

ALTERNATIVE ANODE MATERIALS FOR METHANE OXIDATION IN SOLID OXIDE FUEL CELLS

THÈSE N° 2446 (2001)

PRÉSENTÉE AU DÉPARTEMENT DE CHIMIE

ÉCOLE POLYTECHNIQUE FÉDÉRALE DE LAUSANNE

POUR L'OBTENTION DU GRADE DE DOCTEUR ÈS SCIENCES

PAR

Joseph SFEIR

Ingénieur chimiste diplômé EPF

de nationalité suisse et originaire de Reiden et Wikon (LU)

acceptée sur proposition du jury:

Prof. M. Grätzel, directeur de thèse

Dr H. Middleton, rapporteur

Dr M. Mogensen, rapporteur

Prof. A. Renken, rapporteur

Lausanne, EPFL
2002

*Fange nie an aufzuhören
Höre nie auf anzufangen.*

Table of content

Summary / Résumé	1
Chapter 1 Introduction	
General introduction.....	6
Operating principle and the problematic of solid oxide fuel cells.....	6
Conditions for carbon free run in SOFC – a thermodynamic approach.....	9
Alternative materials for SOFC anodes.....	12
Aim of the thesis.....	14
References.....	15
Appendix.....	19
Chapter 2 Experimental set-up	
Introduction.....	21
Slurry preparation and cell fabrication.....	21
Electrochemical testing	
<i>a. Non-sealed configuration</i>	21
<i>b. Sealed configuration</i>	22
<i>c. Symmetrical configuration</i>	25
References.....	25
Chapter 3 Synthesis, structure, characterization and electrical properties of LaCrO₃-based powders	
Abstract.....	27
Introduction / theory.....	27
<i>Structural symmetry</i>	28
<i>Conductivity</i>	28
<i>Preparation</i>	29
<i>The aim of the present chapter</i>	30
Experimental	
<i>Powder preparation</i>	30
<i>Conductivity measurements</i>	30
<i>Adhesion and morphologies of electrodes</i>	30
Results	
<i>Powder XRD analysis</i>	30
<i>Powder characterization</i>	33
<i>Conductivity</i>	34
<i>Adhesion and morphologies of electrodes</i>	37
Conclusion.....	38
References.....	39
Appendix	
Chapter 4 Evidence of surface reaction with highly substituted LaCrO₃-based anodes	
Abstract.....	56
Introduction.....	56
Experimental	
<i>Powder preparation</i>	56
<i>Cell fabrication</i>	56
<i>Data acquisition</i>	57
Results.....	57
Conclusion.....	64
References.....	64
Chapter 5 Stability of Ca and Sr substituted LaCrO₃ during current treatment	
Abstract.....	66

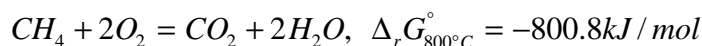
Introduction.....	66
Experimental.....	66
Results.....	67
Discussion.....	69
Conclusion.....	72
References.....	73
Chapter 6 LaCrO₃-based catalysts for oxidation of CH₄ directly on SOFC anodes	
Abstract.....	75
Introduction	
<i>Literature survey on LaCrO₃-based catalysts</i>	75
<i>Background of the present work</i>	75
Methods	
<i>Powder preparation</i>	76
<i>Catalytic tests (steady-state mode)</i>	76
<i>Temperature programmed oxidation and reduction (transient mode)</i>	77
<i>XPS and TEM analysis</i>	77
Results	
<i>Powder characteristics and TPR</i>	78
<i>Effect of O₂</i>	79
<i>Effect of CO₂</i>	83
<i>Effect of H₂O</i>	83
<i>Methane coupling</i>	86
<i>TPO</i>	86
<i>XPS analysis</i>	88
<i>TEM analysis</i>	90
Discussion.....	94
Conclusions.....	102
References.....	103
Appendix.....	105
Chapter 7 LaCrO₃-based anodes: stability considerations	
Abstract.....	110
Introduction.....	110
Estimating thermodynamic properties.....	110
Air solubility limit estimations for Ca and Sr extrapolated from experimental data.....	111
Stability of the Ca, Sr and Ni substituted LaCrO ₃ in oxygen and in reducing atmospheres as well as in corrosive gases (H ₂ , H ₂ O, CO and CO ₂)	
<i>Stability in high oxygen partial pressures (Ca, Sr)</i>	112
<i>Stability in low oxygen partial pressures (Ca, Sr)</i>	113
<i>Volatility diagrams: effect of the gas composition (Ca, Sr)</i>	113
<i>Stability in low oxygen partial pressures (Mg, Mn, Fe, Co, Ni)</i>	117
<i>Kinetically limited decomposition?</i>	118
<i>Interfacial reaction with YSZ</i>	119
Conclusion.....	120
References.....	120
Appendix.....	123
Chapter 8 Preparation of stable LaCrO₃-based anodes and their electrochemical characterization in humidified CH₄ and CO/CO₂	
Abstract.....	131
Introduction.....	131
Experimental	
<i>Powder preparation</i>	131
<i>Slurry preparation and cell fabrication</i>	133
<i>Electrochemical testing and relaxation experiments</i>	133
Results and discussion	

<i>Effect of the sintering temperature</i>	133
<i>Effect of polarization on the cell performance</i>	138
<i>Effect of H₂, CH₄, H₂O, CO/CO₂ on LC polarization</i>	140
<i>Effect of the substituent on the performance of LC anodes</i>	144
<i>Effect of the composite layer composition on the performance of LC anodes</i>	148
Discussion – nature of the electrode reaction.....	150
Conclusion.....	155
References.....	155
Appendix.....	157
Chapter 9 Synthesis, structure, characterization and electrical properties of CeO₂-based powders	
Abstract.....	161
Introduction / theory	
<i>Structural symmetry</i>	161
<i>Conductivity</i>	161
<i>Preparation</i>	163
<i>The aim of the present chapter</i>	163
Experimental	
<i>Powder preparation</i>	163
<i>Conductivity measurements</i>	164
<i>Adhesion, morphologies and chemical compatibility of electrodes on 8YSZ</i>	164
Results	
<i>Powder and pellets preparation and XRD analysis</i>	164
<i>Conductivity</i>	167
<i>Adhesion and electrode morphologies</i>	169
<i>Chemical compatibility with YSZ</i>	172
Conclusions.....	173
References.....	175
Chapter 10 CeO₂-based catalysts for oxidation of CH₄ directly on SOFC anodes	
Abstract.....	178
Introduction.....	178
Methods	
<i>Powder preparation</i>	179
<i>Catalysts tests</i>	179
<i>Temperature programmed oxidation and reduction</i>	179
<i>XPS and TEM analysis</i>	180
Results	
<i>Powder characteristics and TPR</i>	180
<i>Effect of O₂</i>	181
<i>Effect of CO₂</i>	184
<i>Effect of H₂O</i>	185
<i>Methane coupling</i>	186
<i>TPO</i>	186
<i>XPS analysis</i>	187
<i>TEM analysis</i>	188
Discussion.....	190
Conclusions.....	193
References.....	193
Chapter 11 CeO₂-based anodes and their electrochemical characterization in humidified H₂ and CH₄	
Abstract.....	196
Introduction.....	196
Experimental	
<i>Powder and cell preparation</i>	197

<i>Electrochemical testing</i>	197
Results	
<i>Effect of the electrode thickness and morphology</i>	199
<i>Effect of the catalyst on the performance: case of Ni and Cu</i>	204
<i>Effect of the polarization on the performance of the CeNbO anode</i>	204
<i>Effect of H₂, H₂O, CH₂ and P_{O₂} on CeNbO anodes</i>	210
Discussion – Nature of the CeNbO electrode reaction.....	218
<i>Literature survey on ceria-based anodes</i>	227
Conclusion.....	228
References.....	229
General conclusions	232
Acknowledgements	236
List of publications	238
Curriculum Vitae	239

Summary

Fuel Cells are electrochemical devices that are able to directly convert chemical energy to electrical energy, without any Carnot limitation. Hence, their energy efficiencies are relatively high. Among the various types of fuel cells, solid oxide fuel cells (SOFC) are operated at high temperatures and in principle can run on various fuels such as natural gas and hydrogen. As natural gas is sought to become one of the main fuels of the next decades, its direct feed to a SOFC is desirable as the reaction free energy is high



At present, conventional SOFC are operated with pure hydrogen or partially to fully reformed natural gas implying an efficiency penalty. SOFC anodes are generally made of electrocatalytically active Ni-YSZ cermet. Pure CH_4 is not fed directly to the anode, because of problems associated with the anode deactivation and coking as CH_4 leads to the detachment of Ni particles from the YSZ support and their encapsulation by carbon. To overcome this problem, partially oxidized or reformed CH_4 is used.

For SOFCs running on direct CH_4 feed, alternative anode materials to Ni-YSZ, or new anode formulations are necessary. However, in this case, several parameters influence the anode performance and stability. The anodes should withstand reduction at a low P_{O_2} of around 10^{-24} atm, be compatible with the SOFC electrolyte, possess an acceptable conductivity and thermal expansion coefficient, and appropriate catalytic and electrocatalytic properties along with low coking activity.

$LaCrO_3$ and CeO_2 -based materials as well as some metal catalysts were studied here for their potential application as anodes in direct oxidation of CH_4 . This choice of materials was made as lanthanum chromite and ceria-based materials are mixed conductors known to resist quite well to the very reducing conditions in SOFC as they are commonly used for interconnect and electrolyte materials respectively. Moreover, these compounds possess some catalytic activity for CH_4 activation and combustion. $LaCrO_3$ and CeO_2 -based materials show rather low electrical conductivity (on the order of 1 S/cm in reducing conditions), necessitating the application of an extra material for proper current collection. Nevertheless, these oxides possess many of the stringent characteristics cited above.

For SOFC anode purposes, $LaCrO_3$ -based compounds, substituted with Ca, Sr, Mg, Mn, Fe, Co and Ni, were synthesized by a modified citrate route from nitrate precursors. An optimal calcination temperature of $1100^\circ C$ was found to be necessary to obtain XRD-pure yet sinteractive compounds. Conductivity measurements in air and in reducing atmospheres of 10^{-21} atm showed that the La A-site substituents (Ca and Sr) influenced the conductivity more than the Cr B-site substituents (Mg, Mn, Fe, Co and Ni). In humidified H_2 , the total conductivity was maximally of 6.5 S/cm. Surface reaction with YSZ electrolyte was evidenced by SEM, XPS and SIMS, in reducing conditions, especially under current load, when these powders were applied as anodes. A current induced demixing effect was noted for heavily substituted $LaCrO_3$.

Ceria-based compounds, doped with Y, Nb, Pr and Gd, were synthesized through 3 different techniques: the solid-state method, coprecipitation and the $NbCl_5$ route. The coprecipitation route was found to be most appropriate for Y, Pr and Gd, whereas for Nb a modified precipitation and the $NbCl_5$ technique were the most efficient. Co-doping of Nb and Gd or Pr was studied in order to increase the electronic as well as the ionic conductivity in CeO_2 . Among all dopants, Nb was found to promote most the adhesion to YSZ electrolyte sheets. Adding Nb to Gd-doped ceria improved the electrode adhesion on YSZ sheets, but deteriorated its conductivity in oxidizing conditions. No interfacial reaction with YSZ was observed by HRTEM when Nb-doped ceria anodes were sintered on YSZ at $1200^\circ C/4h$.

Catalytic measurements were undertaken with these materials in CH_4 rich atmospheres. Different reaction mixtures were chosen to simulate the various SOFC operating conditions: partial oxidation, CO_2 reforming by recycling and H_2O reforming. Among the different elements, Sr and Ni were found to be the most active substituents for $LaCrO_3$, as they promote all three types of reactions. The combination of both elements is favorable not only for catalytic use, but also for electrode application as they tend to increase the electronic conductivity of the material. Temperature programmed oxidation (TPO) and TEM made on the catalysts after runs in CH_4 , showed a very low carbon coverage over these oxides, except in the case of Fe

substitution, over which carbon deposition was promoted. XPS analysis showed also that all B-site substituted compounds did not segregate after the catalytic runs whereas Ca and Sr (A-site substituents) tended to segregate in H₂ and H₂O rich atmospheres. Thermodynamic calculations, made using correlations developed in literature, show that Ca and Sr are expected to segregate in H₂ and H₂O rich atmospheres as they tend to form volatile hydroxyl species. Also, the thermodynamic stability of the LaCrO₃ was observed to depend much on the substitution.

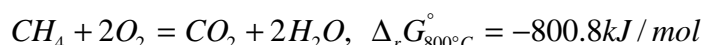
For CeO₂-based oxides, the activity for steam reforming increased from Nb<Gd<Pr, but in all cases the activity towards CH₄ was poor. All three solid solutions did not deposit carbon even under the most reducing conditions as observed by TPO and TEM. From temperature programmed reduction (TPR), Pr-doped ceria showed a higher degree of reduction leading to a higher vacancy concentration. Metallic loading of these catalysts was very sensitive to the sintering and reducing temperature, but in all cases lead ultimately to carbon deposition. Sintering at higher temperatures gave rise to a higher interaction with the CeO₂-based support, as the induction time for carbon deposition was increased. Cu-based alloys loading showed a high resistance to carbon deposition when compared to Ni. By adding Cu to Ni, the overall activity towards CH₄ was reduced and concomitantly the ability to form carbon was reduced.

Electrochemical measurements (I/V curves, impedance spectroscopy) were made on Ca, Sr, Mg, Fe, Co, and Ni substituted LaCrO₃ anodes deposited on 8YSZ sheets. The effects of the sintering temperature, the polarization, the gas and the anode composition, as well as the presence of an adhesion layer made of LaCrO₃-based powder and 8YSZ were taken into account. Ni and Sr substituents were observed to improve the electrocatalytic activity in H₂ as well as in CH₄. The electrocatalytic trend followed almost the catalytic trend in CH₄, LaCrO₃ ≈ LaCr_{0.9}Co_{0.1}O₃ < LaCr_{0.9}Ni_{0.1}O₃ < La_{0.85}Sr_{0.15}CrO₃ < La_{0.85}Sr_{0.15}Cr_{0.9}Ni_{0.1}O₃, and was influenced by the anodes conductivity. The application of an adhesion layer made of the anode material and YSZ fine powders improved the stability of the system. The best cell gave at 877°C, a power output of 450 mW/cm² and 300 mW/cm², with a short circuit current of 1950 mA/cm² and 900 mA/cm², in humidified (3% H₂O) H₂ and CH₄ respectively. CO oxidation rate was observed to be slower than CH₄, and CH₄ slower than H₂. As for the catalytic study, CO₂ had an inhibiting effect on the performance of LaCrO₃, possibly due to a blocking effect of surface carbonates. H₂O had no measurable effect on the H₂ reaction, whereas its effect was observable at high current densities for CH₄.

For ceria, the electrocatalytic properties of Nb and Gd-doped ceria anodes deposited on 8YSZ and 20CGdO electrolytes were analyzed. The effects of the electrode thickness and morphology, the addition of a pore former and Ni or Cu metal catalysts, the polarization as well as the gas composition (H₂, H₂O, CH₄ and CO₂) were taken into account. The low activity of Nb and Gd-doped ceria for the oxidation of CH₄ confirmed the catalytic measurements. No carbon deposition was observed. Similarly to LaCrO₃-based anodes, ceria anodes performance in CH₄ depended much on H₂ oxidation at least at open circuit potential (OCV). Oxygen ion diffusion in the ceria anode is thought to participate in the overall polarization losses, indicating that the anode reaction spreads far away from the triple phase boundary. The best performance reached was of 430 mW/cm² between 850-900°C in H₂. The performance in CH₄ depended much on the presence of a catalyst. At 900°C, with a Pt mesh current collector, the performance was of 350 mW/cm² with a short circuit current of 1050 mA/cm², whereas with an Au mesh it was only of 100 mW/cm² and 420 mA/cm². Cu addition increased the activity of the anode when using an Au mesh.

Résumé

Les piles à combustibles permettent de convertir l'énergie chimique directement en électricité, sans la limitation de Carnot. Leurs rendements théoriques sont relativement élevés. Parmi les différents types de piles à combustibles existants, ceux à électrolyte solide (PCES ou SOFC de l'anglais solid oxide fuel cells) fonctionnent à hautes températures et peuvent en principe accepter tout type de combustibles, tels le méthane et l'hydrogène. Avec la baisse de la réserve mondiale de pétrole, le gaz naturel est appelé à prendre une place plus importante comme source d'énergie fossile. Son utilisation direct dans un système SOFC est en plus avantageuse vue la grande énergie dégagée par la réaction du méthane, principal composant du gaz naturel



A l'heure actuelle, les SOFC opèrent à l'hydrogène ou à des hydrocarbures, principalement le méthane, partiellement ou complètement converties en gaz de synthèse. Les anodes de base des SOFC sont des composites de Ni-YSZ. L'alimentation en méthane pur sur ce genre de structure conduit à la formation de carbone sur les sites de Ni, à la destruction mécanique de l'anode et par conséquent à la perte de fonction de la pile. Pour surmonter ces problèmes, le méthane est donc traité par une oxydation partielle ou par une réaction de reformage qui conduit à la production d'hydrogène et de monoxyde de carbone (gaz de synthèse).

Pour que les SOFC puissent oxyder les hydrocarbures directement, des anodes alternatives ou de nouvelles formulations sont nécessaires. Pour ce faire, les nouvelles anodes doivent répondre à des critères drastiques : elles doivent être stables dans les milieux réducteurs, être compatibles chimiquement avec l'électrolyte, être de bons conducteurs ionique et électronique et posséder de très bonnes activités catalytiques et électrocatalytiques. La déposition de carbone sur l'anode doit être inhibée pour de longues périodes de fonctionnement avec des hydrocarbures.

Dans cette étude, les oxydes chromite de lanthane et cérium ainsi que des catalyseurs métalliques furent étudiés dans le but de leur application en tant qu'anodes pour l'oxydation du méthane. Ce choix repose sur la stabilité de ces oxydes à très hautes températures et très basses pressions d'oxygène. Ces oxydes sont déjà utilisés dans les SOFC en tant qu'interconnecte et électrolyte respectivement. Bien que leurs conductivités soient relativement faibles, nécessitant l'application de collecteurs de courant inertes, ces oxydes possèdent plusieurs des critères cités auparavant.

Pour une application SOFC, des oxydes chromite de lanthane, substitués avec du Ca, Sr, Mg, Mn, Fe, Co or Ni furent synthétisés en passant par la méthode des 'citrate'. Une température optimale de 1100°C fut nécessaire pour obtenir des oxydes purs observés par analyse aux rayons X. Des mesures de conductivité sous air et sous milieu réducteur montrent que la substitution en site A (La) est plus favorable pour la conductivité que celle sur le site B (Cr). Aussi, une réaction de surface entre l'électrolyte (YSZ) et les anodes à base de chromite de lanthane a été observée pour les cas de fortes substitutions en site A. Une décomposition du matériau sous l'effet du courant a été mise en évidence dans ces cas-ci.

Des oxydes de cérium, dopés à l'Y, au Nb, au Pr et au Gd furent également synthétisés. Trois méthodes distinctes furent appliquées : la coprécipitation, la réaction solide-solide et une méthode basée sur le NbCl₅. Pour les solutions solides contenant l'Y, le Pr et le Gd, la coprécipitation est plus adéquate, tandis que pour le Nb la précipitation et la méthode basée sur le précurseur NbCl₅ aboutissent aux meilleurs résultats. Des dopages mixtes entre le Nb et le Gd ou le Pr furent entrepris dans le but de modifier la conductivité du matériau. Parmi tous ces dopants, le Nb favorise le mieux l'adhésion de la cérium sur la zircone. L'adjonction de Nb dans les solution solides avec le Gd aide l'adhésion. Dans le cas des solutions solides avec le Pr, le Nb ne semble pas avoir d'influence. Globalement, le Nb augmente la conductivité électronique mais diminue la conductivité ionique. Des analyses *HRTEM* montrent clairement l'absence de réactions avec la zircone si la température de frittage des anodes à base de cérium est plus petite que ou au moins égale à 1200°C.

Des mesures catalytiques furent entreprises avec ces matériaux dans des atmosphères riches en méthane. Des conditions proches de celles régnantes dans les SOFC furent considérées.

Parmi les différents substituants étudiés dans le cas des oxydes de chromite de lanthane, le Sr et le Ni favorisent l'activité avec le méthane. Une oxydation à température programmée et des

analyses *TEM* effectuées sur ces catalyseurs après fonctionnement sous CH_4 montrent un très faible dépôt de carbone pour tous les substituants à l'exception du Fe, qui montrent une formation épitaxiale de carbone à la surface du catalyseur. Des analyses *XPS* montrent que tous les substituants en site *B* ne s'altèrent pas après les réactions catalytiques, tandis que le Ca et le Sr avaient tendance à se déposer en surface du catalyseur, surtout après traitement sous des atmosphères contenant de l' H_2 et de l' H_2O . Des calculs thermodynamiques confirment ces résultats pour le Ca et le Sr et indiquent que la décomposition des autres chromites de lanthane est inhibée cinétiquement.

Pour les oxydes de cérium, l'activité catalytique augmente du Nb au Gd au Pr, bien qu'elle reste faible. La cérine dépose moins de carbone que les chromites de lanthane. L'adjonction de catalyseurs métallique améliore les performances mais conduit à des dépôts de carbone. Les alliages à base de Cu montrent une plus grande résistance à la déposition de carbone.

Des mesures électrochimiques furent entreprises avec les chromites de lanthane substitués avec du Ca, Sr, Mg, Fe, Co et du Ni déposées sur des électrolytes 8YSZ. Les effets de la température de frittage, de la polarisation, des gaz et de la composition de l'anode ainsi que la présence d'une couche d'adhésion composée de poudre de chromites de lanthane et d'une poudre fine de 8YSZ furent traités. Les substituents Ni et Sr améliorent la performance sous hydrogène et le méthane. Les performances électrocatalytiques avec le CH_4 suivent l'activité catalytique selon l'ordre $\text{LaCrO}_3 \approx \text{LaCr}_{0,9}\text{Co}_{0,1}\text{O}_3 < \text{LaCr}_{0,9}\text{Ni}_{0,1}\text{O}_3 < \text{La}_{0,85}\text{Sr}_{0,15}\text{CrO}_3 < \text{La}_{0,85}\text{Sr}_{0,15}\text{Cr}_{0,9}\text{Ni}_{0,1}\text{O}_3$, et sont influencées par la conductivité électrique. L'insertion d'une couche d'adhésion entre l'électrolyte et l'anode améliore la performance du système. La meilleure cellule a fourni une densité de puissance de 450 mW/cm^2 sous H_2 et de 300 mW/cm^2 sous CH_4 . L'oxydation du CO est plus lente que celle du CH_4 , et celle du CH_4 plus lente que celle de H_2 . Le CO_2 semble inhiber la performance des chromites de lanthane.

Dans le cas des cérines, les propriétés électrocatalytiques de la cérine dopée au Nb et au Gd, déposées sur des électrolytes 8YSZ et 20CGdO ont été étudiées. Les effets de l'épaisseur de l'anode et de sa morphologie, la création d'une porosité supplémentaire, l'addition de catalyseurs métalliques (Ni et Cu), l'effet de la polarisation ainsi que la composition des gaz (H_2 , H_2O , CH_4 et CO_2) furent pris en compte. L'activité des cérines sous CH_4 est relativement faible et aucun dépôt de carbone n'a été mis en évidence. La performance des anodes dans le méthane dépend de la pression partielle de H_2 , du moins dans les conditions proches du circuit ouvert. La diffusion des ions d'oxygène dans l'anode semble être un facteur déterminant dans les pertes de polarisation, indiquant que la réaction électrochimique s'étend au-delà de la zone de contact triple entre l'anode, l'électrolyte et les gaz. La densité de puissance maximale sous H_2 était de 430 mW/cm^2 à $850\text{-}900^\circ\text{C}$. La performance sous CH_4 dépend de la nature du catalyseur utilisé. A 900°C , avec un collecteur de courant en Pt, la densité de puissance maximale mesurée était de 350 mW/cm^2 . Avec un collecteur en Au, la densité de puissance n'atteint plus que 100 mW/cm^2 . L'ajout du Cu améliore l'activité globale du système.

Chapter 1 —

Introduction

Introduction

General introduction

This chapter gives an overview of operating solid oxide fuel cells (SOFC) with hydrocarbon fuels. Due to higher thermodynamic efficiency, fuel cells running on hydrocarbon fuels are shown to be more attractive than hydrogen feeding. Conventional SOFC anodes based on Ni are very sensitive to hydrocarbons. It is shown thermodynamically that SOFC cells should be operated with a steam reformed or carbon dioxide reformed or a partially oxidised hydrocarbon fuel in order to prevent carbon formation. A literature review of the state-of-the-art of the present knowledge on available or potential anode materials for their use with a direct feed of hydrocarbons is presented. Besides the usual fuel processing (reforming or partial oxidation) not many materials have been tested in real SOFC conditions even though several alternative materials were recently suggested. Finally, the aim and structure of the thesis is presented.

Operating principle and challenges of solid oxide fuel cells

Fuel cells are electrochemical devices that are able to directly convert chemical energy to electrical energy, without any Carnot limitation. Hence, as the intermediate physical conversion is absent, their energy efficiencies are relatively high. Like any other electrochemical cell (see for example the Daniel battery of Figure 1a), a fuel cell has an electrolyte, a cathode and an anode. Five different types exist, each having its specific electrolyte, operating temperature and fuel (see Table 1)^{1,2}.

Table 1: Summary of the different fuel cell types.

fuel cell type	abbreviation	working temperature [°C]	fuel	electrolyte
alkaline fuel cell	AFC	100	H ₂	KOH aqueous
polymer electrolyte fuel cell	PEFC	80-110	H ₂	Nafion
phosphoric acid fuel cell	PAFC	150-210	H ₂	H ₃ PO ₄
molten carbonate fuel cell	MCFC	550-650	H ₂ , CO	KLiCO ₃
solid oxide fuel cell	SOFC	600-1000	hydrocarbons	e.g. YSZ

Source ^{1,2}

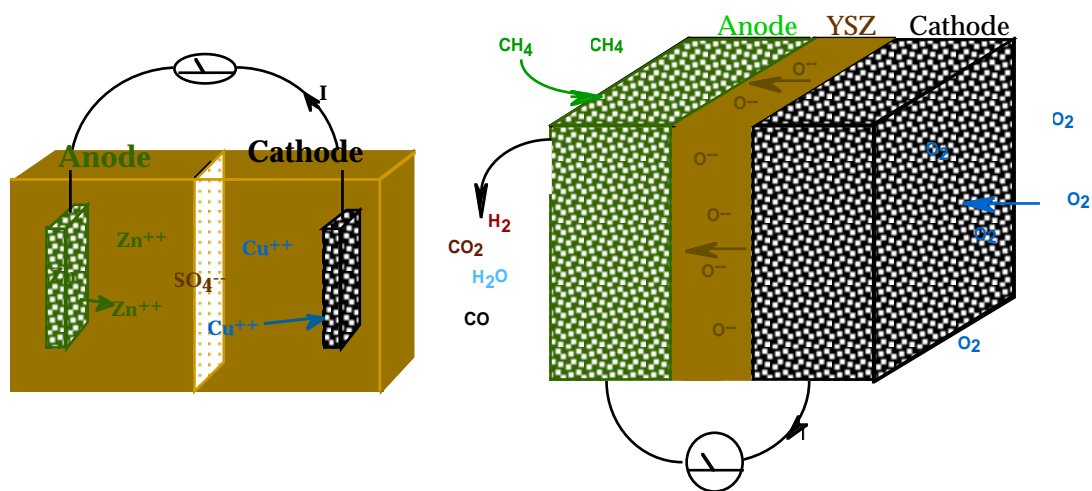


Figure 1: A schematic view of two electrochemical devices. a. Daniel battery, and b. SOF cell.

Among them, Solid Oxide Fuel Cells (SOFC) are operated at high temperatures (600-1000°C) and unlike low temperature fuel cells can run on various fuels such as natural gas (primarily CH₄³), bio-gas, methanol and ethanol, liquified petroleum gas (LPG), naphtha, gasified coal and hydrogen. SOFCs use a solid oxygen ion conducting electrolyte like yttria

stabilised zirconia (YSZ), doped ceria, substituted lanthanum gallate, substituted lanthanum yttriate or aluminate, bismuth oxides, ...⁴. The fuel is oxidised on the anode side and the electrolyte transports the required O²⁻ from the cathode side where oxygen is reduced (see Figure 1b). This oxide transport generates an external electron flow. Due to their high working temperature, SOFCs are able to generate both electricity and high quality heat, which may be used for space heating, steam generation or combined power cycle applications.

The thermodynamic efficiency of a fuel cell depends on the nature of the fuel. It is defined as $\chi = \frac{\Delta_r G_{\text{combustion}}}{\Delta_r H_{\text{combustion}}} = \frac{\Delta_r H_{\text{combustion}} - T\Delta_r S_{\text{combustion}}}{\Delta_r H_{\text{combustion}}}$, where $\Delta_r G_{\text{combustion}}$, $\Delta_r H_{\text{combustion}}$ and $\Delta_r S_{\text{combustion}}$ are the free enthalpy, the enthalpy and the entropy change of the fuel's combustion reaction. It can be seen that, depending on the entropy change of the reaction, this efficiency can be equal or even exceed unity. At 800°C, MeOH, EtOH, CH₄, CO and H₂ have efficiencies of 1.08, 1.08, 1.00, 0.67 and 0.76 respectively (see Table 2). The higher thermodynamic efficiency for MeOH and EtOH is due to an increase of the entropy upon reaction as the combustion leads to more species. Thus, hydrocarbon fuels are not only more easily available in comparison to H₂ but also possess higher thermodynamic efficiencies. Beside that, natural gas (primarily CH₄) is expected to be a major energy vector of the next decades⁵⁻⁸.

Table 2: Summary of the thermodynamic efficiencies at 800°C.

SOFC efficiency (χ) at 800°C Reaction	reaction type	fuel processing		oxidation in SOFC		
		$\Delta_r G$	$\Delta_r H$	$\Delta_r G$	$\Delta_r H$	χ
CH ₄ +2O ₂ =CO ₂ +2H ₂ O	deep oxidation			-800.8	-801.4	1
CH ₄ +0.5O ₂ =CO+2H ₂	partial oxidation	-233.9	-22	-566.9	-779.4	0.73
CH ₄ +H ₂ O=CO+3H ₂	steam reforming	-45.2	226.4	-755.6	-1027.8	0.74
CH ₄ +CO ₂ =2CO+2H ₂	CO ₂ reforming	-44.5	260.4	-756.3	-1061.8	0.71
CO+0.5O ₂ =CO ₂	oxidation			-189.4	-282.5	0.67
H ₂ +0.5O ₂ =H ₂ O	oxidation			-188.7	-248.4	0.76
CH ₃ OH+1.5O ₂ =CO ₂ +2H ₂ O	deep oxidation			-728.2	-673.6	1.08
CH ₃ CH ₂ OH+3O ₂ =2CO ₂ +3H ₂ O	deep oxidation			-1384	-1280	1.08

The calculations were made using HSC 4.1 thermodynamic equilibria calculation software (Outokumpu Research Oy, Finland). $\Delta_r H$ and $\Delta_r G$ are given in kJ/mol.

In real fuel cells, other factors affect the thermodynamic efficiency leading to a decrease in overall cell efficiency. First, the internal losses encountered at the electrodes (known as overpotential losses $\eta_{\text{electrodes}}$) as well as the ohmic losses due to the current flow (IR) in the conductors lead to a drop of the cell potential (Nernst potential). Globally, these losses contribute to the heating of the cell. Thus the efficiency of the chemical conversion to electricity is lowered as the working potential is then given by $E_{\text{cell}} = E_{\text{Nernst}} - (IR + |\eta_{\text{electrodes}}|)$. Thus, for efficient SOFC systems, low ohmic losses in the electrolyte and in the electrodes as well as performing materials are desirable. In state-of-the-art SOFC devices, run on H₂ or partially to fully reformed natural gas, with YSZ as electrolyte and Ni-cermet as anode material, efforts were made to reduce the thickness of the electrolyte and to increase the performance of the anode and the cathode. High current densities were thus achieved with electrolytes of 10 to 40 μm thickness with a Ni-YSZ-cermet anode and a lanthanum strontium manganite perovskite as cathode (see Figure 2 for an example). In literature, Kim et al.⁹ reported 820 mW/cm² power density at 650°C and 1800 mW/cm² at 800°C in H₂ with Ni-YSZ cermet anode-supported SOFC with an electrolyte thickness of 50 to 70 μm .

In fuel cell stack concepts, not all the fuel is utilised over the anode as part of it is usually burned on the rim of the cell, leading to a further heat production. This loss reduces the overall efficiency of the cell furthermore when the total amount of chemical energy is taken into account. This loss is defined as fuel utilisation and given as the ratio of the actual cell current density to the theoretical one if all of the gas would have been converted to electricity $\chi_{\text{fu}} = \frac{i}{i_{\text{max}}}$.

Other losses can add up to the cell's performance due to fuel processing, pumps, ... Globally, as high efficiencies are expected, high benefits for the environment are awaited as CO_x, HC_x and NO_x emissions are cut down. A reduction of about 22% in CO₂ emissions is expected if CH₄ is

used in place of the current fossil fuels for producing electricity, whereas a cut of 12% is foreseeing for automotive power and heating. With methanol, the cuts are even higher for the transportation sector, reaching about 45%. Globally, when using fuel cells instead of combustion engines, the reduction is thus interesting, reaching 61% for CH_4 and CH_3OH ¹¹.

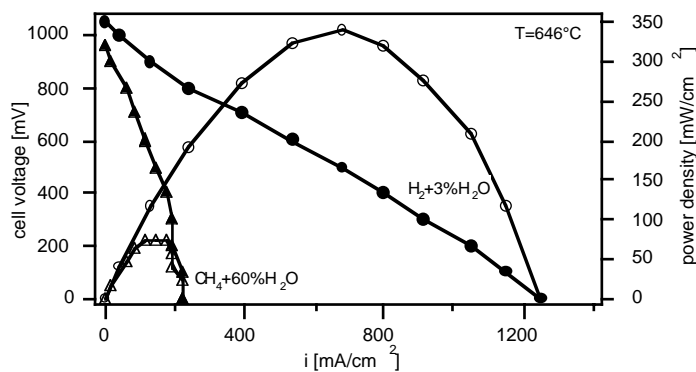


Figure 2: I/V characteristics of a thin film YSZ-Ni-cermet SOFC cell, run in $\text{H}_2+3\%\text{H}_2\text{O}$ and $\text{CH}_4+60\%\text{H}_2\text{O}$ at 646°C (unpublished work). This type of cell has been developed at EPFL¹⁰.

A major problem with conventional Ni-cermet anodes is their high sensitivity towards hydrocarbon feeds and the impurities present in most of them, such as sulphur and chlorine compounds¹². From steam-reforming studies, hydrocarbons have been observed to react heavily with Ni producing large amounts of carbon which lead to poisoning of the metal catalyst (see an example in Figure 3)¹³⁻¹⁷. This occurs through many routes^{13, 15, 18-23}. Pure CH_4 feed on the anode leads for example to the detachment of Ni particles from the YSZ skeleton and their encapsulation by carbon. The formation of carbon filaments made by carbon precipitation at the Ni particles leads to mechanical breakdown of the anode, to deterioration of the electrochemically active Ni-YSZ interface, and also to deactivation of Ni by further encapsulation. For these reasons, hydrocarbons are processed either by steam or CO_2 reforming (equation (1) and (2)) or by partial oxidation (equation (3)) prior to their feed over the anode, but these reactions could be carried out on the anode *in-situ* due to the high catalytic activity of Ni²⁴.

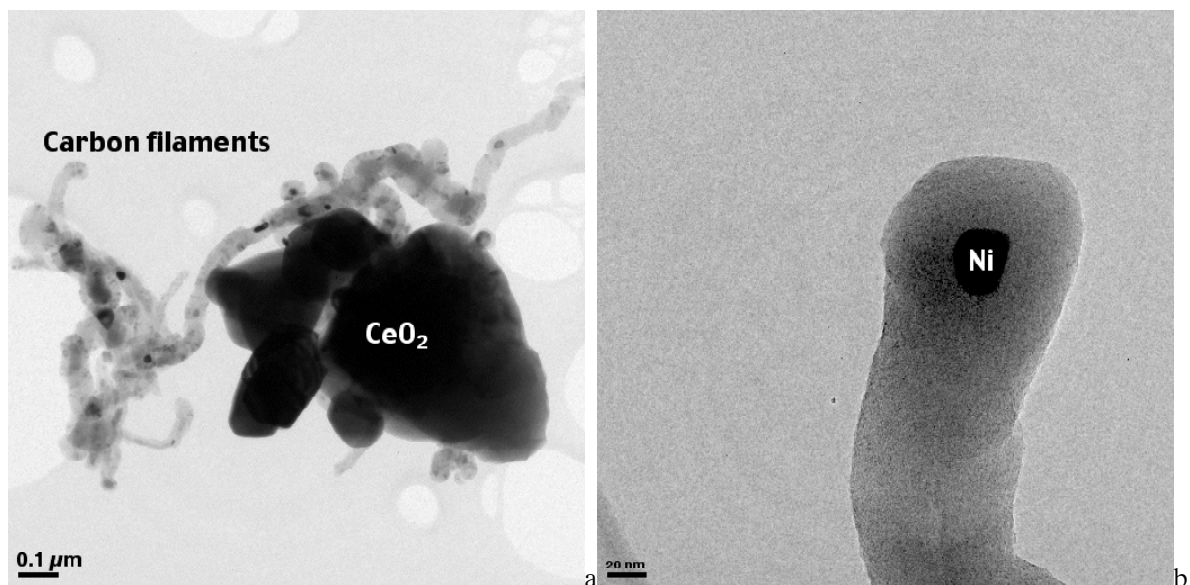
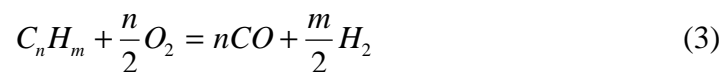
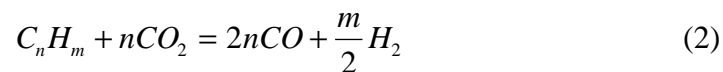
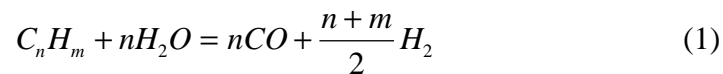


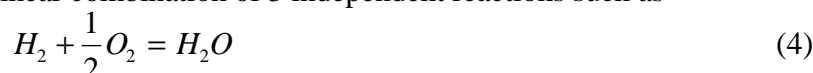
Figure 3: TEM micrographs of CeO_2+Ni catalyst exposed to CH_4 showing C filaments.

The stoichiometries given here do not hold at all temperatures as will be discussed later. Furthermore, by these fuel processings, the thermodynamic efficiencies of the SOFC drop. For the special case of CH_4 , these efficiencies are shown in Table 2. This indicates clearly that direct feed of CH_4 without any prior processing is the most favourable approach. With the present Ni-cermet formulation, such a direct feed is not feasible so that alternative anodes have to be developed for that purpose.

However, in this case, several parameters influence the anode performance and stability. The anode should withstand reduction at a P_{O_2} as low as 10^{-24} atm, be compatible with the YSZ electrolyte, possess acceptable thermal expansion and conductivity and appropriate catalytic and electrocatalytic properties and inhibit carbon deposition.

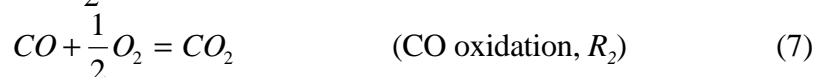
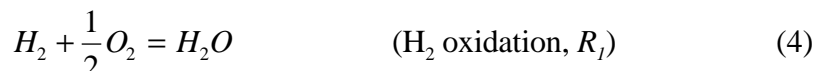
Conditions for carbon free operation in SOFC - a thermodynamic approach

The chemical reactions involving the six different species H_2 , H_2O , CO , CO_2 , CH_4 and O_2 can be described as a linear combination of 3 independent reactions such as

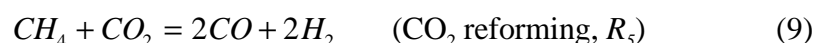
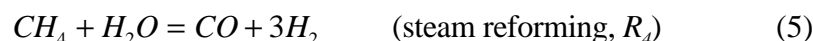


Even though these three reactions are enough to describe the system, many other denominations are used to describe specific reactions. Besides the three above mentioned ones it is often common to consider other reactions. It is possible to divide these reactions in four different categories that are given as follows

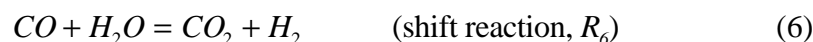
Conversion reactions



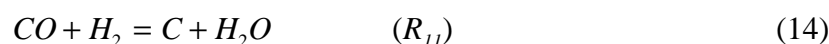
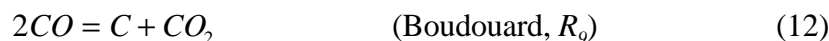
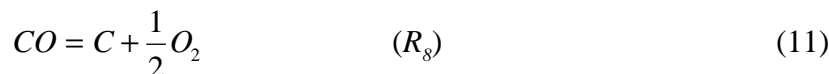
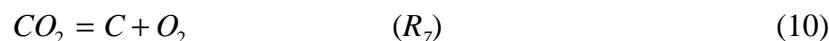
Reforming reactions



Shift reaction



Dissociation reactions



The thermodynamics of these reactions are presented in Figure 4. Among these reactions, CH_4 oxidation (R_3) is the most exothermic (Figure 4b). R_4 and R_5 are endothermic ($\Delta_r H > 0$, not shown here), with the last slightly more favourable at higher temperature (Figure 4c). The reforming reactions are quite unfavourable at $T < 650^\circ\text{C}$ ($P=1$ atm). The shift reaction (R_6) produces CO at $T > 800^\circ\text{C}$, and CO_2 below this temperature (Figure 4c). The Boudouard reaction

(R_9) is favoured at $T < 675^\circ\text{C}$ while CH_4 pyrolysis (R_{10}) takes place at $T > 600^\circ\text{C}$. Thus carbon deposition has two regimes, one at low temperature and the other at high temperature.

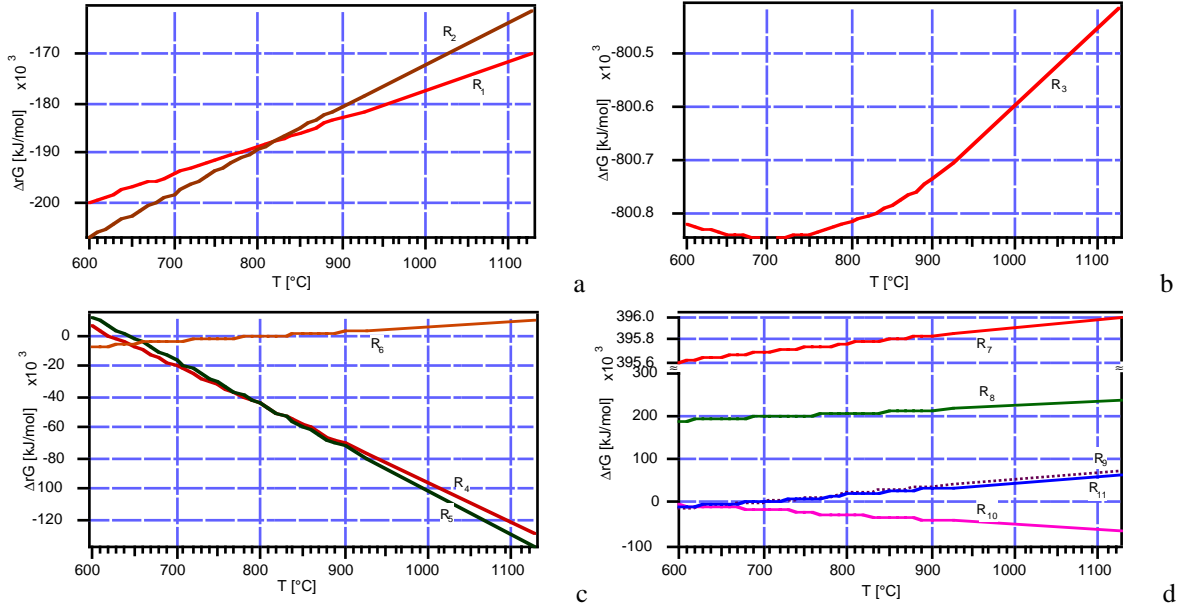
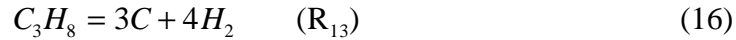
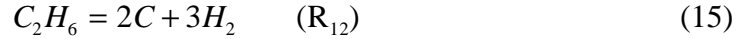


Figure 4: Free enthalpy change with temperature for the different reactions. The plots were made using the thermodynamic data given by Bossel²⁵. $P_{\text{total}} = 1 \text{ atm}$.

Carbon deposition is more likely with higher hydrocarbons such as the reactions



which are more favoured than for CH_4 , which is the most inert compound among hydrocarbons (see Figure 5).

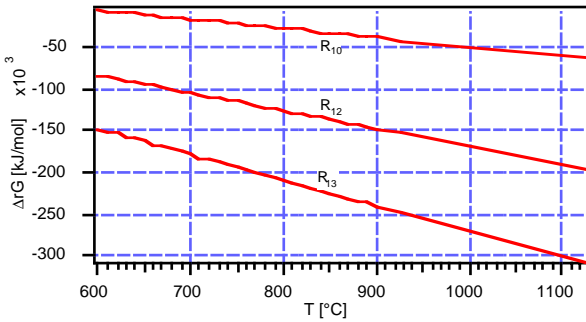


Figure 5: Free enthalpy change with temperature for the R_{10} , R_{12} , R_{13} . The plots were made using the thermodynamic data given by Bossel²⁵. $P_{\text{total}} = 1 \text{ atm}$.

For a common reaction in SOFC, steam reforming of CH_4 (R_4), either externally or internally to the stack, thermodynamic calculations predict carbon deposition at all temperatures if not ‘enough’ steam is added to prevent its formation either by the Boudouard (R_9) or the CH_4 pyrolysis (R_{10}) reactions. Figure 6a shows this aspect at 850°C . Carbon is prevented only when the stoichiometric amount of H_2O is added to CH_4 . As expected, H_2 is the main gas product of CH_4 decomposition. At high enough water content, CO and CO_2 start to form. The evolution of C and in parallel that of oxygen partial pressure with temperature and with steam content is presented in Figure 6b and c. The higher the temperature the less steam is needed for a carbon free run ($\text{H}_2\text{O}/\text{H}_2 \rightarrow 1$). As mentioned before, carbon deposition is harmful for Ni-cermet based anodes as it leads to their porosity blocking and mechanical failure. Also, as C is deposited, the oxygen partial pressure in equilibrium with the solid and gas phases becomes very low leading to high open circuit voltage (OCV) values.

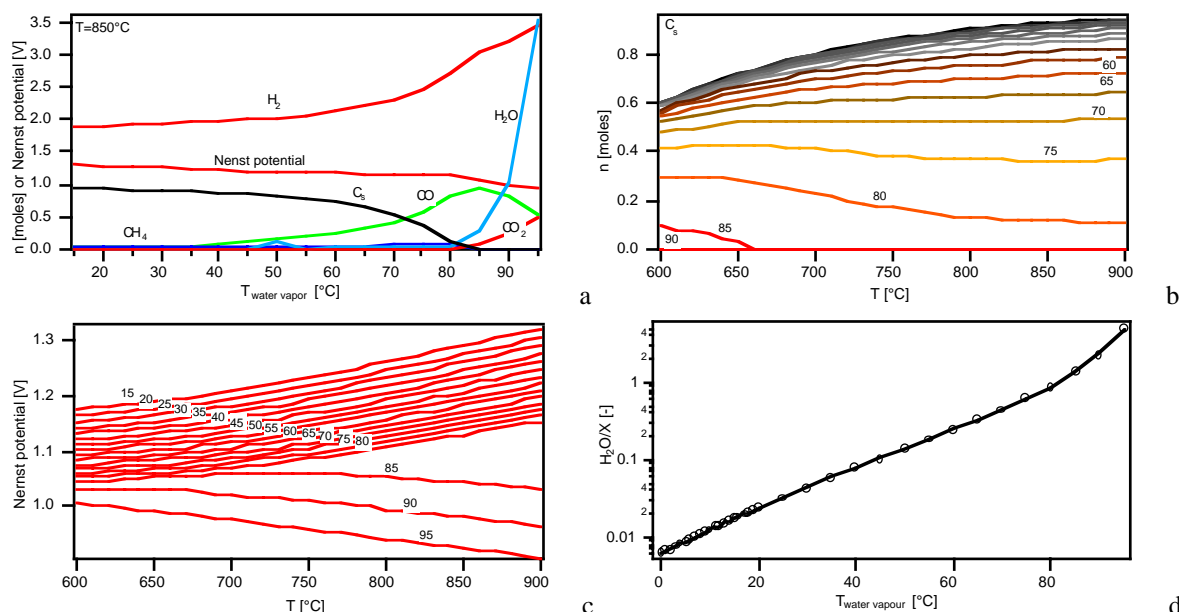


Figure 6: Effect of water content on the carbon deposition from CH_4 feeds. a. the evolution of the gas and solid phases with the H_2O content at 850°C ; b. the evolution of C and c. the oxygen partial pressure with temperature and water content (inset numbers are the water vapour temperature of the bubbler used to saturate CH_4 with water); d. the calculated evolution of the steam content in the gas phase with the water vapour temperature of the bubbler. The calculations (a., b., and c.) were made using a thermodynamic equilibria programme developed by Van herle (Swiss Institute of Technology, Lausanne). $P_{\text{total}} = 1 \text{ atm}$.

Thus optimal H_2O , CO_2 or O_2 to fuel ratios are necessary to work thermodynamically under carbon free conditions. This is shown in Figure 7 for four hydrocarbons. In all cases, it is observed that only at high temperatures ($T \geq 800^\circ\text{C}$) the stoichiometric amount of H_2O , O_2 or CO_2 is required, whereas at lower temperatures much higher values are needed. For steam reforming, almost twice the stoichiometric amount of H_2O is needed at intermediate temperatures ($500\text{--}600^\circ\text{C}$). These ratios are important at OCV where no current is drawn from the cell^{26, 27}. Upon polarisation, H_2 , H_2O and CO_2 are formed locally by the electrochemical reaction. If CH_4 , for example, is diluted or if its concentration corresponds to the stoichiometric amount of the reaction, then no carbon deposition is thermodynamically expected even at lower steam to methane ratios above a certain threshold current²⁷⁻³⁰. This current depends much on the CH_4 partial pressure, flow rate and dilution.

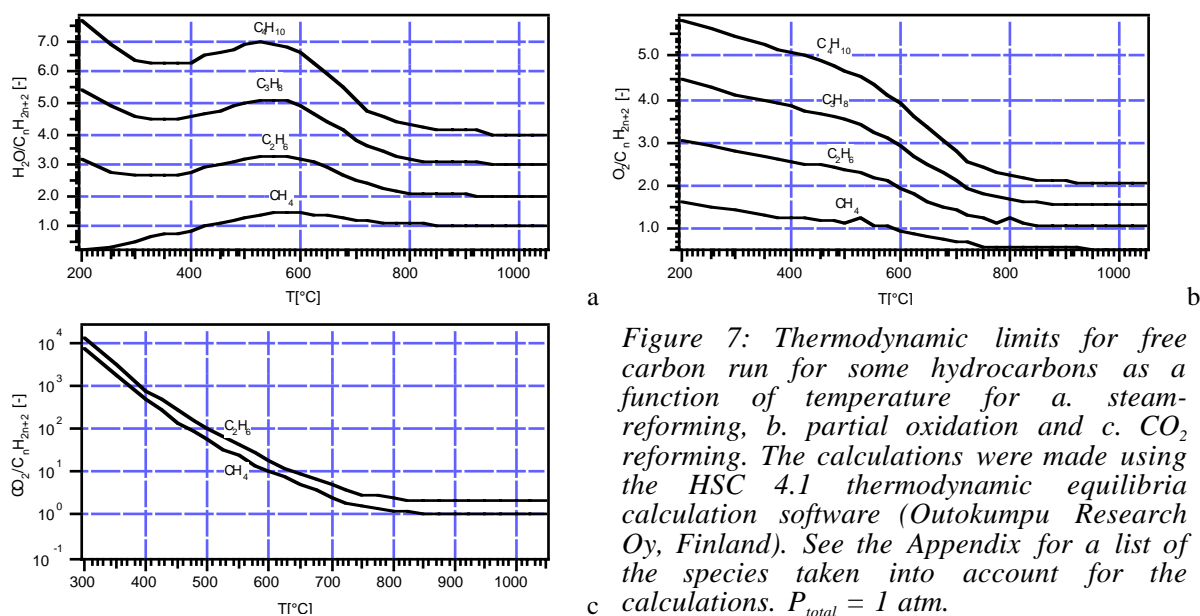


Figure 7: Thermodynamic limits for free carbon run for some hydrocarbons as a function of temperature for a. steam-reforming, b. partial oxidation and c. CO_2 reforming. The calculations were made using the HSC 4.1 thermodynamic equilibria calculation software (Outokumpu Research Oy, Finland). See the Appendix for a list of the species taken into account for the calculations. $P_{\text{total}} = 1 \text{ atm}$.

From a kinetics point of view, many data exist on the steam or carbon dioxide reforming reaction of CH_4 over supported Ni, Fe or noble metals such as Pd, Pt and Rh catalysts for the production of syngas^{15,31,32}. The relative metal activity for steam reforming is $\text{Ru} \approx \text{Rh} > \text{Ni} > \text{Ir} > \text{Pd} \approx \text{Pt} \gg \text{Co} \approx \text{Fe}$, in a trend almost similar to that of CO_2 reforming³³. H_2O and CH_4 show a competitive adsorption mechanism³⁴. Some data are also available for the steam reforming reaction under SOFC conditions^{24,28,29,35-37}. Yentekakis et al.²⁴ and Bebelis et al.³⁵ showed the presence of a non-faradic electrochemical modification of catalytic activity, or NEMCA effect³⁸, inhibiting carbon formation over a Ni-YSZ cermet anode working with $\text{CH}_4 + \text{H}_2\text{O}$. The experimentally measured carbon free limits over the Ni-YSZ cermet anodes match well the thermodynamic forecasts.

Also, fuels like MeOH or EtOH are expected to need less stringent conditions for free carbon runs than their hydrocarbon counterparts (CH_4 and C_2H_6). With MeOH, thermodynamics predict a carbon free run at temperatures above circa 800°C (see Figure 8 and 6d). Such bio-fuels could be easily implemented with the present state-of-the-art Ni-YSZ cermet anodes.

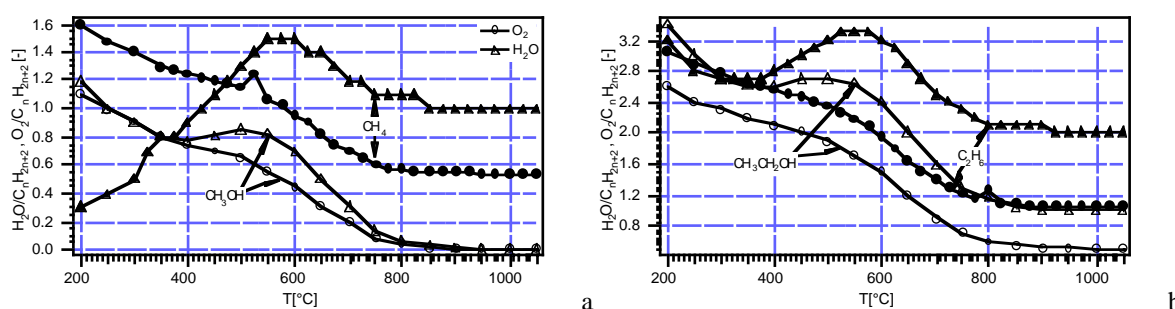


Figure 8: Thermodynamic limits for free carbon runs for a. CH_3OH and b. $\text{CH}_3\text{CH}_2\text{OH}$ compared to CH_4 and C_2H_6 . The calculations were made using the HSC thermodynamic equilibria calculation software (Outokumpu Research Oy, Finland). \blacktriangle H_2O reforming, \bullet O_2 partial oxidation. Open symbols alcohol, closed symbols hydrocarbon. $P_{\text{total}} = 1 \text{ atm}$.

In steam reforming, the modification of Ni-based catalysts by means of additives such as alkalis or Cu, or by higher interactions with the support have been advanced for controlling the carbon formation³⁹⁻⁴⁷. Such approaches could also be implemented for Ni-based cermet anodes. In turn, other types of catalysts showing a milder affinity to hydrocarbons and carbon could be used.

Alternative materials for SOFC anodes

In conventional steam reforming or partial oxidation of CH_4 many catalysts have been advanced in literature. Besides the oxide supported (MgO , SiO_2 , Al_2O_3 , CeO_2 , ...) Fe, Co, Ni, Cu metals and noble metals (Ru, Rh, Pd, Ir, Pt) or metal oxides with or without additives like CeO_2 , oxide-based formulations were also studied⁴⁸⁻⁵¹. NiAl_2O_4 , rare-earth ruthenium pyrochlores ($\text{Ln}_2\text{Ru}_2\text{O}_7$, Ln = lanthanides), Bi_2RuO_7 , $\text{Eu}_2\text{Ir}_2\text{O}_7$, $\text{La}_2\text{MgPtO}_6$, $\text{RhVO}_4/\text{SiO}_2$, are examples^{33,49,52,53}. Most of these oxides did not show carbon deposition in stoichiometric runs and many decomposed to finely dispersed metal particles over the oxide support. Other perovskites, pyrochlores, brownmillerites, bronze-like, ... oxides were advanced as catalysts for CH_4 activation, many of them being quite stable in the reaction conditions. Such examples are LnMO_3 with $M = \text{Al, Ti, V, Cr, Mn, Fe, Co, Ni, Cu, Y}$ and Nb, substituted or not on the A or B sites, TiO_2 , ZnO , Nb_2O_5 , Bi_2O_3 , CeO_2 , lanthanide-based oxides, $(\text{Sr,Ba})\text{CeO}_3$, $\text{Li}(\text{La,Ni})\text{O}_2$, $\text{Sr}(\text{Co,Fe})\text{O}_{3-\delta}$, $\text{Mn}_2\text{O}_3\text{-Na}_2\text{WO}_4/\text{SiO}_2$ and SrTiO_3 , $\text{La}_{0.66}\text{Sr}_{0.34}\text{Ni}_{0.3}\text{Co}_{0.7}\text{O}_3$ and $\text{La}_{0.4}\text{Sr}_{0.6}\text{Fe}_{0.4}\text{Co}_{0.6}\text{O}_3$, $\text{Ca}_{0.8}\text{Sr}_{0.2}\text{Ti}_{0.8}\text{Ni}_{0.2}\text{O}_3$ mixed oxide, $\text{Ca}_{0.8}\text{Sr}_{0.2}\text{Ti}_{0.8}\text{Co}_{0.2}\text{O}_{3-\delta}$, as well as carbides^{33,54-72}.

Among the lanthanide perovskites, LnMO_3 , of the first row transition metal elements, Mn, Fe, Co and Ni, based compounds were found to exhibit interesting oxidative behaviour under co-feed ($\text{CH}_4 + \text{O}_2$) reaction conditions comparable to highly active $\text{Pt}/\text{Al}_2\text{O}_3$. LnCrO_3 were the least active^{56,73}. By substituting Sr on the La site, an increase in activity was observed and related to a higher lattice oxygen availability^{56,58,60}. The lanthanide part did also influence the

catalytic activity towards CH_4 but less than the accompanying transition metals. For the same transition metal element, the reducibility and thus the lattice oxygen availability tended to decrease in the trend $\text{Gd} > \text{Sm} > \text{Nd} > \text{Pr} > \text{La}$, corresponding to a decrease in catalytic activity.^{60, 74.}

^{75.} Alcock et al.⁶⁸ and Doshi et al.⁵⁶ studied the perovskite $\text{La}_{1-x}\text{Sr}_x\text{B}_{1-y}\text{M}_y\text{O}_{3-\delta}$ ($B = \text{Co}, \text{Cr}, \text{Fe}, \text{Mn}, \text{Y}; M = \text{Nb}, \text{Ti}$), the K_2NiF_4 -type superconducting $\text{A}_{1-x}\text{B}_x\text{CuO}_{4-\delta}$ ($A = \text{La}, \text{Nd}; B = \text{Sr}, \text{Ce}$) along with $\text{La}_{0.9}\text{Sr}_{0.1}\text{O}_{1.45}$, La_2O_3 , LaYO_3 , $\text{La}_{0.8}\text{Sr}_{0.2}\text{YO}_{2.9}$, Y_2O_3 and SrO in 30:4:65 $\text{CH}_4:\text{O}_2:\text{He}$ and 2:98 $\text{CH}_4:\text{air}$ for CH_4 coupling and oxidation respectively in order to analyse the effect of the conduction mode on these reactions. They found that for CH_4 oxidation a small p or n -type conduction combined with good oxygen ion conduction was favourable, whereas for CO oxidation p -type conductors are preferred. For CH_4 coupling a high ionic conductivity with low electronic conductivity gives a high C_2 compounds yield. However, of all these materials, the ones with $\text{Cr}, \text{V}, \text{Ti}$ and Nb are reported to be the most stable in reducing atmosphere.

Metallic and ceramic composites were already investigated in SOFC for Ni-based anodes running on humidified H_2 , but also on CH_4 , reformed or partially oxidised internally or in an separate reactor. For H_2 oxidation, Setoguchi et al.⁷⁶ showed the high electrochemical activity of Ni when compared to other metals such as $\text{Au}, \text{Pt}, \text{Pd}, \text{Rh}, \text{Ru}, \text{Co}, \text{Fe}$ and Mn . The ceramic part was also observed to be important as PrO_x promoted the reaction more than Sm -doped CeO_2 and YSZ due to its high oxygen ion mobility. On these types of anodes, internal reforming or partial oxidation are in principle feasible but they induce temperature gradients due to the endothermicity of H_2O or CO_2 reforming and the small exothermicity of O_2 partial oxidation. Examples of internal steam reforming and oxygen or air partial oxidation of hydrocarbons are given in references⁷⁷⁻⁸² where Gd -doped ceria, YSZ or similar ionic conducting electrolytes were used as electrolyte or cermet with Ni, Fe or Pt , in a single as well as in a two chamber SOFC cell. These experiments were conducted in feeds containing at least the thermodynamic ratio of oxygen or water in order to prevent carbon deposition^{28-30, 83, 84}. High power densities could be achieved (400 mW/cm^2 at 700°C for partial oxidation using a $\text{Ni}+\text{Sm}$ doped ceria anode and $\text{Sm}_{0.5}\text{Sr}_{0.5}\text{CoO}_3$ cathode sintered on a $150 \mu\text{m}$ thick Sm doped ceria electrolyte⁸⁰). Many trials were made to increase the performance of these anodes, either by using some additives with Ni (e.g. Mo)⁸⁵⁻⁸⁷ or by increasing the electronic conductivity of the ionic conductor (by using TiO_2 for example⁸⁸). Feeding CH_4 rich feeds leads in principle to carbon deposits. Some studies were also aimed at understanding the mechanism of CH_4 oxidation over Ni or Pt based anodes^{28, 29, 89}.

However, in a very narrow temperature window, where kinetics for carbon deposition are somewhat sluggish, Murray et al. have recently reported a Ni - YSZ cermet run in a pure CH_4 feed for 100 h⁹⁰. This special cell was made of a thin ($2 \mu\text{m}$) Y -doped ceria layer interlayer between a Ni - YSZ cermet and an $8 \mu\text{m}$ thick YSZ electrolyte⁹¹. Power densities of 370 mW/cm^2 versus 480 mW/cm^2 were achieved at 650°C in H_2 and dry CH_4 respectively. Ishihara et al.⁹² reported a run in $\text{CH}_4:\text{O}_2$ ratios of 4, 2 and ∞ at 1000°C over a Ni -based anode deposited over a $\text{La}_{0.9}\text{Sr}_{0.2}\text{Ga}_{0.8}\text{Mg}_{0.2}\text{O}_3$ electrolyte. A power output of 510 mW/cm^2 was achieved in dry CH_4 , with a 30 h stability with no C deposition. Recently also, Cu -based anodes (see also Chapter 10 and 11) were reported to run with pure methane, ethane, 1-butene, n -butane, n -decane, toluene, synthetic diesel and hydrogen^{93, 94} without carbon deposition (3 h run except for CH_4 where the experiments lasted for 12 h). In H_2 a power output of 450 mW/cm^2 was reported versus 250 mW/cm^2 in CH_4 at 800°C using a $60 \mu\text{m}$ thick YSZ electrolyte⁹⁵.

Due to the oxygen availability of an oxide, carbon deposition is generally less liable than on metallic catalysts. Among the first row transition metal perovskites, LaCrO_3 was reported to be the most stable at 1000°C and at very low oxygen partial pressures ($\approx 10^{-21}$ atm), whereas LaMnO_3 , LaFeO_3 , LaCoO_3 and LaNiO_3 decomposed at a P_{O_2} of 10^{-15} , 10^{-17} , 10^{-7} and 10^{-4} atm respectively⁹⁶. LaVO_4 , encountered a phase transition, passing from LaVO_4 to LaVO_3 upon reduction, leading to a change in its volume. This material shows a metallic conductivity ($>150 \text{ S/cm}$) and could be interesting for SOFC application. In SOFC, LaCrO_3 -based catalysts were investigated as catalyst powders for their possible use as anode materials⁹⁷⁻¹⁰¹. These materials were reported to have a mild activity toward CH_4 and to resist much better to carbon deposition than Ni - YSZ cermet. Nevertheless, carbon was formed in some cases above 600°C , but water addition lowered its formation. Horita et al.¹⁰² and Norby et al.¹⁰³ tried $\text{La}_{0.8}\text{Ca}_{0.23}\text{CrO}_3$ and $\text{La}_{0.7}\text{Ca}_{0.3}\text{CrO}_3$ anodes respectively and obtained a low electrochemical performance at 1000°C

(a maximum of 50 mW/cm²) (see also Chapter 3 to 8). Gobal¹⁰⁴ also tried a La_{0.7}Ca_{0.3}CrO₃ anode and observed a power output of 7.5 mW/cm² at 850°C. Vernoux et al.¹⁰¹ worked with cone-shaped LaCrO₃-based micro-electrodes pressed on the surface of YSZ pellets in H₂ and CH₄ and showed that these materials have comparable efficiency to Ni-YSZ cone-electrodes in diluted steam-reforming conditions. Globally, these materials are poor *p*-type conductors but are already used as interconnects for SOFC and show some stability with YSZ⁴.

Nb or Ti modified YSZ was also sought for its use as SOFC anode as Nb and Ti doping add some electronic conductivity to an otherwise ionic conductor¹⁰⁵. In this concept of a whole YSZ cell (as the cathode is an Yb doped YSZ) a maximum power output of 40 mW/cm² (1.5 mm thick YSZ electrolyte) was achieved in H₂ at 915°C with a Y₁₂ZrTi₂₀ anode. In CH₄ a power density of 2 mW/cm² with no carbon deposition was reported at 932°C over a 300 μm thick YSZ electrolyte¹⁰⁶. Similar concepts are advanced by Tuller et al. who worked on Gd-based titanates pyrochlores¹⁰⁷.

Titanates and niobates are known for their high electronic conductivity¹⁰⁸⁻¹¹¹. They attracted attention for their potential use as anodes^{99, 112-117}. Many of these compounds are not very stable in oxidising conditions. The highest conductivities reported at 800°C were for SrNbO₃, Nb₂TiO₇ (Ti_{0.34}Nb_{0.66}O₂ 340 S/cm) and CrTi₂O₅ (177 S/cm). By stabilising these structures, they often end up with lower conductivities. Nb₂O₅, when reduced, possesses also a high conductivity (NbO₂ 398 S/cm at 850°C)¹¹⁸. However, Nb₂O₅ was observed to stick badly on YSZ, even when used as a composite with YSZ (needle-like structure, from our own unpublished work). Na_xWO₃ may be another candidate if stability under reducing conditions can be satisfied.

Other possible anode materials put forward recently are carbides. Horita et al.¹² studied ZrC, WC, TiC and VC. The best choice material was WC due to its thermodynamic stability under reducing conditions. These materials decompose however under current load to their oxide counterparts. One can also imagine to use the mixed conducting materials used in oxygen separation membranes. SrFeCo_{0.5}O_x, developed by Balachandran et al.⁶¹, gave a certain power density at 917°C in CH₄ + 3% H₂O when sintered on a 10% Y-doped ceria electrolyte (see Figure 9, from our own unpublished results). This material has high ionic and electronic conductivities and shows a multiple phase composition¹¹⁹. We also looked also at La_{0.2}Sr_{0.8}Cr_{0.2}Fe_{0.8}O₃ and La_{0.6}Sr_{0.4}Co_{0.2}Fe_{0.8}O₃ from the point of view of catalysis. Weston et al.¹²⁰ studied La_{0.6}Sr_{0.4}Co_{0.2}Fe_{0.8}O₃ in dilute 3:6 CH₄:O₂ for its potential use as anode and Norby et al.¹²¹ used an Au-SrFeO_{3.8} anode deposited on YSZ for the catalytic oxidation of CH₄ cofed with O₂. These materials were observed to be quite unstable in the low oxygen partial pressures encountered at SOFC anodes. Also, CeO₂-based materials could be regarded as potential anodes for CH₄ oxidation (see Chapter 9 to 11). This mixed conductor shows high ionic conduction as well as electronic conduction in low oxygen partial pressures. It has recently been shown that it is a good electrode for H₂ oxidation¹²² and Marina et al.^{123, 124} showed its capacity for CH₄ oxidation (80 mW/cm² at 1000°C). Protonic conductors could also be potential materials for anodes in SOFC.

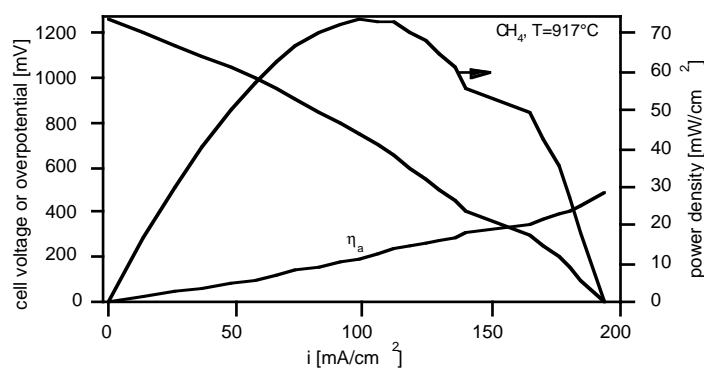


Figure 9: Current/potential-overpotential and power density of a SrFeCo_{0.5}O_x anode deposited on a 10% Y-doped ceria electrolyte. The measurement was performed in a sealed set-up using CH₄ + 3% H₂O (unpublished work).

Aim of the thesis

From the discussion above, the research on hydrocarbon fuel anodes is still not much explored as the number of papers dealing with real electrochemical tests is scarce. However,

many materials are investigated for their potential use as anodes, as long as their stability in reducing conditions is confirmed. The stringent requirements for a SOFC anode working under reducing conditions as well as their fabrication make the development of suitable materials a challenging task.

Many of the materials presented above show middle range conductivity in reducing atmospheres. However, different strategies could be implemented to address many of the problems encountered with anode materials, such as low conductivity (ionic or electronic) and low catalytic activity. Composite materials could be made to supplement one or the other lack in conductivity or to temper or increase the catalytic activity of an anode by proper deposition, doping or alloying with elements of interest. For example, for a low electronic conductor, a current collector layer made of a good metallic conducting oxide (for example one of the Nb or Ti-based bronze-like materials) or an inert metal could serve for that purpose. The poor ionic conductivity might be as well solved by proper doping or by making a composite with a good ionic conductor.

In the present study, three types of materials are considered: LaCrO_3 and CeO_2 -based oxides as well as metallic catalysts such as Cu and Cu-Ni alloys. The oxide materials were chosen for their known stability under reducing conditions, as well as for the many possibilities available for tailoring these oxides by proper substitutions. Two palettes of materials were targeted: *p*-type LaCrO_3 -based perovskite compounds and the *n*-type fluorite CeO_2 . As for the metallic catalysts, as discussed in Chapter 10, they were chosen for their peculiar characteristics with CH_4 .

This work can be divided into two parts: LaCrO_3 -based and metals and CeO_2 -based materials.

1- LaCrO_3 oxides are perovskite materials which allow large variations in their composition. Thus interesting modifications in the electronic as well as in the catalytic properties of the material can be tuned. Chapter 3 is a discussion of the synthesis, structure and physical properties of LaCrO_3 -based powders. Chapter 4 and 5 give evidences of a surface reaction between these oxides and the YSZ electrolyte under fuel cell operation mode (current treatment). The catalytic properties of different LaCrO_3 catalysts substituted with elements such as Mg, Ca, Mn, Fe, Co, Ni and Sr are considered in Chapter 6 while the thermodynamic stability of the same materials is discussed in Chapter 7. Finally, the electrochemical performances of LaCrO_3 -based compounds are presented in Chapter 8.

2- Ceria-based materials synthesis, structure and physical characterisations are presented in Chapter 9. Their catalytic activity as well as those of the metals are discussed in Chapter 10, whereas the electrochemical studies in H_2 and CH_4 are presented in Chapter 11.

References

- (1) Hirschenhofer, J. H.; Stauffer, D. B.; Engleman, R. R.; Klett, M. G. "Fuel Cell Handbook. Fourth Edition," Pearson's Corporation, for U.S. Department of Energy, Office of Fossil Energy, Federal Energy Technology Center, **1999**.
- (2) Kartha, S.; Grimes, P., *Physics Today* **1994**, 54-61.
- (3) Twigg, M. V. *Catalyst Handbook*, 2 ed.; Wolfe Publishing Ltd., **1989**.
- (4) Minh, N. Q., *J. Am. Ceram. Soc.* **1993**, 76, 563-588.
- (5) Campbell, C.; Laherrère, J., *Pour la Science* **1998**, 29-36.
- (6) George, R., *Pour la Science* **1998**, 38-39.
- (7) Anderson, R., *Pour la Science* **1998**, 40-45.
- (8) Fouda, S., *Pour la Science* **1998**, 46-49.
- (9) Kim, J.-W.; Virkar, A. V.; Fung, K.-Z.; Mehta, K.; Singhal, S. C., *J. Electrochem. Soc.* **1999**, 146, 69-78.
- (10) Ihringer, R., Swiss Federal Institut of Technology, EPFL, Lausanne, **2000**.
- (11) Steinberg, M., *Chemtech* **1999**, 31-36.
- (12) Horita, T.; Sakai, N.; Kawada, T.; Yokokawa, H.; Dokiya, M., *J. Electrochem. Soc.* **1995**, 142, 2621-2624.
- (13) Rostrup-Nielsen, J., *Journal of Catalysis* **1977**, 48, 155-165.
- (14) Rostrup-Nielsen, J. R., *Journal of Catalysis* **1974**, 33, 184-201.
- (15) Rostrup-Nielsen, J. R. In *Catalysis, Science and Technology*; Anderson, J. R. and Boudart, M., Eds.; Springer Verlag, **1984**; Vol. 5.

- (16) Rostrup-Nielsen, J. R., *Journal of Catalysis* **1984**, *85*, 31-43.
- (17) Rostrup-Nielsen, J. R.; Alstrup, I. In *Catalysis*; Ward, J. W., Ed.; Elsevier Science Publishers:, **1987**.
- (18) Bokx, P. K. D.; Kock, A. J. H. M.; Boellaard, E.; Klop, W.; Geus, W., *Journal of Catalysis* **1985**, *96*, 454-467.
- (19) Kock, A. J. H. M.; Bokx, P. K. D.; Boellaard, E.; Klop, W.; Geus, W., *Journal of Catalysis* **1985**, *96*, 468-480.
- (20) Boellaard, E.; Bokx, P. K. D.; Kock, A. J. H. M.; Geus, W., *Journal of Catalysis* **1985**, *96*, 481-490.
- (21) Ceyer, S. T.; Yang, Q. Y.; Lee, M. B.; Beckerle, J. D.; Johnson, A. D. *The mechanism for the dissociation of methane on a nickel catalyst.*; Elsevier, **1988**.
- (22) Bartholomew, C. H., *Catal. Rev. -Sci. Eng.* **1982**, *24*, 67-112.
- (23) Kim, M. S.; Rodriguez, N. M.; Baker, R. T. K., *Journal of Catalysis* **1992**, *134*, 253-268.
- (24) Yentekakis, L. V.; Neophytides, S. G.; Kaloyiannis, A. C.; Vayenas, C. G. Third International Symposium on Solid Oxide Fuel Cells, Hawaii, **1993**; p 904-912.
- (25) Bossel, U. "Facts and figures," Swiss Federal Office of Energy, **1992**.
- (26) Ledjeff, K.; Rohrbach, T.; Schaumberg, G. The Second International Symposium on Solid Oxide Fuel Cells, Athens, Greece, **1991**; p 323-333.
- (27) Koh, J.; Kang, B.; Lim, H. C.; Yoo, Y., *Electrochemical and Solid-State Letters* **2001**, *4*, A12-A15.
- (28) Ihara, M.; Abudula, A.; Kato, R.; Sakaki, K.; Komiyama, H.; Yamada, K. Materials and Processes, Les Diablerets, Switzerland, **1997**; p 129-132.
- (29) Ihara, M.; Yokoyama, C.; Abudula, A.; Kato, R.; Komiyama, H.; Yamada, K., *J. Electrochem. Soc.* **1999**, *146*, 2481-2487.
- (30) Horita, T.; Sakai, N.; Kawada, T.; Yokokawa, H.; Dokiya, M., *J. Electrochem. Soc.* **1996**, *142*, 1161-1168.
- (31) Masai, M.; Kado, H.; Miyake, A.; Nishiyama, S.; Tsuruya, S. In *Methane Conversion*; Bibby, D. M., Chang, C. D., Howe, R. F. and Yurchak, S., Eds.; Elsevier Science Publishers:, **1988**.
- (32) Lu, G. Q.; Wang, S., *Chemtec* **1999**, 37-43.
- (33) Tsang, S. C.; Claridge, J. B.; Green, M. L. H., *Catalysis Today* **1995**, *23*, 3-15.
- (34) Frennet, A.; Liénard, G.; Crucq, A.; Degols, L., *Journal of Catalysis* **1978**, *53*, 150-163.
- (35) Bebelis, S.; Neophytides, S.; Vayenas, C. First European Solid Oxide Fuel Cell Forum, Lucerne, Switzerland, **1994**; p 197-206.
- (36) Zanibelli, L.; Flego, C.; Perego, C.; Rizzo, C. First european solid oxide fuel cell forum, Lucerne, Switzerland, **1994**; p 207-216.
- (37) Lee, A. L.; Zabransky, R. F.; Huber, W. J., *Ind. Eng. Chem. Res.* **1990**, *29*, 766-773.
- (38) vayenas, C. G.; Bebelis, S.; Yentekakis, I. V.; Neophytides, S., **1992**.
- (39) Zhuang, Q.; Qin, Y.; Chang, L., *Applied Catalysis* **1991**, *70*, 1-8.
- (40) Vogt, E. T. C.; Dillen, A. J. v.; Geus, J. W. In *Catalyst Deactivation 1987*; Delmon, B. and Froment, G. F., Eds.; Elsevier Science Publishers:, **1987**.
- (41) Wu, X.; Zhang, J.; Chang, L. In *Catalyst Deactivation 1987*; Delmon, B. and Froment, G. F., Eds.; Elsevier Science Publishers:, **1987**.
- (42) Kim, M. S.; Rodriguez, N. M.; Baker, R. T., *Journal of Catalysis* **1991**, *131*, 60-73.
- (43) Rodriguez, N. M.; Kim, M. S.; Baker, R. T., *Journal of Catalysis* **1993**, *140*, 16-29.
- (44) Alstrup, I., *Journal of Catalysis* **1988**, *109*, 241-251.
- (45) Alstrup, I.; Tavares, M. T., *Journal of Catalysis* **1993**, *139*, 513-524.
- (46) Bernardo, C. A.; Alstrup, I.; Rostrup-Nielsen, J. R., *Journal of Catalysis* **1985**, *96*, 517-534.
- (47) Kooten, W. E. J. v.; Kragten, D. D.; Gijzeman, O. L. J.; Geus, J. W., *Surface Science* **1993**, *290*, 302-308.
- (48) Berg, M.; Järås, S., *Applied Catalysis A: General* **1994**, *114*, 227-241.
- (49) Vernon, P. D. F.; Green, M. L. H.; Cheetham, A. K.; Ashcroft, A. T., *Catalysis Letters* **1990**, *6*, 181-186.
- (50) Liu, W.; Flytzani-Stephanopoulos, M., *Journal of Catalysis* **1995**, *153*, 304-316.
- (51) Garbowski, E.; Guenin, M.; Marion, M.-C.; Primet, M., *Applied Catalysis* **1990**, *64*, 209-224.

- (52) Lee, J. H.; Trimm, D. L., *Fuel Processing Technology* **1995**, *42*, 339-359.
- (53) Sokolovskii, V. D.; Coville, N. J.; Parmaliana, A.; Eskendirov, I.; Makao, M., *Catalysis Today* **1998**, *42*, 191-195.
- (54) Hackenberger, M.; Stephan, K.; Kießling, D.; Schmitz, W.; Wendt, G., *Catalysis Today* **1997**, *101-103*, 1195-1200.
- (55) Dubois, J. L.; Cameron, C. J., *Applied Catalysis* **1990**, *67*, 49-71.
- (56) Doshi, R.; Alcock, C. B.; Gunasekaran, N.; Carberry, J. J., *Journal of Catalysis* **1993**, *140*, 557-563.
- (57) McCarty, J. G.; Wise, H., *Catalysis Today* **1990**, *8*, 231-248.
- (58) Seiyama, T., *Catal. Rev. -Sci. Eng.* **1992**, *34*, 281-300.
- (59) Wu, J.; Li, S.; Niu, J.; Fang, X., *Applied Catalysis A: General* **1995**, *124*, 9-18.
- (60) Tejuca, L. G.; Fierro, J. L. G.; Tascon, J. M. D., *Advances in Catalysis* **1989**, *36*, 237-328.
- (61) Balachandaran, U.; Eror, N. G., *Journal of Materials Science* **1988**, *23*, 2676-2682.
- (62) Tsai, C.-Y.; Dixon, A. G.; Moser, W. R.; Ma, Y. H., *AIChE Journal* **1997**, *43*, 2741-2750.
- (63) Gellings, P. J.; Bouwmeester, H. J. M., *Catalysis Today* **1992**, *12*, 1-105.
- (64) Chan, K. S.; Ma, J.; Jaenicke, S.; Chuah, G. K., *Applied Catalysis A: General* **1994**, *107*, 201-227.
- (65) Trovarelli, A., *Catal. Rev. -Sci. Eng.* **1996**, *38*, 439-520.
- (66) Otsuka, K.; Wang, Y.; Sunada, E.; Yamanaka, I., *Journal of Catalysis* **1998**, *175*, 152-160.
- (67) Klvana, D.; Vaillancourt, J.; Kirchnerova, J.; Chaouki, J., *Applied Catalysis A: General* **1994**, *109*, 181-193.
- (68) Alcock, C. B.; Carberry, J. J.; Doshi, R.; Gunasekaran, N., *Journal of Catalysis* **1993**, *143*, 533-538.
- (69) York, A. P. E.; Claridge, J. B.; Marquez-Alvarez, C.; Brungs, A. J.; Tsang, S. C.; Green, M. L. H. 3rd World Congress on Oxidation Catalysis, **1997**; p 711-720.
- (70) Saracco, G.; Scibilia, G.; A. I.; Baldi, G., *Applied Catalysis B: Environmental* **1996**, *8*, 229-244.
- (71) Provendier, H.; Petit, C.; Kiennemann, A. *Studies in Surface Science and Catalysis*, **2000**; p 683-688.
- (72) Hutchings, G. J.; Scurrall, M. S.; Woodhouse, J. R., *Chem. Soc. Rev.* **1989**, *18*, 251-283.
- (73) Fierro, J. L. G.; Tascon, J. M. D.; Tejuca, L. G., *Journal of Catalysis* **1985**, *93*, 83-91.
- (74) Bouwmeester, H. J. M.; Burggraaf, A. J. In *The CRC Handbook of Solid State Electrochemistry*; Gellings, P. J. and Bouwmeester, H. J. M., Eds.; CRC Press; **1997**.
- (75) Matsuda, H.; Ishihara, T.; Mizuhara, Y.; Takita, Y. Third International Symposium on SOFC, Honolulu, Hawaii, **1993**.
- (76) Setoguchi, T.; Okamoto, K.; Eguchi, K.; Arai, H., *J. Electrochem. Soc.* **1992**, *139*, 2875-2880.
- (77) Livermore, S. J. A.; Cotton, J. W.; Ormerod, R. M., *Journal of Power Sources* **2000**, *86*, 411-416.
- (78) Kendall, K.; Williams, D. S., *Platinum Metals Rev.* **1998**, *42*, 164-167.
- (79) Hibino, T.; Hashimoto, A.; Inoue, T.; Tokuno, J.; Yoshida, S.; Sano, M., *J. Electrochem. Soc.* **2000**, *147*, 2888-2892.
- (80) Hibino, T.; Hashimoto, A.; Inoue, T.; Tokuno, J.; Yoshida, S.; Sano, M., *Science* **2000**, *288*, 2031-2033.
- (81) Hibino, T.; Wang, S.; Kakimoto, S.; Sano, M., *Electrochemical and Solid-State Letters* **1999**, *2*, 317-319.
- (82) Asano, K.; Hibino, T.; Iwahara, H., *J. Electrochem. Soc.* **1995**, *142*, 3241-3245.
- (83) Cunningham, R. H.; Ormerod, R. M. Forth European Solid Oxide Fuel Cell Forum, Lucerne, Switzerland, **2000**; p 507-516.
- (84) Onuma, S.; Kaimai, A.; Kawamura, K.; Nigara, Y.; Kawada, T.; Mizusaki, J.; Inaba, H.; Tagawa, H., *J. Electrochem. Soc.* **1998**, *145*, 920-925.
- (85) Finnerty, C. M.; Cunningham, R. H.; Ormerod, R. M. Third European Solid Oxide Fuel Cell Forum, Nantes, France, **1998**; p 217-226.

- (86) Cunningham, R. H.; Finnerty, C. M.; Ormerod, R. M. The Fifth International Symposium on Solid Oxide Fuel Cell, Aachen, Germany, **1997**; p 973-982.
- (87) Cunningham, R. H.; Finnerty, C. M.; Kendall, K.; Ormerod, R. M. The Fifth International Symposium on Solid Oxide Fuel Cell, Aachen, Germany, **1997**; p 965-972.
- (88) Skarmoutsos, D.; Tsoga, A.; Naoumidis, A.; Nikolopoulos, P. *Solid State Ionics*, **1999**; p 439-444.
- (89) Onuma, S.; Kaimai, A.; Kawamura, K.; Nigara, Y.; Kawada, T.; Mizusaki, J.; Tagawa, H., *Solid State Ionics* **2000**, *132*, 309-331.
- (90) Murray, E. P.; Tsai, T.; Barnett, S. A., *Nature* **1999**, *400*, 649-651.
- (91) Tsai, T.; Barnett, S. A., *Solid State Ionics* **1997**, *98*, 191-196.
- (92) Ishihara, T.; Hiei, Y.; Takita, Y., *Solid State Ionics* **1995**, *79*, 371-375.
- (93) Kim, H.; Park, S.; Vohs, J. M.; Gorte, R. J., *J. Electrochem. Soc.* **2001**, *148*, A693-A695.
- (94) Park, S.; Vohs, J. M.; Gorte, R. J., *Nature* **2000**, *404*, 265-267.
- (95) Park, S.; Gorte, R. J.; Vohs, J. M., *J. Electrochem. Soc.* **2001**, *148*, A443-A447.
- (96) Nakamura, T.; Petzow, G.; Gauckler, L. J., *Mat. Res. Bull.* **1979**, *14*, 649-659.
- (97) Baker, R. T.; Metcalfe, I. S., *Applied Catalysis A: General* **1995**, *126*, 297-317.
- (98) Baker, R. T.; Metcalfe, I. S., *Applied Catalysis A: General* **1995**, *126*, 319-332.
- (99) Middleton, P. H.; Steiner, H. J.; Christie, G. M.; Baker, R.; Metcalfe, I. S.; Steele, B. C. H. Proceedings of the Third International Symposium on Solid Oxide Fuel Cells, Hawaii, **1993**; p 542-551.
- (100) Stojanovic, M.; Mims, C. A.; Moudallal, H.; Yang, Y. L.; Jacobson, A. J., *Journal of Catalysis* **1997**, *166*, 324-332.
- (101) Vernoux, P.; Guindet, J.; Gehain, E. Third European Solid Oxide Fuel Cell Forum, Nantes, France, **1998**; p 237-247.
- (102) Horita, T.; Sakai, N.; Kawada, T.; Yokokawa, H.; Dokiya, M. First European Solid Oxide Fuel Cell Forum, Lucerne, Switzerland, **1994**; p 227-236.
- (103) Norby, T.; Osborg, P. A.; Dyrлие, O.; Hildrum, R.; Seiersten, M.; Glenne, R. European Solid Oxide Fuel Cell Forum I, Lucerne, Switzerland, **1994**; p 217-226.
- (104) Gobal, F., *Indian Journal of Chemistry* **1996**, *35A*, 687-689.
- (105) Worrell, W. L.; Han, P.; Uchimoto, Y.; Davies, P. K. Solid Oxide Fuel Cells IV, Yokohama, Japan, **1995**; p 50-57.
- (106) Kelaidopoulou, A.; Siddle, A.; Dicks, A. L.; Kaiser, A.; Irvine, J. T. S. Fourth European Solid Oxide Fuel Cell Forum, Lucerne, Switzerland, **2000**; p 537-546.
- (107) Porat, O.; Heremans, C.; Tuller, H. L., *Solid State Ionics* **1997**, *94*, 75-83.
- (108) Sugimoto, W.; Tahara, T.; Sugahara, Y.; Kuroda, K., *Mat. Res. Soc. Symp. Proc.* **1997**, *453*, 361-366.
- (109) Svensson, G.; Eriksson, L.; Olofsson, C.; Holm, W., *Journal of Alloys and Compounds* **1997**, *248*, 33-41.
- (110) Chavez, J. A.; Gibb, T. C.; West, A. R., *J. Mater. Chem.* **1996**, *6*, 1957-1961.
- (111) Isawa, K.; Sugiyama, J.; Matsuura, K.; Nozaki, A.; Yamauchi, H., *Physical Review B* **1993**, *47*, 2849-2853.
- (112) Steiner, H.-J.; Middleton, P. H.; Steele, B. C. H., *Journal of Alloys and Compounds* **1993**, *190*, 279-285.
- (113) Fagg, D. P.; Kharton, V. V.; Frade, J. R. Solid Oxide Fuel Cell Materials and Mechanisms, Les Diablerets, Switzerland, **2001**; p 71-74.
- (114) Ouweltjes, J. P.; Rietveld, G. Solid Oxide Fuel Cell Materials and Mechanisms, Les Diablerets, Switzerland, **2001**; p 79-84.
- (115) Irvine, J. T. S.; Slater, P. R.; Kaiser, A.; Bradley, J. L.; Holtappels, P.; Mogensen, M. Fourth European Solid Oxide Fuel Cell Forum, Lucerne, Switzerland, **2000**; p 471-477.
- (116) Reich, C. M.; Kaiser, A.; Irvine, J. T. S. Fourth European Solid Oxide Fuel Cell Forum, Lucerne, Switzerland, **2000**; p 517-526.
- (117) Slater, P. R.; Irvine, J. T. S., *Solid State Ionics* **1999**, *120*, 125-134.
- (118) Sakata, K., *J. Phys. Soc. Japan* **1969**, *26*, 867.
- (119) Guggilla, S.; Manthiram, A., *J. Electrochem. Soc.* **1997**, *144*, L120-L122.
- (120) Weston, M.; Metcalfe, I. S., *Solid State Ionics* **1998**, *113-115*, 247-251.

- (121) Norby, T.; Middleton, P. H.; Hansen, E. W.; Dahl, I.; Andersen, A. G., *Chem. Eng. Technol.* **1995**, *18*, 139-147.
- (122) Watanabe, M.; Uchida, H.; Yoshida, M., *J. Electrochem. Soc.* **1997**, *144*, 1739-1743.
- (123) Marina, O. A.; Mogensen, M., *Applied Catalysis A: General* **1999**, *189*, 117-126.
- (124) Marina, O. A.; Bagger, C.; Primdahl, S.; Mogensen, M. Third European Solid oxide Fuel Cell Forum, Nantes, France, **1998**; p 427-436.

Appendix: List of the different gas species used in the gas phase calculations presented in this chapter as well as all over this thesis (using HSC 4.1)

C(g), C₂(g), C₃(g), C₄(g), C₅(g), CH(g), CH₂(g), CH₃(g), CH₄(g), C₂H(g), C₂H₂(g), C₂H₃(g), C₂H₄(g), C₂H₅(g), C₂H₆(g), CH₃OH, CH₃CH₂OH, CO(g), CO₂(g), C₂O(g), C₃O₂(g), COOH(g), H(g), H₂(g), HCO(g), HCOOH(g), HO(g), HO₂(g), H₂O(g), H₂O₂(g), O(g), O₂(g), O₃(g), C(s), Ar(g)

Chapter 2 二

Experimental set-up

Experimental set-up

Introduction

In this chapter the procedures developed for electrode slurries preparation and their application over electrolyte sheets are outlined. The different assemblies used for the electrochemical experiments are described.

Slurry preparation and cell fabrication

Terpineol-ethyl cellulose-based slurries were prepared by mixing electrode powder, terpineol and ethyl cellulose in the proportion of 56.50:39.55:3.95 in isopropanol. The slurries were obtained by evaporating the solvent isopropanol under mechanical stirring on a hot plate. Composite slurries of the electrode with Tosoh 8YSZ (TZ-8Y) powders were also made using different amounts of the electrode material and 8YSZ powders. The electrode pastes were then screen-printed on 8YSZ plates. These were 3 cm x 3 cm or circular ($\phi \approx 2.2$ cm) Kerafol or cast tapes made in-house and sintered at 1500°C/3h. They were then treated in a 10% HF solution as an etching step. A 5 min etching, at 60°C, was implemented in order to remove surface impurities¹. Electrodes of 1 cm² (square tapes) or 0.38 cm² (circular tapes) area were printed. The number of layers and their composition varied from sample to sample. As current collector, an Au electroplated-Pt mesh was pressed in the last layer. In the special case of circular cells used for the sealed configuration (see below), no current collector was fixed at that stage. Au was used in order to prevent CH₄ reaction with Pt, as carbon deposition was observed on bare Pt mesh which ultimately caused cell failure. On the opposite side of the electrolyte, in alignment, a three layered 1 cm² (on square YSZ) or 0.38 cm² (on circular YSZ) lanthanum strontium manganite (LSM, La_{0.85}Sr_{0.15}MnO₃) cathode was deposited along with a Pt mesh current collector. In the case of symmetrical cells (see below and Figure 1c), the same type of anode was applied with an Au electroplated Pt mesh. The cell thus obtained was then sintered under load (thermocompression) between 2 alumina felts with a heating ramp of 90°C/h from room temperature to 600°C to burn the organics, followed by a ramp of 180°C/h until the desired temperature. The cell was then kept at this temperature for 4 h and then allowed to cool down to room temperature. Subsequently, a 5 mm x 3 mm Pt painted electrode was placed 3 mm away from the cathode as a reference electrode. In the case of the circular cells, used in the sealed configuration, a porous Au-anode material paste was painted on the anode as a current collector. This is sintered at 950°C for 1 h with a heating ramp of 180°C/h. A schematic view of the different cells is given in Figure 1.

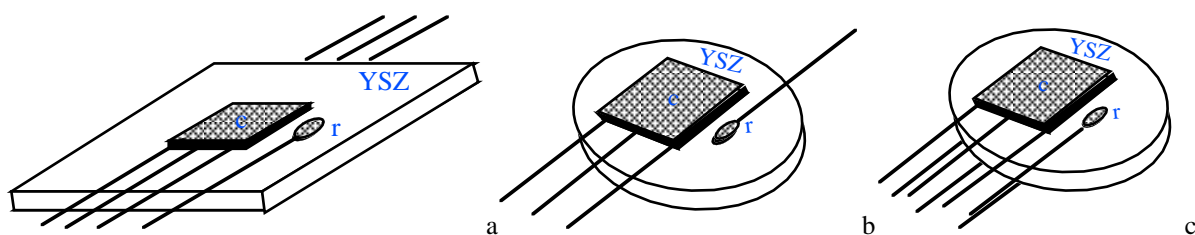


Figure 1: Schematic view of various cells showing the 8YSZ Kerafol electrolyte, the LSM and the Pt-mesh cathode, the Pt reference electrode and on the opposite side the LC anode. a: non-sealed, b: sealed, and c: symmetrical cell.

Electrochemical testing

a. Non-sealed configuration

The *square* cells (type a, Figure 1) were mounted between inconel flanges with porous alumina felts on each side as electrical insulators and gas diffusers. This configuration was not sealed so that the excess fuel burned at the periphery of the cell. The tests were conducted in a Lenton EF 11/8 furnace. The gas inputs - air on the cathode side and fuel on the anode side - were controlled by rotameters, and the fuel line was heated in order to prevent water condensation. A valve allowed to switch between humidified H₂, or CH₄ and dry CO/CO₂

mixtures. Typically, air flow rate was 300 ml/min and the fuel flow rate was 200 ml/min for H_2 and 70 ml/min for CH_4 . Electrical contacts to the cell were made using silver wires welded to the Pt current collectors and taken outside the oven through mullite tubes. The whole system was protected from electrical noise by a Faraday cage connected to the ground. A schematic view of the set-up is shown in Figure 2. The gas humidifier is shown in Figure 3.

After mounting, the cells were heated to $840^\circ C$ in 4 h under 3% humidified H_2 on the fuel side and air on the cathode side. The flange temperature was monitored by a K-type thermocouple pressed on its base, whereas the cell temperature was followed by one S-type (Pt/Pt 10% Rh) thermocouple inserted beneath the anode and protected by alumina wool. The electrochemical characterization was performed in most cases starting from $840^\circ C$ in H_2 followed by overnight polarization at 400 mV. This helped to activate the electrodes, especially the LSM cathode. The temperature was then varied and ultimately the gas was switched to $CH_4 + 3\% H_2O$.

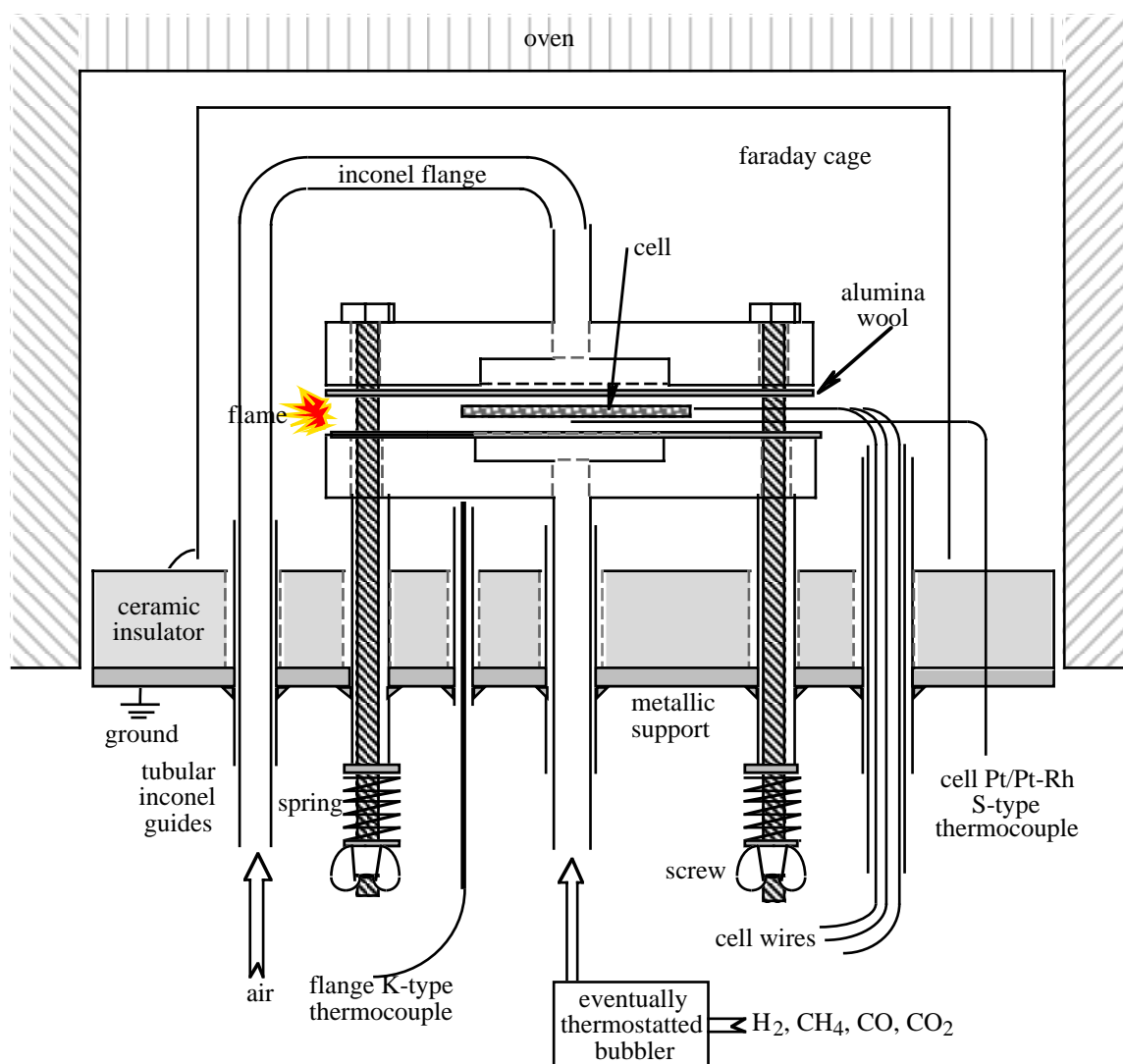


Figure 2: A schematic view of the non-sealed testing set-up (not on scale).

b. Sealed configuration

The circular cells (type b, Figure 1) were mounted over a machined Macor ceramic tube using an Au ring and a home-made soda glass powder as sealing, with the anode facing the inside. The soda glass proved to be the most suitable among various commercial glass seals. The anode was then pressed to an Au mesh-current collector mounted on a Macor machined gas

diffuser, and the whole cell was tightened using a machined Stumatite ceramic pressed to the cathode. This tightening allowed better current collection and higher stability to the seal. The electrical wires were passed through ceramic tubes protected by a metallic tubing or coating serving as a wire shield. The cell was then mounted in a vertical oven (Horst, Germany) and heated to 860°C in 4 h under Ar flow on the anode and air on the cathode, in order to melt the glass seal properly. The fuel gas was introduced just below the anode and extracted by a thin alumina tube at the bottom. At the desired temperature, the fuel gas was switched to humidified H₂ and the cell OCV was monitored to check the seal tightness. The anode gas flow rates were set to 30 ml/min, whereas the cathode air flow rate was of 150 ml/min. The anode gases were all monitored by mass flow controllers, and humidified in an oil thermostatted bubbler. The cell temperature was monitored by a K-type thermocouple placed at the cell height, and occasionally by an S-type thermocouple pressed on the cathode side of the cell. A schematic view is given in Figure 4. The outlet gases (O₂, N₂, Ar, CH₄, H₂, CO, CO₂ and possibly C₂ compounds) were analyzed by gas chromatography through syringe injection (Carlo Erba MFC500 and Gowmac instruments) and by a quadrupole mass spectrometer (Residual Gas Analyser, Spectra, Leda Mass Vision, HF-100, maximum mass of 100 a.m.u.). A Porapak Q column with He as carrier was used for Ar, CH₄, CO₂ and C₂-compounds analysis (Carlo Erba) whereas a Molecular Sieve 5Å with Ar carrier (Gowmac) was used for H₂, O₂, N₂, CH₄ and CO detection.

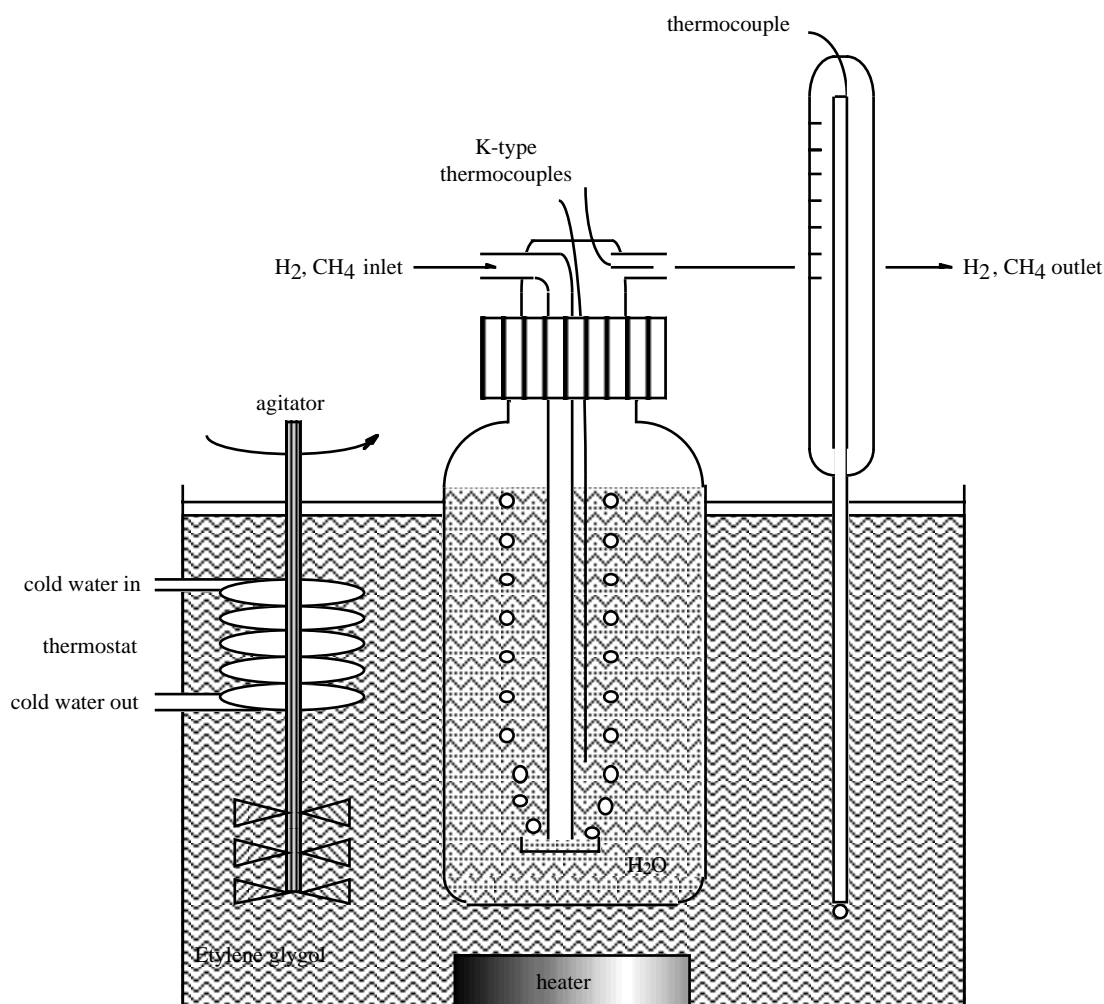


Figure 3: Schematic view of a thermostatted bubbler. The vapor pressure content is monitored by analysing its temperature with a thermocouple set at the gas outlet.

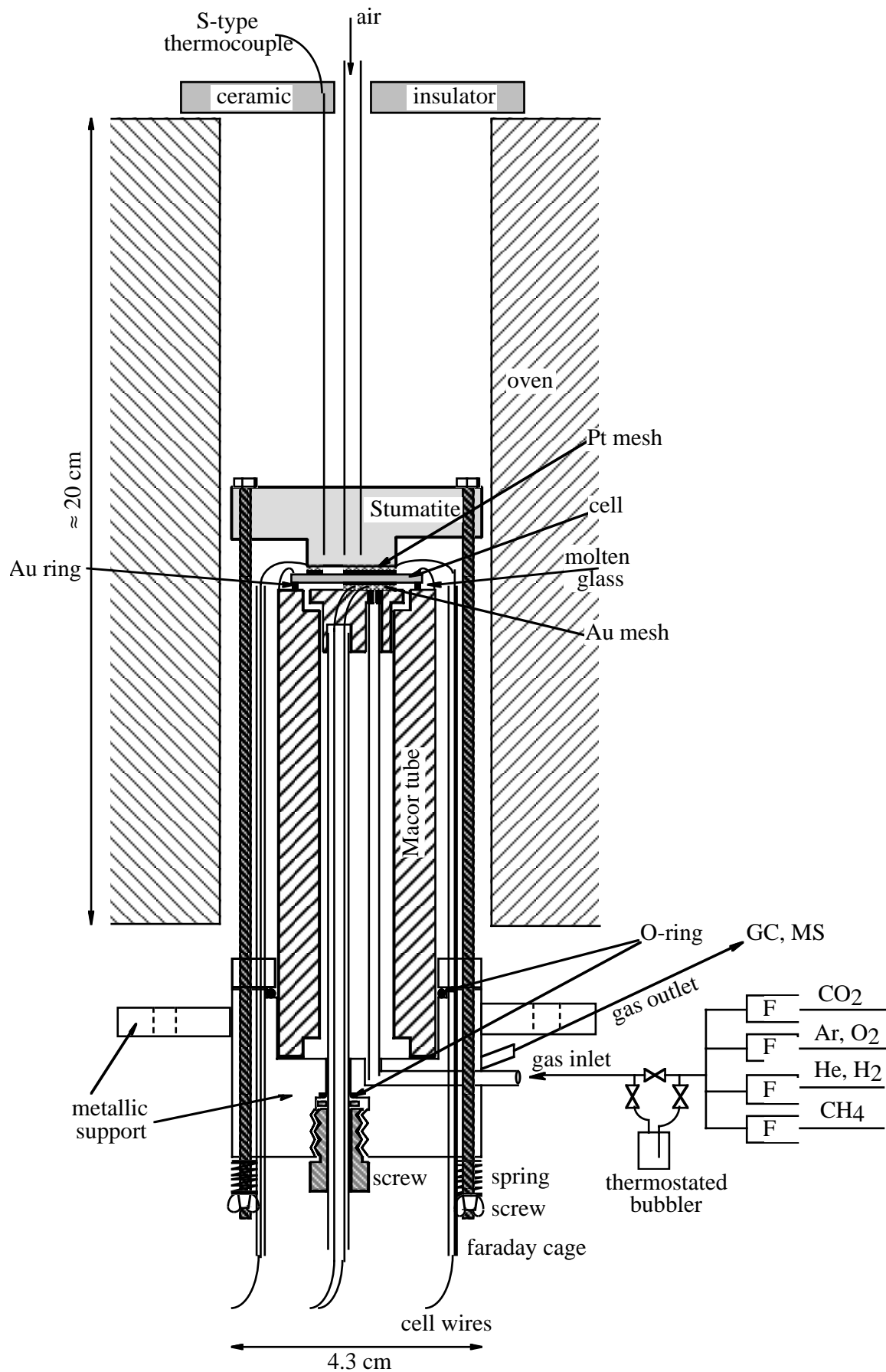


Figure 4: A schematic view of the sealed testing set-up (not on scale).

c. Symmetrical configuration

The circular cells (type c, Figure 1) were mounted in a horizontal quartz tube and electrical oven (Horst, Germany) and the electrical contacts to the cell were made using Au wires welded to the Au electroplated Pt current collectors (Figure 5). A K-type thermocouple, protected in a quartz tube was placed near the cell and served to monitor its temperature.

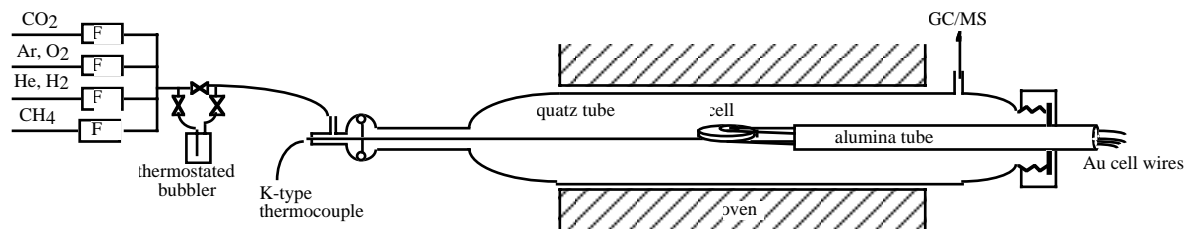


Figure 4: A schematic view of a symmetrical testing set-up (not on scale).

At all stages of the electrochemical characterization, current/potential (I/V) curves were performed on cells of type a and b with a Wenking potentiostat. Impedance spectroscopy was conducted on all cell types with an applied amplitude of 10 mV, using a modified IM5 Zahner impedance analyser. The frequency used ranged from 100 kHz to 40 mHz.

References

- (1) Van herle, J., Ph.D. Thesis Nr. 1187, Swiss Federal Institute of Technology Lausanne (EPFL), 1993.

Chapter 3 三

Synthesis, structure, characterization and electrical properties of LaCrO₃-based powders

Synthesis, structure, characterization and electrical properties of LaCrO₃-based powders

Abstract

Lanthanum or yttrium chromite-based compounds, substituted with Mg, Al, Ca, Mn, Fe, Co, Ni, Cu, Sr and Nb were synthesized by a modified citrate route from nitrate precursors. An optimal calcination temperature of 1100°C was necessary to obtain XRD-pure compounds. Residual, unidentified peaks of low intensity (<2%), not matching the usually admitted orthorhombic lattice structure of these perovskites were detected. However, compounds such as CaCrO₄, CaO, Cr₂O₃, β-CaCr₂O₄, Ca₃(CrO₄)₂, Ca₅(CrO₄)₃, Ca₅(CrO₄)₃O_{0.5} or La₂CrO₆, could not be accounted for by these small intensity peaks. At lower calcination temperatures, secondary phases such as CaCrO₄ and α-CaCr₂O₄ were detected by XRD. Some of the X-ray diffractogrammes were best fitted by considering a monoclinic symmetry rather than the orthorhombic one. When ball-milled, these powders had specific surface areas between 1 and 4.6 m²/g when calcined at 1100°C and 11~68 m²/g at 1000°C. The average particle size was between 0.8 and 3.6 μm. Pellets were made showing liquid phase sintering for the highly La-site substituted compounds, whereas the Cr-substituted LaCrO₃ showed enhanced densification due to the lowering of Cr activity. The electronic conductivity of these pellets was measured in both air and humidified H₂. Conductivities varied between 24 and 0.4 S/cm in air and 6.5 and 0.05 S/cm in humidified H₂, at 800°C. For electrode applications, ball-milling is very crucial to obtain compact and adherent structures.

Introduction / theory

LaCrO₃ belongs to the family of the perovskites^{1,2}. The ideal oxide perovskite-type structure, ABO₃, consists of a cubic array of corner-sharing BO₆ octahedra forming the skeleton of the structure, whose body center position is occupied by the A cation. The perovskite structure is thus a superstructure with the BO₃-type framework, formed by the introduction of A cations, which are generally larger than the B cations. B is a transition metal cation in the six-fold coordination, whereas A is either an alkali, an alkaline earth or a rare earth ion, in a twelve-fold coordination with the oxygen (see Figure 1). The lower limits for the ionic radii of A and B are of 0.9 Å and 0.51 Å in the oxides. On the basis of geometric considerations, a tolerance factor (or Goldschmidt factor) was defined as²

$$t_p = \frac{r_o + r_A}{\sqrt{2}(r_o + r_B)} \quad (1)$$

giving the distortion of the structure compared to the ideal cubic arrangement ($t_p=1$).

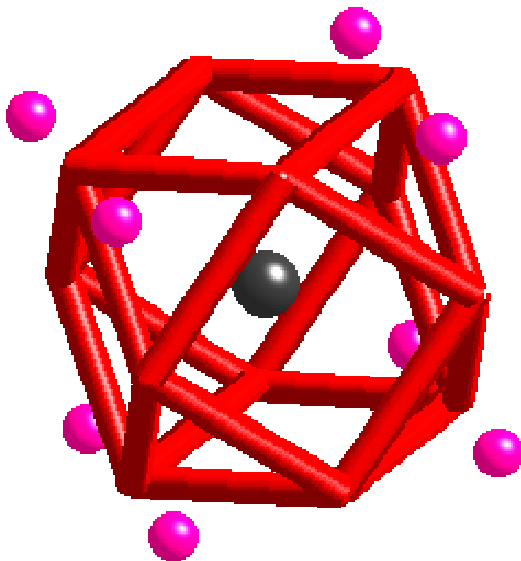


Figure 1: Ideal ABO₃ perovskite cubic structure: spheres on the corner of the cube correspond to Cr, the large atom in the center represent La, while the continuous lines represent the twelve-fold coordination of La with O. This structure was made using the CrystalMaker program.

When the distortion becomes too large, other crystal symmetries such as orthorhombic, rhombohedral or monoclinic appear. The perovskite lattice exists in oxides only between the limits $0.75 < t < 1$. For electroneutrality, the charge distribution in the perovskite can be of the form of $A^+B^{3+}O_3$, $A^{2+}B^{4+}O_3$ or $A^{3+}B^{3+}O_3$.

These materials are easily partially substituted on the A and B sites with alkali, alkaline earth, rare earth or transition metal ions while keeping the perovskite structure, which allows interesting modifications in their catalytic and electronic properties. Clearly, it is the stability of this structure that allows a large departure from stoichiometry. From literature, the stability of the perovskites follows the trend ²⁻⁴



Structural symmetry

At room temperature, LaCrO_3 appears in the orthorhombic crystal symmetry which is a distortion of the ideal cubic structure (see Figure 2). An orthorhombic to a rhombohedral, and a rhombohedral to cubic structural phase transition of LaCrO_3 occurs at around 260°C and 1600° respectively ⁵. The precise transition temperature depends largely on the A and B -site substituents (e.g. 305°C for $\text{LaCr}_{0.75}\text{Mn}_{0.25}\text{O}_3$ ⁶). This phase change causes changes in volume and also a change in the thermal expansion coefficient due to the contraction of the CrO_6 octahedra.

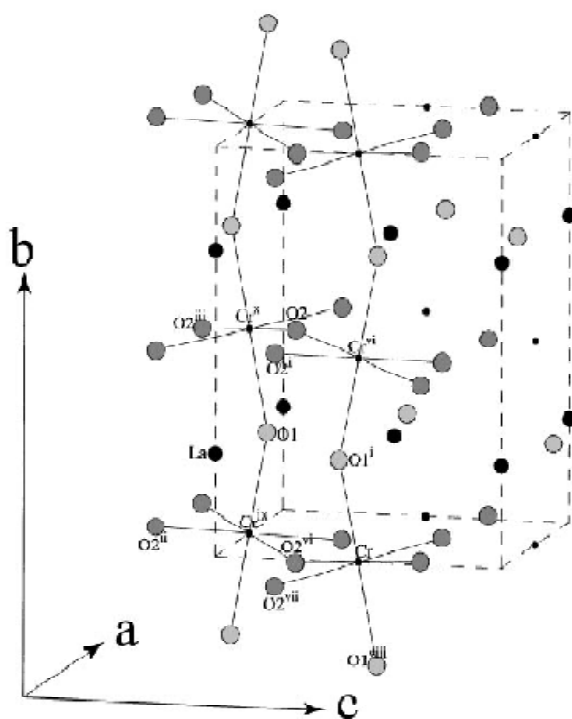
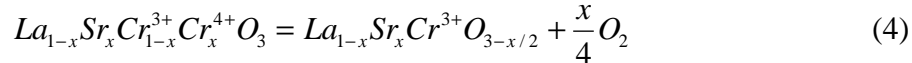


Figure 2: Crystal structure of LaCrO_3 for orthorhombic phase (space group: $Pnma$, 62). Large black, small black, and large gray circles represent La, Cr, O atoms respectively. Taken from Oikawa et al. ⁵.

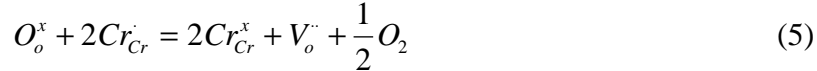
Conductivity

LaCrO_3 -based compounds are semiconductors. Thermogravimetric studies have indicated that in LaCrO_3 the native nonstoichiometric ionic defects are cation vacancies, leading to oxygen-excess stoichiometries ². The conductivity mechanism of substituted LaCrO_3 is consistent with the hopping of polarons in a defect band of localized states at the Fermi energy with a thermopower essentially independent of temperature ⁷. Indeed, by introducing elements such as Ca, Sr, Mg and the transition metals on the La and Cr sites, the substitution being dependent on the ionic radius of the substituent, electronic compensation occurs by the formation of holes at high oxygen partial pressure, i.e. the oxidation of Cr^{III} to Cr^{IV} , or of oxygen vacancies at low P_{O_2} (for some substituents even in air, e.g. Mg ⁸). Thus, p -type

conductivity is dominant in air while the ionic conductivity increases upon reduction. This is best illustrated with Sr substitution



The corresponding defect equilibrium following the *Kröger-Vink* notation is given by



where O_o^x is an oxygen ion in the lattice, $Cr_{Cr}^{\cdot} = Cr^{IV}$, $Cr_{Cr}^x = Cr^{III}$ and $V_o^{\cdot\cdot}$ an oxygen vacancy. The reduction of Cr^{IV} to Cr^{III} leads to a decrease in overall conductivity of the perovskite as it is mainly induced by the holes concentration. The hole conductivity is slightly thermally activated and given by⁸

$$\sigma = \frac{\sigma_o}{T} e^{\frac{-E_a}{RT}} \quad (6)$$

where E_a is the activation energy, R the gas phase constant, T the temperature and σ_o the pre-exponential factor. σ_o can be expressed as^{9,10}

$$\sigma_o = \left(\frac{e^2 a^2}{6k\tau_o}\right)[Cr^{3+}][Cr^{4+}] \quad (7)$$

where e is the elementary electric charge, a the distance of hopping, k the Boltzmann factor, τ_o the average free time (i.e. the inverse of the jump attempt frequency), and $[Cr^{3+}]$ and $[Cr^{4+}]$ the mole fraction of the Cr species. It is worth noting that *n*-type conductivity can also be introduced in LnCrO₃-based perovskites, by doping with elements with high valencies, such as Ti and Nb¹¹.

Preparation

The results of the catalytic activity are reported to be affected by the presence of oxide admixtures and crystallinity^{12,13}. The preparation conditions were in many cases responsible for the structural differences and thus for the differences in the catalytic properties of oxides. A number of methods have been used in the synthesis of perovskites. Some are based on *solid-solid reactions* and some on *liquid-solid reactions*.

In the *solid-solid reactions* method, physical mixtures of single oxide components or other adequate precursors are calcined at high temperatures (>1000°C). Consequently surface areas of perovskites prepared by this route are very low. Another drawback is the lack of homogeneity of the sintered solid so that repeated grinding and firing steps are required¹. An alternative to that could be *microwave synthesis*. Iwasaki et al.¹⁴ reported the microwave synthesis of LaCrO₃ at a temperature of only 440°C reached during very short times (15 min), which is much lower than for the conventional synthesis route (>1200°C), giving rise to a relatively fine powder with a size distribution of 0.4-3.2 μm.

In the *liquid-solid reactions* method, many techniques are available. The simplest method is *dry evaporation*. Using nitrate precursors, LaCrO₃ was synthesized at 1000°C for 24 h leading to a powder of 0.8 m²/g¹⁵. The *explosion method* uses the properties of ammonium nitrate or glycine which is then dry-evaporated giving rise to powders of 30 m²/g after vacuum decomposition at 300°C and calcination in oxygen at 500°C^{1,16}. However, this method leads to inhomogeneities. Another technique is *freeze-drying* which is probably the physical method that preserves most the homogeneity originally present in the solution. Fierro et al.¹⁷ used this method for the synthesis of LaCrO₃, freeze-dried from nitrate precursors at -55°C under vacuum, then heated in air at 650°C for 80 h to yield powders of a *BET* surface area of ≈ 4 m²/g. *Crystallization* of complexes such as oxalates is also a method which is expected to give extremely homogeneous mixed oxide precursors, but the difficulty of preparing the complexes restricts its use. *Coprecipitation* is also similar but some ions do not precipitate in the same pH region¹⁸. *Hydrothermal synthesis* was also used for LaCrO₃ using an autoclave heated at 260°C for 7 days, and the product had a narrow particle size distribution in the range of 1-3 μm¹⁹. *Complexation* in the form of amorphous compounds with a vitreous structure is another chemical procedure which preserves as much as possible the homogeneity present in the

solution. In perovskite-based compounds, this technique is widely used due to the ease of handling and manufacturing. It uses the complexing properties of hydroxyacids, in particular citric acid²⁰. The intermediate complexes in LaCrO₃ are thought to be of the form La[Cr(C₆H₅O₇)₂].2H₂O. Powders of 5 to 7 m²/g surface area were obtained after a calcination step at 1100°C²¹.

The aim of the present chapter

Due to the convenience of the citrate route, we chose this method for the synthesis of the (Y,La)CrO₃-based compounds substituted with Mg, Al, Ca, Mn, Fe, Co, Ni, Cu, Sr and Nb. Hereafter, the synthesis is discussed on the basis of X-ray powder diffraction analysis and the physical characteristics of these powders (i.e. size distribution, surface area and conductivity) are evaluated. Finally, trials were made to produce and stick layers of these compounds over YSZ electrolyte sheets.

Experimental

Powder preparation

Different lanthanum chromite powders were prepared according to the formula La_{1-α}A_αCr_{1-β}B_βO₃ through a modified citrate route, by dissolving the nitrate precursors (Fluka, >99% purity except for Cr(NO₃)₃.9H₂O from Acros, 99%) in 1M aqueous citric acid solution in a ratio of 1:1.2. Most of the water was removed by heating at 80-90°C in vacuum. The gels obtained were heated at 110°C for 20 h, then at 200°C for 2 h and the resulting powders were crushed to size by dry ball-milling. Different calcination temperatures were adopted in order to follow the crystallinity and purity of the final compounds. Different elements were used as substituents: Mg, Al, Ca, Mn, Fe, Co, Ni, Cu, Sr, Nb, Y and La. Al was implemented in a trial to reduce the expansion coefficient of the LaCrO₃ compound. In the case of Nb, Nb₂O₅ (Fluka) was dispersed in the gel solution prior to the firing. La_{0.8}Sr_{0.2}Cr_{0.97}V_{0.03}O₃ powder was obtained from IRD/Denmark in the framework of an European Brite/Euram project.

XRD spectra were acquired on a Siemens D500 diffractometer using CuKα radiation. In some cases, phase indexation was undertaken from XRD analysis using the Appleman unit cell refinement method. Surface area was measured using a BET Micrometrics Gemini 2375 apparatus (N₂ adsorption at 77K). The particle size distribution was measured in a Horiba CAPA-700 analyzer.

Conductivity measurements

LaCrO₃-based compounds were pressed to rods of 13x6x5 mm³ at 100 MPa and sintered at 1500°C for 4 h. The pellets thus obtained were polished with μm diamond paste. *dc* four probe conductivity measurements were carried out in the same set-up as for the symmetrical cell configuration (see Chapter 2), in air, CO/CO₂ mixtures and humidified hydrogen, using Ag paste and Ag leads as current and potential leads. The oxygen partial pressure was monitored by a home-built YSZ sensor placed near the sample.

Adhesion and morphologies of electrodes

Terpineol-ethyl cellulose-based slurries were prepared as described in Chapter 2. 1 cm² electrodes were screen-printed over 8YSZ sheets and sintered at 1000°C, 1050°C, 1100°C, or 1200°C for 4h. Subsequently, the electrodes were treated overnight at 800°C under a flow of H₂ + 3% H₂O. SEM cross-section images were made before and after hydrogen treatment in order to analyze the electrode morphologies.

Results

Powder XRD analysis

Calcination tests were made at 500, 900, 1000, 1100 and 1200°C for 4 h for La_{0.7}Ca_{0.32}CrO₃ and La_{0.85}Sr_{0.15}CrO₃ citrate gels decomposed at 200°C. For each temperature, XRD analyses

were performed (Figures 3 and 4). The powders calcined at 500°C were not pure phase perovskites and contained secondary phases such as CaCrO_4 , $\alpha\text{-CaCr}_2\text{O}_4$ and SrCrO_4 . These three phases persisted until 1000°C , a temperature above which the powders were observed to be made of a single phase. These results are consistent with what has been recently published in literature²². Ca-substituted compounds seemed to be made of one phase already at 1000°C , whereas it was necessary to go to 1100°C for Sr substitution. 1100°C is thus taken to be the best calcination temperature for these oxides. Figure 5 shows the XRD patterns for other LaCrO_3 -based powders. All oxidized powders were indexed following the orthorhombic crystal symmetry (see Appendix for XRD charts of the most important powders of our study).

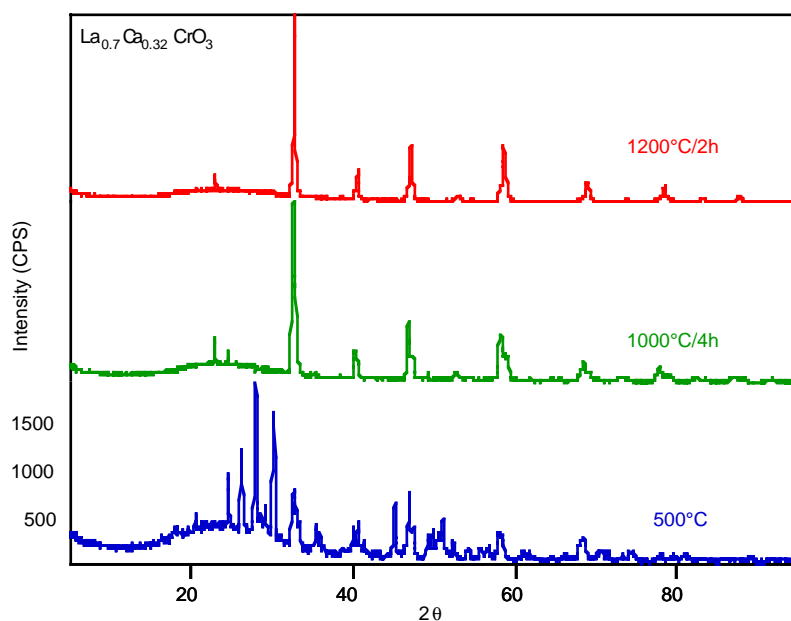


Figure 3: XRD patterns for the $\text{La}_{0.7}\text{Ca}_{0.32}\text{CrO}_3$ powder sintered at 500, 1000 and 1200°C for 4 h. CPS: arbitrary units.

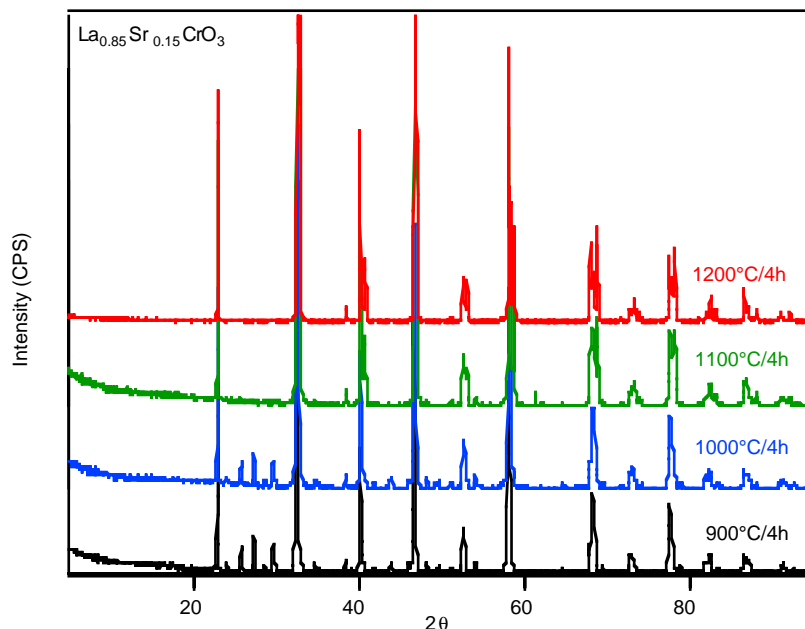


Figure 4: XRD patterns for the $\text{La}_{0.85}\text{Sr}_{0.15}\text{CrO}_3$ powder sintered at 900, 1000, 1100°C and 1200°C for 4 h. CPS: arbitrary units.

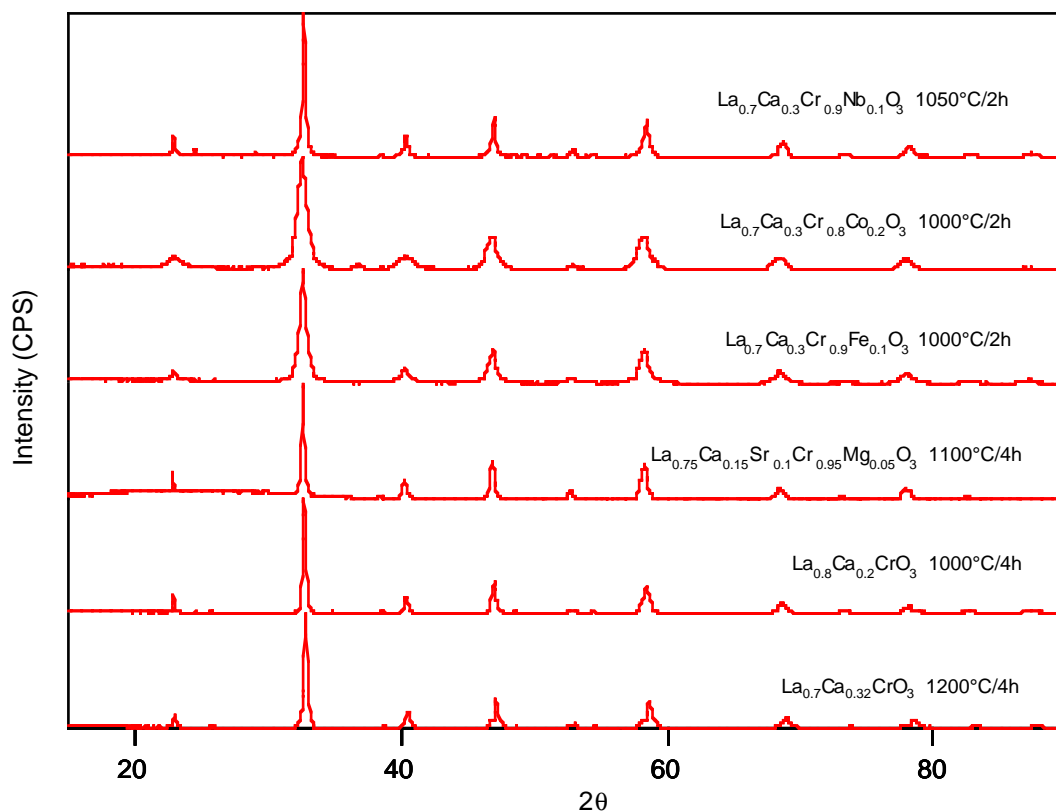


Figure 5: XRD patterns for other calcium substituted LaCrO_3 powders. CPS: arbitrary units.

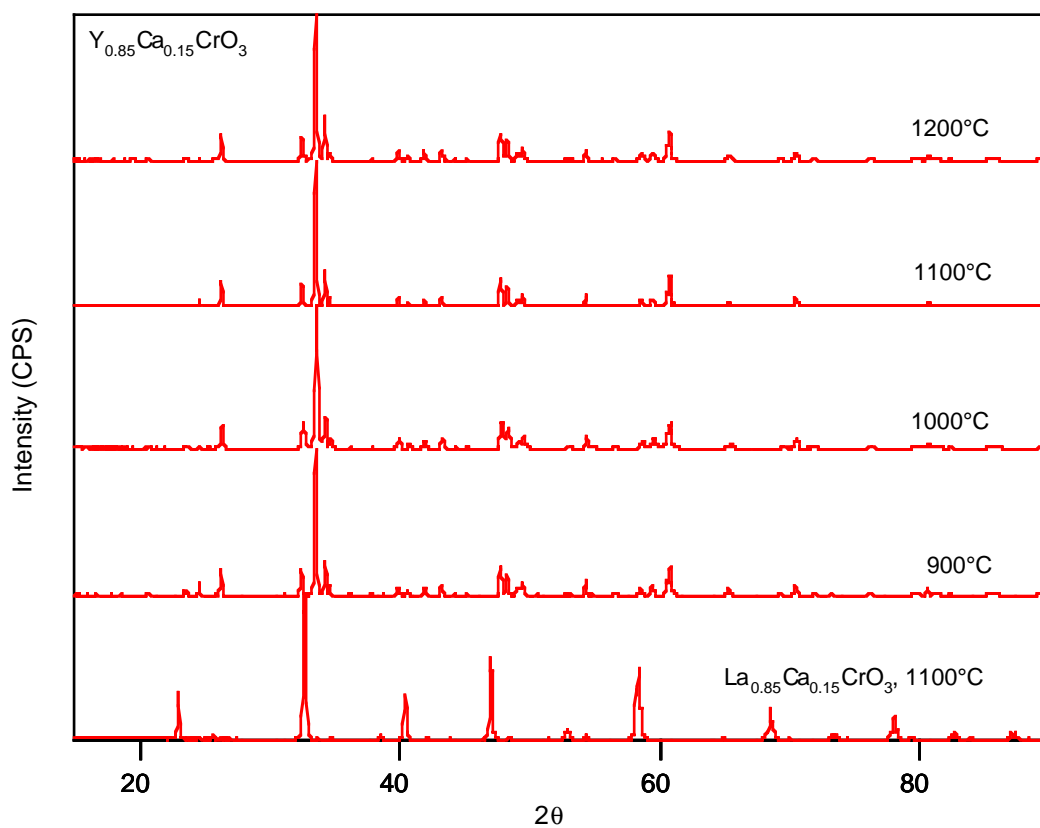


Figure 6: XRD patterns for calcium substituted YCrO_3 powders sintered at 900, 1000, 1100 and 1200°C for 4h. $\text{La}_{0.85}\text{Ca}_{0.15}\text{CrO}_3$ is given as a reference. CPS: arbitrary units.

La_{0.85}Ca_{0.15}CrO₃, La_{0.85}Ca_{0.15}Cr_{0.9}Mg_{0.1}O₃, La_{0.85}Sr_{0.15}CrO₃ and La_{0.85}Sr_{0.15}Cr_{0.9}Mg_{0.1}O₃ were best fitted by the monoclinic crystal symmetry. Such an indexation is also seen for lanthanum manganite according to the *JCPDS* (Joint Committee for Powder Diffraction Society, also known as *PDF*, Powder Diffraction File, edited by the *ICDD*, International Center for Diffraction Data) charts. Sr substituted LaCrO₃²² was reported to have a rhombohedral crystal symmetry. Also, in some cases, residual, low intensity (<2%), unidentified peaks, not matching the lattice structure of these perovskites were detected.

Ca substituted yttrium chromites were also produced but none of them gave the pure phase (Figure 6). Secondary phases such as CaCrO₄ and Cr₂O₃ were observed at all calcination temperatures from 900°C to 1200°C. YCrO₃ is known to be less affected by reduction than LaCrO₃²³. However, due to these secondary phases, the work with Y was discontinued and no optimization was undertaken. All synthesized LaCrO₃-based powders are summarized in Table 1. When reduced, the orthorhombic phase turned into the rhombohedral symmetry. This is a known feature for many LaCrO₃-based oxides²⁴ (see example in Appendix). From literature, an orthorhombic to rhombohedral phase transformation is expected to occur between 750 and 850°C for A and B-site double substitution²².

Table 1: Surface area and average particle size for the LaCrO₃-based powders.

Powder composition	surface area	particle size
	[m ² /g]	[μm]
La _{0.7} Ca _{0.32} CrO ₃	2.0	3.6
La _{0.7} Ca _{0.3} CrO ₃	-	-
La _{0.7} Ca _{0.3} Cr _{0.9} Fe _{0.1} O ₃	68	-
La _{0.7} Ca _{0.3} Cr _{0.9} Co _{0.2} O ₃	31	-
La _{0.7} Ca _{0.3} Cr _{0.9} Cu _{0.1} O ₃	13	-
La _{0.7} Ca _{0.3} Cr _{0.9} Nb _{0.1} O ₃	11	-
La _{0.75} Ca _{0.15} Sr _{0.1} Cr _{0.95} Mg _{0.05} O ₃	1.4	3.8
La _{0.2} Sr _{0.8} Cr _{0.2} Fe _{0.8} O ₃	3.4	4.5
La _{0.95} Mg _{0.05} Cr _{0.75} Al _{0.25} O ₃	4.3	5
La _{0.8} Ca _{0.2} CrO ₃	-	5.9
La _{0.85} Ca _{0.15} CrO ₃	2.6	0.9
La _{0.85} Ca _{0.15} Cr _{0.9} Mg _{0.1} O ₃	1.0	2.6
La _{0.85} Ca _{0.15} Cr _{0.9} Ni _{0.1} O ₃	1.5	1.8
La _{0.85} Sr _{0.15} CrO ₃	2.7	1.0
La _{0.85} Sr _{0.15} Cr _{0.9} Mg _{0.1} O ₃	1.8	2.3
La _{0.8} Sr _{0.2} Cr _{0.97} V _{0.03} O ₃ *	4.6	0.7
LaCrO ₃	2.8	0.8
LaCr _{0.9} Mg _{0.1} O ₃	3.0	1.3
LaCr _{0.9} Mn _{0.1} O ₃	2.3	1.6
LaCr _{0.9} Fe _{0.1} O ₃	2.0	1.1
LaCr _{0.9} Co _{0.1} O ₃	1.4	2.1
LaCr _{0.9} Ni _{0.1} O ₃	1.4	2.1
LaCr _{0.5} Ni _{0.5} O ₃	-	-
Y _{0.85} Ca _{0.15} CrO ₃	-	-

* obtained from IRD, Denmark, within the framework of the European Brite/Euram project BRPR-CT97-0413.

Powder characterization

Powder size distribution and surface area measurements were made for these powders. For measuring the powder size distribution, the powders were dispersed in an aqueous solution of 0.2% Na₄P₂O₇ for the very fine powder (<10 μm) or in ethylene glycol for coarser grains (for >10 μm). Table 1 summarizes these values. Surface areas varied in a narrow window of 1 to 6 m²/g, for the powders calcined at 1100°C (except La_{0.7}Ca_{0.3}Cr_{0.9}Fe_{0.1}O₃, La_{0.7}Ca_{0.3}Cr_{0.9}Co_{0.2}O₃, La_{0.7}Ca_{0.3}Cr_{0.9}Cu_{0.1}O₃ and La_{0.7}Ca_{0.3}Cr_{0.9}Nb_{0.1}O₃ sintered at 1000°C) and are comparatively

lower than the 5 to 7 m²/g reported in literature ²¹ for LaCrO₃ using the same fabrication technique and calcination temperature.

Conductivity

Sintered pellet densities of the different lanthanum chromites varied with the nature of the incorporated element, the substitution of Cr giving rise to a better densification ^{25, 26}. Compared to the XRD calculated density, unsubstituted LaCrO₃ gave low density pellets (63%), whereas the incorporation of Mn, Ni, Co and Mg increased the density to about 97, 95, 94 and 90% respectively. Ca and Sr had less effect in this regard, giving 71 and 67% relative density respectively. Ca excess had an effect on the sinterability as La_{0.7}Ca_{0.32}CrO₃ gave rise to 97% density. A double substitution on the A-site with Ca or Sr and the B-site with Mg or Ni showed an enhanced effect on densification – 97, 98 and 98.5% respectively for La_{0.85}Sr_{0.15}Cr_{0.9}Mg_{0.1}O₃, La_{0.85}Ca_{0.15}Cr_{0.9}Ni_{0.1}O₃, and La_{0.85}Ca_{0.15}Cr_{0.9}Mg_{0.1}O₃. Thus, it is seen that upon the incorporation of elements such as Mg, Mn, Co and Ni, all B-site substituents, the density is enhanced. This effect could be related to the lowered activity of Cr and thus the lowered CrO_x species volatilities which are responsible for the bad sintering of LaCrO₃-based compounds ²⁶. B-site substituent effect was also observed in literature ^{22, 27, 28}. Some of these results are summarized in Table 2.

Table 2: Summary of the conductivity measurements in air and humidified H₂, as well as the XRD characteristics of lanthanum chromite powders.

Pellet composition	Conductivity σ^1 [S/cm]				XRD V [Å ³]	M [g/mol]	d_{theo} [g/cm ³]	pellet % d_{theo}
	air	H ₂ ²	E_a^3 [kJ/mol]					
La _{0.7} Ca _{0.32} CrO ₃	24	0.8	10.98	18.42				97
La _{0.75} Ca _{0.15} Sr _{0.1} Cr _{0.95} Mg _{0.05} O ₃	11	0.5	-	-				95
La _{0.85} Ca _{0.15} CrO ₃	16.01	2.18	5.20	5.47	232.62	224.08	6.40	71
La _{0.85} Ca _{0.15} Cr _{0.9} Mg _{0.1} O ₃	9.65	0.34	13.68	33.82	228.24	221.31	6.44	99
La _{0.85} Ca _{0.15} Cr _{0.9} Ni _{0.1} O ₃	14.76	1.91	9.64	32.28	231.78	224.74	6.44	98
La _{0.85} Sr _{0.15} CrO ₃	-	-	-	-	232.72	231.21	6.60	67
La _{0.85} Sr _{0.15} Cr _{0.9} Mg _{0.1} O ₃	14.73	1.27	6.55	6.46	229.24	228.44	6.62	97
La _{0.8} Sr _{0.2} Cr _{0.97} V _{0.03} O ₃ ⁴	23.78	6.52	5.68	15.08		228.61		
LaCrO ₃	0.42	0.05	6.46	34.98	234.94	238.90	6.75	63
LaCr _{0.9} Mg _{0.1} O ₃	5.11	0.16	16.38	36.72	235.40	236.13	6.66	91
LaCr _{0.9} Mn _{0.1} O ₃	5.43	0.56	17.44	19.85	234.86	239.19	6.76	97
LaCr _{0.9} Fe _{0.1} O ₃	-	-	-	-	235.85	239.28	6.74	-
LaCr _{0.9} Co _{0.1} O ₃	5.84	0.63	20.14	29.97	233.15	239.59	6.82	94
LaCr _{0.9} Ni _{0.1} O ₃	5.41	0.39	7.32	16.58	234.87	239.57	6.77	95
LaCr _{0.5} Ni _{0.5} O ₃	-	-	-	-	233.56	242.25	6.89	-
LaCr _{0.5} Ni _{0.5} O ₃ ⁵	-	-	-	-	349.94	242.25	6.89	-

¹The conductivity has been corrected for the density (see text). ²The P_{O₂} in wet H₂ at 800°C was of 8x10⁻²¹ atm as measured by a home-made YSZ oxygen gas sensor. ³The conductivity was measured between 700 and 900°C. ⁴This powder, calcined at 1000°C, was obtained from IRD, Denmark, within the framework of the European Brite/Euram project BRPR-CT97-0413; by powder-XRD we observed the presence of secondary phases. ⁵The reduced powder at 780°C, in humidified H₂, is rhombohedral. All the other are oxidized, thus orthorhombic.

The conductivity trend observed is comparable to values extrapolated from literature data ²⁹ (Table 3) and followed the concentration of Cr^{IV}, except for LaCr_{0.9}Ni_{0.1}O₃ which is reported to have higher conductivities in air than in our study. Ca or Sr substitution (A-site) gave rise to a higher conductivity in air and in humidified H₂ than B-site substitution, perhaps due to the increase in the hopping distance, as part of the Cr is replaced by another element. Also, as the reduction of the perovskites proceeds, the change in the Cr valence induces an increase in the linear expansion coefficient of the lattice ²⁹, a phenomena which could cause the delamination of LaCrO₃-based electrodes from the surface of a YSZ electrolyte. A summary of available literature values for the thermal expansion coefficients is given in Table 3.

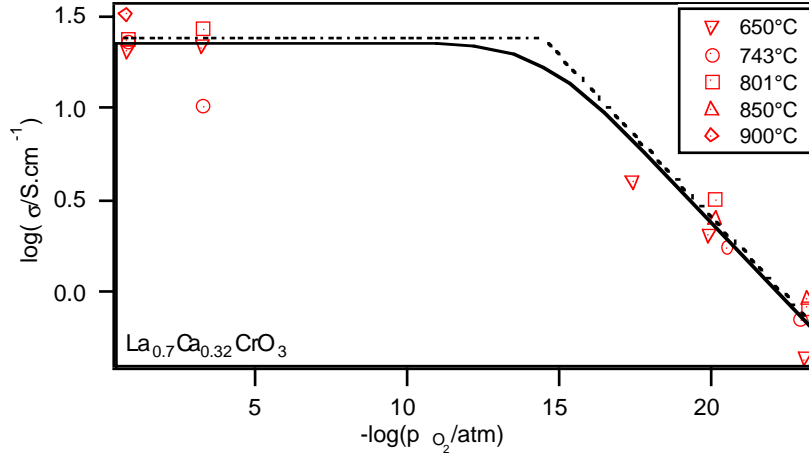


Figure 7: Evolution of the total conductivity with the oxygen partial pressure and temperature. Case of La_{0.7}Ca_{0.32}CrO₃. The effect of temperature is very small. The solid line represents the expected trend of the conductivity¹⁰.

By introducing elements such as Ca, Sr and the transition metals on the La and Cr sites in LaCrO₃, the substitution on the A or B-site depending on the ionic radius of the element, electronic compensation occurs by the formation of holes at high oxygen partial pressure, i.e. the oxidation of Cr^{III} to Cr^{IV}, or of oxygen vacancies at low P_{O₂}²⁹. Thus, upon reduction, the ionic conductivity tends to increase as a consequence of the increasing concentration of oxygen vacancies. However the total conductivity decreases due to the decrease of the hole concentration (see Figure 7 for the case of La_{0.7}Ca_{0.32}CrO₃). Activation energies tend to be higher in reducing atmospheres.

Table 3: Summary of the literature data on similar compositions measured at 1000°C. Also given are the thermal expansion coefficients (TEC) as well as the % linear expansion when the pellet is reduced from air to wet H₂.

Pellet composition	Properties		Conductivity [Ω /cm]		TEC 10 ⁻⁶ /K	% Linear expansion	references
	air	wet H ₂		$E_{a, air}$			
La _{0.9} Ca _{0.1} CrO ₃	12.1-20	1.2-2.7					30,31
La _{0.85} Ca _{0.15} CrO ₃	23					0.12	32,29
La _{0.8} Ca _{0.2} CrO ₃	35.5-40	1.9-4.8				0.2	30,31,29
La _{0.7} Ca _{0.3} CrO ₃	45.7-56	1.9-4.4				0.35	30,31,29
La _{0.9} Sr _{0.1} CrO ₃	8.5	2.1			9.8		30, 33
La _{0.85} Sr _{0.15} CrO ₃	10-20			11.3	10		28, 34
La _{0.8} Sr _{0.2} CrO ₃	16-36.6	6.4				0.17	30,33,29
La _{0.7} Sr _{0.3} CrO ₃	41.5	4.9					30
LaCrO ₃	2.5			7.5	9.5	0	32, 34,29
LaCr _{0.95} Mg _{0.05} O ₃	1.9	1.25					32
LaCr _{0.9} Mg _{0.1} O ₃	5.6	0.27			9.5		32,29
LaCr _{0.8} Mg _{0.2} O ₃	5.9	0.39					30
LaCr _{0.9} Mn _{0.1} O ₃						0.25	29
LaCr _{0.9} Co _{0.1} O ₃					13.1	0.22	32,29
LaCr _{0.9} Ni _{0.1} O ₃	30			9.6		0.24	34,29
LaCr _{0.8} Ni _{0.2} O ₃	57.7			11.2			34
LaCr _{0.7} Ni _{0.3} O ₃	81.8			10			34
La _{0.15} Sr _{0.15} Cr _{0.95} Ni _{0.05} O ₃	38.3			14.3	10.3		28
La _{0.8} Sr _{0.2} Cr _{0.95} Ni _{0.05} O ₃	36.9	1.58					10
La _{0.8} Sr _{0.2} Cr _{0.97} V _{0.03} O ₃	30	12*					35
YSZ					10.3		32

*measured in wet hydrogen at an oxygen partial pressure of 10⁻¹⁶ atm.

Due to the differences in rod densities, all conductivity measurements were normalized for a 100% pellets density by using the approximation

$$d_{eff}/d_{theo} = \sigma_{eff}/\sigma_{theo} \quad (6)$$

where d_{eff} and σ_{eff} are the measured density and conductivity respectively and d_{theo} and σ_{theo} the theoretical density (XRD) and conductivity respectively.

Importantly, no changes were observed for the different pellets before and after the conductivity tests by XRD analysis, indicating that these compounds withstand well the highly reductive conditions used in SOFC. An example is given in Figures 8 and 9 for the $\text{La}_{0.75}\text{Ca}_{0.15}\text{Sr}_{0.1}\text{Cr}_{0.95}\text{Mg}_{0.05}\text{O}_3$ and $\text{LaCr}_{0.9}\text{Ni}_{0.1}\text{O}_3$ systems respectively.

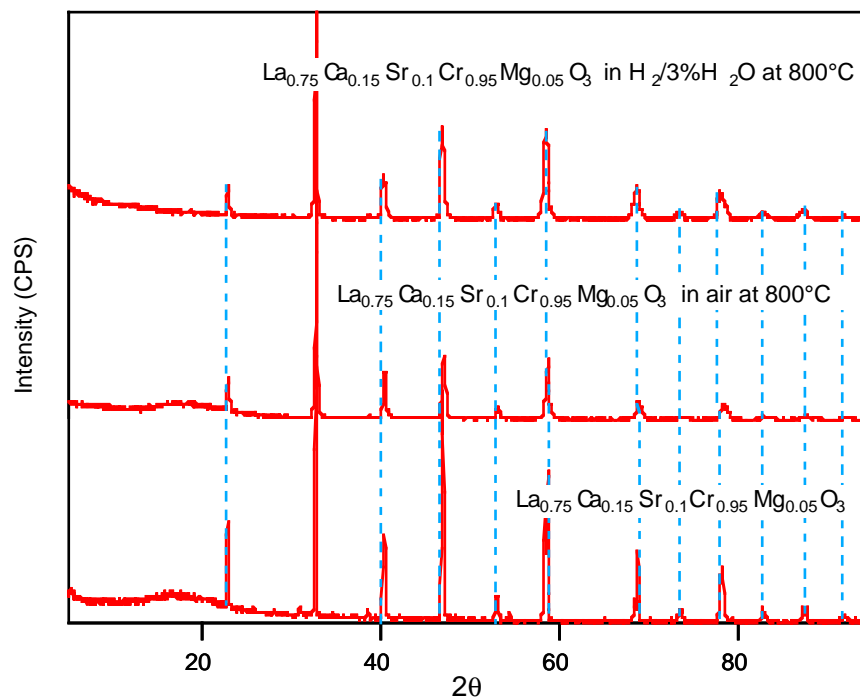


Figure 8: XRD of $\text{La}_{0.75}\text{Ca}_{0.15}\text{Sr}_{0.1}\text{Cr}_{0.95}\text{Mg}_{0.05}\text{O}_3$ pellets, after sintering at 1500°C , after conductivity tests in air, and after conductivity test in humidified H_2 . No changes were observed in the XRD patterns.

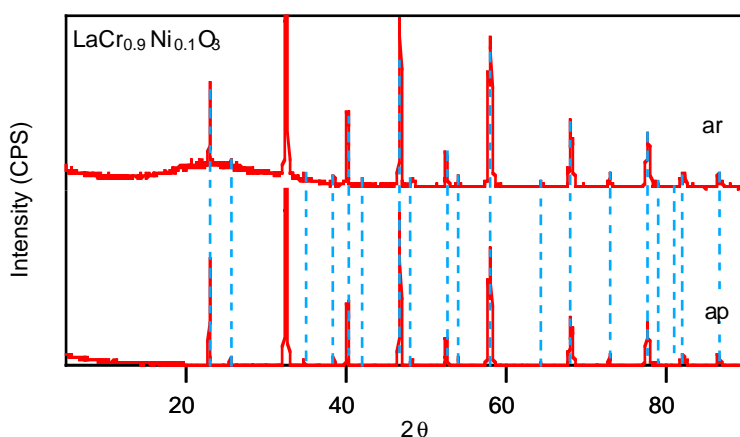


Figure 9: XRD of $\text{LaCr}_{0.9}\text{Ni}_{0.1}\text{O}_3$ powders, ap: as prepared at $1100^\circ\text{C}/4\text{h}$ and ar. after reduction in humidified H_2 . No changes in the XRD patterns are observed.

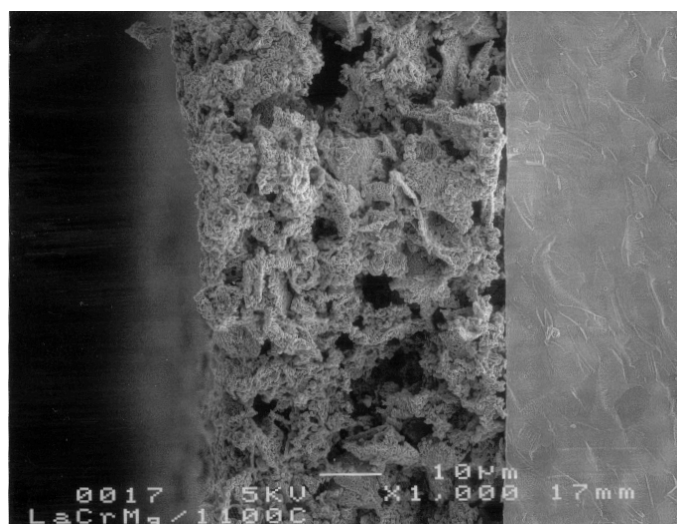


Figure 10: $\text{La}_{0.75}\text{Ca}_{0.15}\text{Sr}_{0.1}\text{Cr}_{0.95}\text{Mg}_{0.05}\text{O}_3$ anode made of unground powders, showing a very loose structure. Sintering temperature: 1100°C/4h.

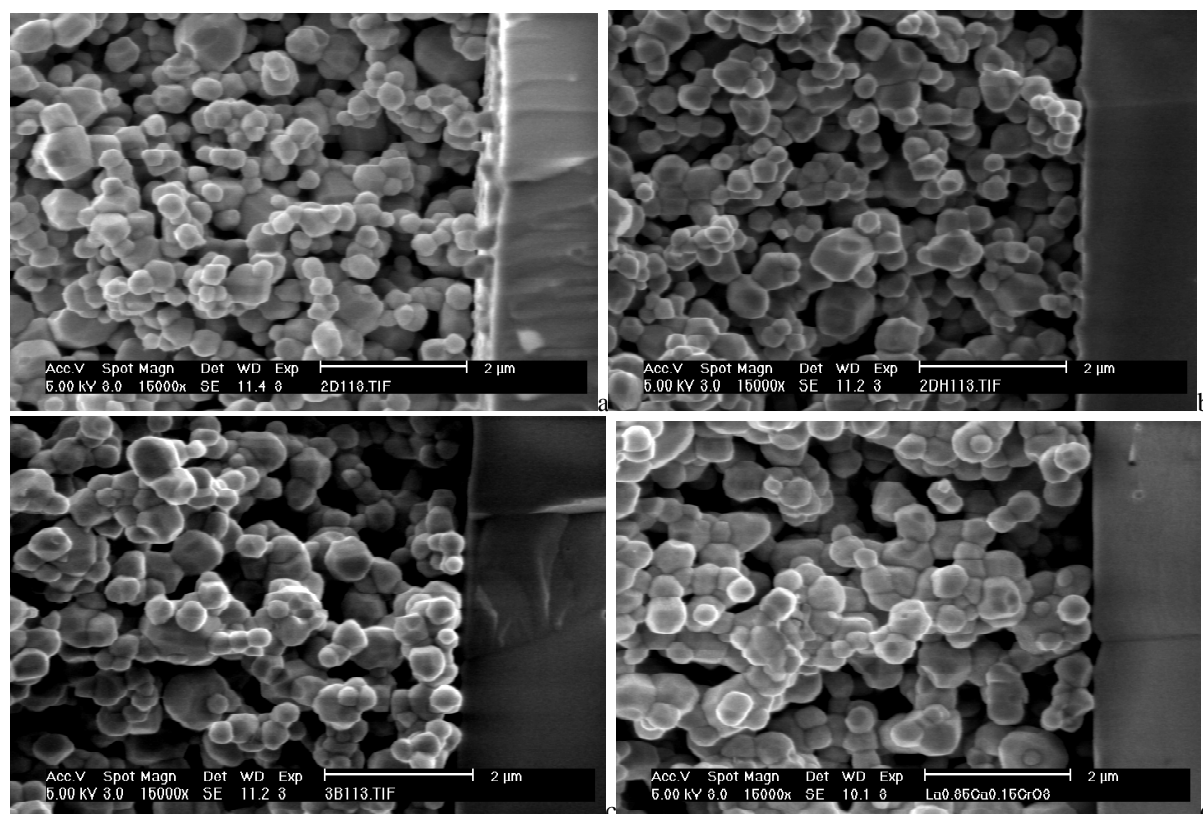


Figure 11: Electrode morphologies for a-b. $\text{La}_{0.85}\text{Sr}_{0.15}\text{CrO}_3$ and c-d. $\text{La}_{0.85}\text{Ca}_{0.15}\text{CrO}_3$ as sintered in air at 1100°C (a and c) and after treatment in humidified H_2 (b and d).

Adhesion and morphologies of electrodes

The adhesion and the morphology of the different electrodes were observed to depend on the powder handling. A grinding step is necessary to break the sheet-like structures originating from the citrate synthesis, as the contact to YSZ was poor (Figure 10). The grinding allows a better surface coverage of the powder on YSZ (Figure 11). The adhesion was observed to depend also on the Ca or Sr substitution levels in LaCrO₃. A-site highly substituted LaCrO₃ adhered much better than the others. By lowering the Ca substitution level from 0.32 to 0.2 or 0.15 it was observed that the sticking decreased. This could be due to surface reaction (see Chapter 4 and 5) as also observed for lanthanum strontium manganites. B-site substituted LaCrO₃ tend to stick less on YSZ when no Ca or Sr is added on the A-site.

The higher the sintering temperature the better is the adhesion. However, above 1100°C, some surface reaction is observed between the electrode and the YSZ. This reaction is easily observed under SEM for the samples with high level of Ca or Sr substitution (e.g. Figure 12, for La_{0.7}Ca_{0.32}CrO₃) or at high temperature for low substitution levels (e.g. Figure 12, for the La_{0.85}Ca_{0.15}CrO₃). Thus, the optimal sintering temperature was observed to be around 1100°C.

When treated in humidified H₂, the sintered electrodes did not present any change in their structure (see Figure 11). Adhesion was not altered.

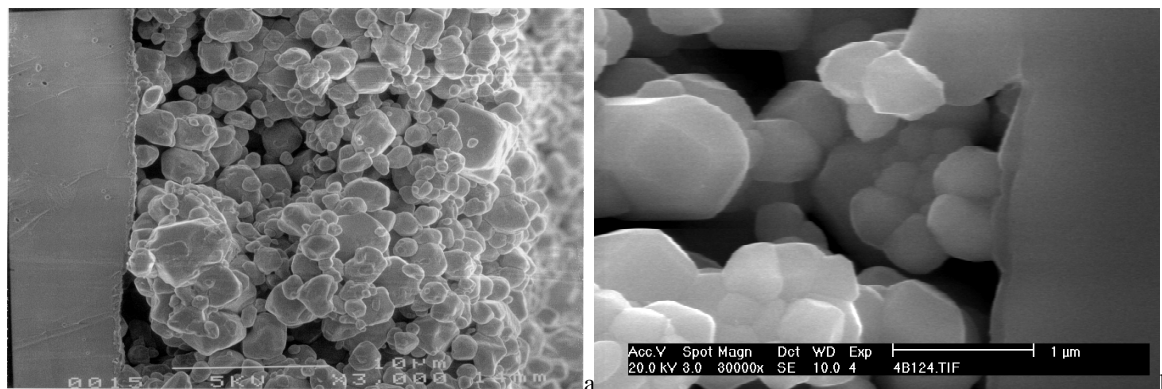


Figure 12: a. La_{0.7}Ca_{0.32}CrO₃ electrode sintered at 1150°C/4h. Some surface reaction is apparent between the electrode and the 8YSZ electrolyte. b. La_{0.85}Ca_{0.15}CrO₃ electrode sintered at 1200°C/4h. EDAX analysis reveal 16% Ca / 40% La / 44% Cr in the visible layer at the interface.

Conclusions

22 different lanthanide chromite-based compositions were produced following a modified citrate route. Different substituents were used: Mg, Al, Ca, V, Mn, Co, Ni, Cu, Sr and Nb. An optimal calcination temperature of 1100°C was necessary to produce single phase compounds. Powers of 1 to 6 m²/g and 0.7 to 6 µm average size were thus obtained. In most cases, residual, unidentified peaks of low intensity (<2%), not matching the usually admitted orthorhombic lattice structure were detected. Conductivity pellets made of some of these compositions sintered at 1500°C showed a conductivity of 5 to 24 S/cm in air versus 0.2 to 6 S/cm in humidified H₂. It was observed that high A-site and mild B-site substitution gave rise to high conductivity and densification. A-site substitution with Ca or Sr is necessary to reach high conductivities. Equivalently, ball-milled powders showed to sinter well at 1100°C over YSZ sheets, and their adhesion depended on the level of A-site substitution. Sintering at higher temperatures lead to surface reaction with YSZ, whereas a lower sintering temperature produced a friable electrode.

References

- (1) Tejuca, L. G.; Fierro, J. L. G.; Tascon, J. M. D., *Advances in Catalysis* **1989**, 36, 237-328.
- (2) Bouwmeester, H. J. M.; Burggraaf, A. J. In *The CRC Handbook of Solid State Electrochemistry*; Gellings, P. J. and Bouwmeester, H. J. M., Eds.; CRC Press; **1997**.
- (3) Matsuda, H.; Ishihara, T.; Mizuhara, Y.; Takita, Y. Third International Symposium on SOFC, Honolulu, Hawaii, **1993**.
- (4) Nakamura, T.; Petzow, G.; Gauckler, L. J., *Mat. Res. Bull.* **1979**, 14, 649-659.
- (5) Oikawa, K.; Kamiyama, T.; Hashimoto, T.; Shimojyo, Y.; Morii, Y., *Journal of Solid State Chemistry* **2000**, 154, 524-529.
- (6) Howard, S. A.; Yau, J.-K.; Anderson, H. U., *J. Am. Ceram. Soc.* **1991**, 75, 1685-1687.
- (7) Webb, J. B.; Sayer, M.; Mansingh, A., *Can. J. Phys.* **1977**, 55, 1725-1731.
- (8) Flandermeyer, B. F.; Nasrallah, M. M.; Sparlin, D. M.; Anderson, H. U., *High Temperature Science* **1985**, 20, 259-269.
- (9) Mori, M.; Yamamoto, T.; Itoh, H.; Abe, T.; Yamamoto, S.; Takeda, Y.; Yamamoto, O. First European Solid Oxide Fuel Cell Forum, Lucerne, **1994**; p 465-473.
- (10) Yasuda, I.; Hishinuma, M., *Solid State Ionics* **1995**, 80, 141-150.

- (11) Holt, A.; Ahlgren, E.; Poulsen, F. W. The Third International Symposium on Solid Oxide Fuel Cell, Honolulu, Hawaii, **1993**; p 562-571.
- (12) Hackenberger, M.; Stephan, K.; Kießling, D.; Schmitz, W.; Wendt, G., *Catalysis Today* **1997**, *101-103*, 1195-1200.
- (13) Gunasekaran, N.; Bakshi, N.; Alcock, C. B.; Carberry, J. J., *Solid State Ionics* **1996**, *83*, 145-150.
- (14) Iwasaki, M.; Takizawa, H.; Uheda, K.; Endo, T.; Shimada, M., *Journal of Materials Science* **1998**, *8*, 2765-2768.
- (15) Collongue, B. d.; Garbowski, E.; Primet, M., *J. Chem. Soc. Faraday Trans.* **1991**, *87*, 2493-2499.
- (16) Chick, L. A.; Bates, J. L.; Pederson, L. R.; Kissinger, H. E. First International Symposium on Solid Oxide Fuel Cells, Hollywood, Florida, **1989**; p 170-187.
- (17) Fierro, J. L. G.; Tascon, J. M. D.; Tejuca, L. G., *Journal of Catalysis* **1984**, *89*, 209-216.
- (18) Sakai, N.; Kawada, T.; Yokokawa, H.; Dokiya, M., *Journal of the Ceramic Society of Japan* **1993**, *101*, 1195-1200.
- (19) Zheng, W.; Pang, W.; Meng, G.; Peng, D., *Journal of Materials Science* **1999**, *9*, 2833-2836.
- (20) Devi, P. S.; Rao, M. S., *Thermochimica Acta* **1989**, *15*, 181-191.
- (21) Saracco, G.; Scibilia, G.; A, I.; Baldi, G., *Applied Catalysis B: Environmental* **1996**, *8*, 229-244.
- (22) Simner, S. P.; Hardy, J. S.; Stevenson, J. W., *J. Electrochem. Soc.* **2001**, *148*, A351-A360.
- (23) Armstrong, T. R.; Stevenson, J. W.; McCready, D. E.; Paulik, S. W.; Raney, P. E., *Solid State Ionics* **1996**, *92*, 213-223.
- (24) Tilset, B. G.; Fjellvåg, H.; Kjekshus, A., *Journal of Solid State Chemistry* **1995**, *119*, 271-280.
- (25) Sfeir, J.; Van herle, J.; McEvoy, A. J., *Journal of the European Ceramic Society* **1999**, *19*, 897-902.
- (26) Yokokawa, H.; Sakai, N.; Kawada, T.; Dokiya, M., *J. Electrochem. Soc.* **1991**, *138*, 1018-1027.
- (27) Jin, F.; Endo, T.; Takizawa, H.; Shimada, M., *Journal of Solid State Chemistry* **1994**, *113*, 138-144.
- (28) Simner, S. P.; Hardy, J. S.; Stevenson, J. W.; Armstrong, T. R. The Sixth International Symposium on Solid Oxide Fuel Cells, Hawaii, **1999**; p 696-705.
- (29) Armstrong, T. R.; Stevenson, J. W.; Pederson, L. R.; Raney, P. E., *J. Electrochem. Soc.* **1996**, *143*, 2919-2925.
- (30) Mori, M.; Sakai, N.; kawada, T.; Yokokawa, H.; Dokiya, M., *Denki Kagaku* **1991**, *59*, 314-319.
- (31) Yasuda, I.; Hikita, T., *J. Electrochem. Soc.* **1993**, *140*, 1699-1704.
- (32) Nasrallah, M. M.; Carter, J. D.; Anderson, H. U.; Koc, R. The Second International Symposium on Solid Oxide Fuel Cells, Athens, Greece, **1991**; p 637-644.
- (33) Meadowcroft, D. B., *Brit. J. Appl. Phys. (J. Phys. D)* **1969**, *2*, 1225-1233.
- (34) Höfer, H. E.; Schmidberger, R., *J. Electrochem. Soc.* **1994**, *141*, 782-786.
- (35) Primdahl, S.; Hansen, J. R.; Grahl-Madsen, L.; Larsen, P. H., *J. Electrochem. Soc.* **2001**, *148*, A74-A81.

Appendix: XRD charts of the most relevant LaCrO₃-based powders

LaCrO ₃	d	I [%]	hkl	2θ	d	I [%]	hkl	2θ	
as produced, 1100°C/4h	3.891	21.6	110	22.838	1.591	19.6	132	57.923	
	3.634	0.3		24.477	1.584	20.3	312	58.199	
CuKα1 λ: 1.5405	3.599	0.3		24.715	1.576	0.6		58.518	
	3.554	0.3		25.033	1.555	0.3	223	59.402	
	3.482	1.4	111	25.562	1.495	0.2	321	62.038	
System: <i>orthorhombic</i> a: 5.4820±0.5x10 ⁻³ b: 5.5176±0.4x10 ⁻³ c: 7.7671±0.9x10 ⁻³ α: 90 β: 90 γ: 90 V: 234.94±0.2x10 ⁻¹ M: 238.90 Z: 4 ρ: 6.75	3.390	0.2		26.269	1.441	0.7	313	64.639	
	2.748	100.0	112	32.558	1.432	0.1		65.071	
	2.696	0.4		33.207	1.379	3.3	040	67.917	
	2.668	0.2		33.560	1.374	9.8	224	68.203	
	2.585	0.8		34.673	1.359	0.3	041	69.082	
	2.482	0.2		36.168	1.350	0.6		69.600	
	2.464	0.2	120	36.437	1.319	0.2	141	71.485	
	2.350	1.0	121	38.278	1.313	0.3	215	71.871	
	2.341	0.5	211	38.430	1.297	1.7	134	72.879	
	2.250	13.2	022	40.044	1.294	1.3	314	73.082	
	2.240	10.9	202	40.236	1.279	0.3	331	74.086	
	2.154	0.5	113	41.911	1.232	3.4	240	77.400	
	Fabrication process: Modified citrate route	2.080	0.2	122	43.464	1.228	7.4	420	77.720
		1.944	32.4	220	46.679	1.221	0.3		78.196
		1.923	0.3		47.240	1.213	0.4	421	78.883
1.886		1.3	221	48.201	1.175	1.5	242	81.962	
1.838		0.1		49.560	1.171	1.9	206	82.284	
1.816		0.2		50.192	1.165	0.1		82.785	
1.782		0.2	213	51.237	1.159	0.5	333	83.320	
1.743		2.4	130	52.441	1.124	2.2	044	86.481	
1.737		5.4	114	52.639	1.119	1.8	404	86.963	
1.728		0.4		52.964	1.109	0.4	423	87.997	
1.693		1.4	311	54.120					
1.673	0.1		54.836						

$\text{LaCr}_{0.9}\text{Mg}_{0.1}\text{O}_3$	d	I [%]	hkl	2θ	d	I [%]	hkl	2θ
as produced, 1100°C/4h	3.891	21.3	110	22.834	1.645	0.3		55.848
	3.483	1.5	111	25.557	1.591	21.3	312	57.919
CuK α 1 λ : 1.5405	3.414	0.5		26.078	1.585	22.7	132	58.156
	3.267	2.0		27.278	1.574	0.7		58.594
	3.189	3.1		27.958	1.557	0.3	223	59.323
System: <i>orthorhombic</i> a: $5.517 \pm 0.1 \times 10^{-2}$ b: $5.489 \pm 0.1 \times 10^{-2}$ c: $7.773 \pm 0.2 \times 10^{-2}$ α : 90 β : 90 γ : 90 V: $235.39 \pm 0.6 \times 10^{-1}$ M: 236.13 Z: 4 ρ : 6.66	3.072	0.4		29.041	1.495	0.2	231	62.039
	2.984	1.4		29.919	1.453	0.1		64.044
	2.822	0.3		31.678	1.442	0.8	133	64.561
	2.751	100.0	112	32.521	1.380	3.8	400	67.878
	2.590	1.0	021	34.603	1.375	11.9	224	68.162
	2.495	0.2		35.960	1.351	0.8	041	69.523
	2.469	0.2	210	36.364	1.311	0.2		71.994
	2.345	1.0	103	38.354	1.297	2.6	330	72.840
	2.285	2.1		39.402	1.294	2.1	042	73.076
	2.250	16.0	202	40.040	1.280	0.5	331	74.005
	2.225	0.5		40.518	1.233	3.9	420	77.362
	2.156	0.7	113	41.874	1.229	9.2	240	77.641
	Fabrication process: Modified citrate route	2.142	0.3		42.163	1.214	0.8	241
2.078		0.2	122	43.523	1.187	0.2	305	80.948
1.967		0.5		46.118	1.175	1.8	422	81.921
1.946		34.4	220	46.642	1.171	2.7	242	82.276
1.887		1.9	221	48.199	1.160	0.6	333	83.241
1.869		1.4		48.680	1.158	0.5	135	83.400
1.830		0.2		49.791	1.125	2.5	404	86.441
1.785		0.3	213	51.120	1.120	2.0	423	86.879
1.739		6.9	114	52.600	1.110	0.5	243	87.919
1.702		0.4	311	53.835	1.102	0.1	414	88.682
1.694		1.7	131	54.078				
1.659	0.7		55.320					

$La_{0.85}Ca_{0.15}CrO_3$	d	I [%]	hkl	2 θ	d	I [%]	hkl	2 θ
as produced, 1100°C/4h	3.872	13.7	002	22.953	1.307	0.2	125	72.203
	3.465	1.2	111	25.686	1.291	1.6	006	73.281
CuK α 1 λ : 1.5405	2.735	100.0	200	32.715	1.288	1.2	402	73.477
	2.667	0.2		33.572	1.273	0.4	331	74.482
	2.576	0.9	201	34.806	1.223	7.6	116	78.119
System: <i>monoclinic</i> a: 5.4695 \pm 0.4 \times 10 ⁻³ b: 5.4913 \pm 0.6 \times 10 ⁻³ c: 7.7455 \pm 0.1 \times 10 ⁻² α : 90 β : 90.56 γ : 90 V: 232.62 \pm 0.5 \times 10 ⁻¹ M: 224.08 Z: 4 ρ : 6.39	2.453	0.1	120	36.599	1.208	0.7	421	79.241
	2.337	1.0	013	38.487	1.182	0.2	143	81.314
	2.237	13.7	022	40.277	1.169	1.3	026	82.444
	2.146	0.4	113	42.079	1.166	1.9		82.721
	2.071	0.2	122	43.675	1.154	0.5	135	83.763
	1.936	30.3	004	46.885	1.119	2.3		87.003
	1.878	1.2	221	48.440	1.115	2		87.396
	1.775	0.2	123	51.446	1.110	0.2	-423	87.906
	1.730	4.0	310	52.880	1.105	0.5		88.442
	1.693	0.3	131	54.117	1.077	0.2	150	91.351
	1.687	1.4	311	54.355	1.073	0.7	510	91.801
	1.673	0.2		54.847	1.061	0.7	511	93.080
	Fabrication process: Modified citrate route	1.583	19.0	024	58.243			
1.578		20.7		58.442				
1.569		1.1		58.798				
1.549		0.2	005	59.636				
1.435		0.7	115	64.925				
1.410		0.1	322	66.244				
1.379		0.2		67.942				
1.372		3.5	040	68.319				
1.368		11.5	400	68.562				
1.360		0.3		69.009				
1.344		0.5	401	69.916				
1.325	0.2		71.077					

$\text{La}_{0.85}\text{Ca}_{0.15}\text{Cr}_{0.9}\text{Mg}_{0.1}\text{O}_3$	d	I [%]	hkl	2θ	d	I [%]	hkl	2θ
as produced, 1200°C/4h	3.876	15.3	110	22.927	1.291	1.8	134	73.241
	3.463	1.3	111	25.704	1.288	1.5	402	73.434
CuK α 1 λ : 1.5405	2.738	100.0	112	32.686	1.274	0.4	331	74.434
	2.721	3.4		32.891	1.223	7.5	116	78.077
	2.708	0.6		33.058	1.218	0.4		78.483
System: <i>orthorhombic</i> a: $5.4675 \pm 0.4 \times 10^{-3}$ b: $5.4895 \pm 0.2 \times 10^{-3}$ c: $7.7325 \pm 0.3 \times 10^{-3}$ α : 90 β : 90 χ : 90 V: $232.08 \pm 0.2 \times 10^{-1}$ M: 221.31 Z: 4 ρ : 6.33	2.576	0.8	201	34.794	1.208	0.9	403	79.239
	2.450	0.2	120	36.645	1.169	1.1	242	82.433
	2.333	1.2	013	38.553	1.166	2.0	422	82.681
	2.233	14.1	202	40.367	1.155	0.4	333	83.709
	2.146	0.6	113	42.073	1.119	2.4	044	86.995
	2.068	0.3	212	43.748	1.115	2.1	404	87.356
	1.937	31.8	220	46.877	1.105	0.6	007	88.394
	1.927	1.4		47.125	1.077	0.4	150	91.363
	1.879	1.1	221	48.407	1.073	1.0	226	91.756
	1.775	0.2	213	51.429	1.062	0.4	511	92.996
	1.730	5.3	114	52.876	1.072	3.3	152	95.923
	1.722	0.3		53.161	1.035	4.2	136	96.202
	Fabrication process: Modified citrate route	1.688	1.6	311	54.321	1.033	6.6	512
1.583		17.5	132	58.237	1.024	0.2	405	97.607
1.578		23.1	204	58.433	0.968	1.2	440	105.400
1.571		1.3		58.724	0.990	0.3	513	102.198
1.548		0.2	223	59.685	0.968	1.2	440	105.400
1.489		0.2	321	62.284	0.967	0.6	008	105.678
1.436		0.6	313	64.880	0.961	0.2	441	106.582
1.373		3.7	040	68.280	0.959	0.2	425	106.823
1.368		13.0	224	68.527	0.940	0.7	350	110.039
1.361		0.4		68.931	0.937	0.6		110.549
1.346		0.4	401	69.841	0.931	0.4		111.597
1.308		0.2	323	72.174	0.915	1.0	060	114.645

$La_{0.85}Ca_{0.15}Cr_{0.9}Mg_{0.1}O_3$	d	I [%]	hkl	2θ	d	I [%]	hkl	2θ
as produced, 1200°C/4h	3.876	15.3	110	22.927	1.218	0.4		78.483
	3.463	1.3	111	25.704	1.208	0.9	116	79.239
CuK α 1 λ : 1.5405	2.738	100.0	200	32.686	1.169	1.1	035	82.433
	2.721	3.4	112	32.891	1.166	2.0	242	82.681
	2.708	0.6	-112	33.058	1.155	0.4	206	83.709
System: <i>monoclinic</i> a: $5.4749 \pm 0.6 \times 10^{-3}$ b: $5.4764 \pm 0.3 \times 10^{-3}$ c: $7.616 \pm 0.1 \times 10^{-2}$ α : 90 β : 89.54 γ : 90 V: $228.24 \pm 0.3 \times 10^{-1}$ M: 221.31 Z: 4 ρ : 6.44	2.576	0.8	021	34.794	1.119	2.4		86.995
	2.450	0.2	120	36.645	1.115	2.1	404	87.356
	2.333	1.2	121	38.553	1.105	0.6	243	88.394
	2.233	14.1	202	40.367	1.077	0.4		91.363
	2.146	0.6		42.073	1.073	1.0	-235	91.756
	2.068	0.3	212	43.748	1.062	0.4	-511	92.996
	1.937	31.8	220	46.877	1.072	3.3		95.923
	1.927	1.4		47.125	1.035	4.2		96.202
	1.879	1.1	221	48.407	1.033	6.6	-152	96.399
	1.730	5.3	222	52.876	0.968	1.2	440	105.400
	1.722	0.3	-222	53.161	0.959	0.2	-441	106.823
Fabrication process: Modified citrate route	1.688	1.6	-131	54.321	0.940	0.7		110.039
	1.583	17.5		58.237	0.937	0.6	018	110.549
	1.578	23.1	132	58.433	0.915	1.0		114.645
	1.571	1.3	-312	58.724	0.914	0.7	-416	114.922
	1.436	0.6	313	64.880	0.912	4.1		115.320
	1.373	3.7		68.280	0.868	0.7		125.199
	1.368	13.0	400	68.527	0.866	0.4		125.549
	1.361	0.4	224	68.931	0.865	1.1	444	125.964
	1.346	0.4	-401	69.841	0.860	0.6	-621	127.323
	1.291	1.8	402	73.241	0.826	1.5		137.639
	1.288	1.5	042	73.434	0.824	1.3		138.361
	1.274	0.4	331	74.434	0.792	1.0		153.402
	1.223	7.5		78.077	0.790	1.0	264	155.072

$\text{La}_{0.85}\text{Sr}_{0.15}\text{CrO}_3$	d	I [%]	hkl	2θ	d	I [%]	hkl	2θ
as produced, 1200°C/4h	3.873	28.1	110	22.945	1.070	1.3	226	92.080
	2.751	100.0	020	32.519	1.039	7.4	152	95.716
CuK α 1 λ : 1.5405	2.728	92.5	200	32.805	1.035	7.2	136	96.202
	2.338	2.3	121	38.477	1.028	6.3	512	97.037
	2.244	29.7	022	40.161	0.969	3.4	440	105.359
System: <i>monoclinic</i> a: $5.4559 \pm 0.1 \times 10^{-3}$ b: $5.5038 \pm 0.1 \times 10^{-3}$ c: $7.7506 \pm 0.2 \times 10^{-3}$ α : 90 β : 90.76 γ : 90 V: $232.720 \pm 0.6 \times 10^{-2}$ M: 231.21 Z: 4 ρ : 6.59	2.217	9.0	202	40.672	0.944	0.7	-154	109.431
	1.937	67.1	220	46.872	0.942	1.7	046	109.760
	1.785	0.6	031	51.119	0.938	0.8	442	110.478
	1.739	6.7	130	52.596	0.932	0.5	514	111.528
	1.726	6.4	114	52.998	0.917	2.0	-352	114.361
	1.589	22.2	-132	58.001	0.914	4.7	028	114.924
	1.584	38.6	132	58.198	0.909	3.8	532	115.838
	1.576	3.1	321	58.516	0.893	1.0	-246	119.244
	1.570	15.1	312	58.766	0.888	0.5	-602	120.371
	1.376	13.2	040	68.080	0.882	0.7	426	121.605
	1.370	2.0	400	68.439	0.870	3.4	-444	124.682
	1.364	15.3	224	68.796	0.863	4.6	444	126.357
	Fabrication process: Modified citrate route	1.316	0.5	-141	71.677	0.949	0.6	-262
1.297		1.9	-134	72.881	0.848	0.5		130.484
1.291		3.1	134	73.236	0.845	0.7	138	131.525
1.281		1.2	402	73.920	0.841	1.0	622	132.841
1.228		10.9	240	77.675	0.829	3.2	064	136.597
1.222		11.7	116	78.161	0.827	2.0	156	137.316
1.173		1.3	-242	82.080	0.819	2.0	604	140.316
1.169		3.5	242	82.438	0.795	1.5	-264	151.600
1.162		2.0	422	83.085	0.792	3.4	048	153.040
1.122		5.1	044	86.720	0.785	2.1	624	157.841
1.109		2.1	404	88.042				
1.079	1.2	-334	91.081					

$La_{0.85}Sr_{0.15}Cr_{0.9}Mg_{0.1}O_3$	d	I [%]	hkl	2 θ	d	I [%]	hkl	2 θ
as produced, 1100°C/4h	3.876	17.1	110	22.925	1.208	0.6	-241	79.236
	3.466	1.3	111	25.680	1.197	0.2	-225	80.119
CuK α 1 λ : 1.5405	2.738	100.0	020	32.684	1.169	1.4	422	82.438
	2.576	1.2	021	34.801	1.166	1.9	-422	82.678
	2.333	1.2	121	38.556	1.154	0.3		83.721
System: <i>monoclinic</i> a: 5.489 \pm 0.1 \times 10 ⁻² b: 5.4717 \pm 0.8 \times 10 ⁻³ c: 7.631 \pm 0.2 \times 10 ⁻² α : 90 β : 89.73 γ : 90 V: 229.24 \pm 0.7 \times 10 ⁻¹ M: 228.44 Z: 4 ρ : 6.62	2.237	14.4	202	40.277	1.120	1.9		86.959
	2.147	0.4		42.046	1.116	1.7		87.321
	2.067	0.4	212	43.752	1.105	0.3		88.370
	1.936	32.6	220	46.881	1.077	0.5	510	91.357
	1.923	1.9		47.231	1.073	0.7	150	91.721
	1.879	0.9	221	48.400	1.062	0.6	-226	93.002
	1.773	0.4	031	51.514				
	1.730	5.1	222	52.876				
	1.688	1.2	-131	54.319				
	1.583	20.1	321	58.240				
	1.578	22.8	132	58.435				
	1.570	1.6	204	58.759				
	Fabrication process: Modified citrate route	1.562	0.4	-204	59.080			
1.549		0.3		59.651				
1.490		0.2	-321	62.246				
1.436		0.8	313	64.882				
1.379		0.5		67.942				
1.373		4.0	400	68.281				
1.368		10.7	040	68.523				
1.346		0.4	041	69.845				
1.291		1.6	330	73.240				
1.288		1.4	042	73.437				
1.273		0.5	-331	74.469				
1.224		7.1	240	78.039				

$\text{LaCr}_{0.9}\text{Mn}_{0.1}\text{O}_3$	d	I [%]	hkl	2θ	d	I [%]	hkl	2θ	
as produced, 1100°C/4h	3.885	20.6	110	22.874	1.229	8.2	332	77.601	
	3.477	1.3	111	25.602	1.213	0.7	241	78.881	
CuK α 1 λ : 1.5405	2.748	100.0	112	32.561	1.174	1.7	422	82.002	
	2.712	1.3		33.005	1.171	2.0	026	82.238	
	2.585	1.1	021	34.681	1.159	0.7	333	83.279	
System: <i>orthorhombic</i> a: $5.5147 \pm 0.4 \times 10^{-3}$ b: $5.4817 \pm 0.6 \times 10^{-3}$ c: $7.769 \pm 0.1 \times 10^{-2}$ α : 90 β : 90 γ : 90 V: $234.86 \pm 0.3 \times 10^{-1}$ M: 239.19 Z: 4 ρ : 6.76	2.345	1.3	103	38.356	1.124	1.8	404	86.481	
	2.248	14.9	202	40.080	1.120	1.4	044	86.881	
	2.240	2.4	022	40.232	1.110	0.5	243	87.919	
	2.155	0.6	113	41.882					
	2.074	0.3	122	43.600					
	1.944	34.0	220	46.683					
	1.886	1.2	221	48.204					
	1.785	0.3	213	51.120					
	1.743	3.0	310	52.443					
	1.739	5.3	222	52.601					
	1.700	0.2	311	53.880					
	1.692	1.5	131	54.150					
	Fabrication process: Modified citrate route	1.590	20.6	312	57.960				
		1.584	19.3	132	58.196				
1.566		0.2		58.916					
1.557		0.3		59.324					
1.495		0.2	105	62.012					
1.441		0.7	133	64.607					
1.380		3.3	400	67.885					
1.374		9.3	224	68.201					
1.350		0.6	041	69.567					
1.318		0.2	411	71.555					
1.297	2.0	314	72.881						
1.278	0.4	331	74.119						

$LaCr_{0.9}Fe_{0.1}O_3$	d	I [%]	hkl	2 θ	d	I [%]	hkl	2 θ	
as produced, 1100°C/4h	3.898	19.7	110	22.798	1.176	1.3	422	81.844	
	3.487	1.6	111	25.524	1.172	1.8	242	82.162	
CuK α 1 λ : 1.5405	2.754	100.0	112	32.482	1.160	0.5	333	83.199	
	2.591	1.0	021	34.598	1.125	2.3	404	86.398	
	2.466	0.2	210	36.399	1.121	1.7	044	86.801	
System: <i>orthorhombic</i> a: 5.5229 \pm 0.7 \times 10 ⁻³ b: 5.4917 \pm 0.7 \times 10 ⁻³ c: 7.776 \pm 0.1 \times 10 ⁻² α : 90 β : 90 γ : 90 V: 235.85 \pm 0.4 \times 10 ⁻¹ M: 239.28 Z: 4 ρ : 6.74	2.347	1.3	103	38.316	1.117	0.2		87.237	
	2.252	14.5	202	40.001	1.111	0.2	243	87.798	
	2.159	0.6	113	41.803					
	2.083	0.2	212	43.400					
	1.947	31.8	220	46.602					
	1.889	1.0	221	48.123					
	1.788	0.3	213	51.040					
	1.740	6.1	114	52.560					
	1.696	1.6	131	54.038					
	1.592	21.0	312	57.880					
	1.587	22.7	024	58.080					
	1.557	0.5	223	59.319					
	Fabrication process: Modified citrate route	1.496	0.2	105	61.980				
		1.443	0.7	133	64.802				
1.381		3.4	400	67.802					
1.375		9.7	224	68.119					
1.352		0.4	041	69.449					
1.314		0.2	125	71.769					
1.299		2.1	314	72.761					
1.296		1.8	134	72.960					
1.280		0.5	331	73.998					
1.229		8.2	240	77.599					
1.214	0.3	043	78.795						
1.190	0.2	413	80.675						

$\text{LaCr}_{0.9}\text{Co}_{0.1}\text{O}_3$	d	I [%]	hkl	2θ	d	I [%]	hkl	2θ	
as produced, 1100°C/4h	3.877	18.0	110	22.916	1.316	0.2	141	71.651	
	3.468	1.2	111	25.665	1.308	0.2	215	72.158	
CuK α 1 λ : 1.5405	2.754	34.3	020	32.484	1.294	1.8	134	73.074	
	2.741	100.0	112	32.643	1.290	1.4	006	73.319	
	2.579	0.9		34.763	1.276	0.4	331	74.279	
System: <i>orthorhombic</i> a: $5.4663 \pm 0.3 \times 10^{-3}$ b: $5.5092 \pm 0.3 \times 10^{-3}$ c: $7.7419 \pm 0.6 \times 10^{-3}$ α : 90 β : 90 γ : 90 V: $233.15 \pm 0.2 \times 10^{-1}$ M: 239.59 Z: 4 ρ : 6.82	2.461	0.1	120	36.483	1.230	3.0	240	77.561	
	2.344	0.3	121	38.364	1.227	6.6	332	77.800	
	2.338	1.0	211	38.480	1.225	8.5	116	77.961	
	2.244	14.1	022	40.153	1.209	0.5	421	79.159	
	2.233	12.5	202	40.358	1.186	0.1	143	80.990	
	2.148	0.4	113	42.032	1.172	1.4	242	82.162	
	1.940	31.9	220	46.796	1.167	2.0	422	82.598	
	1.935	7.6	004	46.907	1.157	0.3	135	83.487	
	1.882	1.1	221	48.319	1.153	0.3	315	83.808	
	1.876	0.5		48.484	1.122	2.5	44	86.684	
	1.780	0.3	123	51.275	1.117	1.8	404	87.242	
	1.741	2.4	130	52.524	1.106	0.4	423	88.313	
	Fabrication process: Modified citrate route	1.733	4.8	114	52.798				
		1.698	0.3	131	53.955				
1.689		1.4	311	54.282					
1.588		19.5	132	58.044					
1.580		21.0	204	58.362					
1.551		0.3	223	59.559					
1.491		0.2	321	62.205					
1.437		0.7	313	64.837					
1.377		3.5	040	68.006					
1.370		11.6	224	68.401					
1.367		2.6	400	68.602					
1.346	0.4		69.807						

<i>LaCr_{0.9}Ni_{0.1}O₃</i>	d	I [%]	hkl	2θ	d	I [%]	hkl	2θ
as produced, 1100°C/4h	3.891	18.8	110	22.838	1.293	1.5	134	73.114
	3.482	1.6	111	25.562	1.278	0.5	331	74.119
CuKα1 λ: 1.5405	2.748	100.0	112	32.556	1.232	3.3	420	77.401
	2.585	1.0	021	34.672	1.228	8.1	116	77.719
	2.350	1.3	211	38.276	1.217	0.2	421	78.554
System: <i>orthorhombic</i> a: 5.5175±0.3x10 ⁻³ b: 5.4824±0.4x10 ⁻³ c: 7.7643±0.6x10 ⁻³ α: 90 β: 90 γ: 90 V: 234.87±0.2x10 ⁻¹ M: 239.57 Z: 4 ρ: 6.77	2.342	1.1	103	38.402	1.213	0.7	241	78.876
	2.271	0.3		39.648	1.193	0.1		80.451
	2.250	13.2	202	40.047	1.188	0.2	413	80.834
	2.240	11.6	022	40.235	1.175	1.4	422	81.966
	2.155	0.5	113	41.877	1.171	1.7	242	82.281
	2.081	0.2	212	43.447	1.167	0.5		82.627
	1.944	33.9	220	46.679	1.159	0.5	333	83.318
	1.886	1.3	221	48.200	1.124	2.4	404	86.482
	1.785	0.3	213	51.125	1.120	1.6	044	86.956
	1.744	2.6	310	52.439	1.109	0.5	243	88.000
	1.738	5.2	222	52.603				
	1.701	0.4	311	53.839				
	Fabrication process: Modified citrate route	1.693	1.7	131	54.116			
1.591		19.8	312	57.926				
1.584		21.1	132	58.197				
1.555		0.4	223	59.407				
1.494		0.2	105	62.064				
1.441		0.9	133	64.636				
1.379		3.6	400	67.916				
1.374		10.5	224	68.204				
1.366		0.6		68.653				
1.350		0.6	041	69.600				
1.314		0.2	215	71.796				
1.297	1.9	314	72.849					

$La_{0.15}Ca_{0.15}Cr_{0.9}Ni_{0.1}O_3$	d	I [%]	hkl	2 θ	d	I [%]	hkl	2 θ	
as produced, 1100°C/4h	3.876	14.1	110	22.926	1.222	7.9	420	78.117	
	3.462	1.1	111	25.711	1.211		043	78.963	
CuK α 1 λ : 1.5405	2.738	100.0	112	32.686	1.208	0.7	225	79.246	
	2.576	1.1	003	34.795	1.169	1.2	242	82.443	
	2.338	1.1	121	38.476	1.166	2.0	422	82.721	
System: <i>orthorhombic</i> a: 5.4620 \pm 0.4 \times 10 ⁻³ b: 5.4895 \pm 0.4 \times 10 ⁻³ c: 7.7314 \pm 0.8 \times 10 ⁻³ α : 90 β : 90 γ : 90 V: 231.81 \pm 0.2 \times 10 ⁻¹ M: 224.74 Z: 4 ρ : 6.44	2.333	0.5		38.561	1.154	0.4	333	83.760	
	2.239	12.7	022	40.246	1.119	2.1	044	87.037	
	2.233	14.6	202	40.363	1.115	1.6	404	87.397	
	2.146	0.6	113	42.075	1.105	0.5	423	88.436	
	2.067	0.3	212	43.753					
	1.936	32.0	220	46.883					
	1.934	13.1	004	46.951					
	1.878	1.1	221	48.435					
	1.776	0.4	123	51.397					
	1.730	4.5	114	52.879					
	1.687	1.5	311	54.351					
	1.583	20.0	132	58.241					
	Fabrication process: Modified citrate route	1.578	22.9	204	58.440				
		1.548		223	59.678				
1.488			105	62.354					
1.435		0.7	313	64.920					
1.373		3.1	040	68.281					
1.368		11.6	224	68.557					
1.345		0.5	401	69.881					
1.342		0.3		70.075					
1.291		1.4	330	73.279					
1.288		1.4	314	73.443					
1.273		0.5	331	74.475					
1.226		240	77.839						

$La_{0.85}Ca_{0.15}Cr_{0.9}Ni_{0.1}O_3$	d	I [%]	hkl	2θ	d	I [%]	hkl	2θ
after long term catalysis (CTL) = reduced	3.864	17.6	012	22.999				
	2.748	100	110	32.562				
CuK α 1 λ : 1.5405	2.721	94.5	104	32.884				
	2.335	2.7	113	38.532				
	2.240	29.5	202	40.233				
System: <i>trigonal</i> a: $5.4996 \pm 0.5 \times 10^{-3}$ b: $5.4996 \pm 0.5 \times 10^{-3}$ c: $13.2743 \pm 0.2 \times 10^{-3}$ α : 90 β : 90 γ : 120 V: $347.69 \pm 0.7 \times 10^{-1}$ M: 224.74 Z: 6 ρ : 6.44	2.212	8.1	006	40.765				
	1.934	81.5	024	46.953				
	1.916	1		47.406				
	1.783	0.6		51.208				
	1.737	8	122	52.644				
	1.724	5.9	116	53.086				
	1.587	28.2	030	58.077				
	1.582	51.4	214	58.279				
	1.566	18.7	018	58.917				
	1.375	17.3	220	68.157				
	1.367	2.4		68.601				
	1.361	16.8	208	68.922				
	Fabrication process: Modified citrate route	1.350	0.6		69.605			
1.296		2.4	312	72.961				
1.290		3.3	036	73.326				
1.279		1	10 10	74.053				
1.227		15.4	134	77.758				
1.220		15.2	128	78.315				
1.172		2.3	042	82.159				
1.168		3.6	226	82.521				
1.160		1.9	02 10	83.243				
1.121		7.1	404	86.804				
1.106	2	00 12	88.283					

<i>LaCr_{0.5}Ni_{0.5}O₃</i>	d	I [%]	hkl	2θ	d	I [%]	hkl	2θ
as produced	3.884	18.9	101	22.880	1.290	1.5	143	73.316
	3.477	1.3	111	25.601	1.276	0.4	313	74.245
CuKα1 λ: 1.5405	2.745	100.0	121	32.601	1.230	3.1	402	77.559
	2.579	1.2	012	34.758	1.226	7.2	161	77.840
	2.342	0.9	211	38.398	1.212	0.5	252	78.960
System: <i>orthorhombic</i> a: 5.5101±0.5x10 ⁻³ b: 7.752±0.1x10 ⁻² c: 5.4678±0.5x10 ⁻³ α: 90 β: 90 γ: 90 V: 233.5578±0.3x10 ⁻¹ M: 242.25 Z: 4 ρ: 6.89	2.246	13.3	220	40.116	1.210	0.6	214	79.121
	2.235	11.4	022	40.321	1.172	1.4	422	82.155
	2.221	0.7		40.597	1.168	1.6	224	82.558
	2.152	0.5	131	41.952	1.157	0.5	333	83.522
	2.075	0.2	221	43.590	1.154	0.4	153	83.712
	1.941	34.5	202	46.762	1.123	2.7	440	86.641
	1.883	1.3	212	48.287	1.117	1.7	044	87.201
	1.783	0.3	231	51.205	1.107	0.4	234	88.204
	1.741	2.5	301	52.519				
	1.735	5.4	222	52.721				
	1.699	0.3	311	53.926				
	1.689	1.6	113	54.275				
Fabrication process: Modified citrate route	1.588	20.4	321	58.036				
	1.581	19.7	042	58.322				
	1.574	0.8		58.596				
	1.552	0.3	232	59.530				
	1.493	0.2	150	62.137				
	1.438	0.9	133	64.802				
	1.378	3.2	400	67.969				
	1.371	10.8	242	68.358				
	1.367	2.8	004	68.599				
	1.346	0.5	014	69.799				
	1.342	0.2		70.069				
1.295	2.0	341	72.999					

$LaCr_{0.5}Ni_{0.5}O_3$	d	I [%]	hkl	2θ	d	I [%]	hkl	2θ
reduced in $H_2+3\%H_2O$ at 780°C for 1 week	3.883	27.9	012	22.885	1.105	0.8	00 12	88.439
	2.799	2.4		31.944				
CuK α 1 λ : 1.5405	2.761	100.0	110	32.396				
	2.725	76.7	104	32.840				
	2.342	1.6	113	38.402				
System: <i>trigonal</i> a: $5.5217\pm 0.6\times 10^{-3}$ b: $5.52166\pm 0.6\times 10^{-3}$ c: $13.25343\pm 0.2\times 10^{-2}$ α : 90 β : 90 γ : 120 V: $349.94\pm 0.7\times 10^{-1}$ M: 242.25 Z: 6 ρ : 6.89	2.250	22.8	202	40.041				
	2.210	5.4	006	40.802				
	2.038	0.6		44.418				
	1.962	1.0		46.242				
	1.940	47.4	024	46.801				
	1.745	6.4	122	52.404				
	1.724	4.4	116	53.076				
	1.611	0.4		57.141				
	1.594	18.0	300	57.799				
	1.587	27.0	214	58.079				
	1.564	9.8	018	58.998				
	1.556	0.6		59.355				
	Fabrication process: Modified citrate route	1.380	9.4	220	67.840			
1.373		0.7		68.235				
1.361		7.1	208	68.919				
1.300		1.4	312	72.680				
1.292		2.0	306	73.195				
1.277		0.6	10 10	74.202				
1.231		7.2	134	77.476				
1.221		6.0	128	78.202				
1.177		0.6	042	81.795				
1.170		1.4	226	82.314				
1.160		0.8	02 10	83.244				
1.125	3.5	404	86.442					

Chapter 4 四

*Evidence of surface reaction with highly substituted
LaCrO₃-based anodes*

Evidence of surface reaction with highly substituted LaCrO₃-based anodes*

Abstract

Lanthanum calcium chromite-based anodes were tested on 8YSZ electrolytes with humidified H₂ or CH₄ between 700 and 900°C. Their performances degraded in both fuels due to the formation of an interfacial layer developed during cell operation, in the case of highly Ca-substituted LaCrO₃, as evidenced by imaging and surface analysis techniques (*SEM-EDAX*, *XPS* and *SIMS*). The anode materials were stable against coking, at sufficiently low temperatures or high current densities. The loss in performance was therefore due to an ohmic increase and to electrode aging.

Introduction

Lanthanum chromites are reported to be very stable under very low oxygen partial pressures of 10⁻²¹ atm¹. By substitution of metals such as Ca, Sr or Mg on La or Cr sites in LaCrO₃, electronic compensation occurs by the formation of holes (i.e. by reduction Cr^{IV} to Cr^{III}) at high oxygen partial pressure or of oxygen vacancies at low P_{O₂}²⁻⁵, these having an impact on the ionic conductivity of the material^{6, 7}. The higher the substitution level the higher is the total conductivity in both oxidizing and reducing atmospheres. Baker et al., Middleton et al. and Norby et al.⁸⁻¹¹ reported that lanthanum calcium chromites show catalytic total or partial oxidation of pure methane with a low level of coking when compared to the Ni-YSZ cermet. These different properties of doped LaCrO₃ are promising for a methane-fed anode. In the present work, we assess the electrochemical behaviour of heavily substituted LaCrO₃ anodes in real SOFC mode using humidified H₂ and CH₄. We are also giving an evidence for the interfacial instability of the material due to a topotactic reaction between the heavily substituted LaCrO₃ and YSZ electrolyte.

Experimental

Powder preparation

Different powders were prepared according to the formula La_{1-α}A_αCr_{1-β}B_βO₃ (see Table 1) by following the citrate procedure, described in Chapter 3. The non-stoichiometric La_{0.7}Ca_{0.32}CrO₃ was obtained from EMPA-Switzerland. All these powders had in common a high level of A-site substitution (0.2~0.32).

Table 1: A summary of the different tested lanthanum chromites.

Electrode composition	Firing temperature
La _{0.7} Ca _{0.32} CrO ₃	As obtained
La _{0.8} Ca _{0.2} CrO ₃	1000°C/4h
La _{0.7} Ca _{0.3} Cr _{0.9} Fe _{0.1} O ₃	1000°C/2h
La _{0.7} Ca _{0.3} Cr _{0.9} Cu _{0.1} O ₃	1100°C/4h
La _{0.7} Ca _{0.3} Cr _{0.8} Co _{0.2} O ₃	1000°C/2h
La _{0.75} Ca _{0.15} Sr _{0.1} Cr _{0.95} Mg _{0.05} O ₃	1100°C/4h

Cell fabrication

On thin HF-etched 8YSZ sheets of 150 to 200 μm thickness, three successive layers of lanthanum chromite organic slurries were screen-printed to form electrodes of 1 cm² area. As current collector, platinum mesh was pressed in the last layer (see Chapter 2). A stoichiometric

*This chapter has been submitted in a shorter version as J. Sfeir, J. Van herle, A. J. McEvoy, 'LaCrO₃-based anodes for methane oxidation', in *Third European Solid Oxide Fuel Cell Forum, Nantes-France, ed. P. Stevens, 1998, 267-276.*

LSM electrode ($\text{La}_{0.85}\text{Sr}_{0.15}\text{MnO}_3$) was symmetrically deposited on the opposite side of each sheet, with a similar Pt current collector. Both sides carried screen-printed reference electrodes of the same respective compositions. The whole structure was thermocompressed at 1100°C for 4 h. This thermocompression was necessary to ensure a good current collection and to minimize the contact losses.

Data acquisition

The cells were tested in both the sealed and the non-sealed configurations (see Chapter 2). For the unsealed set-up, the cells were mounted between inconel flanges with porous alumina felts on each side as electrical insulators and gas diffusers, and tested in a vertical tubular oven. This configuration was not sealed so that the fuel excess burned at the periphery of the cell. The gas inputs were controlled by mass-flow meters. For the fuel (CH_4 or H_2), 3% water was added to the stream. Typical flows were of 300 to 400 ml/min for air and 250 ml/min for the fuel.

Electrical contacts to the cell were made using silver wires welded to the Pt current collector meshes. Separate current and potential leads were used, with a Wenking potentiostat for *dc* measurements or a Zahner IM5 impedance analyser for electrochemical impedance spectroscopy (EIS, typically between 40mHz and 300kHz). These EIS measurements were done both under open circuit conditions and at increasing current densities.

After the measurements, some of the pellets were imaged by SEM and some surface and cross-section analyses were performed (EDAX, low angle XRD, SIMS and Auger-XPS).

Results

Prior to the electrochemical measurement, the cells were usually polarized for several hours at 400 to 700 mV, in order to activate the electrodes. During this initial stage, irrespective of the fuel, the current density started degrading after a brief transient improvement due to the cathode activation. This is illustrated in Figure 1 for the $\text{La}_{0.7}\text{Ca}_{0.32}\text{CrO}_3/\text{YSZ}/\text{LSM}$ system under H_2 . The initial current drawn from this all-ceramic cell was acceptable (short circuit current, i_{sc} , of around $620 \text{ mA}/\text{cm}^2$). The performance dropped to about one third, after a day and ultimately the i_{sc} stabilized at $150 \text{ mA}/\text{cm}^2$.

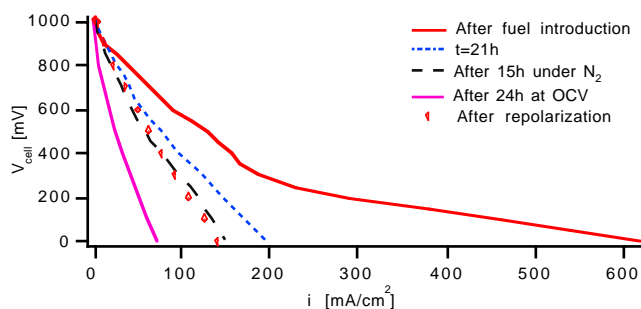


Figure 1: *IV* curves for the $\text{La}_{0.7}\text{Ca}_{0.32}\text{CrO}_3/8\text{YSZ}/\text{LSM}$ system at 830°C with $\text{H}_2+3\%\text{H}_2\text{O}$ fuel.

Interestingly, the cell performance depended on the magnitude of the operating voltage. With increasing anodic overpotential, the polarization impedance, R_p , decreased drastically, e.g. passing from 10 to $2 \Omega\text{cm}^2$ at 800°C in CH_4 , or 2 to $0.7 \Omega\text{cm}^2$ at 900°C in H_2 (Figure 2), when measured at different voltages starting from the open circuit potential (OCV) to short circuit (*sc*). Also, when the cell was left at OCV, its performance degraded drastically (Figure 1 and 3). After polarization at short circuit, the cell resumed to its initial performance. This implies a modification of the electrocatalytic activity of the electrode under current. Also, the increase in the polarization resistance was slow and evolved over a 24 h period indicating a slow reduction process.

The electrode performance was observed to be similar in both the non-sealed and sealed set-up. A difference arose from the measured OCV, where a near theoretical OCV of $\sim 1220 \text{ mV}$ was achieved in the metallic non-sealed set-up against $\sim 903 \text{ mV}$ in the all-ceramic sealed configuration. This discrepancy arose from the possible pyrolysis of CH_4 on the metallic flanges. These electrodes performed much better in H_2 than in CH_4 , i.e. 3.5 to 5 times (e.g. Figure 4).

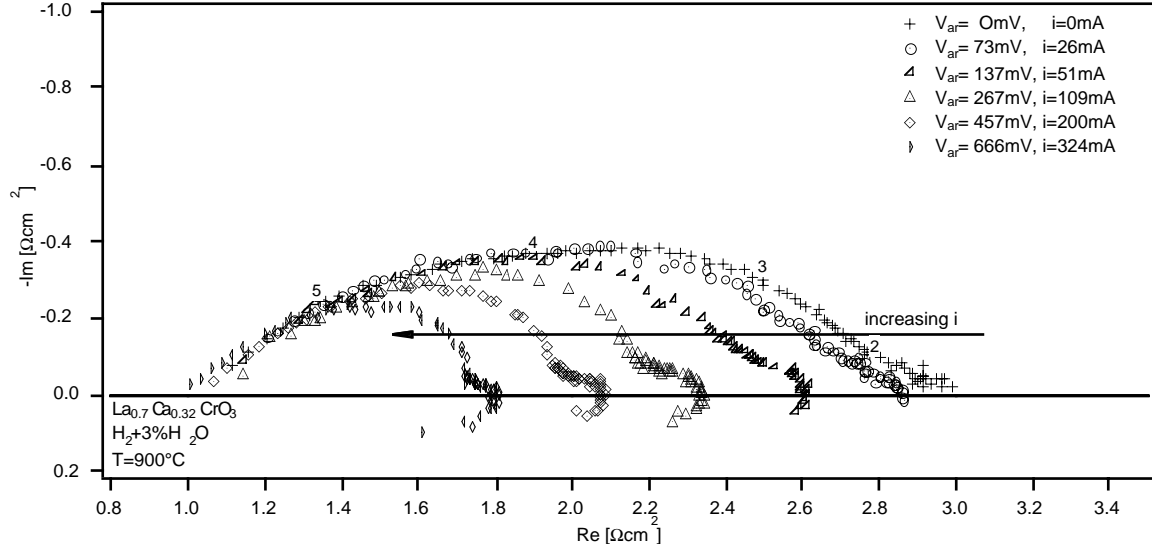
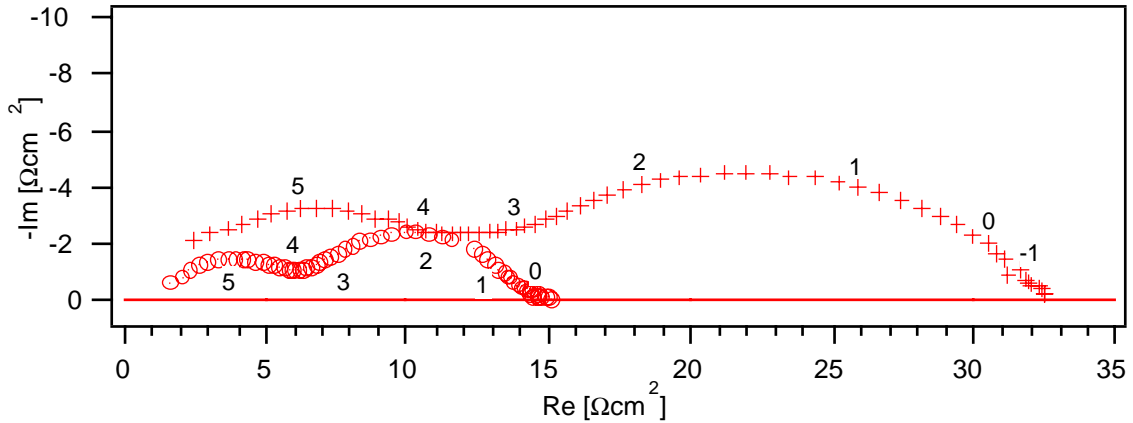


Figure 2: Evolution of the anode impedance with increasing potential, V_{ar} , applied between the anode and the anode reference electrode for the $La_{0.7}Ca_{0.32}CrO_3/8YSZ/LSM$ system at $900^\circ C$.

From the impedance measurements, two to three processes were observed, where the first process was almost unaffected by the nature of the gas phase (Figure 5). Interestingly, H_2O concentration had a tremendous effect on the anode performance by lowering its polarization resistance (Figure 6). The OCV was lowered from 1155 to 1073 mV and the i_{sc} was increased from 135 to 225 mA/cm² when the water content passed from 4 to 42%. The impedance spectra were best fitted by two to three arcs, $LR_e(R_1Y_1)(R_2Y_2)(R_3Y_3)$ circuit, using the Zahner fitting software. Y_i is a constant phase element (CPE)

$$Y_i = Y_{i,o} (j\omega)^n \quad (1)$$

with $Y_{i,o}$ an admittance factor, j the imaginary unit, ω the angular frequency, n the frequency number, R_e the series electrolyte resistance between the reference electrode and the working electrode, R_i a resistance, and L the current/potential collectors inductance.



Impedance response after I/V polarization	R_1 [Ωcm^2]	C_1 [$\mu F/cm^2$]	n_1	R_2 [Ωcm^2]	C_2 [$\mu F/cm^2$]	n_2	R_{tot} [Ωcm^2]	i_{sc} [mA/cm ²]
After OCV for 24 h	11.5	1.1	0.58	20	49	0.53	32	70
After repolarization at i_{sc} for 24 h	4.2	1.5	0.75	8.5	65	0.63	13	150

Figure 3: The effect of polarization on the magnitude of the $La_{0.7}Ca_{0.32}CrO_3$ impedance at $830^\circ C$. Inset numbers mark each decade in frequency. + after OCV; ○ after repolarization.

The activation process of R_1 and R_2 in H_2 are of about 170 kJ/mol, whereas that of the electrolyte series resistance seems to follow quite well that of YSZ (81 kJ/mol). The similarity of the activation energy for the electrolyte indicates no contribution of the electrode conductivity to the ohmic drop as the $\text{La}_{0.7}\text{Ca}_{0.32}\text{CrO}_3$ conductivity activation energy lies at 10.9 and 18.4 kJ/mol in air and humidified H_2 .

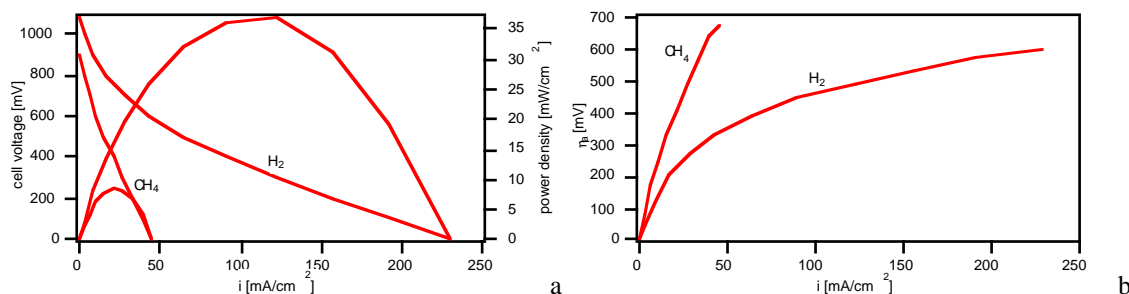
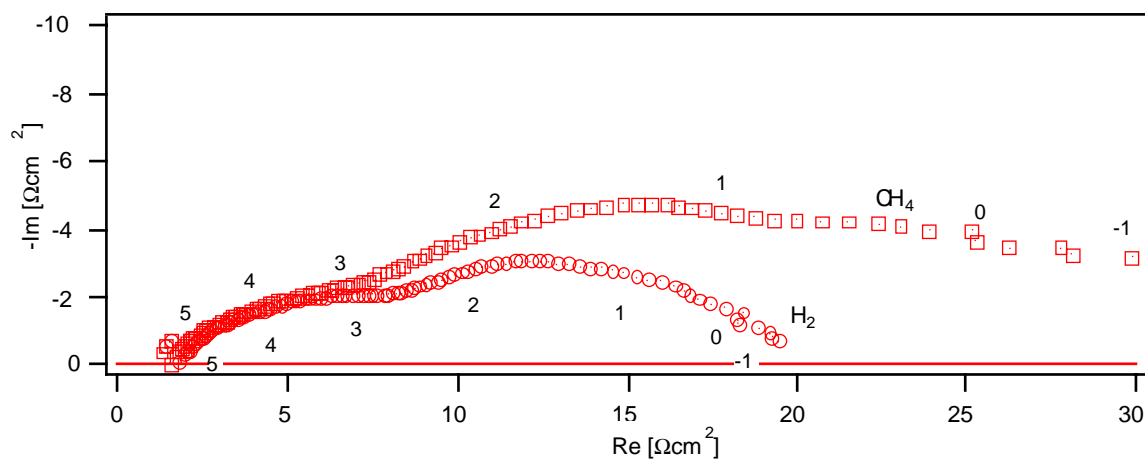


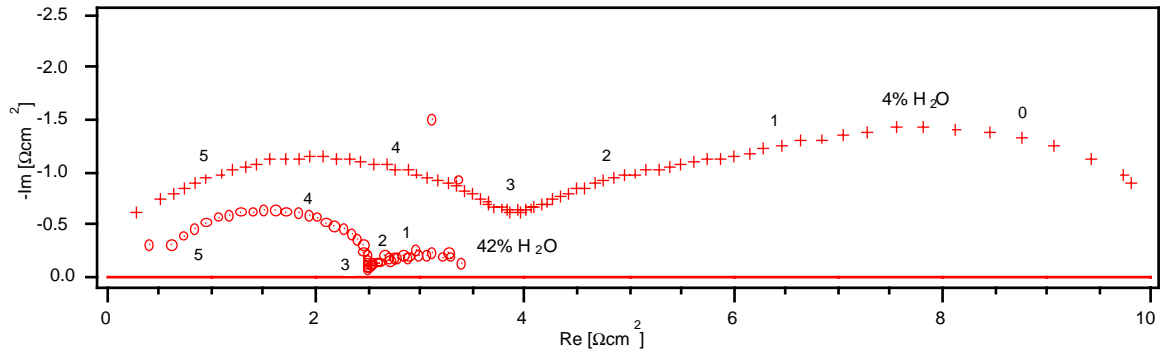
Figure 4: Performance of a $\text{La}_{0.7}\text{Ca}_{0.32}\text{CrO}_3$ anode at 850°C in both humidified H_2 and CH_4 , measured in the sealed configuration. a. I/V and power curves; b. anode overpotential for the two different fuels.

In order to assess the initially rapid and thereafter slower degradations encountered with $\text{La}_{0.7}\text{Ca}_{0.32}\text{CrO}_3$, an experiment was performed in humidified H_2 at high temperature (900°C) in order to accelerate the process (Figure 7). An initial series ohmic loss of $600 \text{ m}\Omega\text{cm}^2$ was observed. This value was higher than expected for a 150 μm thick 8YSZ electrolyte ($\approx 270 \text{ m}\Omega\text{cm}^2$ at 900°C). Polarized at 660 mV, the cell performance degraded rapidly by 75% of the initial current (from 160 mA/cm^2 to 40 mA/cm^2) as shown in the inset of Figure 7. The initially smaller anode impedance response increased from a R_p of $\sim 1.8 \Omega\text{cm}^2$ after 3 h of operation to $\sim 2.7 \Omega\text{cm}^2$ (Figure 8) at 660 mV. Following further polarization at lower cell voltages (300 mV and short circuit), the polarization resistance recovered back to its initial value. Figure 9 shows that after repolarization, the anode overpotential stabilized and did not change much afterwards over 160 h. This rapid degradation is thought to be similar to the one depicted above (Figure 1 and 3) and is related to the slow reduction of the anode.



Impedance response after I/V polarization	R_1 [Ωcm^2]	C_1 [$\mu\text{F}/\text{cm}^2$]	n_1	R_2 [Ωcm^2]	C_2 [$\mu\text{F}/\text{cm}^2$]	n_2	R_{tot} [Ωcm^2]	i_{sc} [mA/cm^2]
$\text{H}_2 + 3\% \text{H}_2\text{O}$	8.4	10.4	0.48	8.8	234	0.68	17.2	230
$\text{CH}_4 + 3\% \text{H}_2\text{O}$	8.3	12.5	0.46	14.3	154	0.68	>30	45

Figure 5: The effect of the gas atmosphere on the $\text{La}_{0.7}\text{Ca}_{0.32}\text{CrO}_3$ impedance at 850°C tested in the sealed configuration. Inset numbers mark each decade in frequency.



Impedance response after I/V polarization	R_1 [Ωcm^2]	C_1 [$\mu\text{F}/\text{cm}^2$]	n_1	R_2 [Ωcm^2]	C_2 [$\mu\text{F}/\text{cm}^2$]	n_2	R_{tot} [Ωcm^2]	i_{sc} [mA/cm^2]
$\text{CH}_4 + 4\% \text{H}_2\text{O}$	3.5	4.6	0.72	3.2	319	0.61	9.7	135
$\text{CH}_4 + 42\% \text{H}_2\text{O}$	1.5	2.8	0.92	0.7	34	0.96	2.9	225

Figure 6: H_2O effect on the polarization resistance of $\text{La}_{0.7}\text{Ca}_{0.32}\text{CrO}_3$ tested at 830°C in CH_4 . Inset numbers mark each decade in frequency.

The degradation was not related to the cathode as its response improved with time during the whole experiment, passing from a R_p at OCV of $2.17 \Omega\text{cm}^2$ to about $0.45 \Omega\text{cm}^2$. It is well known²⁻⁵ that upon reduction, the electronic conductivity of the lanthanum chromite perovskites drops, accompanied by oxygen loss from the lattice. For a dense $\text{La}_{0.7}\text{Ca}_{0.32}\text{CrO}_3$ pellet, the total conductivity was of $0.9 \text{ S}/\text{cm}$ at 850°C in humidified H_2 and $24 \text{ S}/\text{cm}$ in air. The effective conductivity of a porous electrode is well below these values. This implies that the overall conductivity plays a role in the anode performance.

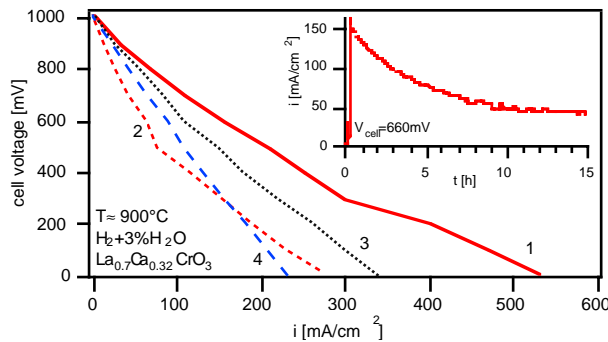


Figure 7: Evolution of the I/V curve for $\text{La}_{0.7}\text{Ca}_{0.32}\text{CrO}_3/8\text{YSZ}/\text{LSM}$ in $\text{H}_2 + 3\% \text{H}_2\text{O}$ at 900°C as a function of time and polarization. 1: after polarization at 660 mV for 3 h ; 2: after polarization at 660 mV for 19 h ; 3: after polarization at 300 mV (running time = 44 h); 4: after polarization at short circuit (running time = 158 h). Inset: the initial rapid current degradation with time ($V_{\text{cell}} = 660 \text{ mV}$).

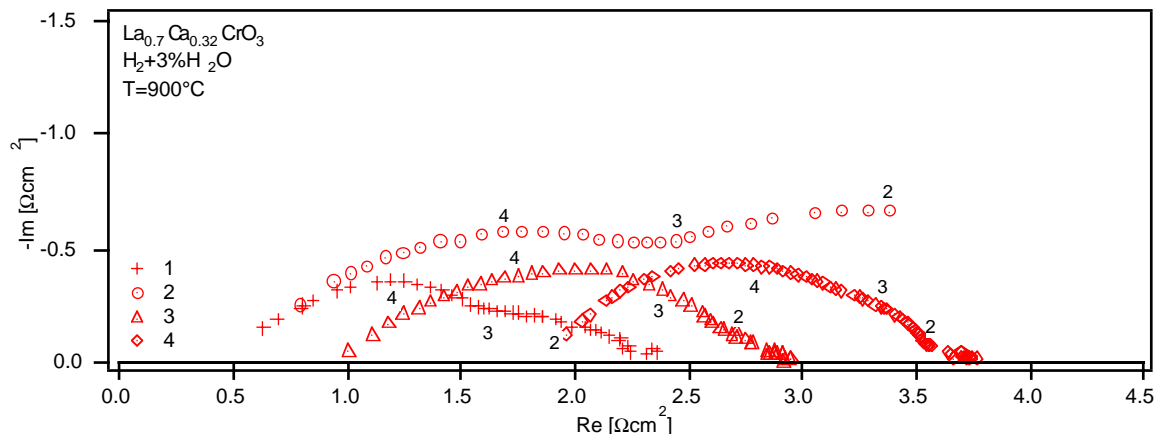


Figure 8: Evolution of the anode impedance at OCV for $\text{La}_{0.7}\text{Ca}_{0.32}\text{CrO}_3/8\text{YSZ}/\text{LSM}$ in $\text{H}_2 + 3\% \text{H}_2\text{O}$ at 900°C . Same indexation as for Figure 7.

Beside this rapid degradation, an additional series ohmic loss, R_e , at the anode side was evidenced by impedance spectroscopy. The R_e increased with time reaching $2 \Omega\text{cm}^2$ after a 160 h run (Figure 8 and 9). *Post-mortem SEM* analysis showed the growth of an interfacial layer of $0.5 \mu\text{m}$ thickness. This layer had a melt like morphology covering the whole surface of the electrolyte (see Figure 10). The topotactic reaction was not visible immediately after the sintering of the anode at $1100^\circ\text{C}/4\text{h}$ (Figure 11) and was thus related to the electrochemical treatment. *EDAX* and *XPS* (e.g. Figure 12) analysis of the tested cell after anode removal revealed the presence of large Ca excess and in some spots the presence of Cr. Only a small amount of La was detected in this layer even after sputter etching the surface (Figure 12). *XPS* established that the electrode grains too exhibited a superficial excess of Ca. *SIMS* revealed that the excess of Ca corresponded to the region where Zr and Y intensities were at their highest (Figure 13). Low angle *XRD* did not reveal any particular peak for CaZrO_3 (Figure 14).

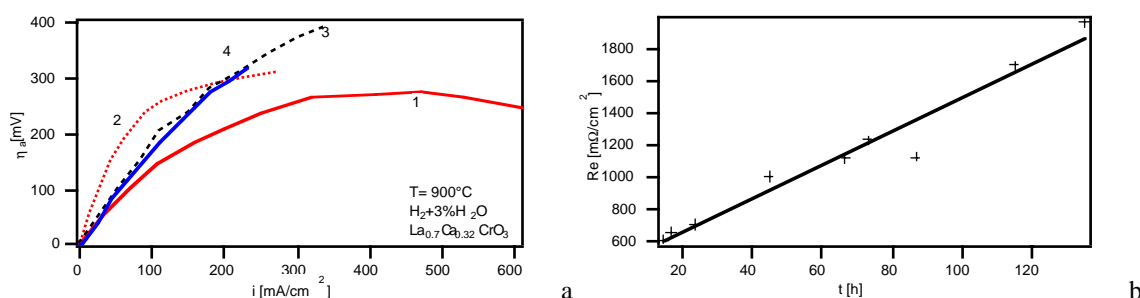


Figure 9: Evolution with time of a. the anode overpotential and b. series resistance for $\text{La}_{0.7}\text{Ca}_{0.32}\text{CrO}_3/8\text{YSZ/LSM}$ in $\text{H}_2 + 3\% \text{H}_2\text{O}$ at 900°C . Same indexation as for Figure 7.

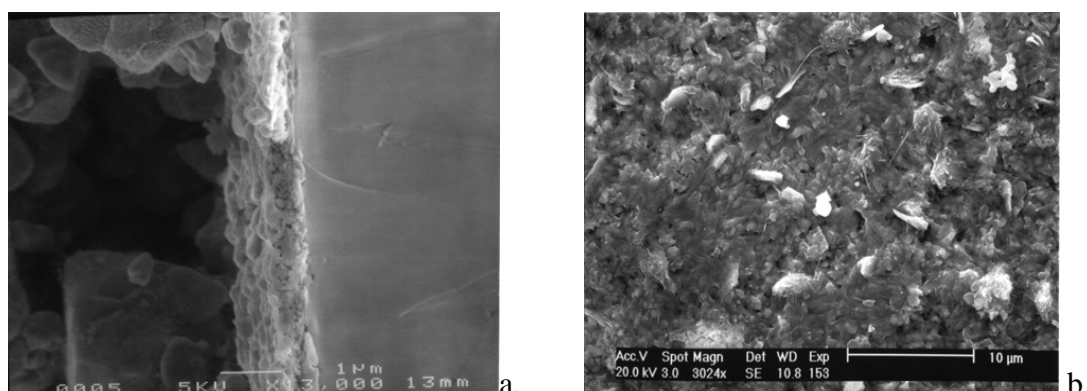


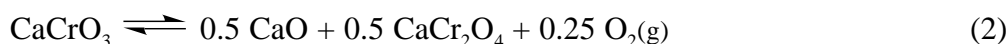
Figure 10: SEM micrographs of the $\text{La}_{0.7}\text{Ca}_{0.32}\text{CrO}_3$ electrode YSZ electrolyte structure. a: cross-section of the cell showing the topotactic layer; b: the reaction layer surface after removal of the electrode.



Figure 11: SEM micrograph of the $\text{La}_{0.7}\text{Ca}_{0.32}\text{CrO}_3$ electrode YSZ electrolyte structure before the electrochemical test.

The literature concerning the stability of these materials indicates the possible formation of an apatite-structured compound, $\text{Ca}_5(\text{CrO}_4)_3\text{O}_{0.5}$, or other $\text{Ca}_m(\text{CrO}_4)_n$ phases which emanate from calcium substituted LaCrO_3 and eventually react with YSZ to form a CaZrO_3 phase¹²⁻¹⁶.

The apatite-like phase is reported to be a good conductor in air (at 900°C , $\sigma_{\text{tot}} \approx 0.6 \text{ S/cm}$) but decomposes in reducing conditions to CaO and CaCr_2O_4 resulting in $\sigma_{\text{tot}} \approx 3.2 \times 10^{-6} \text{ S/cm}$ at 900°C in wet H_2 ¹². The other possible exsolved phase, CaCrO_3 , is also unstable under reducing conditions leading to the following reactions (see Chapter 7):



SIMS analysis pointed out to the possibility of CaZrO_3 formation. Powder diffraction of a 50% YSZ/50% $\text{La}_{0.7}\text{Ca}_{0.32}\text{CrO}_3$ finely mixed powder pressed into a pellet, fired at $1100^\circ\text{C}/4\text{h}$ and subsequently treated for 130 h at 800°C under humidified H_2 did not reveal however any secondary phases (see Figure 15). Perhaps the excess of calcium was dissolved in the YSZ powder without reaching the critical concentration for the formation of CaZrO_3 , or the concentration of the latter was under the level of detection for *XRD*. In the case of an electrode, as the dissolution of an excess of calcium species is hindered, CaZrO_3 formation should be expected as the calcium activity was quite high. However, low angle *XRD* of the YSZ surface, after the anode removal, did not reveal any particular secondary phase indicating here again that the concentration was below the detection limit of the analysis.

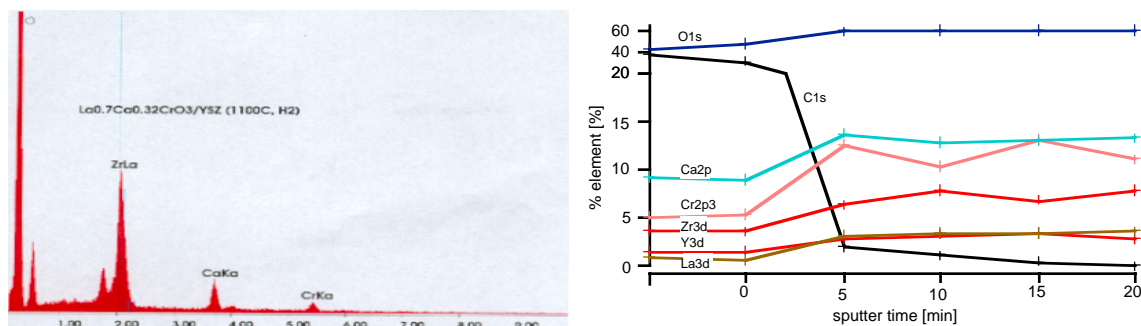


Figure 12: a. EDAX and b. XPS analysis and effect of sputtering of the topotactic reaction shown in Figure 10. Ca and Cr are clearly seen to be the predominant elements in the upper part of the reaction layer, followed by Zr.

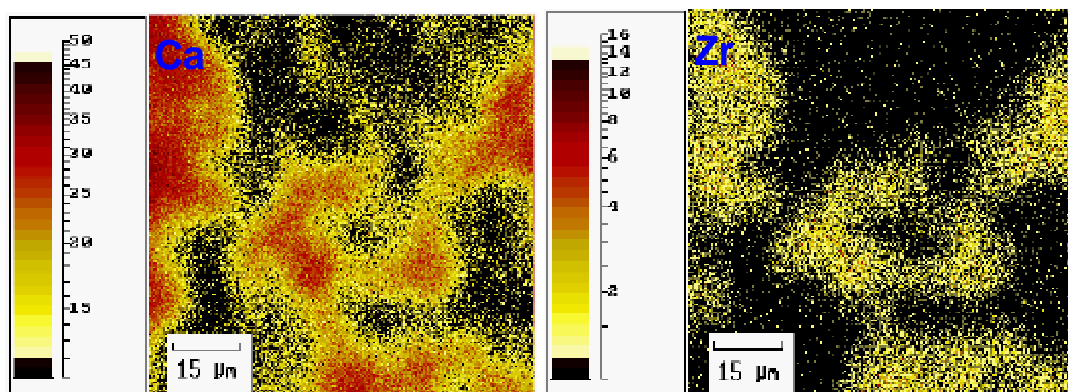


Figure 13: SIMS analysis of the interface of a YSZ/ $\text{La}_{0.7}\text{Ca}_{0.32}\text{CrO}_3$ anode, tested in 3% humidified H_2 at 900°C . The coexistence of Ca and Zr in the same region of the interface indicates the possible formation of CaZrO_3 . Cr and La were not detected in this region.

These materials are very poor conductors and thus can contribute to the observed ohmic loss. Also, Mizusaki et al.¹⁷ reported that the ionic conductivity in SrZrO_3 is 10^{-3} to 10^{-4} times that of YSZ. A rough estimation of the additional ohmic component, if we consider a reaction layer of 0.1 to 0.5 μm (Figure 10) would be of 1 to 5 Ωcm^2 in the case of a dense calcium

zirconate phase and of 3 to 30 Ωcm^2 in the case of a CaO phase. These values are of the same order as the 1.8 Ωcm^2 additional ohmic loss measured on the anode side.

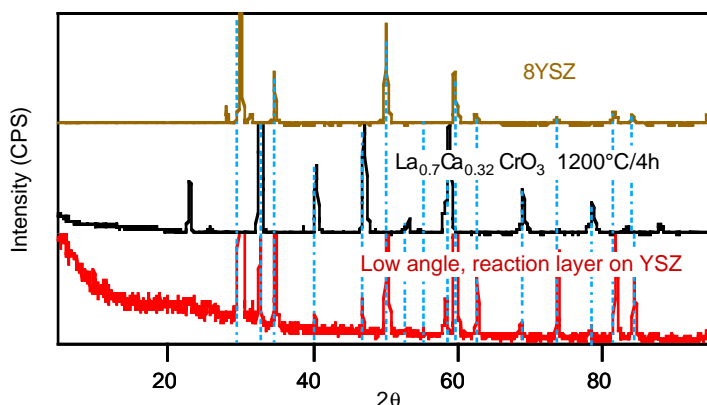


Figure 14: XRD low angle analysis of the reaction layer. No other peaks than for 8YSZ and $\text{La}_{0.7}\text{Ca}_{0.32}\text{CrO}_3$ were detected.

In order to minimize the surface reaction with YSZ and to enhance the overall conductivity and activity of the lanthanum chromites, other compositions were investigated. Stoichiometric lanthanum calcium chromites B-site substituted with other cations (Fe, Co and Cu) were studied. The Co, Fe and Cu compounds, $\text{La}_{0.7}\text{Ca}_{0.3}\text{Cr}_{0.9}\text{Fe}_{0.1}\text{O}_3$, $\text{La}_{0.7}\text{Ca}_{0.3}\text{Cr}_{0.9}\text{Cu}_{0.1}\text{O}_3$ and $\text{La}_{0.7}\text{Ca}_{0.3}\text{Cr}_{0.8}\text{Co}_{0.2}\text{O}_3$, were found to be more reactive than the $\text{La}_{0.7}\text{Ca}_{0.32}\text{CrO}_3$ material and in the case of the Co-containing perovskite, decomposition was observed although this material was reported stable¹⁸. Poor currents and large overpotential drops were measured with these anodes. *Post-mortem* observations showed surface stains on the electrolyte which indicate a topotactic reaction with YSZ. This is compatible with the initial large series ohmic resistances observed by impedance spectroscopy during the electrochemical tests.

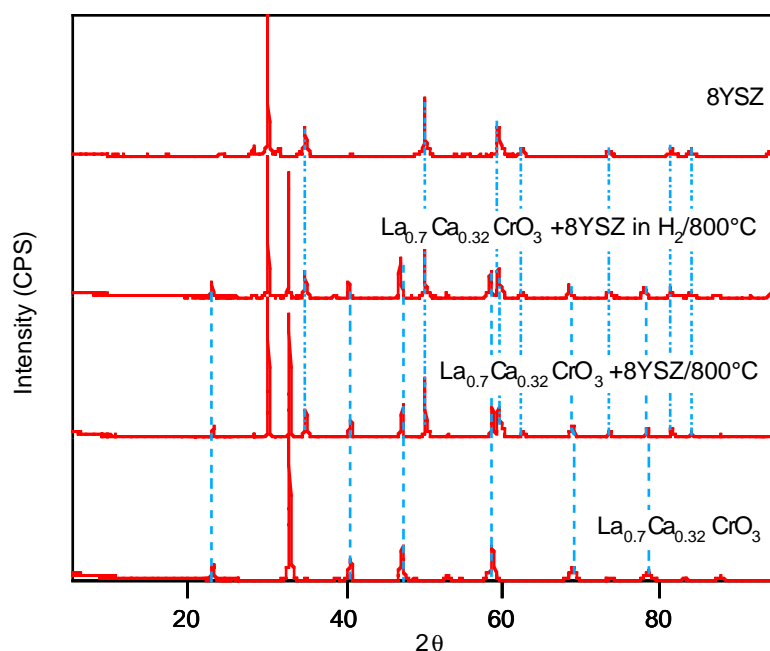


Figure 15: XRD analysis of a $\text{La}_{0.7}\text{Ca}_{0.32}\text{CrO}_3$ and YSZ powder mixture subjected to heat treatment at 800°C in air and humidified H_2 . No reaction was visible within the XRD sensibility limit (about 1%).

Compositions with lower calcium content were also investigated. $\text{La}_{0.8}\text{Ca}_{0.2}\text{CrO}_3$ showed poor adherence on the YSZ and consequently a poor performance ($i_{sc} \approx 80\text{mA}/\text{cm}^2$). Only $\text{La}_{0.75}\text{Ca}_{0.15}\text{Sr}_{0.1}\text{Cr}_{0.95}\text{Mg}_{0.05}\text{O}_3$ seemed more stable under methane than $\text{La}_{0.7}\text{Ca}_{0.32}\text{CrO}_3$ when polarized at intermediate potentials. No surface reaction was detected at 800°C and only small degradation was observed at high temperature (~900°C). However, this material was more sensitive to delamination, because no Ca excess was added. Fine powders improved adhesion to YSZ.

Conclusion

Lanthanum calcium chromite anodes were investigated on YSZ in CH₄ and H₂ at intermediate temperatures. Although they exhibited low performance, these materials were stable against coking unlike Ni-YSZ cermet anodes. At the lower end of the SOFC operating temperature range, the catalytic behaviour of the tested lanthanum chromites kinetically inhibited coking. At higher temperatures, carburization most probably occurred, producing the higher OCV. The degradation of the anode cannot be attributed to carbon formation, as it occurred also with hydrogen fuel. It was more related to the interfacial reaction product of the lanthanum chromite with YSZ, for which imaging and analytical procedures provided good evidence. In the next chapters, further variation of composition was undertaken in order to achieve a stable lanthanum chromite-based anode with a reasonable current output under H₂ and CH₄. This material could then be activated with catalysts or combined with other oxides to form composites with the desired performance.

References

- (1) Nakamura, T.; Petzow, G.; Gauckler, L. J., *Mat. Res. Bull.* **1979**, *14*, 649-659.
- (2) Mizusaki, J.; Yamauchi, S.; Fueki, K.; Ishikawa, A., *Solid State Ionics* **1984**, *12*, 119-124.
- (3) Sakai, N.; Kawada, T.; Yokokawa, H.; Dokiya, M.; Iwata, T., *Journal of Material Science* **1990**, *25*, 4531-4534.
- (4) Flandermeyer, B. F.; Nasrallah, M. M.; Sparlin, D. M.; Anderson, H. U., *High Temperature Science* **1985**, *20*, 259-269.
- (5) Jin, F.; Endo, T.; Takizawa, H.; Shimada, M., *Journal of Solid State Chemistry* **1994**, *113*, 138-144.
- (6) Hassel, B. A. v.; Kawada, T.; Sakai, N.; Yokokawa, H.; Dokiya, M.; Bouwmeester, H. J. M., *Solid State Ionics* **1993**, *66*, 295-305.
- (7) Kawada, T.; Horita, T.; Sakai, N.; Yokokawa, H.; Dokiya, M., *Solid State Ionics* **1995**, *79*, 201-207.
- (8) Baker, R. T.; Metcalfe, I. S., *Applied Catalysis A: General* **1995**, *126*, 297-317.
- (9) Baker, R. T.; Metcalfe, I. S., *Applied Catalysis A: General* **1995**, *126*, 319-332.
- (10) Middleton, P. H.; Steiner, H. J.; Christie, G. M.; Baker, R.; Metcalfe, I. S.; Steele, B. C. H. Proceedings of the Third International Symposium on Solid Oxide Fuel Cells, Hawaii, **1993**; p 542-551.
- (11) Norby, T.; Osborg, P. A.; Dyrлие, O.; Hildrum, R.; Seiersten, M.; Glenne, R. European Solid Oxide Fuel Cell Forum I, Lucerne, Switzerland, **1994**; p 217-226.
- (12) Yasuda, I.; Hishinuma, M., *Solid State Ionics* **1995**, *78*, 109-114.
- (13) Carter, J. D.; Appel, C. C.; Mogensen, M., *Journal of Solid State Chemistry* **1996**, *122*, 407-415.
- (14) Yokokawa, H.; Horita, T.; Sakai, N.; Kawada, T.; Dokiya, M.; Takai, Y.; Todoki, M., *Thermochimica Acta* **1995**, *267*, 129-138.
- (15) Sakai, N.; Kawada, T.; Yokokawa, H.; Dokiya, M., *Journal of the Ceramic Society of Japan* **1993**, *101*, 1195-1200.
- (16) Sakai, N.; Kawada, T.; Yokokawa, H.; Dokiya, M. Science and Technology of Zirconia V, Melbourne, Australia, **1992**.
- (17) Mizusaki, J.; Tagawa, H.; Katou, M.; Hirano, K.; Sawata, A.; Tsuneyoshi, K. The Second International Symposium on Solid Oxide Fuel Cells, Athens, Greece, **1991**; p 487-494.
- (18) Armstrong, T. R.; Stevenson, J. W.; Pederson, L. R.; Raney, P. E., *J. Electrochem. Soc.* **1996**, *143*, 2919-2925.

Chapter 5 五

Stability of Ca and Sr substituted LaCrO₃ during current treatment

Stability of Ca and Sr substituted LaCrO_3 during current treatment*

Abstract

$\text{La}_{0.7}\text{Ca}_{0.32}\text{CrO}_3$, $\text{La}_{0.75}\text{Ca}_{0.15}\text{Sr}_{0.1}\text{Cr}_{0.95}\text{Mg}_{0.05}\text{O}_3$, $\text{La}_{0.85}\text{Ca}_{0.15}\text{CrO}_3$, $\text{La}_{0.85}\text{Ca}_{0.15}\text{Cr}_{0.9}\text{Mg}_{0.1}\text{O}_3$, $\text{La}_{0.85}\text{Sr}_{0.15}\text{CrO}_3$, $\text{La}_{0.85}\text{Sr}_{0.15}\text{Cr}_{0.9}\text{Mg}_{0.1}\text{O}_3$ and $\text{La}_{0.8}\text{Sr}_{0.2}\text{Cr}_{0.97}\text{V}_{0.03}\text{O}_3$ compounds were studied. During high temperature treatment, they were found to exhibit liquid phase sintering except for $\text{La}_{0.85}\text{Ca}_{0.15}\text{CrO}_3$ and $\text{La}_{0.85}\text{Sr}_{0.15}\text{CrO}_3$. Mg enhanced the densification of stoichiometric LaCrO_3 . They were tested electrochemically in reducing atmospheres containing hydrogen, methane and CO/CO_2 . Current was found to affect the stability of the heavily doped samples, whereas the reducing atmospheres did not have a detectable impact. Calcium and/or strontium and chromium-enriched secondary phases were detected after current treatment with $\text{La}_{0.7}\text{Ca}_{0.32}\text{CrO}_3$, $\text{La}_{0.75}\text{Ca}_{0.15}\text{Sr}_{0.1}\text{Cr}_{0.95}\text{Mg}_{0.05}\text{O}_3$ and $\text{La}_{0.8}\text{Sr}_{0.2}\text{Cr}_{0.97}\text{V}_{0.03}\text{O}_3$ samples. $\text{La}_{0.85}\text{Ca}_{0.15}\text{Cr}_{0.9}\text{Mg}_{0.1}\text{O}_3$ and $\text{La}_{0.85}\text{Sr}_{0.15}\text{Cr}_{0.9}\text{Mg}_{0.1}\text{O}_3$ did not degrade during current treatment for 100 h. A current enhanced demixing could be responsible for the segregation. The solubility limit of calcium and strontium in LaCrO_3 is estimated to be low at 800°C (around 15%).

Introduction

Calcium substituted lanthanum chromites (LCC), commonly used as interconnects¹ for solid oxide fuel cells (SOFC), were explored as anodes alternative to the conventional Ni-yttria stabilized zirconia (YSZ)-cermet² (Chapter 4). Thermochemical and electrocatalytic properties of these anodes were assessed in humidified hydrogen and methane fuels at different temperatures². During the electrochemical tests (fuel cell conditions), a rapid degradation of the cell performance was observed. SEM analysis revealed the formation of an interfacial reaction layer between LCC and YSZ. This thin layer was found to be a poor conductor. EDX and ESCA analyses showed that under these reducing conditions, the LCC anodes were enriched with calcium and chromium at the surface. Calcium chromate phases are believed to exsolve from these materials and decompose to CaO which eventually reacts with the YSZ electrolyte to form CaZrO_3 . This phase segregation is also thought to affect the activity of these anodes towards the fuel oxidation.

In order to ascertain these observations and to follow the possibility of stabilizing these materials against reduction, the behavior of some LCCs with different doping levels was investigated in different atmospheres and by current treatment.

Experimental

$\text{La}_{0.7}\text{Ca}_{0.32}\text{CrO}_3$ (LCC1) powder was acquired from EMPA, Switzerland, whereas $\text{La}_{0.8}\text{Sr}_{0.2}\text{Cr}_{0.97}\text{V}_{0.03}\text{O}_3$ (LSCV) was obtained from IRD, Denmark. $\text{La}_{0.75}\text{Ca}_{0.15}\text{Sr}_{0.1}\text{Cr}_{0.95}\text{Mg}_{0.05}\text{O}_3$ (LCSCM), $\text{La}_{0.85}\text{Ca}_{0.15}\text{CrO}_3$ (LCC2), $\text{La}_{0.85}\text{Sr}_{0.15}\text{CrO}_3$ (LSC) and $\text{La}_{0.85}\text{Ca}_{0.15}\text{Cr}_{0.9}\text{Mg}_{0.1}\text{O}_3$ (LCCM) and $\text{La}_{0.85}\text{Sr}_{0.15}\text{Cr}_{0.9}\text{Mg}_{0.1}\text{O}_3$ (LSCM) powders were prepared following a modified citrate procedure from nitrate precursors (see Chapter 3).

Ball-milled, these powders were then pressed as bars of $13 \times 6 \times 5 \text{ mm}^3$ at 100 kPa and sintered at 1550°C for 4 h. Densities varied between 95 and 97% of theoretical for LCC1, LCSCM, LCCM and LSCM whereas LCC2 and LSC pellets were quite porous (67 and 72% dense respectively). It was observed that the addition of Mg enhanced noticeably the sinterability of stoichiometric lanthanum chromites (see for example Figure 6-c, 6-d). Subsequently, they were polished with μm diamond paste and ultrasonically washed with ethanol. Some were cut in length into two or three pieces.

dc four probe conductivity measurements were carried out at 800°C for 100 h on the bars (except for LCC2 and LSC for their high porosity as discussed in Chapter 3) in air and reducing conditions, especially in $\text{H}_2 + 3\% \text{H}_2\text{O}$, to analyze the effect of current and of gas

* This chapter has been submitted in a shorter version as J. Sfeir, J. Van herle and A. J. McEvoy, 'Stability of calcium substituted lanthanum chromites used as SOFC anodes for methane oxidation', *J. Europ. Ceram. Soc.*, 19, 1999, 897-902.

atmosphere on the stability of these materials. Silver-paint was applied as electrodes and silver or platinum wires were used as contacts. Constant currents of 10 to 30 mA were applied corresponding to about 100 to 300 mA/cm², and the voltage monitored with time. The oxygen partial pressure was measured simultaneously by a YSZ sensor placed near the sample.

Other rods were subjected for 100 h to different atmospheres like air, 80%CO/20%CO₂, CH₄+3%H₂O or H₂+3%H₂O without current treatment. All rods were later examined by SEM and EDAX and some also by XRD.

Results

As discussed in Chapter 3, by substitution of elements such as Ca, Sr and Mg on the La or Cr sites in LaCrO_3 (LC), electronic compensation occurs by the formation of holes at high oxygen partial pressure, i.e. the oxidation of Cr^{III} to Cr^{IV} , or of oxygen vacancies at low P_{O_2} . In our measurements at 800°C, the conductivities in air increased with the dopant concentration and amounted to 24, 16, 11, 7, 15 and 24 S/cm for LCC1, LCC2, LCSCM, LCCM, LSCM and LSCV respectively. After passing from air to humidified hydrogen ($P_{\text{O}_2} \approx 10^{-21}$ atm) and applying a current to the samples, the conductivities decreased over a period of 20 h, then increased again to stabilize at an intermediate value. In this atmosphere they reached only 0.8, 2.2, 0.5, 0.34-1, 1.3 and 6.5 S/cm respectively. As expected^{3,4}, the conductivities at low oxygen partial pressures are quite low, except for the LSCV composition.

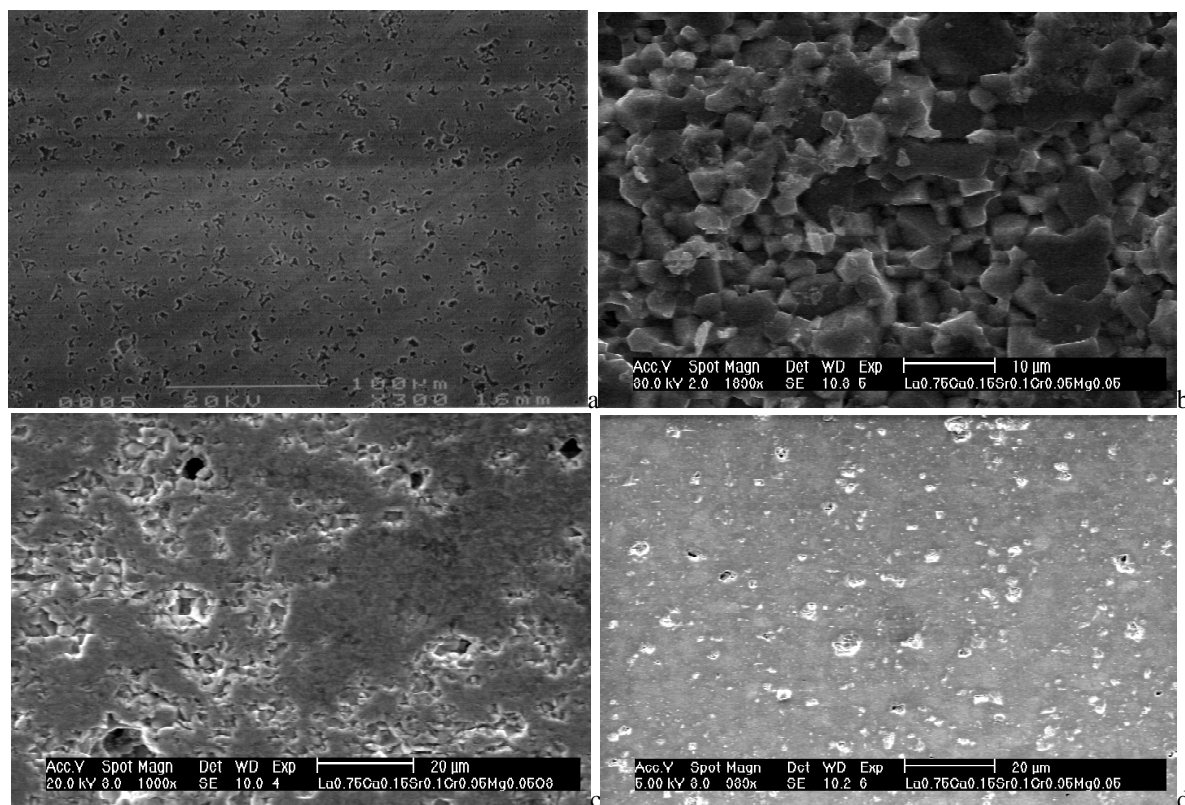


Figure 1: SEM micrographs of $\text{La}_{0.75}\text{Ca}_{0.15}\text{Sr}_{0.1}\text{Cr}_{0.95}\text{Mg}_{0.05}\text{O}_3$ (LCSCM) rods. a. as such, polished surface; b. cross-section of a current treated rod in humidified H_2 at 800°C; c. surface of a wet methane treated rod at 800°C; d. surface of a CO/CO_2 treated rod at 800°C.

From post-mortem analyses, LCC1 and LCSCM exhibited cracks and were found to be fragile when compared to the initial material. SEM analysis showed (e.g. Figure 1-b) that these two materials broke rather intragranularly. LCCM and LSCM did not display a similar behaviour.

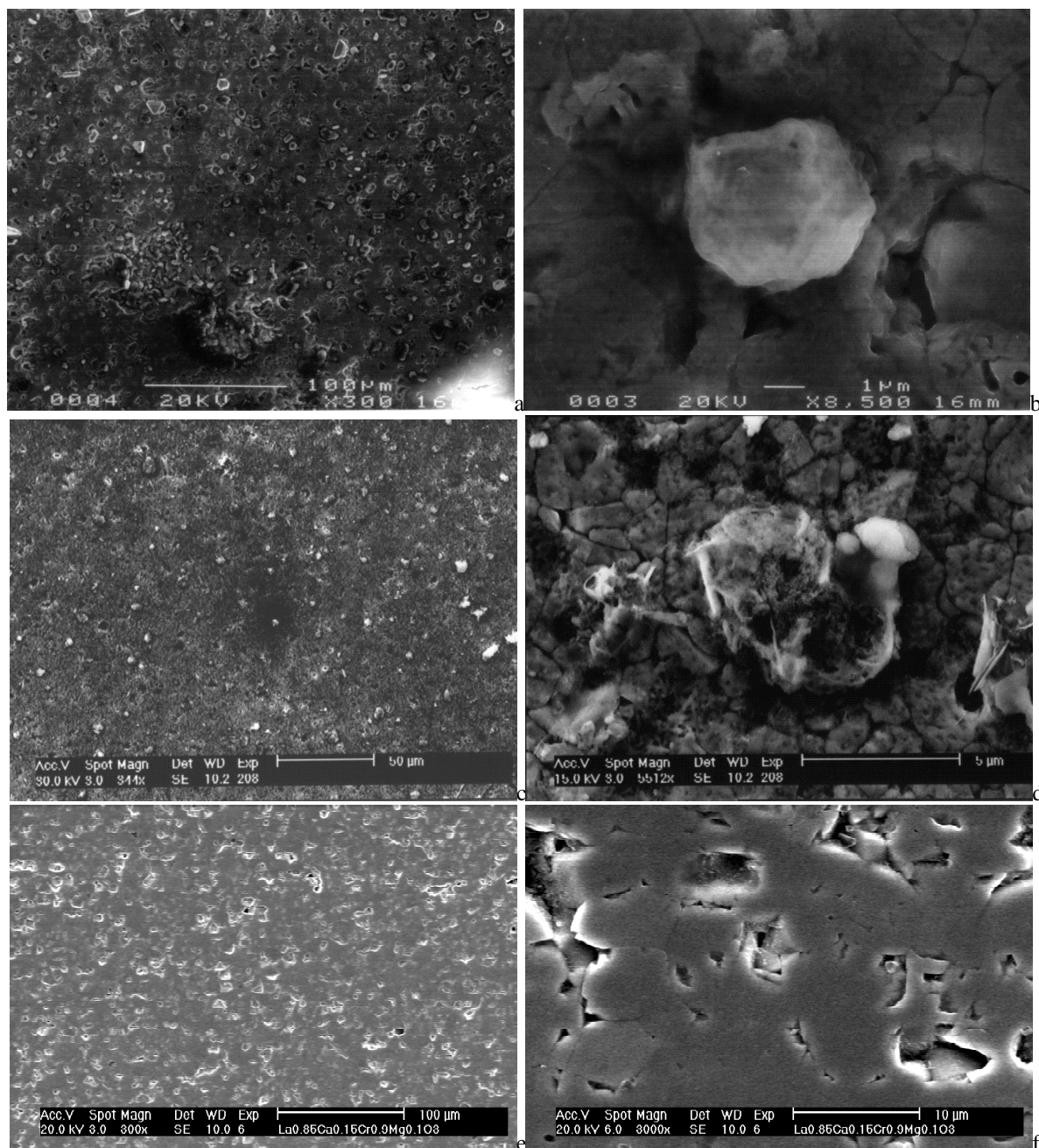


Figure 2: Surface SEM micrographs of: a-b. $\text{La}_{0.7}\text{Ca}_{0.32}\text{CrO}_3$ (LCC1); c-d. $\text{La}_{0.75}\text{Ca}_{0.15}\text{Sr}_{0.1}\text{Cr}_{0.95}\text{Mg}_{0.05}\text{O}_3$ (LCSCM); e-f. $\text{La}_{0.85}\text{Ca}_{0.15}\text{Cr}_{0.9}\text{Mg}_{0.1}\text{O}_3$ (LCCM) rods subjected for 100 h to current treatment in humidified hydrogen ($T=800^\circ\text{C}$). Only LCC1 and LCSCM exhibited secondary phase exsolution.

SEM micrographs of the LCC1 and LCSCM conductivity rods showed also the presence of exsolved phases as depicted in Figure 2. LSCV had a similar behaviour (Figure 3). Semi-quantitative EDAX analysis revealed secondary phases enriched with calcium, strontium and chromium with only small amounts of lanthanum which might stem from the underlying bulk. Si impurities were also detected. The exact nature of these phases is not confirmed as XRD analysis did not reveal any extra phase (XRD detection limit is of about 1%). However, from EDAX analysis, $(\text{Ca,Sr})\text{O}$ as well as $(\text{Ca,Sr})_x\text{Cr}_y\text{O}_z$ are thought to exist on the surface. Figure 4 shows two different EDAX spectra, one for a freshly polished LCSCM surface and the other for the LCSCM rod subjected to the conductivity test. After a further thermal treatment in air, we observed a melt-like form covering the surface (Figure 5). As to LCCM, the conductivity sample had a different behaviour and no secondary phases were detected (Figure 2-e,f).

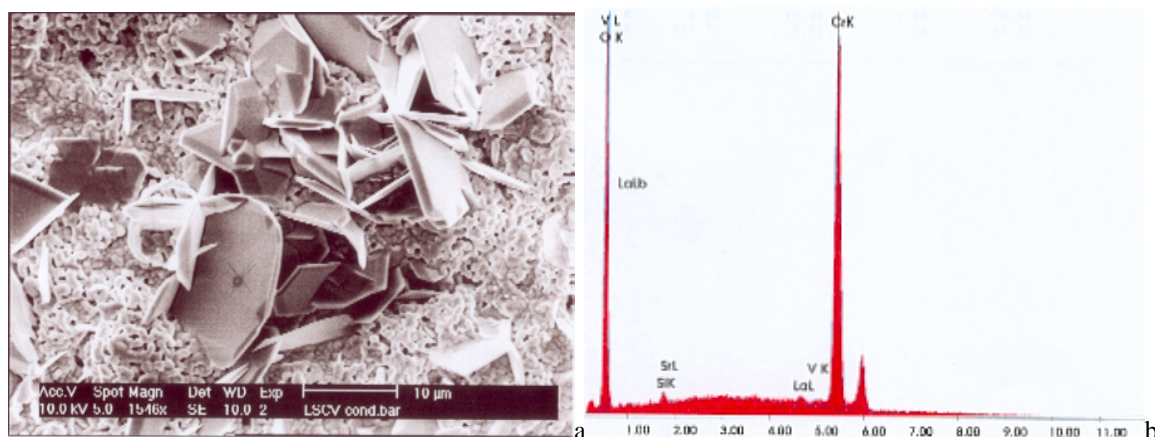


Figure 3: a. Surface SEM micrograph of LSCV showing Cr enrichment (97%) as slabs after the conductivity measurements. b. EDAX analysis of these slabs.

Further EDAX investigations on cross-sections and on repolished bar surfaces did not reveal any particular phase segregation within the bulk. This behaviour confirm parallel observations on porous LCC1 anodes where superficial calcium and chromium excess was detected by ESCA within a few nm depth.

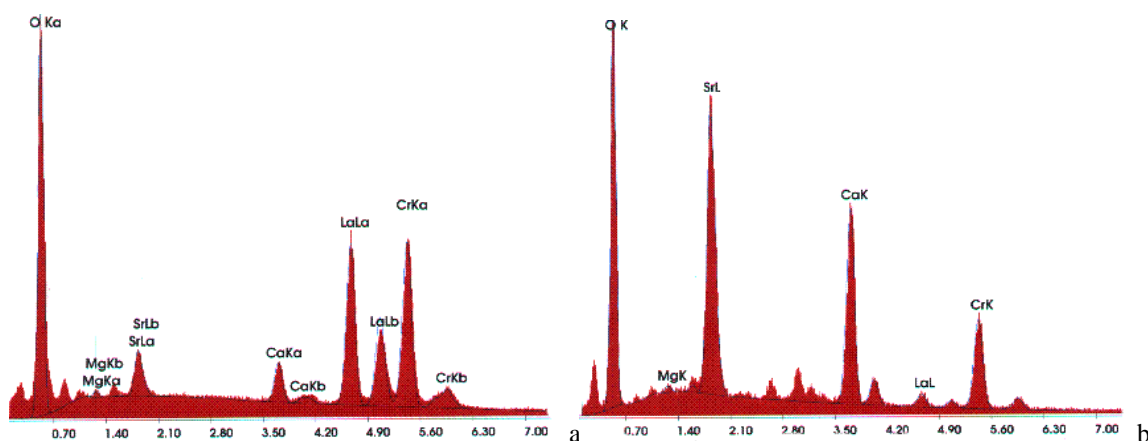


Figure 4: EDAX analysis on a. polished LCSCM surface, as seen in figure 1-a, and b. current treated LCSCM in humidified hydrogen and corresponding to the structure of figure 2-d

Other polished LCSCM rods were subjected to different gas mixtures. The results presented in Figure 1-c,d and 6-b indicate no detectable secondary phase exsolution when the polished rods were only thermally treated in humidified CH_4 , CO/CO_2 and humidified H_2 . No indication of carbonate growth was evidenced. Similarly, LCC1, LCCM and LCC2 did not degrade when treated in wet hydrogen (Figure 6-a,c,d). The same was observed with LSC and LSCM. These materials are thus quite stable even under such reducing atmospheres.

Surface analysis on fresh unpolished samples revealed melt-like layers at the grain boundaries (see Figure 7) suggesting a liquid phase sintering process. High levels of Ca, Sr, Cr and Mg along with some Si were found there. Obviously, these layers are cleaned away when the samples are polished.

Discussion

The behaviour just described indicates that the current treatment has an impact on the stability of these materials. We observed in Chapter 3 that screen-printed substituted LaCrO_3 , sintered at 1100°C on YSZ sheets, did not generate any relevant topotactic reaction, even when treated for 100 h at 800°C in humidified hydrogen. In a fuel cell test however, a rapid

degradation was noticed and related to the formation of a melt-like interfacial layer ² (Chapter 4).

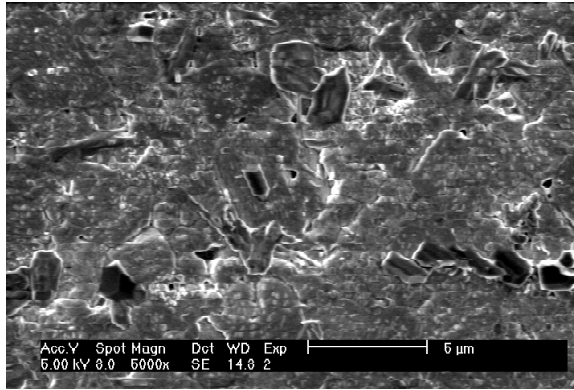


Figure 5: Surface SEM micrograph of LCSCM, first current treated in $\text{H}_2 + 3\%\text{H}_2\text{O}$, then followed by a thermal treatment in air. The secondary phases exsolved during current treatment seem to melt.

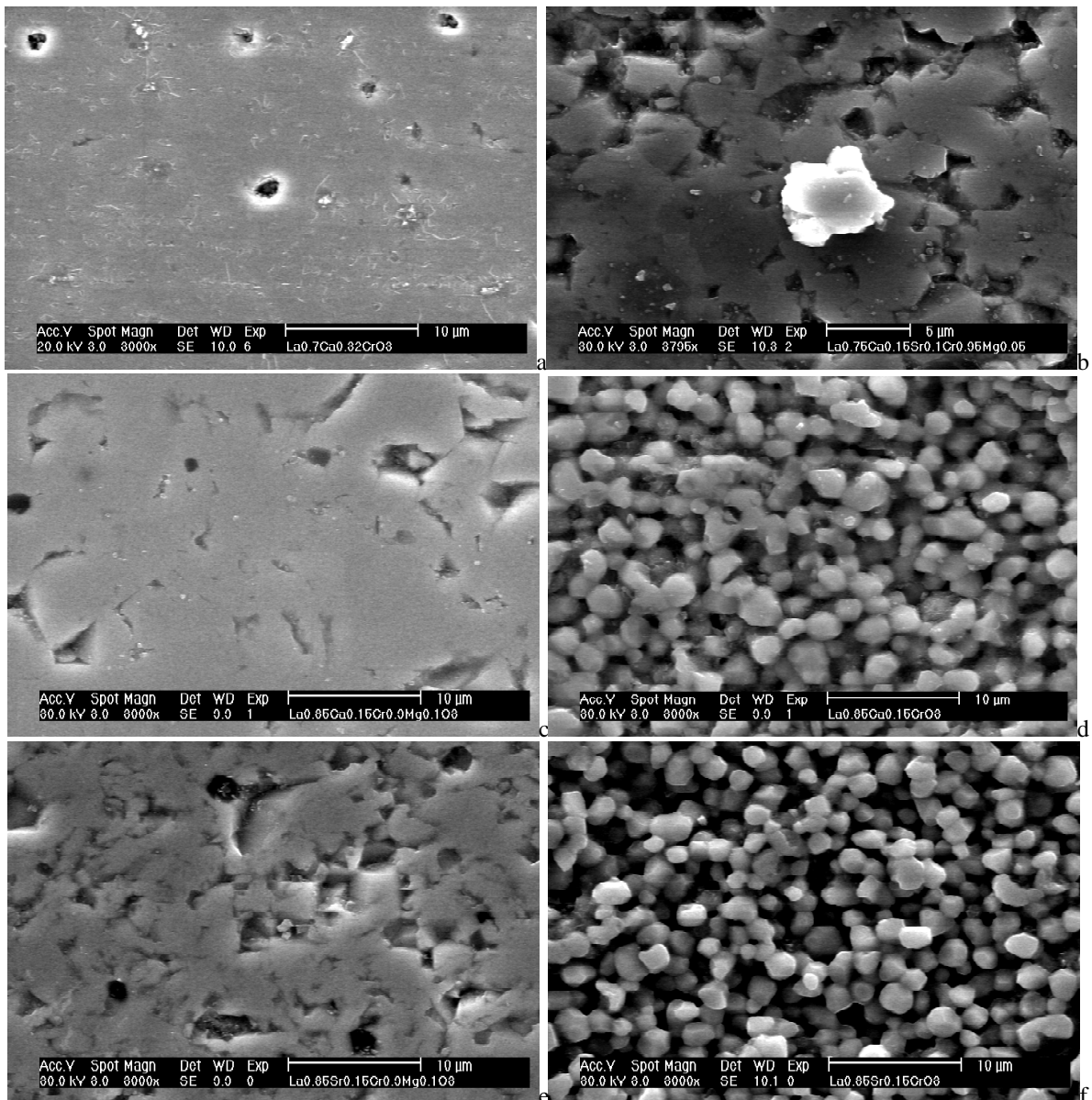


Figure 6: Surface SEM micrographs of wet hydrogen treated rods of: a. $\text{La}_{0.7}\text{Ca}_{0.32}\text{CrO}_3$ (LCC1); b. $\text{La}_{0.75}\text{Ca}_{0.15}\text{Sr}_{0.1}\text{Cr}_{0.95}\text{Mg}_{0.05}\text{O}_3$ (LCSCM); c. $\text{La}_{0.85}\text{Ca}_{0.15}\text{Cr}_{0.9}\text{Mg}_{0.1}\text{O}_3$ (LCCM); d. $\text{La}_{0.85}\text{Ca}_{0.15}\text{CrO}_3$ (LCC2); e. $\text{La}_{0.85}\text{Sr}_{0.15}\text{Cr}_{0.9}\text{Mg}_{0.1}\text{O}_3$ (LSCM) and $\text{La}_{0.85}\text{Sr}_{0.15}\text{CrO}_3$ (LSC). The addition of 10% Mg on the B-side enhanced the sinterability of $\text{La}_{0.85}\text{Ca}_{0.15}\text{CrO}_3$ and $\text{La}_{0.85}\text{Sr}_{0.15}\text{CrO}_3$.

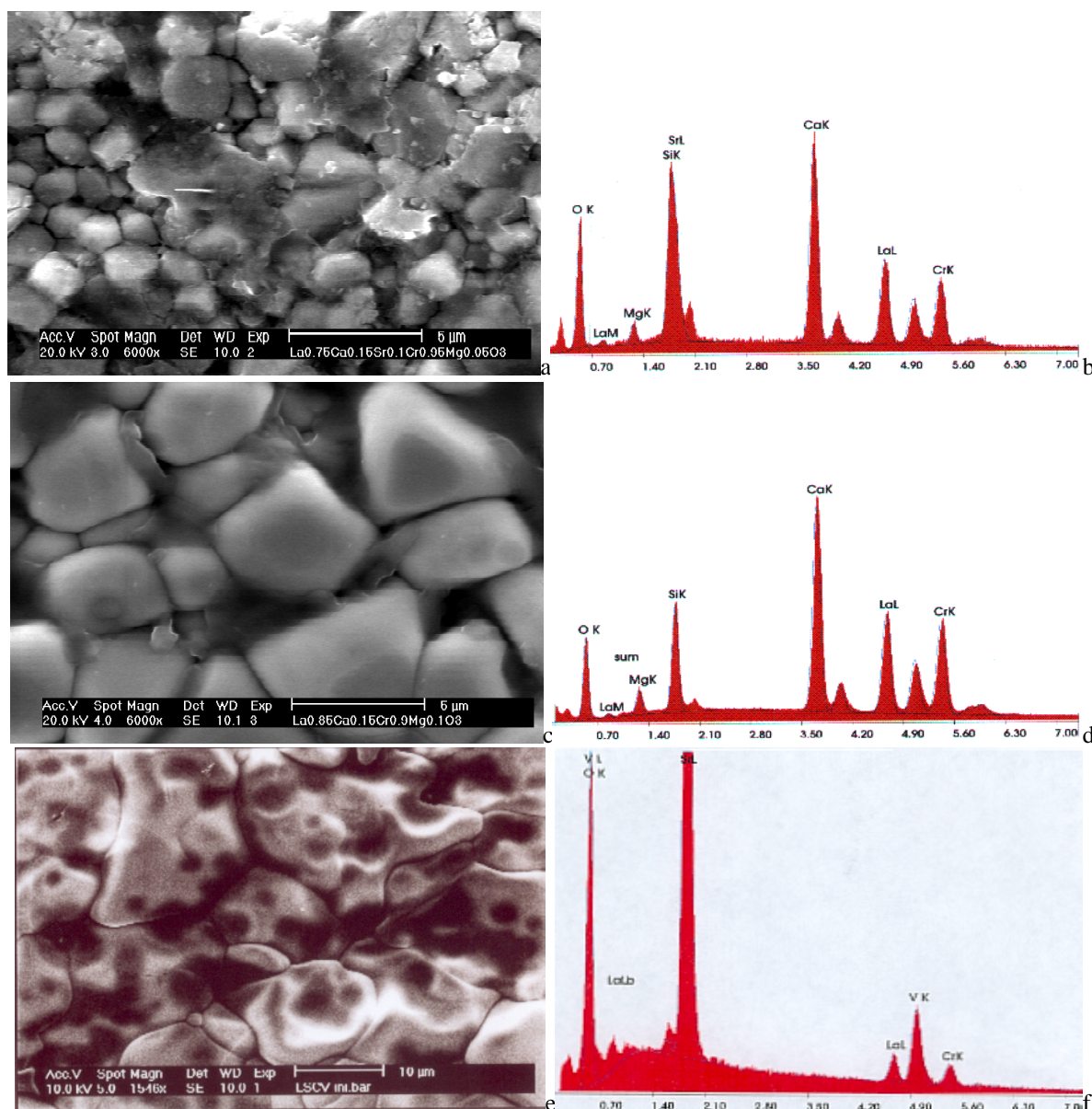


Figure 7: SEM micrographs and subsequent EDX analyses of: a-b. LSCM, c-d. LCCM and e-f. LSCV unpolished rods sintered at 1550°C . Melt-like structures can be seen corresponding to enriched Ca, Sr, Mg, Cr and Si phases. The shown EDX spectra are taken in the melt-like areas of the micrographs.

The exsolved secondary phases, $(\text{Ca}_m(\text{CrO}_4)_n$ and CaO), are suspected to react with YSZ and to form CaZrO_3 , as evidenced by the overlapping of SIMS analyses for Ca and Zr² (Chapter 4).

Substituted LCs ($\text{La}_{1-x}\text{Ca}_x\text{Cr}_{0.9}\text{Ni}_{0.1}\text{O}_3$ ($x = 0.2, 0.3$ and 0.4) and $\text{La}_{0.7}\text{Sr}_{0.3}\text{Cr}_{1-y}\text{Co}_y\text{O}_3$ ($y = 0-0.2$)) were already reported^{5,6} to degrade in reducing atmospheres due to a destabilizing effect of the substituents. Sakai et al. and Nishiyama et al.^{7,8} observed $\text{Ca}_m(\text{CrO}_4)_n$ and $\text{Sr}_m(\text{CrO}_4)_n$ migration on both sides of $\text{La}(\text{Ca,Sr})\text{Cr}(\text{Co})\text{O}_3$ compounds under an oxygen potential gradient and concomitant current flow at 1000°C . This phenomena may be related to a demixing effect^{9,10}. For the LC materials, Sakai et al.⁷ reported that within a few nm (≈ 5 nm) of the surface, a calcium rich region existed at grain boundaries as evidenced by AES measurements. A compositional change in such a thin region would however be undetectable by EDAX. $(\text{Ca,Sr})_m(\text{CrO}_4)_n$ phases are known to be present in highly substituted LCs^{11,12} and also in LCs whose *A*-site to *B*-site ratio exceed a narrow window of stability¹¹. These phases are responsible for the dense sintering of these materials, and are thought to ultimately redissolve in the material which make them quite difficult to detect by XRD. By annealing at a lower

temperature than the fabrication temperature, these phases should segregate¹³⁻¹⁵. However, as no detectable degradation was observed on polished rods thermally treated in oxidizing or reducing gas mixtures, the demixing should be slow or at least occurring along the grain boundaries.

The fact that current, more than reducing conditions, seemed to affect the stability and this might be related to current enhanced demixing. When a multi-component material is subjected to a gradient of a thermodynamic force, e.g. a gradient of chemical potential, a redistribution of the composition, or kinetic demixing, may occur in the homogeneous structure due to the difference of mobility or valences of the structural cations^{9, 10, 16}. Potential gradient induced demixing was observed in some materials such as $\text{Co}_{1-x}\text{Mg}_x\text{O}$, Fe_2SiO_4 and NiTiO_3 ¹⁷. The electrotransport-induced demixing effect was observed in $(\text{Co,Mg})\text{O}$ and $(\text{ZrO}_2, \text{Y}_2\text{O}_3)$ ¹⁸, $(\text{Co,Ni})\text{O}$ ¹⁹, $\text{Co}_{1-x}\text{Ga}_x\text{O}$ ²⁰ and $(\text{Mn}_x\text{Fe}_{1-x})_3\text{O}_4$ ¹⁶.

In literature, measurements done on cation tracer bulk diffusion in LaCrO_3 -based materials showed that Cr diffusion is slower than La, Ca and O diffusion, with bulk diffusion coefficients of 1×10^{-21} , $10^{-19.75}$, 10^{-19} and 2.2×10^{-16} m^2/s respectively. In the grain boundary, Cr, O and Ca have diffusion coefficients of 1.6×10^{-15} , $2 \times 10^{-11} \sim 6 \times 10^{-15}$ and $10^{-13} \sim 10^{-12}$ m^2/s respectively²¹⁻²⁵. Sr is expected to have similar diffusion coefficients as Ca. The Ca to Cr tracer diffusion coefficient ratio is of 93.5 for the bulk and 63-636 for the grain boundary. This difference is quite high and expected to favor the demixing. An electric field would thus induce this process and lead to the migration of the cations.

As some report in literature indicates a rapid equilibration between the secondary phases and the LCs with temperature¹³, the effect highlighted here might be related to the migration of the cations in the grain boundary region. Thus, the gas atmosphere composition would not play much of a role in the segregation, unless some phase instability occurs under reducing conditions, or by chemical reaction with a particular gas component. The appearance of secondary phases on the surface of the heavily substituted LCs, observed only after current treatment, clearly points to the electrotransport-induced demixing.

Ca and Sr are thus expected to segregate preferentially and this seemed to be the case for the LCC1 and LCSCM as Cr and Mg surface concentrations were very low, related to the LC phases. However, for the LSCV, Cr slabs were observed after the conductivity tests. It is not very clear what influence V has on this system.

Finally, the fact that LCCM and LSCM materials did not present any phase exsolution indicates that the solubility limit of calcium and strontium is quite low at least at 800°C (around 15%). Carter et al.¹³ reported a solubility limit of 20% for calcium at 900°C , and Sakai et al.²⁶ observed a phase segregation using XRD measurements in the $\text{La}_{0.7}\text{Ca}_{0.32}\text{CrO}_3$ system.

Conclusion

The present results indicate the liquid phase sintering of $\text{La}_{0.7}\text{Ca}_{0.32}\text{CrO}_3$, $\text{La}_{0.75}\text{Ca}_{0.15}\text{Sr}_{0.1}\text{Cr}_{0.95}\text{Mg}_{0.05}\text{O}_3$, $\text{La}_{0.85}\text{Ca}_{0.15}\text{Cr}_{0.9}\text{Mg}_{0.1}\text{O}_3$ and $\text{La}_{0.85}\text{Sr}_{0.15}\text{Cr}_{0.9}\text{Mg}_{0.1}\text{O}_3$. Exsolved secondary phases, enriched with calcium and/or strontium and chromium oxides, were observed on sintered bars. Mg was found to enhance the densification of these materials.

These materials appear to be stable in reducing atmospheres such as humidified hydrogen and methane. No carbonate growth was evidenced. Current flow, more than the reducing conditions, seemed to affect the stability of these materials when subjected to low oxygen partial pressures. Secondary phase exsolution was observed at the surface of polished sintered rods when current treated at 800°C , in the case of the heavily substituted materials. However, no bulk segregation was observed in polished surfaces and in cross-sections. This indicates a demixing effect enhanced by current. Equally, the solubility limit of calcium in LaCrO_3 appeared low. $\text{La}_{0.85}\text{Ca}_{0.15}\text{Cr}_{0.9}\text{Mg}_{0.1}\text{O}_3$ and $\text{La}_{0.85}\text{Sr}_{0.15}\text{Cr}_{0.9}\text{Mg}_{0.1}\text{O}_3$ compound, with a low Ca/Sr concentration, did not exhibit such exsolutions.

Overall, the behaviour described above gave evidence of the surface reactions which could occur between a porous LC anode and YSZ. The exsolution, and thus the surface reaction, might be enhanced in a porous structure. Lowering the substituent amount, whose concentration does not affect the conductivity of LaCrO_3 at low oxygen partial pressures, is thus needed to get a stable LaCrO_3 -based anode.

References

- (1) Minh, N. Q., *J. Am. Ceram. Soc.* **1993**, *76*, 563-588.
- (2) Sfeir, J.; Van herle, J.; McEvoy, A. J. Third European Solid Oxide Fuel Cell Forum, Nantes-France, **1998**; p 267-276.
- (3) Armstrong, T. R.; Stevenson, J. W.; Pederson, L. R.; Raney, P. E., *J. Electrochem. Soc.* **1996**, *143*, 2919-2925.
- (4) Sakai, N.; Kawada, T.; Yokokawa, H.; Dokiya, M.; Iwata, T., *Journal of Material Science* **1990**, *25*, 4531-4534.
- (5) Sammes, N. M.; Ratnaraj, R., *Journal of Materials Science Letters* **1996**, *15*, 55-56.
- (6) Christie, G. M.; Middleton, P. H.; Steele, B. C. H. The Third International Symposium on Solid Oxide Fuel Cells, Hawaii, **1993**; p 315-324.
- (7) Sakai, N.; Kawada, T.; Yokokawa, H.; Dokiya, M. Science and Technology of Zirconia V, Melbourne, Australia, **1992**.
- (8) Nishiyama, H.; Aizawa, M.; Yokokawa, H.; Horita, T.; Sakai, N.; Dokiya, M.; Kawada, T., *J. Electrochem. Soc.* **1996**, *143*, 2332-2341.
- (9) Schmalzried, H.; Laqua, W., *Oxidation of Metals* **1981**, *15*, 339-353.
- (10) Schmalzried, H., *Reactivity of Solids* **1986**, *1*, 117-137.
- (11) Chick, L. A.; Liu, J.; Stevenson, J. W.; Armstrong, T. R.; McCready, D. E.; Maupin, G. D.; Coffey, G. W.; Coyle, C. A., *J. Am. Ceram. Soc.* **1997**, *80*, 2109-2120.
- (12) Sakai, N.; Kawada, T.; Yokokawa, H.; Dokiya, M.; Kojima, I., *J. Am. Ceram. Soc.* **1993**, *76*, 609-616.
- (13) Carter, J. D.; Sprenkle, V.; Nasrallah, M. M.; Anderson, H. U. Proceedings of the Third International Symposium on Solid Oxide Fuel Cells, Honolulu, Hawaii, **1993**; p 344-353.
- (14) Kindl, B.; Carter, J. D. High Temperature Electrochemical Behaviour of Fast Ion and Mixed Conductors, Risø National Laboratory, Roskilde, Denmark, **1993**; p 275-280.
- (15) Berg, R. W. High Temperature Electrochemistry: Ceramics and Metals, Risø National Laboratory, Roskilde, Denmark, **1996**; p 175-180.
- (16) Hong, J.; Yoo, H., *Solid State Ionics* **1998**, *113-115*, 265-270.
- (17) Bouwmeester, H. J. M.; Burggraaf, A. J. In *The CRC Handbook of Solid State Electrochemistry*; Gellings, P. J. and Bouwmeester, H. J. M., Eds.; CRC Press:, **1997**.
- (18) Monceau, D.; Filal, M.; Tebtoub, M.; Petot, C.; Petot-Ervas, G., *Solid State Ionics* **1994**, *73*, 221-225.
- (19) Teller, O.; Martin, M., *Solid State Ionics* **1997**, *101-103*, 475-478.
- (20) Teller, O.; Martin, M., *Ber. Bunsenges. Phys. Chem.* **1997**, *101*, 1377-1380.
- (21) Kawada, T.; Horita, T.; Sakai, N.; Yokokawa, H.; Dokiya, M., *Solid State Ionics* **1995**, *79*, 201-207.
- (22) Horita, T.; Ishikawa, M.; Yamaji, K.; Sakai, N.; Yokokawa, H.; Dokiya, M., *Solid State Ionics* **1998**, *108*, 383-390.
- (23) Horita, T.; Ishikawa, M.; Yamaji, K.; Sakai, N.; Yokokawa, H.; Dokiya, M., *Solid State Ionics* **1999**, *124*, 301-307.
- (24) Sakai, N.; Yamaji, K.; Horita, T.; Negishi, H.; Yokokawa, H., *Solid State Ionics* **2000**, *135*, 469-474.
- (25) Akashi, T.; Nanko, M.; Maruyama, T.; Shiraishi, Y.; Tanabe, J. Solid Oxide Fuel Cells V, Aachen, Germany, **1997**; p 1263-1272.
- (26) Sakai, N.; Kawada, T.; Yokokawa, H.; Dokiya, M., *Journal of the Ceramic Society of Japan* **1993**, *101*, 1195-1200.

Chapter 6 六

LaCrO₃-based catalysts for oxidation of CH₄ directly on SOFC anodes

LaCrO₃-based catalysts for oxidation of CH₄ directly on SOFC anodes*

Abstract

Catalytic properties of substituted lanthanum chromites were investigated for their use as anode materials for direct methane oxidation in solid oxide fuel cells (SOFC). Different reaction mixtures were chosen to simulate the various SOFC operating conditions: partial oxidation, CO₂ reforming by recycling and H₂O reforming. All experiments were performed in CH₄ rich environments. Alkaline earth elements such as Ca, Sr and Mg, and first series transition metals - Mn, Fe, Co and Ni - were substituted into the LaCrO₃ lattice. Three different catalytic behaviours were observed depending on the substituents. The Ni substituted powders showed the highest activity towards CH₄. Ni substitution showed also interesting H₂O and CO₂ reforming activities. For all catalysts, except in the case of Fe-substituted LaCrO₃, only a small amount of carbon was found on the surface (1~3 monolayers). Among the A-site and B-site substituents, Sr- and Ni-substituted LaCrO₃ were found as the most active and the most suitable oxides for a SOFC anode purpose.

Introduction

Literature survey on LaCrO₃-based catalysts

LaCrO₃, La_{0.8}Sr_{0.2}CrO₃ and LaCr_{0.8}Nb_{0.2}O₃ were investigated as combustion catalysts in 2% CH₄ in air and were found to be the least active oxides among other transition metal lanthanum perovskites¹⁻⁵. However, La_{0.8}Sr_{0.2}CrO₃ was found as the most active among other La_{0.8}Sr_{0.2}MO₃ (M = Fe, Co, Mn and Y) for the CO oxidation (2% CO in air)³. This low activity was related to the poor ionic conductivity³, oxygen adsorption and lattice oxygen availability of these materials for the activation and oxidation of CH₄^{2, 6}. Al₂O₃ and MgAl₂O₄ supported LaCrO₃ showed increased activity when compared to the unsupported LaCrO₃, in 1:4:95 CH₄:O₂:N₂ gas mixture⁷. The increase in activity was explained by an increase of the dispersion state of the perovskite phase. Similarly, LaCr_{1-x}Mg_xO₃ (x = 0-0.5) was dispersed over MgO supports and high activities were observed in 1.5:18:80.5 CH₄:O₂:He⁸. The high dispersion of these catalysts (submicron powders of 15~20 m²/g surface area) as well as the measured high adsorption energies for O₂ (-168~-188 kJ/mol) were thought to be relevant. LaCr_{1-x}Ni_xO₃ catalysts were also investigated in 25:12.5:62.5 CH₄:O₂:He⁹. Again, oxygen adsorption and CH₄ activation were observed to affect the reaction. In general, the activity increased upon substitution as in the case of Mg. However, the supported perovskites (LaCrO₃ and LaCr_{1-x}Mg_xO₃) showed higher activities than the unsupported ones (LaCrO₃, LaCr_{1-x}Mg_xO₃ and LaCr_{1-x}Ni_xO₃). Baker et al.^{10, 11} worked with A-site and B-site substituted LaCrO₃ (La_{0.8}Ca_{0.2}CrO₃ and La_{0.8}Ca_{0.2}Cr_{0.9}(Co,Ni)_{0.1}O₃) in 5:95 CH₄:He or 5:3:92 CH₄:H₂O:He mixtures. They found that these perovskites resisted much better to carbon deposition than a Ni-YSZ-cermet anode. Nevertheless, they observed carbon deposition at a temperature above 600°C, where methane cracking began to take place. Water addition lowered carbon formation. For the Co and Ni substituted-La_{0.8}Ca_{0.2}CrO₃, they observed partial decomposition of the compounds. It is worth noting that all experiments on LaCrO₃-based perovskites exposed in literature used dilute methane, in contrast to the present study. Also, only a few reports⁹⁻¹¹ had the purpose of applying these materials as anodes for SOFCs.

Background of the present work

Calcium substituted lanthanum chromites were previously explored as alternative anodes to Ni-YSZ by the present authors¹² (Chapter 4). A small degradation was observed and was related to a progressive reduction of the electrode as well as a topotactic reaction between excess Ca or Sr with YSZ¹²⁻¹⁴ (Chapter 5). This reaction is however inhibited when low substitution levels are adopted (around 15% on the A-site)^{13, 14}. The lanthanum calcium and/or strontium

* This chapter has been submitted in a shorter version as J. Sfeir, P. A. Buffat, P. Möckli, N. Xanthopoulos, R. Vasquez, H. J. Mathieu, J. Van herle and K. R. Thampi, 'Lanthanum Chromite Based Catalysts for Oxidation of Methane Directly on SOFC Anodes', *J. Catalysis*, 202, 2001, 229-244

chromite compounds were observed to inhibit coking but their overall electrocatalytic activity was found to be low under pure methane feed¹². In this work, because of the stability of LaCrO_3 based materials, an attempt was made to increase their catalytic activity by substituting them with catalytically active Mn, Fe, Co and Ni. Since we intend to use them as SOFC anode materials for direct methane feeding, different gas reaction mixtures were chosen to simulate the various SOFC operating conditions under catalytic conditions.

Methods

Powder preparation

Different lanthanum chromite powders were prepared through a modified citrate route¹⁵ (Chapter 3). In order to tune the activity of the lanthanum chromite, different alkaline earth and transition metal substituents were considered: 15% for Ca and Sr (A-site), and 10% for Mg, Mn, Fe, Co and Ni (B-site). Low substitution levels on the A-site were used to prevent segregation of secondary phases^{13, 14} (Chapter 5). Ca and Sr also help to achieve good adhesion of chromites to the YSZ surface, necessary for the cell's mechanical stability and better current collection.

Catalytic tests (steady-state mode)

0.2 to 0.5 g of the freshly prepared catalyst was introduced in a quartz tube of 20 cm length (0.9 cm i.d.; 12 cm heated zone) and placed between two quartz wool plugs, as a 3 mm thick powder bed. A thermocouple protected in a quartz tube was placed in the catalyst bed and served to monitor the powder temperature. The same catalyst was used for the whole series of gas compositions. All gas input and output lines of the reactor were heated to 150°C to prevent water condensation. This configuration is shown in figure 1.

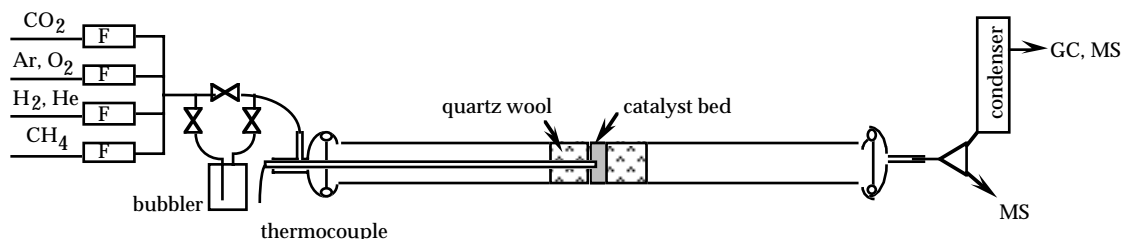


Figure 1: Schematic view of the catalytic reactor. *F* represents the massflow controllers. For steam-reforming reactions, the gas mixture was saturated with H_2O using a thermostated bubbler. All gas lines, before and after the reactor, were heated to prevent water condensation. The thermocouple, used to monitor the catalyst temperature, was placed directly inside the catalyst bed. GC or MS were used to monitor the reaction in the steady-state mode, whereas MS analysis was performed in the transient measurements.

In order to assess the oxidation activities, different gas compositions were considered: a 5:1 $\text{CH}_4:\text{O}_2$ mixture for the partial oxidation condition; a 5:1:0.6 $\text{CH}_4:\text{O}_2:\text{CO}_2$ mixture for CO_2 recycling-reforming behavior and a 56:y:x $\text{CH}_4:\text{Ar}:\text{H}_2\text{O}$, ($x+y=44$), for steam reforming operation. The 5:1 ratio for $\text{CH}_4:\text{O}_2$ was taken so as to simulate a current intensity of about 100 mA/cm^2 , or 400 mA/cm^2 in the deep oxidation and partial oxidation mode respectively. CH_4 , O_2 , CO_2 , Ar and He feed rates were monitored by mass-flow controllers (Bronkhorst), whereas H_2O was saturated using a bubbler maintained at a controlled temperature. The gas flow rate was adjusted for an hourly space-velocity of approximately 19000 h^{-1} (v/v) (see Appendix A for the definition of these terms). The system operated at atmospheric pressure and the inlet pressure was followed with a pressure gauge to monitor any flow blocking due to carbon build-up. Wagner-Weisz-Wheeler modulus, gas film resistance calculations¹⁶, as well as the experimentally observed gas mixture flow rates indicated no mass transfer limitations (see Appendix A). Both the reaction products and the inlet gas mixtures were analysed by gas chromatography through syringe injection (Carlo Erba MFC500 and Gowmac instruments) after water condensation. A Porapak Q column with He as carrier was used for Ar, CH_4 , CO_2 and C_2 compounds analysis (Carlo Erba) whereas a Molecular Sieve 5Å in Ar carrier (Gowmac)

was used for H_2 , O_2 , CH_4 and CO detection. The gases were calibrated by syringe injection using different volumes of each gas. For CH_4 , H_2 , CO and CO_2 a calibration cylinder was also used (standard of 1% of each in N_2 , from Supelco). Measurements were made at steady state conditions (approximately 1 h after temperature stabilization).

The results of the catalytic tests are given as % conversion of CH_4 , % selectivity of CO , C_2s and H_2 , C_2s yields and as turn-over frequency all defined in Appendix A.

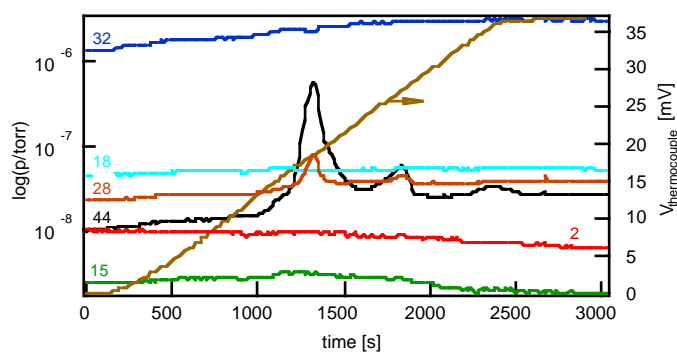


Figure 2: A TPO experiment after a catalytic run in a 56:40:3 CH_4 :Ar: H_2O gas mixture over $\text{LaCr}_{0.9}\text{Ni}_{0.1}\text{O}_3$. The oxidant used was 16.6:83.4 O_2 :He, and the heating rate was set to $25^\circ\text{C}/\text{min}$. The graph shows the evolution of the MS signal for the different masses monitored during the heating stage (2: H_2 ; 15: CH_4 ; 18: H_2O ; 28: $\text{CO}/\text{CO}_2/\text{N}_2$; 32: O_2 ; 44: CO_2). A net CO_2 (mass 44) peak can be observed. The temperature of the catalyst was monitored in parallel, and served to convert the time axis into temperature. This graph has not been corrected for the sensitivity factors of the different gases.

Temperature programmed oxidation and reduction (transient mode)

At the end of each run, temperature programmed oxidation (TPO) in 20 ml/min He with 4 ml/min O_2 was undertaken in order to estimate the carbon deposition, after having cooled the reactor to room temperature in He (in typically 40 min time). An online quadrupole mass spectrometer (Residual Gas Analyser, Spectra, Leda Mass Vision, HF-100, maximum mass of 100 a.m.u.) which allowed a quantitative analysis of the outlet gas (CH_4 , CO , CO_2 , H_2 , H_2O , O_2) was used for detection.

Temperature programmed reduction (TPR) of lanthanum chromite powders pre-oxidized at 900°C for 1 h was performed in 9% H_2 in Ar with a total flow rate of 55 ml/min. The water produced during this reaction was followed by the online mass spectrometer.

The heating rate for both TPO and TPR was set at $25^\circ\text{C}/\text{min}$. Figure 2 illustrates a typical TPO experiment after a catalytic run in a 56:40:3 CH_4 :Ar: H_2O gas mixture. The temperature programmed techniques which have proved to be very useful for investigating oxygen adsorption, reactions activation energies, etc., are described in more detail by Falconer et al.¹⁷

XPS and TEM analysis

Surface analysis was performed by X-ray photoelectron spectroscopy (XPS), in a Perkin Elmer Phi 5500 and a Kratos Axis Ultra Instruments using $\text{MgK}\alpha$ radiation in the first and $\text{AlK}\alpha$ in the second (except for the Mg doped lanthanum chromite, where $\text{AlK}\alpha$ radiation was used). Samples were pressed on an indium sheet fixed on the sample holder. All spectra were analyzed and fitted using the instruments' softwares. Peak positions were corrected by shifting the $\text{C}1\text{s}$ peak to 285 eV. Labelling of the different Cr, La, alkali earth and transition metal elements was done by comparison with literature data. In the case of $\text{La}_{0.85}\text{Ca}_{0.15}\text{Cr}_{0.9}\text{Ni}_{0.1}\text{O}_3$, XPS analysis was performed before and after several Ar^+ sputtering steps, in order to estimate the surface enrichment of the powder.

TEM analysis was performed in a Philips EM430T instrument at 300 kV equipped with an EDS X-ray spectrometer. Carbon film on copper grids were impregnated by the powder dispersed in methanol.

Results

Powder characteristics and TPR

After ball-milling, lanthanum chromite powders showed a specific *BET* surface area between 1 and 3 m²/g and a particle size distribution centered at 1 to 2.6 μm, as shown in Table 1 (see also Chapter 3).

Table 1: Summary of the different powders characteristics as well as the activation energies E_a in 5:1 CH₄:O₂, 56:41:3 and 56:20:24 CH₄:Ar:H₂O gas mixtures.

Catalyst composition	mass [g]	surface area [m ² /g]	particle size d_{50} [μm]	E_a 5:1 CH ₄ :O ₂ [kJ/mol]	E_a 3% H ₂ O [kJ/mol]	E_a 24% H ₂ O [kJ/mol]
La _{0.85} Ca _{0.15} CrO ₃	0.40	2.6	0.9	82±4 (6)	173±8 (5)	215±7 (4)
La _{0.85} Ca _{0.15} Cr _{0.9} Mg _{0.1} O ₃	0.46	1.0	2.6	98±7 (6)	192±28 (5)	329±5 (3)
La _{0.85} Ca _{0.15} Cr _{0.1} Ni _{0.1} O ₃	0.26	1.5	1.8	109±8 (4) ^a 45±1 (7) ^b	126±39 (4)	na
La _{0.85} Sr _{0.15} CrO ₃	0.60	2.7	1.0	86±40 (3)	182±42 (4)	214±9 (5)
La _{0.85} Sr _{0.15} Cr _{0.9} Mg _{0.1} O ₃	0.56	1.8	2.3	90±5 (7)	164±11 (5)	192±3 (4)
LaCrO ₃	0.27	2.8	0.8	97±5 (4)	272±14 (3)	189±26 (4)
LaCr _{0.9} Mg _{0.1} O ₃	0.21	3.0	1.3	116±5 (4)	193±9 (3)	199±24 (4)
LaCr _{0.9} Mn _{0.1} O ₃	0.47	2.3	1.6	85±5 (4)	116±3 (3)	166±6 (5)
LaCr _{0.9} Fe _{0.1} O ₃	0.49	2.0	1.1	98±7 (4)	234±26 (4)	190±7 (4)
LaCr _{0.9} Co _{0.1} O ₃	0.31	1.4	2.1	121±6 (6)	145±15 (4)	174±1 (4)
LaCr _{0.9} Ni _{0.1} O ₃	0.43	1.4	2.1	116±1 (4) ^b	43±10 (3)	107±10 (4)

The number of points used for the Arrhenius plots are given in parentheses. na: not available, ^a: before activation, ^b: after activation

Figure 3 shows TPR spectra for the different lanthanum chromite catalysts pre-oxidised at 900°C for 1 h. Two peaks were observed at 364-420 and 446-527°C depending on the substituent. No other peaks could be identified. The total amount of atomic O lost by reduction was calculated by integrating the corrected water peaks (mass 18) measured by MS. The samples substituted with Ca and Sr were reduced by 0.08 and 0.06 O/LC molecule, respectively. The calculated values from

$$La_{1-x}(Ca, Sr)_x Cr_{1-x}^{3+} Cr_x^{4+} O_3 = La_{1-x}(Ca, Sr)_x Cr^{3+} O_{3-x/2} + \frac{x}{2} O_2 \quad (1)$$

correspond to $x/2$ ($x=0.15$), i.e. 0.075, and matches well with the experimental results. The Mg, Mn, Fe, Co and Ni substituted LCs were reduced to an equivalent of 0.09, 0.026, 0.025, 0.031, and 0.064 O/LC molecule compared to a calculated value from

$$LaCr_{1-x}(Mg, Mn, Fe, Co, Ni)_x O_3 = LaCr_{1-x}^{3+}(Mg, Mn, Fe, Co, Ni)_x O_{3-x/2} + \frac{x}{2} O_2 \quad (2)$$

of 0.05 ($x/2$, $x=0.1$) if the dopant is divalent. LC gave an amount of 0.02 O/molecule of LC. For the latter compound Fierro et al.¹⁸ state a value of 0.006 O/molecule. Our measurement is about 3 times higher. Estimated values of the non-stoichiometry (δ), based on Armstrong et al.¹⁹ thermogravimetric measurements, obtained by subtracting the measured δ of the La_{0.7}Ca_{0.3}Cr_{0.9}M_{0.1}O₃ (M = transition elements) powders from the base material La_{0.7}Ca_{0.3}CrO₃, amount to 0.02, 0.06, 0.04, 0.03, 0.07 and 0.07 for the Mg, Ca, Mn, Fe, Co and Ni substitution respectively. These values were higher, for the transition metals, than in our measurements. Overall, our results indicate that Fe and Mn ($\delta = 0.025$ and 0.026) were in the trivalent state while Co ($\delta = 0.031$) had mixed valencies (III and II), whereas Ni was in the divalent state. This is in agreement with literature where it is stated that up to a substitution limit of about 0.4 on the Cr site, the Ni is expected to be divalent²⁰, whereas the Co is stated to be in the trivalent state in the whole range of substitutions in LaCrO₃²¹ - the same is expected for Fe and Mn¹⁹. A double substitution on the A and B sites gives rise to a higher degree of reduction: 0.09 for Ca-Ni, 0.14 for Sr-Ni, 0.124 for Ca-Mg and 0.155 for Sr-Mg substitution respectively, compared with the

expected nominal value of 0.125. This indicates that the transition metal substituted LCs did not decompose and that in the special case of $\text{LaCr}_{0.9}\text{Ni}_{0.1}\text{O}_3$ and $\text{La}_{0.85}\text{Ca}_{0.15}\text{Cr}_{0.9}\text{Ni}_{0.1}\text{O}_3$, Ni^{II} did not undergo a further reduction.

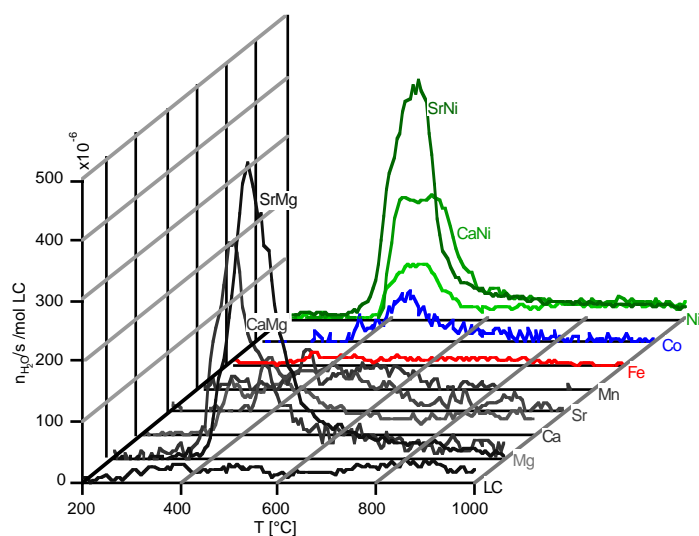


Figure 3: TPR (temperature programmed reduction) in 9:91 H_2 :Ar with a total flow rate of 55 ml/min, and a heating rate of 25°C/min. The measurements were done on pre-oxidized lanthanum chromites in pure oxygen, at 900°C for 1 h. The analysis was made by MS.

Table 2: TPR starting reduction temperatures and estimated heat of partial reduction of an oxide, q_s .

Compounds	T [°C]	q_s [kJ/mol]
$\text{LaCr}_{0.9}\text{Co}_{0.1}\text{O}_3$	361	73.5
$\text{LaCr}_{0.9}\text{Ni}_{0.1}\text{O}_3$	360	73.2
$\text{LaCr}_{0.9}\text{Mn}_{0.1}\text{O}_3$	359	72.8
$\text{La}_{0.85}\text{Ca}_{0.15}\text{CrO}_3$	338	64.9
$\text{La}_{0.85}\text{Sr}_{0.15}\text{CrO}_3$	310	53.9

Moreover, part of the water produced by TPR should be attributed to adsorbed hydroxyl groups and surface oxygen¹⁵. The low temperature shoulder corresponds to adsorbed or adsorbed surface oxygen whereas the high temperature shoulder is assigned to lattice oxygen¹⁵. Generally, the two former adsorbed species desorbed more easily from Ca than from Sr and transition metal substituted LCs. For the transition elements the reduction started at almost the same temperature. These starting reduction temperatures are summarized in Table 2. Also, by using the correlations developed in literature²²⁻²⁷ (see Appendix B), relating the heat of partial reduction of an oxide, q_s , and the inverse of the starting reduction temperatures, it is possible to estimate the heat released during the reactions (1) and (2). From the TPR and the q_s thus calculated, the lattice oxygen seems to be more stabilized by Sr>Ca>Mg. For the transition elements, lattice oxygen is more easily removed and follows the order Mn>Ni>Co. There is no experimental data available in literature to verify these values. These q_s values are smaller than the reported values for Fe_2O_3 , Co_3O_4 and NiO (260.4, 257.9 and 237.8 kJ/mol respectively)²⁶, indicating the higher stability of lanthanum chromites.

Effect of O_2

Figure 4a shows the steady state curves obtained by reacting the 5:1 CH_4 : O_2 gas mixture on various catalysts. The total flow rate was set to 50 mlN/min. The reactions started in the range between 300° to 600°C, depending on the nature of the substituent in LaCrO_3 (LC). In this low temperature part of the curves, O_2 was entirely consumed by CH_4 to form CO_2 and H_2O - low H_2 and CO selectivities, as seen in Figure 4b and 4c -, thus showing total oxidation (reaction (3)). The CH_4 conversion reached here a maximum of 10%, O_2 being the limiting factor in the reactions





It is only above 700°C that an observable net partial oxidation occurred (reaction (4)). Tests carried out in the blank reactor, under the different gas mixtures, showed no reaction occurring in the gas phase below 700°C , while at higher temperatures, the gases reacted to produce CO_2 , CO and H_2O ; CO is also formed by water gas shift reaction:



with methane conversion reaching 15%, at 900°C , for the blank reactor. On these curves, the thermodynamic limits were also represented. These gas phase thermodynamic equilibrium calculations were made using the Gibbs Free Energy Minimization method of the HSC-4.1, thermodynamic equilibria calculation software, from Outokumpu Research Oy, Finland (see Chapter 1, the Appendix, for a list of the different species taken into account for the calculations).

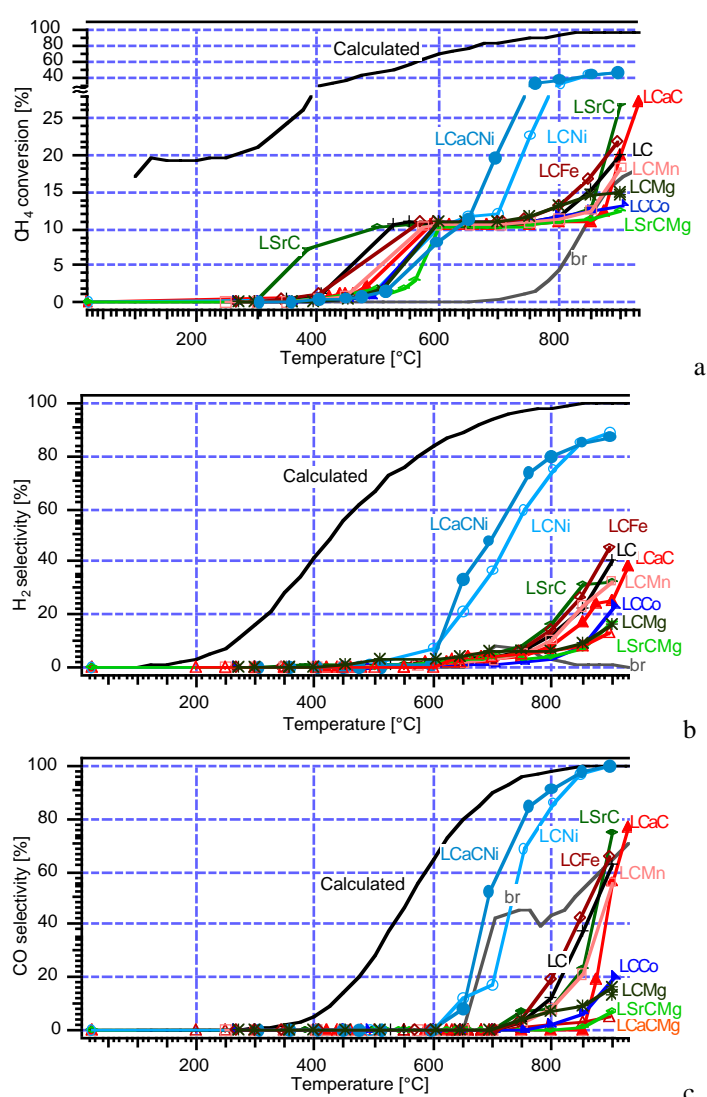


Figure 4: CH_4 conversion and H_2 and CO selectivities as a function of temperature for the various catalysts in 5:1 $\text{CH}_4:\text{O}_2$. The calculated CH_4 conversion takes into account carbon deposition. For the CO selectivity based on the thermodynamic calculations, the deposited carbon was not incorporated in the selectivity ratio, as shown in c.

The high level of methane thermodynamic conversion observed is due to carbon deposition likely to form under reductive conditions. In these calculations, graphitic carbon was used as the most stable solid carbon species formed in the gas phase. It is clearly seen that the calculated conversion in the 5:1 CH_4 : O_2 gas mixture differs much from the experimental results, indicating low coking levels on the lanthanum chromites oxides.

All catalysts had their temperatures cycled from room temperature to 900°C and then back to ambient, in order to verify the reproducibility of steady state values. In some cases, a hysteresis in % CH_4 conversion occurred whereby a higher conversion was noticed, during cooling, at a given temperature, when compared to the heating cycle.

For comparing the activity of various catalysts, the oxidation behaviour of lanthanum chromites was evaluated at the temperature at which 50% O_2 conversion occurs. It is observed that among the alkaline earth elements, Sr ($T \approx 390^\circ\text{C}$) is best for promoting oxidation, whereas Mg impedes it ($T \approx 550^\circ\text{C}$), with Ca at an intermediate level ($T \approx 500^\circ\text{C}$), when compared to pure LC ($T \approx 450^\circ\text{C}$). The same trend is reported in the literature¹ for Ca or Sr substituted LaMO_3 ($M = \text{Mn, Fe, Co}$) combustion catalysts. Since $\text{La}_{0.85}\text{Ca}_{0.15}\text{CrO}_3$ and $\text{La}_{0.85}\text{Sr}_{0.15}\text{CrO}_3$ have the same surface areas and particle size distributions (Table 1), this behaviour seems to be independent of such parameters. A double substitution Ca and Mg or Sr and Mg shifted the temperature to higher values, compared to Mg substitution alone ($T \approx 570^\circ\text{C}$ for $\text{La}_{0.85}\text{Ca}_{0.15}\text{Cr}_{0.9}\text{Mg}_{0.1}\text{O}_3$; $T \approx 620^\circ\text{C}$ for $\text{La}_{0.85}\text{Sr}_{0.15}\text{Cr}_{0.9}\text{Mg}_{0.1}\text{O}_3$). This latter change could also be related to the decrease in the surface area and the increase in the average particle size of the catalysts upon Mg substitution (see Table 1). Such effects were also reported by Arai et al.². For the various transition metal elements, the observed trend was as follows: Fe (475°C) < Mn (500°C) < Co \approx Ni (540°C).

This trend is also qualitatively followed when the activity is evaluated on the basis of methane conversion and product selectivities, where three different patterns are distinctly noticed with our catalysts:

1. Case A: $\text{La}_{0.85}\text{Sr}_{0.15}\text{Cr}_{0.9}\text{Mg}_{0.1}\text{O}_3$ (LSrCMg) $\text{La}_{0.85}\text{Ca}_{0.15}\text{Cr}_{0.9}\text{Mg}_{0.1}\text{O}_3$ (LCaCMg), $\text{La}_{0.85}\text{Cr}_{0.9}\text{Mg}_{0.1}\text{O}_3$ (LCMg) and $\text{LaCr}_{0.9}\text{Co}_{0.1}\text{O}_3$ (LCCo), showed complete oxidation (reaction (3)) at high temperatures, exhibiting a negative catalytic effect when compared to the blank reactor (br) alone or the base material LaCrO_3 (LC), possibly by inhibiting the radical reactions in the gas phase;
2. Case B: $\text{La}_{0.85}\text{Ca}_{0.15}\text{CrO}_3$ (LCaC), $\text{LaCr}_{0.9}\text{Mn}_{0.1}\text{O}_3$ (LCMn), $\text{LaCr}_{0.9}\text{Fe}_{0.1}\text{O}_3$ (LCFe) and LaCrO_3 (LC) catalysts showed activities similar to that of the blank reactor and indicated a preference for water-gas shift (reaction (5)) at high temperatures;
3. Case C: $\text{La}_{0.85}\text{Sr}_{0.15}\text{CrO}_3$ (LSrC), $\text{LaCr}_{0.9}\text{Ni}_{0.1}\text{O}_3$ (LCNi), and $\text{La}_{0.85}\text{Ca}_{0.15}\text{Cr}_{0.9}\text{Ni}_{0.1}\text{O}_3$ (LCaCNi) significantly favoured the reforming reaction at high temperatures with an increase in the methane conversion and CO and H_2 selectivities, the reforming being almost complete according to reaction (4) for the Ni containing compounds above 800°C.

In terms of turn-over frequency (*TOF*), calculated as the number of moles of CH_4 reacted per second per unit surface area of the catalyst, regardless of product selectivity, the classification at 850°C follows the order of substitution $\text{Ca} < \text{Sr} < \text{Mg} < \text{Mn} < \text{LC} < \text{Fe} < \text{Co} < \text{CaMg} < \text{SrMg} < \text{Ni} < \text{CaNi}$ (see Figure 5).

Table 3 summarizes the activity of the different catalysts at 800°C. Activities of all catalysts were stable over one day or more, except for Ni-containing LC (case C). In the latter, the initial conversion was low and comparable to that of LCCo (10% CH_4 conversion). The activity increased over a period of 20 h and reached full reforming level of about 40% CH_4 conversion (5:1 CH_4 : O_2 initial mixture), at 900°C (see figure 6a). This activity was sustained for more than 360 h at 800°C (see figure 6b).

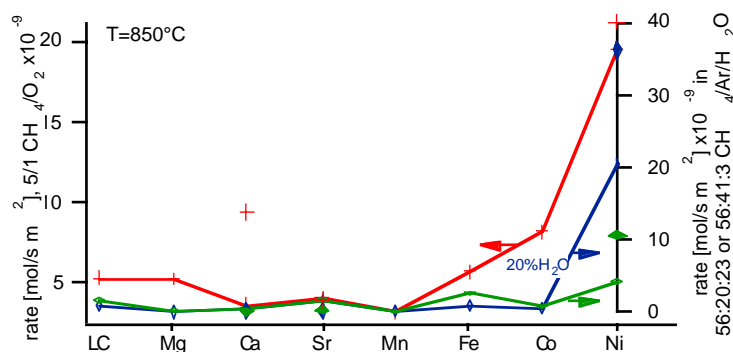


Figure 5: Summary of the turn-over frequencies in the different gas mixtures, at 850°C.

Apparent activation energies for the oxidation reactions were determined at conversions below 10%. Their errors were estimated from the error of the Arrhenius plot slope errors. They vary between 82 and 121 kJ/mol (Table 1). They are in general agreement with data published for different gas compositions: 101 (2:1:5 CH_4 : O_2 :He) or 120.4 (2 vol% CH_4 in air) to 142 kJ/mol (1.5:4.2:94.3 CH_4 : O_2 :He) for LaCrO_3 ^{1,4,5,9}, 120 to 147 kJ/mol for $\text{La}_{0.8}\text{Ca}_{0.2}\text{CrO}_3$ (5% CH_4 in He)¹⁰, 90 to 100 kJ/mol for $\text{LaCr}_{0.75}\text{Ni}_{0.25}\text{O}_3$ (2:1:5 CH_4 : O_2 :He)⁹, and 91.1, 76.1, 92.4 and 81.1 kJ/mol for LaMnO_3 , LaFeO_3 , LaCoO_3 and LaNiO_3 (2 vol% CH_4 in air)¹, compared to 115.4 kJ/mol for Pt(1 wt%) Al_2O_3 and 257.1 kJ/mol for the noncatalytic thermal reaction¹². In comparison, the activation energy of oxygen adsorption is of 16.4 kJ/mol on LaCrO_3 and LaMnO_3 ^{18,28} and 38 kJ/mol on LaNiO_3 ⁶.

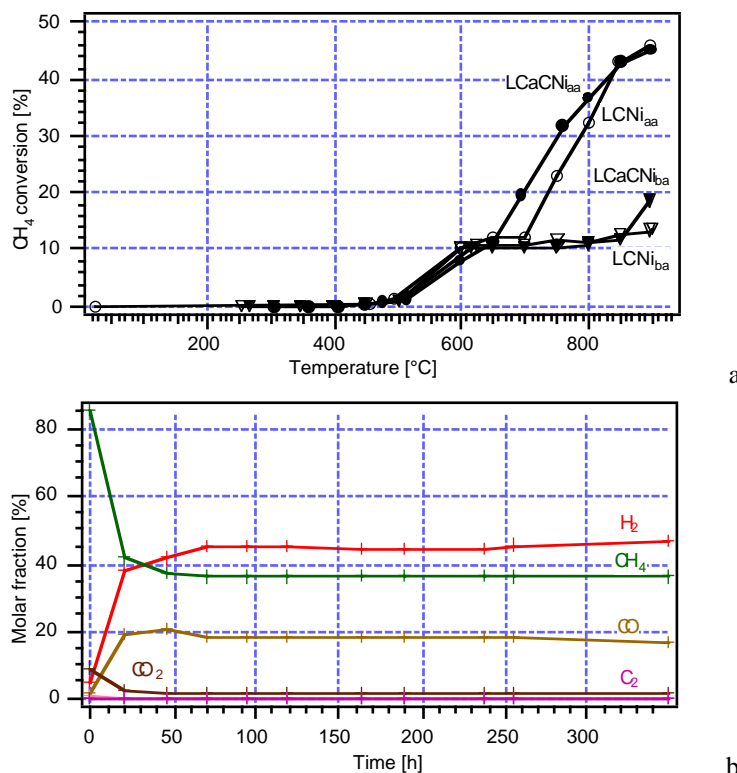


Figure 6: a: Initial versus activated $\text{LaCr}_{0.9}\text{Ni}_{0.1}\text{O}_3$ and $\text{La}_{0.85}\text{Ca}_{0.15}\text{Cr}_{0.9}\text{Ni}_{0.1}\text{O}_3$; ba and aa stand for before activation and after activation respectively. b: The evolution of the activity of $\text{La}_{0.85}\text{Ca}_{0.15}\text{Cr}_{0.9}\text{Ni}_{0.1}\text{O}_3$ over time at 800°C.

Table 3: Summary of the activity in the different gas mixtures at 800°C.

Catalyst composition	Reaction at 800°C		
	% methane conversion (in parentheses: number of carbon monolayers)		
	5:1 CH ₄ :O ₂	CH ₄ :O ₂ :CO ₂	CH ₂ :H ₂ O
Maximum conversion possible	40 ^a	52 ^b	24 ^c
La _{0.85} Ca _{0.15} CrO ₃	10.7 (0.6)	- (0.0)	0.39 (2.2)
La _{0.85} Ca _{0.15} Cr _{0.9} Mg _{0.1} O ₃	11.2 (-)	10.2 (-)	0.04 (-)
La _{0.85} Ca _{0.15} Cr _{0.9} Ni _{0.1} O ₃	36.7 (0.7)	37.8 (0.8)	18.70 (3.3)
La _{0.85} Sr _{0.15} CrO ₃	11.3 (0.0)	10.9 (0.0)	1.22 (0.4)
La _{0.85} Sr _{0.15} Cr _{0.9} Mg _{0.1} O ₃	10.9 (0.0)	10.8 (0.0)	0.22 (0.0)
LaCrO ₃	11.8 (0.3)	11.1 (0.5)	0.50 (1.7)
LaCr _{0.9} Mg _{0.1} O ₃	13.1 (1.7)	12.4 (1.5)	0.05 (1.1)
LaCr _{0.9} Mn _{0.1} O ₃	11.2 (0.0)	11.0 (0.0)	0.79 (1.1)
LaCr _{0.9} Fe _{0.1} O ₃	13.1 (2.6)	12.0 (0.5)	0.62 (69.4)
LaCr _{0.9} Co _{0.1} O ₃	11.5 (0.0)	11.1 (0.0)	0.21 (0.0)
LaCr _{0.9} Ni _{0.1} O ₃ ^d	32.1 (0.4)	48.2 (-)	16.6 (1.9)

The maximum conversion possible were calculated following ^a: CH₄ + 0.5 O₂ = CO + 2 H₂; ^b: CH₄ + 0.5 O₂ = CO + 2 H₂ and CH₄ + CO₂ = 2 CO + 2 H₂; ^c: CH₄ + H₂O = CO + 3 H₂; ^d: activity after 20 h run; -: not measured. The number of carbon monolayers integrated from TPR measurements is given in parentheses.

Effect of CO₂

Figure 7 shows the influence of CO₂ on the oxidation reaction of methane (5:1:0.6 CH₄:O₂:CO₂ gas mixture). Table 3 summarizes the activity of the different catalysts at 800°C. It is observed that in all catalysts, except the Ni containing compounds, CO₂ reforming was small at high temperature. The curves follow the same steady-state trend as with the 5:1 CH₄:O₂ runs, and at T ≥ 750°C the gas-shift reaction (reaction (5)) took place over some catalysts by a concomitant increase in CO and decrease in H₂ selectivity (see Figure 7b and c) when compared with the 5:1 CH₄:O₂ runs (Figure 4b and c). Separate experiments in 5:1:0.6 CH₄:Ar:CO₂ (without O₂) confirmed the low CO₂ reforming ability on some of these materials. On the other hand, almost full CO₂-reforming,



took place on LCNi, LCaCNi and to some extent on LSrC (all materials of case C mentioned above). CO₂ reforming is relevant for SOFC operations, where a fraction of the product CO₂ could be recycled along with the natural gas feed. In the case of the A-site substituted LCs, CO₂ might have an inhibiting effect on the reaction with methane as its conversion (Figure 7a) is somehow lower than in the case of the 5:1 CH₄:O₂ gas mixture (Figure 4a), probably due to carbonates formation.

Effect of H₂O

Figure 8 displays the steam reforming reaction in a 56:20:24 CH₄:Ar:H₂O mixture and Table 3 summarizes the activity of the different catalysts at 800°C in the same gas mixture. Here again, we observe three different behaviours depending on the catalyst composition as recorded for the oxidation of methane. In most cases, CH₄ conversion was very low (≤ 1%, see Table 3) and quite independent of the water content. The reaction order with respect to P_{H₂O} varied with temperature, changing from a positive order at high temperatures to a negative one at low temperatures (Table 4). It was near zero for the cases where steam had little effect on the reaction (case A). LC, LSrC and LCMn were slightly affected by water (case B) whereas the Ni containing powders showed high conversion of water at T ≥ 800°C (case C) following the overall reaction,



Also, the CO selectivity diminished in all cases when the water content was increased from 3 to 23%, indicating that the reverse water-gas shift reaction (5) was fast. Table 5 summarizes the CO selectivities at 900°C in 56:20:24 and 56:41:3 CH₄:Ar:H₂O.

If the activity is expressed in terms of the turn-over frequency, the classification of the substituents follows, at 850°C , the order $\text{Mg} < \text{Mn} < \text{LC} \approx \text{Co} \approx \text{Ca} < \text{Sr} < \text{Fe} < \text{Ni} < \text{CaNi}$.

Apparent activation energies in 56:41:3 and 56:20:24 CH_4 :Ar: H_2O were calculated at conversions below 10% (see Table 1). They varied between 43 and 272 kJ/mol for 56:41:3 CH_4 :Ar: H_2O and depended on the fraction of water vapor, where the values tended to be higher with increasing steam content. Steam reforming on Ni based catalysts is reported to have an activation energy between 20 and 160 kJ/mol²⁹, the latter representing the activation energy in the absence of diffusion limitations³⁰.

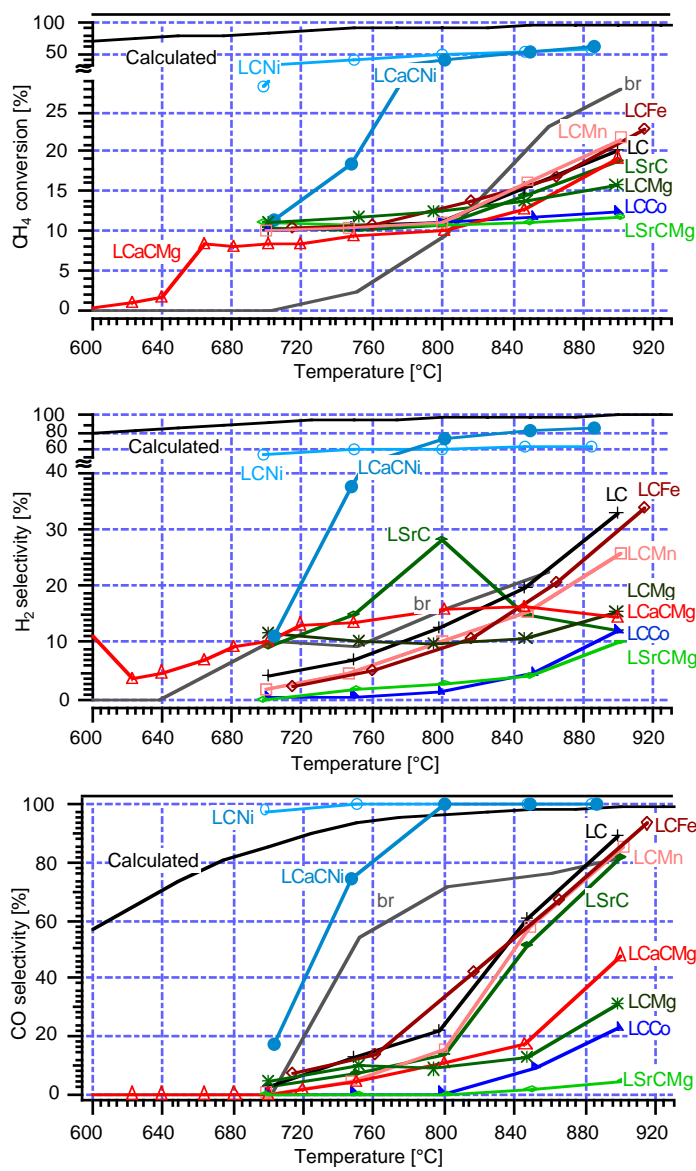


Figure 7: CH_4 conversion and H_2 and CO selectivities as a function of temperature for the various catalysts in 5:1:0.6 CH_4 : O_2 : CO_2 . The calculated CH_4 conversion takes into account carbon deposition. For the CO selectivity based on the thermodynamic calculations, the deposited carbon was not incorporated in the selectivity ratio, as shown in c.

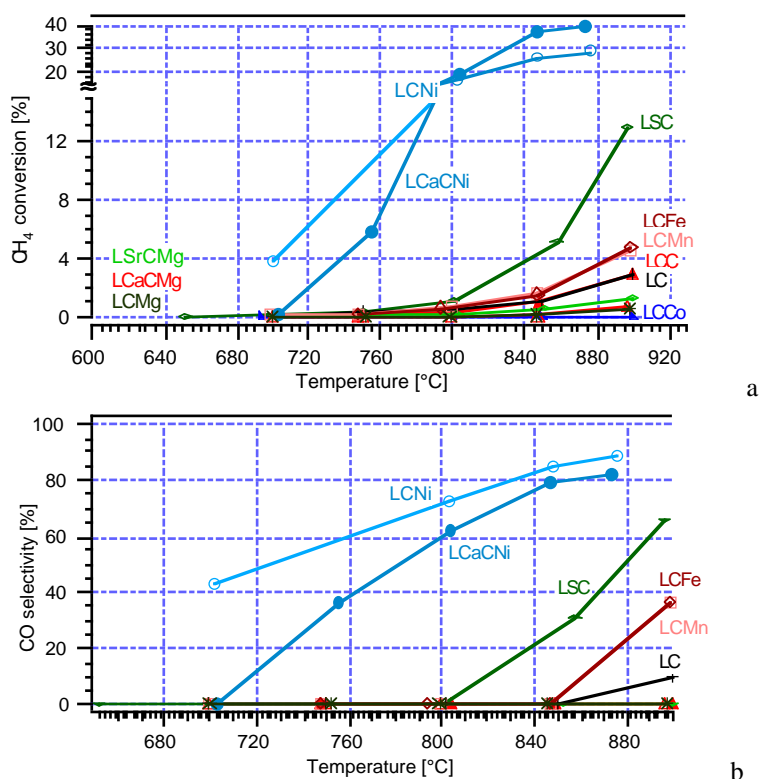


Figure 8: CH_4 conversion and CO selectivity as a function of temperature for the various catalysts in 56:20:24 CH_4 :Ar: H_2O .

Table 4: Reaction orders for water at different temperatures.

Compounds	900°C	850°C	800°C	750°C	700°C	600°C
$\text{La}_{0.85}\text{Ca}_{0.15}\text{CrO}_3$	1.2	0.2	0.3	-0.2	-0.2	
$\text{La}_{0.85}\text{Ca}_{0.15}\text{Cr}_{0.9}\text{Mg}_{0.1}\text{O}_3$		0.8	-1.4			
$\text{La}_{0.85}\text{Ca}_{0.15}\text{Cr}_{0.9}\text{Ni}_{0.1}\text{O}_3$					-0.5	
$\text{La}_{0.85}\text{Sr}_{0.15}\text{CrO}_3$			-0.5	-0.2	-0.3	-0.5
$\text{La}_{0.85}\text{Sr}_{0.15}\text{Cr}_{0.9}\text{Mg}_{0.1}\text{O}_3$	0.0	0.1	0.1	0.0	-0.1	
LaCrO_3	-0.5	-0.3	-0.1			
$\text{LaCr}_{0.9}\text{Mg}_{0.1}\text{O}_3$	0.1	-0.1	-0.1			
$\text{LaCr}_{0.9}\text{Mn}_{0.1}\text{O}_3$	1.4		1.1		0.8	
$\text{LaCr}_{0.9}\text{Fe}_{0.1}\text{O}_3$	-0.2					
$\text{LaCr}_{0.9}\text{Ni}_{0.1}\text{O}_3$	0.2	0.0	-0.1		-0.1	

These values were obtained from two different water concentrations except for the case of $\text{La}_{0.85}\text{Ca}_{0.15}\text{CrO}_3$ where 4 different concentrations were taken into account.

Table 5: CO selectivity as a function of the steam content in the 56:x:y ($x+y=44$) CH_4 :Ar: H_2O gas mixture at 900°C.

Powder versus CO selectivity	CO selectivity	
	24% H_2O	3% H_2O
$\text{La}_{0.85}\text{Ca}_{0.15}\text{CrO}_3$	0	99
$\text{La}_{0.85}\text{Ca}_{0.15}\text{Cr}_{0.9}\text{Mg}_{0.1}\text{O}_3$	0	33
$\text{La}_{0.85}\text{Ca}_{0.15}\text{Cr}_{0.9}\text{Ni}_{0.1}\text{O}_3$	81	100
$\text{La}_{0.85}\text{Sr}_{0.15}\text{CrO}_3$	65	100
$\text{La}_{0.85}\text{Sr}_{0.15}\text{Cr}_{0.9}\text{Mg}_{0.1}\text{O}_3$	0	42
LaCrO_3	10	96
$\text{LaCr}_{0.9}\text{Mg}_{0.1}\text{O}_3$	0	0
$\text{LaCr}_{0.9}\text{Mn}_{0.1}\text{O}_3$	36	80
$\text{LaCr}_{0.9}\text{Fe}_{0.1}\text{O}_3$	36	91
$\text{LaCr}_{0.9}\text{Co}_{0.1}\text{O}_3$	0	0
$\text{LaCr}_{0.9}\text{Ni}_{0.1}\text{O}_3$	88	100

Methane coupling

Only small amounts ($\leq 1\%$) of C_2 compounds (C_2H_2 , C_2H_4 and C_2H_6) were observed in almost all cases for the oxidative coupling environment of 5:1 CH_4 : O_2 with the exception of Mg-substituted LC (16 to 24% at 900°C), the blank reactor (22% at 900°C, 56% at 700°C), LCCo (7% at 900°C) and LCaC (5% at 900°C). CO_2 increased slightly the coupling reaction, while in the blank reactor it rised to 82% at 900°C. H_2O addition suppressed C_2 compound formation totally except for the case of Mg substituted LCs where it only decreased (from 73 to 45% for LCaCMg, 33 to 19% for LSrCMg and 23 to 19% for LCMg when passing from 56:20:23 to 56:41:3 CH_4 :Ar: H_2O , at 900°C). This illustrates the low methane oxidative coupling activity of these catalysts (see Table 6). It is worth noting that prior to the activation of the LCNi and LCaCNi, their activity was similar to LCCo with high methane coupling selectivities.

Table 6: Summary of the oxidative coupling of methane over the lanthanum chromite catalysts at 850°C.

Catalyst composition	C_2 selectivity and yield [%], 850°C		Gas mixture			
	5:1 CH_4 : O_2		CH_4 : O_2 : CO_2		CH_4 : H_2O	
$\text{La}_{0.85}\text{Ca}_{0.15}\text{CrO}_3$	3.9	0.42	-	-	0	0
$\text{La}_{0.85}\text{Ca}_{0.15}\text{Cr}_{0.9}\text{Mg}_{0.1}\text{O}_3$	11.7	1.31	18.3	1.86	49.9	0.02
$\text{La}_{0.85}\text{Ca}_{0.15}\text{Cr}_{0.9}\text{Ni}_{0.1}\text{O}_3$, before	9.2	1.06				
$\text{La}_{0.85}\text{Ca}_{0.15}\text{Cr}_{0.9}\text{Ni}_{0.1}\text{O}_3$, after	0.6	0.22	0.1	0.05	0	0
$\text{La}_{0.85}\text{Sr}_{0.15}\text{CrO}_3$	1.6	0.18	1.9	0.21	0	0
$\text{La}_{0.85}\text{Sr}_{0.15}\text{Cr}_{0.9}\text{Mg}_{0.1}\text{O}_3$	7.8	0.85	9.6	1.05	11.2	0.024
LaCrO_3	1.0	0.12	1.8	0.19	0	0
$\text{LaCr}_{0.9}\text{Mg}_{0.1}\text{O}_3$	23.7	3.10	23.7	2.94	0	0
$\text{LaCr}_{0.9}\text{Mn}_{0.1}\text{O}_3$	1.8	0.20	2.13	0.23	0	0
$\text{LaCr}_{0.9}\text{Fe}_{0.1}\text{O}_3$	0.5	0.06	2.6	0.31	0	0
$\text{LaCr}_{0.9}\text{Co}_{0.1}\text{O}_3$	8.5	0.97	10.6	1.18	0	0
$\text{LaCr}_{0.9}\text{Ni}_{0.1}\text{O}_3$, before	13.2	1.64				
$\text{LaCr}_{0.9}\text{Ni}_{0.1}\text{O}_3$, after	0.7	0.24	0	0	0	0

The first column for each gas mixture corresponds to the selectivity whereas the second correspond to the yield, all given in percentage.

TPO

Temperature programmed oxidation (TPO) experiments were started from room temperature to 1000°C after running the catalytic reactions for about one day or more. They show that in all cases, except for LCFe, the amount of carbon estimated was less than 2-3 monolayers (results are summarized in Table 3), normalized to the total surface of the catalysts. The average surface area of a carbon atom on the surface of the perovskites was assumed to be of 0.018 nm^2 , as the covalent radius of carbon is given to be 77 pm ³¹. In the case of LCaCNi a

total of 2 monolayers were estimated by integrating the CO_2 peaks signal after the run in 5:1 $\text{CH}_4:\text{O}_2$ (360 h). In 56:41:3 $\text{CH}_4:\text{Ar}:\text{H}_2\text{O}$, 3.3 and 3.5 monolayers were deposited on the same catalyst after 30 h and 160 h respectively, indicating that the total amount of carbon deposited did not change much. Similarly, measurements done on LCaC with dry and humidified methane, showed that the total amount of carbon deposited with time tended to level off to 1~2 monolayers (see Figure 9) indicating that, at that point, the rate of coking might be equal to that of gasification of carbon or that all the catalytically active sites for coking are blocked by the deposited carbon. Thus, apart from the Fe substituted LC, the other catalysts do not seem to build-up carbon, in the contrary of Ni-YSZ-cermet, the conventional SOFC anode.

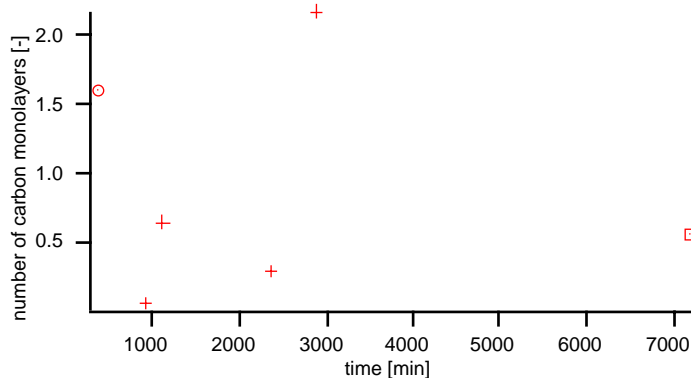


Figure 9: Amount of carbonaceous species deposited on $\text{La}_{0.85}\text{Ca}_{0.15}\text{CrO}_3$ with time, measured by TPO after catalytic runs at 850°C in (O) dry methane, (+) 3% wet methane and (\square) 5:1 $\text{CH}_4:\text{O}_2$.

From these TPO experiments (see Figure 10 for an example), different peaks of CO_2 have been observed at around 300, 400, 500-600, 700-800 and 900°C , corresponding to different types of carbon deposits, some being more stable than others. This is summarized in Table 7. They may be related to the different carbon species reported by Rostrup-Nielsen²⁹ and Bartholomew³² for Ni: adsorbed atomic (dispersed, surface carbide), bulk carbide, polymeric amorphous filaments or films, vermicular and graphitic (crystalline, films) carbon which reacted with H_2 in temperature programmed reaction hydrogenation (TPRH) at 200, 400, 400-600 and $550\text{--}850^\circ\text{C}$. As can be seen from Table 7, for some catalysts, some peaks appeared in the three different gas composition used.

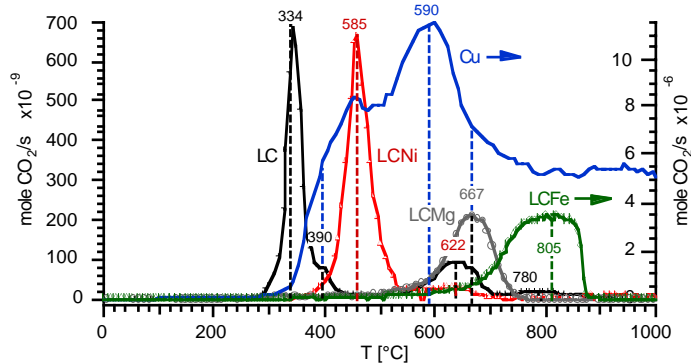


Figure 10: Temperature programmed oxidation (TPO, $25^\circ\text{C}/\text{min}$, 20 mlN/min He + 4 mlN/min O_2) on (+) LC, (o) LCMg, (\diamond) LCFE and (Δ) LCNi after catalytic runs in 56:41:3 $\text{CH}_4:\text{Ar}:\text{H}_2\text{O}$. A (-) CuO catalyst run in 5:1 $\text{CH}_4:\text{O}_2$ is also shown for a comparison with a metal catalyst (see Chapter 10). In the case of copper ($0.5 \text{ m}^2/\text{g}$), the carbon deposited was such that its oxidation was not complete at the highest temperature used.

5:1 $\text{CH}_4:\text{O}_2$	1 st peak	2 nd peak	3 rd peak	4 th peak	5 th peak	6 th peak
Catalyst composition/ temperature [°C]						
$\text{La}_{0.85}\text{Ca}_{0.15}\text{CrO}_3$?					
$\text{La}_{0.85}\text{Ca}_{0.15}\text{Cr}_{0.9}\text{Mg}_{0.1}\text{O}_3$	-	-	-	-	-	-
$\text{La}_{0.85}\text{Ca}_{0.15}\text{Cr}_{0.9}\text{Ni}_{0.1}\text{O}_3$	-	293	-	507	-	-
$\text{La}_{0.85}\text{Sr}_{0.15}\text{CrO}_3$?					
$\text{La}_{0.85}\text{Sr}_{0.15}\text{Cr}_{0.9}\text{Mg}_{0.1}\text{O}_3$	-	-	-	-	-	-
LaCrO_3	?					
$\text{LaCr}_{0.9}\text{Mg}_{0.1}\text{O}_3$	-	-	-	-	748	918
$\text{LaCr}_{0.9}\text{Mn}_{0.1}\text{O}_3$	-	318	401	-	-	-
$\text{LaCr}_{0.9}\text{Fe}_{0.1}\text{O}_3$	-	-	-	-	-	829
$\text{LaCr}_{0.9}\text{Co}_{0.1}\text{O}_3$	-	-	-	-	-	-
$\text{LaCr}_{0.9}\text{Ni}_{0.1}\text{O}_3$	97	261	-	515	699	825
$\text{La}_{0.85}\text{Ca}_{0.15}\text{Cr}_{0.9}\text{Ni}_{0.1}\text{O}_3$, LTC	-	-	-	638	742	847

5:1:0.6 $\text{CH}_4:\text{O}_2:\text{CO}_2$	1 st peak	2 nd peak	3 rd peak	4 th peak	5 th peak	6 th peak
Catalyst composition/ temperature [°C]						
$\text{La}_{0.85}\text{Ca}_{0.15}\text{CrO}_3$?					
$\text{La}_{0.85}\text{Ca}_{0.15}\text{Cr}_{0.9}\text{Mg}_{0.1}\text{O}_3$	-	-	-	-	-	-
$\text{La}_{0.85}\text{Ca}_{0.15}\text{Cr}_{0.9}\text{Ni}_{0.1}\text{O}_3$	-	287	-	605	-	886
$\text{La}_{0.85}\text{Sr}_{0.15}\text{CrO}_3$?					
$\text{La}_{0.85}\text{Sr}_{0.15}\text{Cr}_{0.9}\text{Mg}_{0.1}\text{O}_3$	-	-	-	-	-	-
LaCrO_3	?					
$\text{LaCr}_{0.9}\text{Mg}_{0.1}\text{O}_3$	-	318	355	-	774	932
$\text{LaCr}_{0.9}\text{Mn}_{0.1}\text{O}_3$	-	318	401	-	-	-
$\text{LaCr}_{0.9}\text{Fe}_{0.1}\text{O}_3$	125	-	-	580	-	-
$\text{LaCr}_{0.9}\text{Co}_{0.1}\text{O}_3$	-	-	-	-	-	-
$\text{LaCr}_{0.9}\text{Ni}_{0.1}\text{O}_3$?					

56:20:23 $\text{CH}_4:\text{Ar}:\text{H}_2\text{O}$	1 st peak	2 nd peak	3 rd peak	4 th peak	5 th peak	6 th peak
Catalyst composition/ temperature [°C]						
$\text{La}_{0.85}\text{Ca}_{0.15}\text{CrO}_3$?					
$\text{La}_{0.85}\text{Ca}_{0.15}\text{Cr}_{0.9}\text{Mg}_{0.1}\text{O}_3$	-	-	-	-	-	-
$\text{La}_{0.85}\text{Ca}_{0.15}\text{Cr}_{0.9}\text{Ni}_{0.1}\text{O}_3$	-	-	417	600	791	-
$\text{La}_{0.85}\text{Sr}_{0.15}\text{CrO}_3$?					
$\text{La}_{0.85}\text{Sr}_{0.15}\text{Cr}_{0.9}\text{Mg}_{0.1}\text{O}_3$	-	-	-	-	-	-
LaCrO_3	-	334	390	603	782	-
$\text{LaCr}_{0.9}\text{Mg}_{0.1}\text{O}_3$	-	-	-	-	667	918
$\text{LaCr}_{0.9}\text{Mn}_{0.1}\text{O}_3$	-	350	-	-	-	-
$\text{LaCr}_{0.9}\text{Fe}_{0.1}\text{O}_3$	-	-	-	-	-	829
$\text{LaCr}_{0.9}\text{Co}_{0.1}\text{O}_3$	-	-	-	-	-	-
$\text{LaCr}_{0.9}\text{Ni}_{0.1}\text{O}_3$	-	-	-	585	622	-
$\text{La}_{0.85}\text{Ca}_{0.15}\text{Cr}_{0.9}\text{Ni}_{0.1}\text{O}_3$, LTC	-	334	402	592	679	-

Table 7: Summary of the TPO temperature peaks. The measurements were made at 25°C/min, in 20 mlN/min He + 4 mlN/min O_2 , after the different catalytic runs. ?: not measured or uncertain.

XPS analysis

XPS analysis was conducted on freshly prepared powders as well as on used catalyst samples. The measurements were done on an area of approximately $100 \mu\text{m}^2$. The XPS peak positions for the different elements were adjusted by shifting the carbon 1s peak to 285 eV. After deconvolution, average peak positions were: $3d_{5/2}$ La_I, 834.5 eV and La_{II} 838.5 eV; $2p_{3/2}$ Cr_I 576 eV and Cr_{II} 579 eV; $2p_{3/2}$ Ca 346.4 eV; $3d_{5/2}$ Sr 133.8 eV; $2p_{3/2}$ Mn 642.2 eV; $2p_{3/2}$ Fe 711 eV; $2p_{3/2}$ Co 780.5 eV; O_I 529.1 eV and O_{II} 531 eV. This is summarized in Appendix C. $2p_{3/2}$ Ni peak could not be resolved because it overlapped with La 3d peaks. As no Ni satellite peak was observed around 870 eV, it was concluded that the surface concentration of Ni, on the

Ni substituted LCs, was below the detection limit ($\approx 1\%$). The Mn, Fe, Co and Ni peak intensities were quite low as illustrated in Figure 11. La and Cr peaks remained at the same position independently of the substitution (Appendix D).

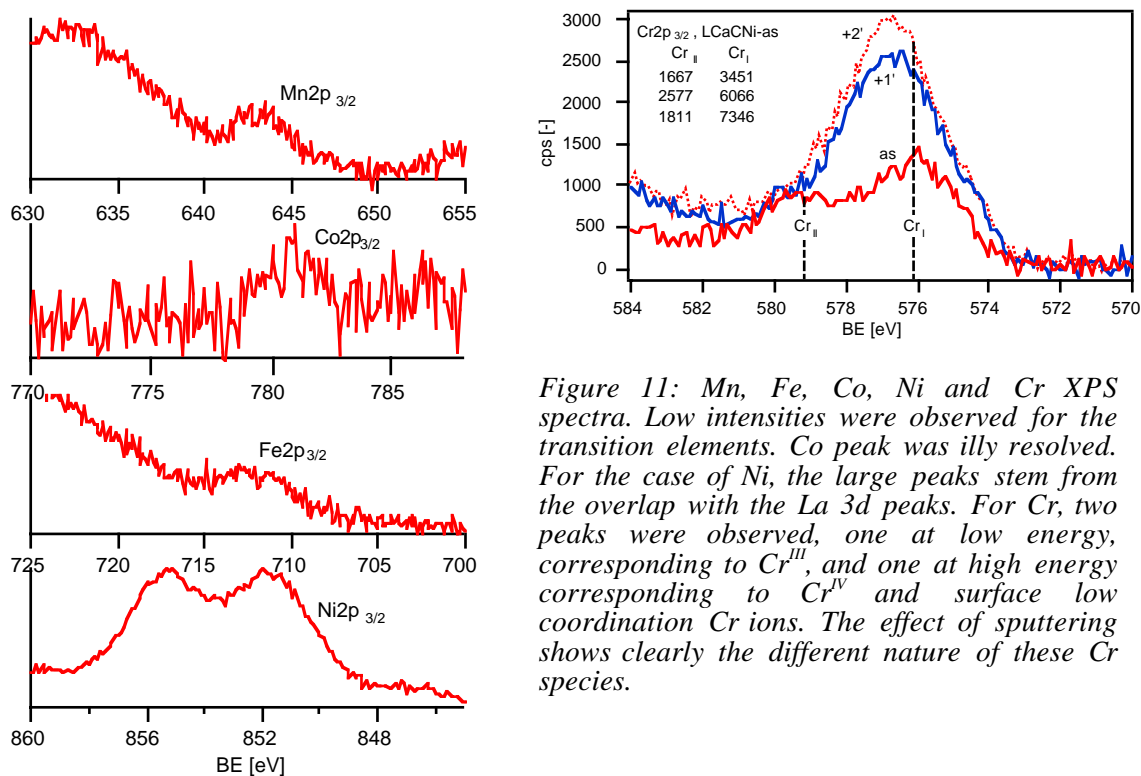


Figure 11: Mn, Fe, Co, Ni and Cr XPS spectra. Low intensities were observed for the transition elements. Co peak was illy resolved. For the case of Ni, the large peaks stem from the overlap with the La 3d peaks. For Cr, two peaks were observed, one at low energy, corresponding to Cr^{III}, and one at high energy corresponding to Cr^{IV} and surface low coordination Cr ions. The effect of sputtering shows clearly the different nature of these Cr species.

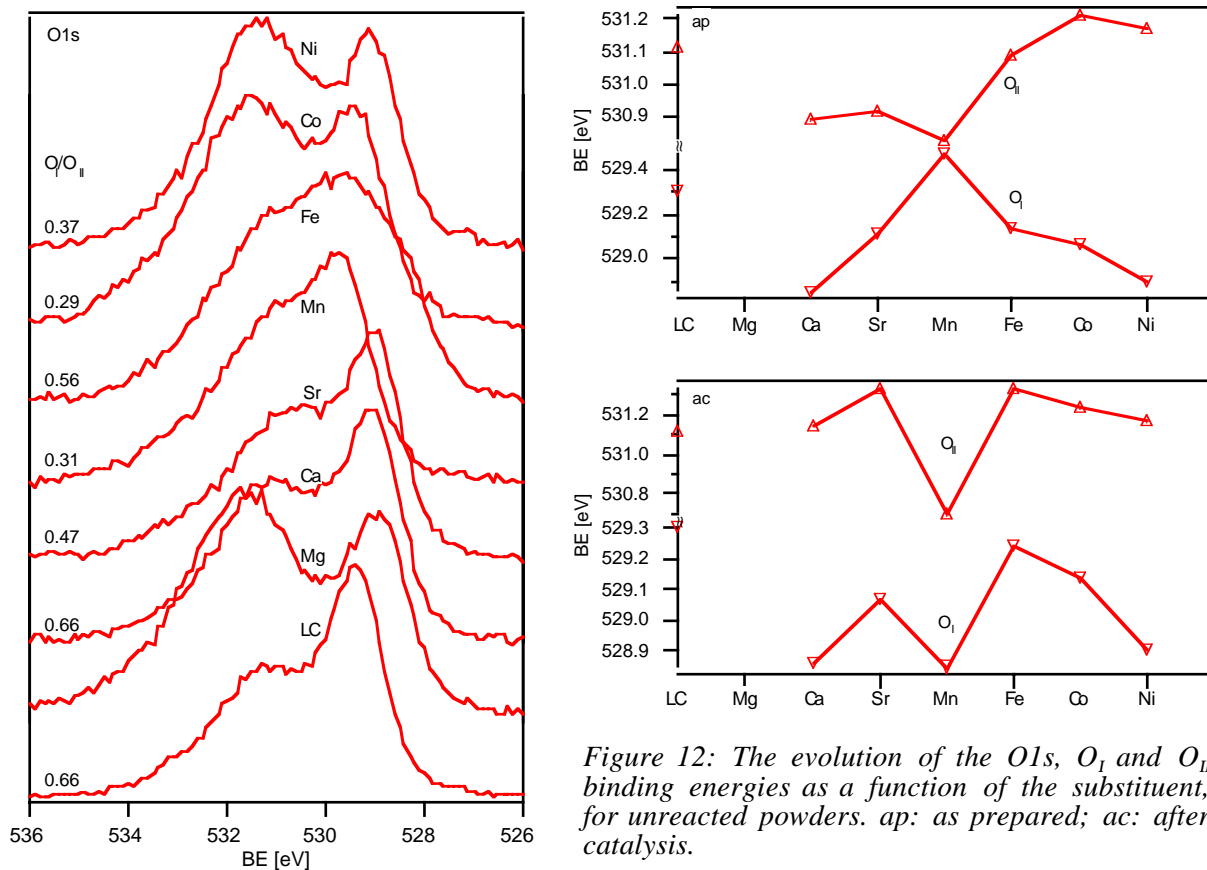


Figure 12: The evolution of the O1s, O_I and O_{II} binding energies as a function of the substituent, for unreacted powders. ap: as prepared; ac: after catalysis.

The $\text{O}1s$ peaks, O_I and O_{II} , corresponding to the lattice oxygen and adsorbed oxygen and hydroxyl groups respectively, fluctuate slightly with the substitution. The binding energy (BE) of O_I decreases from Mn to Ni and from Mn to Ca while for O_{II} it increases from Mn to Ni whereas it is almost unchanged for Ca and Sr, as illustrated in Figure 12. The high binding energy $\text{O}1s$ peak was previously reported to increase with the nature of the LaMO_3 perovskites, from $M = \text{Cr}$ to Ni, whereas the low binding energy $\text{O}1s$ did not fluctuate much¹⁵.

Ni carbides were not observed on samples of LCNi and LCaCNi after catalysis, as a carbon peak specific to carbides was not observed. The concentration of the different species are summarized in Table 8. It is seen that in all cases but the LC, LCC, LCCNi and LSC powders, La is present in excess. This could stem from the preparation procedure. Next, Ca and Sr are seen to segregate strongly on the surface. This segregation is enhanced after the catalytic runs (from 10 to 22% for Ca and 10 to 14% for Sr). Ca seems to segregate more easily than Sr. In the case of a fresh $\text{La}_{0.85}\text{Ca}_{0.15}\text{Cr}_{0.9}\text{Ni}_{0.1}\text{O}_3$ powder, the La, Cr and Ca peaks vary with time after sputtering with Ar^+ ; after 2 min sputtering time, the La, Cr and Ca concentrations pass successively from 39 to 49%, 49 to 42% and 12 to 9% respectively. The gas atmosphere is observed to have an effect on the surface segregation of Ca as observed on LCaCNi samples exposed at 800°C to air, CO_2 or $\text{H}_2+3\%\text{H}_2\text{O}$ atmospheres for more than 100 h (bottom of Table 8). Wet hydrogen clearly increased the segregation of Ca, whereas air and CO_2 had no effect.

Table 8: Summary of the XPS surface analysis given in percent of the sum of the total metal elements.

XPS analysis [%]	La/Cr	Mg	Ca	Sr	Mn	Fe	Co	Ni	Ca, Sr	Mg, Mn, Fe, Co, Ni
Catalyst composition								*	nominal	nominal
LaCrO_3 , ap	0.9									
$\text{LaCr}_{0.9}\text{Mg}_{0.1}\text{O}_3$, ap	2.9	5.3								5
$\text{LaCr}_{0.9}\text{Mg}_{0.1}\text{O}_3$, ac	2.8	4.9								5
$\text{La}_{0.85}\text{Ca}_{0.15}\text{CrO}_3$, ap	1.0		10						7.5	
$\text{La}_{0.85}\text{Ca}_{0.15}\text{CrO}_3$, ac	1.0		22						7.5	
$\text{La}_{0.7}\text{Ca}_{0.32}\text{CrO}_3$, ap	1.0		39						16	
$\text{La}_{0.85}\text{Sr}_{0.15}\text{CrO}_3$, ap	0.9			10					7.5	
$\text{La}_{0.85}\text{Sr}_{0.15}\text{CrO}_3$, ac	0.8			14					7.5	
$\text{LaCr}_{0.9}\text{Mn}_{0.1}\text{O}_3$, ap	1.2				5					5
$\text{LaCr}_{0.9}\text{Mn}_{0.1}\text{O}_3$, ac	1.3				5.7					5
$\text{LaCr}_{0.9}\text{Fe}_{0.1}\text{O}_3$, ap	1.1					7.3				5
$\text{LaCr}_{0.9}\text{Fe}_{0.1}\text{O}_3$, ac	1.2					8.7				5
$\text{LaCr}_{0.9}\text{Co}_{0.1}\text{O}_3$, ap	1.2						1.9			5
$\text{LaCr}_{0.9}\text{Co}_{0.1}\text{O}_3$, ac	1.3						2.8			5
$\text{LaCr}_{0.9}\text{Ni}_{0.1}\text{O}_3$, ap	1.6							?		5
$\text{LaCr}_{0.9}\text{Ni}_{0.1}\text{O}_3$, ac	1.9							?		5
$\text{La}_{0.85}\text{Ca}_{0.15}\text{Cr}_{0.9}\text{Ni}_{0.1}\text{O}_3$, ap	1.0		10					?	7.5	5
$\text{La}_{0.85}\text{Ca}_{0.15}\text{Cr}_{0.9}\text{Ni}_{0.1}\text{O}_3$, ac	0.8		21					?	7.5	5
$\text{La}_{0.85}\text{Ca}_{0.15}\text{Cr}_{0.9}\text{Ni}_{0.1}\text{O}_3$, H_2	1.2		15					?	7.5	5
$\text{La}_{0.85}\text{Ca}_{0.15}\text{Cr}_{0.9}\text{Ni}_{0.1}\text{O}_3$, CO_2	1.0		9					?	7.5	5
$\text{La}_{0.85}\text{Ca}_{0.15}\text{Cr}_{0.9}\text{Ni}_{0.1}\text{O}_3$, air	1.2		6					?	7.5	5

ap: as prepared; ac: after catalysis; *: Ni peak could not be resolved because of overlapping with La 3d peaks. A Ca rich LaCrO_3 ($\text{La}_{0.7}\text{Ca}_{0.32}\text{CrO}_3$) is also given to illustrate the high segregation effect of A-site substituents.

TEM analysis

TEM analyses were performed on the LCNi, LCaCNi and LCFE powders before and after catalysis. It was observed that in the case of LCaCNi, carbon formation was limited to some LCaCNi grains with small islets of Ni attached to them, as illustrated in Figure 13a. These Ni islets had a mean particle size of 20 to 50 nm. The carbon was deposited around the Ni islets on the LCaCNi surface and formed well defined graphitic films, shown in Figure 13b. These had a thickness of around 5 nm and seemed to grow in parallel to the surface of LCaCNi particules.

Some of the films were observed to be amorphous in electron diffraction mode (see Figure 13c). These Ni particles seemed to adhere well on the grain surface and none was observed away from the surface.

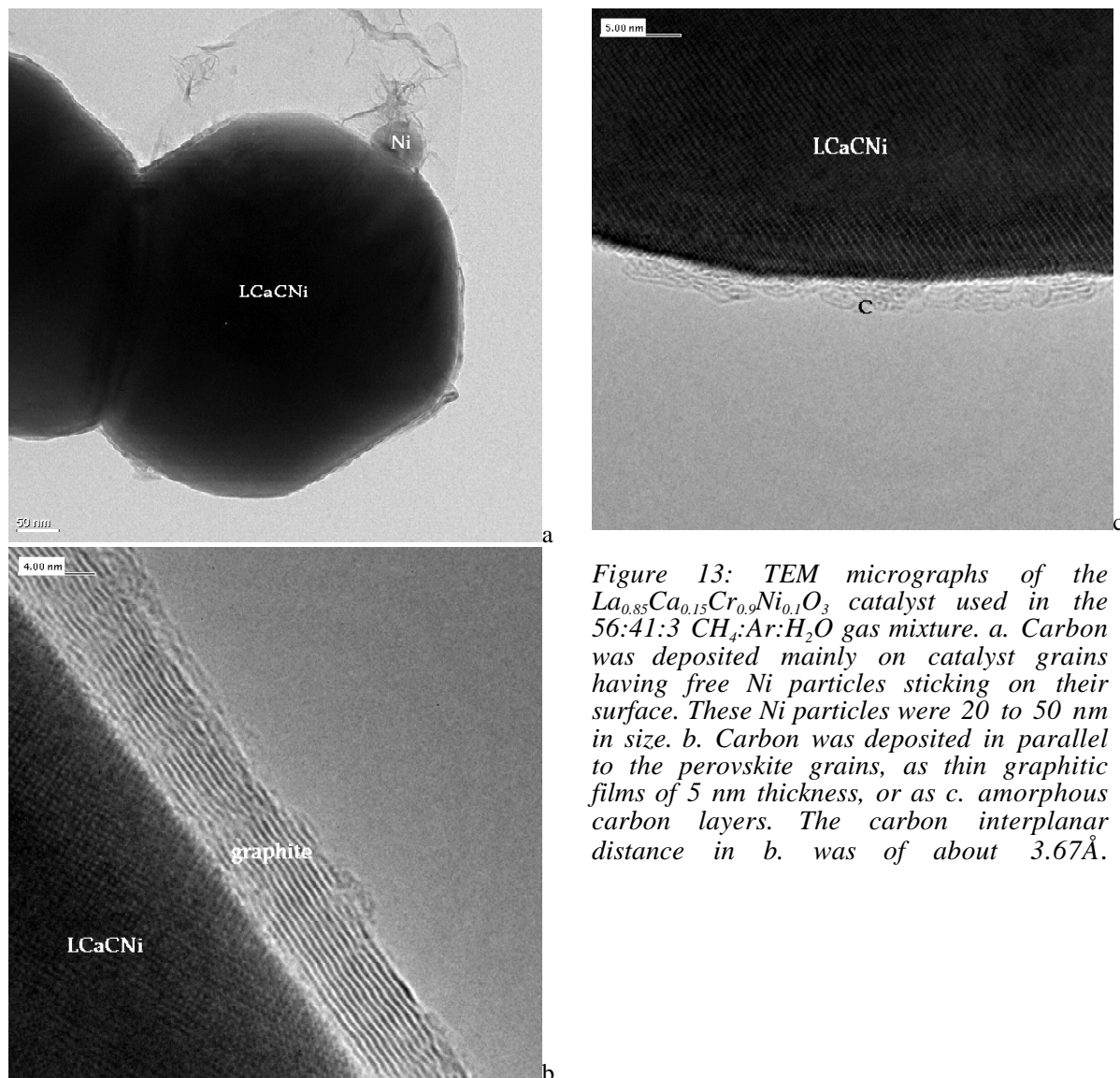


Figure 13: TEM micrographs of the $\text{La}_{0.85}\text{Ca}_{0.15}\text{Cr}_{0.9}\text{Ni}_{0.1}\text{O}_3$ catalyst used in the 56:41:3 CH_4 :Ar: H_2O gas mixture. a. Carbon was deposited mainly on catalyst grains having free Ni particles sticking on their surface. These Ni particles were 20 to 50 nm in size. b. Carbon was deposited in parallel to the perovskite grains, as thin graphitic films of 5 nm thickness, or as c. amorphous carbon layers. The carbon interplanar distance in b. was of about 3.67\AA .

The particles free of Ni islets did not grow any carbon films. The composition of LCaCNi, measured on a large number of grains, did not change for particles with or without the Ni islets within accuracy of *EDS* microanalysis (50 s acquisition time). Ni islets were found on the free surface of LCaCNi and in some cases in the bottle neck between two grains, as shown in Figure 14 for the reoxidized catalyst.

The origin of free Ni is not very clear, but it was possible to observe it on top of what seems to be a CaCr_2O_4 phase. This is well illustrated in Figure 15a-b. This phase is known to be one of the impurities that forms during the fabrication of Ca substituted LCs¹³ (Chapter 5).

Another impurity was the CaCrO_4 (or CaCrO_3) phase as shown in Figure 16a-b. This phase was not observed either by *XRD* diffraction as it seemed amorphous taking the form of a melt like structure (see Figure 17a-b). The CaCrO_4 was observed on free surfaces as well as in the bottle neck between two grains (see Figure 18a-b). A Ca rich phase, which could also be a calcium chromate phase, was sometimes observed in grain boundaries (see Figure 19a). The surface of the grains seemed to be clean as observed by *HRTEM* (Figure 19b).

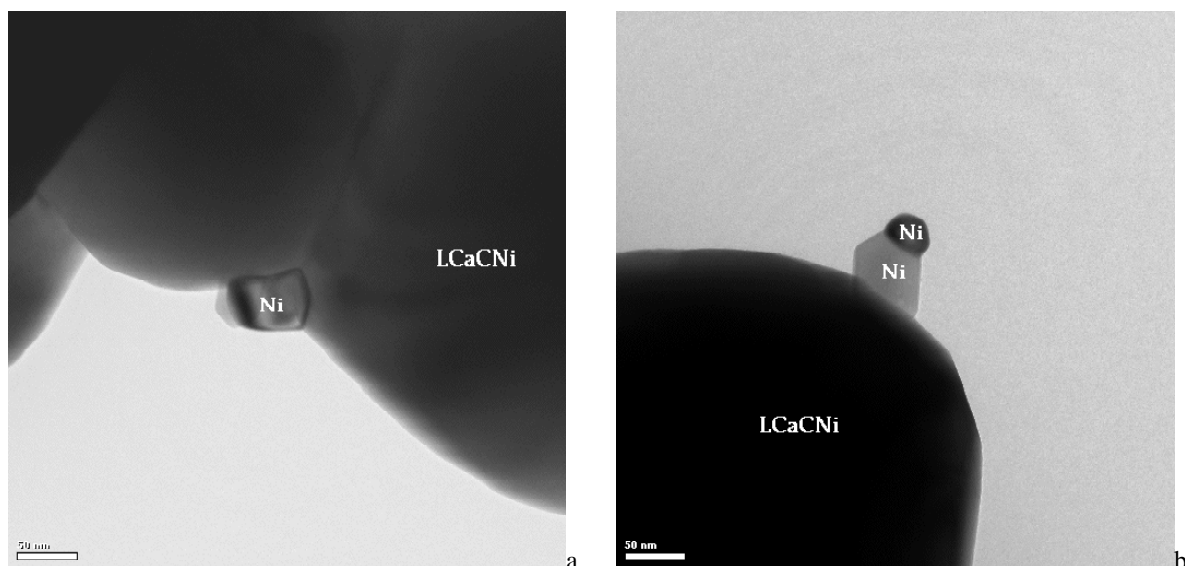


Figure 14: Ni islets as observed by TEM on $\text{La}_{0.85}\text{Ca}_{0.15}\text{Cr}_{0.9}\text{Ni}_{0.1}\text{O}_3$ catalyst. Ni was found a: in the bottle neck of two grains and b: on the free surface of a grain.

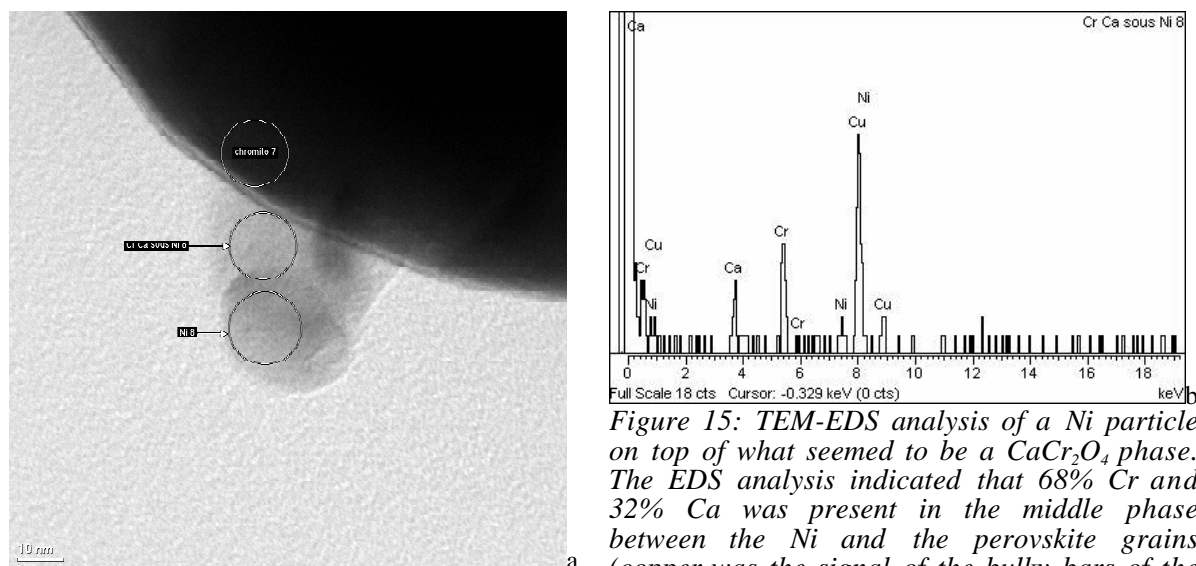
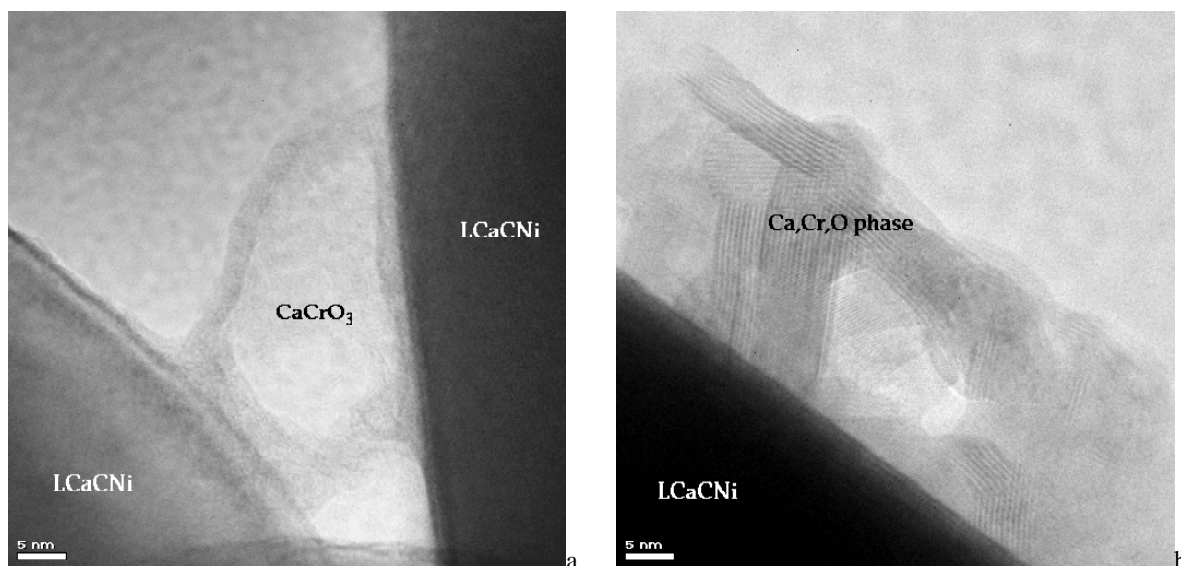
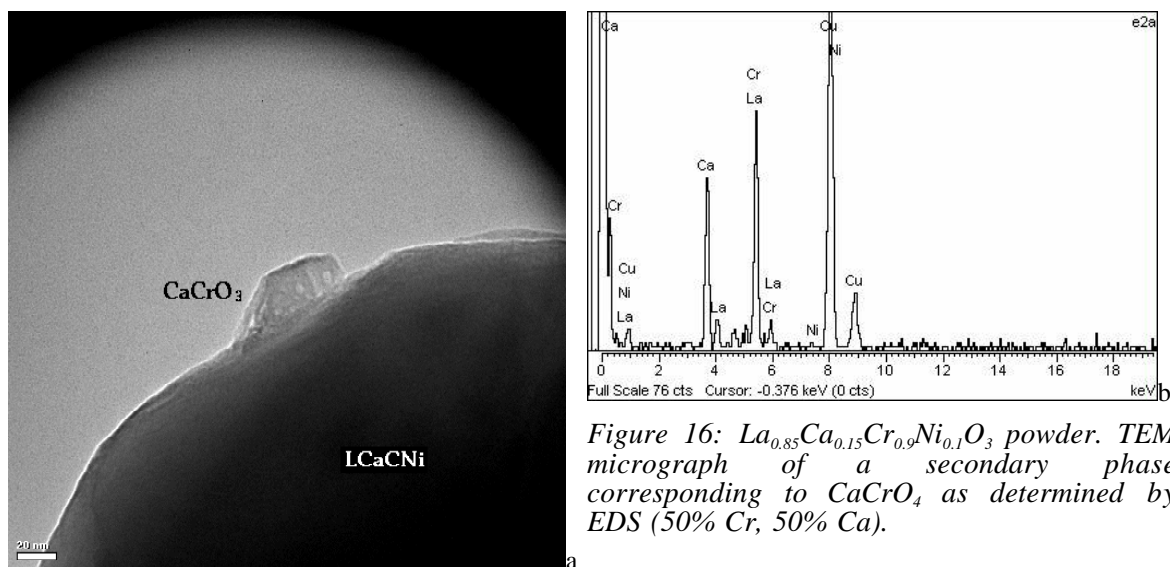


Figure 15: TEM-EDS analysis of a Ni particle on top of what seemed to be a CaCr_2O_4 phase. The EDS analysis indicated that 68% Cr and 32% Ca was present in the middle phase between the Ni and the perovskite grains (copper was the signal of the bulky bars of the Cu sample holder).

On the LCNi powders, no Ni islets were observed (Figure 20a). It was however possible to observe some spots on or inside some grains (Figure 20b). Diffraction analysis show that this might stem from secondary phases precipitated in the lattice. It was not possible to analyze the surface composition of the LCNi and LCaCNi grains by HRTEM, as the electron beam tended to destroy the first layers rapidly. Very narrow surface segregation might exist on oxides, leading to changes in their catalytic activity^{33, 34}.

LCFe did not show any Fe segregation of any kind. Chemical analysis measurements done on a large number of grains showed very similar compositions within accuracy of EDS microanalysis (50 s acquisition time). The carbon deposition and its structure depended on the temperature of the reaction. Almost no carbon was found at 800°C. Figure 21a-d show two different carbons after the run in 56:41:3 CH_4 :Ar: H_2O at 850°C. A major component was the soot-like carbon which was deposited in many cases on kinks (see Figure 21d). The step-edge perovskite atoms can be considered as low-coordinate ions (CUS, coordinately unsaturated sites), showing marked electron donor properties, and thus having higher activity toward methane³⁵. The other carbon represent amorphous films which had thicknesses of about 20 nm (see Figure 21b,c). However, the carbon coverage was low at 850°C. Running the catalyst at

900°C lead to structured graphitic films (see Figure 22b,c) along with graphitic filaments (see Figure 22a,c,d) running from the surface of the grains. At this temperature, carbon coverage was quite significant. From the TEM micrographs these filaments seemed to build-up epitaxially to the surface of the LCFE powder (Figure 22d). The interplanar distance measured on the micrograph 22d is of 3.82Å, whereas the one for the carbon was of 3.57Å at the interphase, or 3.48Å in the filament (3.35Å for well crystallized graphitic carbon, 3.57Å as an average for graphite on these perovskites). These values were quite close. Beside that, there was also a clear continuity between the grain's planes and the carbon filament as indicated by the black lines of Figure 22d. Also, the interplanar distance measured on the carbon film of Figure 22c was of 3.56Å in the well crystallized part.



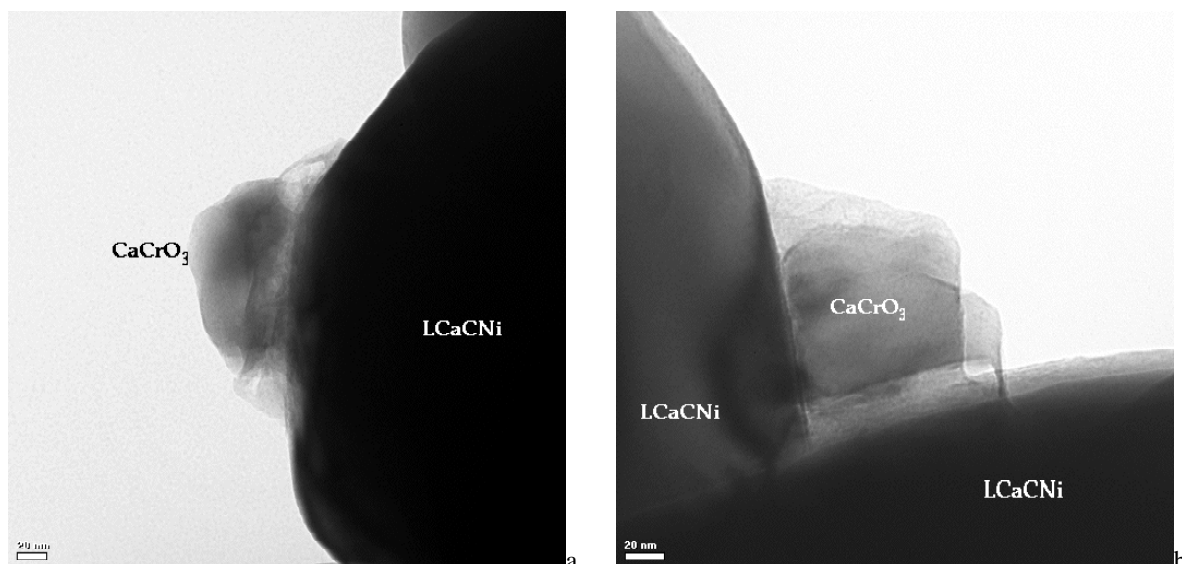


Figure 18: TEM micrographs of CaCrO_4 observed on $\text{La}_{0.85}\text{Ca}_{0.15}\text{Cr}_{0.9}\text{Ni}_{0.1}\text{O}_3$ on a: free surfaces as well as in b: the bottle neck between two grains.

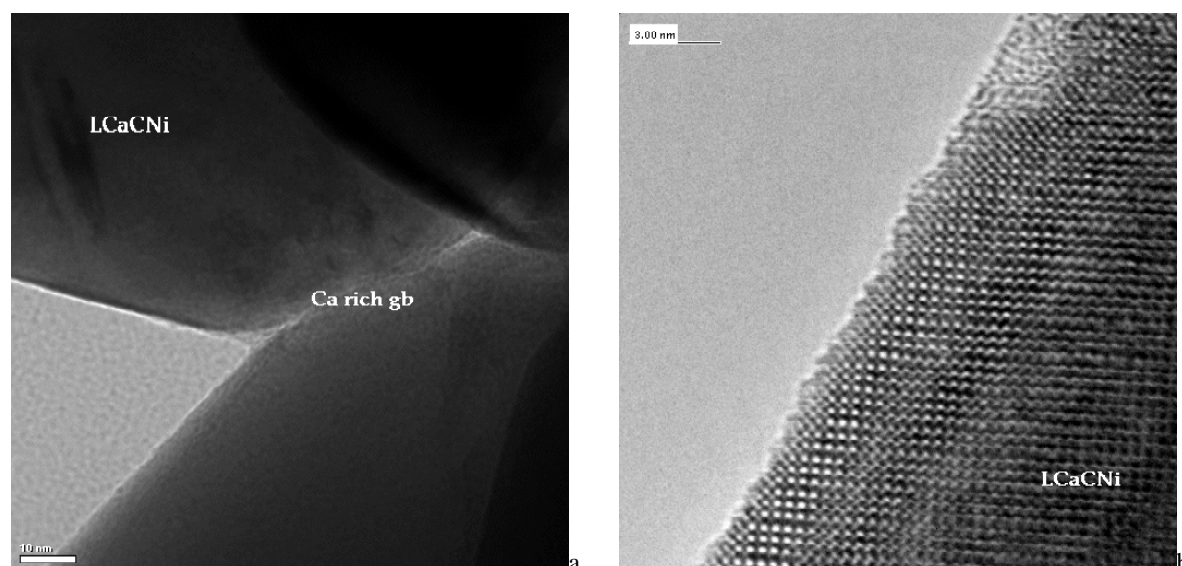


Figure 19: TEM on $\text{La}_{0.85}\text{Ca}_{0.15}\text{Cr}_{0.9}\text{Ni}_{0.1}\text{O}_3$ powder. a: A Ca rich phase, which could also be a calcium chromate phase, was sometimes observed in grain boundaries. b: The surface of the grains seem to be clean as observed by HRTEM, as there is a continuity between the bulk and the surface of the grain.

Discussion

In XPS spectra the $2p_{3/2}$ Mn peak was located at 642.2 eV, which is close to that of Mn^{III} (641.9 eV)³⁶. Fe seems to be in the trivalent state as its binding energy (BE) was in the range of 710.5 to 711.7 eV (711.3 eV for Fe_2O_3 ,³⁷). The BE of Co corresponded to both Co^{II} and Co^{III} ³⁸. With Ni, however, no peak was observed. Overall, these results corroborate well with measured TPR spectra where mixed valencies were observed for Co ($\delta = 0.031$) and a valency of III for Mn and Fe as δ was close to that of LC. From TPR, Ni is thought to be in the divalent state.

The two observed Cr peaks can be assigned to Cr^{III} (576.1 eV,³⁷) and Cr of a higher valency (579 eV). The high valency Cr can be either Cr^{IV} or surface Cr where its coordination sphere is not complete¹⁵.

The two peaks of oxygen can be attributed to lattice oxygen O_I (529 eV) and to adsorbed oxygen and hydroxyl O_{II} (531 eV)¹⁵ - it was not deconvoluted into two further peaks because of overlapping. This agrees well with the *TPR* results where two peaks were observed, one for the surface adsorbed oxygen species and another for the lattice oxygen. The lattice oxygen O_I binding energy seemed to decrease from Mn to Ni (see Figure 12) as expected from the stability of the LaMO_3 oxides³⁹, indicating that oxygen vacancies were easily formed on Ni substituted LCs compared to other substitutions. Also, O_I *BE* increased from Ca to Sr. From thermodynamic calculations based on values in the literature^{40, 41}, Sr substituted LC reduces however more readily than Ca with a difference of ≈ 11 kJ/mol (for $x=0.15$)¹⁴ (Chapter 7). The O_{II} peak increased from Mn to Ni, with Mn having the lowest *BE*. This corroborates well with *TPR* measurements and indicates that oxygen adsorbs more on the Ni=Co>Fe>Mn substituted LCs. However, the total amount of O_I s did not change for the different substituents. From *TPR*, the Sr substitution caused more oxygen to desorb than did Ca substitution. This difference in desorption could explain the higher activity of L SrC when compared to L CaC (50% O_2 conversion at 390°C for Sr- versus 500°C for Ca substituted LC, and *TOF* of 3.9×10^{-9} for Sr versus 3.5×10^{-9} for Ca at 850°C in 5:1 $\text{CH}_2:\text{O}_2$) as more oxygen from the lattice was available for the reaction.

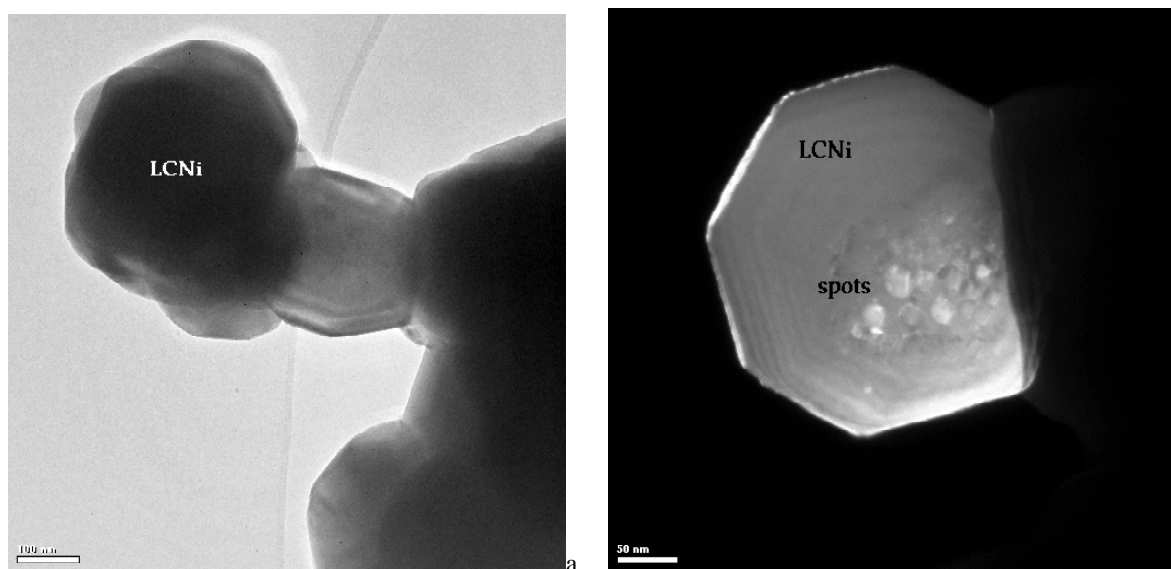


Figure 20: TEM on the $\text{LaCr}_{0.9}\text{Ni}_{0.1}\text{O}_3$ powders, a: no Ni islets were observed; b: it was however possible to observe some spots on or inside some grains. On that grain it is also possible to see a step-like structure.

This effect was also observed on the doubly substituted LC (Sr or Ca/Mg and Sr or Ca/Ni). For the transition elements, the trend was similar as the *TOF* was of $3.1, 5.6, 8.0$ and 19.5×10^{-9} for Mn, Fe, Co and Ni respectively, following in proportion the total amount of oxygen species desorbed by *TPR* (Mn 0.026 \approx Fe 0.025 < Co 0.031 < Ni 0.064) and the O_I *BE* trend. This suggests that a relation exists between the reducibility and the catalytic activity on these oxides. This relation is already observed in literature for simple oxides²⁷, and for perovskites^{2, 6}. They clearly showed a trend between oxygen adsorption, reducibility and the activity of oxides for oxidation reactions.

Surface concentration of the different elements showed that surface segregation was important for Ca and Sr substitution. The Ni islets, observed on the L CaCNi powders, were most probably related to the liquid phases (calcium chromates) produced during sintering as the L CNi powder did not present any free Ni. In literature, the collapse of heavily doped A-site $\text{LaCr}_x(\text{Ni},\text{Co})_y\text{O}_3$ (0.2-0.3 Sr, 0.2-0.4 Ca) in wet hydrogen was reported⁴²⁻⁴⁴, alongside to the formation of melt-like chromate phases⁴⁴. In this study, two secondary phases, CaCrO_3 and CaCr_2O_4 , were observed on the L CaCNi powder (see Figures 15 and 16) and, in some cases, they were attached to Ni islets (see Figure 15). The *XPS* results indicated no surface segregation for Ni (Table 8). This clearly indicates that the catalytic activity of the L CaCNi was not directly related to the Ni islets as the L CNi had a similar catalytic behavior.

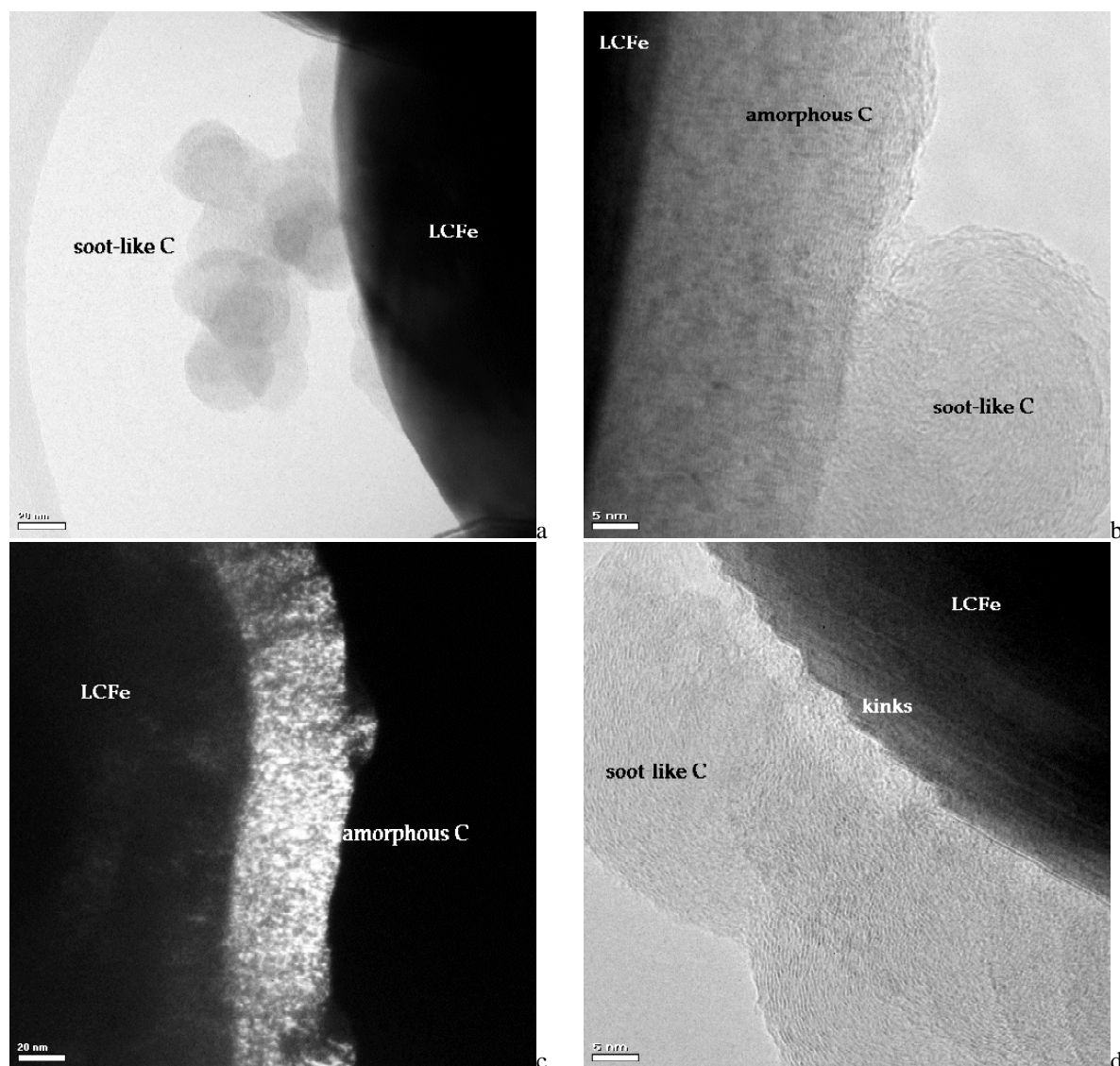


Figure 21: TEM micrographs of different types of carbon deposited over $\text{LaCr}_{0.9}\text{Fe}_{0.1}\text{O}_3$ at 850°C after catalytic runs in the 56:41:3 CH_4 :Ar: H_2O gas mixture. a: soot-like carbon; b: amorphous carbon films of ≈ 20 nm thickness as observed in the c: dark file mode; d: carbon formation around kinks on the grains' surface.

XRD, *XPS* and *TEM* measurements conducted on freshly prepared as well as on tested LCNi and LCaCNi powders, showed no change in the composition due to catalysis. This was also true for the iron substituted catalyst based on *XPS* and *TEM* data and for the other transition metal substituted catalysts based on *XRD* and *XPS* measurements. On the other hand, Ca and Sr segregation measured by *XPS* was significant, as observed already in the past^{12, 13} (Chapter 4). *XPS* analysis on LCaCNi powders, exposed to different atmospheres (humidified H_2 , CO_2 and air), show clearly the effect of humidified hydrogen on Ca segregation (see Table 8). Interestingly, Ni did not segregate during these tests. Preliminary thermodynamic calculations show that H_2 and H_2O lead to a higher loss of Sr and Ca due to the formation of volatile hydroxyl species whereas CO , CO_2 and O_2 had almost no effect¹⁴ (Chapter 7). Our results may indicate that the Ca and Sr solubilities are below 15% of the La site. Sfeir et al.¹³ and Peck et al.⁴⁰ have reported a value for Sr in LC of 15% at 850°C and of 10% at 950°C respectively, whereas Carter et al.⁴⁵ and Sfeir et al.¹³ indicate a solubility limit for Ca in LC of 20% at 900°C and 15% at 800°C respectively. Moreover, Mg, Mn, Fe, Co and Ni do not segregate further after the catalytic runs, indicating that they may not destabilize the perovskite structure. This is in accordance with *TPR* results, which shows clearly that all of the LC catalysts did not undergo total reduction of the *B*-site substituent.

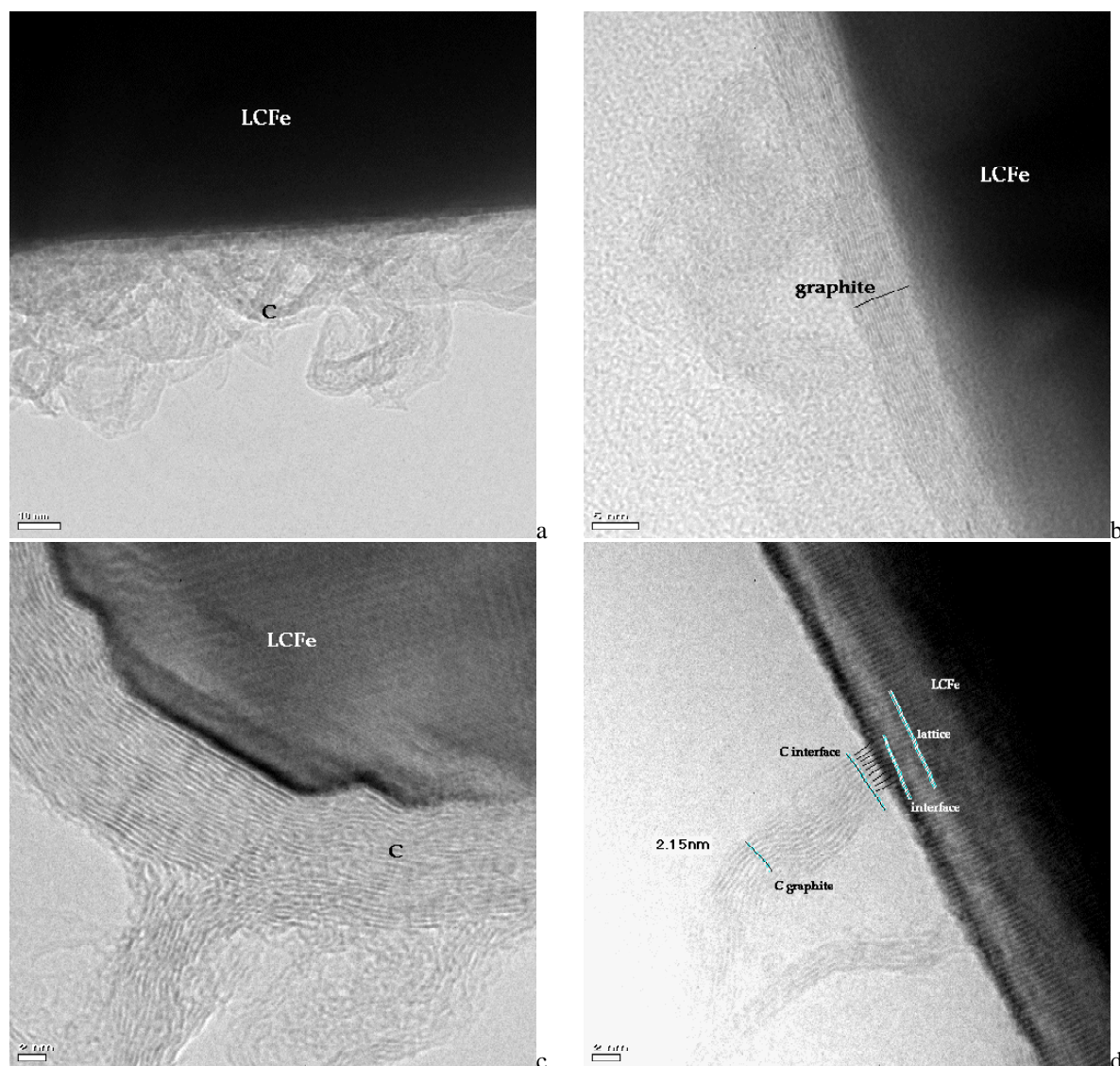


Figure 22: TEM micrographs of different types of carbon deposited over $\text{LaCr}_{0.9}\text{Fe}_{0.1}\text{O}_3$ at 900°C after catalytic runs in the 56:41:3 CH_4 :Ar: H_2O gas mixture. a, c and d: filamentous carbon; b and c: graphitic carbon films. Epitaxial growth of carbon filaments is clearly observed in d, where the interplanar distance for the perovskite follow closely the one for the carbon fillament, the planes being continuous.

Our thermodynamic calculations based on the ideal solid solution model used by Yokokawa et al.⁴⁶ indicate further that the Fe and Ni substituted LCs would decompose at a P_{O_2} of 1.26×10^{-23} and 3.16×10^{-16} respectively, to yield the metal and the LaCrO_3 phase, while Mg, Ca, Sr, Mn and Co would decompose to the metal oxide and LaCrO_3 phases at a P_{O_2} of 1.6×10^{-14} , 1.0×10^{-19} , 1.6×10^{-26} , 6.3×10^{-24} and 1.9×10^{-14} respectively¹⁴ (Chapter 7). Christie et al.⁴⁴, Baker et al.¹¹ and Sammes et al.^{42, 43} have previously observed the partial decomposition of heavily doped A-site $\text{LaCr}_{1-x}(\text{Co}, \text{Ni})_x\text{O}_3$. The TPR and XPS results in this study for the Ni and Co substituted LCs indicate clearly the destabilizing effect of the A-site substituent. XRD measurements made on a $\text{LaCr}_{0.5}\text{Ni}_{0.5}\text{O}_3$ powder, exposed for 1 week at 780°C to $\text{H}_2 + 3\% \text{H}_2\text{O}$, showed no demixing (Figure 23). This is in accordance with the results published by Stojanovic et al.⁹. Our present experimental results suggest that the decomposition of LCs is hindered kinetically.

However, it is not very clear why a slow change in the catalytic activity was observed over a period of 20 h in the 5:1 CH_4 : O_2 gas mixture for both Ni-substituted LCs (Figure 6b). We

previously observed a slow change in the conductivity of different LC rods over the same period of time. The change in activity could be related to a slow reduction process (Chapter 8).

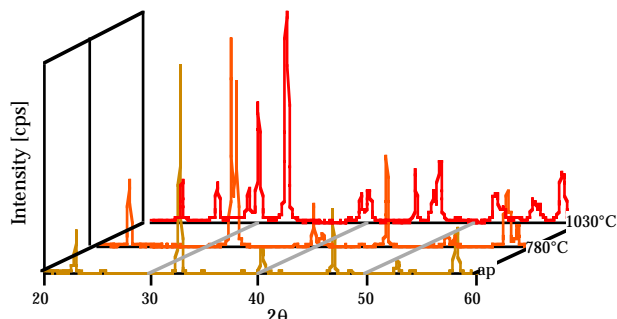


Figure 23: XRD on $\text{LaCr}_{0.5}\text{Ni}_{0.5}\text{O}_3$ powder exposed 1 week to 3% wet H_2 . The as prepared powder (ap) is orthorhombic, the one reduced at 780°C is rhombohedral, whereas the one reduced at 1030°C could not be resolved and has most probably decomposed (Ni , LaCrO_3 ?). The spectra were recorded from 2θ of 5 to 90 (see Appendix Chapter 3).

If we try to correlate the XPS observations with the apparent activities of the different LCs, we observe that in the 5:1 $\text{CH}_4:\text{O}_2$ gas mixture, the activity follows the trend of the O_{II} and O_I BE, i.e., the activity increases with the strength of the oxygen adsorption, and the easiness of reduction of the lattice. Overall, the change in activity with the substitution, if expressed as turn over frequency (TOF), is observed to be very marginal in the case of Mg, Ca, Sr and Mn. For Fe, Co and Ni, the substitution induces a higher activity when compared to the LC base material. Moreover, for the Mn and Co substitution the activity is lower than in the base materials, LaMnO_3 and LaCoO_3 , where higher valencies, Mn^{IV} and Co^{IV} , are formed upon substitution with Sr or Ca (e.g. at 850°C , $\text{TOF} \approx 2 \times 10^{-6}$ and only 8×10^{-9} moles of $\text{CH}_4/\text{m}^2\text{s}$ for methane oxidation on $\text{La}_{0.8}\text{Sr}_{0.2}\text{CoO}_3$ ¹ and $\text{LaCr}_{0.9}\text{Co}_{0.1}\text{O}_3$, this study, respectively, i.e. 250 times lower in the LC). This could be due to the low valencies of Mn and Co in LC (Mn^{III} and $\text{Co}^{III, II}$). Also, a double substitution with Ca or Sr and a B-site substituent had an effect on the activity. The TOF increased from 5.1×10^{-9} for LCMg to 9.8×10^{-9} for LCaCMg, but stayed constant for Ni substituted LC, being of 1.9×10^{-8} for LCNi and 2.1×10^{-8} for LCaCNi at 850°C , in 5:1 $\text{CH}_4:\text{O}_2$. This could also be correlated with the conductivities of the catalysts (1 to 1.27 S/cm for LCaCMg and LSrCMg versus 0.16 S/cm for LCMg, and 1.91 S/cm for LCaCNi versus 0.39 S/cm for LCNi, in wet hydrogen (Chapter 3)), related to higher hole and oxygen vacancies conductivities. In literature, CH_4 oxidation over perovskites was described by a parallel reaction of CH_4 with weakly held chemisorbed surface oxygen, at low temperature, and with lattice oxygen at high temperatures. The reaction mechanism at low temperatures was either expressed as a Rideal-Eley² or a Mars and van Krevelen⁹ mechanism. Globally the reaction rate was expressed as

$$r = k_1 P_{\text{CH}_4}^n P_{\text{O}_2}^m + k_2 P_{\text{CH}_4} \quad (8)$$

with k_1 and k_2 the rate constants for the adsorbed oxygen reaction and the lattice oxygen reaction respectively, and n and m the orders of the reactions in respect to CH_4 and O_2 , n and m being near to 1 and 0.5 in most cases. In detailed experiments with $\text{La}_x\text{Sr}_y\text{MnO}_3$, Arai et al.² determined activation energies of 59~85 kJ/mol and 105~166 kJ/mol for the reaction with adsorbed oxygen and with lattice oxygen, respectively. The adsorption energies for oxygen were in this case of 274~291 kJ/mol. In the case of LaFeO_3 McCarty et al.⁵ determined activation energies of 81 kJ/mol and 133 kJ/mol respectively. Also, the activation energy for the diffusion coefficients of oxygen ion vacancies in LaFeO_3 and LaCoO_3 and $\text{La}_{0.6}\text{Sr}_{0.4}\text{CoO}_3$ was found to be of 75 ± 21 kJ/mol, a value near to the activation energy of the reaction with lattice oxygen⁵. The heat of oxygen adsorption over LaCrO_3 is of 20 kJ/mol¹⁸, indicating a physisorption. By substituting with Mg, the heat of adsorption was reported to increase to 168~188 kJ/mol, indicating a chemisorption⁸. Activation energies for the LCs in the 5:1 $\text{CH}_4:\text{O}_2$ gas mixture vary in this study between 82 and 121 kJ/mol indicating that the mechanism is somehow similar. Globally, there is an increase in the activation energy from Mn to Ni. This could be due to the fact that lattice oxygen is more active in the case of Ni than in Mn, and that oxygen adsorption is

increasing, as could be concluded from the *TPR* and *XPS O1s* measurements. A similar behaviour is seen for Ca and Sr. The CO_2 inhibiting effect on methane oxidation over A-site substituted LCs could be related to the surface segregation of Ca and Sr. These basic sites might interact with CO_2 to form carbonates which block the catalytically active sites for oxidation. Such inhibition was reported on the La_2O_3 catalyst⁴⁷ and interpreted as the interaction of CO_2 with active oxide species responsible for methane and oxygen activation. The effect of surface segregation over perovskites activity was also discussed by Gunasekaran et al.⁴

A thorough analysis of the product distribution in the case of the methane-steam reaction indicates that the main reaction is steam-reforming leading to CO and H_2 . When going from 3 to 23% water, the CO selectivity was reduced (see Table 5). In most cases water had no influence on the CH_4 conversion, so that this change in selectivity is related to a fast reverse water gas shift reaction (reaction (5)). The low steam-reforming capacities of these perovskites might be related to the fact that the surface coverage with hydroxyl groups is low as observed by infrared and *in situ* diffuse reflectance infrared spectroscopy (*DRIFT*) over LaCrO_3 ¹⁸ and La_2O_3 ³⁵ respectively, even though the hydroxyl radicals are reported to be easily formed over La_2O_3 with an activation energy of 125 kJ/mol⁴⁸. Equivalently, the lifetime of adsorbed CH_4 is reported to be short as measured by *TAP* (Temporal Analysis of Products) on La_2O_3 and Sm_2O_3 ^{47, 49}. Furthermore, the active sites for water and methane adsorption are believed to be similar^{47, 48}. In this work, the order of the reaction for water on LCs was near zero and it changed from negative to positive values with temperature (Table 4). The activation energy of the reaction also increased with the steam content (Table 1). This might be a hint for a competitive coverage of adsorbed species on multiple sites⁵⁰, i.e. adsorption on the same active sites. Baker et al.^{10, 11} showed previously that methane dissociation is promoted over LCs and that the diluted methane reacted with adsorbed or lattice oxygen species. However, when using wet methane, they found that the reaction proceeded mainly through reaction with water. It is worth to note that all experiments on perovskites reported in literature used diluted methane, in contrast to the present study.

Among the substituents used in this study, only the Ni and Sr substitution increased CH_4 conversion indicating that these substituents do promote CH_4 dissociation. The low conversion of methane in the other substitutions is thought to be responsible for the low OCVs (open circuit voltages) measured with some of these anodes in SOFC tests. The situation seems to be similar to gold anodes (OCV \approx 700mV). Theoretical OCVs for SOFC cells using air at the cathode and a 56:41:3 CH_4 :Ar: H_2O gas mixture at different anodes, were calculated (see Table 9) based on the actual exhaust gas composition, using HSC 4.1 thermodynamic equilibria calculation software (Outokumpu Research Oy, Finland). For the calculation, the unreacted CH_4 was considered to be inert and equivalent to Ar. The calculated OCV of 880, 914 and 934 mV at 800°C for LSrCMg , LCaCMg and $\text{La}_{0.7}\text{Ca}_{0.3}\text{Cr}_{0.9}\text{Fe}_{0.1}\text{O}_3$ respectively, is close to the measured values of 862 (Figure 24), 892 and 928 mV respectively. $\text{La}_{0.7}\text{Ca}_{0.32}\text{CrO}_3$ gave an OCV of 903 mV at 854°C.

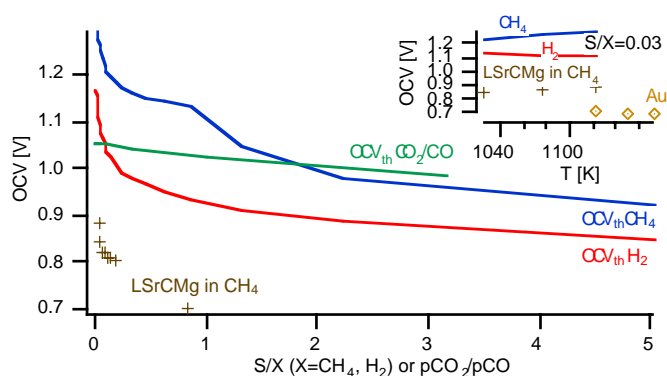


Figure 24: OCV measurements as a function of the steam to carbon ratio (S/C) and temperature in a glass sealed set-up (Chapter 2) for the $\text{La}_{0.85}\text{Sr}_{0.15}\text{Cr}_{0.9}\text{Mg}_{0.1}\text{O}_4/\text{YSZ}/\text{LSM}$ system (+). The thermodynamic equilibria for different gases are also shown along with measured values for an Au electrode (\diamond).

These OCVs agree well when considering the oxygen partial pressure determined by the $P_{\text{H}_2\text{O}}/P_{\text{H}_2}$ and $P_{\text{CO}_2}/P_{\text{CO}}$ equilibria from the $\text{H}_2 + 1/2 \text{O}_2 = \text{H}_2\text{O}$ and $\text{CO} + 1/2 \text{O}_2 = \text{CO}_2$ reactions. The theoretical OCV for the CH_4 reaction is 1205 mV at 800°C. Furthermore, impedance spectroscopy measurements done during electrochemical tests on symmetrical cells

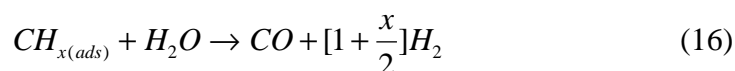
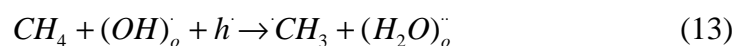
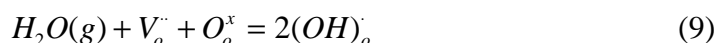
at OCV show that the reaction sequences had the same order of reaction for H_2 and CH_4 , whereas the activation energies were different. This indicates that the reactions are governed by CH_4 activation to yield the reactive hydrogen species followed by the removal of the carbonaceous species on the catalyst surface to form syngas.

Table 9: Estimated OCVs, in 56:41:3 CH_4 :Ar: H_2O , at 800°C.

Catalyst composition	P_{O_2} [atm]	OCV [mV]
Theoretical	4.80E^{-24}	1205
$\text{La}_{0.85}\text{Ca}_{0.15}\text{CrO}_3$	3.76E^{-19}	944
$\text{La}_{0.85}\text{Ca}_{0.15}\text{Cr}_{0.9}\text{Mg}_{0.1}\text{O}_3$	3.68E^{-18}	892
$\text{La}_{0.85}\text{Ca}_{0.15}\text{Cr}_{0.9}\text{Ni}_{0.1}\text{O}_3$	1.81E^{-23}	1174
$\text{La}_{0.85}\text{Sr}_{0.15}\text{CrO}_3$	7.11E^{-21}	1036
$\text{La}_{0.85}\text{Sr}_{0.15}\text{Cr}_{0.9}\text{Mg}_{0.1}\text{O}_3$	5.96E^{-18}	881
LaCrO_3	1.32E^{-18}	915
$\text{LaCr}_{0.9}\text{Mg}_{0.1}\text{O}_3$	1.17E^{-16}	812
$\text{LaCr}_{0.9}\text{Mn}_{0.1}\text{O}_3$	3.92E^{-19}	943
$\text{LaCr}_{0.9}\text{Fe}_{0.1}\text{O}_3$	7.80E^{-19}	928
$\text{LaCr}_{0.9}\text{Co}_{0.1}\text{O}_3$	1.19E^{-17}	865
$\text{LaCr}_{0.9}\text{Ni}_{0.1}\text{O}_3$	7.29E^{-22}	1089

The OCV were calculated from the exhaust gas composition by considering the unreacted CH_4 to be equivalent to Ar.

On the basis of these observations, a simplified reaction sequence for the steam-reforming as well as the partial oxidation could be proposed^{35,47,51} as:



with reaction (9) and (11)-(12) in competition with each other, $\text{V}_\text{o}^{\cdot\cdot}$, $\text{O}_\text{o}^{\text{x}}$, $\text{O}_\text{o}^{\cdot}$, $(\text{OH})_\text{o}^{\cdot}$, $(\text{H}_2\text{O})_\text{o}^{\cdot\cdot}$, h^{\cdot} , CH_3^{\cdot} and CH_3O^- representing the doubly charged oxygen ion vacancy, the oxygen O^{\cdot} and $\text{O}^{\cdot\cdot}$ on the normal lattice position, a positive hydroxyl-group on regular oxygen position, a doubly charged adsorbed water molecule, the electron hole in valence band, a methyl radical and a methoxide ion respectively. CH_4 dissociation is considered as homolytic as the energy of dissociation in the gas phase into the methyl and hydrogen radicals is of 422 kJ/mol, whereas the energy of heterolytic dissociation is much higher, 1309 and 1741 kJ/mol for the positively and negatively charged methyl ions respectively, even though the reversible adsorption of methane is thought to proceed through a heterolytic dissociation ($\text{CH}_3^{\cdot} + \text{H}^{\cdot}$)^{35,47,49,52}. This was also taken in agreement with kinetic isotopic effects measurements^{47,49}. $\text{O}_\text{o}^{\cdot}$ was proposed to be the most stable oxygen species on the surface of oxides⁵¹. On La_2O_3 , theoretical studies concluded that the formation of $\text{O}_\text{o}^{\cdot}$ pairs requires an energy of only 9.6 kJ/mol⁴⁸. Equation (9)

is reported to be rapid, i.e. at equilibrium, at 900°C ⁴⁸. It is thought that CH_4 activation is the rate determining step (equation (12)), in accordance with reference⁴⁹. Also, formaldehyde might also be an intermediate in the oxidation of methyl radicals from methoxide ions. The formaldehyde dissociates easily to CO and H_2 at these high temperatures⁵³.

Table 10: Estimation of the number of total and step-edge sites, in sites/ m^2 , over orthorhombic $\text{LaCrO}_3(1,0,1)$ and $(0,2,0)$ planes.

Plane	total $V_o^{\cdot\cdot}$	total Cr sites	total M	total $r/V_o^{\cdot\cdot}$ [%]	total r/M [%]
(1,0,1)	2.21×10^{17}	6.66×10^{18}	6.66×10^{17}	1.4	0.5
(0,2,0)	2.21×10^{17}	3.34×10^{18}	3.34×10^{17}	1.4	0.9
Step-edge Plane	$V_o^{\cdot\cdot}$	Cr sites	M	$r/V_o^{\cdot\cdot}$ [%]	r/M [%]
(1,0,1)	1.10×10^{16}	3.33×10^{17}	3.33×10^{16}	27.2	9.0
(0,2,0)	1.11×10^{16}	1.67×10^{17}	1.67×10^{16}	27.1	18.0

For the respective $(1,0,1)$ and $(0,2,0)$ planes a lattice surface area of $7.75 \times 7.75 \text{ \AA}^2$ and $5.47 \times 5.47 \text{ \AA}^2$ was considered. The rate (r) of 3×10^{15} molecules/ m^2s of CH_4 converted (a TOF of 5×10^{-9} mol/ m^2s) was compared to the respective step-edge sites. M stands for the transition metal ion and $V_o^{\cdot\cdot}$ for the oxygen ion vacancy. As an order of magnitude, CH_4 has a surface area of approximately $3.45 \times 10^{-20} \text{ m}^2$ (CSChem3Dpro program).

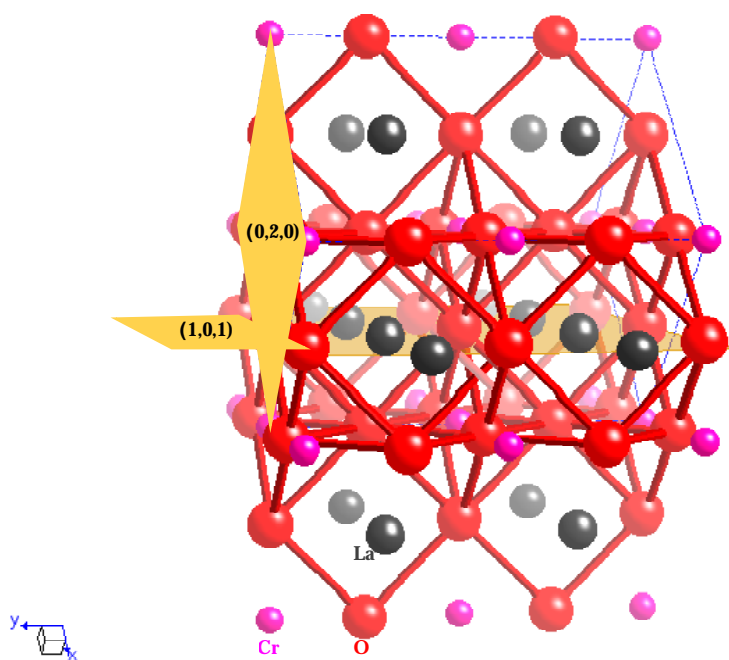


Figure 25: Lattice construction of the LaCrO_3 orthorhombic phase (ideal structure). From the interplanar distance of the $\text{LaCr}_{0.9}\text{Fe}_{0.1}\text{O}_3$ grain in Figure 22d, it is possible to index the phase as a $(1,0,1)$ or $(0,2,0)$ plane following Miller's indexation. These planes (in yellow) are made only of the La-oxide or transition metals-oxides sublayers. They correspond to about 37 and 9% intensity according to the JCPDS chart No 70-1024 for orthorhombic LaCrO_3 . Balls red: oxygen; black: lanthanum and pink: chromium ions. This structure was made using the CrystalMaker program.

Part of this sequence could also explain the oxidative coupling of CH_4 related to the Mg based catalysts. Mg substitution enhances the coupling reaction of LC, probably by radical formation. MgO is indeed known as a good coupling catalyst⁵⁴. The coupling activity is further enhanced in LCs when a double substitution with Mg and Ca or Sr is considered. This is related to the increase in the hole conductivity and in the vacancy concentration, increasing thus the possibility to form $O_o^{\cdot\cdot}$ active sites, or even to the higher La/Cr ratio (Table 7), as La_2O_3 is known to generate methyl radicals. The increase of the steam content blocks these active sites. An alternative interpretation for the effect of steam on the coupling reaction could be assigned to the quenching effect of water on the radical $\cdot\text{CH}_3$, or even to the reaction of $\cdot\text{OH}$, formed on the catalyst surface and liberated in the gas phase⁴⁸, with gaseous methyl radicals. On the other hand, Ni substitution promotes the dissociation of methane and its subsequent reaction with water to syngas.

According to Lacombe et al.³⁵, the step-edge atoms, presenting a number of nearest neighbour ions of the opposite sign lower than those for surface and bulk atoms, i.e. low coordinated ions, might be considered as responsible for total oxidation on La₂O₃. By assuming that the low index planes are the most represented planes on the surface of the LC powders¹⁸, it is possible to estimate the number of vacancy and transition metal ions (*M*) sites on these step-edges which are given to mobilize 5~10% of the total surface atoms³⁵ (Table 10). The calculation gives that for a reaction rate of about 3×10^{15} molecules/m²s of converted CH₄ (a *TOF* of 5×10^{-9} mol/m²s), about 27% and 9% of the respective step-edge V_o^{\bullet} and transition metal species could be involved in the reaction.

Finally, the *TPO* results show the very low carbon coverage on lanthanum chromites, except for the LCFE powder. This indicates that these materials withstand coking and do not seem to promote it. Even in the case of the most active catalyst in our study (LCaCNi), carbon did not build up with time, and most of it is related to the presence of the free Ni-islets. The activity is moreover sustained for more than 360 h, indicating that carbon formation does not seem to poison the catalytic sites of the LCaCNi powder. Also, comparing the *TPO* results with *TEM* analysis shows that the pronounced *TPO* peak at 829°C observed for the LCFE powder could be related to graphitic carbon, whereas on Ni substituted LCs we observe some amorphous carbon (580-600°C) and thin film graphite (620-790°C). The low temperature peaks could be related to low coverage adsorbed carbon species like methane or related radicals. Another observation is that the type of carbon does not seem to vary a lot with the gas mixture used (Table 7). Beside that, from the interplanar distance of the LCFE grain on which carbon filaments were observed to grow (Figure 22d), it is possible to index the phase as a (1,0,1) or (0,2,0) plane following Miller's indexation. These planes have intensities of only 37 and 9% respectively, according to the *JCPDS* chart No 70-1024 for LaCrO₃. Also, these two planes are made only of the La-oxide or transition metals-oxides sublayers (see Figure 23). According to Iwamoto et al.²⁷ simple oxides with a metal ion in the d⁰ or d¹⁰ configuration are poor methane oxidation catalysts, so that the La-oxide layers should be quite inert to methane. Therefore, the transition metal-oxides sublayers are thought to be responsible for the growth of the carbon filaments.

From the different *TEM* micrographs made on LCaCNi powder catalysts, the interplanar distances for the carbon in the films grown on the surface of the grains (see Figure 13b for an example) were observed to vary between 3.42Å and 4.80Å. For the LCFE system, the interplanar distances varied between 3.89Å and 4.63Å for the soot-like carbon, 3.54Å and 5.14Å for the filaments, and 3.56Å and 5.22Å for the carbon films. These are larger than the expected interplanar distance for graphite (3.35Å), indicating that the deposited carbon films are more or less graphitized. Their oxidation temperature could thus be affected accordingly depending on their structure.

Also, from Figure 13b and c, it is possible to measure the interplanar distance for the LCaCNi grains. They correspond to the (1,0,1) or (0,2,0) plane, and to the (2,1,1) or (1,3,0) or (1,1,2) or (0,3,1) plane respectively. The (0,2,0) and (1,3,0) planes have an intensity of 100% and 8% respectively, as taken from our *XRD* measurements indexation of LCaCNi. The (0,3,1) plane has an intensity of 41.5% if LaCrO₃ phase is considered (*JCPDS* chart No 70-1024). Figure 25b shows similarly a (1,0,1) or (0,2,0) plane.

Conclusions

By substituting the inactive LaCrO₃ catalyst with alkaline earth and first series transition metal elements, a noticeable improvement in activity towards methane conversion is achieved. For the LaCrO₃ compounds, three different behavioral patterns were observed depending on the catalyst composition. It was observed that among the alkaline earth elements, Mg had an inhibiting effect whereas Ca and Sr substitution improved the catalytic activity for CH₄ oxidation, and CO₂ and H₂O reforming reactions. Transition metal substitution experiments on the *B*-site indicate that Co has an inhibiting effect whereas Mn and Fe showed an enhancement in activity when compared to the activity of the base material, LaCrO₃. The LaCrO₃ activity is however not modified drastically. On the other hand, Ni substitution causes a considerable change in the turn-over frequency (4 fold when compared to LaCrO₃). Among the transition metal substituents, Co and Mn showed the lowest cracking activity whereas Fe deposited high amounts of C. Thus by suitable substitution of the stable but inactive LaCrO₃ catalyst with Ni,

we have been able to produce an improved catalyst for CH₄ oxidation, with low coking activity. Also, these experiments were done in methane rich atmospheres, simulating real SOFC conditions.

References

- (1) Seiyama, T., *Catal. Rev. -Sci. Eng.* **1992**, *34*, 281-300.
- (2) Arai, H.; Yamada, T.; Eguchi, K.; Seiyama, T., *Applied Catalysis* **1986**, *26*, 265-276.
- (3) Doshi, R.; Alcock, C. B.; Gunasekaran, N.; Carberry, J. J., *Journal of Catalysis* **1993**, *140*, 557-563.
- (4) Gunasekaran, N.; Bakshi, N.; Alcock, C. B.; Carberry, J. J., *Solid State Ionics* **1996**, *83*, 145-150.
- (5) McCarty, J. G.; Wise, H., *Catalysis Today* **1990**, *8*, 231-248.
- (6) Fierro, J. L. G.; Tascon, J. M. D.; Tejuca, L. G., *Journal of Catalysis* **1985**, *93*, 83-91.
- (7) Collongue, B. d.; Garbowski, E.; Primet, M., *J. Chem. Soc. Faraday Trans.* **1991**, *87*, 2493-2499.
- (8) Saracco, G.; Scibilia, G.; A, I.; Baldi, G., *Applied Catalysis B: Environmental* **1996**, *8*, 229-244.
- (9) Stojanovic, M.; Mims, C. A.; Moudallal, H.; Yang, Y. L.; Jacobson, A. J., *Journal of Catalysis* **1997**, *166*, 324-332.
- (10) Baker, R. T.; Metcalfe, I. S., *Applied Catalysis A: General* **1995**, *126*, 297-317.
- (11) Baker, R. T.; Metcalfe, I. S., *Applied Catalysis A: General* **1995**, *126*, 319-332.
- (12) Sfeir, J.; Van herle, J.; McEvoy, A. J. Third European Solid Oxide Fuel Cell Forum, Nantes-France, **1998**; p 267-276.
- (13) Sfeir, J.; Van herle, J.; McEvoy, A. J., *Journal of the European Ceramic Society* **1999**, *19*, 897-902.
- (14) Sfeir, J. Solid Oxide Fuel Cell Materials and Mechanisms, Les Diablerets, Switzerland, **2001**.
- (15) Tejuca, L. G.; Fierro, J. L. G.; Tascon, J. M. D., *Advances in Catalysis* **1989**, *36*, 237-328.
- (16) Levenspiel, O. *Chemical reaction engineering*, 3 ed.; John Wiley & Sons, **1999**.
- (17) Falconer, J. L.; Schwarz, J. A., *Catal. Rev. -Sci. Eng.* **1983**, *25*, 141-227.
- (18) Fierro, J. L. G.; Tejuca, L. G., *Journal of Catalysis* **1984**, *87*, 126-135.
- (19) Armstrong, T. R.; Stevenson, J. W.; Pederson, L. R.; Raney, P. E., *J. Electrochem. Soc.* **1996**, *143*, 2919-2925.
- (20) Höfer, H. E.; Kock, W. F., *J. Electrochem. Soc.* **1993**, *140*, 2889-2894.
- (21) Tilset, B. G.; Fjellvåg, H.; Kjekshus, A., *Journal of Solid State Chemistry* **1995**, *119*, 271-280.
- (22) Sachtler, W. M. H.; Dorgelo, G. J. H.; Fahrenfort, J.; Voorhoeve, R. J. H. Proceedings of the Fourth International Congress in Catalysis, Moscow, **1968**; p 454-465.
- (23) Roiter, V. A.; Golodets, G. I.; Pyatnitskii, Y. I. Proceedings of the Fourth International Congress on Catalysis, Moscow, **1968**; p 466-477.
- (24) Pankratiev, Y. D., *React. Kinet. Catal. Lett.* **1982**, *20*, 255-259.
- (25) Golodets, G. I., *Theoretical and Experimental Chemistry* **1965**, *1*, 506-510.
- (26) Golodets, G. I.; Pyatnitskii, Y. I.; Goncharuk, V. V., *Theoretical and Experimental Chemistry* **1968**, *4*, 31-35.
- (27) Iwamoto, M.; Yoda, Y.; Yamazoe, N.; Seiyama, T., *The Journal of Physical Chemistry* **1978**, *82*, 2564-2570.
- (28) Fierro, J. L. G.; Tascon, J. M. D.; Tejuca, L. G., *Journal of Catalysis* **1984**, *89*, 209-216.
- (29) Rostrup-Nielsen, J. R. In *Catalysis, Science and Technology*; Anderson, J. R. and Boudart, M., Eds.; Springer Verlag; **1984**; Vol. 5.
- (30) Twigg, M. V. *Catalyst Handbook*, 2 ed.; Wolfe Publishing Ltd., **1989**.
- (31) Cotton, F. A.; Wilkinson, G.; Gaus, P. L. *Basic inorganic chemistry*, Second ed.; John Wiley & Sons, **1987**.
- (32) Bartholomew, C. H., *Catal. Rev. -Sci. Eng.* **1982**, *24*, 67-112.
- (33) Nowotny, J., *Solid State Ionics* **1988**, *28-30*, 1235-1243.
- (34) Scanlon, P. J.; Bink, R. A. M.; Berkel, F. P. F. v.; Christie, G. M.; Ijzendoorn, L. J. v.; Brongersma, H. H.; Welzenis, R. G. v., *Solid State Ionics* **1998**, *112*, 123-130.

- (35) Lacombe, S.; Geantet, C.; Mirodatos, C., *Journal of Catalysis* **1994**, *151*, 439-452.
- (36) Strohmeier, B. R.; Hercules, D. M., *J. Phys. Chem.* **1984**, 4922-4929.
- (37) Sugimoto, K.; Seto, M.; Tanaka, S.; Hara, N., *J. Electrochem. Soc.* **1993**, *140*, 1586-1592.
- (38) Helfland, M. A.; Clayton, C. R.; Diegle, R. B.; Sorenson, N. R., *J. Electrochem. Soc.* **1992**, *139*, 2121-2128.
- (39) Nakamura, T.; Petzow, G.; Gauckler, L. J., *Mat. Res. Bull.* **1979**, *14*, 649-659.
- (40) Peck, D. H.; Hilpert, K.; Miller, M.; Korbertz, D.; Nickel, H. "Untersuchungen zur Verdampfung und Thermodynamik von Perowskiten auf der Basis von LaCrO₃ für Hochtemperatur-Brennstoffzellen mit Festelektrolyt (SOFC)," Forschungszentrum Jülich GmbH, Institut für Werkstoffe der Energietechnik, **1996**.
- (41) Yasuda, I.; Hishinuma, M., *J. Electrochem. Soc.* **1996**, *143*, 1583-1590.
- (42) Sammes, N. M.; Ratnaraj, R., *Journal of Materials Science Letters* **1996**, *15*, 55-56.
- (43) Sammes, N. M.; Ratnaraj, R., *Journal of Materials Science* **1997**, *32*, 687-692.
- (44) Christie, G. M.; Middleton, P. H.; Steele, B. C. H. The Third International Symposium on Solid Oxide Fuel Cells, Hawaii, **1993**; p 315-324.
- (45) Carter, J. D.; Sprenkle, V.; Nasrallah, M. M.; Anderson, H. U. Proceedings of the Third International Symposium on Solid Oxide Fuel Cells, Honolulu, Hawaii, **1993**; p 344-353.
- (46) Yokokawa, H.; Sakai, N.; Kawada, T.; Dokiya, M., *Solid State Ionics* **1992**, *52*, 43-56.
- (47) Lacombe, S.; Zanthoff, H.; Mirodatos, C., *Journal of Catalysis* **1995**, *155*, 106-116.
- (48) Hewett, K. B.; Anderson, L. C.; Rosynek, M. P.; Lunsford, J. H., *J. Am. Chem. Soc.* **1996**, *118*, 6992-6997.
- (49) Martin, G. A.; Mirodatos, C., *Fuel Processing Technology* **1995**, *42*, 179-215.
- (50) Frennet, A.; Liénard, G.; Crucq, A.; Degols, L., *Journal of Catalysis* **1978**, *53*, 150-163.
- (51) Gellings, P. J.; Bouwmeester, H. J. M., *Catalysis Today* **2000**, *58*, 1-53.
- (52) Utiyama, M.; Hattori, H.; Tanabe, K., *Journal of Catalysis* **1978**, *53*, 237-242.
- (53) Lee, J. H.; Trimm, D. L., *Fuel Processing Technology* **1995**, *42*, 339-359.
- (54) Dubois, J. L.; Cameron, C. J., *Applied Catalysis* **1990**, *67*, 49-71.

Appendix A: Calculation procedures and definition of terms for catalysis

Evaluation of the molar flow rates of the different gases used in the catalytic measurements

From the gas chromatography measurements, the molar flow rates of all gases are derived from

$$n_{(CH_4, CO, CO_2, O_2, H_2, Ar)} [mol/s] = \frac{V_{(CH_4, CO, CO_2, O_2, H_2, Ar)} \times 101300 \times Q}{V_{tot} \times R \times T_{room}} \quad A-1$$

with $V_{(CH_4, CO, CO_2, O_2, H_2, Ar)}$ and V_{tot} , the volume of the species and the total volume injected in the gas chromatograph respectively, given in m³, Q the flow rate in m³/s, R the gas phase constant (8.314 J/mol.K) and T_{room} the room temperature in Kelvin (about 22°C). As the water leaving the reactor is condensed prior to the GC analysis, the water molar flow rate is estimated from

$$n_{H_2O_{out}} = 2(n_{CH_4, in} - n_{CH_4, out}) + n_{H_2O, in} - n_{H_2} - n_{C_2H_2} - 2n_{C_2H_4} - 3n_{C_2H_6} \quad A-2$$

with the *in* and *out* subscripts standing for the initials of inlet and outlet respectively. Also, the carbon deposited as function of time can be estimated from the following mass balance

$$n_C [mol/s] = 0.5 \times (n_{H_2} + 2(n_{O_2, in} - n_{O_2, out}) + 4(n_{CO_2, in} - n_{CO_2, out}) - 3n_{CO} - 3n_{C_2H_2} - 2n_{C_2H_4} - n_{C_2H_6}) \quad A-3$$

In almost all cases, the amount of carbon is so low that this number is very small and negligible.

Definition of terms

The definitions of the different terms used in this section are summarized hereafter.
CH₄ conversion

$$X_{CH_4} [\%] = \frac{n_{CH_4, in} - n_{CH_4, out}}{n_{CH_4, in}} \times 100 \quad A-4$$

CO, CO₂, C₂s and H₂ selectivities

$$S_{CO} [\%] = \frac{n_{CO}}{n_{CO} + (n_{CO_2, out} - n_{CO_2, in}) + 2(n_{C_2H_2} + n_{C_2H_4} + n_{C_2H_6})} \times 100 \quad A-5$$

$$S_{CO_2} [\%] = \frac{n_{CO_2, out} - n_{CO_2, in}}{n_{CO} + (n_{CO_2, out} - n_{CO_2, in}) + 2(n_{C_2H_2} + n_{C_2H_4} + n_{C_2H_6})} \times 100 \quad A-6$$

$$S_{C_2} [\%] = 100 - (S_{CO} + S_{CO_2}) \quad A-7$$

$$S_{H_2} [\%] = \frac{n_{H_2}}{n_{H_2} + n_{H_2O}} \times 100 \quad A-8$$

C₂s yield

$$Y_{C_2s} [\%] = \frac{n_{C_2H_2} + n_{C_2H_4} + n_{C_2H_6}}{n_{CH_4, in}} \times 100 = \frac{S_{C_2s} [\%] \times X_{CH_4} [\%]}{100} \quad A-9$$

Turn-over frequency (TOF)

$$TOF_{CH_4} [mol/s.m^2] = \frac{n_{CH_4, in} - n_{CH_4, out}}{a} \quad A-10$$

with a the unit surface area of the catalyst in m².

The space-velocity defines the number of reactor volumes of feed at specified conditions which can be treated in unit time

$$s[h^{-1}] = \frac{Q}{V_{reactor}} \quad A-11$$

with $V_{reactor}$ the volume of the reactor.

Determining controlling resistances to the reaction ¹⁶

Interpretation of experiments becomes difficult when more than one resistance affects the rate. Many factors can influence the rate of reactions on particles, as summarized in Table A-1. Two kinds of resistances are considered: the film resistance and the pore resistance.

Table A-1: Factors which influence the rate of reaction of particles ¹⁶.

Rate influencing factor	Porous catalyst particle	Catalyst coated surface
Surface reaction	Yes	Yes
Pore diffusion	Yes	No
Particle ΔT	Not too likely	No
Film ΔT	Sometimes	Rare
Film mass transfer	Not too likely	Yes

Film resistance

Experiments can be devised to see whether the conversion changes at different gas velocities but at identical weight-time. An example is given in Table A-2 for the case of LSrCMg run at 680°C in the 5:1 CH₄:O₂ gas mixture.

Table A-2: The impact of the flow rate in ml/min on the gas exhaust composition in the case of LSrCMg run at 680°C in the 5:1 CH₄:O₂ gas mixture.

Flow rate	%CH ₄	%CO	%CO ₂	%H ₂	%H ₂ O	X _{CH₄}	S _{CO₂}	S _{H₂}
30.1	73.78	0	8.74	0.38	17.10	10.59	100	2.18
50.0	73.64	0	8.79	0.38	17.20	10.66	100	2.14
78.4	73.20	0	8.93	0.40	17.46	10.87	100	2.24

We see clearly that there is almost no impact of the flow rate on the reaction kinetics, thus indicating no mass transport limitations.

It is possible to calculate whether film resistance to mass transport is important by comparing the observed first-order rate constant based on the volume of particle with the mass transfer coefficient for that type of flow. For fluid passing through a packed bed of particles

$$\frac{k_g d_p}{D_e} = 2 + 1.8 \text{Re}^{1/2} \text{Sc}^{1/3}, \text{Re} > 80 \quad A-12$$

with Re , the Reynolds number

$$\text{Re}[-] = \frac{d_p \cdot v \cdot \rho}{\mu} \quad A-13$$

and Sc , the Schmid number

$$\text{Sc}[-] = \frac{\mu}{\rho \cdot D_e} \quad A-14$$

and k_g the mass transfer coefficient of the gas film, d_p the particles mean diameter, μ the viscosity of the fluid, ρ the density of the fluid, v the fluid flow rate, and D_e the effective molecular diffusion coefficient. Thus we have roughly

$$k_g \sim \frac{1}{d_p} \quad \text{for small } d_p \text{ and } v \quad A-15$$

$$\text{or } k_g \sim \frac{V^{1/2}}{d_p^{1/2}} \quad \text{for large } d_p \text{ and } v \quad \text{A-16}$$

To see whether film mass transfer resistance is important, $k_{obs}V_p$ should be compared to $k_g a$, with k_{obs} the measured rate constant, V_p the particles mean volume and a the particle mean surface area. If the two terms are of the same order of magnitude gas film resistance affects the rate. On the other hand, if $k_{obs}V_p$ is much smaller than $k_g a$, this resistance has no effect. k_{obs} is calculated from

$$TOF = k_{obs} P_{CH_4}^n P_{O_2, H_2O, CO_2}^m \quad \text{A-17}$$

Pore resistance

Experimentally, this can be resolved by comparing rates for different pellet sizes and noting the drop in activation energy of the reaction with rise in temperature, couple with a possible change in reaction order. It is also possible to calculate the Wagner-Weisz-Wheeler modulus, M_w , given as

$$M_w = L^2 \frac{k_{obs}}{D_e} \quad \text{A-18}$$

with L the characteristic size of a porous particle defined as

$$\left(\frac{\text{volume of particle}}{\text{exterior surface available for reactant penetration}} \right) \quad \text{A-19}$$

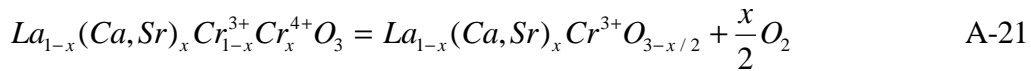
which reduces to $d_p/6$ for spherical particles. If this modulus is less than 0.15 than the reaction runs in a diffusion-free regime. Above 4, the reaction shows a strong diffusion resistance.

Appendix B: Correlations between catalytic and thermodynamic parameters²³

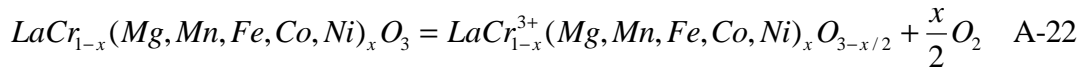
The relationship between kinetics and thermodynamics of ionic and radical processes is usually expressed by correlations of the Brönsted equation type

$$k = gK^\alpha \quad \text{A-20}$$

where k is the rate constant, K the equilibrium constant of the elementary stage, g and α constant values for a series of reactions. In heterogeneous catalysis this correlation also holds, provided that radical or ionic character is inherent not only to initial catalyst but also to intermediate compound of the latter with reagents. The analysis of a large body of experimental material²²⁻²⁶ shows that it is thus possible to correlate the reaction rate of different reactions (methane combustion for example) with the heat of partial reduction of an oxide catalyst, q_s . In the LaCrO₃ system this heat is released during the following reactions



or



Following this approach, for a specified reaction an optimum catalyst, chosen among the same family of catalysts, should have a q_s very near to half the value of the heat of the overall reaction. Thus volcano curves are expected within a family of catalysts. One way to measure this heat of partial reduction is by mean of a TPR measurement using hydrogen. In this case, the rate of reduction of the oxide by hydrogen is related to the inverse of the absolute temperature at which the reduction starts

$$r_{H_2} = \frac{1}{T_{H_2}} \quad \text{A-23}$$

so that the following proportionality holds

$$q_s \approx \text{const.} \frac{1}{T_{H_2}} \quad \text{A-24}$$

It is thus possible to estimate the q_s in a family of oxides from 2 or 3 known couples (q_s ; T_{H_2}) by using the simple correlation given by equation A-24.

Appendix D: Summary of the average peak positions in XPS

ESCA analysis Catalyst composition	C	O _{II}	O _I	Element	Position [eV]	FWHM	Area
LaCrO ₃	285	531.1	529.3	La3d _{5/2}	834.4	2.9	20806
				Cr2p _{3/2}	576.1	2.3	8979
La _{0.85} Ca _{0.15} CrO ₃ , ap	285	530.9	528.9	La3d _{5/2}	834.3	3.0	16954
				Cr2p _{3/2}	575.9	2.5	6995
				Ca2p _{3/2}	346.5	2.0	1352
La _{0.85} Ca _{0.15} CrO ₃ , ac	285	531.1	529.0	La3d _{5/2}	834.0	3.1	5762
				Cr2p _{3/2}	575.6	2.3	2800
				Ca2p _{3/2}	346.4	2.1	1119
La _{0.85} Sr _{0.15} CrO ₃ , ap	285	530.9	529.1	La3d _{5/2}	834.5	2.9	15999
				Cr2p _{3/2}	576.1	2.5	6976
				Sr3d _{5/2}	133.8	1.2	849
La _{0.85} Sr _{0.15} CrO ₃ , ac	285	531.3	529.1	La3d _{5/2}	834.2	2.9	9145
				Cr2p _{3/2}	576.0	2.5	4729
				Sr3d _{5/2}	133.8	1.4	722
LaCr _{0.9} Mn _{0.1} O ₃ , ap	285	530.8	529.5	La3d _{5/2}	834.6	2.8	10169
				Cr2p _{3/2}	576.3	2.5	3119
				Mn2p _{3/2}	642.4	3.3	942
LaCr _{0.9} Mn _{0.1} O ₃ , ac	285	530.7	528.9	La3d _{5/2}	834.2	3.3	11793
				Cr2p _{3/2}	576.1	2.9	3769
				Mn2p _{3/2}	642.1	3.6	1074
LaCr _{0.9} Fe _{0.1} O ₃ , ap	285	531.1	529.1	La3d _{5/2}	834.3	3.1	18345
				Cr2p _{3/2}	576.0	2.7	6523
				Fe2p _{3/2}	710.5	4.8	1506
LaCr _{0.9} Fe _{0.1} O ₃ , ac	285	531.3	529.2	La3d _{5/2}	834.5	3.1	9970
				Cr2p _{3/2}	576.1	2.5	3122
				Fe2p _{3/2}	711.7	4.9	1074
LaCr _{0.9} Co _{0.1} O ₃ , ap	285	531.2	529.1	La3d _{5/2}	834.7	3.2	10875
				Cr2p _{3/2}	576.1	2.8	3220
				Co2p _{3/2}	780.5	3.1	569
LaCr _{0.9} Co _{0.1} O ₃ , ac	285	531.2	529.1	La3d _{5/2}	834.5	3.1	10823
				Cr2p _{3/2}	575.8	2.2	2796
				Co2p _{3/2}	780.5	2.7	470
LaCr _{0.9} Ni _{0.1} O ₃ , ap	285	531.2	528.9	La3d _{5/2}	834.8	3.3	25158
				Cr2p _{3/2}	576.1	2.8	5468
				Ni2p _{3/2}	851.6	3.2	16968

Chapter 7 七

LaCrO₃-based anodes: stability consideration

LaCrO₃-based anodes: stability considerations*

Abstract

LaCrO₃ based materials have been studied as alternative anodes to the conventional Ni-YSZ cermet. Thermodynamic calculations as well as experimental work have been conducted in an attempt to analyze the stability of this system when doped with Mg, Ca, Sr, Mn, Fe, Co and Ni. Various gas atmospheres were simulated (air, humidified hydrogen, CO and CO₂). It was possible to correlate some of the experimental results (electrochemical, XRD, XPS-Auger, SIMS and TEM-EDS) with the thermodynamic calculations. It was calculated that Sr and Mn substitution maintains the stability of the perovskite even in the severe reducing conditions used in SOFC, whereas the other substitutions destabilize the system. Experimentally, transition metal substituted LaCrO₃ did not decompose readily in the reducing atmospheres containing wet hydrogen or methane indicating that the demixing is at least kinetically hindered.

Introduction

In solid oxide fuel cells (SOFC), lanthanum chromites, LaCrO₃, were investigated for their use as interconnect materials for cell stacking and potentially as cathode¹ and anode² electrocatalysts. These perovskite materials are reported to be quite stable in both oxidative and reductive atmospheres³. They can be easily substituted on the *A* and *B* sites with alkali earth and transition metal elements respectively, which allows interesting modifications of their electronic as well as their catalytic properties⁴. In the literature, many reports focus on the doping effect of alkali earth (Mg, Ca, Sr) as well as transition metal (Co, Ni, Cu) elements on the conductivity, sintering and stability behaviour of these materials. Less work is however done on catalysis, electrocatalysis and the effect of corrosive gases.

We previously explored calcium and / or strontium and magnesium substituted lanthanum chromites as alternative anodes to Ni-YSZ cermet⁵ (Chapter 4). These materials were observed to inhibit coking but their overall electrocatalytic activity was found to be low under pure methane feed. Also, a small degradation was observed and was related to a progressive reduction of the electrode as well as a topotactic reaction between excess Ca or Sr with YSZ. It was also found that part of this degradation could originate from an electrochemical demixing effect⁶ (Chapter 5). This reaction was however reduced when low substitution levels were adopted (around 15% on the *A*-site). Characterization measurements done on powders of different compositions subjected to methane rich atmospheres during catalytic measurements, showed surface enrichments of Sr and Ca following the exposure to particular gases⁷ (Chapter 6). In the present study, a chemical thermodynamic analysis was undertaken in the perspective of understanding the stability, the solubility limit of substituents as well as the effect of oxidative, reductive and corrosive gases (air, wet hydrogen, CO and CO₂) on (Mg, Ca, Sr, Mn, Fe, Co, Ni)-substituted LaCrO₃. Trials were made to correlate these estimations with experimental results based on electrochemical, XRD, SEM, SIMS, XPS-Auger and TEM-EDS characterizations.

Estimating thermodynamic properties

The thermodynamic data for most of the different substituted LaCrO₃ species used in this study are not available in the literature so that the thermodynamic parameters for these phases had to be estimated. For that purpose, the different LaCrO₃ phases were treated as ideal solid solutions of LaCrO₃ and MCrO₃, and LaCrO₃ and LaCr_{0.5}M_{0.5}O₃ for the *A*-site and *B*-site *M*-substituents respectively, following a procedure developed by Yokokawa et al.⁸⁻¹⁰. The molar Gibbs free energy for the ideal solid solution was taken as:

$$G_{\text{perovskite}} = \sum x_i \Delta_f G_i^\circ + RT \sum x_i \ln(x_i) \quad (1)$$

*This chapter has been submitted in a shorter version as J. Sfeir, 'LaCrO₃-based anodes: stability considerations', in *Solid Oxide Fuel Cell Materials and Mechanisms*, IEA-ESF, Diablerets 2001, 55-67.

where x_i is the mole fraction of species i in the solution, $\Delta_f G_i^\circ$ the standard Gibbs free energy of formation of species i , and R the gas constant. The standard entropy of the perovskite oxides was derived from the following expression:

$$\Delta_r S_{298}^\circ = 10 \text{ J/molK} = S_{298, \text{perovskite}}^\circ - \sum x_i S_{298, \text{binary oxide}}^\circ \quad (2)$$

where $\Delta_r S_{298}^\circ$ was set to 10 J/molK according to Yokokawa et al.⁸, the binary oxides stand for the La₂O₃, Cr₂O₃ and the other element oxides by supposing the following kind of reaction



The heat capacity coefficients were estimated using:

$$\alpha_{\text{perovskite}} = \sum x_i \alpha_{\text{binary oxide}} \quad (4)$$

Also, in order to estimate the enthalpy of formation $\Delta_f H_{298}^\circ$ of the LaCr_{0.5}M_{0.5}O₃, LaCr_{0.5}M_{0.5}O_{2.75} and LaM_{0.5}Cr_{0.5}O_{2.75} phases, the correlation relating the stabilization energy, δ , to $\Delta_f H_{298}^\circ$ and the tolerance factor (Goldschmid), t_p , derived by Yokokawa et al.⁸ was used (see Appendix A):

$$\delta [\text{kJ/mol}] = -90 + 720(1 - t_p) = \Delta_f H_{298, \text{perovskite}}^\circ - \sum x_i \Delta_f H_{298, \text{binary oxide}}^\circ \quad (5)$$

$$\text{and } t_p = \frac{r_O + r_A}{\sqrt{2}(r_O + r_B)} \quad (6)$$

with r_O , r_A and r_B the mean Shannon ionic radii¹¹ of the O , A and B sites respectively. The transition metal substituents were taken in the low spin state. The difference with a high spin state is at most of 1.5%.

The non-stoichiometry, δ , was taken into account by treating the non-stoichiometric compounds as ideal solid solutions of LaCrO₃ and LaM_{0.5}Cr_{0.5}O_{2.75} or LaCr_{0.5}M_{0.5}O_{2.75} for the A -site and B -site M -substituents respectively. In the case of Ca and Sr substitutions, the thermodynamic data for LaM_{0.5}Cr_{0.5}O_{2.95} were corrected by using the experimental K_{ox} published by Yasuda et al.¹² and Peck et al.¹³ from:

$$\Delta_f G_{\text{La}_{1-x}(\text{Ca,Sr})_x \text{CrO}_3, T}^\circ = \Delta_f G_{\text{La}_{1-x}(\text{Ca,Sr})_x \text{CrO}_{3-\delta}, T}^\circ + \delta \Delta_{ox} G_T^\circ \quad (7)$$

$$\text{and } \ln K_{ox} = -\frac{\Delta_{ox} H^\circ}{RT} + \frac{\Delta_{ox} S^\circ}{R} \quad (8)$$

The evolution of K_{ox} for Ca substitution was extrapolated from Yasuda et al.'s thermogravimetric data¹² using the same slope for the x dependency of $\Delta_{ox} H^\circ$ and $\Delta_{ox} S^\circ$ as for the Sr substitution given by Peck et al.¹³ (see Appendix A). For Mg substitution the value given by van Dierten was used⁹. For the other substituents, no experimental data for K_{ox} nor non-stoichiometry data were available in literature so that no correction was possible. The summary of the thermodynamic data thus generated is given in Appendix B.

The thermodynamic equilibrium calculations were made using the HSC-4.1, thermodynamic equilibria calculation software, from Outokumpu Research Oy, Finland, using the thermodynamic data delivered in the software package as well as thermodynamic data obtained from literature^{8,9,13,14} and other laboratories. The different species taken into account for these calculations are listed in the Appendix C. Neither melts or mixed Ruddlesden-Popper phases nor hydroxylapatite-like oxides were taken into account. These compounds were however reported to coexist with the LaCrO₃-based perovskites¹⁵⁻²⁰.

Air solubility limit estimations for Ca and Sr extrapolated from experimental data

The experimental solubility limit, x , for Sr in LaCrO₃ is reported to be 0.1 and 0.31 at 950°C in air and 1600°C in 10⁻⁹ atm. of oxygen respectively^{13,21}, 0.1 at 1100°C²², or 0.07 at 650°C in air²³. For Ca, the solubility limit in air is 0.15 at 800°C⁶, 0.31 and 0.22 at 950°C in air and at

1600°C in 10⁻⁹ atm. of oxygen respectively²⁰, 0.12 at 650°C in air²³, and 0.2, 0.3 and 0.4 at 900, 1000 and 1030°C in air respectively²⁴. This correlates well with the data recently published by Miyoshi et al.²².

Furthermore, the main secondary phase which experimentally coexists, at low temperatures (≈1200°C), with the La_{1-x}Sr_xCrO₃ perovskite phase is SrCrO₄, with small amounts of other phases such as Sr_{2.67}Cr₂O₈ and La_{1.6}Cr₇O₄₄^{13, 19, 22, 23, 25}. For the case of Ca, it is reported that CaCrO₄ forms predominantly^{6, 20, 22-24, 26}. Also, Sfeir et al.⁷ observed by TEM a CaCrO₄ secondary phase on high Ca substituted LaCrO₃. The origin of the difference in the minor secondary phases composition reported in literature was partly rationalized by Chick et al.²⁶.

Based on these results, La_{1-x}(Ca,Sr)_xCrO₃ phases were assumed to be formed as an ideal solution between LaCrO₃ and (Ca,Sr)CrO₃. From the ‘symmetrical regular solutions model’^{27, 28} we have for the (A,B)_nO system:

$$G_{ss} = \underbrace{(x_A \mu_{A_nO}^\circ + x_B \mu_{B_nO}^\circ)}_{G^\circ} + \underbrace{\{nRT(x_A \ln x_A + x_B \ln x_B)\}}_{G_{mix}} + \underbrace{(nx_A x_B W_G)}_{GX_s} \quad (9)$$

with, G_{ss} the molar free energy of solution, x_A mole fraction of A_nO and x_B mole fraction of B_nO ($x_A + x_B = 1$) and $W_G = W_{H1bar} - TW_S$, the interaction parameter (no ordering or clustering of atoms is assumed). The evolution of x with temperature is then given by (see Appendix D):

$$\ln\left(\frac{x}{1-x}\right) = \frac{W_G}{RT}(2x-1) \quad (10)$$

This allows the estimation of W_G from the experimental data and the plot of the expected solubility limit for Ca and Sr in function of temperature as shown in Figure 1.

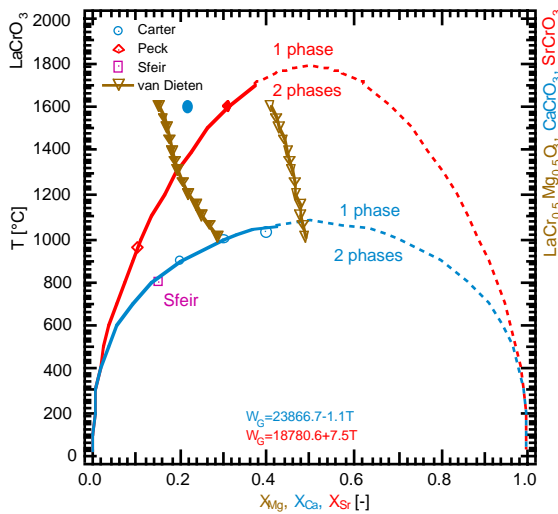


Figure 1: The solubility limit of La_{1-x}Ca_xCrO₃ and La_{1-x}Sr_xCrO₃ as extrapolated from experimental results^{6, 13, 24} using the ‘symmetrical regular solutions model’. The solubility limit of Mg⁹ is also given to illustrate the case of a B-site substitution. It does not follow the regular model. (○, ▽) open symbols refer to air whereas (●, ▼) solid symbols refer to a low oxygen partial pressure of about 10⁻⁸ atm for Mg and Ca respectively. It is observed that for Ca²⁰ and Mg⁹, the solubility limit decrease in reducing conditions. Sr¹⁹ does not seem to be affected.

Stability of the Ca, Sr and Ni substituted LaCrO₃ in oxygen and in reducing atmospheres as well as in corrosive gases (H₂, H₂O, CO and CO₂)

Stability in high oxygen partial pressures (Ca, Sr)

La_{1-x}Ca_xCrO₃ and La_{1-x}Sr_xCrO₃ stability under high oxygen partial pressures is depicted in Figure 2 as a function of x . The reaction equations shown here were chosen among others because they depict the easiest reaction path. In air, the stability region with Ca is wider than with Sr. The solubility of Sr under oxygen, calculated at 800°C, lies near 0.07, as expected from the extrapolated value taken from Figure 1. Ca substitution, however, seems to be more favourable in our calculations than reported in literature. The thermodynamic parameters estimated for La_{1-x}Ca_xCrO₃ are such that the species have become too stable. However, no attempt was undertaken to adjust these parameters.

Stability in low oxygen partial pressures (Ca, Sr)

Figure 3 shows the stability of $\text{La}_{1-x}\text{Ca}_x\text{CrO}_3$ and $\text{La}_{1-x}\text{Sr}_x\text{CrO}_3$, as a function of x , under low oxygen partial pressures corresponding to the working atmosphere of an anode in $3\% \text{H}_2\text{O} + \text{H}_2$ or CH_4 . These calculations indicate that, for the A-site substitution, Ca would highly destabilize the LaCrO_3 phase whereas Sr would be expected to preserve the perovskite phase even under the lowest oxygen partial pressures encountered on the anode side. It is only at the highest temperature (1000°C) that Ca-containing species enters the stability region in contact with humidified H_2 . The lower solubility limit of calcium under low oxygen partial pressure is also observed experimentally at 1600°C , in 10^{-9} atm. by Peck et al.²⁰, whereas Sr solubility is reported to increase in low P_{O_2} ²¹. Thus, the Sr substitution could be more appropriate than Ca for an anode purpose.

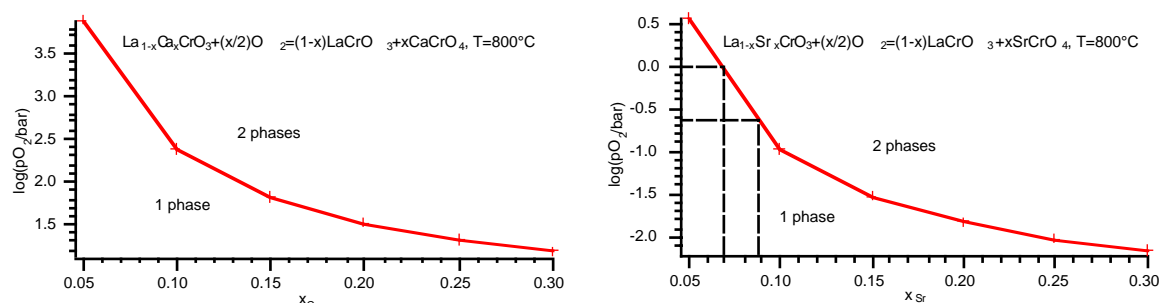


Figure 2: $\text{La}_{1-x}\text{Ca}_x\text{CrO}_3$ and $\text{La}_{1-x}\text{Sr}_x\text{CrO}_3$ stability at 800°C , under high oxygen partial pressures as a function of x .

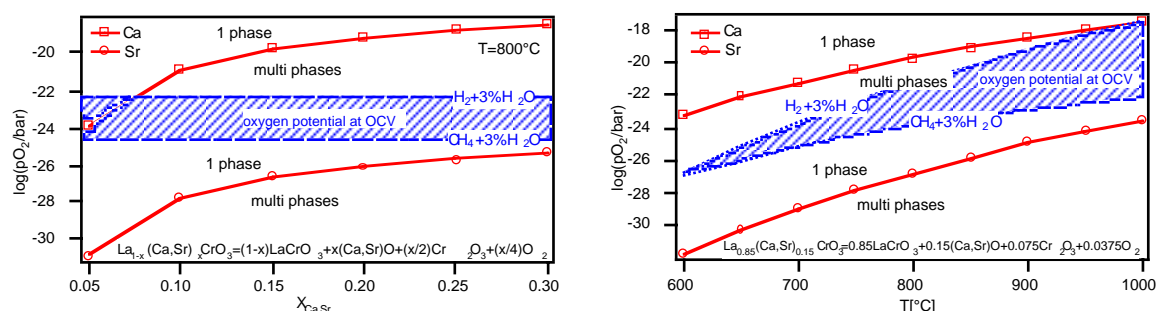


Figure 3: $\text{La}_{1-x}\text{Ca}_x\text{CrO}_3$ and $\text{La}_{1-x}\text{Sr}_x\text{CrO}_3$ stability under low oxygen partial pressures as a function of x , at 800°C , and the effect of temperature on $x=0.15$.

Volatility diagrams: effect of the gas composition (Ca, Sr)

Figure 5 shows the volatility diagrams of LaCrO_3 , $\text{La}_{0.85}\text{Ca}_{0.15}\text{CrO}_3$ and $\text{La}_{0.93}\text{Sr}_{0.07}\text{CrO}_3$ systems, at 800°C . These were drawn following the procedure described by Lou et al.^{29, 30}, and by piling up different diagrams, as shown in Figure 4 for the case of the $\text{Sr}_x\text{Cr}_y\text{O}_z$. These diagrams were set up by generating ≈ 1200 reactions for both Sr and Ca substitutions, by checking the thermodynamic stability of each phase combination and deriving valid phase relations. The chemical reactivity of the materials is determined by the behavior of the most reactive components. The substitution level of $x = 0.15$ and 0.07 for Ca and Sr respectively was chosen based on the solubility limit at 800°C in air as extrapolated from Figure 1. From these diagrams, it is clearly observed that the stability region of LaCrO_3 is modified by substitution with Ca and Sr, as discussed above. In reducing atmospheres, Ca substitution is expected to be less favourable than Sr. The stability domain of the different species is expressed as bold lines and given as a function of the oxygen partial pressure. Further, these diagrams show, for simplification, an abrupt decomposition of the perovskites in reducing atmospheres, whereas it should be seen as a continuous change, as expressed by Figure 3. Weight loss due to vaporization is normally considered important only if the vapour pressure of the evaporating species is higher than 10^{-8} atm.²⁹ This limit is presented on the volatility diagrams as a dotted horizontal line. Taking into account the non-stoichiometry, introduced by the reduction of the perovskite, did not modify much the stability diagrams of Ca- and Sr-substituted LaCrO_3 .

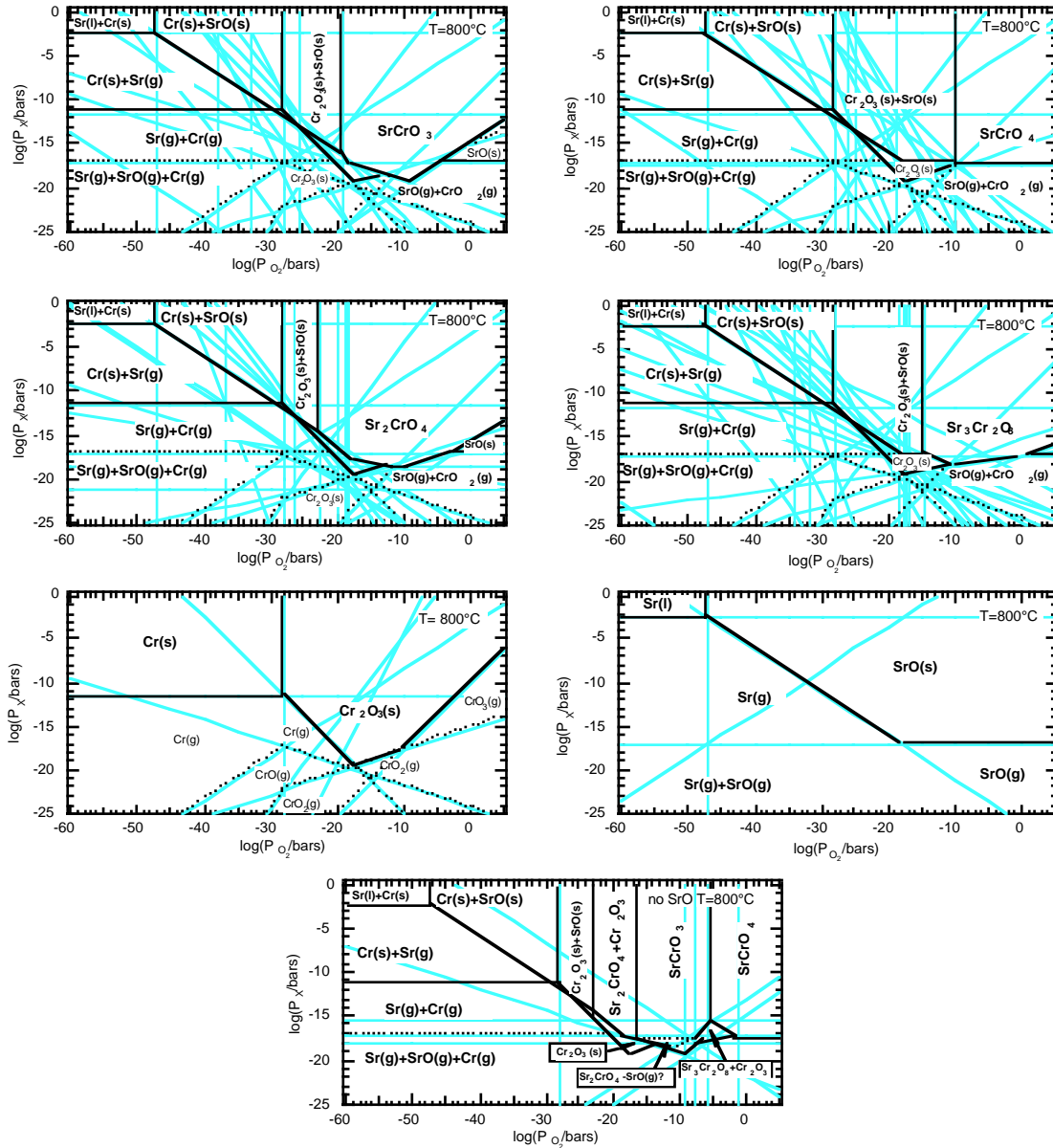
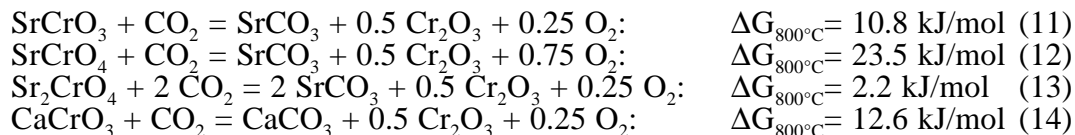
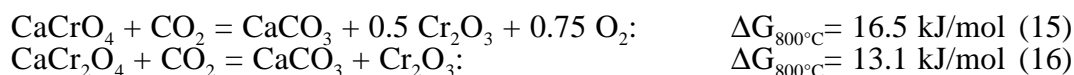


Figure 4: Example of the volatility diagram of the $Sr_xCr_yO_z$ phase drawn following the procedure described by Lou et al.^{29, 30}, and by piling up different diagrams. 6 volatility diagrams were necessary to obtain the final $Sr_xCr_yO_z$ phase volatility diagram. The blue lines represents the different equilibria taken into account to build up the diagrams.

H₂O is observed to have a large effect on the stability of these perovskites, as seen from the increased volatility arising from hydroxy-volatile Cr, Ca and Sr compounds (dashed lines in Figure 5). The volatility of the Ca- and Sr-substituted compounds are increased by eight orders of magnitude at middle P_{O_2} ranges of 10^{-20} atm. It is clearly seen that Ca is more volatile than Sr as the partial pressures for Ca hydroxyles are higher. H₂ has a similar effect as shown in Figure 6. In the absence of the thermodynamic data for the rare earth carbonates as well as for Cr, only Ca and Sr carbonates were considered. From that simplified approach, CO and CO₂ are expected to have almost no effect on the stability of these perovskites, as shown in the diagrams and as far as no carbon is formed and no secondary phases are present. The effect of the latter is given as:





These reaction – 11, 12, 14 and 15 - proceed at a P_{O_2} of 1.5×10^{-9} , 4.1×10^{-7} , 5.5×10^{-11} and 3.3×10^{-5} atm. respectively. The effect of carbon was not analyzed (carbide formation, reducing agent). The meaning of all the lines shown are described in more details by Lou et al.^{29,30}

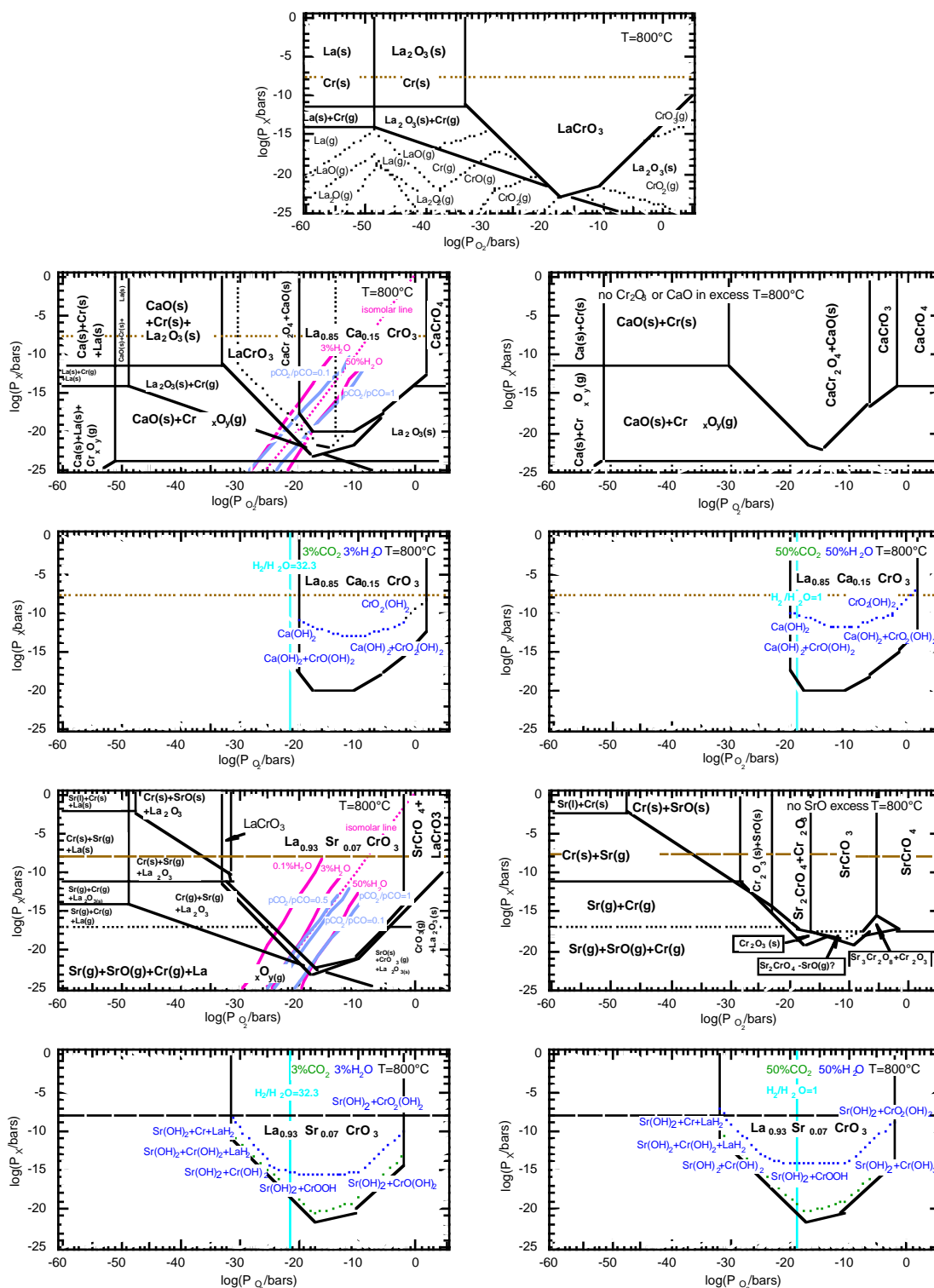


Figure 5: Volatility diagrams for the LaCrO_3 , $\text{La}_{0.85}\text{Ca}_{0.15}\text{CrO}_3$ and $\text{La}_{0.93}\text{Sr}_{0.07}\text{CrO}_3$ systems, at 800°C . The effect of H_2O and CO_2 is also highlighted. H_2 has a similar effect to H_2O . The complexity of the $(\text{Ca},\text{Sr})_x\text{Cr}_y\text{O}_z$ phase diagrams is also shown for the case where CaO , SrO and Cr_2O_3 are not in excess. The presence of impurities can modify much the secondary phases composition.

Correlation of these calculations with experimental results is possible. The volatility diagrams show that the surrounding gas phase in equilibrium at different P_{O_2} with LaCrO₃ is essentially made up of CrO₃(g), CrO₂(g), Cr(g) and LaO(g) (see Figure 5, case of LaCrO₃). This agrees well with measurements made at 1600°C by Peck et al.³¹

The changes in composition of the chromium gas phase as a function of oxygen partial pressure are also well predicted in our diagrams when compared to the reported one at 950°C by Hilpert et al.³². Similarly, as shown in Figure 5, CrO₂(OH)₂(g) is predicted to be the dominant Cr gaseous species in humidified atmospheres, in accordance with literature³². Also, the secondary phase for the Ca-substitution is predicted to be CaCr₂O₄ in reducing atmospheres in accordance with Peck et al.²⁰

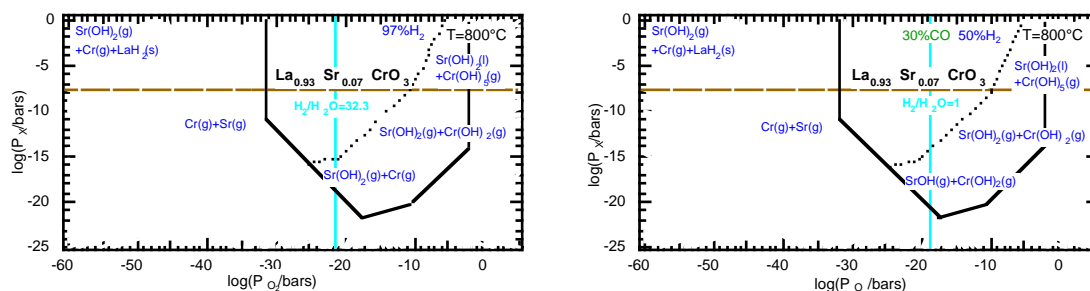


Figure 6: The effect of H₂ on the volatility of La_{0.93}Sr_{0.07}CrO₃ system. CO does not influence the stability of the perovskite.

Table 1: Summary of the XPS surface analysis given in percent of the sum of the total metal elements. ap: as prepared; ac: after catalysis with CH₄. The last three lines show the influence of some gases on the surface segregation⁷.

XPS analysis [%]	La/Cr	Mg	Ca	Sr	Mn	Fe	Co	Ni	Ca, Sr	Mg, Mn, Fe, Co,
Catalyst composition								*	nominal	Ni nominal
LaCrO ₃ , ap	0.9									
LaCr _{0.9} Mg _{0.1} O ₃ , ap	2.9	5.3								5
LaCr _{0.9} Mg _{0.1} O ₃ , ac	2.8	4.9								5
La _{0.85} Ca _{0.15} CrO ₃ , ap	1.0		10						7.5	
La _{0.85} Ca _{0.15} CrO ₃ , ac	1.0		22						7.5	
La _{0.7} Ca _{0.32} CrO ₃ , ap	1.0		39						16	
La _{0.85} Sr _{0.15} CrO ₃ , ap	0.9			10					7.5	
La _{0.85} Sr _{0.15} CrO ₃ , ac	0.8			14					7.5	
LaCr _{0.9} Mn _{0.1} O ₃ , ap	1.2				5					5
LaCr _{0.9} Mn _{0.1} O ₃ , ac	1.3				5.7					5
LaCr _{0.9} Fe _{0.1} O ₃ , ap	1.1					7.3				5
LaCr _{0.9} Fe _{0.1} O ₃ , ac	1.2					8.7				5
LaCr _{0.9} Co _{0.1} O ₃ , ap	1.2						1.9			5
LaCr _{0.9} Co _{0.1} O ₃ , ac	1.3						2.8			5
LaCr _{0.9} Ni _{0.1} O ₃ , ap	1.6							?		5
LaCr _{0.9} Ni _{0.1} O ₃ , ac	1.9							?		5
La _{0.85} Ca _{0.15} Cr _{0.9} Ni _{0.1} O ₃ , ap	1.0		10					?	7.5	5
La _{0.85} Ca _{0.15} Cr _{0.9} Ni _{0.1} O ₃ , ac	0.8		21					?	7.5	5
La _{0.85} Ca _{0.15} Cr _{0.9} Ni _{0.1} O ₃ , H ₂	1.2		15					?	7.5	5
La _{0.85} Ca _{0.15} Cr _{0.9} Ni _{0.1} O ₃ , CO ₂	1.0		9					?	7.5	5
La _{0.85} Ca _{0.15} Cr _{0.9} Ni _{0.1} O ₃ , air	1.2		6					?	7.5	5

*: Ni peak could not be resolved because of overlapping with La 3d peaks.

XPS measurements made on $x=0.15$ for Ca- and Sr-substituted LaCrO₃ show a small excess of these elements on the surface of freshly prepared samples (see Table 1). This could stem from the preparation procedure⁷. It was previously observed that a calcination temperature of at least 1100°C was necessary to produce an XRD pure perovskite, as shown in Figure 7 for the

case of $\text{La}_{0.85}\text{Sr}_{0.15}\text{CrO}_3$. However, as reported in literature, pure substituted LaCrO_3 has a very narrow window and secondary phases beneath XRD detection level would be always expected^{7, 10, 26}. Also, the slow cooling of the calcined powder could also cause a demixing of Ca or Sr rich compounds, as the solubility limit is low at room temperature, as discussed above. Another explanation could be the melts responsible of the sintering of the LaCrO_3 -based compounds which are left on the surface of the perovskites as very thin layers⁶ (Chapter 5).

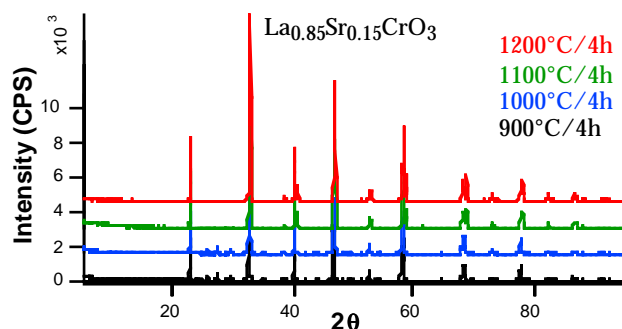


Figure 7: XRD analysis of the phase formation in the $\text{La}_{0.85}\text{Sr}_{0.15}\text{CrO}_3$ system. Secondary phases appear at temperatures below 1100°C . At low temperatures, secondary phases such as CaCrO_4 and La_2CrO_6 were detected.

Table 1 also shows a surface enrichment of the perovskites with Ca or Sr substitution upon treatment in reducing atmospheres. It is clearly seen that, for runs of 100 h, wet hydrogen has an effect on the segregation, whereas air or CO_2 do not affect the system much (the three last lines in Table 1). Ca is seen to segregate more readily than Sr and this could be eventually explained by the lower stability limit in H_2 or the higher volatility of Ca, as discussed above. Cr, on the other hand, did not segregate as the La/Cr ratio did not change much after catalysis.

Stability in low oxygen partial pressures (Mg, Mn, Fe, Co, Ni)

The lanthanum nickelate system is quite complicated showing a large variation in non-stoichiometry and composition^{3, 33, 34}. This is also the case for the other transition metal lanthanum oxides studied here. For the stability calculations, only LaNiO_3 , La_2NiO_4 , $\text{La}_4\text{Ni}_3\text{O}_{10}$ and $\text{LaCr}_{1-x}\text{Ni}_x\text{O}_3$ were considered. Figure 8 exposes the solubility limit of $\text{LaCr}_{1-x}\text{Ni}_x\text{O}_3$ as a function of temperature and oxygen partial pressure. As for Mg⁹ substitution, the solubility limit varies with the oxygen partial pressure. Ni substitution, B-site, is seen to be thermodynamically less favored than Ca, in reducing atmospheres. However, XRD measurements made on a $\text{LaCr}_{0.5}\text{Ni}_{0.5}\text{O}_3$ powder, exposed for 1 week at 780°C to $\text{H}_2 + 3\% \text{H}_2\text{O}$ showed no demixing (see Figure 9).

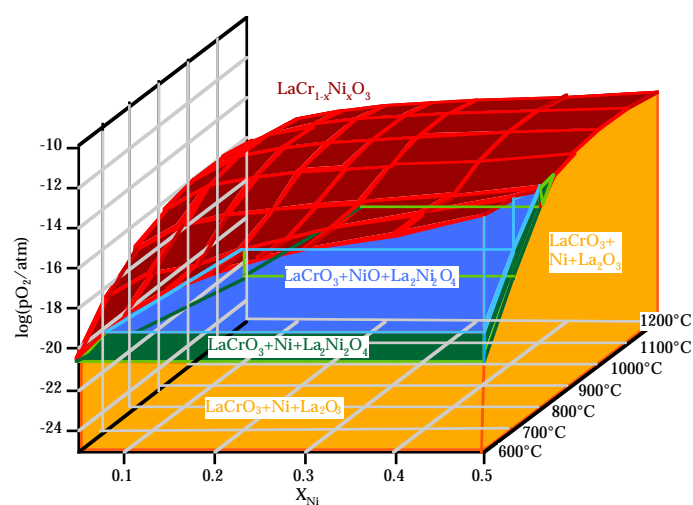


Figure 8: Estimated solubility limit of $\text{LaCr}_{1-x}\text{Ni}_x\text{O}_3$. The solubility is a function of p_{O_2} as in the case of $\text{LaCr}_1\text{Mg}_x\text{O}_3$ ⁹. In these calculations, the non-stoichiometry was not taken into account.

Also, our catalytic runs in 3% $\text{H}_2\text{O} + \text{CH}_4$ and in 5:1 $\text{CH}_4:\text{O}_2$ on $\text{LaCr}_{0.9}\text{Ni}_{0.1}\text{O}_3$ and $\text{La}_{0.85}\text{Ca}_{0.15}\text{Cr}_{0.9}\text{Ni}_{0.1}\text{O}_3$ powders did not cause any phase segregation⁷. This indicates that the decomposition of the Ni-substituted LaCrO_3 is kinetically hindered. The same has been previously observed in literature for another (Mg) B-site substituted LaCrO_3 ⁹.

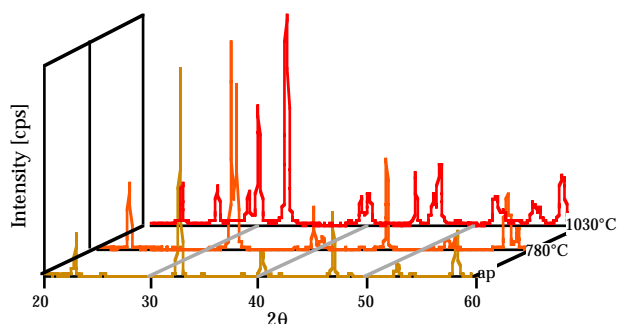


Figure 9: XRD on LaCr_{0.5}Ni_{0.5}O₃ powder exposed 1 week to 3% wet H₂. The as prepared powder (ap) is orthorhombic, the one reduced at 780°C is rhombohedral, whereas the one reduced at 1030°C could not be resolved and has most probably decomposed.

Our thermodynamic calculations, limited to the very few compounds taken into account, indicate further that, at 850°C, the Fe substituted LCs would decompose at a P_{O_2} of 1.26×10^{-23} , to yield the metal and the LaCrO₃ phase, while with Mg, Ca, Sr, Mn and Co the LC should decompose to the metal oxide and LaCrO₃ phases at a P_{O_2} of 1.6×10^{-14} , 1.0×10^{-19} , 1.6×10^{-26} , 6.3×10^{-24} and 1.9×10^{-14} atm respectively. In these systems, no chemical thermodynamic analysis was undertaken in the perspective of understanding the effect of corrosive gases (air, wet hydrogen, CO and CO₂).

However, Mg, Mn, Fe and Co did not segregate further after the catalytic runs (see Table 1), indicating that they may not destabilize the perovskite structure. This is in accordance with experimental temperature programmed reduction (TPR) results⁷, which showed clearly that all of the LC catalysts did not undergo total reduction of the B-site substituent. Our experimental results suggest that the decomposition of these LCs is hindered kinetically.

Kinetically limited decomposition?

In literature, measurements done on cation tracer bulk diffusion in LaCrO₃-based materials showed that Cr diffusion is slower than La, Ca and Sr diffusion by one to two orders of magnitude³⁵⁻³⁹ (see Table 2). This might also explain the differences, after catalysis, in surface composition between A-site- and B-site-substituted LaCrO₃. Tracer grain boundary diffusion coefficients are also higher for Ca and Sr than for Cr by about two orders of magnitude³⁸. In both cases Ca diffusion is faster than Sr diffusion³⁶. This could also explain the difference in the segregation. The effect of P_{O_2} on the cation diffusion coefficients is not very clear^{36, 37}. However, in air, the tracer grain boundary diffusion coefficients for the cations and the anion are of the same order of magnitude.

Also, as previously observed (Chapter 4 and 5), current induced the demixing of Ca/Sr-rich substituted LaCrO₃ leading to the deposition of a 1 nm thick Ca/Sr rich layer over porous anode structures. As the Ca grain boundary diffusion coefficient is of the same magnitude as the oxygen anions grain boundary diffusion coefficient (Table 2), the presence of a potential gradient or the flow of a current in the LaCrO₃-based anode might then have an effect on the migration of these cations on the surface of the anode grains. Their migration would proceed in the opposite direction to the electrons and oxygen anions, leading to their segregation on the anode/YSZ interface, and ultimately to an interfacial reaction with the electrolyte.

Table 2: Tracer bulk diffusion and grain boundary diffusion coefficients (D_{bulk} , $D_{g.b.}$), at 1000°C, and their activation energies, taken from references³⁵⁻³⁹.

Compound	level of substitution	element diffusing	D_{bulk} [m ² /s]	E_a [kJ/mol]	$D_{g.b.}$ [m ² /s]	E_a [kJ/mol]
LCC	Ca 0.25	Cr	1.07×10^{-21}	213	1.57×10^{-15}	266
	Ca 0.3	O	2.2×10^{-16}	-	$2 \times 10^{-11} \sim 6 \times 10^{-15}$	-
	Ca 0.25	Ca	10^{-19}	222	$10^{-13} \sim 10^{-12}$	192
LC		La	$10^{-19.75}$	482	-	-

Interfacial reaction with YSZ

Beside Ni who may form mixed phases with YSZ¹⁴ (see Appendix C), the pyrochlore phase, La₂Zr₂O₇, is the main reaction product of LaMO₃ with YSZ, $M = \text{Mg, Mn, Fe and Co}$ ⁴⁰. Figure 10 shows the interfacial reaction at 800°C between La_{1-x}Ca_xCrO₃, La_{1-x}Sr_xCrO₃ or LaCr_{1-x}Ni_xO₃ and YSZ as a function of x . From these thermodynamic calculations, La₂Zr₂O₇ does not form under SOFC conditions for Ca and Sr whereas (Ca,Sr)ZrO₃ is readily obtained. Sr-substituted LaCrO₃ is observed to be more stable toward these reactions. Ni forms readily La₂Zr₂O₇ as nickel zirconates are reported to be unstable⁴⁰. These results indicate that the surface reactions between YSZ and the LaCrO₃ based anodes could be of importance, in reducing conditions, even at low temperatures. However, there is no experimental evidence (*SEM* analysis) that the anode itself reacted directly with YSZ, unless treated above 1100°C.

As seen in Figure 10, a $x=0.15$ of Ca- or Sr-, or a $x=0.1$ of Ni-substituted LaCrO₃ is not expected to react with YSZ at 1200°C in air. LaCrO₃ is expected to be very stable toward YSZ, both in reducing and oxidizing conditions, unless Cr dissolves into YSZ⁴¹ which would allow the resulting precipitated La₂O₃ to react with YSZ following reaction (18).

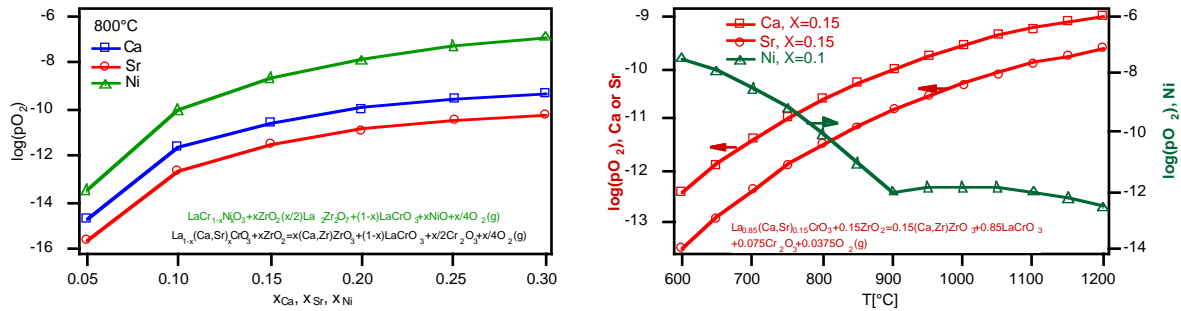
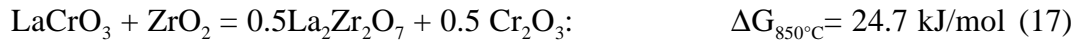
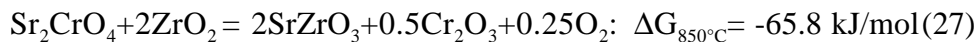
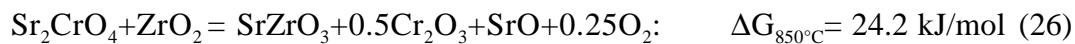
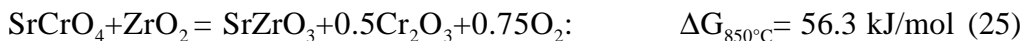
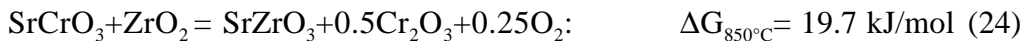
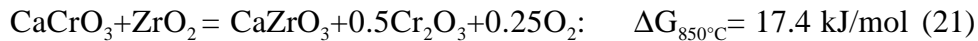
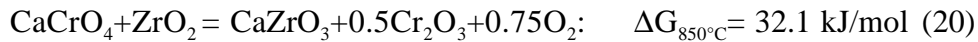


Figure 10: Interfacial reaction at 800°C between La_{1-x}Ca_xCrO₃, La_{1-x}Sr_xCrO₃ or LaCr_{1-x}Ni_xO₃ and YSZ as a function of x . When sintering a La_{0.85}Ca_{0.15}CrO₃, La_{0.85}Sr_{0.15}CrO₃ or LaCr_{0.9}Ni_{0.1}O₃ at temperatures of 1100°C to 1200°C no reaction is expected with YSZ.

Experimentally, CaO and calcium oxychromates, Ca_m(CrO₄)_n, exsolved from a La_{0.7}Ca_{0.32}CrO₃ anode were observed to react readily with YSZ at 900°C to form CaZrO₃ as assessed from impedance spectroscopy⁵ and XPS-Auger-SIMS analysis as shown in Figure 11. The CaZrO₃ or SrZrO₃ formation could be attributed to some of the following reactions:



These reactions - 20, 21, 23, 25, 26 and 27 - are already favorable below a P_{O_2} of 2.6×10^{-5} atm at 850°C. This indicates clearly that secondary phases could play an important role in the anode degradation, and thus should be minimized.

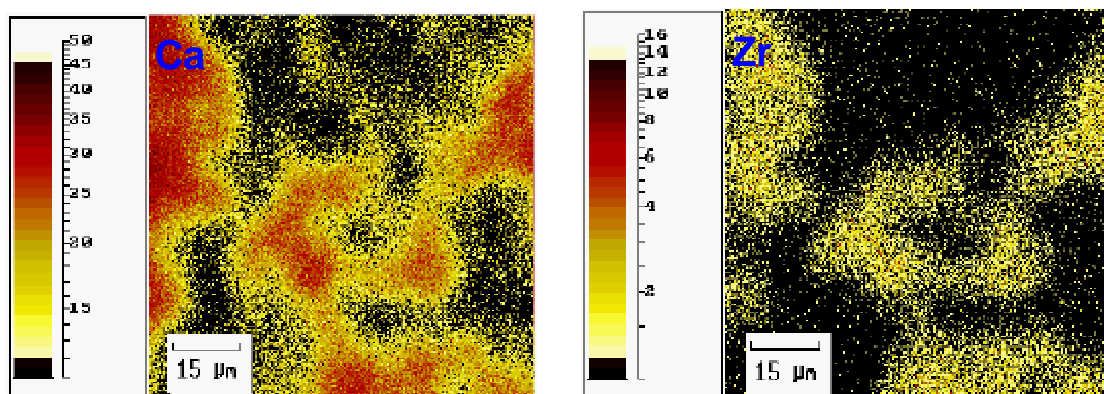


Figure 11: SIMS analysis of the interface of a YSZ/La_{0.7}Ca_{0.32}CrO₃ anode, tested in 3% wet H₂ at 900°C⁵. The coexistence of Ca and Zr in the same region of the interface indicates the possible formation of CaZrO₃. Cr and La were not detected in this region.

Conclusions

LaCrO₃-based compounds' stability was assessed, based on thermodynamic as well as experimental results. It was found that on the A-site, Sr substitution is more favorable than Ca in reducing atmospheres. H₂O and H₂ are expected to corrode the perovskites, as the volatility of the Ca, Sr and Cr are more pronounced due to the formation of hydroxy-species. Furthermore, the higher the substitution with Ca or Sr the larger the destabilization of the perovskite, both in air and in reducing atmospheres – the LaCrO₃ seems to accommodate more Sr in reducing atmospheres. The secondary phases formed during the decomposition could react readily with YSZ at 800°C, as observed experimentally. Overall, the LaCrO₃ are thermodynamically quite reactive toward YSZ but this was not observed experimentally unless treated above 1100°C. Also, Mg, Mn, Fe, Co and Ni, B-site-substituted compounds, although thermodynamically unstable, are quite stable experimentally suggesting that the decomposition of B-site substituted LCs is hindered kinetically. The A-site substitution seems to be more problematic.

References

- (1) Mori, M.; Sakai, N.; Kawada, T.; Yokokawa, H.; Dokya, M., *Denki Kagaku* **1990**, *58*, 528-532.
- (2) Norby, T.; Osborg, P. A.; Dyrлие, O.; Hildrum, R.; Seiersten, M.; Glenne, R. European Solid Oxide Fuel Cell Forum I, Lucerne, Switzerland, **1994**; p 217-226.
- (3) Nakamura, T.; Petzow, G.; Gauckler, L. J., *Mat. Res. Bull.* **1979**, *14*, 649-659.
- (4) Tejuca, L. G.; Fierro, J. L. G.; Tascon, J. M. D., *Advances in Catalysis* **1989**, *36*, 237-328.
- (5) Sfeir, J.; Van herle, J.; McEvoy, A. J. Third European Solid Oxide Fuel Cell Forum, Nantes-France, **1998**; p 267-276.
- (6) Sfeir, J.; Van herle, J.; McEvoy, A. J., *Journal of the European Ceramic Society* **1999**, *19*, 897-902.
- (7) Sfeir, J.; Buffat, P. A.; Möckli, P.; Xanthopoulos, N.; Vasquez, R.; Mathieu, H. J.; Van herle, J.; Thampi, K. R., *Journal of Catalysis* **2001**, *202*, 229-244.
- (8) Yokokawa, H.; Sakai, N.; Kawada, T.; Dokiya, M., *J. Electrochem. Soc.* **1991**, *138*, 1018-1027.
- (9) Van Dielen, V., Ph.D. thesis, Technische Universiteit Delft, **1995**.
- (10) Yokokawa, H.; Sakai, N.; Kawada, T.; Dokiya, M., *Solid State Ionics* **1992**, *52*, 43-56.
- (11) Shannon, R. D.; Prewitt, C. T., *Acta Cryst.* **1969**, *B25*, 925-946.
- (12) Yasuda, I.; Hishinuma, M., *J. Electrochem. Soc.* **1996**, *143*, 1583-1590.
- (13) Peck, D. H.; Hilpert, K.; Miller, M.; Korbertz, D.; Nickel, H. "Untersuchungen zur Verdampfung und Thermodynamik von Perowskiten auf der Basis von LaCrO₃ für Hochtemperatur-Brennstoffzellen mit Festelektrolyt (SOFC)," Forschungszentrum Jülich GmbH, Institut für Werkstoffe der Energietechnik, **1996**.
- (14) Yokokawa, H.; Sakai, N.; Kawada, T.; Dokiya, M., *J. Electrochem. Soc.* **1991**, *138*, 2719-2727.

- (15) Yasuda, I.; Hishinuma, M., *Solid State Ionics* **1995**, 78, 109-114.
- (16) Sakai, N.; Kawada, T.; Yokokawa, H.; Dokiya, M.; Kojima, I., *J. Am. Ceram. Soc.* **1993**, 76, 609-616.
- (17) Sakai, N.; Kawada, T.; Yokokawa, H.; Dokiya, M., *Journal of the Ceramic Society of Japan* **1993**, 101, 1195-1200.
- (18) Yokokawa, H.; Horita, T.; Sakai, N.; Kawada, T.; Dokiya, M.; Takai, Y.; Todoki, M., *Thermochimica Acta* **1995**, 267, 129-138.
- (19) Peck, D. H.; Miller, M.; Hilpert, K., *Solid State Ionics* **1999**, 123, 59-65.
- (20) Peck, D. H.; Miller, M.; Hilpert, K., *Solid State Ionics* **1999**, 123, 47-57.
- (21) Peck, D. H.; Miller, M.; Nickel, H.; Das, D.; Hilpert, K. The Fourth International Symposium on Solid Oxide Fuel Cells, **1995**; p 858-868.
- (22) Miyoshi, S.; Yashiro, K.; Onuma, S.; Kaimai, A.; Kawamura, K.; Nigara, Y.; Kawada, T.; Mizusaki, J. Forth European Solid Oxide Fuel Cell Forum, Lucerne, Switzerland, **2000**; p 881-887.
- (23) Chick, L. A.; Bates, J. L.; Maupin, G. D. The Second International Symposium on Solid Oxide Fuel Cells, Athens, Greece, **1991**; p 621-628.
- (24) Carter, J. D.; Sprenkle, V.; Nasrallah, M. M.; Anderson, H. U. Proceedings of the Third International Symposium on Solid Oxide Fuel Cells, Honolulu, Hawaii, **1993**; p 344-353.
- (25) Berg, R. W. High Temperature Electrochemistry: Ceramics and Metals, Risø National Laboratory, Roskilde, Denmark, **1996**; p 175-180.
- (26) Chick, L. A.; Liu, J.; Stevenson, J. W.; Armstrong, T. R.; McCready, D. E.; Maupin, G. D.; Coffey, G. W.; Coyle, C. A., *J. Am. Ceram. Soc.* **1997**, 80, 2109-2120.
- (27) Wood, B. J.; Fraser, D. G. *Elementary thermodynamics for geologists*; Oxford University Press, **1976**.
- (28) Oonk, H. A. J. *Phase theory. The thermodynamics of heterogeneous equilibria*; Elsevier Scientific Publishing Company, **1981**.
- (29) Lou, V. L. K.; Mitchell, T. E.; Heuer, A. H., *J. Am. Ceram. Soc.* **1985**, 68, 49-58.
- (30) Lou, V. L. K.; Heuer, A. H. High Temperatures-High Pressures., Petten, The Netherlands, **1990**; p 33-52.
- (31) Peck, D. H.; Miller, M.; Kobertz, D.; Nickel, H.; Hilpert, K., *J. Am. Ceram. Soc.* **1996**, 79, 3266-3272.
- (32) Hilpert, K.; Das, D.; Miller, M.; Peck, D. H.; Weiß, R., *J. Electrochem. Soc.* **1996**, 143, 3642-3647.
- (33) Moriga, T.; Usaka, O.; Nakabayashi, I.; Kinouchi, T.; Kikkawa, S.; Kanamaru, F., *Solid State Ionics* **1995**, 79, 252-255.
- (34) Höfer, H. E.; Kock, W. F., *J. Electrochem. Soc.* **1993**, 140, 2889-2894.
- (35) Kawada, T.; Horita, T.; Sakai, N.; Yokokawa, H.; Dokiya, M., *Solid State Ionics* **1995**, 79, 201-207.
- (36) Horita, T.; Ishikawa, M.; Yamaji, K.; Sakai, N.; Yokokawa, H.; Dokiya, M., *Solid State Ionics* **1998**, 108, 383-390.
- (37) Horita, T.; Ishikawa, M.; Yamaji, K.; Sakai, N.; Yokokawa, H.; Dokiya, M., *Solid State Ionics* **1999**, 124, 301-307.
- (38) Sakai, N.; Yamaji, K.; Horita, T.; Negishi, H.; Yokokawa, H., *Solid State Ionics* **2000**, 135, 469-474.
- (39) Akashi, T.; Nanko, M.; Maruyama, T.; Shiraiishi, Y.; Tanabe, J. Solid Oxide Fuel Cells V, Aachen, Germany, **1997**; p 1263-1272.
- (40) Yokokawa, H.; Sakai, N.; Kawada, T.; Dokiya, M. Science and Technology of Zirconia, **1993**; p 59-68.
- (41) Yokokawa, H.; Sakai, N.; Kawada, T.; Dokiya, M. The Second International Symposium on Solid Oxide Fuel Cells, Athens, Greece, **1991**; p 663-670.
- (42) Katsura, T.; Kitayama, K.; Sugihara, T.; Kimizuka, N., *Bulletin of the Chemical Society of Japan* **1975**, 48, 1809-1811.
- (43) Katsura, T.; Sekine, T.; Kitayama, K.; Sugihara, T., *Journal of Solid State Chemistry* **1978**, 23, 43-57.
- (44) Kamata, K.; Nakajima, T.; Nakamura, T., *Mat. Res. Bull.* **1979**, 14, 1007-1012.
- (45) Petrov, A. N.; Kropanev, A. Y.; Zhukovskii, V. M., *Russian Journal of Physical Chemistry* **1984**, 58, 26-28.

- (46) Yokokawa, H.; Kawada, T.; Dokiya, M., *J. Am. Ceram. Soc.* **1989**, 72, 152.
- (47) Tilsted, B. G.; Fjellvåg, H.; Kjekshus, A., *Journal of Solid State Chemistry* **1995**, 119, 271-280.
- (48) Marti, P. E., Swiss Federal Institute of Technology Zürich, **1994**.
- (49) Navrotsky, A. In *Perovskite: A structure of great interest to geophysics and materials science*; Navrotsky, A. and Weidner, D. J., Eds.; American Geophysical Union:, **1989**; Vol. 45.
- (50) Mizusaki, J.; Yamauchi, S.; Fueki, K.; Ishikawa, A., *Solid State Ionics* **1984**, 12, 119-124.
- (51) Yasuda, I.; Hikita, T., *J. Electrochem. Soc.* **1993**, 140, 1699-1704.
- (52) Atkins, P. W. *Physical Chemistry*, Sixth ed.; Oxford University Press, **1998**.

Appendix A: Literature background concerning the derivation of the thermodynamic parameters of substituted LaCrO_3 using an empirical correlation

The nature of the correlations

Katsura et al.^{42, 43}, Kamata et al.⁴⁴ and Petrov et al.⁴⁵, among others, pointed out that the standard Gibbs free energy or the enthalpy of formation of lanthanoid-Mn, Fe, Co-perovskites (LnMnO_3 , LnFeO_3 or LnCoO_3) from Ln_2O_3 and the metal oxides changes proportionally with the tolerance factor. This is well illustrated in Figure A-1 for the cases of LnMnO_3 and LnFeO_3 perovskites where the stabilization energy, ∂ ,

$$\partial[\text{kJ/mol}] = \Delta_f H_{298, \text{perovskite}}^\circ - \sum x_i \Delta_f H_{298, \text{binary oxide}}^\circ \quad \text{A-1}$$

is shown to vary linearly with the tolerance factor t_p

$$t_p = \frac{r_O + r_A}{\sqrt{2}(r_O + r_B)} \quad \text{A-2}$$

Figure A-1 shows clearly that the fitted lines for both systems lie very near to each other and that it is possible to extrapolate the stabilization energy for a whole family of lanthanides. Such linear correlations were also derived for respective $A^{3+}-M^{3+}$, $A^{2+}-M^{4+}$ and A^+-M^{5+} perovskites. Yokokawa et al.^{8, 10, 46} were able to establish a correlation for many types of perovskites and to extract successfully the thermodynamic parameters for systems whose thermodynamic data are not yet experimentally available.

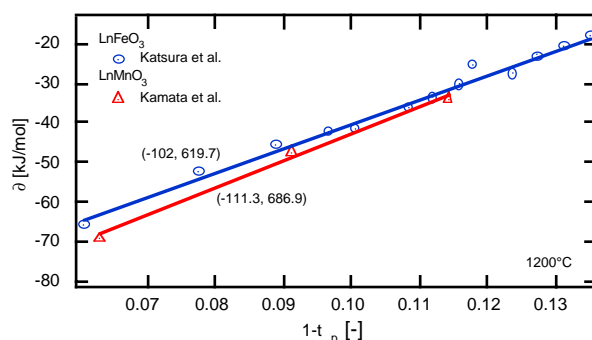


Figure A-1: Evolution of the stabilization energy, ∂ , at 1200°C , for the LnMnO_3 and LnFeO_3 perovskites as a function of the tolerance factor. Data are taken from Kamata et al.⁴⁴ and Katsura et al.⁴³. Ln: La, Nd, Sm, Eu, Gd, Tb, Dy, Ho, Er, Tm, Yb, Lu and Y.

Based on Yokokawa's work, the stabilization energy for the LaCrO_3 -based compounds at 298 K were calculated from the following expression for the $A^{3+}B^{3+}\text{O}_3$ -type perovskites⁸

$$\partial[\text{kJ/mol}] = -90 + 720(1 - t_p) \quad \text{A-3}$$

This is shown in figure A-2. The derivation of $\Delta_f H_{298}^\circ$ for the $\text{LaCr}_{0.5}\text{M}_{0.5}\text{O}_3$ systems is thus possible by considering the binary constituent oxides, La_2O_3 , Cr_2O_3 (Cr^{III}) and M_2O_3 in the case of $M = \text{Mn, Fe, Co}$ and Ru , and La_2O_3 , CrO_2 (Cr^{IV}) and MO in the case of $M = \text{Mg, Ni, Cu}$ and Zn , and then using equation A-1. The valence number of Mn, Fe and Co was assumed to be of III whereas Ni was assumed to be divalent in accordance with our TPR measurements⁷ (Chapter 6). This is also confirmed in literature where it is stated that, up to a substitution limit of about 0.4 on the Cr site, the Ni is expected to be divalent³⁴, whereas the Co is stated to be in the trivalent state in the whole range of substitutions in LaCrO_3 ⁴⁷.

For the divalent Mg, Ni, Cu and Zn, Cr ions are forced in the IV state, in air, so that the CrO_2 species is taken instead of Cr_2O_3 when using equation A-1. Although the CrO_2 species is not

stable at high temperatures, this approach is reported to give good approximates as it has been illustrated previously by Yokokawa et al.⁸

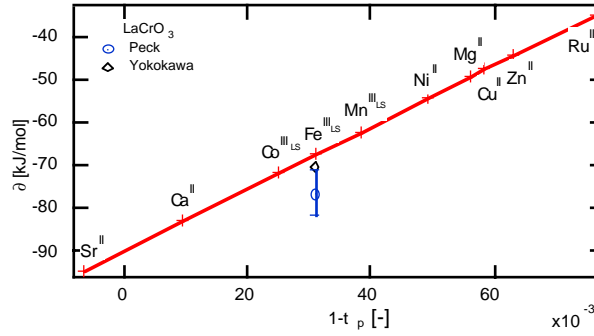


Figure A-2: Estimates for the stabilization energy, ∂ , at room temperature, for the LaCrO_3 -based compounds, based on equation A-3. For LaCrO_3 this correlation gives an estimate which is close to the experimentally measured value³¹.

For the tolerance factor, t_p , used in equation A-3, r_A and r_B , which are the mean Shannon radii¹¹ (see Table A-1) for the La (A) and Cr (B) sites, are estimated from the average of the La and (Ca, Sr) ionic radii in the case of $\text{La}_{0.5}(\text{Ca, Sr})_{0.5}\text{CrO}_3$ and Cr and (Mg, Mn, Fe, Co, Ni, Cu, Zn, Ru) ionic radii in the case of $\text{LaCr}_{0.5}(\text{Mg, Mn, Fe, Co, Ni, Cu, Zn, Ru})_{0.5}\text{O}_3$. A-site ions are 12-coordinated and the B-site ions are 6-coordinated.

Table A-1: Shannon¹¹ radii for the different elements used in this study.

Element	Ionic radius	Element	Ionic radius
La	1.46	Ni ^{II}	0.83
Cr ^{IV}	0.69	Cu ^{II}	0.87
Cr ^{III}	0.76	Zn ^{II}	0.89
Mg ^{II}	0.86	Ru ^{III}	0.82
Ca ^{II}	1.49	Y ^{III}	1.29
Sr ^{II}	1.58	Ce ^{III}	1.43
Mn ^{III}	0.72	Pr ^{III}	1.43
Fe ^{III}	0.69	Sm ^{III}	1.38
Co ^{III}	0.67	Gd ^{III}	1.34

A-site substituents are 12-coordinated whereas B-site substituents are 6-coordinated. Some of the A-site radii are not available in the 12-coordination so that these radii were estimated by multiplying the 8-coordination radii by 1.12 as reported by Petrov et al.⁴⁵. The oxygen radius is 1.27 nm.

For the Ca- and Sr-substituted LaCrO_3 , ∂ were obtained after estimation of the $\Delta_f H_{298}^\circ$ from the ideal solid solution approximation by mixing LaCrO_3 and $(\text{Ca, Sr})\text{CrO}_3$ following equation (1) and in agreement with the nature of the secondary phases coexisting with the perovskite phase. Such estimates for the $\Delta_f H_{298}^\circ$ allow to follow the change in the stability of the lanthanoid chromites as shown in figure A-3. The result show clearly that La is the most stable substituent, in accordance with experimental results for other perovskites ($\text{Ln}(\text{Mn, Fe, Co})\text{O}_3$)^{42-45, 48}.

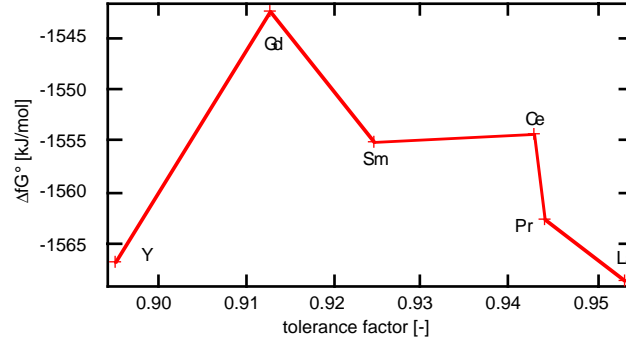


Figure A-3: The estimated Gibbs free energy of formation for different LnCrO₃ compounds.

Another approach to estimate the thermodynamic properties of perovskite-like structures has been reported in literature. It is based on estimates derived from the Madelung energy as reported, for example, by Navrotsky⁴⁹.

Estimating the non-stoichiometry from literature data

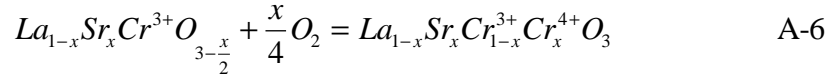
The non-stoichiometry of the La_{1-x}Sr_xCrO₃ system was measured by Mizusaki et al.⁵⁰ as a function of the oxygen partial pressure between 1000°C and 1300°C. From these measurements they were able to extract the enthalpy and entropy of oxidation, $\Delta_{ox}H^\circ$ and $\Delta_{ox}S^\circ$ (see Table A-2), defined by

$$\ln K_{ox} = -\frac{\Delta_{ox}H^\circ}{RT} + \frac{\Delta_{ox}S^\circ}{R} \quad A-4$$

where K_{ox}

$$K_{ox} = \frac{[O_o^x][Cr_{Cr}^\bullet]^2}{[V_o^{\bullet\bullet}][Cr_{Cr}^x]^2 \sqrt{pO_2}} \quad A-5$$

is obtained from



By fitting for the different compositions of Table A-2, we have

$$\Delta_{ox}H^\circ [kJ/mol] = -327.5 + 263.4x \quad A-5$$

$$\Delta_{ox}S^\circ [J/molK] = -114.9 + 146.7x \quad A-6$$

It is thus possible to estimate the Gibbs free energy of the non-stoichiometric perovskite from the stoichiometric one estimated following the procedures described above, using

$$\Delta G_{La_{1-x}Sr_xCr_{1-x}^{3+}Cr_x^{4+}O_3, T}^\circ = \Delta G_{La_{1-x}Sr_xCr^{3+}O_{3-\delta}, T}^\circ + \delta \Delta_{ox}G^\circ \quad A-7$$

with

$$\Delta_{ox}G^\circ = -RT \ln K_{ox} \quad A-8$$

Table A-2: Values of $\Delta_{ox}H^\circ$ and $\Delta_{ox}S^\circ$ for the La_{1-x}Sr_xCrO₃ system, derived in the temperature range of 1000°C to 1300°C by Mizusaki et al.⁵⁰.

x	$\Delta_{ox}H^\circ$ [kJ/mol]	$\Delta_{ox}S^\circ$ [J/mol K]
0.1	-302.9	-100.4
0.2	-272.0	-85.8
0.3	-250.2	-71.1

For the Ca substitution, the same holds. For that purpose, data published by Yasuda et al.⁵¹ were used. From their study it was possible to extract the $\Delta_{ox}H^\circ$ and $\Delta_{ox}S^\circ$ for the composition of $x=0.3$, in the temperature range of 900-1050°C as shown in Table A-3.

Table A-3: Experimental and fitted values of non-stoichiometry in the La_{0.7}Ca_{0.3}CrO₃ system⁵¹.

T [°C]	1/T [1/K]	K_{ox}	$\ln(K_{ox})$	ΔG_{ox} [kJ/mol]	ΔH_{ox}° [kJ/mol]	ΔS_{ox}° [J/mol K]
900	8.53x10 ⁻⁴	6.73x10 ⁷	18.02	-175.78	-261.03	-72.93
950	8.18x10 ⁻⁴	2.17x10 ⁷	16.89	-171.76		
1000	7.86x10 ⁻⁴	7.31x10 ⁶	15.80	-167.27		
1050	7.56x10 ⁻⁴	3.34x10 ⁶	15.02	-165.23		

As no literature data was found, the variation of $\Delta_{ox}H^\circ$ and $\Delta_{ox}S^\circ$ with x was taken to be similar to the case of Sr (i.e. the same slope with x),

$$\Delta_{ox}H^\circ[\text{kJ/mol}] = -340.1 + 263.4x \quad \text{A-9}$$

$$\Delta_{ox}S^\circ[\text{J/molK}] = -114.9 + 146.7x \quad \text{A-10}$$

For the other substituents, no experimental data for K_{ox} nor for non-stoichiometry data were available in literature so that no correction was possible and the estimates were taken as such.

Evaluation of the thermodynamic properties as a function of temperature

The temperature dependence of the heat capacity can be estimated using the Kelley equation

$$C_p = A + B \cdot 10^{-3} \cdot T + C \cdot 10^5 \cdot T^{-2} + D \cdot 10^{-6} \cdot T^2 \quad \text{A-11}$$

where A , B , C and D are coefficients estimated from experimental data (taken, for example, from the HSC database) or the correlations presented above (equation (3)).

The evolution of the enthalpy of formation with temperature is given by

$$\Delta_f H_T^\circ = \Delta_f H_{298.15}^\circ + \int_{298.15}^T C_p dT + \sum \Delta H_{tr} \quad \text{A-12}$$

with ΔH_{tr} the enthalpy of transformation of the substance.

The dependence of the entropy with temperature is given by

$$S_T^\circ = S_{298.15}^\circ + \int_{298.15}^T \frac{C_p}{T} dT + \sum \frac{\Delta H_{tr}}{T_{tr}} \quad \text{A-13}$$

with T_{tr} the temperature of phase transformation.

From the above, it is thus possible to estimate the Gibbs free energy of a reaction



at a given temperature by

$$\Delta_r G_T = \Delta_r H_T - T \Delta_r S_T \quad \text{A-15}$$

where

$$\Delta_r H_T = (\gamma \Delta_f H_{T,C}^\circ + \delta \Delta_f H_{T,D}^\circ) - (\alpha \Delta_f H_{T,A}^\circ + \beta \Delta_f H_{T,B}^\circ) \quad \text{A-16}$$

$$\text{and} \quad \Delta_r S_T = (\gamma S_{T,C}^\circ + \delta S_{T,D}^\circ) - (\alpha S_{T,A}^\circ + \beta S_{T,B}^\circ) \quad \text{A-17}$$

Appendix B: Generated thermodynamic parameters for the compounds of the substituted LaCrO₃ phases. The heat capacity is given as C_p [kJ/molK] = $A + B 10^{-3} T + C 10^5 T^{-2} + D 10^{-6} T^2$, with T in Kelvin

Compounds	ΔH°_{298} [kJ/mol]	S°_{298} [J/mol K]	A	B	C	D
LaCrO ₃	-1534.40	114.00	119.30	12.05	-14.64	0.00
La _{0.5} Ca _{0.5} CrO ₃	-1420.51	106.69	128.10	20.51	-4.95	-0.95
La _{0.5} Ca _{0.5} CrO _{2.75}	-1201.35	101.47	106.9	18.04	-3.05	-1.90
La _{0.5} Sr _{0.5} CrO ₃	-1416.21	115.41	126.06	25.77	-3.37	-3.03
La _{0.5} Sr _{0.5} CrO _{2.75}	-1173.24	110.19	104.9	23.31	-1.47	-3.98
LaCr _{0.5} Mg _{0.5} O ₃	-1546.07	112.64	131.08	17.97	-12.18	-0.13
LaCr _{0.5} Mg _{0.5} O _{2.75}	-1521.42	107.42	109.88	15.51	-10.29	-1.08
LaCr _{0.5} Mn _{0.5} O ₃	-1483.34	121.57	111.81	21.99	-8.23	-0.95
LaCr _{0.5} Mn _{0.5} O _{2.75}	-1421.56	123.81	109.19	17.28	-6.70	-0.95
LaCr _{0.5} Fe _{0.5} O ₃	-1455.40	115.81	110.51	32.68	-8.57	-0.95
LaCr _{0.5} Fe _{0.5} O _{2.75}	-1372.62	122.75	111.34	17.53	-6.51	-0.95
LaCr _{0.5} Co _{0.5} O ₃	-1314.66	118.62	111.16	27.34	-8.40	-0.95
LaCr _{0.5} Co _{0.5} O _{2.75}	-1351.23	120.44	111.61	13.36	-3.46	1.22
LaCr _{0.5} Ni _{0.5} O ₃	-1370.03	118.18	270.06	-508.55	-38.60	577.77
LaCr _{0.5} Ni _{0.5} O _{2.75}	-1209.77	112.95	248.85	-511.02	-36.70	576.8
LaCr _{0.5} Cu _{0.5} O ₃	-1321.82	120.48	131.44	19.40	-10.56	0.00
LaCr _{0.5} Cu _{0.5} O _{2.75}	-1161.77	115.78	110.24	16.94	-8.66	-0.95
LaCr _{0.5} Zn _{0.5} O ₃	-1415.73	121.00	129.82	19.33	-9.61	0.00
LaCr _{0.5} Zn _{0.5} O _{2.75}	-1255.78	112.95	108.62	16.87	-7.71	-0.95

Appendix C: List of the species taken into account for the calculations

- H₂(g), H₂O(g), O₂(g), Ar(g), CO(g), CO₂(g),
- Cr(s), Cr(g), CrOH(g), CrO(g), Cr(OH)₂(g), Cr₂O₃(s), Cr(OH)₃(g), CrOOH(g), CrO₂(g), Cr(OH)₃(g), CrO(OH)₂(g), CrO(OH)₃(g), Cr(OH)₅(g), CrO(OH)₃(g), CrO₂OH(g), CrO₃(g), Cr(OH)₆(g), CrO(OH)₄(g), CrO₂(OH)₂(g),
- La(s), La(g), LaH₂(s), La₂O(g), LaO(g), La₂O₂(g), La₂O₃(s), La₂O₂(g),
- Mg(s), MgO(s),
- Ca(s), CaO(s), CaH(g), CaH₂(s), CaOH(g), Ca(OH)₂(g), CaCO₃(s), CaCrO₃(s), CaCrO₄(s), CaCr₂O₄(s), Ca₂CrO₄(s), Ca₃Cr₂O₇(s), Ca₃Cr₂O₈(s), Ca₅(CrO₄)₃(s), Ca₅(CrO₃)₄O(s), Ca₁₀(CrO₄)₇(s),
- Sr(l), Sr(g), SrH(g), SrOH(g), SrO(s), Sr(OH)₂(l), Sr(OH)₂(g), SrCO₃(s), SrCrO₃(s), SrCrO₄(s), Sr₂CrO₄(s), Sr₃Cr₂O₈(s),
- Mn(s), MnO(s), Mn₂O₃(s), Mn₃O₄(s),
- Fe(s), FeO(s), Fe₂O₃(s), Fe₃O₄(s), FeCr₂O₄(s),
- Co(s), CoO(s), Co₂O₃(s), CoCr₂O₄(s),
- Ni(s), NiO(s), Ni₂O₃(s), NiCr₂O₄(s),
- Cu(s), CuO(s),
- Zn(s), ZnO(s),
- La₂CrO₄(s), La₂CrO₆(s), La₂(CrO₄)₃(s), LaCrO₄(s), LaCr_{1-x}Mg_xO₃(s), LaCaCrO₄(s), LaCa₂Cr₂O₇(s), La₃Ca₂O₇(s), La_{1-x}Ca_xCrO₃(s), La_{1-x}Ca_xCrO_{3-δ}(s), LaSrCrO₄(s), La_{1-x}Sr_xCrO₃(s), La_{1-x}Sr_xCrO_{2-δ}(s), LaCr_{1-x}Mn_xO₃(s), LaCr_{1-x}Fe_xO₃(s), LaCr_{1-x}Co_xO₃(s), LaNiO₃(s), LaNiO₄(s), La₄Ni₃O₁₀(s), LaCr_{1-x}Ni_xO₃(s), LaCr_{1-x}Cu_xO₃(s), LaCr_{1-x}Zn_xO₃(s),
- ZrO₂(s), CaZrO₃(s), SrZrO₃(s), La₂Zr₂O₇(s), La₂NiZrO₄(s), La₄Ni₂ZrO₁₀(s)

Appendix D: Derivation of the solubility limit from the ‘symmetrical regular solutions model’^{27, 28}

Entropy of mixing

If we consider 1 mole of a solid solution between AO and BO. The entropy of (A,B)O may be considered to be made up of the thermal and mixing contributions. In solid solution the thermal contribution is negligible²⁷. The entropy of mixing can be derived from statistical thermodynamics using the Boltzmann formula⁵²

$$S_{mix} = k \ln W \quad \text{A-18}$$

with k , the Boltzmann constant and W , the permutability, i.e. the total number of possible atomic configurations in the mixture, given as

$$W = \frac{N!}{N_A! \cdot N_B!} \quad \text{A-19}$$

where N_A and N_B atoms are randomly distributed over N positions. By developing equation A-18, we obtain

$$S_{mix} = -kN[x_A \ln x_A + x_B \ln x_B] \quad \text{A-20}$$

with x_A and x_B the molar fraction of A and B respectively, with $x_A + x_B = 1$. By considering 1 mole of the solid solution, equation A-20 becomes

$$S_{mix} = -nR[x_A \ln x_A + x_B \ln x_B] \quad \text{A-21}$$

where n is the number of position in each formula unit on which mixing takes place in a general formula (A,B)_nO, and R , the gas phase constant.

Solubility limit

If we consider a system made up of n_A moles of the A_nO oxide and n_B moles of the B_nO oxide and if we suppose that these two oxides are allowed to mix ideally to form one homogeneous solid solution (A,B)_nO, with randomly mixed atoms of A and B than the free energy of the solid solution is given by:

$$G_{ss} = n_A \mu_{A_nO}^o + n_B \mu_{B_nO}^o + nRT(n_A \ln x_A + n_B \ln x_B) \quad \text{A-22}$$

$$\text{or} \quad G'_{ss} = \frac{G_{ss}}{n_A + n_B} = x_A \mu_{A_nO}^o + x_B \mu_{B_nO}^o + nRT(x_A \ln x_A + x_B \ln x_B) \quad \text{A-23}$$

$$\text{or} \quad G'_{ss} = x_A \mu_{A_nO} + x_B \mu_{B_nO} \quad \text{A-24}$$

where μ^o and μ the standard chemical potential and the chemical potential, and n , the number of position in each formula unit of (A,B)_nO, taken from equation A-21. Substituting $(1-x_A)$ for x_B in A-23 and A-24 and differentiating with respect to x_A we have:

$$\left(\frac{\partial G'_{ss}}{\partial x_A} \right)_{P,T} = \mu_{A_nO}^o - \mu_{B_nO}^o + nRT(\ln x_A - \ln(1-x_A)) \quad \text{A-25}$$

$$\text{and} \quad \mu_{A_nO} = G'_{ss} + (1-x_A) \left(\frac{\partial G'_{ss}}{\partial x_A} \right)_{P,T} \quad \text{A-26}$$

Substituting A-25 in A-26 we get the chemical potential of A_nO:

$$\mu_{A_nO} = \mu_{A_nO}^o + nRT \ln x_A \quad \text{A-27}$$

If we consider now the non-ideal contribution to the free energy, G^{xs} , taking the interchange energy, W_G , between A and B sites, and by assuming that the entropy of mixing is not altered by the non-ideal interactions and that there is no ordering or clustering of atoms, then we have:

$$G^{xs} = nx_Ax_BW_G = nx_A(1-x_A)W_G \quad \text{A-28}$$

G^{xs} should be added to A-23. W_G is defined, at a pressure of 1 bar, as:

$$W_G = W_{H_{1bar}} - TW_S \quad \text{A-29}$$

The chemical potential of A_nO is changed to:

$$\mu_{A_nO} = \mu_{A_nO}^o + nRT \ln x_A + nW_G(1-x_A)^2 \quad \text{A-30}$$

The departures of activities from ideality is also expressed in terms of activity as:

$$\mu_{A_nO} = \mu_{A_nO}^o + nRT \ln \gamma_A x_A \quad \text{A-31}$$

Combining A-30 and A-31 gives the value of γ as:

$$RT \ln \gamma_A = W_G(1-x_A)^2 = W_G x_B^2 \quad \text{A-32}$$

If a miscibility gap appears we have an equilibrium between the two phases such as

$$\mu_{A_nO}^\alpha = \mu_{A_nO}^\beta \quad \text{A-33}$$

$$\text{and } \mu_{B_nO}^\alpha = \mu_{B_nO}^\beta \quad \text{A-34}$$

with α and β standing for the A_nO and B_nO phases respectively. Using equations A-31 and A-32 for both A and B species we obtain finally the equation describing the evolution of the solubility limit with temperature as:

$$\ln \left(\frac{x_B}{1-x_B} \right) = \frac{W_G}{RT} (2x_B - 1) \quad \text{A-35}$$

Practically, if there is a miscibility gap in a system made of A_nO and B_nO , and if we can suppose that the system follows the regular model then

- (a) this miscibility gap should be symmetrical, i.e. the crest of the surface should be centered at $x_A=0.5$, with the two branches lying symmetrically to $x_A=0.5$;
- (b) the structures of A_nO , B_nO and $(A,B)_nO$ must be the same;
- (c) no ordering is assumed.

From experimental measurements, made at different temperatures, it is possible to calculate W_G at any temperature then use equation A-35 to estimate the solubility limit as a function of temperature.

Chapter 8 八

Preparation of stable LaCrO₃-based anodes and their electrochemical characterization in humidified H₂, humidified CH₄ and CO/CO₂

Preparation of stable LaCrO_3 -based anodes and their electrochemical characterization in humidified H_2 , humidified CH_4 and CO/CO_2

Abstract

Electrocatalytic properties of Ca, Sr, Mg, Fe, Co and Ni substituted lanthanum chromites deposited on 8YSZ electrolytes were studied using I/V and impedance analysis. The effects of the sintering temperature, the polarization, the gas and the anode composition, as well as the presence of an adhesion layer made of LaCrO_3 and 8YSZ were taken into account. The polarization resistance is observed to decrease significantly for anodes sintered at lower temperatures and after current treatment. The application of an adhesion layer between the electrode and the YSZ considerably improved the stability of the system. Ni substitution was observed to have a beneficial effect on the performance of the cell under CH_4 feed. A direct relationship between the electric conductivity and catalytic activity and the electrocatalytic performance was evidenced. The electrocatalytic activity follows the trend $\text{LaCrO}_3 \approx \text{LaCr}_{0.9}\text{Co}_{0.1}\text{O}_3 < \text{LaCr}_{0.9}\text{Ni}_{0.1}\text{O}_3 < \text{La}_{0.85}\text{Sr}_{0.15}\text{CrO}_3 < \text{La}_{0.85}\text{Sr}_{0.15}\text{Cr}_{0.9}\text{Ni}_{0.1}\text{O}_3$, in a similar manner to the steam-reforming and oxidation activities of the same materials used as catalysts. The best cell gave at 877°C , a power output of $450 \text{ mW}/\text{cm}^2$ and $300 \text{ mW}/\text{cm}^2$, with a short circuit current of $1950 \text{ mA}/\text{cm}^2$ and $900 \text{ mA}/\text{cm}^2$, in humidified (3% H_2O) H_2 and CH_4 respectively. This cell sustained a direct CH_4 feed for 136 h at 877°C . In general, two rate limiting processes were fitted from the impedance analysis. The overall activation energy of both processes was between 80 and 190 kJ/mol. The oxidation of CH_4 was masked by the oxidation of H_2 . CO oxidation rate was observed to be slower than CH_4 , and CH_4 slower than H_2 . As for the catalytic study, CO_2 had an inhibiting effect on the performance of LaCrO_3 , possibly due to a blocking effect of surface carbonates. H_2O had no measurable effect on the H_2 reaction, whereas its effect was observable at high current densities for CH_4 .

Introduction

In Chapter 4, we explored calcium and / or strontium substituted lanthanum chromites as alternative anodes to Ni-YSZ¹. These materials were observed to inhibit coking but their overall electrocatalytic activity was found to be low under pure methane feed. Also, a degradation was observed and was related to a progressive reduction of the electrode as well as a topotactic reaction between excess Ca or Sr with YSZ. This reaction was however inhibited when low substitution levels were adopted (around 15% on the A-site)² (Chapter 5). Following experimental tests based on powder characterization (XRD , SEM , TEM , EDS), conductivity and catalytic tests^{2,3} (Chapter 4, 5 and 6) and thermodynamic calculations⁴ (Chapter 7) it could be possible to choose an appropriate composition from different substituents (Mg, Ca, Sr, Mn, Fe, Co, Ni, Cu and Nb).

In this chapter, following the previous measurements, an attempt was made to apply different LaCrO_3 powders as electrodes for their use as anode in methane. Different parameters were addressed. The effects of the sintering temperature, the polarization, the gas and the anode composition, as well as the presence of an adhesion layer made of lanthanum chromite and 8YSZ were taken into account. Ca, Sr, Mg, Co and Ni substituents were investigated.

Experimental

Powder preparation

Different lanthanum chromite powders were prepared according to the formula $\text{La}_{1-\alpha}\text{A}_\alpha\text{Cr}_{1-\beta}\text{B}_\beta\text{O}_3$ through a modified citrate route⁵, as described in Chapter 3. These powders were previously characterized by XRD , XPS , TEM-EDS and catalytic tests³ (Chapter 3 and 6).

Table 1: Summary of the different anodes used in this study. The nature of the perovskite, the layer thickness, the sintering temperature, as well as the anode composition were varied. The composite (LCs + YSZ) thickness were observed to be of 5 μm by EDAX-SEM.

Perovskite	Cell Nr	Nr of layers 1 st layer	Composite %8YSZ	Screen printer Screen	Nr of layers 2 nd layer	Screen printer Screen	3 rd layer	Anode abbreviation	Sintering temperature [°C]
<i>La_{0.85}Sr_{0.15}Cr_{0.9}Ni_{0.1}O₃</i>	E2c	3	-	250mesh, 50 μ	-	-	-	LSrCNi	1200
<i>La_{0.85}Sr_{0.15}Cr_{0.9}Ni_{0.1}O₃</i>	E2d	3	-	250mesh, 50 μ	-	-	-	LSrCNi	1100
<i>La_{0.85}Sr_{0.15}Cr_{0.9}Ni_{0.1}O₃</i>	E2f	3	-	250mesh, 50 μ	-	-	-	LSrCNi	1050
<i>La_{0.85}Sr_{0.15}Cr_{0.9}Ni_{0.1}O₃</i>	E7b	1	21.8	325mesh, 30 μ	3	250mesh, 50 μ	-	LSrCNi	1100
<i>La_{0.85}Sr_{0.15}Cr_{0.9}Ni_{0.1}O₃</i>	E2b	1	44.3	325mesh, 30 μ	3	250mesh, 50 μ	-	LSrCNi	1200
<i>La_{0.85}Sr_{0.15}Cr_{0.9}Ni_{0.1}O₃</i>	E2e	1	44.3	325mesh, 30 μ	2	250mesh, 50 μ	-	LSrCNi	1100
<i>La_{0.85}Sr_{0.15}Cr_{0.9}Ni_{0.1}O₃</i>	E2g	1	44.3	325mesh, 30 μ	2	250mesh, 50 μ	-	LSrCNi	1050
<i>La_{0.85}Sr_{0.15}Cr_{0.9}Ni_{0.1}O₃</i>	E5h	1	44.3	325mesh, 30 μ	3	250mesh, 50 μ	LaCr _{0.5} Ni _{0.5} O ₃	LSrCNi	1100
<i>La_{0.85}Sr_{0.15}Cr_{0.9}Ni_{0.1}O₃</i>	E7c	1	44.3	325mesh, 30 μ	1	250mesh, 50 μ	-	LSrCNi	1100
<i>La_{0.85}Sr_{0.15}CrO₃</i>	E5b	4	-	250mesh, 50 μ	-	-	-	LSrC	1100
<i>La_{0.85}Sr_{0.15}CrO₃</i>	E5a	1	44	325mesh, 30 μ	3	250mesh, 50 μ	-	LSrC	1100
LaCrO₃	E5f	1	44	325mesh, 30 μ	3	250mesh, 50 μ	-	LC	1100
<i>LaCr_{0.9}Co_{0.1}O₃</i>	E5i	1	44	325mesh, 30 μ	3	250mesh, 50 μ	-	LCCo	1100
<i>LaCr_{0.9}Ni_{0.1}O₃</i>	E5e	1	44.8	325mesh, 30 μ	3	250mesh, 50 μ	-	LCNi	1100
<i>LaCr_{0.9}Mg_{0.1}O₃</i>	B41	3	-	250mesh, 50 μ	-	-	-	LCMg	1100
<i>La_{0.85}Ca_{0.15}Cr_{0.9}Mg_{0.1}O₃</i>	B20	3	-	250mesh, 50 μ	-	-	-	LCaCMg	1100
<i>La_{0.85}Ca_{0.15}Cr_{0.9}Mg_{0.1}O₃</i>	B29	2	-	250mesh, 50 μ	-	-	-	LCaCMg	1100
<i>La_{0.85}Sr_{0.15}Cr_{0.9}Mg_{0.1}O₃</i>	B21	4	-	250mesh, 50 μ	-	-	-	LSrCMg	1100
<i>La_{0.85}Sr_{0.15}Cr_{0.9}Mg_{0.1}O₃</i>	B24	3	-	250mesh, 50 μ	-	-	-	LSrCMg	1100
<i>La_{0.85}Sr_{0.15}Cr_{0.9}Mg_{0.1}O₃</i>	B30	3	-	250mesh, 50 μ	-	-	-	LSrCMg	1100
<i>La_{0.85}Sr_{0.15}Cr_{0.9}Mg_{0.1}O₃</i>	B37	3	-	250mesh, 50 μ	-	-	-	LSrCMg	1050
<i>La_{0.85}Sr_{0.15}Cr_{0.9}Mg_{0.1}O₃</i>	E5d	4	-	250mesh, 50 μ	-	-	-	LSrCMg	1100

Cell numbers in bold and in italic are measurements made in the symmetrical and sealed set-up configurations respectively.

Slurry preparation and cell fabrication

Terpineol-ethyl cellulose-based slurries were prepared with the proportion of 56.50:39.55:3.95 ceramic powder:terpineol:ethyl cellulose, using isopropanol as a solvent, as described in Chapter 2. Composite slurries of LCs (substituted LaCrO_3) with Tosoh 8YSZ (TZ-8Y) powders were also made using appropriate amounts of LCs and 8YSZ powders (Table 1). The LC-based pastes were then screen-printed on 8YSZ electrolytes. The number of layers and their composition varied from sample to sample (Table 1). The cells were prepared following the procedure detailed in Chapter 2. The cells thus obtained were then sintered under load (thermocompression) between 2 alumina felts. A heating ramp of $90^\circ\text{C}/\text{h}$ from room temperature to 600°C was used in order to burn the organics, followed by a ramp of $180^\circ\text{C}/\text{h}$ until the desired temperature indicated in Table 1. The cell was then kept at this temperature for 4 h and then allowed to cool down to room temperature.

The parameters addressed in this study are the lanthanum chromite composition, the presence of an adhesion layer made of LC + 8YSZ composite between the YSZ electrolyte and the anode, the sintering temperature and the number of anode layers. The fact of using Pt meshes on the anode side, with their known activity toward CH_4 , does not prevent to compare the different electrodes, as the preparation conditions were similar. Also, Au electroplating should prevent Pt from reacting heavily with CH_4 .

Electrochemical testing and relaxation experiments

All three testing configurations were used in this study (see Chapter 2). For the systematic study in the non-sealed configuration, the electrochemical characterization were performed in most cases starting from 840°C in H_2 followed by a 1 night polarization at 400 mV in order to activate the electrodes, specially the LSM cathode. The temperature was then raised to 900°C and ultimately the gas was switched to $\text{CH}_4 + 3\% \text{H}_2\text{O}$.

Humidified H_2 and CH_4 were used in all set-ups in order to prevent excessively reducing conditions which might decompose the electrodes^{4,6}. At all stages, current/potential (I/V) curves were performed on cells of type a and b with a Wenking potentiostat. Impedance spectroscopy was conducted with an applied amplitude of 10 mV using a modified IM5 Zahner impedance analyzer on all cell types. The frequency ranged from 100 kHz to 40 mHz. After the measurements, the pellets' cross-sections were imaged by a Philips XLF30 secondary electron microscope (*SEM*). Some *EDAX* analysis was also performed in order to identify the interfacial composition between YSZ and the LCs as well as to estimate the composites layer thickness.

LC rods of $13 \times 6 \times 5 \text{ mm}^3$ were pressed at 100 MPa and sintered at 1500°C for 4 h. The pellets thus obtained were polished with a μm diamond paste. Transient measurements were performed in a quartz tube, similar to the one used for catalysis (Chapter 6), specially designed with a small gas volume to allow for rapid gas change. For this purpose, thinner rods ($\approx 500 \mu\text{m}$) were used. *dc* four probe conductivity measurements were carried out in air and humidified hydrogen, using Ag paste and Ag leads as current and potential lines. The oxygen partial pressure was monitored by a home-built YSZ sensor placed near the sample.

This kind of measurement was done in order to estimate the surface exchange coefficient and the oxygen diffusion coefficient, in an attempt to investigate the possibility of surface exchange limitations in the electrode reactions.

Results and discussion

Effect of the sintering temperature

Prior to the electrochemical tests, half cells were made by screen-printing $\text{La}_{0.85}\text{Ca}_{0.15}\text{Cr}_{0.9}\text{Mg}_{0.1}\text{O}_3$, $\text{La}_{0.85}\text{Sr}_{0.15}\text{Cr}_{0.9}\text{Mg}_{0.1}\text{O}_3$ and $\text{La}_{0.85}\text{Sr}_{0.15}\text{Cr}_{0.9}\text{Ni}_{0.1}\text{O}_3$ slurries on YSZ pellets. For these compositions, different sintering temperatures were investigated (1050 - 1200°C). Subsequently, these half cells were treated in $\text{H}_2 + 3\% \text{H}_2\text{O}$ at 800°C for several hours. After cooling to room temperature, the adherence and the morphology of the electrodes were verified by abrasion tests (using a cutter) and in some cases by *SEM* imaging. Firing at 1100°C was optimal, whereas lower temperatures gave poor adherence while firing at 1200°C produced some surface reaction with YSZ¹.

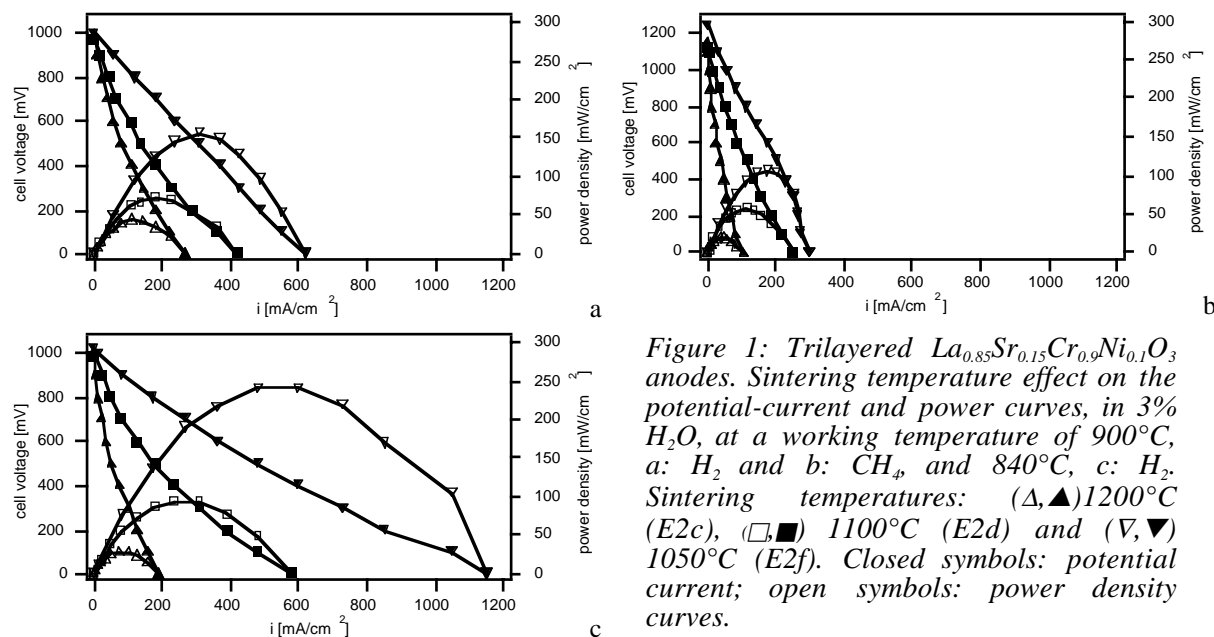


Figure 1: Trilayered $\text{La}_{0.85}\text{Sr}_{0.15}\text{Cr}_{0.9}\text{Ni}_{0.1}\text{O}_3$ anodes. Sintering temperature effect on the potential-current and power curves, in 3% H_2O , at a working temperature of 900°C , a: H_2 and b: CH_4 , and 840°C , c: H_2 . Sintering temperatures: (Δ, \blacktriangle) 1200°C (E2c), (\square, \blacksquare) 1100°C (E2d) and ($\nabla, \blacktriangledown$) 1050°C (E2f). Closed symbols: potential current; open symbols: power density curves.

The effect of the sintering temperature was also studied in more detail with the two systems, $\text{La}_{0.85}\text{Sr}_{0.15}\text{Cr}_{0.9}\text{Ni}_{0.1}\text{O}_3$ and 55.7:44.3 $\text{La}_{0.85}\text{Sr}_{0.15}\text{Cr}_{0.9}\text{Ni}_{0.1}\text{O}_3$:8YSZ, by electrochemical means. I/V curves were taken and impedance spectroscopy analyses performed in $\text{H}_2 + 3\% \text{H}_2\text{O}$ or $\text{CH}_4 + 3\% \text{H}_2\text{O}$ as fuel, at two temperatures, 840°C and 900°C , with unsealed cells sintered at 1050°C , 1100°C and 1200°C . I/V curves and power outputs, as well as anode overpotential (η_a) values are given in Figures 1 to 4. In Figure 1, initial performance was highest for the anodes sintered at the lowest temperature (1050°C). These, however, degrade more rapidly than those fired at 1100°C . Also, Figure 1 shows an inferior output at 900°C (a), compared to 840°C (c), at which temperature the test was initiated. This therefore indicates rapid degradation during testing between 840°C and 900°C

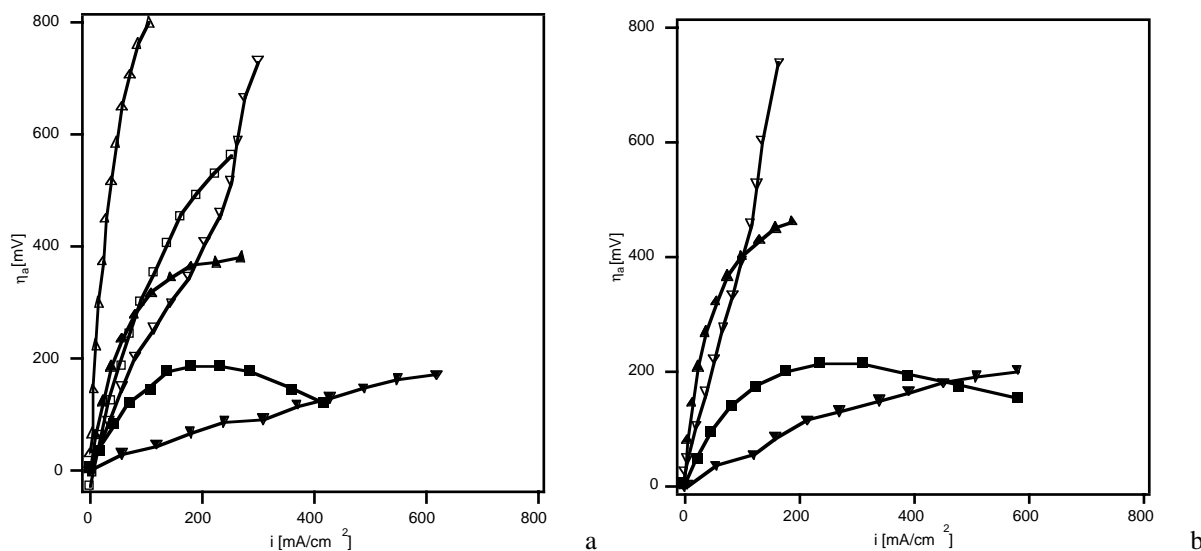


Figure 2: Trilayered $\text{La}_{0.85}\text{Sr}_{0.15}\text{Cr}_{0.9}\text{Ni}_{0.1}\text{O}_3$ anodes. Sintering temperature effect on the anode overpotential, in 3% H_2O , at a working temperature of a: 900°C , and b: 840°C . Sintering temperatures: (Δ, \blacktriangle) 1200°C (E2c), (\square, \blacksquare), 1100°C (E2d) and ($\nabla, \blacktriangledown$) 1050°C (E2f). Closed symbols: H_2 ; open symbols: CH_4 .

In the case of $\text{La}_{0.85}\text{Sr}_{0.15}\text{Cr}_{0.9}\text{Ni}_{0.1}\text{O}_3$, the current output was higher and the overpotential lower, in both humidified H_2 and CH_4 , when the cell was sintered at $1050^\circ\text{C} > 1100^\circ\text{C} > 1200^\circ\text{C}$ (Figure 1,2). The maximum power output reached at 900°C in humidified H_2 at the sintering

temperature of 1050°C was of 250 mW/cm² with a short circuit current of almost 1200 mA/cm². However, the cell performance was only stable when sintered at 1200°C. For the 1100°C and 1050°C sintering, the performance degraded rapidly with time as observed by impedance spectroscopy. The anodic polarization resistance values, R_p , for the cell sintered at 1050°C increased by 2.25 times overnight, while the anodic electrolyte resistance, R_e , changed by a factor of 1.2, resulting in the rapid degradation of the current output (Table 2). Also, the R_p s were significantly higher with increasing sintering temperatures, increasing 37 and 11 times in humidified H₂ at 840°C and 900°C respectively, and 7 times in humidified CH₄ at 900°C, between cells sintered at 1050°C and 1200°C. SEM micrographs show densification of the anode structure the higher the sintering temperature (Figure 5). The mean anode grain size was of 1 μm at 1200°C whereas it was in the submicron scale at lower sintering temperatures. From the micrographs, the structure seemed to be more loose at 1050°C as after the test some delamination was observed. SEM-EDAX analysis made on the 1200°C sintered anode showed a topotactic reaction between the La_{0.85}Sr_{0.15}Cr_{0.9}Ni_{0.1}O₃ electrode and the YSZ, most probably due to SrZrO₃ formation (Figure 7).

Table 2: Summary of the initial electrolyte and polarization resistances at OCV, R_e and R_p respectively, given in units of Ω.cm².

Anode composition	Cell Nr	Sintering temperature [°C]	H ₂ 840°C		H ₂ 900°C		CH ₄ 840°C		CH ₄ 900°C		800°C	800°C
			R_e	R_p	R_e	R_p	R_e	R_p	R_e	R_p	σ_{air}	σ_{H_2}
La _{0.85} Sr _{0.15} Cr _{0.9} Ni _{0.1} O ₃	E2c	1200	1	15	1.1	7.9	0.7	34	0.9	25	14.8	1.9
La _{0.85} Sr _{0.15} Cr _{0.9} Ni _{0.1} O ₃	E2d	1100	1	2.5	1.2	2.6	-	-	0.8	6.2		
La _{0.85} Sr _{0.15} Cr _{0.9} Ni _{0.1} O ₃	E2f	1050	0.7	0.4	0.9	0.7	0.7	4	0.8	3.6		
		overnight	0.86	0.9	0.8							
La _{0.85} Sr _{0.15} Cr _{0.9} Ni _{0.1} O ₃	E7b ¹	1100	0.32	0.16	0.27	0.11	0.29	-	0.26	-		
La _{0.85} Sr _{0.15} Cr _{0.9} Ni _{0.1} O ₃	E2b	1200	1.07	4.6	1.17	2.8	1	6.8	0.9	5		
La _{0.85} Sr _{0.15} Cr _{0.9} Ni _{0.1} O ₃	E2e	1100	1	1.4	1	0.5	0.54		0.5	2.8		
La _{0.85} Sr _{0.15} Cr _{0.9} Ni _{0.1} O ₃	E2g	1050	1.8	1.6	1.6	0.9			1	5.1		
La _{0.85} Sr _{0.15} Cr _{0.9} Ni _{0.1} O ₃	E5h	1100	2.7	1.8	2.2	1.4			1.1	4		
La _{0.85} Sr _{0.15} Cr _{0.9} Ni _{0.1} O ₃	E7c	1100										
La _{0.85} Sr _{0.15} CrO ₃	E5b	1100									2.6	0.9
La _{0.85} Sr _{0.15} CrO ₃	E5a	1100	0.5	1	0.5	0.5	0.6	2.4	0.4	2.1		
LaCrO ₃	E5f	1100	9.6	13	8.8	5.6	7.1	23	8.8	13	0.4	0.05
LaCr _{0.9} Co _{0.1} O ₃	E5i	1100	1.6	7	1.4	3.4	1.4	19	1.4	9.9	5.8	0.6
LaCr _{0.9} Ni _{0.1} O ₃	E5e	1100	3.9	5.1	2.7	3.3	5	24	2	9	5.4	0.4
LaCr _{0.9} Mg _{0.1} O ₃	B41	1100									5.1	0.16
La _{0.85} Ca _{0.15} Cr _{0.9} Mg _{0.1} O ₃	B20	1100									9.7	0.3
La _{0.85} Ca _{0.15} Cr _{0.9} Mg _{0.1} O ₃	B29	1100	0.5 ²	19.5								
	after polarization		0.37	2.3			0.7					
La _{0.85} Sr _{0.15} Cr _{0.9} Mg _{0.1} O ₃	B21	1100	0.4 ³	21.5							14.7	1.3
	after polarization		0.37	1.7			0.85	6.1				
La _{0.85} Sr _{0.15} Cr _{0.9} Mg _{0.1} O ₃	B24	1100	0.4	32			0.4	35				
La _{0.85} Sr _{0.15} Cr _{0.9} Mg _{0.1} O ₃	B30	1100	17.6	9.1								
La _{0.85} Sr _{0.15} Cr _{0.9} Mg _{0.1} O ₃	B37	1050										
La _{0.85} Sr _{0.15} Cr _{0.9} Mg _{0.1} O ₃	E5d	1100	1.2	1.3	1.4	1.6	1	6	1.1	6.2		

The conductivities, σ , in air and in humidified H₂ (3% H₂O), are given in units of S/cm. It is to be noted that the conductivities of La_{0.85}Ca_{0.15}Cr_{0.9}Ni_{0.1}O₃ and La_{0.85}Sr_{0.15}CrO₃ are those of the Ca substituted compounds, as these values were not measured for the Sr substitution. ¹: cell temperature of 864°C and 874°C instead of 840°C and 900°C; ²: 828°C; ³: 800°C. Bold numbers correspond to measurements made after the cell degradation.

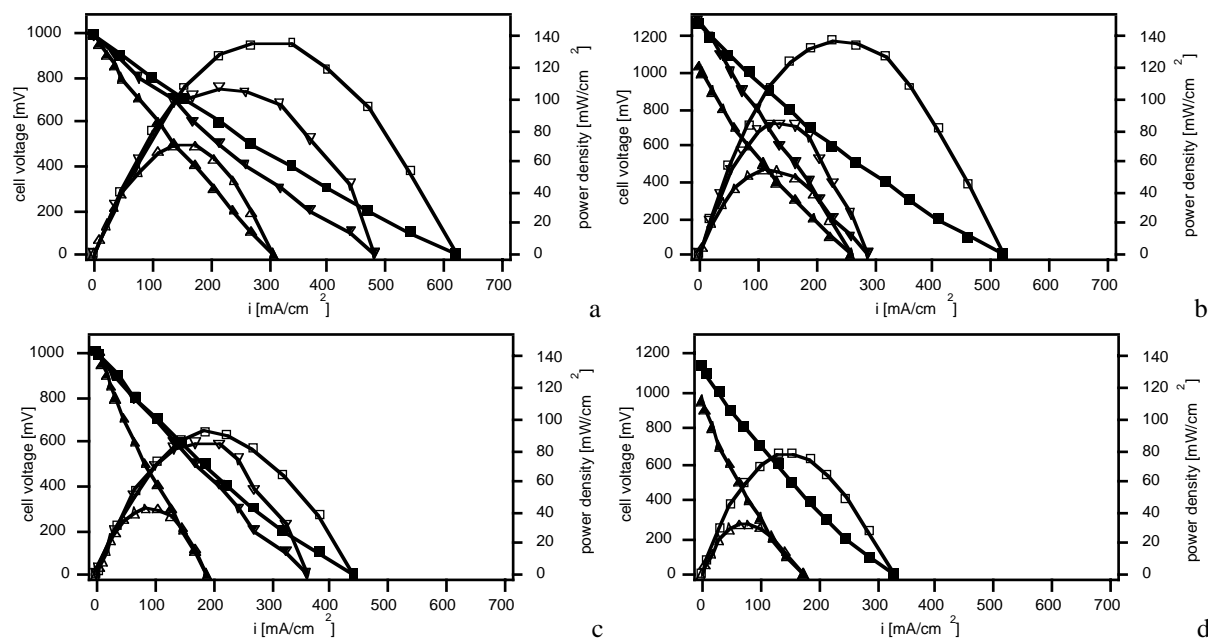


Figure 3: 1 layer of 55.7:44.3 $\text{La}_{0.85}\text{Sr}_{0.15}\text{Cr}_{0.9}\text{Ni}_{0.1}\text{O}_3$ +8YSZ composite anode, covered with 3 layers of $\text{La}_{0.85}\text{Sr}_{0.15}\text{Cr}_{0.9}\text{Ni}_{0.1}\text{O}_3$. Sintering temperature effect on the potential-current and power curves, in 3% H_2O , at a working temperature of 900°C, a: H_2 and b: CH_4 , and 840°C, c: H_2 and d: CH_4 . Sintering temperatures: (Δ , \blacktriangle) 1200°C (E2b), (\square , \blacksquare), 1100°C (E2e) and (∇ , \blacktriangledown) 1050°C (E2g). Closed symbols: potential current; open symbols: power density curves.

For 55.7:44.3 $\text{La}_{0.85}\text{Sr}_{0.15}\text{Cr}_{0.9}\text{Ni}_{0.1}\text{O}_3$:8YSZ, the current output is higher and the overpotential lower when the cell was sintered at 1100°C < 1050°C < 1200°C, in both humidified H_2 and CH_4 (Figure 3,4). The maximum power output reached at 900°C at the sintering temperature of 1100°C was of 140 mW/cm^2 with a short circuit current of more than 600 mA/cm^2 in humidified H_2 and 500 mA/cm^2 in humidified CH_4 . It is interesting to see that the power outputs in humidified H_2 and CH_4 are of the same order. The cell performances were stable over a period of more than 1 day for the cases of sintering at 1200°C and 1100°C. For the sintering temperature of 1050°C, the stability was less pronounced, and this was most probably due to delamination as observed *post-mortem* by SEM. YSZ composites seem to sinter badly at 1050°C. As for the case of $\text{La}_{0.85}\text{Sr}_{0.15}\text{Cr}_{0.9}\text{Ni}_{0.1}\text{O}_3$ anodes, the higher the sintering temperature the denser the electrodes (Figure 6). The mean thickness of the adhesion composite layer was estimated by line-scan EDAX analysis to be of approximately 5 μm . The R_e and R_p followed a similar trend with sintering temperature, i.e., 1100°C < 1050°C < 1200°C (Table 2). The R_p was lowered by a factor of 3 and 5.6 in humidified H_2 at 840°C and 900°C respectively, and 1.8 in humidified CH_4 at 900°C, between the sintering temperature of 1200°C and 1100°C.

It is thus observed that in both cases, the R_e was higher than the expected value for YSZ electrolyte. For a 150 μm thick Kerafol 8YSZ plate, the electrolyte ohmic loss is expected to be of 0.38 and 0.27 Ωcm^2 at 840°C and 900°C respectively. Also, in both $\text{La}_{0.85}\text{Sr}_{0.15}\text{Cr}_{0.9}\text{Ni}_{0.1}\text{O}_3$ and 55.7:44.3 $\text{La}_{0.85}\text{Sr}_{0.15}\text{Cr}_{0.9}\text{Ni}_{0.1}\text{O}_3$:8YSZ anodes, the sintering temperature of 1100°C was optimal. This temperature was adopted hereafter. The application of an adhesive layer also seemed to increase the stability of the system, as in the absence of the layer delamination was observed to occur rapidly.

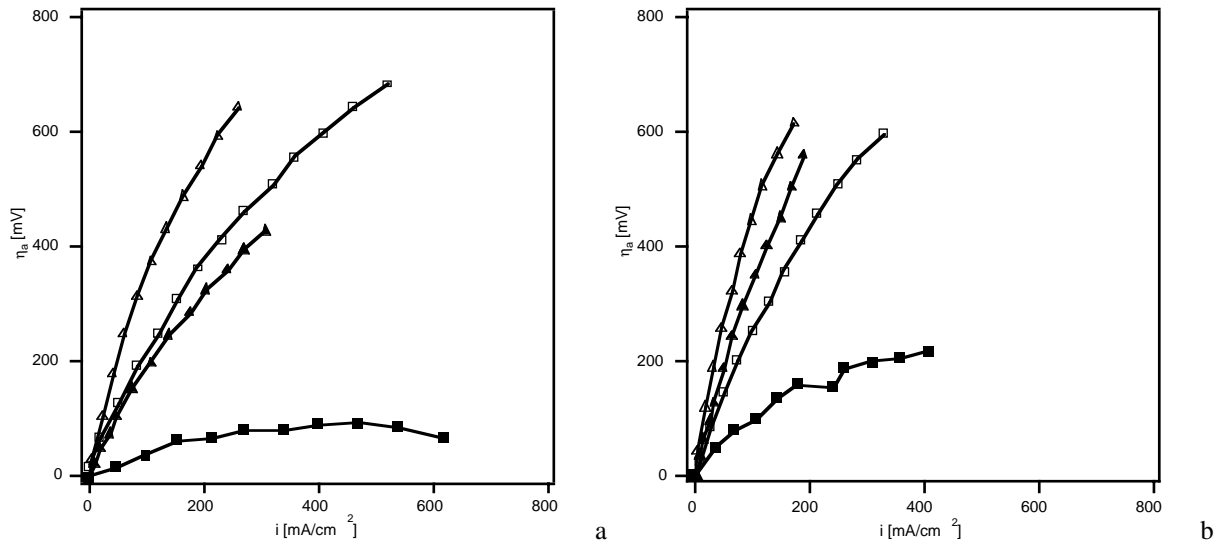


Figure 4: 1 layer of 55.7:44.3 $\text{La}_{0.85}\text{Sr}_{0.15}\text{Cr}_{0.9}\text{Ni}_{0.1}\text{O}_3$ +8YSZ composite anode covered with 3 layers of $\text{La}_{0.85}\text{Sr}_{0.15}\text{Cr}_{0.9}\text{Ni}_{0.1}\text{O}_3$. Sintering temperature effect on the anode overpotential, in 3% H_2O , at a working temperature of a: 900°C , and b: 840°C . Sintering temperatures: (Δ , \blacktriangle) 1200°C (E2b) and (\square , \blacksquare) 1100°C (E2e). Closed symbols: H_2 ; open symbols: CH_4 .

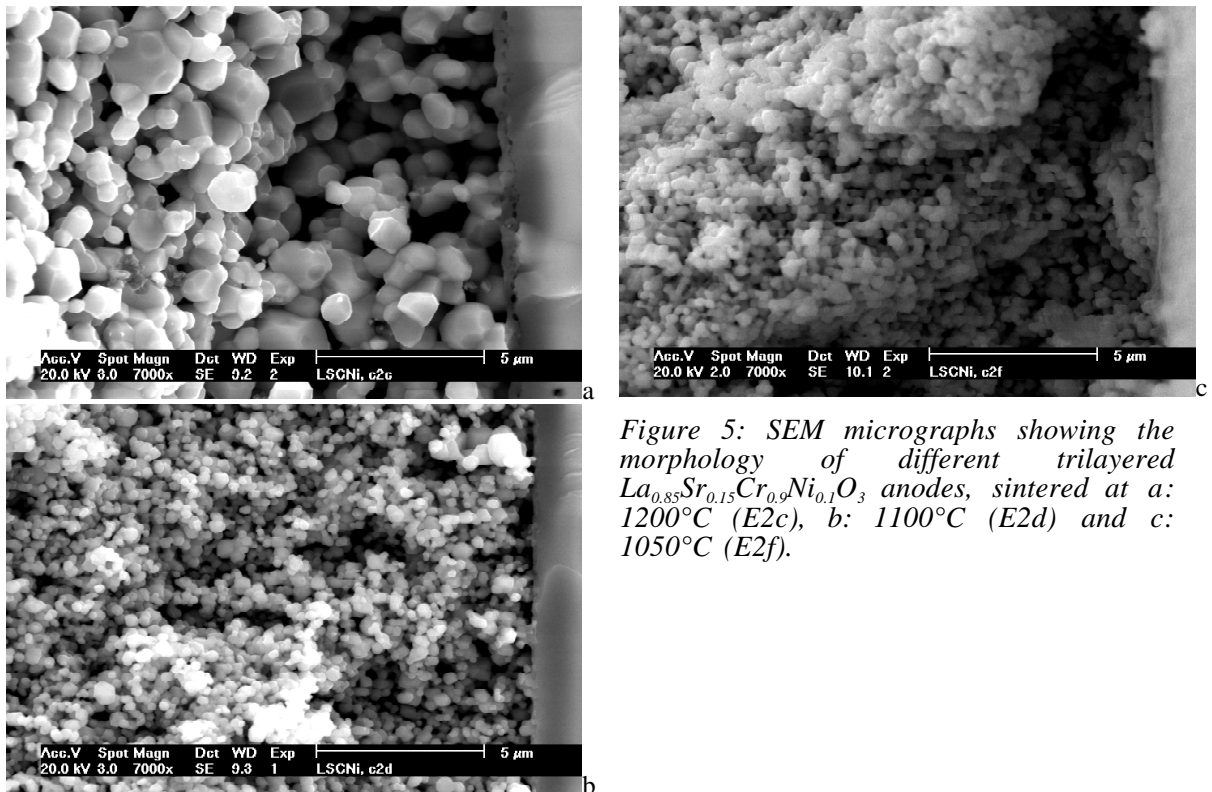


Figure 5: SEM micrographs showing the morphology of different trilayered $\text{La}_{0.85}\text{Sr}_{0.15}\text{Cr}_{0.9}\text{Ni}_{0.1}\text{O}_3$ anodes, sintered at a: 1200°C (E2c), b: 1100°C (E2d) and c: 1050°C (E2f).

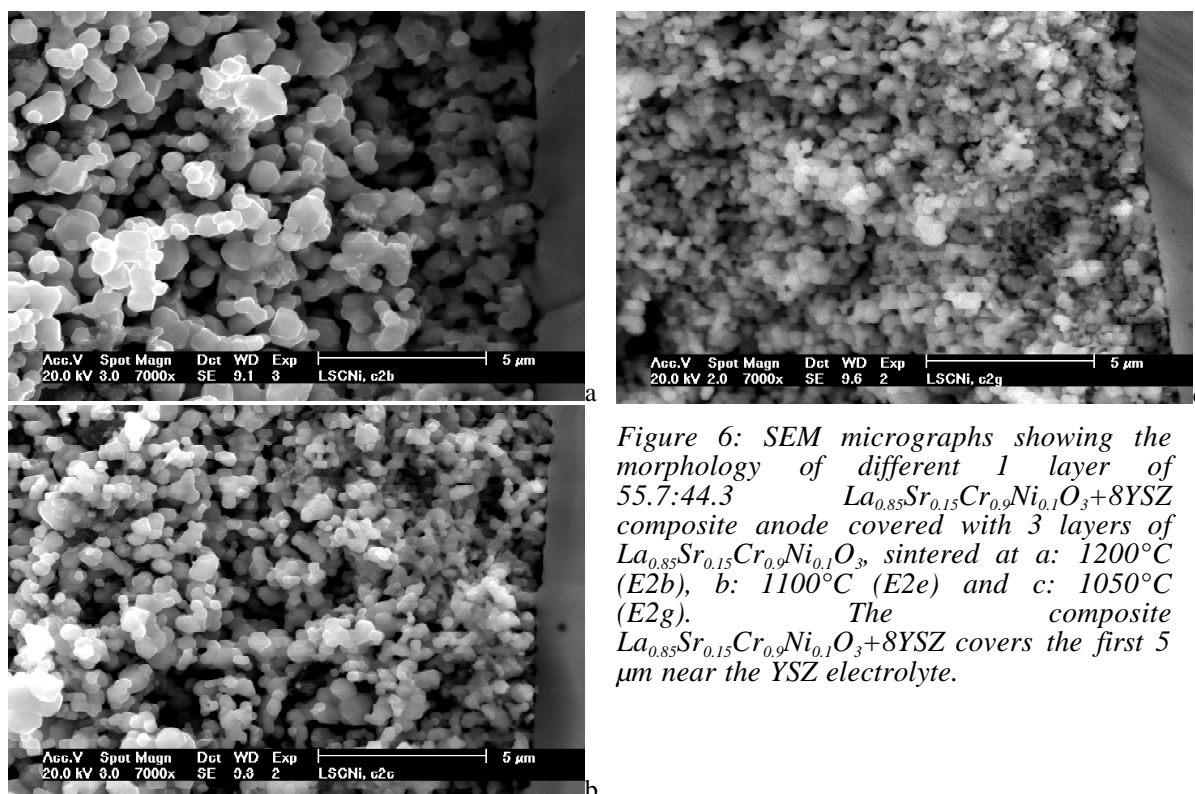


Figure 6: SEM micrographs showing the morphology of different 1 layer of 55.7:44.3 $\text{La}_{0.85}\text{Sr}_{0.15}\text{Cr}_{0.9}\text{Ni}_{0.1}\text{O}_3+8\text{YSZ}$ composite anode covered with 3 layers of $\text{La}_{0.85}\text{Sr}_{0.15}\text{Cr}_{0.9}\text{Ni}_{0.1}\text{O}_3$, sintered at: a: 1200°C (E2b), b: 1100°C (E2e) and c: 1050°C (E2g). The composite $\text{La}_{0.85}\text{Sr}_{0.15}\text{Cr}_{0.9}\text{Ni}_{0.1}\text{O}_3+8\text{YSZ}$ covers the first 5 μm near the YSZ electrolyte.

Effect of polarization on the cell performance

The impedance analysis of two sets of anodes, a LaCaCrMg (B29) and a LaSrCrMg (B21), sintered at 1100°C , show clearly the influence of polarization on the anode formation (Table 2). Prior to the passage of current, the polarization resistance, R_p , measured in humidified H_2 at 850°C , were of 19.5 and 21.5 Ωcm^2 , for the first and the second electrode respectively. After one night polarization, these resistances dropped to 2.3 and 1.7 Ωcm^2 respectively, by a factor of approximately 10 (see Figure 8). The summit frequencies tended to increase after polarization. The drop in the polarization resistance occurred in general after 1 h of polarization. This phenomenon is similar to that observed on LSM electrodes ⁷.

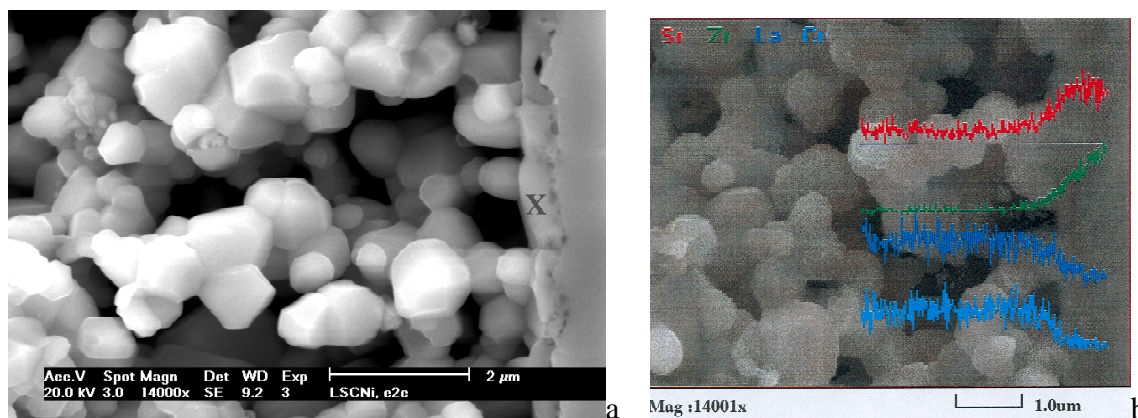


Figure 7: SEM micrographs of $\text{La}_{0.85}\text{Sr}_{0.15}\text{Cr}_{0.9}\text{Ni}_{0.1}\text{O}_3$ (E2c) anode showing a: a topotactic change at the interface (in the X region), and b: an EDAX linescan analysis of the same region, indicating possibly the formation of a SrZrO_3 phase (there is an uncertainty in the quantitative analysis of Sr and Zr as their EDAX peaks overlap).

Also, upon current flow, the impedance response showed an activated process, as the total R_p dropped by a factor of 2 between OCV and 400 mV in humidified H_2 (Figure 9). This correlates well with the overpotential-current evolution (Figure 10) where a net activation process is observed upon polarization. The impedance responses were best fitted by a three arcs

$LR_e(R_1Y_1)(R_2Y_2)(R_3Y_3)$ circuit, using the Zahner fitting software. Y_i is a constant phase element (CPE)

$$Y_i = Y_{i,0}(j\omega)^n \quad (1)$$

with $Y_{i,0}$ an admittance factor, j the imaginary unit, ω the angular frequency ($2\pi f$, f being the frequency), n the frequency power, R_e the series electrolyte resistance between the reference electrode and the working electrode, R_i a resistance, and L the current/potential collectors and instrumentation inductance. One physical interpretation of $Y_{i,0}$ is as a distributed capacitance, as when $n=1$, this value reduces to a capacitance, C . L , the inductance was added in this manner after trials made with ceramic resistors and capacitors, which were best interpreted by taking into account the current and potential leads' inductance. L was constant, with some variation between measurements. This simple equivalent circuit was chosen as no knowledge of the reaction mechanism was available. This approach condenses however the data and allows for their interpretation. The general values for n_1, n_2, n_3 and L were 0.76-0.9, 0.8-1, 0.85-0.9, and 643 nH, and the mean fitting error was of 0.1-0.4%, whereas the maximum error was of 1-4%.

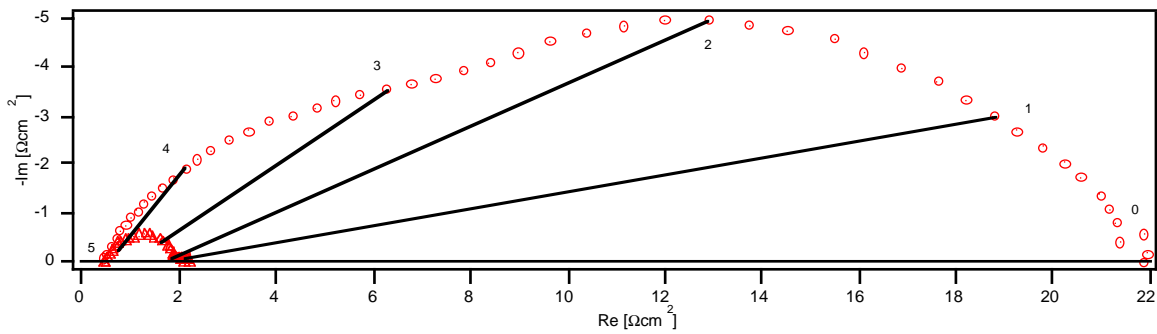


Figure 8: $\text{La}_{0.85}\text{Sr}_{0.15}\text{Cr}_{0.9}\text{Mg}_{0.1}\text{O}_3$ anode (B21). Effect of the cell polarization on the anode impedance at OCV. (O) initial anode impedance, after H_2 introduction at 850°C ; (Δ) the same impedance after polarization in H_2 . Inset numbers mark each decade in frequency.

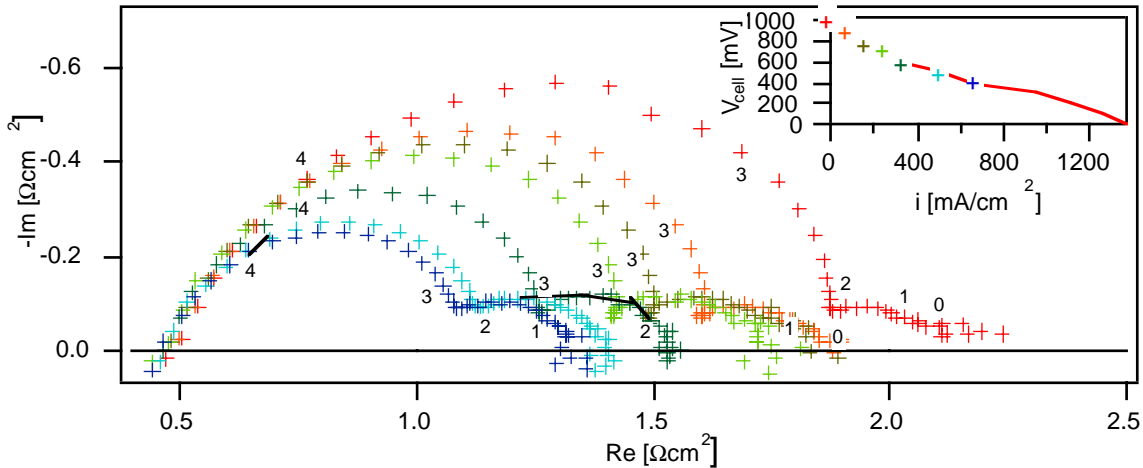


Figure 9: Electrocatalysis on $\text{La}_{0.85}\text{Sr}_{0.15}\text{Cr}_{0.9}\text{Mg}_{0.1}\text{O}_3$ anode (B21). The anode R_p decreases upon polarization at 1010, 900, 800, 700, 600, 500 and 400 mV in $\text{H}_2 + 3\%\text{H}_2\text{O}$, at 850°C . Inset numbers mark each decade in frequency.

When the anode was polarized, the series ohmic resistance tended to decrease (Figure 11). Between OCV and 400 mV, the current density rose to about $350 \text{ mA}/\text{cm}^2$, and the R_e was lowered by about 15%. This might be due to the increase of the anodic oxygen potential which would lead to an increase of the overall electronic conductivity of the electrode, as the electronic conductivity of the lanthanum chromites is of the p -type. For the LSrCMg, the conductivity in air was of $\approx 15 \text{ S}/\text{cm}$ whereas it dropped to only $1.3 \text{ S}/\text{cm}$ in humidified hydrogen (Table 2).

The evolution of R_1 - C_1 , R_2 - C_2 and R_3 - C_3 with the anodic overpotential is shown in Figure 16. R_1 and R_2 decreased while R_3 increased with the overpotential. C_1 , C_2 and C_3 also decreased with the polarization. Average summit frequencies, given as

$$f_i[\text{Hz}] = \frac{1}{2\pi R_i C_i}, \quad (2)$$

were of 10 kHz, 4 kHz and 23 Hz for the first, second and third arc respectively. Upon aging, all the R values increased at zero current, as well as C_1 and C_2 , C_3 being almost unchanged (Figure 13). This is due as previously discussed to the absence of the adhesive composite layer. The power output was observed consequently to decrease (Figure 12). Eventually, the degradation ceased and a stable value was reached (Figure 12). The evolution of R_3 and C_3 with the H_2O partial pressure (Figure 14), R_3 decreasing and C_3 slightly increasing, could be a hint of a gas conversion impedance⁹ (see Appendix A). This fact was confirmed by the absence of this third arc when a symmetrical cell configuration was used (see Figure 15).

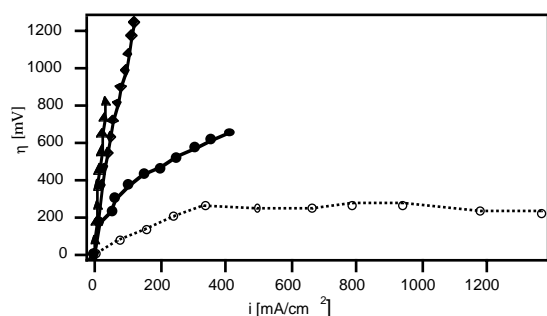


Figure 10: $\text{La}_{0.85}\text{Sr}_{0.15}\text{Cr}_{0.9}\text{Mg}_{0.1}\text{O}_3$ anode (B21). Overpotential in humidified H_2 and CH_4 , and in dry CO_2/CO (ratio ≈ 0.14), at 850°C . Aging time: H_2 , initial (\circ) and final (\bullet) performance, $P_{\text{CO}_2}/P_{\text{CO}} \approx 0.14$ (\blacktriangle) and CH_4 (\blacklozenge).

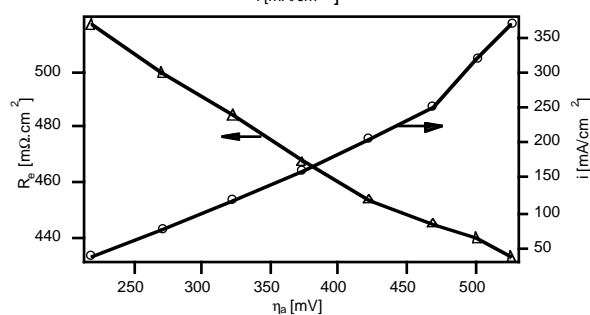


Figure 11: $\text{La}_{0.85}\text{Sr}_{0.15}\text{Cr}_{0.9}\text{Mg}_{0.1}\text{O}_3$ anode (B21). Overpotential effect on the series resistance, R_s , at 850°C . $\text{H}_2 + 3\%\text{H}_2\text{O}$.

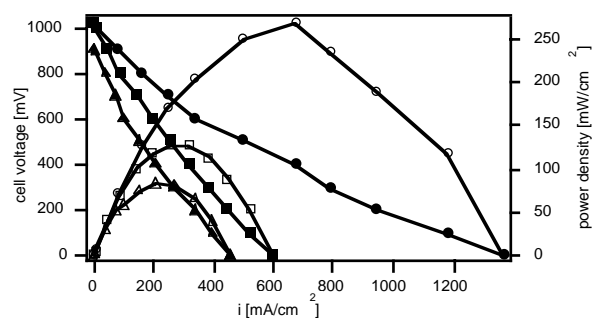


Figure 12: $\text{La}_{0.85}\text{Sr}_{0.15}\text{Cr}_{0.9}\text{Mg}_{0.1}\text{O}_3$ anode (B21). Aging effect on the stability of the anode power and current density output. $T=850^\circ\text{C}$, $\text{H}_2 + 3\%\text{H}_2\text{O}$. Aging time: 6h 35 (\bullet), 70h 45 (\blacktriangle) and 265h 50 (\blacksquare).

Effect of H_2 , CH_4 , H_2O , CO/CO_2 on LC polarization

The theoretical OCVs in the gas phase versus air were calculated using the HSC-4.1 gas phase thermodynamic equilibria calculation software. In $\text{H}_2 + 3\%\text{H}_2\text{O}$ estimates of -1139 mV at 850°C and -1035 mV at 900°C were obtained, while in $\text{CH}_4 + 3\%\text{H}_2\text{O}$ the values rose to -1260 mV at 850°C and -1290 mV at 900°C . The experimental OCV in hydrogen was typically of -1000 ~ -1030 mV (see for example Figure 1 and 3), an acceptable value in view of the open configuration of the testing set-up. In methane, the value was quite high, around -1200 mV (see for example Figure 1 and 3). These values were typical for all tests made in the unsealed configuration. The OCV in CH_4 was however higher than the expected OCVs calculated from previous catalytic measurements³ (Chapter 6). Measurements done in the sealed configuration with LCaCMg and LSrCMg electrodes gave on the contrary OCVs matching well these

predicted values in CH_4 ³ (Chapter 6). The measured OCV for LSrCMg was of 862 mV (Figure 16), matching well the previous estimate of 880 mV, based on the catalytic study. The low potential is not due to air leakage to the anode chamber, as the OCV in wet hydrogen was of -1089 mV, a value which did not change after contacting the anode with CH_4 (i.e., the process is reversible). Also, in this configuration, OCV measurements made as a function of the steam to carbon ratio ($\text{H}_2\text{O}/\text{CH}_4$) (Figure 16) and MS gas analysis of the anode gas exhaust in the case of LSrCMg indicated that the oxygen partial pressure was determined primarily by the $P_{\text{H}_2\text{O}}/P_{\text{H}_2}$ equilibrium from the $\text{H}_2 + 1/2 \text{O}_2 = \text{H}_2\text{O}$ reaction. The $\text{H}_2\text{O}/\text{H}_2$ ratio was of 3.4-3.9, while the ratio of CO_2/CO was of 0.6.

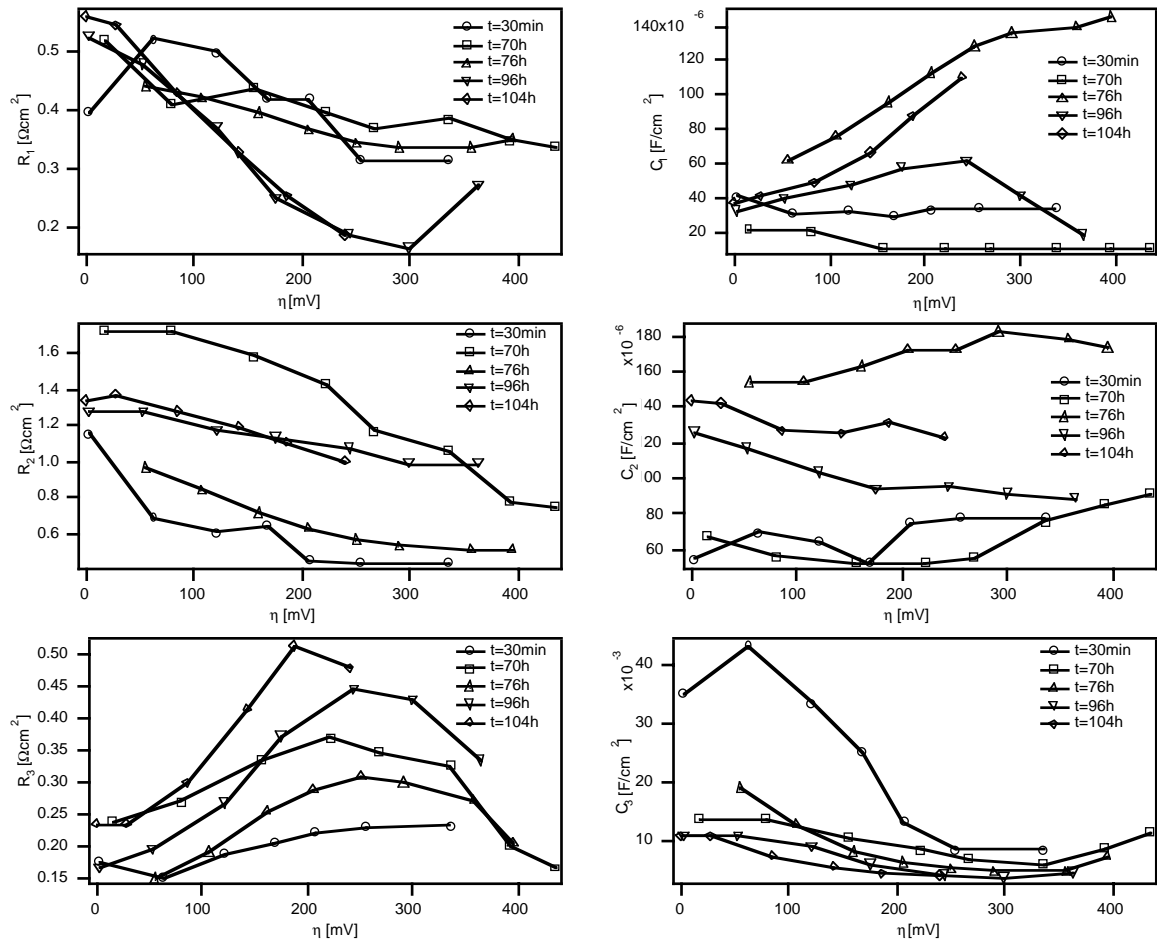


Figure 13: $\text{La}_{0.85}\text{Sr}_{0.15}\text{Cr}_{0.9}\text{Mg}_{0.1}\text{O}_3$ anode (B21). Polarization effect on the rate limiting processes, R_1 - C_1 , R_2 - C_2 and R_3 - C_3 . $T=850^\circ\text{C}$, in $\text{H}_2 + 3\%\text{H}_2\text{O}$.

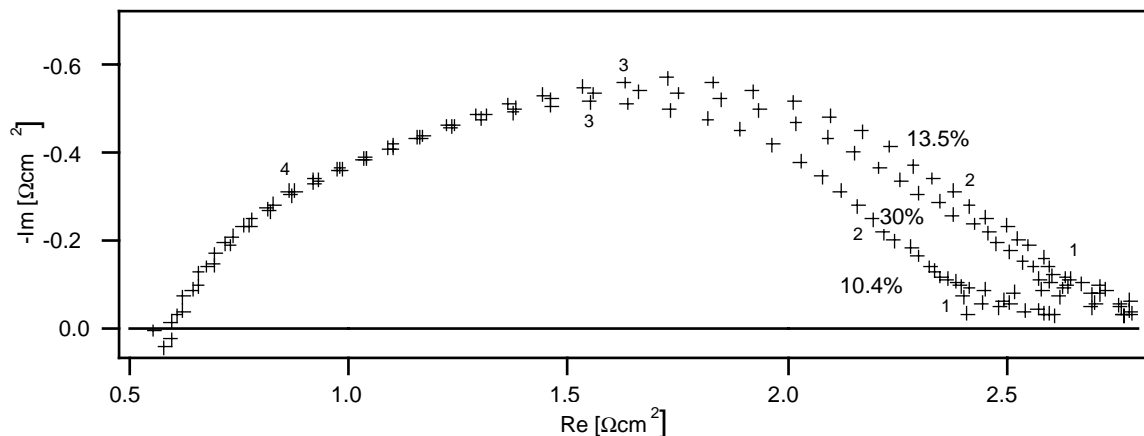


Figure 14: $\text{La}_{0.85}\text{Sr}_{0.15}\text{Cr}_{0.9}\text{Mg}_{0.1}\text{O}_3$ anode (B21). H_2O effect on the impedance spectra in H_2 , at OCV and 850°C . Inset numbers in % refer to the % of H_2O in H_2 .

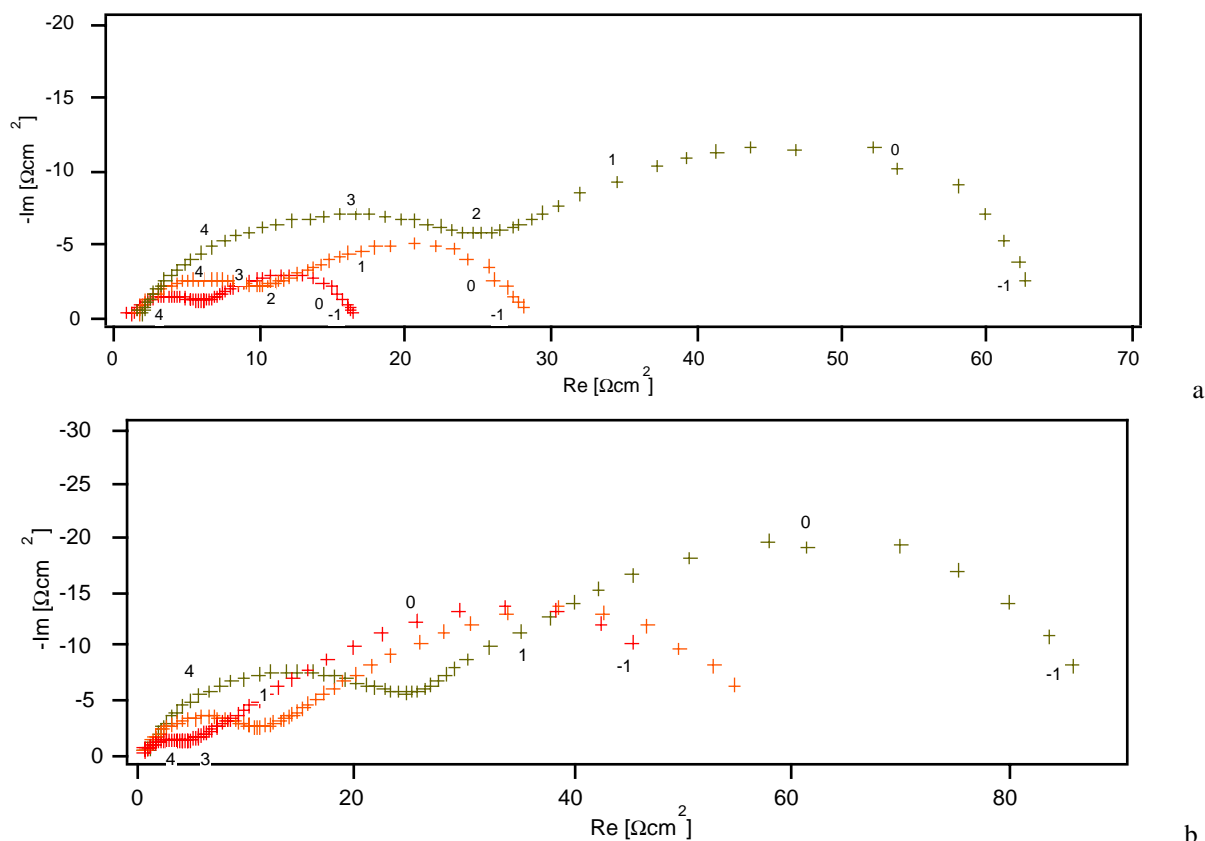


Figure 15: $\text{La}_{0.85}\text{Sr}_{0.15}\text{Cr}_{0.9}\text{Mg}_{0.1}\text{O}_3$ anode (B24). Effect of the working temperature on the initial (before polarization) OCV impedance spectra. a: H_2 , b: CH_4 , + 3% H_2O . Inset numbers mark each decade in frequency. Absence of gas conversion impedance (third arc) because of symmetrical setup.

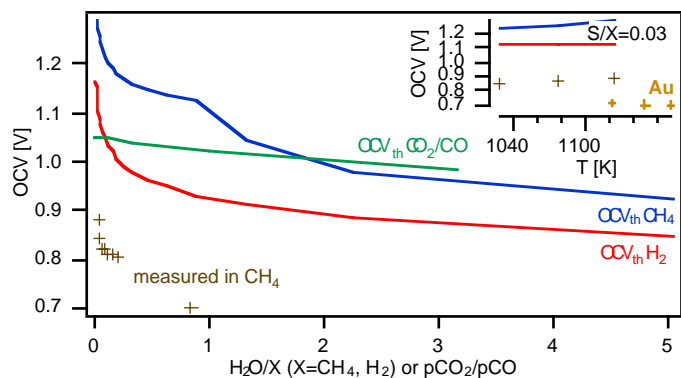
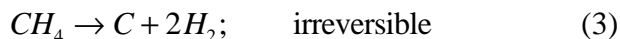


Figure 16: $\text{La}_{0.85}\text{Sr}_{0.15}\text{Cr}_{0.9}\text{Mg}_{0.1}\text{O}_3$ anode, in the sealed configuration (B30). OCV measurements as a function of the steam to carbon ratio (S/C) and temperature. The thermodynamic equilibria for different gases are also shown along with measured values for an Au electrode. 8YSZ plat of 110 μm , $R_e \approx 17.6 \Omega\text{cm}^2$, 22 mA/cm^2 at short circuit in humidified H_2 with an OCV of 1089 mV.

By considering the following reactions



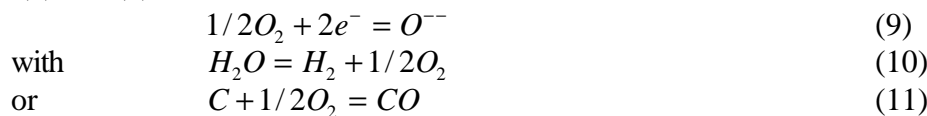
and



and



where equation (7) and (8) can be considered the contraction of



and considering CH_4 as an inert gas (like Ar) then using the measured exhaust gas composition (H_2 , H_2O , CO and CO_2), the thermodynamic calculation (HSC-4.1) gave an OCV between 858 and 865 mV (Figure 16), also in agreement with the other values. From these calculations, the carbon activity was estimated to $\sim 10^{-5}$, hence confirming the absence of carbon deposition. Also, the estimated CH_4 conversion was of 0.3% in good agreement with the catalytic steam-reforming tests (0.22%). LCaCMg anodes performed equivalently (Figure 17). The situation was similar for Au anodes (inset Figure 16), where an OCV of ≈ 700 mV was slowly attained in humidified CH_4 . Non-ideal electromotive forces were also observed in literature on Au electrodes deposited over zirconia for sensors with hydrocarbon gases and O_2 ^{10, 11}. This mixed potential that developed, being dependent on kinetic factors, is expected to be a strong function of the electrode material. Thus, the discrepancy between the expected and actual OCV in the open set-up could be related to some methane pyrolysis over the metallic flange, rather than coking over the LC perovskites as no carbon build up was observed by temperature programmed oxidation analysis (TPO) in catalytic runs in humidified CH_4 over the same catalysts³ (Chapter 3). Dry hydrogen is then expected to reach the anodes after the pyrolysis. Nevertheless, all tests made in methane gave the same OCVs, independently of the anode composition, so that this phenomenon is not expected to have any influence when comparing the different substituents.

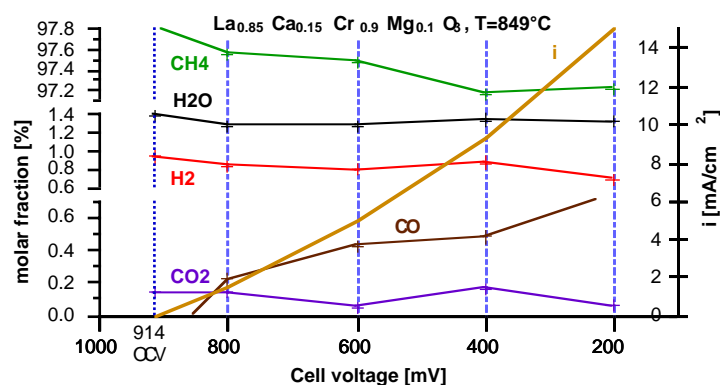


Figure 17: $\text{La}_{0.85}\text{Ca}_{0.15}\text{Cr}_{0.9}\text{Mg}_{0.1}\text{O}_3$ anode (B20). MS analysis of the gas composition at the outlet of the sealed cell. Cell voltage effect on the CH_4 conversion at 850°C . The low current density is thought to stem from bad current collection in the free standing contacts. $R_e \approx 17.6 \Omega\text{cm}^2$, 8YSZ plate of $110 \mu\text{m}$ and $30 \text{mlN}/\text{min}$ CH_4 flow.

The performance of LC anodes in humidified H_2 , CH_4 and dry CO/CO_2 fuels is depicted in Figures 10 and 18, in the case of the L SrCMg system. The power output increases and the overpotential decreases in the order of $\text{CO}-\text{CH}_4-\text{H}_2$. The R_p changed at 850°C from 9.2 to 6.1 to $1.7 \Omega\text{cm}^2$ from CO to CH_4 to H_2 . This indicates that the electrochemical oxidation rate of H_2 was higher than for CH_4 which was in turn higher than for CO . Increasing the CO_2/CO ratio reduced further the cell performance (Figure 19), with the R_p increasing to $17.2 \Omega\text{cm}^2$ – the OCV passed from 1003 to 882 mV, as expected. This indicates some inhibiting effect of CO_2 , as observed earlier³. The inhibition could be related to the surface segregation of Ca or Sr on these materials, as these elements are basic sites capable of interacting with CO_2 to form carbonates. The latter could block the catalytically active sites for oxidation. Such inhibition was reported on La_2O_3 catalysts¹² and interpreted as the interaction of CO_2 with active oxide species responsible for methane and oxygen activation. Moreover, CO_2 reforming was observed to be quite low with the basic LC compounds³ (Chapter 6).

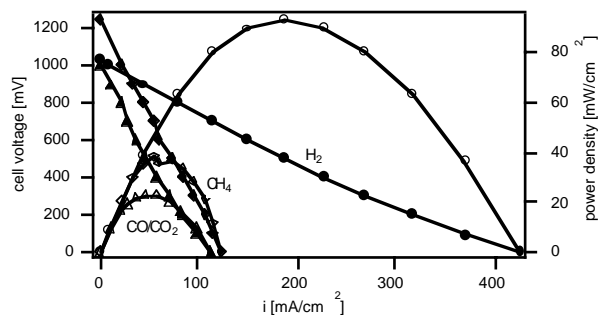


Figure 18: $\text{La}_{0.85}\text{Sr}_{0.15}\text{Cr}_{0.9}\text{Mg}_{0.1}\text{O}_3$ anode (B21). Effect of the gas composition on the anode performance. In : H_2 and CH_4 , + 3% H_2O and dry CO_2/CO (ratio of 0.14), at 850°C.

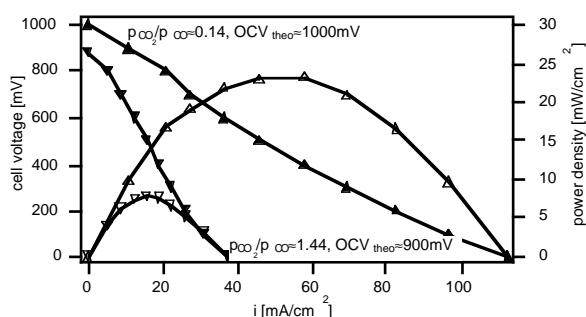


Figure 19: $\text{La}_{0.85}\text{Sr}_{0.15}\text{Cr}_{0.9}\text{Mg}_{0.1}\text{O}_3$ anode (B21). Effect of the CO_2/CO ratio on the cell performance at 850°C. Total fuel flowrate of 200 ml/min.

The impedance spectra obtained for humidified H_2 and CH_4 have similar appearances, as shown for the case of a symmetrical L SrCrMg cell in Figure 15. In this case two arcs were observed with summit frequencies of about 4.5 kHz and 45 Hz in H_2 and 4 kHz and 18 Hz in CH_4 at 850°C. The second arc seemed the most sensitive to the gas atmosphere, as R_1 and C_1 were similar in both humidified H_2 and CH_4 , while R_2 was about 5.6 times higher in CH_4 ($2.5 \Omega\text{cm}^2$ in H_2 and $14 \Omega\text{cm}^2$ in CH_4) respectively, while C_2 was 2.6 time less in CH_4 , $702 \mu\text{F}$ in H_2 and $275 \mu\text{F}$ in CH_4 . Water was previously observed to have almost no effect on the catalytic activity of L SrCrMg and L CaCrMg . In the electrochemical experiment of Figure 16, water modified the OCV values as the $\text{H}_2\text{O}/\text{H}_2$ ratio was changed at higher humidity values. Also, the higher the working temperature, the better the cell performance, with a temperature limit of about 850°C, below which the performance is poor, in both H_2 and CH_4 (Figure 20). The effect of water on the polarization losses were almost negligible (see Figure 14 for H_2 and 21 for CH_4). In methane, the effect of water was only observed at high current densities (Figure 21). This goes in parallel with the previous report³ (Chapter 6) of the poor steam reforming ability of the basic LC oxides in catalytic mode.

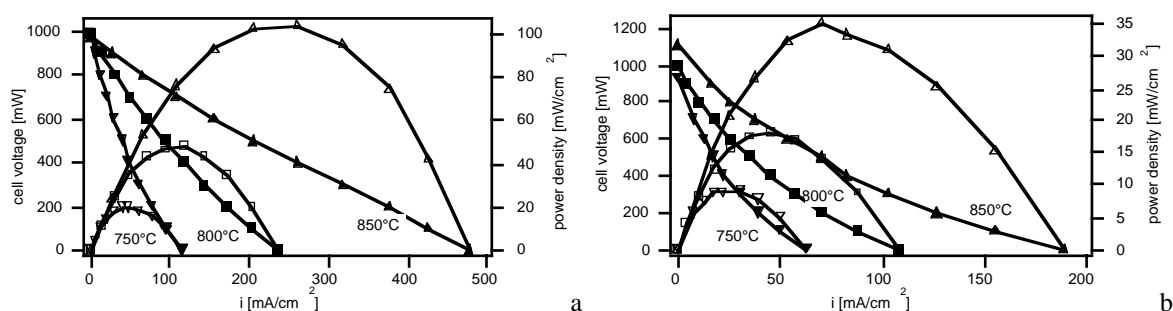


Figure 20: $\text{La}_{0.85}\text{Ca}_{0.15}\text{Cr}_{0.9}\text{Mg}_{0.1}\text{O}_3$ anode (B29). Effect of the temperature on the anode performance in a: H_2 and b: CH_4 , 3% H_2O .

Effect of the substituent on the performance of LC anodes

Four different lanthanum chromite anodes were considered for the analysis of the substitution effect: LaCrO_3 as base material, $\text{La}_{0.85}\text{Sr}_{0.15}\text{CrO}_3$, $\text{LaCr}_{0.9}\text{Co}_{0.1}\text{O}_3$ and $\text{LaCr}_{0.9}\text{Ni}_{0.1}\text{O}_3$. These electrodes were made of 1 composite $\approx 56:44$ lanthanum chromite-based powder:YSZ layer, and 3 layers of the lanthanum chromite-based powder, and were sintered at the optimal temperature of 1100°C. As discussed before, this structure allowed a higher stability

and a better adhesion of the electrode. The composite layer thickness was estimated by SEM-EDAX analysis to 5 μm in all cases. The electrodes morphology observed were quite similar, showing the fine composite layer, and the coarser lanthanum chromite-based layer (Figure 22). The electrode grains followed roughly the initial particle size distribution of the starting lanthanum chromite-based powders, i.e., d_{50} of 0.8 μm , 1.0 μm , 2.1 μm and 2.1 μm for LaCrO_3 , $\text{La}_{0.85}\text{Sr}_{0.15}\text{CrO}_3$, $\text{LaCr}_{0.9}\text{Co}_{0.1}\text{O}_3$ and $\text{LaCr}_{0.9}\text{Ni}_{0.1}\text{O}_3$. All these electrodes stuck quite well on the YSZ electrolyte substrate, even after electrochemical testing. These tests were made in the unsealed configuration set-up.

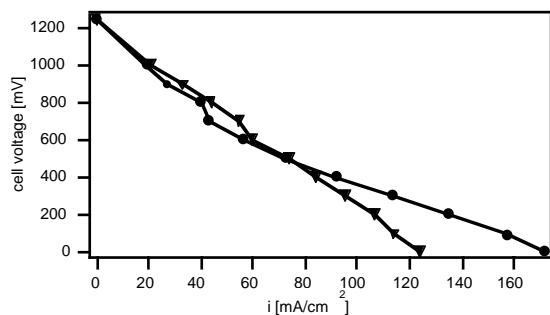


Figure 21: $\text{La}_{0.85}\text{Sr}_{0.15}\text{Cr}_{0.9}\text{Mg}_{0.1}\text{O}_3$ anode (B21). H_2O effect on CH_4 oxidation at 850°C . (▼) 4.8% H_2O ($S/C \approx 0.05$) and (●) 10.4% H_2O ($S/C \approx 0.116$).

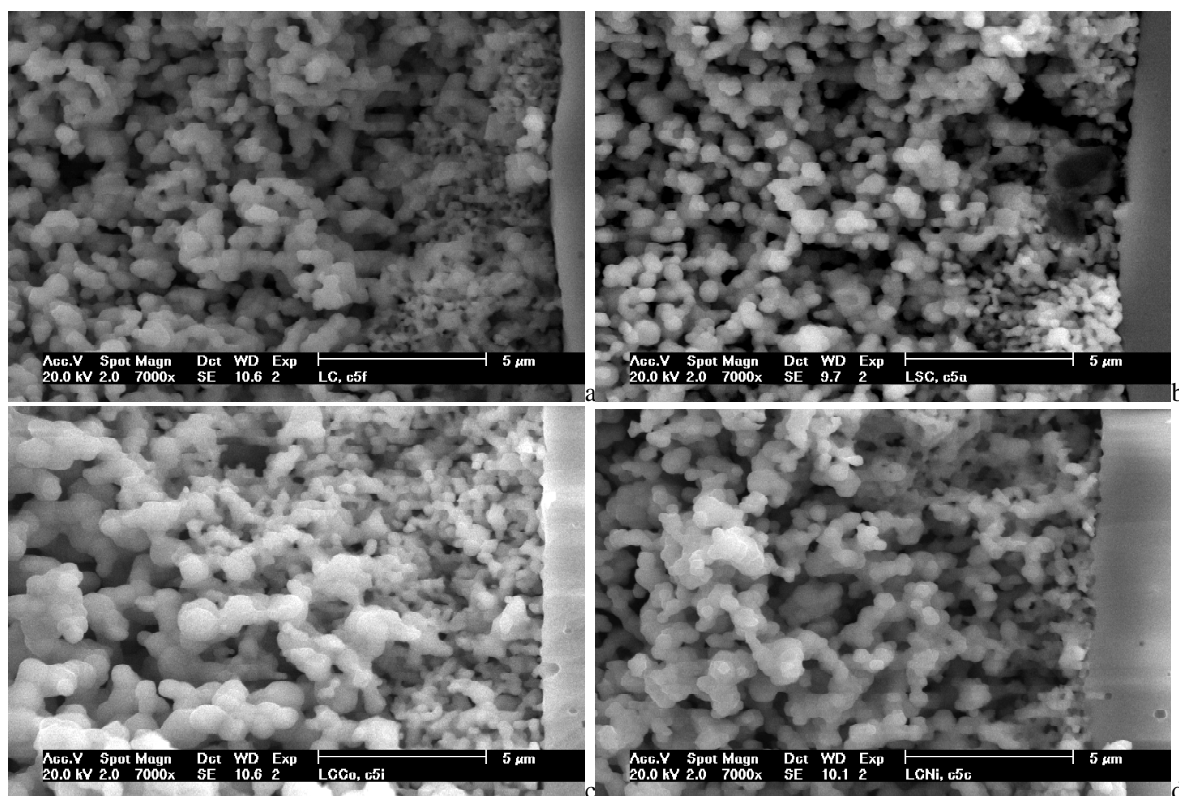


Figure 22: SEM micrographs showing the morphology of different 1 layered 56:44 lanthanum chromite + 8YSZ, + 3 layered lanthanum chromite composite anodes, sintered at 1100°C for 4 h. The thickness of the composite lanthanum chromite + 8YSZ was 5 μm near the YSZ electrolyte. a: LaCrO_3 (E5f), b: $\text{La}_{0.85}\text{Sr}_{0.15}\text{CrO}_3$ (E5a), c: $\text{LaCr}_{0.9}\text{Co}_{0.1}\text{O}_3$ (E5I) and d: $\text{LaCr}_{0.9}\text{Ni}_{0.1}\text{O}_3$ (E5e).

The potential-current and power curves were affected by the substituent in LaCrO_3 (Figure 23). Globally, upon Sr, Co or Ni substitution, the LaCrO_3 base material activity increased both in humidified hydrogen and methane. The R_e and R_p were lowered significantly in the trend $\text{LC} > \text{LCCo} > \text{LCNi} > \text{LSrC}$. The R_e was lowered by a factor of 19 at 840°C and 17.6 at 900°C in humidified H_2 , and 11.8 at 840°C and 22 at 900°C in humidified CH_4 (Table 2). For the R_p , the factor was of 13 at 840°C and 11 at 900°C in humidified H_2 , and 9.6 at 840°C and 6.2 at 900°C in humidified CH_4 from LC to LSrC (Table 2). The evolution of the R_e , corrected from the

expected ohmic loss of half of a $150\ \mu\text{m}$ thick Kerafol 8YSZ electrolyte, as a function of the electric conductivity of the different lanthanum chromites, was linear in both temperature ranges (Figure 24). The similar trend was observed with the R_p . The higher the electronic conductivity, the lower the R_p . This indicates clearly that the electronic conductivity has an influence on the global performance of these anodes.

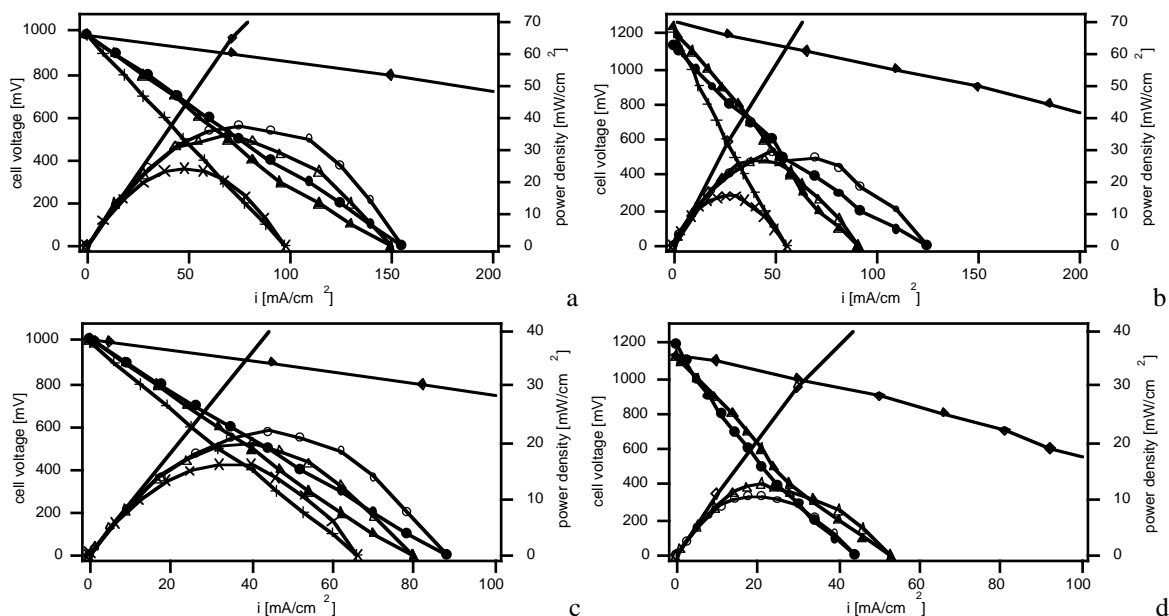


Figure 23: 1 layer of 56:44 lanthanum chromite:YSZ composite anode covered with 3 layers of LC sintered at $1100^\circ\text{C}/4\text{h}$. Substituent effect on the potential-current and power curves, in 3% H_2O at 900°C , a: H_2 and b: CH_4 , and 840°C , c: H_2 and d: CH_4 . (+, ×) LaCrO_3 (E5f), (◇, ◆) $\text{La}_{0.85}\text{Sr}_{0.15}\text{CrO}_3$ (E5a), (Δ, ▲) $\text{LaCr}_{0.9}\text{Co}_{0.1}\text{O}_3$ (E5i) and (●, ○) $\text{LaCr}_{0.9}\text{Ni}_{0.1}\text{O}_3$ (E5e). The $\text{La}_{0.85}\text{Sr}_{0.15}\text{CrO}_3$ anode performance is not fully shown, and is used to indicate the difference existing with the B-site substituted LCs.

The substitution effect on the LaCrO_3 electrode performance is better depicted by the overpotential curves in Figure 25. The overpotential loss trend was $\text{LC} \approx \text{LCCo} > \text{LCNi} > \text{LSrC} > \text{LSrCNi}$ in humidified H_2 at 840°C and 900°C and humidified CH_4 at 840°C , and $\text{LC} > \text{LCCo} > \text{LCNi} > \text{LSrC} > \text{LSrCNi}$ in CH_4 at 900°C . The overpotential losses of LC and LCCo laid very near together even though the electronic conductivity of LCCo was 6 times higher than for LC. This indicates that the substituent plays also an important role in the electrocatalytic activity. Previously, in Chapter 6, the catalytic activity of these different oxides were assessed in methane rich gas mixtures (5:1 $\text{CH}_4:\text{O}_2$, 5:1:0.6 $\text{CH}_4:\text{O}_2:\text{CO}_2$ and 56:x:y $\text{CH}_4:\text{Ar}:\text{H}_2\text{O}$ ($x+y=44$))³. It was observed that the activity, expressed as a turn-over frequency (TOF), followed the order of $\text{LC} \approx \text{LCCo} < \text{LSrC} < \text{LCNi} < \text{LSrCNi}$ at 850°C in wet CH_4 . A direct relationship between the electronic and catalytic activity and the electrocatalytic performance is thus evidenced here.

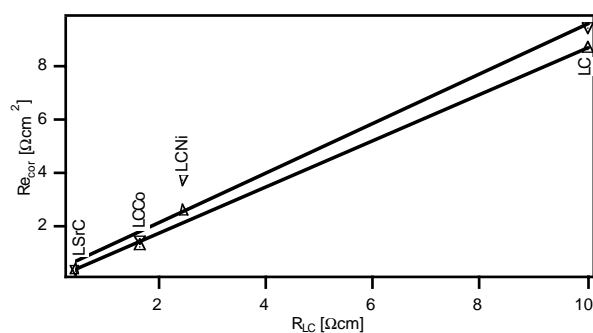


Figure 24: Evolution of the corrected electrolyte resistance, $R_{e,corr}$ on the anode side, in function of the lanthanum chromites conductivity (measured in Chapter 3) showing an additional ohmic drop in the adhesive layer. The $150\ \mu\text{m}$ thick 8YSZ Kerafol electrolyte is supposed to give an ohmic drop of $0.38\ \Omega\text{cm}^2$ and $0.27\ \Omega\text{cm}^2$ at 850°C (▽) and 900°C (Δ) respectively.

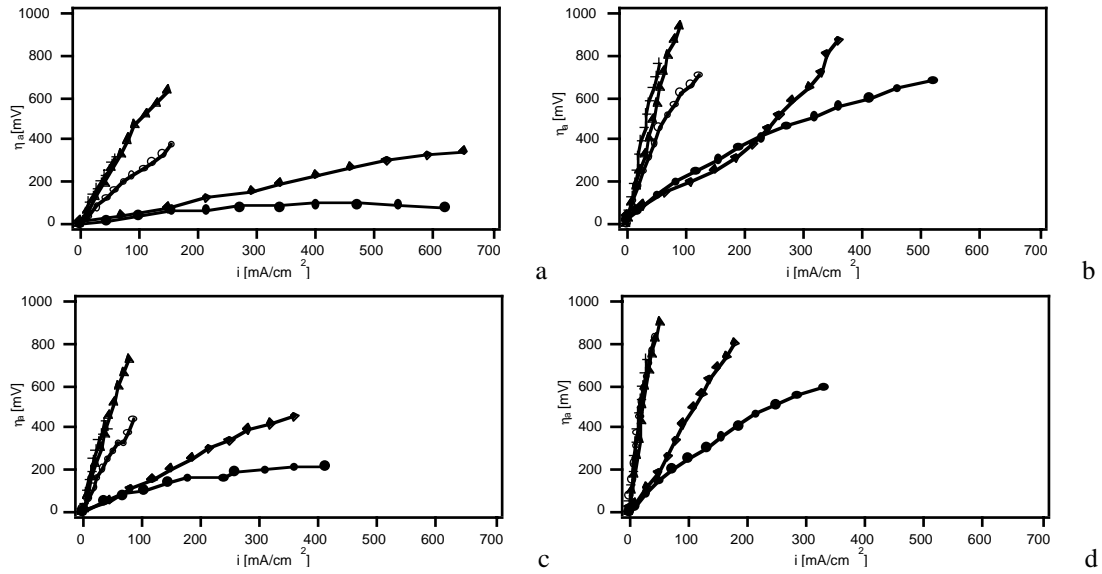


Figure 25: 1 layer of 56:44 lanthanum chromite:YSZ composite anode covered with 3 layers of LC sintered at $1100^\circ\text{C}/4\text{h}$. Substituent effect on the overpotential curves, in 3% H_2O at 900°C , a: H_2 and b: CH_4 , and 840°C , c: H_2 and d: CH_4 . (+) LaCrO_3 , (E5f), (◆) $\text{La}_{0.85}\text{Sr}_{0.15}\text{CrO}_3$ (E5a), (▲) $\text{LaCr}_{0.9}\text{Co}_{0.1}\text{O}_3$ (E5i), (○) $\text{LaCr}_{0.9}\text{Ni}_{0.1}\text{O}_3$ (E5e) and (●) $\text{La}_{0.85}\text{Sr}_{0.15}\text{Cr}_{0.9}\text{Ni}_{0.1}\text{O}_3$ (E2e).

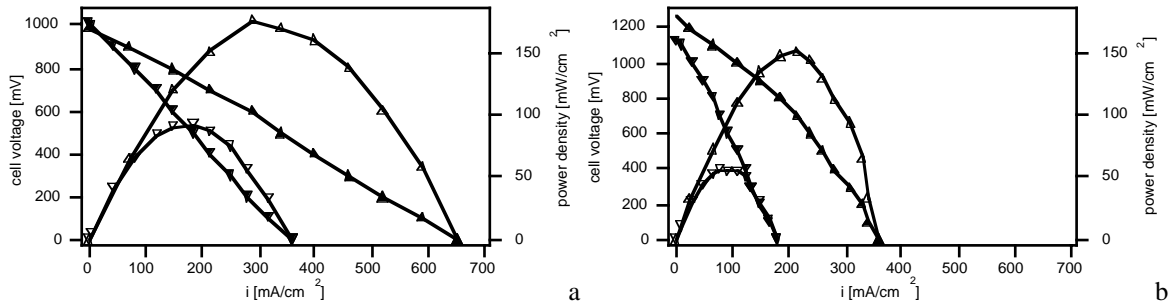


Figure 26: 1 layer of 56:44 $\text{La}_{0.85}\text{Sr}_{0.15}\text{CrO}_3+8\text{YSZ}$ composite anode covered with 3 layers of $\text{La}_{0.85}\text{Sr}_{0.15}\text{CrO}_3$ (E5a), sintered at 1100°C . Potential-current curves in a: H_2 and b: CH_4 , in 3% H_2O , at a working temperature of (▲, △) 900°C , and (▼, ▽) 840°C .

Ni substitution is further observed to enhance the performance of the cell in methane. By addition of Ni on the Cr site of L_{Sr}C, its performance in CH_4 increased markedly (compare Figure 3 and 26). Whereas the short circuit current was of $650\text{ mA}/\text{cm}^2$ in humidified H_2 and $350\text{ mA}/\text{cm}^2$ in humidified CH_4 over a L_{Sr}C anode, it was of $620\text{ mA}/\text{cm}^2$ in H_2 , whereas of $520\text{ mA}/\text{cm}^2$ in CH_4 over L_{Sr}CNi at 900°C . Methane is thus better activated over the Ni substituted compounds. In this case, the power outputs were similar in hydrogen and methane.

A trial has been made to further increase the activity of L_{Sr}CNi anode by adding one more layer made of $\text{LaCr}_{0.5}\text{Ni}_{0.5}\text{O}_3$. No effect of this layer was observed in hydrogen nor methane (Table 2).

Also, the difference between A-site substituents, Ca and Sr, lies in the difference in R_p , with a lower value for Sr substitution ($2.3\ \Omega\text{cm}^2$ for Ca versus $1.7\ \Omega\text{cm}^2$ for Sr, Table 2). Beside that, the previous thermodynamic calculations (Chapter 7) showed the higher stability of the Sr versus Ca-substituted LC and the increasing solubility of Sr in reducing atmospheres⁴. However, the sintering process of Ca versus Sr incorporated in LaCrO_3 is known to be more favorable due to the lower melting temperature of CaCrO_4 or the like ($1000\text{--}1020\text{--}1120^\circ\text{C}$ ^{13, 14}) than for SrCrO_4 (1253°C ^{14, 15}). If secondary phases are left behind during the powder preparation and the anode sintering, these phases would then react readily with YSZ to form

SrZrO_3 ^{3,4}. B-site substituted LC are expected to be more stable, as their demixing seems to be hindered kinetically^{4,16}.

Effect of the composite layer composition on the performance of LC anodes

The 44% YSZ composite anodes were observed to be more stable over time than the ones without YSZ (0%) as exposed in the case of L_{Sr}CNi (compare Figure 1-2 and 3-4). This was also observed for the L_{Sr}C anodes. However, the initial performance of these L_{Sr}C and L_{Sr}CNi anodes were higher in the non-composite form. Indeed, lower R_p and R_e were observed (Table 2), giving rise to a higher power output. These values degraded however very rapidly by a factor of 2.25 and 1.2 respectively. This loss in performance was predominantly due to delamination. Further, LC lacking A-site substituent (Ca or Sr) were very sensitive to delamination and their power output was hence reduced (e.g., Figure 27 for LCMg).

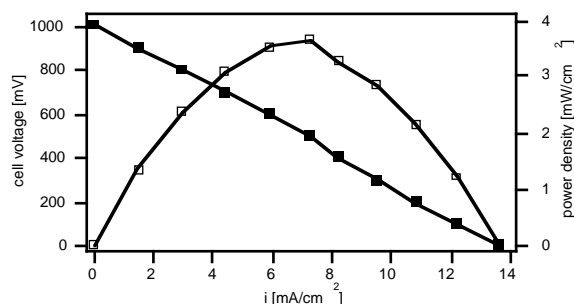


Figure 27: $\text{LaCr}_{0.9}\text{Mg}_{0.1}\text{O}_3$ anode (B41). Very low power output is obtained without an intermediate adhesive layer. $T = 830^\circ\text{C}$ in wet H_2 .

The two extremes used in the composite anodes were 0% YSZ and 44% YSZ. A 22% YSZ composite anode, the lower limit allowed for a percolating structure¹⁷, was also investigated in the case of the L_{Sr}CNi anode. Figure 28 shows the potential-current and the power output of the cell in humidified H_2 or CH_4 at different temperatures. The short circuit current and the power output were increased by a factor of 1.43 in CH_4 , and by 4.44 in H_2 at 840°C , when compared with the 44% YSZ composite anode. As a result of a high current density, the passage of current induced a local increase of the anode temperature (Figure 29a) as measured by the thermocouple placed beneath the electrode (see Chapter 2, Figure 2).

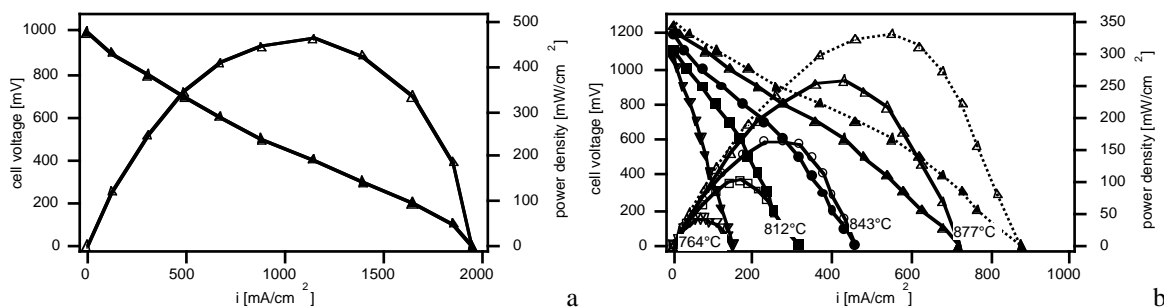


Figure 28: 1 layer of 78.2:21.8 $\text{La}_{0.85}\text{Sr}_{0.15}\text{Cr}_{0.9}\text{Ni}_{0.1}\text{O}_3 + 8\text{YSZ}$ composite anode covered with 3 layers of $\text{La}_{0.85}\text{Sr}_{0.15}\text{Cr}_{0.9}\text{Ni}_{0.1}\text{O}_3$ anode (E7b), sintered at 1100°C . Potential-current curves in a: H_2 (at 874°C) and b: $\text{CH}_4 + 3\% \text{H}_2\text{O}$. Two curves for $T=877^\circ\text{C}$ are shown: one taken after 1 h (dotted line), the other after 136 h

In this system, the ohmic resistances are lowered significantly, by a factor of 3. However these losses are still higher than the expected losses for a $150 \mu\text{m}$ 8YSZ Kerafol (e.g., $0.38 \Omega\text{cm}^2$ at 850°C). The temperature dependence of these losses is given in Figure 29b. An activation energy of $55 \pm 5 \text{ kJ/mol}$ was measured, a value lower than the expected 77 kJ/mol for 8YSZ Kerafol plates, showing still the effect of the electrode conductivity on R_e . On the other hand, the anode overpotentials were significantly lowered (Figure 30) compared to the 0% and 44 YSZ extremes (Figures 2 and 4). This cell configuration sustained direct CH_4 oxidation at 877°C for 136 h, almost without degradation (a small degradation was observed in the first 24 h). The addition of 22% YSZ seemed thus to favor the performance of the anode.

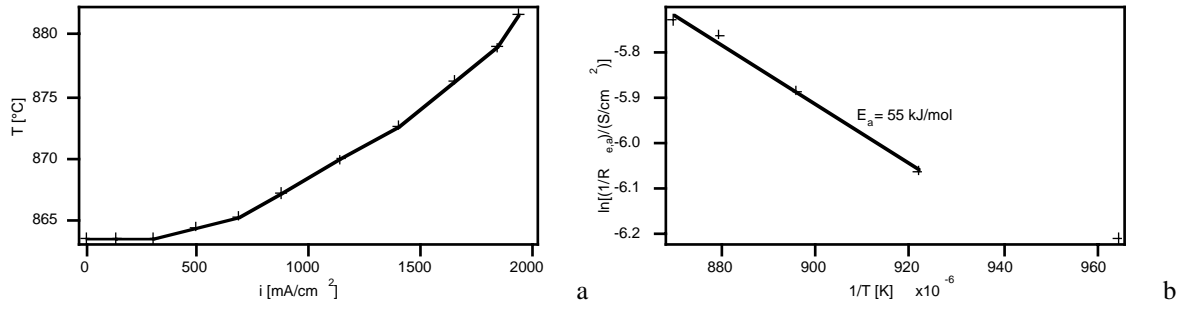


Figure 29: 1 layer of 78.2:21.8 $\text{La}_{0.85}\text{Sr}_{0.15}\text{Cr}_{0.9}\text{Ni}_{0.1}\text{O}_3$ +8YSZ composite anode covered with 3 layers of $\text{La}_{0.85}\text{Sr}_{0.15}\text{Cr}_{0.9}\text{Ni}_{0.1}\text{O}_3$ composite anode (E7b), sintered at 1100°C . a: The increase of the anode temperature as a function of the current density in $\text{H}_2 + 3\% \text{H}_2\text{O}$ at 874°C ; b: The temperature dependence of the anodic electrolyte resistance R_e in $\text{CH}_4 + 3\% \text{H}_2\text{O}$.

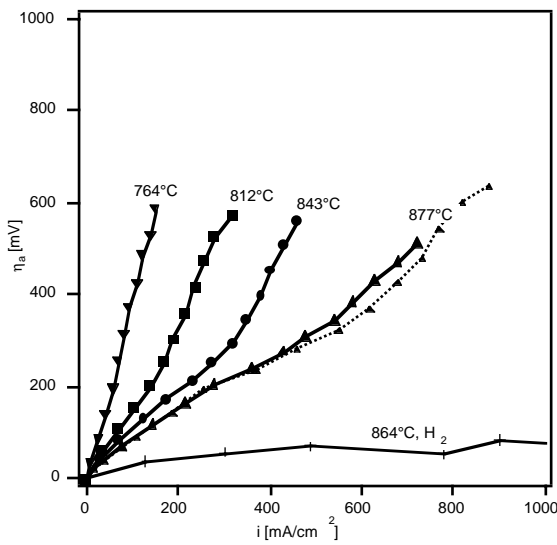


Figure 30: 1 layer of 78.2:21.8 $\text{La}_{0.85}\text{Sr}_{0.15}\text{Cr}_{0.9}\text{Ni}_{0.1}\text{O}_3$ +8YSZ composite anode covered with 3 layers of $\text{La}_{0.85}\text{Sr}_{0.15}\text{Cr}_{0.9}\text{Ni}_{0.1}\text{O}_3$ (E7b), sintered at 1100°C . Overpotential curves in H_2 (at 874°C) and $\text{CH}_4 + 3\% \text{H}_2\text{O}$.

Effect of the anode thickness on the overall performance

The anode thickness deposited above the composite electrode was reduced from 3 to 1 layer. The anode performance showed to increase as exposed in Figure 31 when compared to the case of 3 layers (Figure 3). However, the long term stability was poor. The time degradation of R_e was lower than that of R_p , indicating that a small degradation of R_e modifies R_p drastically.

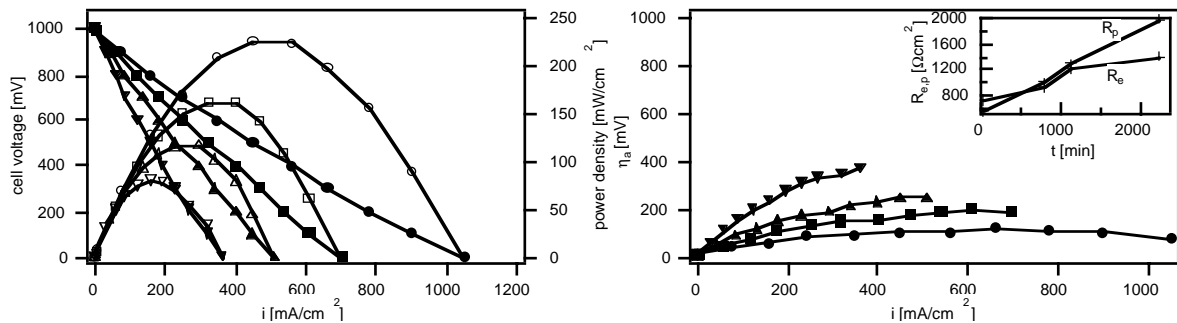


Figure 31: 1 layer of 55.7:44.3 $\text{La}_{0.85}\text{Sr}_{0.15}\text{Cr}_{0.9}\text{Ni}_{0.1}\text{O}_3$ +8YSZ composite anode covered with 1 layer of $\text{La}_{0.85}\text{Sr}_{0.15}\text{Cr}_{0.9}\text{Ni}_{0.1}\text{O}_3$ (E7c). Stability of the system in $\text{H}_2 + 3\% \text{H}_2\text{O}$ at 900°C . Effect of time on the stability: (O, ●) 0.8 h, (□, ■) 13 h (Δ, ▲) 19 h and (▽, ▼) 38 h.

Discussion - nature of the electrode reaction

The sintering temperature and the incorporated elements were shown to have an effect on the anodic electrolyte resistance. An optimum temperature of 1100°C was necessary to stick efficiently the electrode on the YSZ electrolyte and to prevent the formation of a topotactic reaction leading to SrZrO_3 . Sintering at a lower temperature lead to the delamination of the electrode. A better stability was further obtained by adding an adhesion layer in between the LC anode and YSZ. The series resistance was thus observed to be very sensitive to the nature of the interface (about $1 \Omega\text{cm}^2$ for the 0% and 44% YSZ composite adhesive layer and $0.32 \Omega\text{cm}^2$ for the 22% YSZ composite adhesive layer (see Table 2)). An additional ohmic loss was also stemming from the low conductivities of these perovskites. From the measured electronic conductivity in reducing conditions a $200 \text{ m}\Omega\text{cm}^2$, $25 \text{ m}\Omega\text{cm}^2$, $16 \text{ m}\Omega\text{cm}^2$ and $11 \text{ m}\Omega\text{cm}^2$ loss are expected for dense LC, LCNi, LCCo and LSrC electrodes of $100 \mu\text{m}$ thickness and 1 cm^2 surface area respectively. Due to the porosity of the working electrodes, an ohmic loss higher by a factor of about 10 could be expected¹⁸ (i.e. 2000, 250, 160 and $110 \text{ m}\Omega\text{cm}^2$).

Table 3: Summary of the R_p activation energies.

Anode composition	Cell Nr	Sintering temperature [$^\circ\text{C}$]	$R_p E_a$ [kJ/mol]		E_a [kJ/mol]	
			$\text{H}_2+3\%\text{H}_2\text{O}$	$\text{CH}_4+3\%\text{H}_2\text{O}$	σ_e , air	σ_e , H_2
$\text{La}_{0.85}\text{Sr}_{0.15}\text{Cr}_{0.9}\text{Ni}_{0.1}\text{O}_3$	E2c	1200	116		9.7	32.3
$\text{La}_{0.85}\text{Sr}_{0.15}\text{Cr}_{0.9}\text{Ni}_{0.1}\text{O}_3$	E2d	1100				
$\text{La}_{0.85}\text{Sr}_{0.15}\text{Cr}_{0.9}\text{Ni}_{0.1}\text{O}_3$	E2f	1050		19		
$\text{La}_{0.85}\text{Sr}_{0.15}\text{Cr}_{0.9}\text{Ni}_{0.1}\text{O}_3$	E7b	1100				
$\text{La}_{0.85}\text{Sr}_{0.15}\text{Cr}_{0.9}\text{Ni}_{0.1}\text{O}_3$	E2b	1200	87	56		
$\text{La}_{0.85}\text{Sr}_{0.15}\text{Cr}_{0.9}\text{Ni}_{0.1}\text{O}_3$	E2e	1100	186			
$\text{La}_{0.85}\text{Sr}_{0.15}\text{Cr}_{0.9}\text{Ni}_{0.1}\text{O}_3$	E2g	1050	104			
$\text{La}_{0.85}\text{Sr}_{0.15}\text{Cr}_{0.9}\text{Ni}_{0.1}\text{O}_3$	E5h	1100	49?			
$\text{La}_{0.85}\text{Sr}_{0.15}\text{Cr}_{0.9}\text{Ni}_{0.1}\text{O}_3$	E7c	1100				
$\text{La}_{0.85}\text{Sr}_{0.15}\text{CrO}_3$	E5b	1100			5.2	5.4
$\text{La}_{0.85}\text{Sr}_{0.15}\text{CrO}_3$	E5a	1100	125	24		
LaCrO_3	E5f	1100	152	103	6.4	34.9
$\text{LaCr}_{0.9}\text{Co}_{0.1}\text{O}_3$	E5i	1100	131	118	20.1	29.9
$\text{LaCr}_{0.9}\text{Ni}_{0.1}\text{O}_3$	E5e	1100	79	177	7.3	16.6
$\text{La}_{0.85}\text{Sr}_{0.15}\text{Cr}_{0.9}\text{Mg}_{0.1}\text{O}_3$	E5d	1100			6.6	6.5

The conductivity E_a for LSrC and LSrC*Ni* were taken to be those of LCaC and LCaC*Ni*. In comparison, $\sigma_{\text{O}^{2-}}$ is of 87 kJ/mol, as taken from reference¹⁹.

The effect of the substituent on the R_p losses was also significant. This implies that the conductivity played also a role in the electrode reactions. This is in contradiction with the result of Primdahl et al. who argued that conductivity should not have any influence on their $\text{La}_{0.8}\text{Sr}_{0.2}\text{Cr}_{0.97}\text{V}_{0.03}\text{O}_3$ electrode²⁰. Apparent activation energies for the different R_p s are summarized in Table 3. These values vary in general between 80 and 190 kJ/mol. As for the electronic conductivity, it had a higher activation energy in H_2 than in air, with values varying between 5 and 20 kJ/mol in air and 5 and 32 kJ/mol in wet H_2 , whereas the ionic conductivity varied, in the case of $\text{La}_{1-x}\text{Sr}_x\text{Cr}_{1-y}\text{Ni}_y\text{O}_3$, between 87 ($x = 0.2, y = 0.05$), 142 ($x = 0.2, y = 0$)²¹ and 93²¹ or 137¹⁹ kJ/mol ($x = 0.35, y = 0$) and 77 kJ/mol for $\text{La}_{0.7}\text{Ca}_{0.3}\text{CrO}_3$ ²¹. Correspondingly, the activation energy for the ionic leak current density, which takes into account the variation of the vacancy concentration between two different gas atmospheres, is between 130 and 195 kJ/mol²¹. Beside that, conductivity transient measurements made on thin rods of LCaC*Ni* and LCaC*Mg* at 800°C , upon a rapid change of the gas atmosphere from air to wet H_2 (using Ar), indicated a slow exponential decrease in the conductivity with time (Figure 32). The behavior was reversible upon reoxidation giving rise to the same initial conductivity in air. A trial was made to analyze this behavior using the concept of oxygen diffusion in the materials, taking into account the surface exchange and the diffusion coefficients. A rough estimation of the exchange coefficient, κ , taking a mean value for the vacancy diffusion coefficient $D_{\text{v}_o} \cdot 800^\circ\text{C}$ of $1.2 \times 10^{-6} \text{ cm}^2/\text{s}$ ^{19, 21} gave an approximate value of about 10^{-6} to 10^{-7}

cm/s, which could indicate a surface limiting process for the reduction. Yasuda et al. ¹⁹ presented a coefficient $D_{v_o} \dots_{850^\circ\text{C}}$ of 5.62×10^{-7} cm²/s and κ of 1×10^{-4} cm/s measured in air using a similar technique for the compound $\text{La}_{0.8}\text{Sr}_{0.2}\text{Cr}_{0.95}\text{Ni}_{0.05}\text{O}_3$. Taking the concept of Adler et al. ^{22, 23} depicting the length δ of the reaction zone on the electrode,

$$\delta \approx \sqrt{\frac{(1-\varepsilon) L_c}{\tau a}} \quad (12)$$

$$\text{with } L_c = \frac{D^*}{\kappa} \quad (13)$$

$$\text{and } D^* = f D_{v_o} \frac{c_v}{c_{mc}} \quad (14)$$

where ε is the porosity (taken as 0.3), a the surface area (taken as 10000 cm²/cm³), τ the solid phase tortuosity (taken as 1, but is a constant that varies between 1 and 10 for porous bodies ²⁴, and was found to be of 14.5 for YSZ-Ni cermet anodes with pores of a few μm ²⁵), D^* the tracer diffusion coefficient, f the correlation factor (taken as unity ²⁶), c_{mc} the concentration of oxygen sites in the mixed conductor determined from the lattice parameter ($\approx 1.9 \times 10^{-2}$ mol/cm³ for the LCs), and c_v the vacancy concentration (around 10^{-3} mol/cm³ for the LCs), it could be possible to roughly estimate a reaction length of 2 to 4 μm inside the electrode structure. In air, κ is around 10^{-4} cm/s. A more accurate evaluation of $D_{v_o} \dots$ and κ could be obtained from more reliable data. Such a change in the exchange coefficient could explain the slow reduction process. This preliminary evaluation could also explain the slow degradation of the activity of the lanthanum chromites over a period of about 20 h observed during polarisation. Reoxidation of the material leads thus to a reversible activity. It also could give more insight on the mechanism of the reaction. It may be interesting to evaluate partial oxidation on the chromite ($\text{CH}_4 + \text{O}_2$), O_2 possibly hindering the extreme reduction of the electrode. This along with the activation energies and the correlation with the electrode conductivity might indicate a chemical process limitation related to the perovskite surface.

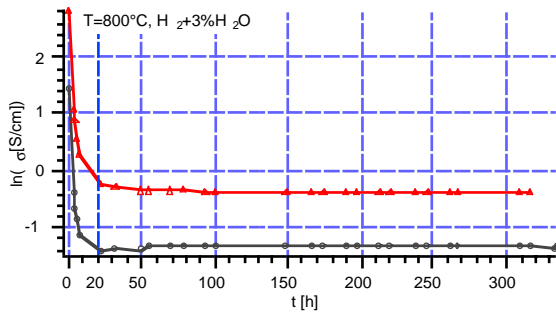


Figure 34: Slow decrease of the conductivity with time, when the gas atmosphere of the pellets of (Δ) LCaCNi and (\circ) LCaCMg is switched from air to $\text{H}_2 + 3\% \text{H}_2\text{O}$.

Also, by Adler et al. ^{22, 23}, a chemical impedance Z_{chem} was defined relating the $D_{v_o} \dots$ and κ , as

$$R_{chem} [\Omega \cdot \text{cm}^2] = \left(\frac{RT}{2F^2} \right) \sqrt{\frac{\tau}{(1-\varepsilon)c_v D_{v_o} a \kappa c_{mc}}} \quad (15)$$

$$C_{chem} [F] = \frac{2F^2 (1-\varepsilon) c_v \delta}{ART} \quad (16)$$

$$Z_{chem} = R_{chem} \sqrt{\frac{1}{1 - j\omega(C_{chem}R_{chem})}} \quad (17)$$

$$\text{with } A = \frac{1}{2} \frac{\partial \ln(P_{O_2})}{\partial \ln(c_v)} \quad (18)$$

By taking into account the values of D_{v_o} and κ of Yasuda et al.¹⁹ and our estimates for κ in humidified H_2 , as well as an estimate of A obtained from nonstoichiometry studies of $\text{La}_{0.9}\text{Sr}_{0.1}\text{CrO}_{3-\delta}$ ²⁷, the difference in behavior between an unpolarized and a polarized electrode could be interpreted as a local change in the activity of the electrode related to its reduction and thus to the decrease of the surface exchange coefficient. By polarizing the electrode, a partial reoxidation will occur leading to the increase in the surface exchange coefficient. This will lead to a decrease in the impedance polarization resistance, R_p . In Table 4, a trial was made to estimate and summarize this expected change.

Table 4: Effect of the κ on a presumed chemical impedance, at 850°C.

Parameters	values	Calculated values	air	wet H_2
τ	1	δ [μm]	1.4	14.4
ε	0.3	D^* [cm^2/s]	2.96×10^{-8}	2.96×10^{-8}
A	647.5	C_{chem} [F/cm^2]	3.10×10^{-4}	3.10×10^{-3}
a [cm^2/cm^3]	10000	R_{chem} [Ωcm^2]	0.18	1.83
κ_{air} [cm/s]	1×10^{-4}	f_{max} [Hz]	2799	28
κ_{H_2} [cm/s]	1×10^{-6}	L_c [cm]	2.96×10^{-4}	2.96×10^{-2}
D_{v_o} [cm^2/s]	5.62×10^{-7}			

Values of references¹⁹ and²⁷ were used and estimates for τ and ε were taken from reference²². N.B. If τ is taken as 14.5 then R_{chem} should be multiplied by 3.8 and the f_{max} should be divided by 3.8.

To apply this on our system, an example of an unpolarized electrode is taken from the symmetrical cell analysis (B24), where two processes were observed by impedance spectroscopy, with activation energies of 139 kJ/mol and 122 kJ/mol in humidified H_2 , and 95 kJ/mol and 24 kJ/mol in humidified CH_4 for R_1 and R_2 respectively (Figure 33). The C_1 activation energy did not vary much with temperature and gases (Figure 33), with a value of about $10 \mu\text{F}/\text{cm}^2$ (see also Figure 13). C_2 seemed to be less affected by the temperature with values of 630 to $250 \mu\text{F}/\text{cm}^2$ (2.5 time less) in humidified H_2 and CH_4 respectively. Globally, by comparing with the results previously shown in Figure 13 (B21), the second process (R_2 - C_2) had a resistance of $5 \Omega\text{cm}^2$ and a C of $794 \mu\text{F}/\text{cm}^2$ ($f_{max} = 40$ Hz) for the unpolarized cell (B24) versus $1.3 \Omega\text{cm}^2$ and $100 \mu\text{F}/\text{cm}^2$ ($f_{max} = 1224$ Hz) for the polarized cell (B21), at 850°C and in humidified H_2 . This might indicate that the second process is related to the chemical impedance described by Adler et al.²². Primdahl et al., on the basis of H_2/D_2 isotopic effect studies, suggested that this process might be related to H_2 adsorption or to a chemical reaction step²⁰. Furthermore, the potential capacitance of charged adsorbed species can be estimated by

$$C = \frac{q}{V} = \frac{nNF}{U} \quad (19)$$

where n is the charge of a species, N the number of moles of the charged species, $F = 96500$ C and U the impedance spectroscopy sinusoidal potential perturbation (in the order of 10 mV). From the above mentioned reasoning (Adler), the reaction zone was estimated as being of 1 μm or less. Taking an anode of 50% porosity, the total volume of LC would be of $1 \times 10^{-4} \text{ cm}^3$ or an equivalent mass of about $66 \times 10^{-5} \text{ g}$ ($d = 6.6 \text{ g}/\text{cm}^3$). The adsorption area of H^+ is given as 3 \AA^2 ²⁸. Taking the surface area of the anode into account, an estimate of 3.6×10^{-8} moles of adsorbed

H^+ can be given. During the impedance cycle only few of these are converted, thus the max capacitance would be of 3.5 mF/cm^2 , in the same range as the measured capacitance for C_2 .

Also, hydrogen adsorption on NiO and its oxygen vacancies is reported to be of 96.4 kJ/mol , whereas hydrogen diffusion over YSZ is reported to be of 119.5 to 159.9 kJ/mol ^{29, 30}. These values are not far from the measured activation energies of both processes. However, the first process, (R_1 - C_1), due to R_1 's lower sensitivity to the gas atmosphere and to equally low values of C_1 ($10\text{--}20 \text{ }\mu\text{F/cm}^2$) in CH_4 and H_2 (Figure 33) and to its potential independent behavior (Figure 13), at least before the cell's degradation in the case of B21, might be related to a chemical step or to charge transfer^{31, 32}. The double layer capacitance model predict a maximum of $30 \text{ }\mu\text{F/cm}^2$ at a minimum spacing of 0.3 \AA , equal to $1/4$ the diameter of an oxide ion. The summit frequency for the first process was of 5 kHz for the unpolarized and 10 kHz for the polarized one. In general, in both processes, the summit frequency tended to increase as the cell was polarized, showing an electrocatalyzed process.

In both processes, gas diffusion as well as gas conversion impedances could be ignored (see Appendix A), as the summit frequencies of these kind of losses would range between 15 and 400 Hz . This was estimated for humidified H_2 and CH_4 on the basis of literature^{9, 33} by taking into account the testing configuration and the interdiffusion coefficient of H_2O in H_2 and H_2 in CH_4 . Similarly, estimates for CO_2/CO fuels indicated negligible losses too.

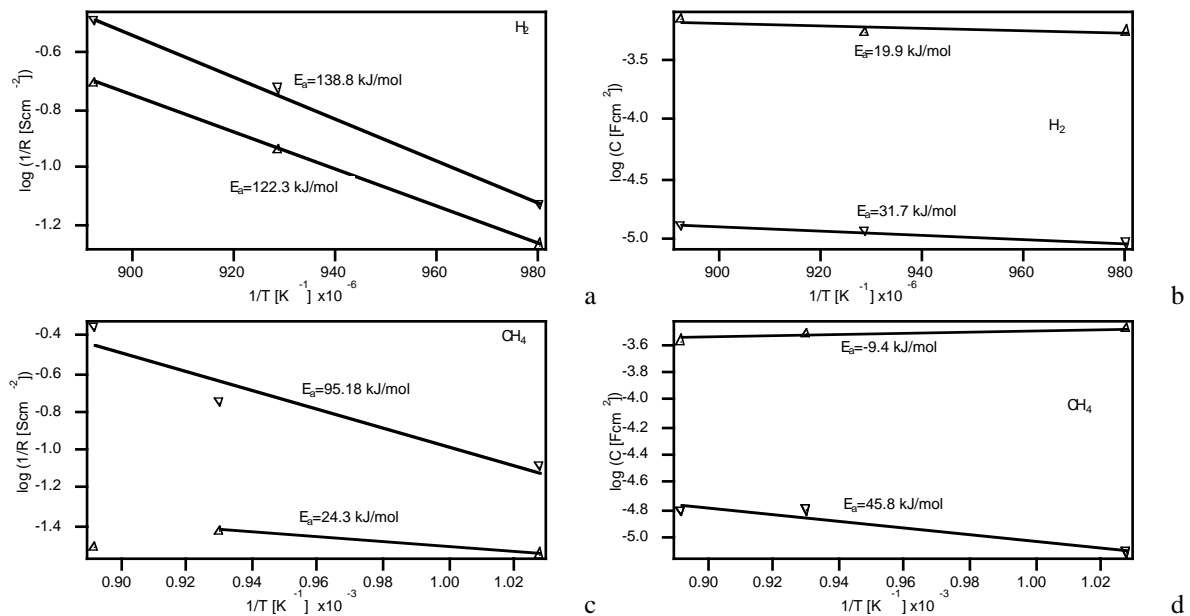


Figure 33: $\text{La}_{0.85}\text{Sr}_{0.15}\text{Cr}_{0.9}\text{Mg}_{0.1}\text{O}_3$ anode (B24). Arrhenius plot for the 2 processes in a-b. wet H_2 and c-d. in wet CH_4 . (▼, ▼) first process (R_1 - C_1) and. (▲, ▲) second process (R_2 - C_2). n_1 : 0.53-0.65; n_2 : 0.57-0.7; $L \approx 800\text{nH}$, maximum error 1.2-4%.

The effect of the substituent on the polarization of the cell cited above indicates furthermore that the catalytic effect has an important role in the electroactivity of these materials. In methane the activity follows the same trend as for the catalytic tests (Chapter 6) made in CH_4 rich atmospheres³ (Figure 25). Ni incorporation had also a positive effect in wet H_2 (Figure 25). Thus total conductivity of the electrode material was an important factor in the performance but it was also tempered by the catalytic activity (ex. LCCo has a higher conductivity than Ni but a lower catalytic and electrocatalytic activity).

Also, as the OCVs of the LCs in wet CH_4 were governed by the $\text{H}_2/\text{H}_2\text{O}$ equilibrium over the electrode, it is reasonable to suggest that H_2 oxidation was masking the overall CH_4 electrooxidation process as observed in the case of CeO_2 based anodes (see Chapter 11), at least under low current densities. This H_2 stems from the local steam-reforming of CH_4 , with a CH_4 conversion of no more than 0.3%, in accordance with previous catalytic runs. From the MS gas analysis of sealed LCaCMg and LSrCMg cells, H_2 concentration was observed to be low, being of about 0.5~1% (Figures 16 and 17). Even though there were both CO and CO_2 in the gas

surrounding the anode with a ratio of $\text{CO}_2/\text{CO} \approx 0.6$, CO oxidation seemed not to affect the anode potential. As pointed out previously, the anode polarization resistance under $\text{CO}-\text{CO}_2$ gas mixture was much higher than in CH_4 or H_2 . The R_p s were of 1.7 in H_2 , 6.1 in CH_4 and 9.2 to 17.2 Ωcm^2 in CO_2/CO of 0.14 and 1.44. Thus the kinetics of CO oxidation are about 1.5 to 2.8 times lower than for CH_4 , and 5.4 to 10.2 times lower than for H_2 . The low OCV values did not reflect the direct oxidation of CH_4 , but rather that of H_2 and in much lower proportion CO oxidation. This might be the reason for this OCV effect. Norby et al.³⁴ have shown that the presence of water prevented carbon deposition over a $\text{La}_{0.7}\text{Ca}_{0.3}\text{CrO}_3$ anode which lead in the case of dry CH_4 to very high OCVs of 1500 mV. This might indicate, that the electrode impedance in humidified CH_4 might be related to hydrogen rather than CO or C as C direct oxidation was observed to be very slow over metallic and oxide electrodes³⁵⁻³⁷.

The MS analysis of the anode gas composition under current load shows that all the methane consumed corresponds to the faradaic current. From the analysis, CO seemed to increase with current, and H_2 to decrease, when compared to OCV (i.e. catalytic reaction). It is not very clear whether the mean reaction is partial oxidation, with a concomitant oxidation of H_2 , or oxidation of H_2 with concomitant removal of carbon species by water. Steam reforming of CH_4 can be excluded in the case of LCaCMg , as its rate was of only 1.2×10^{-10} mol/m²s at 850°C (whereas of 1.7×10^{-9} and 1.1×10^{-8} mol/m²s for LSrC and LCaCNi respectively)⁴, a low value compared to the rate of CH_4 consumption (about 4.4×10^{-8} mol/s), unless a NEMCA (Non-faradic Electrochemical Modification of Catalytic Activity) effect is taking place³⁸.

On these bases, a possible scheme for the mechanism of the reaction is depicted in Figure 34. Combining the mechanism proposed in Chapter 6 based on the catalytic results and on literature data, CH_4 might dissociate over the LC to yield a methyl radical which could lead further to a carbonaceous species or to a formaldehyde intermediates. The formaldehyde is known to be an intermediate in the oxidation of methyl radical from methoxide ions, and it dissociates easily to CO and H_2 at these high temperatures³⁹. This species is also known to exist as a gas phase intermediate⁴⁰. The carbonaceous species could either be electrochemically oxidized or gasified by H_2O , leading H_2 and CO. The adsorbed hydrogen species can undergo a surface diffusion and react electrochemically to produce water, which in turn would gasify carbon. A rapid gas shift reaction would also ensure the conversion of part of the CO to CO_2 .

LSrCNi might be performing much better as its steam and CO_2 reforming activities were observed to be the highest among the series of LCs studied. As the overall polarization losses tended to decrease as the catalytic activity increased, it might be interesting to further optimize the Ni content of the LSrCNi series. In catalytic mode at least, CH_4 combustion in 2:1:5 $\text{CH}_4:\text{O}_2:\text{He}$ gas mixture, Stojanovic et al.⁴¹ found that the rate increased by a factor of about 100 from $x = 0$ to $x = 1$ in $\text{LaCr}_{1-x}\text{Ni}_x\text{O}_3$. An optimum might exist for our purpose by taking into account the instability of the LSrCNi matrix⁴ (Chapter 7).

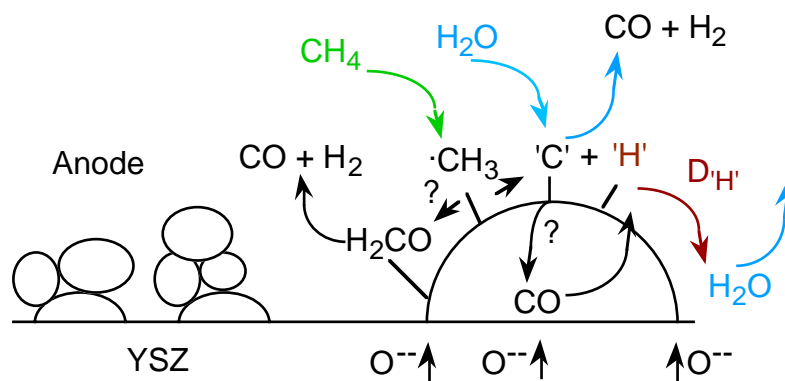


Figure 34: Possible mechanism for the electrochemical reaction of methane on LCs. Formaldehyde, CH_2O , is reported to be formed in many cases in literature³⁹.

Further, H_2O did not seem to favor the electrocatalytic reaction in the case of LCaCMg and LSrCMg , at least at the low current densities, in accordance with previous catalytic measurements. On the contrary, CO_2 inhibited the reaction, and as in the case of the catalytic

reactions, and this is thought to be related to the formation of surface carbonates, as CO and CO_2 are thought to adsorb on the same catalytic sites⁴².

Finally, Sr and Ni substitution turn out to be favorable for the catalytic as well as for the electrocatalytic activities. Sr addition is required to enhance the electronic conductivity of the electrode. Sr is better than Ca from the thermodynamic point of view and also for it allows a lower expansion of the LaCrO_3 . Ni substitution, reduces further this expansion⁴³ (see Chapter 3). Also, in the continuity of the previous work² (Chapter 4 and 5), the lowering of the Ca or Sr concentration proved to be beneficial from the electrochemical stability point of view.

Conclusions

The electrocatalytic properties of Ca, Sr, Mg, Co or Ni substituted lanthanum chromites deposited on 8YSZ electrolytes were compared under humidified H_2 and CH_4 . The nature of the substituent was observed to have an influence on the anodic ohmic and polarization resistances. Globally, the higher the conductivity, the better is the performance of the electrode. However, the catalytic activity of the electrode material was also observed to play a role in the electrochemical reaction. The polarization losses in humidified methane were observed to decrease almost in the same trend as the increase in the catalytic activity, i.e. $\text{LaCrO}_3 \approx \text{LaCr}_{0.9}\text{Co}_{0.1}\text{O}_3 < \text{LaCr}_{0.9}\text{Ni}_{0.1}\text{O}_3 < \text{La}_{0.85}\text{Sr}_{0.15}\text{CrO}_3 < \text{La}_{0.85}\text{Sr}_{0.15}\text{Cr}_{0.9}\text{Ni}_{0.1}\text{O}_3$. A direct relationship between the electronic and catalytic activities and the electrocatalytic performance was evidenced. Also, the surface exchange coefficient might have an influence on the performance of the cell, as it was observed to decrease upon reduction of the electrode material.

Generally, lanthanum chromite performances were higher in H_2 than in CH_4 and in turn higher than in CO_2/CO . OCV measurements made on sealed cells were very sensitive to $\text{H}_2/\text{H}_2\text{O}$ equilibrium rather than to the whole gas composition produced after the partial steam-reforming reaction taking place on the surface of the electrodes. H_2 oxidation could be thought to mask CH_4 oxidation. Further, full oxidation did not seem to take place over $\text{La}_{0.85}\text{Ca}_{0.15}\text{Cr}_{0.9}\text{Mg}_{0.1}\text{O}_3$, at least at low current densities. H_2O did not seem to favor the electrocatalytic reaction, at least at the low current densities, in accordance with previous catalytic measurements. In the contrary, CO_2 had an influence on the cell polarization, and as in the case of the catalytic reactions, this is thought to be related to the formation of surface carbonates.

From the impedance analyses, 2 limiting processes were identified. The first one might be related to charge transfer or to a chemical step, while the second might stem from a chemical process dealing with H_2 . The direct influence of H_2 on the cell performance was also observed on gold and on CeO_2 -based anodes (Chapter 11).

The cells were observed to be more stable when the anodes were sintered at 1100°C . At higher sintering temperatures, some topotactic reactions were observed, linked with the formation of $(\text{Sr},\text{Ca})\text{ZrO}_3$ at the interface with YSZ. Further, the stability of the electrode was increased by intercalating a composite layer between the electrolyte and the electrode. The best performance was obtained with a 1 layer of $78.2:21.8 \text{ La}_{0.85}\text{Sr}_{0.15}\text{Cr}_{0.9}\text{Ni}_{0.1}\text{O}_3 + 8\text{YSZ}$ covered with 3 layers of $\text{La}_{0.85}\text{Sr}_{0.15}\text{Cr}_{0.9}\text{Ni}_{0.1}\text{O}_3$, with a power output of $450 \text{ mW}/\text{cm}^2$ in H_2 and $300 \text{ mW}/\text{cm}^2$ in CH_4 , at 875°C . The measured R_p in H_2 was of $0.11 \Omega\text{cm}^2$. The performance of the electrode was sustained for 136 h in methane. As pointed out by the previous studies on catalysis and on the thermodynamics of the LaCrO_3 -based materials, Sr and Ni elements turned out to be the most favorable substituents for the electrocatalysis. Sr addition is required to enhance the electronic conductivity of the electrode. Sr is better than Ca from the thermodynamic point of view and also for it allows a lower expansion of the substituted LaCrO_3 under reducing conditions. Ni substitution reduces further this expansion.

References

- (1) Sfeir, J.; Van herle, J.; McEvoy, A. J. Third European Solid Oxide Fuel Cell Forum, Nantes-France, **1998**; 267-276.
- (2) Sfeir, J.; Van herle, J.; McEvoy, A. J., *Journal of the European Ceramic Society* **1999**, *19*, 897-902.
- (3) Sfeir, J.; Buffat, P. A.; Möckli, P.; Xanthopoulos, N.; Vasquez, R.; Mathieu, H. J.; Van herle, J.; Thampi, K. R., *J. Catalysis* **2001**, *202*, 229-244.

- (4) Sfeir, J. in "Solid Oxide Fuel Cell Materials and Mechanisms", Joint Topical Meeting, IEA-ESF, Les Diablerets, Switzerland, **2001**, 55-67.
- (5) Tejuca, L. G.; Fierro, J. L. G.; Tascon, J. M. D., *Advances in Catalysis* **1989**, 36, 237-328.
- (6) Metcalfe, I. S.; Baker, R. T., *Catalysis Today* **1996**, 27, 285-288.
- (7) Widmer, S. L., Ph.D. thesis Nr. 1732, Swiss Federal Institute of Technology, Lausanne, **1997**.
- (8) Macdonald, J. R. *Impedance Spectroscopy. Emphasizing Solid Materials and Systems*; John Wiley & Sons, **1987**.
- (9) Primdahl, S.; Mogensen, M., *J. Electrochem. Soc.* **1998**, 145, 2431-2438.
- (10) Hibino, T.; Kuwahara, Y.; Wang, S.; Kakimoto, S.; Sano, M., *Electrochemical and Solid-State Letters* **1998**, 1, 197-199.
- (11) Mukundan, R.; Brosha, E. L.; Brown, D. R.; Garzon, F. H., *Electrochemical and Solid-State Letters* **1999**, 2.
- (12) Lacombe, S.; Zanthoff, H.; Mirodatos, C., *Journal of Catalysis* **1995**, 155, 106-116.
- (13) Yokokawa, H.; Horita, T.; Sakai, N.; Kawada, T.; Dokiya, M.; Takai, Y.; Todoki, M., *Thermochimica Acta* **1995**, 267, 129-138.
- (14) Sakai, N.; Kawada, T.; Yokokawa, H.; Dokiya, M. Science and Technology of Zirconia V, Melbourne, Australia, **1992**.
- (15) Simner, S. P.; Hardy, J. S.; Stevenson, J. W.; Armstrong, T. R., *Solid State Ionics* **2000**, 128, 53-63.
- (16) Glenne, R.; Horst, J. A.; Jørgensen, S.; Norby, T.; Seiersten, M., *Surface and Interface Analysis* **1994**, 22, 275-279.
- (17) Corbin, S. F.; Apté, P. S., *J. Am. Ceram. Soc.* **1999**, 82, 1693-1701.
- (18) Kleinlogel, C. M., ETHZ, Ph.D. thesis, Swiss Federal Institut of Technology, Zürich, **1999**.
- (19) Yasuda, I.; Hishinuma, M., *Solid State Ionics* **1995**, 80, 141-150.
- (20) Primdahl, S.; Hansen, J. R.; Grahl-Madsen, L.; Larsen, P. H., *J. Electrochem. Soc.* **2001**, 148, A74-A81.
- (21) Yasuda, I.; Hishinuma, M., *J. Electrochem. Soc.* **1996**, 143, 1583-1590.
- (22) Adler, S. B.; Lane, J. A.; Steele, B. C. H., *J. Electrochem. Soc.* **1996**, 143, 3554-3564.
- (23) Adler, S. B., *Solid State Ionics* **1998**, 111, 125-134.
- (24) Cussler, E. L. *Diffusion. Mass transfert in fluid systems*, 2 ed.; Cambridge University Press, **1997**.
- (25) Kim, J.-W.; Virkar, A. V.; Fung, K.-Z.; Mehta, K.; Singhal, S. C., *J. Electrochem. Soc.* **1999**, 146, 69-78.
- (26) Kawada, T.; Horita, T.; Sakai, N.; Yokokawa, H.; Dokiya, M., *Solid State Ionics* **1995**, 79, 201-207.
- (27) Mizusaki, J.; Yamauchi, S.; Fueki, K.; Ishikawa, A., *Solid State Ionics* **1984**, 12, 119-124.
- (28) Primdahl, S.; Mogensen, M., *J. Electrochem. Soc.* **1997**, 144, 3409-3419.
- (29) Holtappels, P.; Haart, L. G. J. d.; Stimming, U., *J. Electrochem. Soc.* **1999**, 146, 1620-1625.
- (30) Holtappels, P.; Vinke, I. C.; Haart, L. G. J. d.; Stimming, U., *J. Electrochem. Soc.* **1999**, 146, 2976-2982.
- (31) Robertson, N. L.; Michaels, J. N., *J. Electrochem. Soc.* **1991**, 138, 1494-1499.
- (32) Bockris, J. O. M.; Reddy, A. K. N. *Modern Electrochemistry*, 3 ed.; Plenum/Rosetta, **1977**.
- (33) Primdahl, S.; Mogensen, M., *J. Electrochem. Soc.* **1999**, 146, 2827-2833.
- (34) Norby, T.; Osborg, P. A.; Dyrлие, O.; Hildrum, R.; Seiersten, M.; Glenne, R. European Solid Oxide Fuel Cell Forum I, Lucerne, Switzerland, **1994**; 217-226.
- (35) Horita, T.; Sakai, N.; Kawada, T.; Yokokawa, H.; Dokiya, M. First European Solid Oxide Fuel Cell Forum, Lucerne, Switzerland, **1994**; 227-236.
- (36) Horita, T.; Sakai, N.; Kawada, T.; Yokokawa, H.; Dokiya, M., *J. Electrochem. Soc.* **1995**, 142, 2621-2624.
- (37) Horita, T.; Sakai, N.; Kawada, T.; Yokokawa, H.; Dokiya, M., *J. Electrochem. Soc.* **1996**, 142, 1161-1168.
- (38) Vayenas, C. G.; Bebelis, S.; Yentekakis, I. V.; Neophytides, S., **1992**.

- (39) Lee, J. H.; Trimm, D. L., *Fuel Processing Technology* **1995**, 42, 339-359.
 (40) Shi, C.; Xu, M.; Rosynek, M. P.; Lunsford, J. H., *J. Phys. Chem.* **1993**, 97, 216-222.
 (41) Stojanovic, M.; Mims, C. A.; Moudallal, H.; Yang, Y. L.; Jacobson, A. J., *Journal of Catalysis* **1997**, 166, 324-332.
 (42) Tilset, B. G.; Fjellvåg, H.; Kjekshus, A.; Slagtern, Å.; Dahl, I., *Applied Catalysis A: General* **1996**, 147, 189-205.
 (43) Armstrong, T. R.; Stevenson, J. W.; Pederson, L. R.; Raney, P. E., *J. Electrochem. Soc.* **1996**, 143, 2919-2925.

Appendix A: Gas diffusion, gas conversion and concentration polarization impedances ^{9, 25, 33}

Gas conversion impedance ⁹

Gas conversion impedance is an effect of the passage of current on an electrode in a finite gas flow rate. Gas conversion is not detected when the reference electrode serving to monitor the working electrode is placed in the same gas as this working electrode, or in a symmetric configuration (Chapter 2, Figure 5) where both electrodes are submitted to the same gas atmosphere. Gas conversion impedance is detected in measurement setups (Chapter 2, Figures 2 and 4) where the electrode is characterized against a stable reference potential, e.g. the reference is placed in air and it is used to sense the anode.

The problem arises due to the small local perturbation induced by the impedance measurement, based on a complex potential signal of an amplitude of ± 10 mV, leading to a complex ac current signal. Even, at open circuit potential (OCV), this perturbation will lead to a local change in the gas composition, e.g. the local oxidation of H₂ to H₂O. This change results in the appearance of a concentration difference which is monitored by the reference electrode set at a fixed oxygen potential, e.g. air. This concentration perturbation can be expressed according to the Nernst equation. Based on a continuously stirred tank reactor (CSTR) model, Primdahl et al. ⁹ proposed the following expressions for the conversion impedance, with the limitation that the perturbation is less than the inlet concentration of the gas in question ($\Delta x_{H_2O} \ll x_{i,H_2O}$ and $\Delta x_{H_2} \ll x_{i,H_2}$):

$$R_g = \frac{RT}{4F^2 J_i} \left(\frac{1}{x_{i,H_2O}} + \frac{1}{x_{i,H_2}} \right) \quad A-1$$

$$C_g = \frac{4F^2 PV}{(RT)^2 A} \frac{1}{\frac{1}{x_{i,H_2O}} + \frac{1}{x_{i,H_2}}} \quad A-2$$

$$f_g = \frac{J_i ART}{2\pi PV} \quad A-3$$

where x_i is the inlet mole fraction of the gas, J_i the inlet area-specific gas flow rate (mol/m²s), P the absolute pressure, A the anode area, and V the CSTR volume of the measurement setup. R_g , C_g and f_g are the impedance real resistance, the impedance capacity and the impedance summit frequency. Results for humidified H₂ and CH₄ as a function of the expected H₂O concentration are summarized in Table A-1. The same is done for CO as a function of the CO₂/CO ratio in Table A-2.

Table A-1: Summary of the gas conversion impedances in humidified H₂ and CH₄, as a function of the water content, at 850°C.

in H ₂ or CH ₄	30%H ₂ O	3%H ₂ O	0.3%H ₂ O	0.03%H ₂ O	0.003%H ₂ O	0.0003%H ₂ O
R_g [Ωcm^2]	1.1×10^{-3}	7.9×10^{-3}	7.71×10^{-2}	0.77	7.71	77.08
C_g [F/cm ²]	4.54	0.63	6.5×10^{-2}	6.5×10^{-3}	6.5×10^{-4}	6.5×10^{-5}
f [Hz]	32	32	32	32	32	32

The CSTR volume was taken as 1 cm² x 100 μm, and the J_i was estimated to 10.84 mol/m²s. The bold values correspond to the expected values for H₂ whereas the italic ones are for CH₄.

Table A-2: Summary of the gas conversion impedance in CO₂/CO, at 850°C.

in CO ₂ /CO	0.14	1.44
R _g [Ωcm ²]	2.1x10 ⁻³	9.6x10 ⁻⁴
C _g [F/cm ²]	4.54	4.54
f [Hz]	16	37

Gas diffusion impedance³³

The presence of a stagnant gas layer over the porous anode can lead to a so-called gas diffusion impedance. As with the gas conversion impedance, this concentration gradient can be expressed according to the Nernst equation. Primdahl et al.³³ have shown that this impedance can be described by the following:

$$R_D = \left(\frac{RT}{2F} \right)^2 \frac{l}{PD_{eff}} \left(\frac{1}{x_{H_2,b}} + \frac{1}{x_{H_2O,b}} \right) \quad A-4$$

$$f_D \approx \frac{2.53D_{eff}}{2\pi l^2} \quad A-5$$

where P is the pressure, D_{eff} the effective diffusion coefficient, F , R and T have the usual meaning, x_i the molar fraction of species i in the bulk gas and l the stagnant layer thickness. Results for humidified H₂ and CH₄ and CO₂/CO are given in Table A-3.

Table A-3: Summary of the gas diffusion impedance in H₂, CH₄ and CO₂/CO gases, at 850°C.

Results for	H ₂	3%H ₂ O	CH ₄	0.003% H ₂ O	0.0003% H ₂ O	CO	0.14	1.44
R _d [Ωcm ²], l=0.5cm	H ₂ O/H ₂	0.39	H ₂ /CH ₄	48.13	481.30	CO/CO ₂	6.1x10 ⁻²	2.7x10 ⁻²
C _d [F/cm ²]		2.6x10 ⁻²		2.6x10 ⁻⁴	2.6x10 ⁻⁵		0.92	2.07
f [Hz]		16		13	13		3	3
R _d [Ωcm ²], l=0.1cm		7.7x10 ⁻²		9.63	96.26		1.2x10 ⁻²	5.5x10 ⁻³
C _d [F/cm ²]		5.1x10 ⁻³		5.1x10 ⁻⁵	5.1x10 ⁻⁶		0.18	0.41
f[Hz]		403		322	322		70	70

The effective diffusion coefficients were taken as: H₂O in H₂ (10 cm²/s), H₂ in CH₄ (8 cm²/s) and CO in CO₂ (1.75 cm²/s).

Concentration polarization²⁵

Relatively large anode thickness requires the incorporation of a concentration polarization. Based on the gas diffusion theory applied on porous electrodes, Kim et al.²⁵ estimated a concentration polarization at OCV given by the following expressions

$$R_{conc}(i=0) = \frac{RT}{4F} \left\{ \frac{1}{i_{cs}} + \frac{2}{i_{as}} \left(1 + \frac{P_{H_2}^\circ}{P_{H_2O}^\circ} \right) \right\} \quad A-6$$

$$\text{with} \quad i_{as} = \frac{2FP_{H_2}^\circ D_{a(eff)}}{RTl_a} \quad A-7$$

$$i_{cs} = \frac{4Fp_{\text{O}_2}^{\circ} D_{c(\text{eff})}}{\left(\frac{P - P_{\text{O}_2}^{\circ}}{P}\right) RTl_c} \quad \text{A-8}$$

$$D_{a(\text{eff})} = \frac{D_a \varepsilon_a}{\tau_a} \quad \text{A-9}$$

and

$$D_{c(\text{eff})} = \frac{D_b \varepsilon_c}{\tau_c} \quad \text{A-10}$$

where i_{sc} and i_{sa} are the limit cathodic and anodic current, $P_{\text{H}_2}^{\circ}$, $P_{\text{H}_2\text{O}}^{\circ}$ and $P_{\text{O}_2}^{\circ}$ the inlet partial pressure of H_2 , H_2O and O_2 , P the total pressure, l_a and l_c the anode and cathode thickness, ε_a and ε_c the anode and cathode porosity, τ_a and τ_c the anode and cathode tortuosity, D_a the binary diffusion coefficient on the anode side (between H_2 and H_2O), and D_b the binary diffusion coefficient on the cathode side (between O_2 and N_2). Results for the anode are summarized in Table A-4.

Table A-4: Summary of the concentration polarization for the anode as a function of the electrode thickness.

Parameters	electrode thickness		$D_{\text{H}_2\text{-H}_2\text{O}}$	$D_{\text{O}_2\text{-N}_2}$
	$l=1\text{mm}$	$l=0.1\text{mm}$		
i_{as}	0.924	9.242	0.91cm ² /s	0.22cm ² /s
i_{cs}	0.122	1.225		
$R_{\text{conc}(0)}$	1.94	0.194		

Chapter 9 九

Synthesis, structure, characterization and electrical properties of CeO₂-based powders

Synthesis, structure, characterization and electrical properties of CeO₂-based powders

Abstract

Nb, Y, Pr and Gd doped CeO₂ materials were prepared using 3 different techniques: the solid-state method, the coprecipitation and the NbCl₅ route. The coprecipitation method was most effective for the Y, Pr and Gd doped compounds. In the case of Nb, the coprecipitation or the NbCl₅ routes were best suited. Powders of 1 to 18 m²/g were synthesized. Among all substituents, Nb enhanced most the CeO₂ densification. Nb was also observed to induce the highest electronic conductivity in ceria, both in air and in humidified H₂. However, concomitant doping with Gd and Nb pointed to a negative effect of Nb on the total conductivity in air of Gd-doped ceria. Nevertheless, Nb induced a marked electronic conductivity in reduced conditions. CeO₂-based electrodes showed poor adhesion on YSZ electrolytes unless doped with Nb. In that case, a sintering temperature of 1100°C/4h was necessary to make the electrode stick. The adhesion did not deteriorate in reducing atmospheres. Finally, CeO₂-based electrodes are thought to be stable towards solid state reaction with YSZ when sintered at 1200°C or less, as observed by HRTEM analysis.

Introduction / theory

Structural symmetry

CeO₂ belongs to the family of fluorites such as ZrO₂¹. It appears in cubic face-centered crystal symmetry, with the Ce atoms in the corner and in the center of each of its faces, and the oxygen atoms inside (tetrahedral holes) the lattice at a distance of (1/4, 1/4, 1/4) (see Figure 1). Like for LaCrO₃, Ce can be substituted by a wide range of other elements such as La, Pr, Sm, Gd, Y, Zr, Nb and Ca with different solubilities.

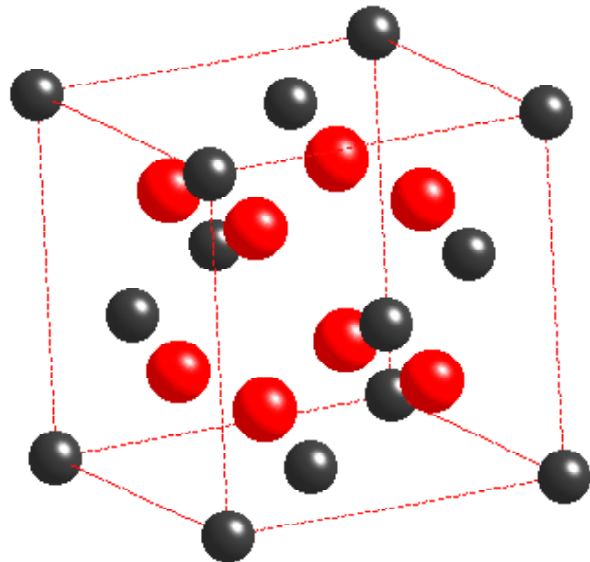
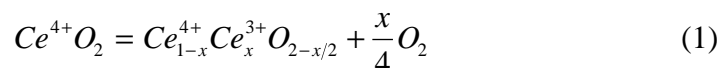


Figure 1: CeO₂ cubic structure in the Fm3m space group. Ce atoms are in the corner and in the face centers of the cube. Oxygen atoms (slightly bigger) are in the lattice. Each Ce is surrounded by 8 O located at the summit of a cube, whereas each O is located at the top of a tetrahedron. The structure was drawn using the JCPDS chart No 34-394 and the CrystalMaker program.

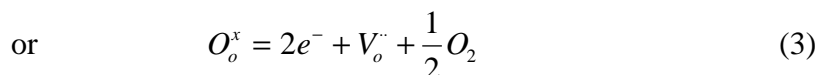
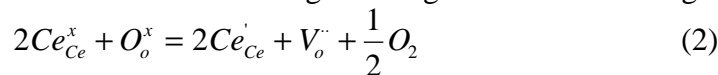
Conductivity

CeO₂-based compounds are semiconductors. Like LaCrO₃-based oxides, they are nonstoichiometric and can be written as CeO_{2-δ}. The composition of these oxides can be varied over a wide range of δ (from 0 to 0.5) by reduction. The removal of oxygen creates electrons as well as ionized oxygen vacancies, V_O^{••}, in the lattice. These materials are thus ionic and n-type semiconductors, and as for LaCrO₃, the electronic conductivity mechanism is consistent with the hopping of small polarons¹⁻³. The migration of a small polaron requires the hopping of both the

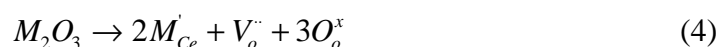
electron and the polarized atomic configuration from one site to an adjacent one. In this case, the hopping proceeds between neighboring Ce⁴⁺ and Ce³⁺ sites, created by reduction as



The corresponding defect equilibrium written following the Kröger-Vink notation is given by ³

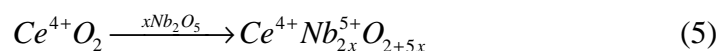


where O_o^x is an oxygen ion in the lattice, $Ce_{Ce}' = Ce^{III}$, $Ce_{Ce}^x = Ce^{IV}$ and V_o'' is an oxygen vacancy. Additional oxygen can be removed from the material when dopants of valence lower than 4+ are incorporated in the lattice, such as the trivalent La, Sm, Gd and Y elements, or divalent Ca ^{4,5}. This happens according to ⁶

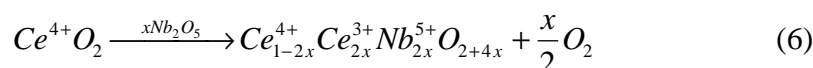


where M_{Ce}' is the doping element on a cerium site. The increase of the vacancy concentration leads to the enhancement of ionic conductivity. This makes these oxides alternative materials to the 8YSZ electrolyte (3 times higher ionic conductivity than 8YSZ at 800°C). The ionic transference number is near one at high P_{O_2} . At a P_{O_2} value of $\sim 10^{-15}$ atm, the electronic conductivity created by Ce^{IV} reduction becomes equal to the ionic contributions. Further below that P_{O_2} , the electronic conduction dominates.

The doping with elements of valence higher than 4+, such as Nb (5+) leads either to the incorporation of the excess oxygen as interstitials ⁷



or to an electronic compensation leading to cerium reduction



i.e to an increase in the electronic conductivity. The electronic conductivity can be expressed in the same manner as for LaCrO₃-based oxides (Chapter 3) ⁶

$$\sigma_e = \left(\frac{e^2 a^2}{kT\tau_o} \right) [Ce^{3+}] [Ce^{4+}] e^{\frac{-E_a}{RT}} \quad (7)$$

whereas the ionic conductivity is dependent on the vacancy concentration ⁴.

Among all substituents, Sm, Gd and Y are preferred as they allow high ionic conductivities, a high level of substitution as well as phase stability ^{4, 6, 8-10}. Sm and Pr seem to induce a high resistance to reduction ^{8, 11}. Pr, Zr and, as discussed before, Nb induce electronic conductivity ^{6, 7, 12-17}.

Ceria oxide doped with elements such as Ca, Sr, Ba, Y, Zr, Nb, La, Pr, Nd, Sm, Eu, Gd, Dy, Ho, Er, Tm, Yb and Lu have been investigated in the cited literature. They all show relatively high conductivities at intermediate temperatures compared to 8YSZ. The solubility in ceria of the above mentioned oxide varies a lot. Ca and Sr are reported to have a solubility of 15 to 23% and 9% respectively ¹⁸⁻²⁰, Y of more than 33% ²¹ and Nb of 1.4% ⁷ (800°C-1000°C). The rare earth oxides are soluble to more than 20 atom %. However, the solubility limit at low temperature might be lower as evidenced in the case of La (20% at 1600°C and 15% at 400°C) ⁴.

The maximum conductivity concentration has been reported to be of 8% for Ca ¹⁹, 3% for Sr ²⁰, 1.2% for Nb ⁷ and 20% for the Y and the rare earth dopant ^{5, 8, 22}. This suggests that the preferred trivalent or divalent dopant concentration is that which yields to approximately 5% of the oxygen sublattice sites vacant. However, the difficulty encountered in the fabrication of such materials have led to a relative paucity and scattered conductivity data.

Preparation

As with LaCrO₃, many techniques are applicable. However, in literature, three main techniques are commonly used: the solid state reaction between CeO₂ and M₂O₃, MO₂ or M₂O₅ at 1300°C or above (950°C for CaO)^{4, 8, 13, 18, 23}, the explosion method⁶, and oxalate or NH₃ precipitation^{5, 12, 21, 23-25}. The last method yields very fine powders as the calcination temperature is of 700-800°C^{25, 26}.

The aim of the present chapter

For our purpose, Y, Gd, Pr and Nb-doped CeO₂ were studied for their potential use as electrodes for direct CH₄ oxidation, with the two first elements to increase the ionic conductivity and the last two elements to analyze the effect of the electronic conductivity on the electrode reaction. A double substitution with Gd or Pr and Nb was also undertaken as for an anode purpose, a concomitant high ionic and electronic conductivity is desirable. Besides that, Pr is known to have interesting catalytic activity when used in SOFC²⁷ and to be the most active catalyst among rare earth oxides^{28, 29}, and Nb oxides to be a methane activating catalysts. Different fabrication techniques were used in order to optimize the powder characteristics. Conductivity measurements were undertaken for some of these materials, and trials were made to produce adhering layers of these compounds on YSZ electrolyte sheets. Finally, TEM observations were undertaken in order to monitor the interfacial reactivity between 8YSZ and CeO₂-based electrodes.

Experimental

Powder preparation

Different methods were used to produce the different ceria powders. For the Y, Pr and Gd doped powders, the oxalate coprecipitation method was used by dissolving the appropriate amounts of the different nitrate precursors in aqueous solution (1 M), added under stirring to a neutral dilute oxalic acid aqueous solution (0.05 M). The cerium nitrate was provided from Wako Chemicals, Japan, whereas the other compounds were purchased from Fluka. The resulting precipitate was then vacuum-filtered, washed with distilled water and isopropanol. Subsequently, the precipitate was dried overnight at 50°C, then calcined between 700 to 1500°C for 1 h. Y, Pr and Gd doped ceria powders are yellowish, reddish to purple and whitish respectively. CeO₂ is also yellowish.

The Nb element does not possess any nitrate salt, and all the Nb water soluble salts are expensive organometallics. For producing Nb-doped ceria powders, three different routes were tried: (1) the solid state route by mixing Nb₂O₅ and the other oxides followed by calcination at 1550°C; (2) the precipitation in oxalic acid aqueous solution where the appropriate amount of Nb₂O₅ was dispersed, followed by calcination at 1400°C; (3) the dissolution of nitrate precursors of Ce and Y or Gd or Pr, and NbCl₅ in 2-propanone (acetone) under heat and stirring, followed by decomposition on a hot plate and calcination at 1100°C. An alternative to the last method is to dissolve the NbCl₅ in 2,4-pentadione (acetyl acetone) in order to make a water soluble complex, then add the cerium nitrate and decomposing the whole under stirring on a hot plate. The calcination temperature is varied from 800 to 1100°C.

For the solid state method, appropriate mixtures of CeO₂, Gd₂O₃ and Nb₂O₅ all provided by Kojundo Chemicals, Japan, 99.9%, of a needle-like structure of 0.3~1 μm or less as observed by SEM, were prepared by wet ball-milling in ethanol using 0.2 wt% sorbitan palmitate as dispersant. Ball-milling was carried out with zirconia balls. This was followed by uniaxially pressing the dry powder into pellets at 100 to 200 MPa. Dry ball-milling was also tried. The sintering temperature was varied between 1400 and 1600°C. Nb₂O₅ is reported to melt between 1450 and 1485°C³⁰ so that to obtain the desired composition the material was first fired at 1400°C, then further calcined at 1550°C.

A dry grinding step ended the fabrication process and was also used at intermediate steps. The different produced powders are summarized in Table 1. XRD measurements were performed on all powders in order to detect impurities.

Table 1: Summary of the different synthesized powders.

Powder composition	surface area [m ² /g]	particle size <i>d</i> ₅₀ [μm]
CeO ₂	≈20	≈0.5
Ce _{0.8} Gd _{0.2} O _{1.9}	≈20	≈0.5
Ce _{0.88} Gd _{0.12} O _{1.94}	≈20	≈0.5
Ce _{0.8} Y _{0.2} O _{1.8}	15.3	0.8
Ce _{0.85} Y _{0.15} O _{1.925}	≈20	≈0.5
Ce _{0.6} Pr _{0.4} O _{1.8}	17.98	≈0.5
Ce _{0.8} Pr _{0.2} O _{1.9}	≈20	≈0.5
Ce _{0.85} Pr _{0.15} O _{1.925}	≈20	≈0.5
Ce _{0.992} Nb _{0.008} O _{2-d}	6.1~6.4	0.8~1
Ce _{0.872} Gd _{0.12} Nb _{0.008} O _{2-d}	0.89	1
Ce _{0.84} Gd _{0.12} Nb _{0.04} O _{2-d}		
Ce _{0.82} Gd _{0.12} Nb _{0.06} O _{2-d}		
Ce _{0.8} Gd _{0.12} Nb _{0.08} O _{2-d}		
Ce _{0.597} Pr _{0.398} Nb _{0.0047} O _{2-d}		

Conductivity measurements

Rods of CeO₂-based compounds of 13x6x5 mm³ were pressed at 100 MPa, and sintered at 1500°C for 4 h. A 4-probe technique measurement was used. A slow change in conductivity was observed at low oxygen partial pressures, and the conductivity reached stable values after more than 5 h. Oxygen partial pressures were controlled by appropriate mixing of O₂/Ar, CO/CO₂ or H₂/H₂O.

Adhesion, morphologies and chemical compatibility of electrodes on 8YSZ

Terpineol-ethyl cellulose-based slurries were prepared from CeO₂, Ce_{0.8}Y_{0.2}O_{1.9}, Ce_{0.6}Pr_{0.4}O_{1.8}, Ce_{0.85}Pr_{0.15}O_{1.925}, Ce_{0.8}Gd_{0.2}O_{1.9}, Ce_{0.992}Nb_{0.008}O_{2-d}, and Ce_{0.6}Pr_{0.4}Nb_{0.005}O_{2-d}, sintered at different temperatures, as described in Chapter 2. 1 cm² electrodes were screen-printed over 8YSZ sheets and sintered at different temperatures in order to verify the adhesion of these electrodes. Subsequently, some of these electrodes were treated overnight at 800°C under a flow a H₂ + 3%H₂O. SEM cross-section images were made before and after hydrogen treatment in order to analyze the electrode morphologies. Finally, one TEM analysis was performed on a Ce_{0.992}Nb_{0.008}O₂ electrode sintered at 1200°C over a 8YSZ sheet in an attempt to understand the sticking mechanism of this particular composition as well as to monitor any interfacial reaction with 8YSZ which might be detrimental to the overall conductivity of the cell.

Results

Powder and pellets preparation and XRD analysis

Powder produced by the oxalate coprecipitation method (i.e. Y, Pr and Gd doped ceria) gave the pure phase after a calcination step of 800°C. For the NbCl₅ route, firing at 800°C was not enough. However, when calcined at 1100°C for 4 h, the powder turned green, a typical color for reduced ceria centers (Ce³⁺)³¹.

For the solid-state method, in order to obtain reproducible conditions, the powder size, the ball-milling time, the pressing conditions and the firing temperature were followed. These parameters were studied on Ce_{0.88}Gd_{0.12}O_{1.94}, then transposed to the Nb-doped solutions. Powders of 1 to 2 μm diameter agglomerates allowed a better densification and produced crack free pellets of 95% of the theoretical density compared to 80% in the case of coarser powder (10 μm or more). Ball-milling had an impact on the densification. The effect of the dispersant was also remarkable in that it enabled near theoretical densities to be achieved. Compaction showed little effect between 100 and 200 MPa. Better green densities were obtained for the latter pressure whereas final densification was better for samples pressed at 100 MPa. Finally, the pellets showed full densification at 1550°C / 8 h and the reminiscence of small enclosed pores at 1400°C / 8 h. A grain growth is observed from 1400 to 1550°C, passing from 0.6 μm at 1400°C

to 1.5 μm at 1500°C to 2 to 3 μm at 1550°C. Reducing the sintering time to 4 h reduces the densification (from 98 to 96 % at 1550°C).

The presence of Nb allows a better densification of doped ceria, beginning at 1400°C for low Nb content. In the case of Ce_{0.84}Gd_{0.12}Nb_{0.04}O_{2.8}, fired at 1400°C / 12 h, full densification was reached. The grain size was of 2 μm compared to 0.6 μm in the case of Ce_{0.88}Gd_{0.12}O_{1.94} fired at the same temperature. For high Gd content (30 and 43%) full densification was not reached.

The X-ray patterns of ceria and gadolinia are very similar. However, in all solid solutions reported here, the main phase observed was that of the cubic ceria phase. Gd-doped ceria did not show any secondary phases at least up to ~ 43% Gd content, as expected from literature³². In the case of Gd/Nb-doped ceria, a trace of a secondary phase was observed in the case of 6% and 8% Nb doped Ce_{0.88}Gd_{0.12}O_{1.94}. The secondary phase could be related to the fergusonite structure of the orthoniobate CeNbO₄, but other phases could also be suggested such as CeNb₃O₉, CeNb₅O₁₄, GdNbO₄ or Ce₂O₃. The ceria orthoniobate was reported to be formed when Nb₂O₅ exceeds its solubility limit of 0.6~0.8% in ceria. Rich Nb phases were observed by electron microprobe analysis.

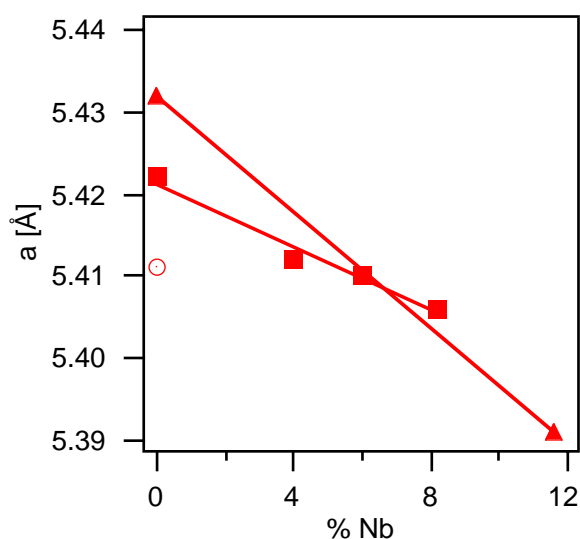


Figure 2: Evolution of the cubic lattice parameter of Nb doped Ce_{1-x}Gd_xO_{2-x/2} as a function of Nb content. (■) Ce_{0.88}Gd_{0.12}O_{1.94}; (▲) Ce_{0.57}Gd_{0.43}O_{1.785}; (○) CeO₂ from reference³².

With increasing Nb content, the lattice parameter decreased as expected from the difference in the ionic sizes of Nb^V, Ce^{IV} and Gd^{III} (0.66, 0.97 and 1.06 Å respectively³³). There is almost a linear decrease in the lattice parameter, going from 0 to 8% Nb in Ce_{0.88}Gd_{0.12}O_{1.94}.

Optically, pellets made of these powders had different colors. For the low Gd concentration solution (12% Gd), the colors go from yellow for the 4% Nb to green-yellow for a 6% Nb to olive-green for the 8% Nb doped powder. It has been reported³¹ that such a color transition is indicative for the presence of Ce^{III}. The olive-green color is observed in Ce₂O₃. Some reports point to the fact that when Ce is in excess in ceria-niobia solid solutions, Ce reduces to the Ce^{III} state without affecting the Nb^V oxidation state^{34, 35}. This indicates that Nb dissolution in ceria leads to an important reduction as would have been expected from the substitutional mechanism (equation (6)). In the Gd rich solutions (30 and 43% Gd) the color is that of Gd doped ceria, even though the Nb content is relatively high (8 and 12%). This contrasts with the substitutional mechanism and could possibly be related to the interstitial or vacancy annihilation mechanism.

Globally, the solid-state and coprecipitation (in the case of Nb) methods require a high calcination temperature (> 1400°C) in order to obtain a pure phase. For the NbCl₅ route and the coprecipitation method (except for Nb), a much lower calcination temperature leads to the pure phase and also to very fine powders. Figure 3 shows XRD spectra of the Ce_{0.992}Nb_{0.008}O_{2.8} made by NbCl₅ and coprecipitation routes along with the Ce_{0.6}Pr_{0.4}Nb_{0.005}O_{2.8} powder made by coprecipitation. Also, these results show that it is possible to combine the effect of Gd and Nb in order to increase Nb solubility in CeO₂ solutions. The introduction of oxygen vacancies allows the accommodation of the oxygen excess from Nb₂O₅ into the structure of CeO₂.

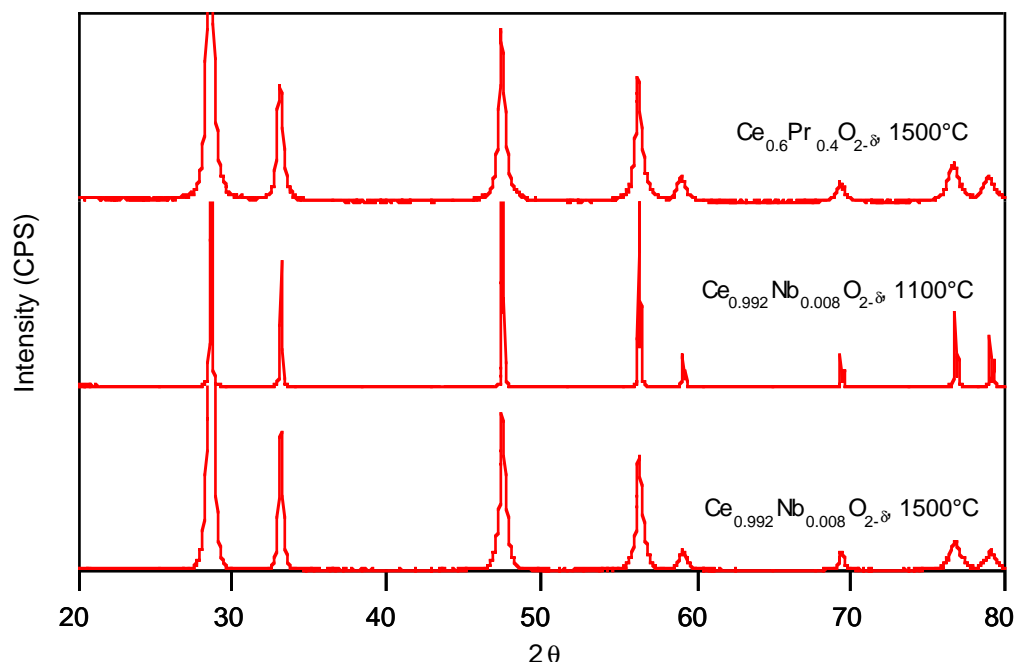


Figure 3: XRD patterns for the Nb and Pr-doped CeO₂ prepared by the solid-state (Nb-1500°C), the NbCl₅ (Nb-1100°C) and the coprecipitation (Pr-1500°C) methods.

Only few of these powders were characterized for their powder size distribution and their surface area (see Table 1). Y and Gd doped ceria prepared by the coprecipitation method gave a average particle size distribution of 0.5 μm, after sintering at 700°C/1 h. Nb-doped ceria prepared by the modified coprecipitation method gave an average particle size of 0.77 μm and a surface area of 6.14–6.39 m²/g, after sintering at 1500°C/1 h and ball-milled for 64 h. Ce_{0.6}Pr_{0.4}O_{1.8} coprecipitated gave a surface area of 17.98 m²/g.

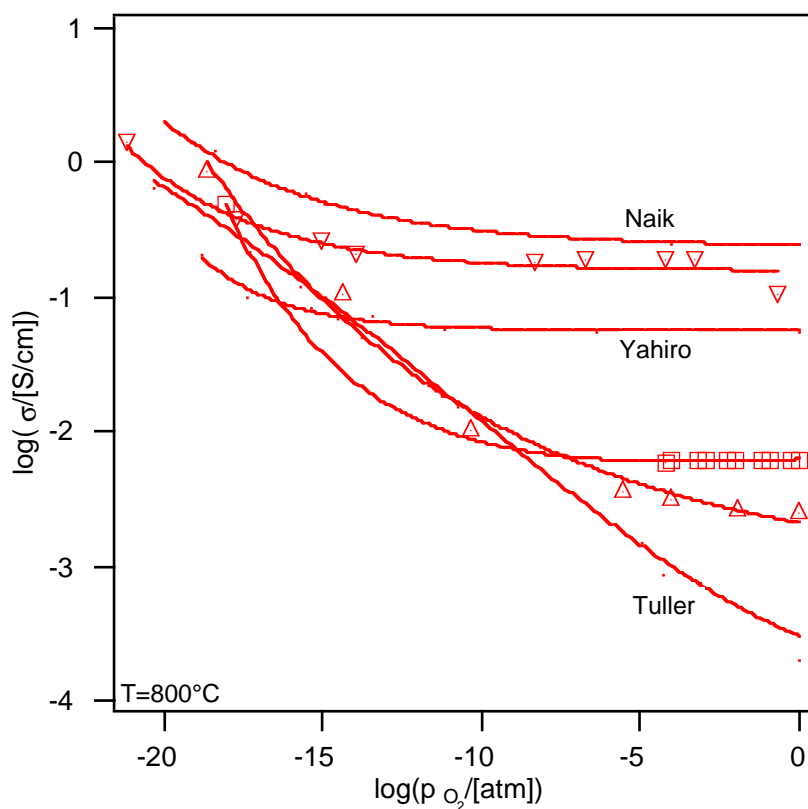


Figure 4: Effect of oxygen partial pressure on the total conductivity of CeO₂ solutions at 800°C. (Δ) Ce_{0.82}Gd_{0.12}Nb_{0.06}O_{2.8}; (□) Ce_{0.84}Gd_{0.12}Nb_{0.04}O_{2.8}; (▽) Ce_{0.992}Nb_{0.008}O_{2.8} CeO₂ (Tuller), Ce_{0.8}Gd_{0.2}O_{1.9} (Yahiro) and Ce_{0.992}Nb_{0.008}O_{2.8} (Naik) taken from references^{3, 7, 8} are also given for comparison.

Conductivity

The total electrical conductivity of most materials are shown in Figure 4 and 5 as a function of the oxygen partial pressure and temperature. The general behaviour of these conductivities are similar to the other CeO₂ solid solutions. A P_{O_2} independent region between 1 and 10⁻⁸ atm is observed indicating that the conductivity is overwhelmingly controlled by the extrinsic conductivity. The stability region becomes narrower at higher temperatures due to an increase in the intrinsic conductivity of CeO₂.

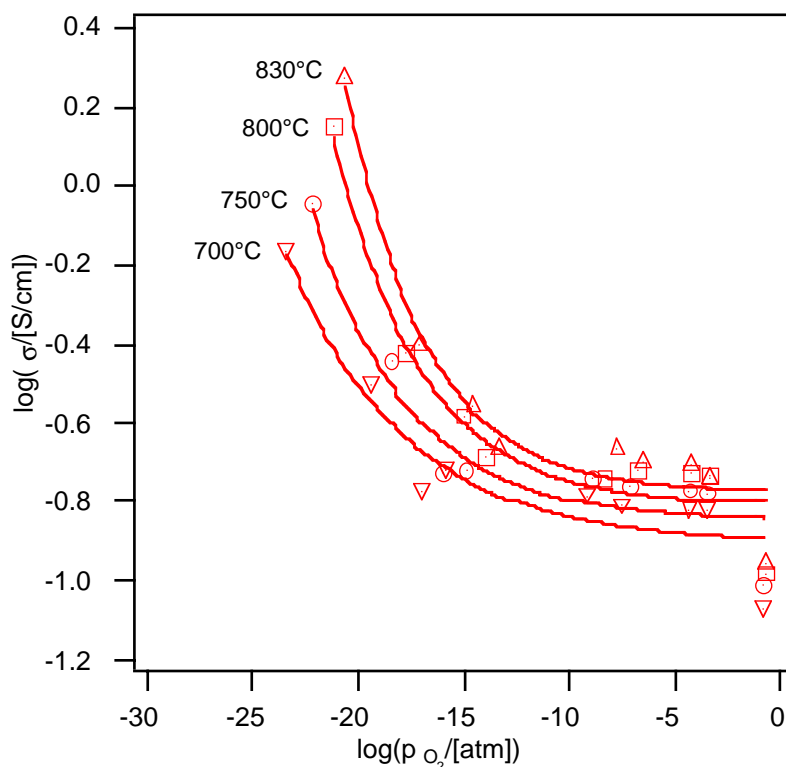


Figure 5: $Ce_{0.992}Nb_{0.008}O_{2-\delta}$ conductivity as a function of temperature and oxygen partial pressure.

The total conductivity in air is a factor of 10 higher for the 6% and 8%, and 30 times for the 4% Nb solutions compared to pure CeO₂. However, compared to pure Ce_{0.88}Gd_{0.12}O_{1.94}, the conductivities in air are lower. The higher the Nb content in Ce_{0.88}Gd_{0.12}O_{1.94}, the lower is the conductivity. Doping with only 0.8% Nb results in an enhancement of a factor of 1250 for CeO₂ conductivity, being of 0.25 S/cm, a value almost one order of magnitude higher than Gd doped ceria. These observations contrast with the reported change in color, which change to olive-green indicating higher Ce^{III} content. Also, our conductivity measurements for Ce_{0.992}Nb_{0.008}O_{2-δ} are slightly lower than what Naik et al. reported⁷.

An Arrhenius plot of the conductivity gives activation energies for Ce_{0.8}Gd_{0.12}Nb_{0.08}O_{2-δ}, Ce_{0.82}Gd_{0.12}Nb_{0.06}O_{2-δ}, and Ce_{0.84}Gd_{0.12}Nb_{0.04}O_{2-δ} between 77 and 97 kJ/mol which correspond more to the activation energy of the ionic process (85 kJ/mol)^{4, 5} (Figure 6). For Ce_{0.992}Nb_{0.008}O_{2-δ}, the activation energy in air corresponds to a small polaron hopping process of the conductivity mechanism of pure CeO₂ (18~51 kJ/mol)^{1, 7}, whereas it shifts to higher values at low oxygen partial pressures (Figure 6).

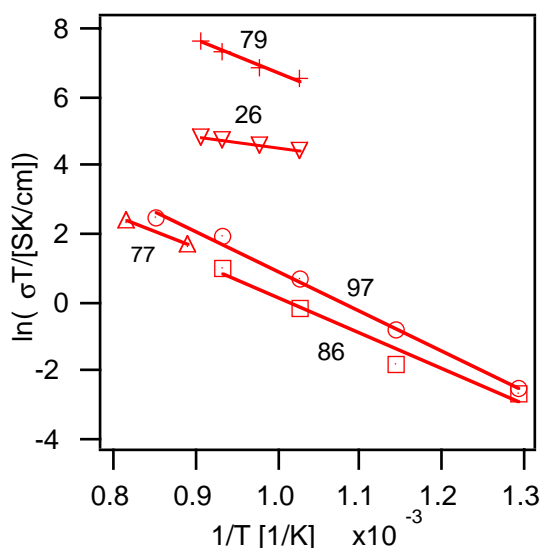


Figure 6: Arrhenius plots for the (O) $Ce_{0.84}Gd_{0.12}Nb_{0.04}O_{2-\delta}$ (□) $Ce_{0.82}Gd_{0.12}Nb_{0.06}O_{2-\delta}$ (Δ) $Ce_{0.84}Gd_{0.12}Nb_{0.08}O_{2-\delta}$ (∇) $Ce_{0.992}Nb_{0.008}O_{2-\delta}$ in air and (+) $Ce_{0.992}Nb_{0.008}O_{2-\delta}$ in humidified H_2 , with a P_{O_2} of about 10^{-22} atm, Inset numbers correspond to the activation energy given in kJ/mol.

If we consider that Nb is introduced in $Ce_{0.88}Gd_{0.12}O_{1.94}$ following an electronic and vacancy mechanism where the Nb_2O_5 excess oxygen is taken by the oxygen vacancies arising from Gd substitution, then the total conductivity could be expected to be proportional to that of the remaining vacancies in the structure. For one Gd, one Nb could then be dissolved considering the fact that for two Gd one vacancy arises and that for two Nb one oxygen is in excess. This approach would mean that a 4%Nb-12%Gd doped ceria is in fact a 8%Gd ceria solution, the 6%Nb-12%Gd doped ceria a 6% Gd doped ceria, etc. However, the Nb-Gd solutions show lower conductivities than expected (Figure 7). This difference might partially be related to the appearance of ceria orthoniobate ($CeNbO_4$) as evidenced by XRD, in the case of the 6 or 8%Nb-12%Gd doped ceria. This secondary phase is known to have a total conductivity of around 0.01 S/cm. These results contrast with Nauer et al.'s¹² who found that a 3% Nb doping of a praseodimium-ceria solution did not worsen its conductivity.

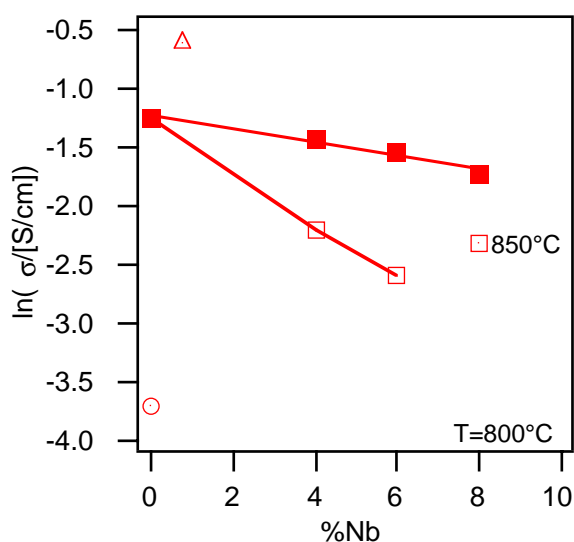


Figure 7: Compared conductivities of the Nb-doped $Ce_{0.88}Gd_{0.12}O_{1.94}$ solution with equivalently doped $Ce_{1-x}Gd_xO_{2-x/2}$: (O) pure ceria from reference³; (Δ) $Ce_{0.992}Nb_{0.008}O_{2-\delta}$ from reference⁷; (□) Nb-doped $Ce_{0.88}Gd_{0.12}O_{1.94}$ solutions and (■) the equivalently doped $Ce_{1-x}Gd_xO_{2-x/2}$.

From these results we conclude that 0.8%Nb shows the highest conductivity, in air. For low oxygen partial pressure, the total conductivity tends to be slightly higher than with pure ceria. The electronic conductivity with Nb is higher as with purely ionic Gd-doped ceria (Figure 4). Adding Nb to the Gd-doped ceria therefore induces an increase in the electronic conductivity. However, a precise control of Nb concentration is necessary in order to prevent the precipitation of secondary poorly conducting phases like $CeNbO_4$. For an anode purpose, Nb seems to be the best dopant, as it allows a higher conductivity in more oxidizing atmospheres than the other studied dopants. The conductivity of Pr-doped CeO_2 solutions were not studied but reports

indicate that a conductivity of 0.1 S/cm, i.e. 2.5 times less than Ce_{0.992}Nb_{0.008}O_{2-δ}, could be achieved with 50%Pr-3%Nb at 800°C whose main contribution to conductivity is electronic^{12, 13}, making them also interesting materials for anodes. The ionic conductivity of these two CeO₂ solutions is expected to increase under reducing conditions (see equation (3)). Pressed rods of the Ce_{0.6}Pr_{0.4}O_{2-δ} composition, sintered at 1500°C/4h, seemed to sinter but crumbled at room temperature. We were thus not able to make any conductivity test for this material. This might be due to changes in the valence number of Ce or Pr between high and low temperatures, giving rise to high thermal expansion. Generally, CeO₂-based solutions are more prone to reduction than LaCrO₃-based materials³⁶. In reducing conditions, CeO₂ expands as much as 2%⁶ versus 0.25 to 0.35% for heavily substituted LaCrO₃, unsubstituted LaCrO₃ having almost no measurable expansion between air and humidified H₂³⁷. Table 2 summarizes some reported values for the conductivity and thermal expansion of CeO₂-based compounds.

Table 2: Summary of some literature data on doped-ceria solutions.

Powder	σ , 800°C* [S/cm]	t_i	E_a [kJ/mol] air	P_{O_2} * [atm] 800°C	σ , 1000°C [S/cm] *	TEC [10 ⁻⁶ K ⁻¹]
CeO ₂	0.0003	0.35	18.3-50		≈2	9.7-12.3
Ca	0.042-0.056	0.99	81-74		2.4	12.8
Y	0.029		102-94	1x10 ⁻¹²		
Nb	0.25	5x10 ⁻⁴	17.3		5	
La	0.048	1	86-78	8x10 ⁻¹⁰		
Pr	0.1	≈0.5	84		1.2	10-11
Nd	0.059-0.031	1	99.7-75	2x10 ⁻¹³		
Sm	0.094-0.042	1	82-79.4	8x10 ⁻¹⁵	0.3	
Gd	0.055-0.038	0.99	68-85.4	2x10 ⁻¹³	1.4	12.5
Dy	0.077	0.98	89.6	8x10 ⁻¹²		
Ho	0.064	1	95.4			
Er	0.057	0.97	98.3			
Tm	0.056	1	96.4			
Yb	0.056-0.031	1	98.3-93.9	1x10 ⁻¹²		
YSZ	0.030	1				10.8

Data taken from references^{2, 4, 6-9, 12, 16, 18, 38-40}. t_i = ionic transference number; P_{O_2} * = the P_{O_2} at which $\sigma_i = \sigma_e$. * taken in air; * taken at a P_{O_2} of 10⁻¹⁵ atm. Doped ceria has the Ce_{0.8}M_{0.2}O_{2-δ} formula, with M the dopant.

Adhesion and electrode morphologies

The adhesion and the morphology of the different CeO₂-based electrodes were observed to depend on the powder handling and on the nature of the dopant. Ceria-based powders were observed to possess a needle-like morphology, which prevented proper adhesion on YSZ sheets (e.g. Figure 8) or (Y,Gd) doped ceria pellets. Calcining at high temperature and ball-milling were needed to achieve spherical powders, more prone to sinter.

Pure CeO₂ calcined at 700°C, 1200°C or 1400°C with subsequent ball-milling showed no adhesion at all when sintered at 1100°C, 1200°C or 1300°C. These electrodes were very friable, even though some kind of reaction occurred on top of the YSZ sheets at the higher sintering temperatures. This could be explained by the ease of reduction of CeO₂ at high temperature and the subsequent mismatch in expansion with YSZ^{13,41} (Table 2). 15 to 20% Y or Gd-doped ceria behaved in a similar way but powders calcined at 1450°C adhered to YSZ sheets when sintered at 1100°C or 1150°C (see Figure 9). The adhesion was enhanced when the sintering occurred under mildly reducing conditions (Ar). However, when the electrodes were reduced in humidified H₂, delamination occurred in most cases. A doping level of 15 or 20% was chosen for it represents the highest ionic conductivity value at the working temperature of 800 to 900°C. Sintering of the same electrodes over 15% Y doped ceria did not improve the sticking much.

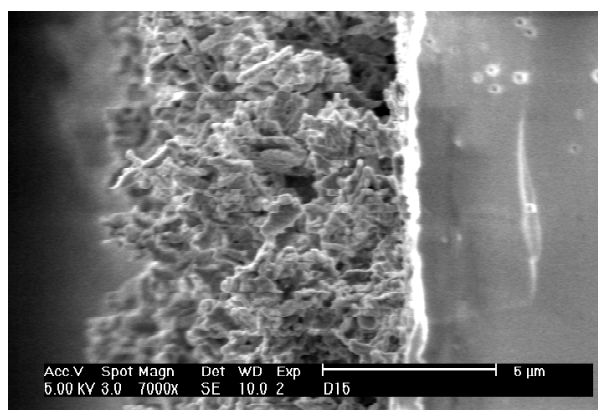


Figure 8: SEM micrograph of a $\text{Ce}_{0.8}\text{Gd}_{0.2}\text{O}_{1.9}$ electrode sintered at $1200^\circ\text{C}/4\text{h}$. The powder was used after calcination at $800^\circ\text{C}/1\text{h}$ and subsequent grinding.

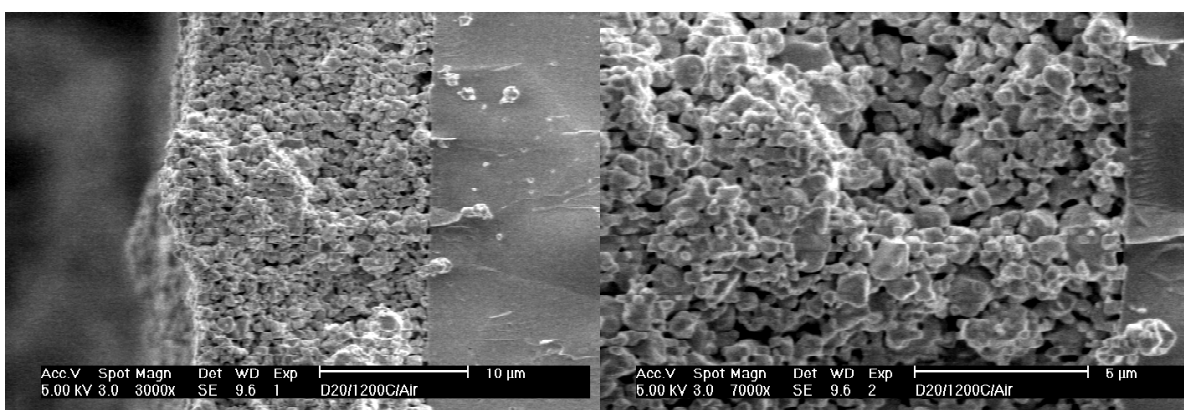


Figure 9: SEM micrographs of a $\text{Ce}_{0.8}\text{Gd}_{0.2}\text{O}_{1.9}$ electrode sintered at $1200^\circ\text{C}/4\text{h}$. The powder was used after calcination at $1450^\circ\text{C}/4\text{h}$ and subsequent ball-milling. The electrode seems to stick well, but is seen to possess a low porosity.

Pr-doped ceria behaved similarly to pure CeO_2 , and calcination at 700°C , 1200°C or 1400°C with subsequent ball-milling did not improve the sticking of the powder even after sintering at 1100°C to 1300°C . Pr seemed to present needle-like powders. At all sintering steps Pr seemed to diffuse into YSZ producing a reddish domain. Sintering of the same powder over 15%Y doped ceria pellets did not improve the adhesion, as the electrodes were observed to be friable.

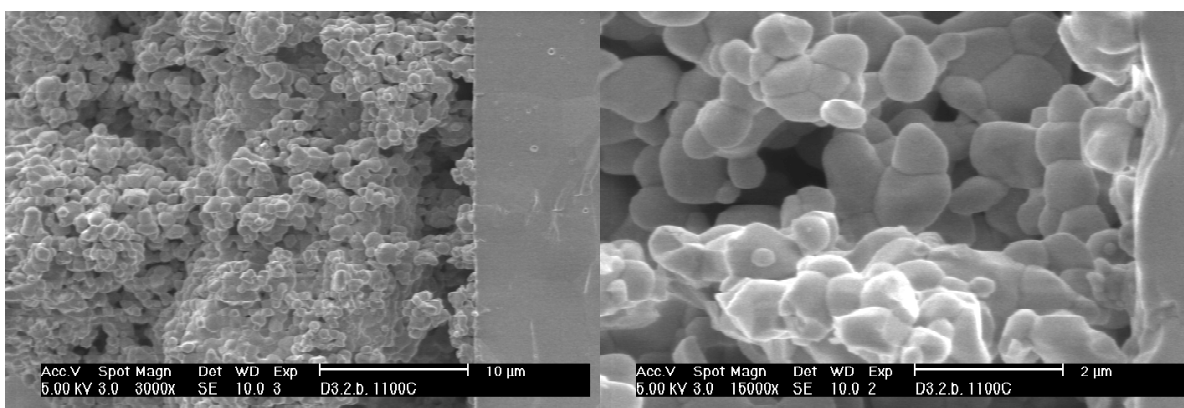


Figure 10: $\text{Ce}_{0.992}\text{Nb}_{0.008}\text{O}_{2.8}$ electrode morphology as observed by SEM. Electrodes obtained from powders made following the NbCl_5 route calcined at 1100°C and sintered at $1100^\circ\text{C}/4\text{h}$.

Only the $\text{Ce}_{0.992}\text{Nb}_{0.008}\text{O}_{2.8}$ composition adhered well on YSZ sheets. Both powder batches produced from the coprecipitation and from the NbCl_5 route gave good results. The electrode structure was quite dense (see Figures 10 and 11). This electrode adhered well at the temperature of 1100°C and tended to fully densify beyond 1300°C (see Figure 11). The analysis of the

electrode morphology indicates some kind of a melting process as all the grains seemed to present a rounded shape at 1100°C , and some melt-like forms appeared at and above 1300°C . Also, the adhesion was maintained even after reduction in humidified H_2 at 800°C . However, as for the Y and Gd-doped ceria, the electrodes seemed too dense, having a low porosity when compared to LaCrO_3 -based electrodes

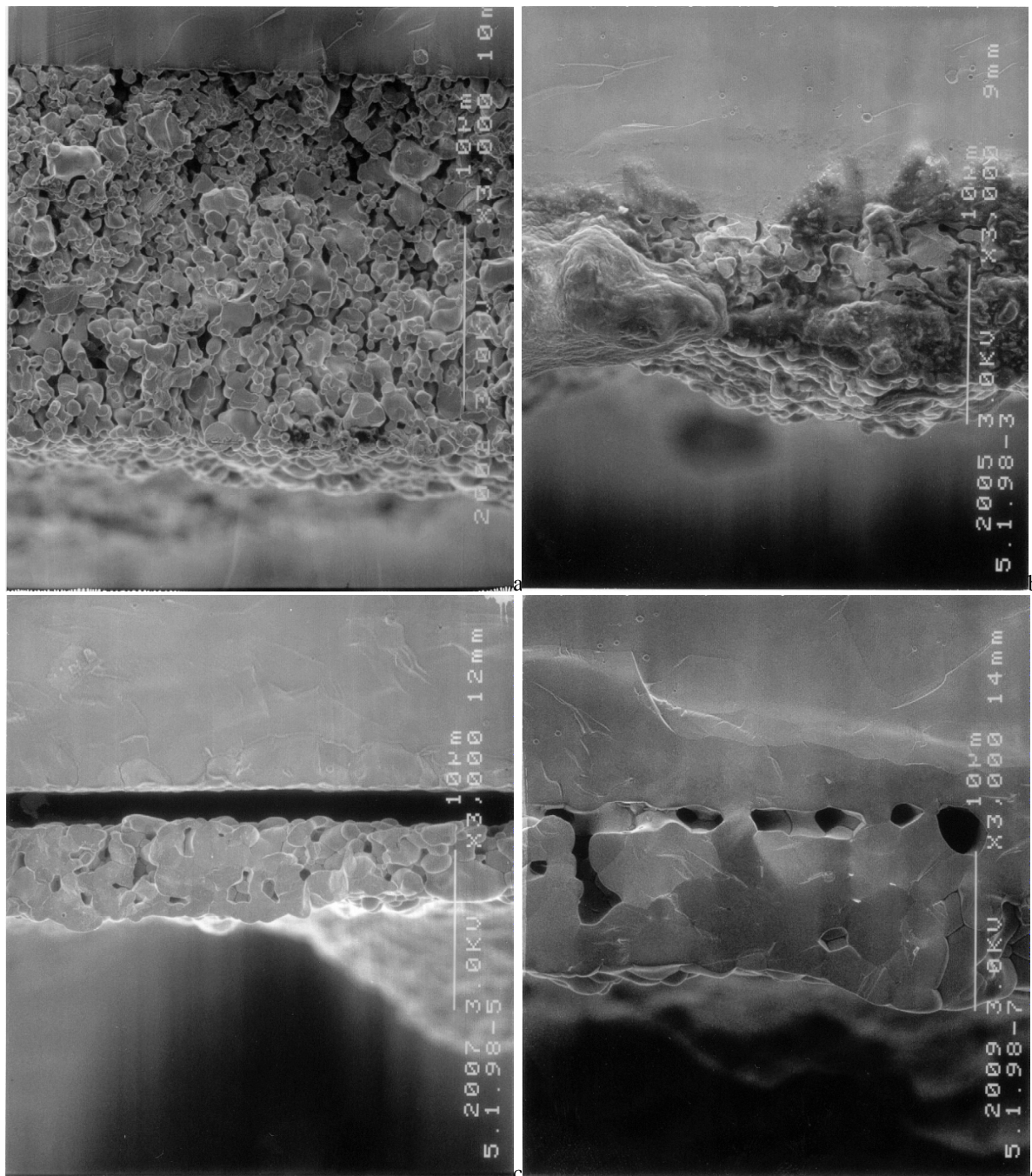


Figure 11: $\text{Ce}_{0.992}\text{Nb}_{0.008}\text{O}_{2.8}$ electrode morphology as observed by SEM. Electrodes obtained from powders made following the coprecipitation route, sintered at a. 1200°C , b. 1300°C , c. 1400°C and d. 1450°C for 4 h. The structure is quite dense at 1200°C and the electrode tends to form a melt like structure. The adhesion is strong after sintering at 1200°C and the electrode sinters completely at 1450°C . The interface shows voids at 1450°C , probably due to the interdiffusion of the species (Kirkendall-void).

The effect of Nb is not very clear. Test made with pure Nb_2O_5 (as it is also a good conductor at reduced atmospheres) sintered over YSZ sheets at different temperatures showed some kind

of surface doping on YSZ sheets. Nb has been reported to react with and dissolve in zirconia⁴². Interestingly, Nb₂O₅ did not stick on YSZ, most probably due to its needle-like powder, which could not be much rounded even by ball-milling. In the ceria electrode the presence of Nb might then promote adhesion by reaction. Furthermore, Nb has been shown to reduce the expansion coefficient of ceria-based materials¹³. However, under reduced oxygen potential, due to additional Ce^{IV} to Ce^{III} reduction, the material is bound to expand (about 1% expansion⁶) in a same manner to Y or Gd-doped CeO₂. The high initial sticking seems thus to prevent the porous structure from delaminating. Furthermore, Baumard et al. also observed that Nb addition to CeO₂ induced a densification process starting at 1200°C, leading to high relative densities⁴¹. Thus, for the anode, Nb seems to be one of the best dopant, both from the conductivity and adhesion point of views.

Addition of Nb to a Ce_{0.88}Gd_{0.12}O_{1.94} solution allowed a better adhesion on YSZ sheets. However, no effect was observed for the Ce_{0.6}Pr_{0.4}O_{2.8} composition. Multilayer variations were also attempted by mixing Ce_{0.992}Nb_{0.008}O_{2.8} with 8YSZ from Tosoh, Japan, or Magnesium Elektron, U.K., at different ratios (40/60 or 20/80). This procedure might be fruitful in future as in the case of LaCrO₃-based materials. Also, addition of catalysts such as Ni and Ru was made either by impregnation or by prior mixing of nitrate precursors with the electrode slurry. The last procedure proved to be detrimental as the electrodes tended to delaminate after reduction.

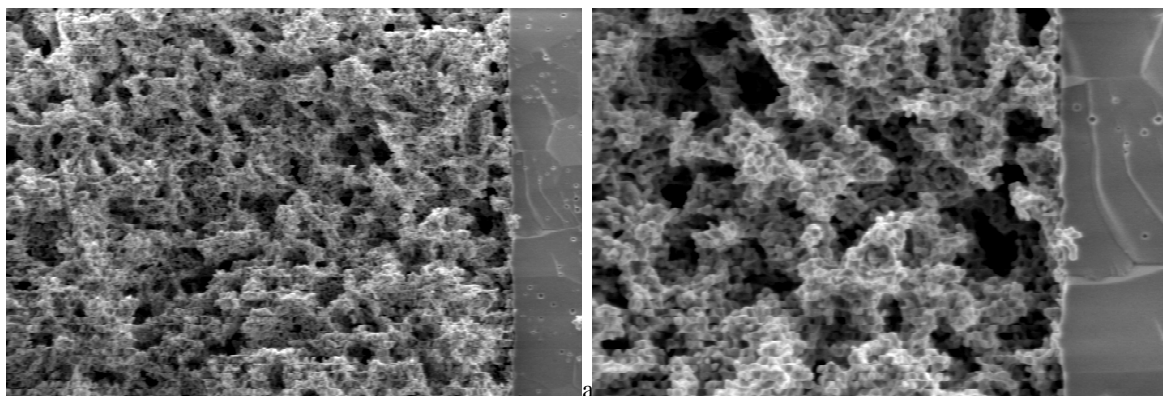


Figure 12: SEM microstructure of a porous anode made by the addition of Teflon balls (50 vol%), sintered at 1200°C/4h. This distance ——— corresponds approximately to 10 μm and 5 μm in the first and second micrograph respectively. Magnification: a.3000x and b.7000x.

Trials were also made to increase the porosity of CeO₂-based anodes. For this purpose, carbon powder (Printex 85 Furnace Black from Degusa, Germany) and Teflon balls (Dolder Teflon micropowder MP 1200, 2-4 μm, from Dolder, Basel, Switzerland) were mixed at 50 vol% with the anode powder during the slurry fabrication using terpineol and ethyl cellulose. The slurries were subsequently well mixed using a triple roll ball-mill. The carbon powder induced a very fine porosity below the μm scale. Teflon balls, however, allowed to get expanded structures as the one shown in Figure 12. This kind of structure allowed the impregnation of catalyst made of Cu and Ni using aqueous nitrate solutions. The highest loading reached was of 17 wt% of Cu, Ni or Ni-Cu catalyst (see Figure 13).

Chemical compatibility with YSZ

CeO₂, ZrO₂ and Y₂O₃ form solid solutions of the fluorite structure. The ternary solution possesses also an immiscibility gap^{43, 44}. CeO₂ is thought to dissolve to about 40% in YSZ at 1600°C⁴⁴. However, CeO₂ reacts with YSZ to yield mixed conducting solutions, having lower ionic conductivity than pure ceria^{14, 15, 45, 46}. This reaction is thus expected to increase the ohmic resistance at the anode electrolyte interface.

Due to the good adhesion of the Ce_{0.992}Nb_{0.008}O_{2.8} electrode, this was taken as model for the interfacial analysis of any possible reaction between ceria and YSZ during sintering at 1200°C, the highest sintering temperature allowed before full densification (see above). One electrode was thus sintered at 1200°C/4h (see Figure 14). The sample was made slimmer by ionic

bombardment. Different line-scan analyses were performed over the prepared sample (see Figure 15). By *EDS*, Nb peaks overlap with Y and Zr peaks. No image profile for Nb was thus possible and no knowledge could be gained in order to understand the adhesion mechanism of this precise composition. However, from the concentration profile of Ce and Zr, it is thought that no interdiffusion occurred between the anode and the support at the μm and nm scale, within experimental errors. Some Zr was observed on the anode very far from the interface, $> 5 \mu\text{m}$, and symmetrically some Ce was observed on YSZ and this is thought to stem from the ionic ablation (specimen preparation) in the region of interest.

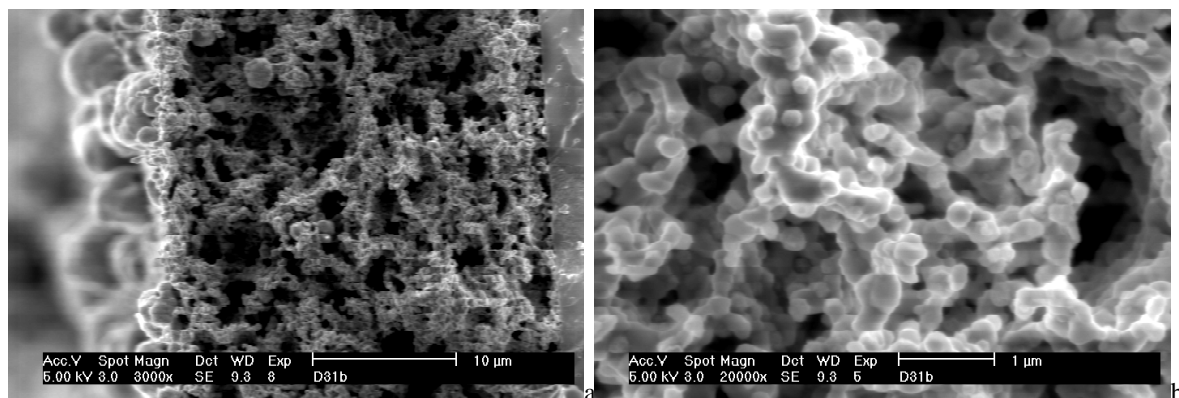


Figure 13: SEM micrograph of a $CeGdO$ anode impregnated with Cu. a: Not all the Cu penetrates the structure and some is deposited on the surface of the electrode; b. Cu tends to produce small droplets inside the anode.

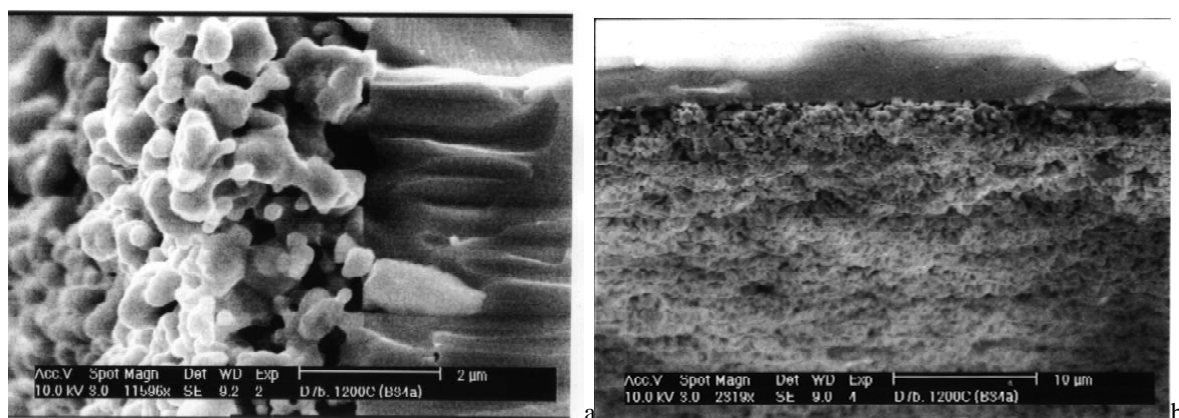


Figure 14: SEM microstructure of a $Ce_{0.992}Nb_{0.008}O_{2.\delta}$ anode sintered at $1200^\circ\text{C}/4\text{h}$. a. cross-section and b. surface (tilt 20°), of the pellet used for interdiffusion analysis by HRTEM.

Mitsuyasu et al. indicate no interdiffusion between YSZ and Y-doped ceria using powders and contacted pellets couples, when the sintering temperature was $\leq 1100^\circ\text{C}$ ^{47, 48}. They detected a surface reaction at 1300°C , 1500°C and 1700°C . At that temperature, the interdiffusion length was of $15 \mu\text{m}$. Our results indicate clearly that even at 1200°C no detectable reaction is to be expected.

Conclusions

Different CeO_2 -based powders were prepared using three different techniques. Oxalate coprecipitation was used for Y, Pr and Gd doped ceria all synthesized at $700^\circ\text{C}/1\text{h}$. Nb doped ceria was synthesized following a modified route, using Nb_2O_5 or $NbCl_5$ as precursors. Some of these powders were characterized for their particle size distribution and their surface area. It was observed that Nb induced a higher electronic conductivity in pure CeO_2 , but a concomitant doping with Gd had a negative effect on the total conductivity in air. Among all these powders, $Ce_{0.992}Nb_{0.008}O_{2.\delta}$ adhered best on YSZ electrolyte sheets and withstood the reducing conditions. From these physical and mechanical results, Nb-doped ceria seems to be the most suitable ceria

candidate for an anode material. However, as for LaCrO_3 -based materials, a composite electrode with YSZ would likely allow also other compositions to adhere to the electrolyte. Finally, ceria was observed to be relatively inert to YSZ when sintered at temperatures $\leq 1200^\circ\text{C}$, as evidenced by *HRTEM*.

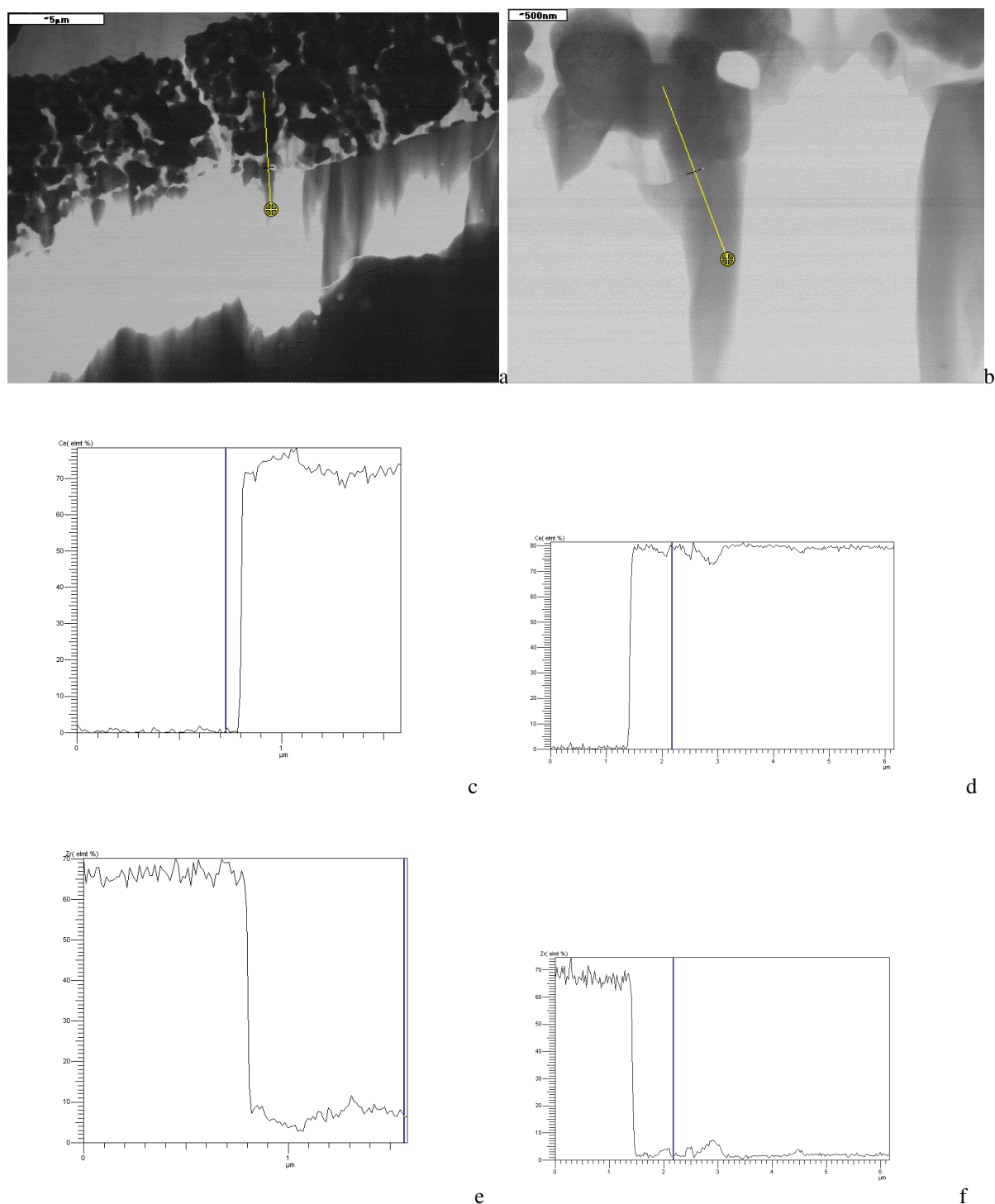


Figure 15: *HRTEM* line-scan chemical analysis. a-b. TEM micrographs of one studied region. c-d. Ce and e-f. Zr profile following the line. The high Zr content in the ceria layer is thought to be an artefact because of the ionic ablation (specimen preparation for TEM). Overall and within experimental error, no interdiffusion is thought to occur between YSZ and $\text{Ce}_{0.992}\text{Nb}_{0.008}\text{O}_{2-\delta}$ anode when the system is fired at $T \leq 1200^\circ\text{C}$.

References

- (1) Tuller, H. T.; Nowick, A. S., *J. Phys. Chem. Solids* **1977**, 38, 859-867.
- (2) Naik, I. K.; Tien, T. Y., *J. Phys. Chem. Solids* **1978**, 39.
- (3) Tuller, H. L.; Nowick, A. S., *J. Electrochem. Soc.* **1979**, 126, 209-217.
- (4) Dirstine, R. T.; Blumenthal, R. N.; Kuech, T. F., *J. Electrochem. Soc.* **1979**, 126, 264-269.
- (5) Faber, J.; Geoffroy, C.; Roux, A.; Sylvestre, A.; Abélard, P., *Appl. Phys. A* **1989**, 49, 225-232.
- (6) Mogensen, M.; Lindegaard, T.; Hansen, U. R.; Mogensen, G., *J. Electrochem. Soc.* **1994**, 141, 2122-2128.
- (7) Naik, I. K.; Tien, T. Y., *J. Electrochem. Soc.* **1979**, 126, 562-566.
- (8) Yahiro, H.; Eguchi, K.; Arai, H., *Solid State Ionics* **1989**, 36, 71-75.
- (9) Balazs, G. B.; Glass, R. S., *Solid State Ionics* **1995**, 76, 155-162.
- (10) Kudo, T.; Obayashi, H., *J. Electrochem. Soc.* **1975**, 122, 142-147.
- (11) Maricle, D. L.; Swarr, T. E.; Karavolis, S., *Solid State Ionics* **1992**, 52, 173-182.
- (12) Nauer, M.; Ftikos, C.; Steele, B. C. H., *Journal of the European Ceramic Society* **1994**, 14, 493-499.
- (13) Ftikos, C.; Nauer, M.; Steele, B. C. H., *Journal of the European Ceramic Society* **1993**, 12, 267-270.
- (14) Calès, B.; Baumard, J. F., *J. Electrochem. Soc.* **1984**, 131, 2407-2413.
- (15) Bentzen, J. J.; Schwartzbach, H., *Solid State Ionics* **1990**, 40/41, 942-946.
- (16) Takasu, Y.; Sugino, T.; Matsuda, Y., *Journal of Applied Electrochemistry* **1984**, 14, 79-81.
- (17) Gouet, M.; Lô, S.; Delebarre, H.; Guillou, M., *High Temperatures-High Pressures*. **1981**, 13, 51-56.
- (18) Yahiro, H.; Eguchi, Y.; Eguchi, K.; Arai, H., *Journal of Applied Electrochemistry* **1988**, 18, 527-531.
- (19) Blumenthal, R. N.; Brugner, F. S.; Garnier, J. E., *J. Electrochem. Soc.* **1973**, 120, 1230-1237.
- (20) Blumenthal, R. N.; Garnier, J. E., *Journal of Solid State Chemistry* **1976**, 16, 21-34.
- (21) Van herle, J.; Horita, T.; Kawada, T.; Sakai, N.; Yokokawa, H.; Dokiya, M., *Journal of the European Ceramic Society* **1996**, 16, 961-973.
- (22) Kudo, T.; Obayashi, H., *J. Electrochem. Soc.* **1976**, 123, 415-419.
- (23) Riess, I.; Braunshtein, D.; Tannhauser, D. S., *Journal of the American Ceramic Society* **1981**, 64, 479-485.
- (24) Duran, P.; Moure, C.; Jurado, J. R., *Journal of Materials Science* **1994**, 29, 1940-1948.
- (25) Drago, A. L.; Domingues, L. P., *Journal of the American Ceramic Society* **1982**, 65, 253-259.
- (26) Wendlandt, W. W., *Analytical Chemistry* **1958**, 30, 58-61.
- (27) Bay, L.; Horita, T.; Sakai, N.; Ishikawa, M.; Yamaji, K.; Yokokawa, H., *Solid State Ionics* **1998**, 113-115, 363-367.
- (28) Netzer, F. P.; Bertel, E. *Handbook on the Physics and Chemistry of Rare Earth*, **1982**.
- (29) Takasu, Y.; Nishibe, S.; Matsuda, Y., *Journal of Catalysis* **1977**, 49, 236-239.
- (30) *CRC Handbook of Chemistry and Physics*, 57 ed.; CRC Press, **1976-1977**.
- (31) In *Gmelin Handbuch der Anorganischen Chemie*, 49, TB3.
- (32) McCullough, J. D.; Britton, J. D., *Journal of the American Ceramic Society* **1952**, 74, 5225-5227.
- (33) Shannon, R. D.; Prewitt, C. T., *Acta Cryst.* **1969**, B25, 925-946.
- (34) Godina, N. A.; Panova, T. I.; Keler, E. K., *Izvestiya Akademii Nauk SSSR, Neorganicheskie Materialy* **1971**, 7, 1205-1208.
- (35) Kasimov, G. G.; Samsonova, N. D.; Sorokina, M. F.; Finkel'shtein, L. D., *Izvestiya Akademii Nauk SSSR, Neorganicheskie Materialy* **1978**, 14, 301-304.
- (36) Wang, S.; Inaba, H.; Tagawa, H.; Dokiya, M.; Hashimoto, T., *Solid State Ionics* **1998**, 107, 73-79.
- (37) Armstrong, T. R.; Stevenson, J. W.; Pederson, L. R.; Raney, P. E., *J. Electrochem. Soc.* **1996**, 143, 2919-2925.

- (38) Carter, S.; Chater, R. J.; Kajda, J.; Liddicott, K. M.; Kilner, J. A.; Steele, B. C. H. Proceedings of the first international symposium on ionic and mixed conducting ceramics., **1989**; p 84-94.
- (39) Hayashi, H.; Kanoh, M.; Quan, C. J.; Inaba, H.; Wang, S.; Dokiya, M.; Tagawa, H., *Solid State Ionics* **2000**, *132*, 227-233.
- (40) Wang, S.; Kobayashi, T.; Dokiya, M.; Hashimoto, T., *J. Electrochem. Soc.* **2000**, *147*, 3606-3609.
- (41) Baumard, J. F.; Gault, C.; Argoitia, A., *Journal of the Less-Common Metals* **1987**, *127*, 125-130.
- (42) Höftberger, M.; Gritzner, G., *Scripta Metallurgica et Materialia* **1995**, *32*, 1237-1241.
- (43) Yokokawa, H.; Horita, T.; Sakai, N.; Dokiya, M.; Van Herle, J.; Kim, S., *Denki Kagaku* **1996**, *64*, 690-691.
- (44) Hinatsu, Y.; Muromura, T., *Mat. Res. Bull.* **1986**, *21*, 1343-1349.
- (45) Reidy, R. F.; Simkovich, G., *Solid State Ionics* **1993**, *62*, 85-97.
- (46) Sammes, N. M.; Cai, Z., *Solid State Ionics* **1997**, *100*, 39-44.
- (47) Mitsuyasu, H.; Nonaka, Y.; Eguchi, K., *Solid State Ionics* **1998**, *113-115*, 279-284.
- (48) Mitsuyasu, H.; Nonaka, Y.; Eguchi, K.; Arai, H., *Journal of Solid State Chemistry* **1997**, *129*, 74-81.

Chapter 10 †

CeO₂-based catalysts for oxidation of CH₄ directly on SOFC anodes

CeO₂-based catalysts for oxidation of CH₄ directly on SOFC anodes

Abstract

Catalytic properties of Nb, Pr and Gd doped ceria were investigated for their use as anode materials for direct methane oxidation in SOFC. Impregnation of some of these catalysts with Ni, Cu, Ni-Cu or Ru was also undertaken in order to tune their activity. Different reaction gas mixtures were chosen to simulate the various SOFC operating conditions: partial oxidation, CO₂ and H₂O reforming. All experiments were performed in CH₄ rich environments. In steam reforming, the activity for pure ceria solutions increased from Nb<Gd<Pr, but in all cases the activity towards CH₄ was poor. All three solutions did not deposit carbon even under the most reducing conditions as observed by temperature-programmed oxidation (TPO) and TEM. Pr doping showed a higher degree of reduction leading to a higher vacancy concentration. Metallic loading of these catalysts was very sensitive to the sintering and reducing temperature, but in all cases lead ultimately to carbon deposition. Sintering at higher temperatures gave rise to a higher interaction with the CeO₂-based support, as the induction time for carbon formation was increased. Also, Cu-based alloys showed a higher resistance to carbon. By adding Cu to Ni, the overall activity towards CH₄ was reduced and concomitantly their ability to form carbon was reduced. However, these catalysts were very sensitive to the reduction as well as the operative temperature, perhaps due to a surface segregation of Cu. Some results showed that such cermet catalysts could be operated as anodes with methane feed.

Introduction

In this study, because of the stability of CeO₂-based compounds in reducing atmospheres, attempt was made to study the effect of Nb, Pr and Gd on the activity of these oxides. These elements were chosen as Nb doping was found to promote the adhesion of CeO₂ over YSZ sheets, but also induced electronic conductivity, Pr induces a redox effect (Pr^{III} and Pr^{IV}) and Gd increases the ionic conductivity of ceria (Chapter 9). Pr doping was considered even though its solution with ceria was observed not to adhere on YSZ sheets. But as stated in Chapter 9, composite electrodes with YSZ, as for LaCrO₃, could be a solution for this problem. As for LaCrO₃-based solutions, different gas compositions were considered and reaction promoters made of metallic catalysts were also studied. Not all catalysts were studied extensively under the different conditions. In an attempt to increase their activity, metal loading with Ni, Cu, Cu-Ni and Ru was undertaken. This concept uses well known steam-reforming catalysts, but also an attempt is made to study metals with low affinity and solubilities to carbon such as Cu, Au and Ag. For these elements no carbide is known (Table 1). Also, Mo was chosen as it possesses a stable carbide form under reducing conditions, having an interesting catalytic activity with CH₄

Table 1: Summary of metal elements with their known carbidic or carbon solubility limits*.

Element	Phases, solubility of carbon
Fe	martensite, Fe ₄ C, Fe ₃ C, Fe ₅ C ₂ , Fe ₇ C ₃ , Fe ₂ C
Co	Co ₃ C, Co ₂ C
Ni	Ni ₃ C (metastable)
Cu	0.0104 at% at 800°C
Mo	MoC and others
Pd	2.5 at% at 800°C
Ag	0.011 at% at 1660°C and diminishes with T
Ir	max. 3.12 at% at 2296°C
Pt	0.41 at% at 800°C
Au	max. 0.082 at% at 1027°C or 0.02 at% at 800°C

*Source ^{2, 3}

Methods

Powder preparation

Ce_{0.8}Gd_{0.2}O_{1.9} and Ce_{0.85}Pr_{0.15}O_{2-δ} powders were made following the coprecipitation method, whereas the Ce_{0.992}Nb_{0.008}O_{2-δ} was fabricated following the modified coprecipitation or the NbCl₅ method, all described in Chapter 9. Gd and Pr-doped ceria were calcined at 800°C. The Nb-doped ceria produced by the modified coprecipitation method was calcined at 1400°C, whereas the powder produced by the NbCl₅ route was calcined at 1100°C. All powders were subsequently ball-milled.

1wt% Ni or Ru-loaded Ce_{0.992}Nb_{0.008}O_{2-δ} was prepared by impregnating the powder with a Ni nitrate or a Ru chloride (Fluka 99%) solution in 2-propanol. After evaporating the solvent, the composites thus obtained were calcined *in-situ* during the catalytic test runs.

Co and Cu oxides as well as Ni_{1-x}Cu_xO were made starting from nitrate precursors (Fluka 99%) dissolved in water in the case of the Ni-Cu solutions and decomposed at 500°C in air. Mo was obtained from an industrial source as fibers. Some cermets with the Ce_{0.992}Nb_{0.008}O_{2-δ} solution were also made by impregnation. Another method was to coprecipitate the ceria powder with the Cu or Cu-Ni oxides and calcine the composite at 700°C/1h. Table 2 summarizes the different powders studied and some of their physical characteristics.

Table 2: Summary of the different powders used in this study.

Powder composition	surface area [m ² /g]	particle size <i>d</i> ₅₀ [μm]
Ce _{0.992} Nb _{0.008} O _{2-δ} (CeNbO)	6.4	0.8
Ce _{0.85} Pr _{0.15} O _{2-δ} (CePrO)	≈20	≈0.5
Ce _{0.8} Gd _{0.2} O _{2-δ} (CeGdO)	≈20	≈0.5
Co oxide	2.82	5.35
Cu oxide	0.47	
Mo		
Ni _{0.65} Cu _{0.35} O	11.23	0.75
1% Ni-Ce _{0.992} Nb _{0.008} O _{2-δ}		
1% Ru-Ce _{0.992} Nb _{0.008} O _{2-δ}		
30% Cu-Ce _{0.992} Nb _{0.008} O _{2-δ}		
30% (80% Cu-20% Ni)-Ce _{0.992} Nb _{0.008} O _{2-δ}		

Catalyst tests

0.2 to 0.5 g of the freshly prepared catalyst was introduced in the same set-up described in Chapter 6. Different gas compositions were used: a 5:1 CH₄:O₂ mixture for the partial oxidation condition, a 5:1:0.6 CH₄:O₂:CO₂ for combined reforming and a 56:y:x CH₄:Ar:H₂O, (x+y=44), for steam reforming operation. The gas flow rate was adjusted for an hourly space-velocity of approximately 19000 h⁻¹ (v/v). The testing conditions and the gas treatment and analysis were similar to those described in Chapter 6.

Temperature programmed oxidation and reduction

At the end of each run, a temperature programmed oxidation (TPO) in 20 ml/min He with 4 ml/min O₂ was undertaken in order to estimate the carbon deposition using an online quadrupole mass spectrometer. The heating rate was of 25°C/min.

Temperature programmed reductions (TPR) were undertaken on Nb, Pr and Gd doped ceria, in 9% H₂ in Ar with a total flow rate of 55 ml/min. The water produced during this reaction was followed by the online spectrometer.

XPS and TEM analysis

XPS was performed on Nb, Pr and Gd doped ceria, in a Kratos Axis Ultra Instrument using MgK α radiation. TEM analysis was performed in a Philips EM430T instrument at 300 kV equipped with an EDS X-ray spectrometer, over the 1 wt% Ni-Ce_{0.992}Nb_{0.008}O_{2- δ} , the Co and Cu-based catalysts. Carbon films on copper grids, used as sample holders, were impregnated by the catalysts powders dispersed in methanol.

Results

Powder characteristics and TPR

After ball-milling, the different powders were analyzed for their BET and particle size distribution. These are summarized in Table 2.

Figure 1 shows TPR spectra for the Nb, Pr and Gd doped ceria preoxidized at 900°C for 1 h. Three peaks were observed in the case of Pr at 525, 670 and 857°C; one for Gd at 898°C and one for Nb at 898°C. No other peaks could be clearly identified for Nb and Gd. The exact position of these peaks might be influenced by the surface area of the samples (6 m²/g for Nb and \approx 20 m²/g for Gd, Pr)⁴. The total amount of atomic O lost by reduction was calculated by integrating the corrected water peaks (mass 18) measured by MS (Figure 1). If we consider that Pr introduces mainly ionic conductivity in air, i.e. the valency is Pr^{III}, as for Gd, the initial oxygen content of the compound would be of 1.925, that of Gd being of 1.9. If we consider that the main substitution mechanism for Nb follows the electronic compensation route (Chapter 9), then the expected O content would be of 1.9997. The expected molar weight of these oxides are quite similar and estimated at 171.73, 171.04 and 173.94 g/mol for Nb, Pr and Gd doping respectively. By reducing these oxides, 0.228, 0.144 and 0.092 moles of O are removed (i.e. the non-stoichiometry δ) from Pr, Nb and Gd respectively. These values account for an oxygen content of about 1.69, 1.81 and 1.85, for Pr, Gd and Nb respectively. The non-stoichiometry is thus quite high in these oxides when compared to LaCrO₃-based oxides (11-5% versus 4% only). Also, these results are consistent with nonstoichiometry data given for pure and 10 or 20% Gd doped ceria by Wang et al.⁵, where an oxygen content of 1.7 is reached at a P_{O₂} of 10⁻²⁰ atm at 1000°C.

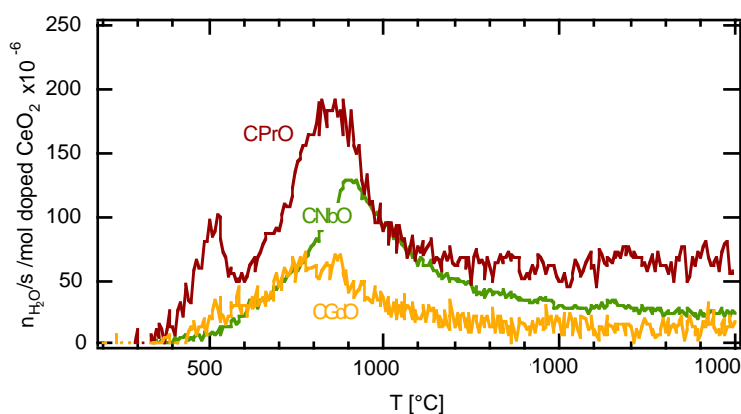
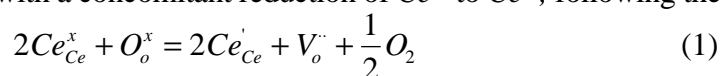


Figure 1: TPR (temperature programmed reduction) in 9:91 H₂:Ar with a total flow rate of 55 ml/min. The measurements were done on pre-oxidized powders, in pure oxygen, at 900°C for 1 h. The analysis is made by MS.

From the nonstoichiometry data of Wang et al.⁵, the reduction of 10% Gd doped ceria starts at around 10⁻²⁰ atm of oxygen, at low temperatures. The main peak observed by TPR starts at around 500°C in all three substitution cases. Thus, this reduction peak can be related to the removal of lattice oxygen with a concomitant reduction of Ce^{IV} to Ce^{III}, following the relation



The first peak in the Pr substitution, as it does not appear in the case of Nb, might be related to the reduction of Pr, most probably from Pr^{IV} to Pr^{III}⁶, or might be due to the reduction of the most easily reducible surface capping oxygen as a similar but small peak was observed for

CGdO in the same region. Such a peak was observed for CeO₂ at around 497°C⁷. The fact that CNbO did not show such a peak might be related to the surface area of the powder⁷. In the TPR analysis this peak should be related to the removal of surface oxygen or hydroxyl groups.

Interestingly, reduced ceria-based powders behaved also differently when exposed to air at room temperature. Reduced Nb, Pr and Gd doped ceria powders were blackish to grey. By contacting the Pr powder with air, it oxidized instantaneously and recovered its reddish color. The Gd powder oxidized slowly until its initial color was recovered. The Nb sample, however, did not oxidize, at least within the first 5 min.

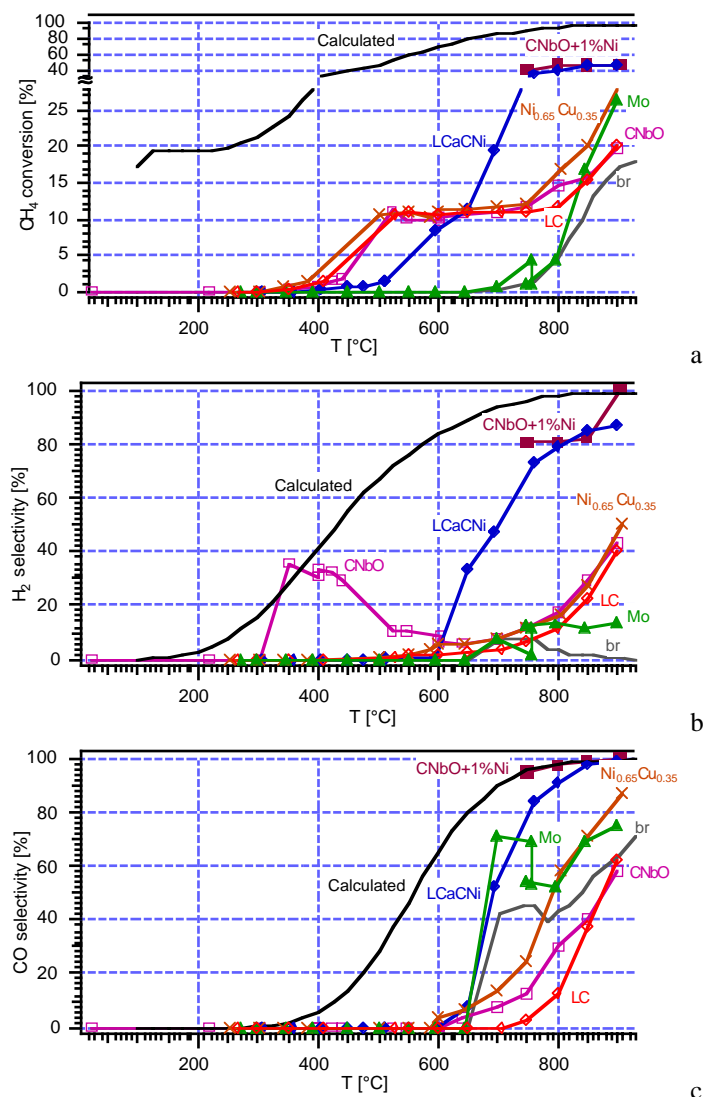
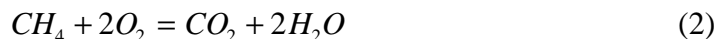


Figure 2: CH₄ conversion and H₂ and CO selectivities as a function of temperature for some of the catalysts in 5:1 CH₄:O₂. Calculated CH₄ conversion takes into account carbon deposition. For the CO selectivity based on the thermodynamic calculations, the deposited C was not incorporated in the selectivity ratio of c.

Effect of O₂

Figure 2 shows the steady state curves obtained by reacting a 5:1 CH₄:O₂ gas mixture on the Nb-doped and on the Ni_{0.65}Cu_{0.35}O catalysts. The La_{0.85}Ca_{0.15}Cr_{0.9}Ni_{0.1}O₃ and LaCrO₃ catalysts are also given for comparison. The total flow rate was set to 50 mlN/min. Globally, CeNbO and Ni-Cu catalysts behaved similarly to LaCrO₃. The reactions started around 400°C. In the middle temperature range, O₂ was entirely consumed by CH₄ to form CO₂ and H₂O as

H₂ and CO selectivities were low (Figure 2b and 2c), thus showing total oxidation (reaction (2)). In this region, the CH₄ conversion reached a maximum of 10%, O₂ being the limiting factor in the reaction.



In the lowest temperature region below 600°C, CeNbO showed an increase in the H₂ selectivity, whereas the CO selectivity was negligible. This might reflect a particular reaction where CH₄ is dissociating and H₂ and CO₂ are formed, following the overall reaction



This type of oxidation was not found over the Ni-Cu or the LaCrO₃ catalysts. It should be noted that this occurred in the region of low CH₄ conversion. Also, it is only above 700°C that an observable net partial oxidation occurs (reaction (4)) as with LaCrO₃



For the Ni containing catalysts, CeNbO+1%Ni and LCaCNi, the methane conversion was quite high giving rise to high H₂ and CO selectivities starting from 650°C. A conversion of 40% was attained, representing the total conversion of O₂ into syngas (reaction (4)).

For the Ni-Cu catalyst, the observed activity was in between the two last categories. To start with, the catalyst was brought to 980°C in 92:8 He:H₂ at a heating rate of 25°C/min. It is to be noted that under these reaction conditions, Cu and Ni were in the metallic rather than in an oxide form as the oxygen partial pressure was low. The measurements were then made from high to low temperatures. During this run, which lasted for about 20 h, no carbon build-up was observed. In a subsequent test, a freshly reduced catalyst at 800°C/1h in a flow of 5:5 H₂/N₂ was subjected to the same gas atmosphere at a constant temperature of 850°C. The activity was sustained only over a period of 18 h, after which carbon began to build up, resulting in a blocking of the flow-through reactor. At the same time, the powder temperature started to drop indicating the decrease in the exothermic CH₄ conversion. Working at a 3:1 CH₄:O₂ mixture improved the stability of the catalyst as carbon deposition was noticed after 25 h. Ni alone reacted readily with CH₄, and in the gas mixture of 5:1 CH₄:O₂, the reaction proceeded rapidly (20 min) to form a large carbon deposit. It is thus interesting to note that Cu seemed to moderate the high activity of Ni. Cu alone was a mild catalyst leading to 12% CH₄ conversion at 850°C but it also deposited C.

Co on the contrary was quite active with a 42% CH₄ conversion at 850°C, depositing C after 3 h. Mo showed a mild activity of 20% CH₄ conversion at 900°C but it was found to form oxide species with oxygen leading to its transport to the cold part of the reactor (i.e. evaporation-recondensation). Molybdenum was chosen as it is known to form stable carbides under reducing conditions with interesting oxidative activities¹.

Tests carried out in the blank reactor, under the various gas mixtures, showed that no reaction was occurring below 700°C, while at higher temperatures, the gases reacted to produce CO₂, CO and H₂O; CO was also formed by water gas shift reaction



CH₄ conversion reached 15%, at 900°C in the case of the blank reactor (see Figure 2, whereas in Chapter 6, the thermodynamic limits were also represented).

Thus globally, the reactivity of CH₄ over these different catalysts, in the gas mixture of 5:1 CH₄:O₂, taking the conversion of CH₄ as parameter followed the trend CeNbO+1%Ni>Co>Ni-Cu>Mo>CeNbO>Cu. Table 3 summarizes the activity of the different catalysts at 850°C. For comparison, LaCrO₃ and La_{0.85}Ca_{0.15}Cr_{0.9}Ni_{0.1}O₃ were added to indicate the low end and the high end of activity observed in the previous study (Chapter 6).

In terms of turn-over frequency (*TOF*), calculated as defined in Chapter 6, the trend is different: Cu>Co>CeNbO+1%Ni>Ni-Cu>CeNbO. For the metallic oxides, the *TOF* was calculated on the basis of the oxide surface area and not the reduced metal surface area, as these were not measured.

Table 3: Summary of the activity in the different gas mixtures at 850°C.

Powder composition	mass [g]	X 5:1 CH ₄ :O ₂	TOF [mol/sm ²]	E _a [*] [kJ/mol]	X CH ₄ :O ₂ :CO ₂	TOF [mol/sm ²]	X CH ₄ :H ₂ O	TOF [mol/sm ²]	E _a [*] [kJ/mol]
Maximum conversion possible		40 ^a			52 ^b		5.4 ^c		
Ce _{0.992} Nb _{0.008} O _{2-δ}	0.48	16	1.74x10 ⁻⁹		16	1.61x10 ⁻⁹	0.3	7.57x10 ⁻¹¹	114.8
Ce _{0.85} Pr _{0.15} O _{2-δ}	0.24						2.7	2.28x10 ⁻¹⁰	218.0
Ce _{0.8} Gd _{0.2} O _{2-δ}	0.17						1.3	1.48x10 ⁻¹⁰	224.0
Co oxide	0.33	42	1.41x10 ⁻⁸						
Cu oxide	0.41	12	1.97x10 ⁻⁸						
Mo	0.26	20		72.5					
Ni _{0.65} Cu _{0.35} O	0.32	20	1.83x10 ⁻⁹	99.5					
1%Ni-Ce _{0.992} Nb _{0.008} O _{2-δ}	0.73	45	2.88x10 ⁻⁹		61	4.71x10 ⁻⁹	9.0	4.79x10 ⁻¹⁰	-
1%Ru-Ce _{0.992} Nb _{0.008} O _{2-δ}	0.33						5.3	1.65x10 ⁻⁹	-
30%Cu-Ce _{0.992} Nb _{0.008} O _{2-δ} ^d	0.28						0.3		
30%(80%Cu-20%Ni)-Ce _{0.992} Nb _{0.008} O _{2-δ} ^d	0.33						7.5		
LaCrO ₃	0.27	15	5.18x10 ⁻⁹	97	15	7.04x10 ⁻⁹	1.7	1.57x10 ⁻⁹	272.0
La _{0.85} Ca _{0.15} Cr _{0.9} Ni _{0.1} O ₃	0.26	40	2.12x10 ⁻⁸	45	52	2.88x10 ⁻⁸			

The maximum conversion possible was calculated following: ^a CH₄ + 0.5 O₂ = CO + 2 H₂; ^b CH₄ + CO₂ = 2 CO + 2 H₂ and ^c CH₄ + H₂O = CO + 3 H₂. ^d measured at 800°C. * derived at low conversion rates.

Apparent activation energies for the oxidation reactions of some of these oxides were determined at conversions below 10%. Ni-Cu and CeNbO catalysts had activation energies of 99.5 and 97.9 kJ/mol respectively, whereas Mo was thermally activated with 72.5 kJ/mol. A value of 117 kJ/mol was calculated for the noncatalytic thermal reaction in the same quartz reactor.

Effect of CO₂

Figure 3 shows the influence of CO₂ on the oxidation reaction of CH₄ in 5:1:0.6 CH₄:O₂:CO₂ gas mixture. Table 3 summarizes the activity of the different catalysts at 850°C. By adding CO₂ to the 5:1 CH₄:O₂ gas mixture, no increase in the reaction is observed over CeNbO as for LaCrO₃. CO₂ reforming is small, and increases only at high temperatures as shown in Figure 4. At T ≥ 800°C, the gas shift reaction (reaction (5)) takes place by a concomitant increase in CO and decrease in H₂ selectivity (see Figure 3b and c) when compared with the 5:1 CH₄:O₂ runs (Figure 2b and c). Thus there is no CO₂ inhibiting effect as is the case for the lanthanum chromites (except those doped with Sr and Ni, Chapter 6).

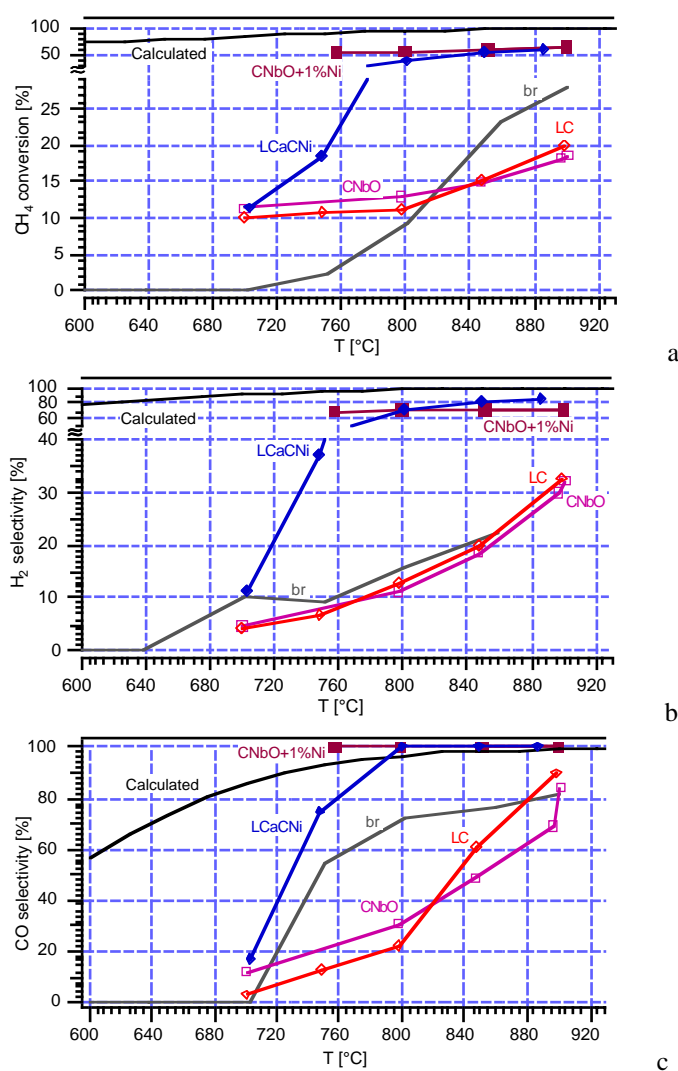


Figure 3: CH₄ conversion and H₂ and CO selectivities as a function of temperature for two of the catalysts in 5:1:0.6 CH₄:O₂:CO₂. The calculated CH₄ conversion takes into account carbon deposition. For the CO selectivity based on the thermodynamic calculations, the deposited carbon was not incorporated in the selectivity ratio, as shown in c.

By adding 1% Ni to the CeNbO, full reforming of CO₂ was observed following the reaction



Its activity is somewhat higher than that of La_{0.85}Ca_{0.15}Cr_{0.9}Ni_{0.1}O₃. Also, the conversion is slightly higher (61%) as the inlet gas mixture was slightly more oxidative than for the other tests.

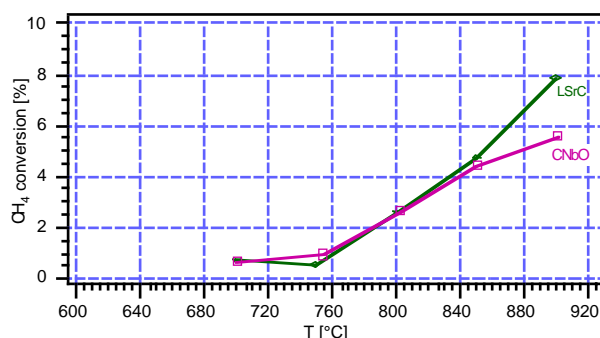


Figure 4: CH₄ reforming in 5:1:0.6 CH₄:Ar:CO₂.

Effect of H₂O

Figure 5 displays the steam reforming reaction



in a 56:41:3 CH₄:Ar:H₂O mixture while Table 3 summarizes the activity of the different catalysts at 850 °C. Here again, the CeNbO catalyst is observed to have a low activity toward CH₄, as its conversion is only 2% at 900 °C. This value is even lower than with LaCrO₃. By adding a metallic catalyst like Ni or Ru, the activity is increased. However, the conversion was observed in these both cases to be higher than expected indicating C formation. Indeed, if all water is consumed without C deposition, a CH₄ conversion of only around 5% is awaited. Ru is observed to induce less carbon than Ni. These cermet catalysts, however, eventually plugged the reactor during the run.

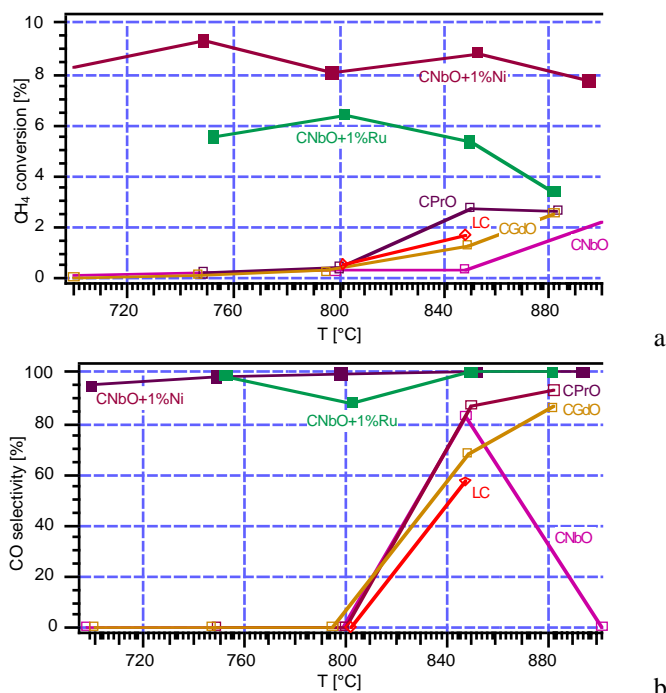


Figure 5: CH₄ conversion and CO selectivity as a function of temperature for some catalysts in 56:41:3 CH₄:Ar:H₂O.

Tests were also made with Cu-based catalysts. The 30%Cu-70%CeNbO composition heated to 700°C in Ar and subsequently reduced with H₂ for 20 min, showed a CH₄ conversion of only 0.25% at 800°C, but ultimately carbon deposited and slowly plugged the reactor. It was observed that with the cermet catalysts, the conditioning of the powders had an effect on their stability towards CH₄. For example, a 30%(80%Cu-20%Ni)-70%CeNbO compound deposited carbon (CH₄ conversion of 7.5%) after 20 min time when the catalyst was reduced at 750°C, while it sustained its activity at 800°C for more than 120 h when reduced prior to its use for 20 min in H₂ at 830°C (CH₄ conversion of 3.5%). Such an interaction, between the metal and ceria is reported to be generally promoted by a reducing pretreatment⁷. This indicates clearly that the activity of Ni can be controlled by copper addition, leading thus to a carbon free reaction. However, as for the pure copper, the activity tended to decrease after a while, indicating that the system should be kept under enough oxidative conditions to prevent C deposition. The fact that Ru and Ni deposited C might be due to the low sintering temperature of these catalysts.

Also, ceria-based catalysts showed a small difference between the dopants. Nb-doped ceria was observed to have the lowest activity, followed by CeGdO and CePrO. Methane conversion in 3%H₂O at 850 and 800°C respectively was as follows: 0.3% and 0.2% for Nb, 1.3% and 0.3% for Gd and 2.7% and 0.4% for Pr. In comparison, LaCrO₃ gave a conversion of 1.7% (Table 3). Globally, the activity trend was CeNbO+1%Ni>CeNbO+1%Ru>30%(80%Cu-20%Ni)-70%CeNbO>CePrO>CeGdO>30%Cu-70%CeNbO=CeNbO.

Apparent activation energies were measured for some of these catalysts and are summarized in Table 3. They vary between 114.8 for CeNbO to 224 for CeGdO and 218 kJ/mol for CePrO. Otsuka et al.⁸ reported an activation energy of 160 kJ/mol for CH₄ oxidation over CeO₂. LaCrO₃ was thermally activated with 272 kJ/mol. The Ru and Ni containing CeNbO catalysts showed a slightly negative activation energy which might indicate a deactivation due to carbon deposition⁹. In comparison, steam reforming on Ni based catalysts is reported to have an activation energy between 20 and 160 kJ/mol¹⁰, the latter representing the activation energy in the absence of diffusion limitations¹¹.

The reaction order with respect to P_{H₂O} varied with temperature for CeNbO, being -0.7 at 750°C, -0.02 at 800°C and 0.2 at 900°C. For CeNbO+1%Ni the reaction order was of 0.7 at 850°C. Also, the higher the water content, the lower the CO selectivity (e.g. 83% for 3%H₂O versus 0% for 20%H₂O in the case of CeNbO), very similar to what was observed with LaCrO₃-based catalysts.

Methane coupling

As for LaCrO₃-based oxides, methane coupling was quite low. Of all studied catalysts, only CNbO, Mo, Co, Cu and Ni_{0.65}Cu_{0.35}O produced some C₂ compounds, in the 5:1 CH₄:O₂ gas mixture with or without CO₂ (6, 28, 0.5, 3 and 1.4% selectivity at 850°C for these oxides respectively). The addition of H₂O suppresses the CH₄ coupling completely as it is evident from the fact that all catalysts studied in 50:41:3 CH₄:Ar:H₂O did not produce C₂ species. Among rare earth oxides, CeO₂ was reported to release very few methyl radicals as its acidic sites contribute to scavenge these radicals leading to their oxidation to CO_x compounds^{7,12}.

TPO

Temperature programmed oxidation (TPO) experiments were started from room temperature to 1000°C after running the catalyst for one day or more in CH₄ containing fuel. Nb, Pr or Gd doped ceria presented negligible carbon deposition (e.g. 2×10⁻¹⁰ mol CO₂ produced, i.e. 4.5×10⁻⁷ carbon layer for Pr doping). This is much less than what was observed on LaCrO₃-based catalysts. The temperatures at which carbon was burned were quite low, between 160 and 380°C representing most probably adsorbed carbonaceous species. A broad low intensity peak around 650-715°C was also observed (e.g. Figure 6). On the other hand, Ce_{0.992}Nb_{0.008}O_{2.8} impregnated with 1% Ni or Ru showed build-up of carbon. This carbon amounted to more than 14 carbon monolayers in some cases depending on the run time. Cu catalysts showed the same behavior, when run beyond the onset time after which carbon started to deposit. Some of the results in 50:41:3 CH₄:Ar:H₂O are summarized in Table 4.

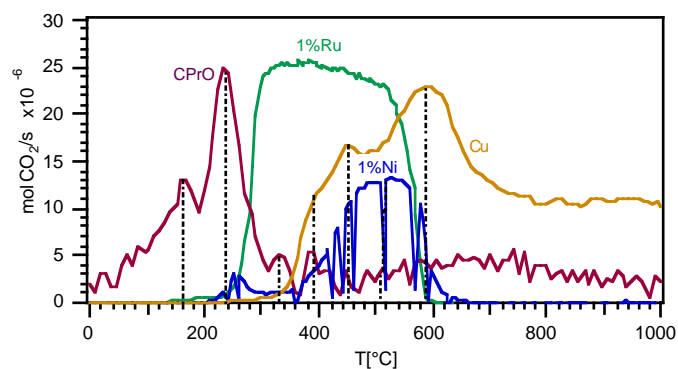


Figure 6: Temperature programmed oxidation (TPO, 25°C/min, 20 mlN/min He + 4 mlN/min O₂) on Ce_{0.85}Pr_{0.15}O_{2-δ} (x1000), Ce_{0.992}Nb_{0.008}O_{2-δ} + 1%Ru (x1), Ce_{0.992}Nb_{0.008}O_{2-δ} + 1%Ni (x3) and Cu (x2). All were made after a catalytic run in 56:41:3 CH₄:Ar:H₂O except for Cu (5:1 CH₄:O₂). The amount of C deposited on metal catalysts depended on the reaction time. Multipliers in parentheses indicate the number of times the curves have been magnified.

Table 4: Summary of the TPO temperature peaks and the total corresponding number of monolayers. The measurements were made after a run in 50:41:3 CH₄:Ar:H₂O.

Catalyst composition / temperature [°C]	1 st peak	2 nd peak	3 rd peak	4 th peak	5 th peak	monolayers
Ce _{0.992} Nb _{0.008} O _{2-δ}	-	-	-	-	-	0
Ce _{0.85} Pr _{0.15} O _{2-δ}	158.7	234.1	329.9	379.1	664.5	0
Ce _{0.8} Gd _{0.2} O _{2-δ}	-	286.7	-	-	715	0
Ce _{0.992} Nb _{0.008} O _{2-δ} + 1%Ni	-	271	-	-	540	19
Ce _{0.992} Nb _{0.008} O _{2-δ} + 1%Ru	-	-	330	-	540	80

XPS analysis

XPS analysis was conducted on the used catalysts samples. The XPS peak positions for the different elements were adjusted by shifting the carbon 1s peak to 285 eV. The average peak positions were as: 3d Ce, 880 eV; 3d Nb, 206.1 eV; 3d Pr, 930 eV; 4d Gd, 140.2 eV and 1s O, 528.6 eV. XPS peaks for the different species are shown in Figure 7.

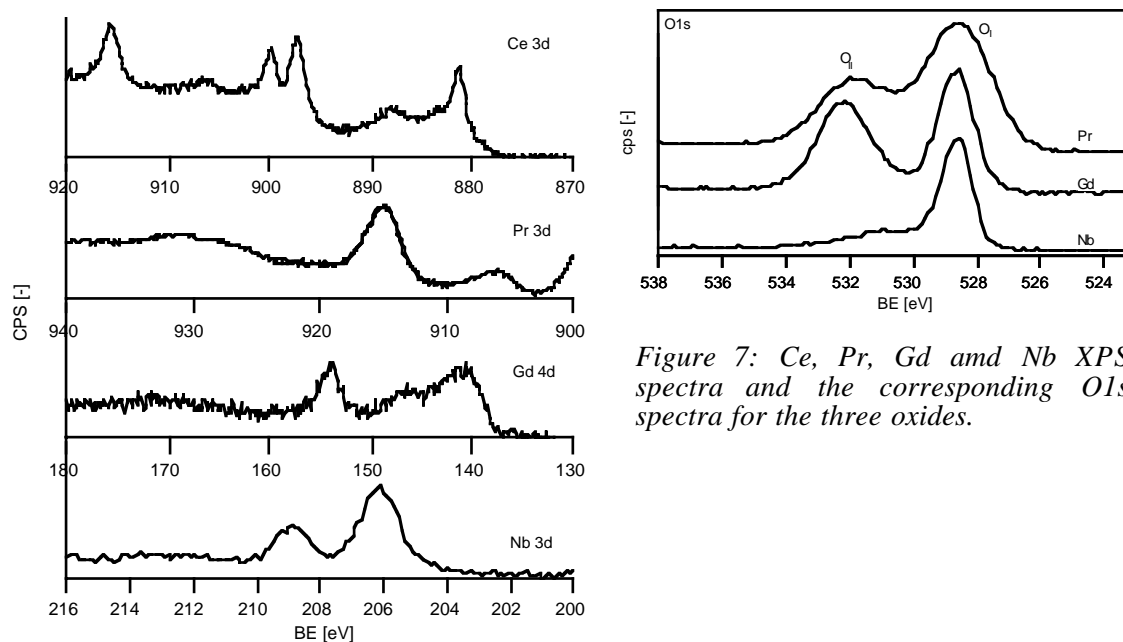


Figure 7: Ce, Pr, Gd and Nb XPS spectra and the corresponding O1s spectra for the three oxides.

XPS analysis reveals surface segregation on the ceria powders. As summarized in Table 5, Nb and Gd tended to segregate in a very high proportion whereas Pr followed the nominal value. In literature, LEIS analysis showed that the outer 5 monolayers of Ce_{0.8}Gd_{0.2}O_{1.9} were enriched with Gd, with the Ce/Gd ratio changing from 1 at the outermost surface to 4.2 in the bulk¹³. Our results for Gd go in the same direction, even though the analysis depth is expected to be quite higher in the XPS technique. The surface concentration change could have a

detrimental effect on the conductivity as it is known that at higher Gd content the ionic conductivity decreases.

Table 5: Summary of the XPS surface analysis given in percent of the sum of the total metal *M* elements.

XPS analysis [%] Catalyst composition	Nb	Ce	Pr	Gd	Nominal concentration	Ce/M surface	Ce/M nominal
Ce _{0.992} Nb _{0.008} O _{2-δ}	24.2	75.8			0.8	3.1	124
Ce _{0.85} Pr _{0.15} O _{2-δ}		81.0	19.0		15	4.3	5.6
Ce _{0.8} Gd _{0.2} O _{2-δ}		58.9		41.1	20	1.4	4

TEM analysis

TEM analyses were performed on the CeNbO+1%Ni, 30%Cu-70%CeNbO, 30%(80%Cu-20%Ni)-70%CeNbO and on Co catalysts. They confirmed the previous measurements and showed clearly the carbon formation over these catalysts.

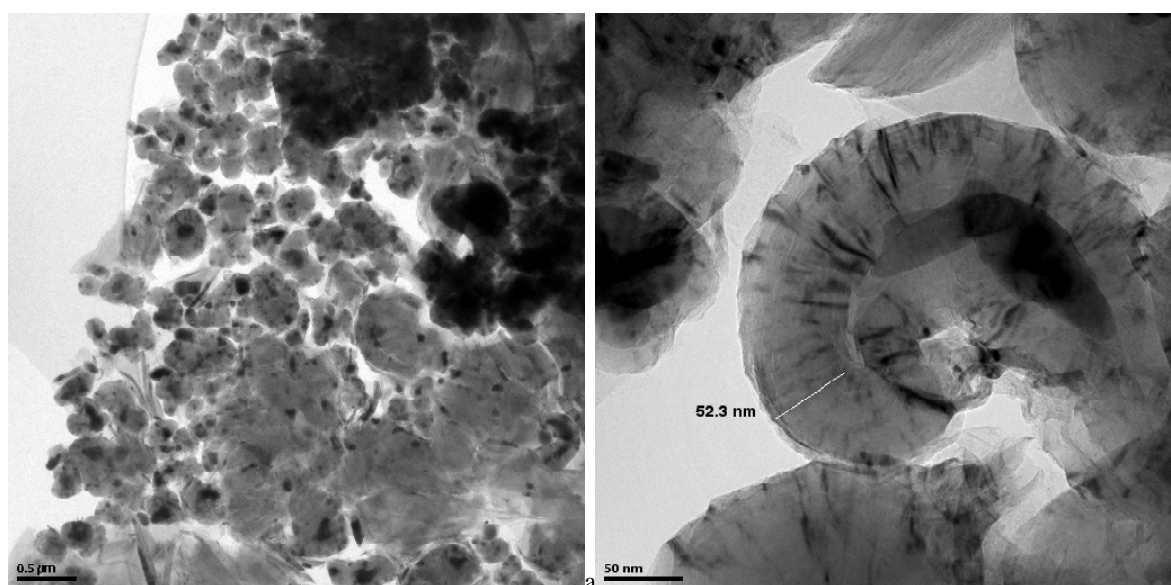


Figure 8: TEM micrographs of Co catalyst after 3 h run in 5:1 CH₄:O₂. Graphitic carbon films cover the Co particles either a. completely or b. partially.

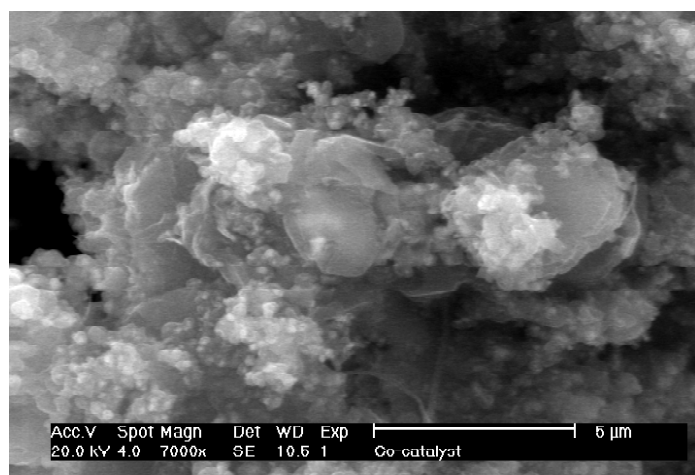


Figure 9: SEM micrograph of the Co catalyst immersed in carbon. This is the same catalyst as the one studied by TEM (Figure 8),

As shown in Figure 8a, Co formed a large amount of carbon deposits after 3 h run in 5:1 CH₄:O₂. Graphitic carbon was observed to encapsulate the Co particles, either totally (Figure 8a, the black spots corresponding to Co) or partially, by precipitating on one side and slowly covering the metallic particle (e.g. Figure 8b). No filamentous carbon could be observed. The

carbon layers had varying thicknesses with a typical value of about 50 nm. Interestingly, this high amount of carbon could also be observed by SEM-EDAX (Figure 9).

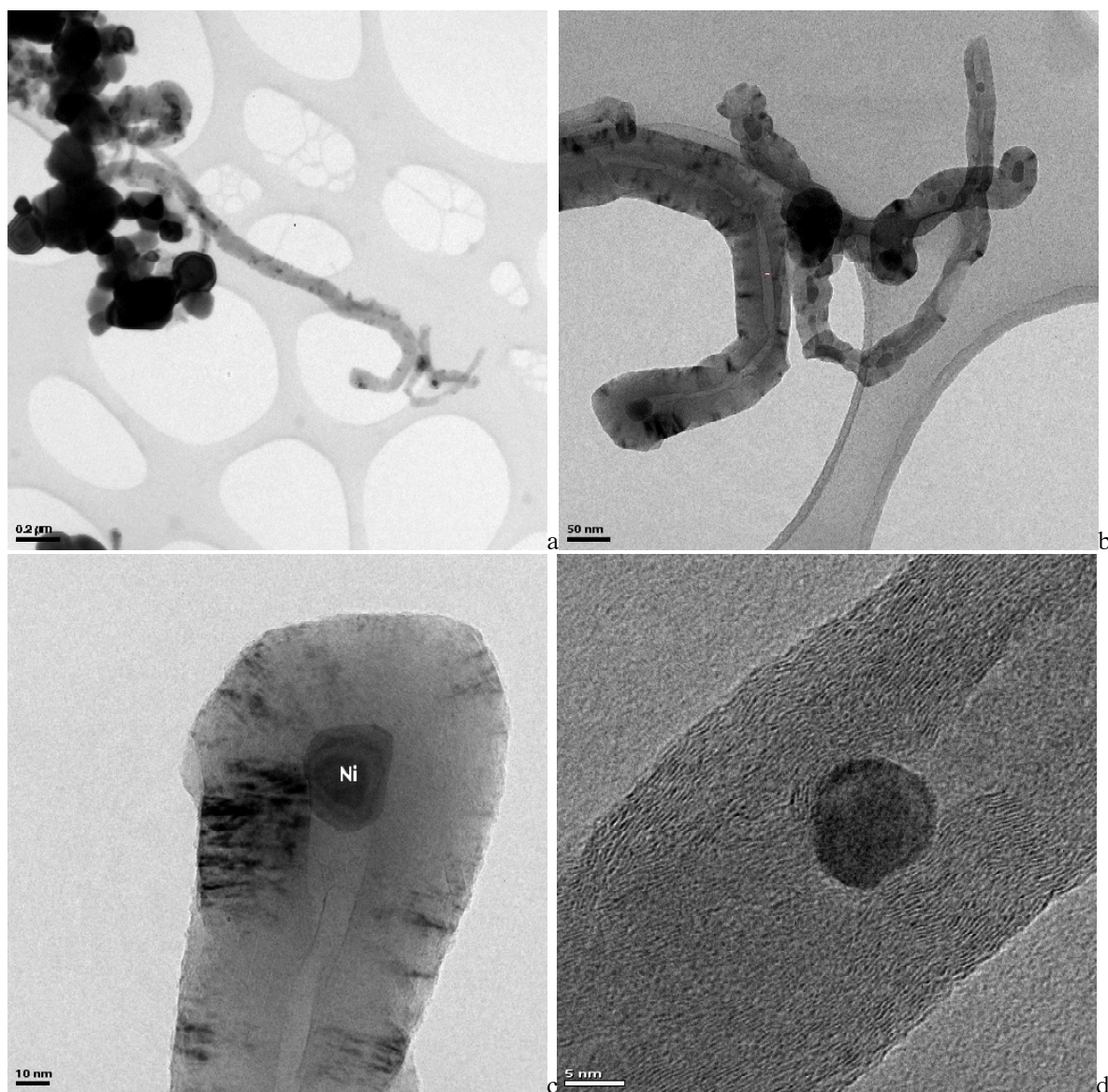


Figure 10: TEM micrographs of CeNbO+1%Ni catalyst. a. Filamentous carbon growing from a ceria powder with b. a Ni particle at its top. c. and d. are enlargements of some of these Ni particles sitting in tubular filaments having a central hole beneath the metallic catalyst. This catalyst was run in 56:41:3 CH₄:Ar:H₂O gas mixture.

Also, CeNbO+1%Ni catalysts showed the formation of high amounts of filamentous carbon, grown around free Ni particles. These filaments, 50 to 100 nm thick, were observed to reach 2 to 3 μm of length (see Figure 10a). The filamentous carbon was well graphitized (Figure 10c-d). Many spots were observed within these filaments corresponding to Ni particles (see Figure 10b-d). Inner holes were observed within them and in many cases Ni particles were completely covered by carbon. Such kind of filaments are commonly observed over Ni-catalysts¹⁴. The Ni particles had varying sizes, some being larger than 100 nm and other being below 20 nm. Many of these particles were observed to sit in the center of the filaments (e.g. Figure 10d), as if they were left behind by a larger Ni particle, sitting on the top of the filaments (Figure 10b). Such kind of material loss was reported in literature of Ni catalysts¹⁵. Interestingly, these filaments seemed to grow from the surface of the CeNbO where the Ni particle seemed to sit. Hence, the metal particles were lifted off the support, moving outward on top of the growing filaments. On the other hand, Ni free CeNbO powders did not show carbon growth of any kind,

thus confirming the absence of carbon deposits over Nb, Pr or Gd-based ceria powders as observed by TPO (e.g. Figure 11a-b).

The Cu-based CeNbO cermets showed also carbon deposition. However the carbon structures were somehow in-between those of Co and Ni catalysts. Filamentous carbon of the so-called primary carbon filament type¹⁴, spiral carbon filaments¹⁵ and encapsulating carbon films were identified (see Figure 12). In the Cu-Ni catalyst, a higher concentration of Ni than the nominal one was observed in the particles responsible for filament growth.

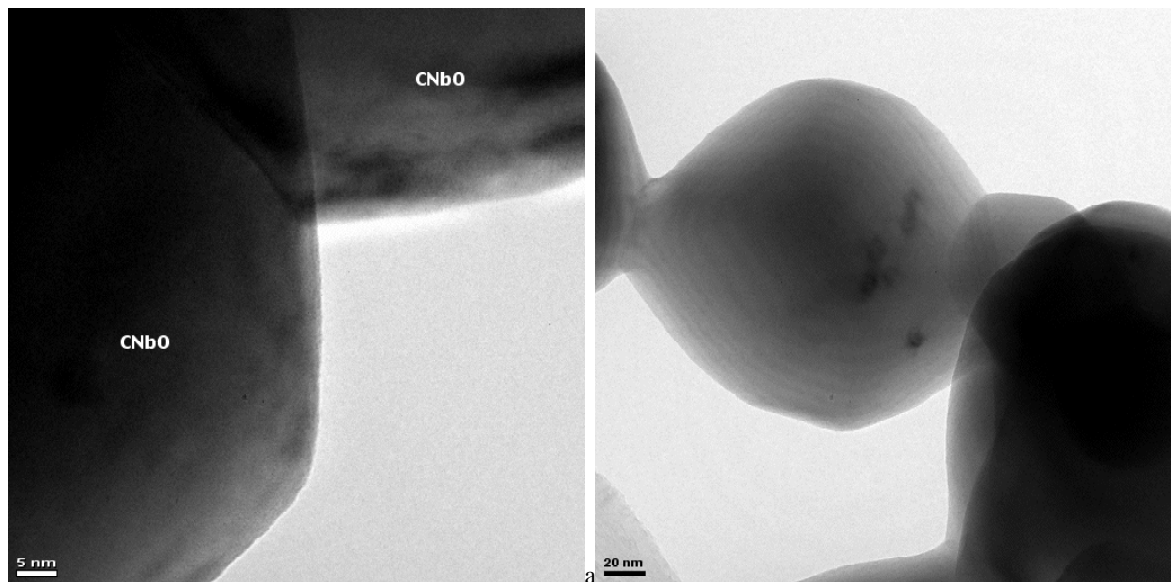


Figure 11: TEM of CeNbO grains showing clearly the absence of any carbon growth of any kind. On these grains it is also possible to see a step-like structure.

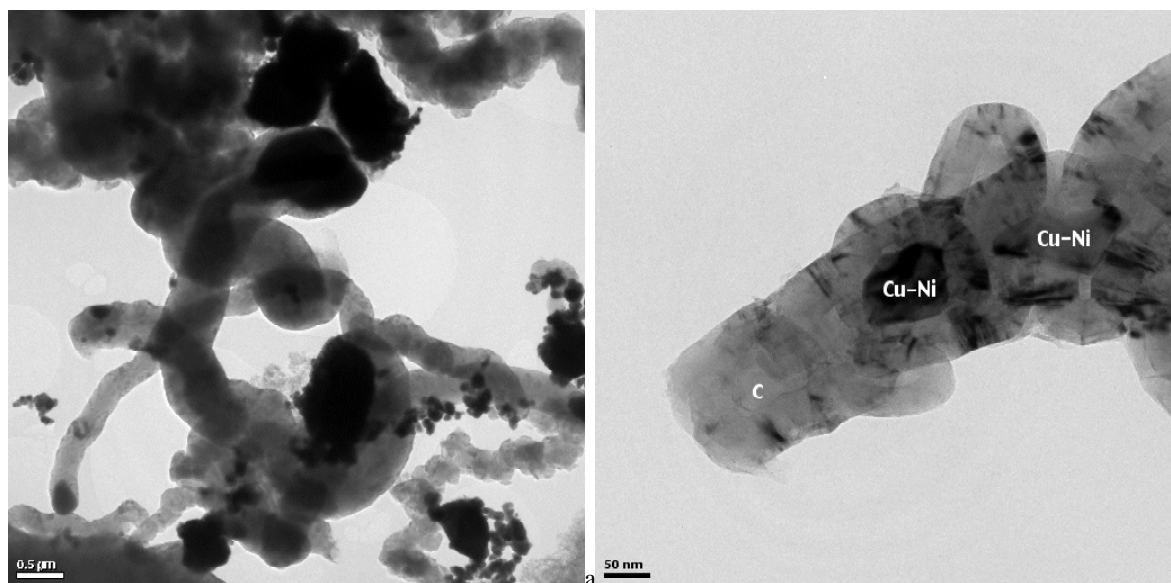


Figure 12: TEM of Cu-based CeNbO catalysts. a: 30%Cu-70%CeNbO showing some twisted and primary carbon filaments and encapsulating films. b: 30%(80%Cu-20%Ni)-70%CeNbO.

Discussion

TPR analysis of the three different ceria compounds doped with Nb, Pr and Gd show the high non-stoichiometry reached upon reduction. Ceria is known for its high storage capacity for oxygen^{16,17}. As discussed in the previous chapter, a high difference between the oxidized and the reduced state of these ceria compounds might account for the difference in adhesion over YSZ sheets. The difference in non-stoichiometry between Nb and Gd doped ceria follows also equally well the conductivity change observed previously (Chapter 9). The high oxygen

evolution with Pr doping compared to Nb is quite significant. The highest activity for steam-reforming was observed over CePrO, followed by CeGdO then CeNbO. The activity seems to be higher, the higher the vacancy concentration in the bulk generated by the reduction as δ amounted to 1.69, 1.81 and 1.85 for Pr, Gd and Nb doping. These values correspond to *TPR* conditions (1000°C, 5% H₂ in Ar). Thus, the ionic conductivity seems to play a role in the overall activity as Nb is expected to have the lowest ionic but the highest electronic conductivity among the three different dopants. The effect seems to be more important at temperatures higher than 850°C as CH₄ conversion was of 2.7, 1.3 and only 0.4% for Pr, Gd and Nb respectively. Among these dopants, Pr is known to show both electronic and ionic conductivity¹⁸, whereas CeNbO is only an electronic and CeGdO an ionic conductor at high P_{O_2} .

Also, the higher non-stoichiometry of Pr doped ceria could be accounted for by the higher reducibility of PrO_x oxides when compared to the other lanthanide oxides¹⁹. PrO_x above all was observed to show the highest isotopic exchange of molecular oxygen.

However, the surface segregation observed by *XPS* over Nb and Gd-doped ceria raise the question of the influence of such a high concentration on the superficial ionic conductivity of these oxides. Gd doped ceria is known to have lower ionic conductivity, by up to an order of magnitude, when doped above or below 20%²⁰ (at 800°C).

Nevertheless, low methane coupling, affected by water, and overall low activity towards CH₄ show that the global behavior of CeO₂ is similar to that of LaCrO₃-based compounds. The reaction order toward H₂O was observed to be negative at low temperatures and positive at higher ones ($\geq 900^\circ\text{C}$), as much as with LaCrO₃. However, the effect of water could be higher in ceria oxides as for LaCrO₃. Hewett et al.²¹ have shown no hydroxyl radical formation over CeO₂ when treated with H₂O at 900°C. *FTIR* analysis has shown that hydroxyl groups were still bound to the surface at 800°C⁴, probably indicating strong interaction. In parallel, CeO₂ is known to have a higher hydrogen solubility²²⁻²⁴ and possibly a high interaction with H₂⁸. Pr doping might promote this effect as it was demonstrated for Pr-added YSZ²⁵. The storage of hydrogen is said to lead to the formation of a H_yCeO_{2-x} bronze-like species⁴. Beside that, oxygen vacancies are known to participate in different oxidation reaction such as CO oxidation²⁶. The overall reaction mechanism might be as well very similar to that over LaCrO₃, but instead of hole conduction, one has to consider electron hopping in ceria (i.e. in the reaction equations developed in Chapter 6, one has to bare in mind the relation

$$h + e' = 0 \quad (8)$$

wherever needed). If this is the case, the nature of the electronic conductivity does not affect the catalyst activity for methane oxidation. However, CeO₂ presents some differences with LaCrO₃. CeO₂ has strong acid sites which lead the oxidation of the methyl radicals²⁷. CO₂ does not inhibit the oxidation reaction, and CO oxidation has been reported to be facile⁷. Also, in the reducing conditions of an anode, CeO₂ seems to deposit less C than LaCrO₃-based oxides. However, the high doping level in CeO₂ used in this study does not seem to enhance much the overall activity of this material when compared to the LaCrO₃-based compounds. The addition of an extra catalyst seems thus needed. This catalyst, such as Ni or Cu, can be either impregnated on ceria, as studied here, or added as a dopant (2-3%).

A major problem in processing methane containing feeds over metal catalysts is extensive carbon deposition. The present study shows that for all these catalysts, even when supported on the CeNbO, carbon was deposited (see the *TEM* figures). Dissociation of CH₄ to adsorbed carbon atoms is considered to be a prerequisite, i.e. an intermediate in the steam-reforming reaction^{10, 14, 28, 29}. Filamentary carbon is seen to be the most detrimental form of carbon as it leads to the lift off of the metal catalyst of the support (see Figure 10) and eventually to the destruction of the anode. The mechanism of such filament formation has been treated in literature and seems to be related to the dissolution of C by carbide formation and its subsequent deposition as graphitic layers around the metal particle^{14, 28, 29}. This seems to be the case for Fe, Co and Ni at least³⁰.

Thus the use of metal less liable to carbide formation and carbon dissolution and possibly a higher interaction with the support might prevent carbon formation. Cu is one such candidate along with Au, Ag and Ru (see Table 1).

Data concerning Cu are somewhat contradictory. Chambers et al.³¹ reported no C deposition over Cu at 600°C when using ethylene. Kim et al.³² report that CH₄ did not

decompose over Cu or Cu-Ni catalysts at temperatures above 740°C and below 900°C. Ponec³³, Rodriguez et al.³² and Bernardo et al.³⁴ indicated no CH₄ adsorption over Cu. Our results with Cu showed, however, that it did deposit carbon even though after a long induction period. Nevertheless, Cu did temper the Ni activity, preventing the catalyst of immediate desactivation as demonstrated for Ni_{0.65}Cu_{0.35} and 30% (80%Cu-20%Ni)-70%CeNbO in slightly humidified (≈3%) CH₄. Literature on Ni-Cu alloys is also contradictory, but as with pure Cu some reports indicated a high carbon resistance while others showed the formation of C filaments^{15, 34}. It seems that these different effects might stem not only from impurities in the CH₄ used but also from H₂ and CO and surface segregation of Cu over Ni-Cu alloy^{9, 32, 35}. However, all of these reports observed some kind of activity change upon Ni alloying with Cu.

The effect of high temperature treatment (850°C) observed in the case of 30% (80%Cu-20%Ni)-70%CeNbO might be related to a stronger metal to support interaction but also to the surface segregation of Cu on the alloy^{32, 35-38}. The effect of Cu over Ni might be related to a change in the adsorption sites as observed by *in situ* diffraction analysis³⁵.

Globally, the metallic particles dispersed over the ceria-based support promote the dissociation of CH₄, while the oxide provides the oxygen or hydroxyl species necessary to the removal of the carbonaceous species left behind on the metal following the global reactions



Heating the composite at higher temperature might lead to a better interaction but also to a dispersion effect of ceria over the metal as observed by Hardacre et al. in the case of Pt-ceria catalysts used for CO oxidation³⁹. Strong metal ceria interaction were also observed for Ni⁴⁰ and Rh⁴¹.

Our result shows that for SOFC purposes the addition of Cu could be viable as long as the cell is kept under polarization. The catalytic runs in 56:41:3 CH₄:Ar:H₂O indicate that an expected OCV (see Chapter 6) of about 820 mV can be achieved with 30%Cu-70%CeNbO at 800°C. This value could be increased by adding Ni as 30% (80%Cu-20%Ni)-70%CeNbO is expected to give an OCV of about 950 mV at 800°C. These OCV estimates were made following the same approximations as in Chapter 6, i.e. by considering the unreacted CH₄ as inert, playing no role in the reaction. In comparison, the expected OCVs for the CNbO, CGdO and CPRo are of 764, 781 and 800 mV at 800°C respectively. The calculated OCV for CNbO agreed well with the sealed SOFC measurements using this powder as electrodes, where the experimental OCV was of 806 mV at 850°C.

A trial with a 50/50 wt% Ni_{0.65}Cu_{0.35}/YSZ cermet sintered at 1300°C/4h over a YSZ sheet gave a mild activity (see Figure 13). At these high sintering temperatures Cu was observed to diffuse through the electrolyte. The cell resisted during the whole experiment time. Interestingly, the performance under H₂ was lower than in CH₄, and this might be related to a low chemisorption of H₂ over Cu^{35, 42}.

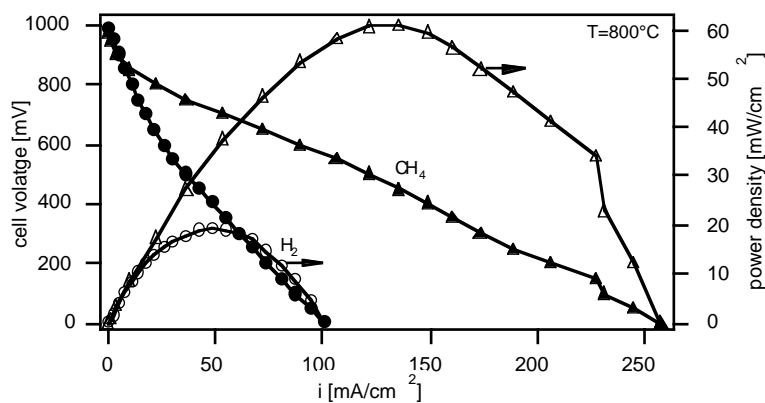


Figure 13: I/V and power density of a 50/50 wt% Ni_{0.65}Cu_{0.35}/YSZ cermet sintered at 1300°C/4h over a YSZ sheet. The cell was first run under H₂ then under humidified (3%H₂O) CH₄. The OCV under CH₄ was of 985 mV.

Recent reports from literature show that cells made of Cu and CeO₂ in a composite with YSZ gave a powder density of 150 mW/cm² in n-butane and even 250 mW/cm² in CH₄ at 800°C⁴³⁻⁴⁵. This shows that such an approach could be viable for an SOFC purpose.

Conclusions

Ceria-based catalysts have shown a poor activity toward CH₄ activation, at least with the three dopants studied (Nb, Pr and Gd). The higher activity was reached with 15%CePrO followed by 20%CeGdO and 0.8%CeNbO. In 3% humidified CH₄, methane conversion was of 2.7, 1.3 and 0.4% at 850°C respectively. This poor activity is equivalent to unsubstituted LaCrO₃ (1.7%). Interestingly, all three did not deposit carbon and seemed to resist much better to CH₄ cracking than LaCrO₃-based catalysts. Globally, the activity of these oxides seemed to be higher the higher the electronic and ionic conductivity as in the case of Pr-doping. However, XPS measurements revealed a high surface segregation in the case of Nb- and Gd-doping which could affect the ionic conductivity. The use of CePrO is advantageous for its higher activity in CH₄ and its expected higher OCV.

Cermet compounds of metallic Ni, Ni-Cu, Cu and Ru were studied in order to enhance the total activity of ceria. Impregnation of 1%Ni or Ru allowed an increase of the activity but at the same time the growth of filamentous carbon around metallic particles, evidenced by TEM, lifted the catalyst off the support leading eventually to the plugging of the reactor. Cu alone resisted longer to CH₄, as a long induction period was needed before carbon precipitation. Interestingly, alloying Ni with Cu allowed to temper the activity of Ni and limit carbon deposition. A strong interaction with the support, reached by high temperature treatment, was observed and found to be necessary for this improved performance. However, over sufficiently long period the catalyst inevitably deposited carbon indicating the necessity to polarize such a material if used as anodes. A preliminary trial with a 50/50 wt% Ni_{0.65}Cu_{0.35}/YSZ cermet sintered at 1300°C/4h over a YSZ sheet showed the viability of such an approach.

References

- (1) York, A. P. E.; Claridge, J. B.; Marquez-Alvarez, C.; Brungs, A. J.; Tsang, S. C.; Green, M. L. H. 3rd World Congress on Oxidation Catalysis, **1997**; p 711-720.
- (2) *Binary alloy phase diagrams*; American Society for Metals, **1986**.
- (3) *Alloy Phase Diagrams*; The Materials Information Society, **1992**.
- (4) Laachir, A.; Perrichon, V.; Badri, A.; Lamotte, J.; Catherine, E.; Lavalley, J.-C.; El-Fallah, J.; Hilaire, L.; Normand, F. I.; Quéméré, E.; Sauvion, G. N.; Touret, O., *J. Chem. Soc. Faraday Trans.* **1991**, 87, 1601-1609.
- (5) Wang, S.; Inaba, H.; Tagawa, H.; Dokiya, M.; Hashimoto, T., *Solid State Ionics* **1998**, 107, 73-79.
- (6) Brauer, G.; Willaredt, B., *Journal of the Less-Common Metals* **1978**, 61, 83-89.
- (7) Trovarelli, A., *Catal. Rev. -Sci. Eng.* **1996**, 38, 439-520.
- (8) Otsuka, K.; Wang, Y.; Sunada, E.; Yamanaka, I., *Journal of Catalysis* **1998**, 175, 152-160.
- (9) Bartholomew, C. H., *Catal. Rev. -Sci. Eng.* **1982**, 24, 67-112.
- (10) Rostrup-Nielsen, J. R. In *Catalysis, Science and Technology*; Anderson, J. R. and Boudart, M., Eds.; Springer Verlag; **1984**; Vol. 5.
- (11) Twigg, M. V. *Catalyst Handbook*, 2 ed.; Wolfe Publishing Ltd., **1989**.
- (12) Campbell, K. D.; Zhang, H.; Lunsford, J. H., *J. Phys. Chem.* **1988**, 92, 750-753.
- (13) Scanlon, P. J.; Bink, R. A. M.; Berkel, F. P. F. v.; Christie, G. M.; Ijzendoorn, L. J. v.; Brongersma, H. H.; Welzenis, R. G. v., *Solid State Ionics* **1998**, 112, 123-130.
- (14) Boellaard, E.; Bokx, P. K. D.; Kock, A. J. H. M.; Geus, W., *Journal of Catalysis* **1985**, 96, 481-490.
- (15) Kim, M. S.; Rodriguez, N. M.; Baker, R. T. K., *Journal of Catalysis* **1992**, 134, 253-268.
- (16) Liu, W.; Flytzani-Stephanopoulos, M., *Journal of Catalysis* **1995**, 153, 304-316.
- (17) Liu, W.; Sarofim, A.; Flytzani-Stephanopoulos, M., *Mat. Res. Soc. Symp. Proc.* **1994**, 344, 145-150.
- (18) Takasu, Y.; Sugino, T.; Matsuda, Y., *Journal of Applied Electrochemistry* **1984**, 14, 79-81.
- (19) Rosynek, M. P., *Catal. Rev. -Sci. Eng.* **1977**, 16, 111-154.
- (20) Kudo, T.; Obayashi, H., *J. Electrochem. Soc.* **1976**, 123, 415-419.

- (21) Hewett, K. B.; Anderson, L. C.; Rosynek, M. P.; Lunsford, J. H., *J. Am. Chem. Soc.* **1996**, *118*, 6992-6997.
- (22) Sakai, N.; Yamaji, K.; Horita, T.; Yokokawa, H.; Hirata, Y.; Sameshima, S.; Nigara, Y.; Mizusaki, J., *Solid State Ionics* **1999**, *125*, 325-331.
- (23) Nigara, Y.; Mizusaki, J.; Kawamura, K.; Kawada, T.; Ishigame, M., *Solid State Ionics* **1998**, *113-115*, 347-354.
- (24) Nigara, Y.; Kawamura, K.; Kawada, T.; Mizusaki, J.; Ishigame, M., *J. Electrochem. Soc.* **1999**, *146*, 2948-2953.
- (25) Bay, L.; Horita, T.; Sakai, N.; Ishikawa, M.; Yamaji, K.; Yokokawa, H., *Solid State Ionics* **1998**, *113-115*, 363-367.
- (26) Gellings, P. J.; Bouwmeester, H. J. M., *Catalysis Today* **2000**, *58*, 1-53.
- (27) Choudhary, V. R.; Rane, V. H., *Journal of Catalysis* **1991**, *130*, 411-422.
- (28) Bokx, P. K. D.; Kock, A. J. H. M.; Boellaard, E.; Klop, W.; Geus, W., *Journal of Catalysis* **1985**, *96*, 454-467.
- (29) Kock, A. J. H. M.; Bokx, P. K. D.; Boellaard, E.; Klop, W.; Geus, W., *Journal of Catalysis* **1985**, *96*, 468-480.
- (30) Liu, B. X.; Wang, J.; Cheng, X. Y.; Fang, Z. Z., *Phys. Stat. Sol. A* **1991**, *128*, K71-K75.
- (31) Chambers, A.; Rodriguez, N. M.; Baker, R. T. K., *J. Phys. Chem.* **1995**, *99*, 10581-10589.
- (32) Kim, M. S.; Rodriguez, N. M.; Baker, R. T., *Journal of Catalysis* **1991**, *131*, 60-73.
- (33) Ponec, V., *International Journal of Quantum Chemistry* **1977**, *12*, 1-12.
- (34) Bernardo, C. A.; Alstrup, I.; Rostrup-Nielsen, J. R., *Journal of Catalysis* **1985**, *96*, 517-534.
- (35) Rodriguez, N. M.; Kim, M. S.; Baker, R. T., *Journal of Catalysis* **1993**, *140*, 16-29.
- (36) Vogt, E. T. C.; Dillen, A. J. v.; Geus, J. W. In *Catalyst Deactivation 1987*; Delmon, B. and Froment, G. F., Eds.; Elsevier Science Publishers:, **1987**.
- (37) Zhuang, Q.; Qin, Y.; Chang, L., *Applied Catalysis* **1991**, *70*, 1-8.
- (38) Wu, X.; Zhang, J.; Chang, L. In *Catalyst Deactivation 1987*; Delmon, B. and Froment, G. F., Eds.; Elsevier Science Publishers:, **1987**.
- (39) Hardacre, C.; Ormerod, R. M.; Lambert, R. M., *J. Phys. Chem.* **1994**, *98*, 10901-10905.
- (40) Maubert, A.; Martin, G. A.; Praliaud, H.; Turlier, P., *React. Kinet. Catal. Lett.* **1984**, *24*, 183-186.
- (41) Fornasiero, P.; Monte, R. D.; Rao, G. R.; Kaspar, J.; Meriani, S.; Trovarelli, A.; Graziani, M., *Journal of Catalysis* **1995**, *151*, 168-177.
- (42) Frennet, A., *Catal. Rev. -Sci. Eng.* **1974**, *10*, 37-68.
- (43) Park, S.; Craciun, R.; Vohs, J. M.; Gorte, R. J., *J. Electrochem. Soc.* **1999**, *146*, 3603-3605.
- (44) Park, S.; Gorte, R. J.; Vohs, J. M., *J. Electrochem. Soc.* **2001**, *148*, A443-A447.
- (45) Craciun, R.; Park, S.; Gorte, R. J.; Vohs, J. M.; Wang, C.; Worell, W. L., *J. Electrochem. Soc.* **1999**, *146*, 4019-4022.

Chapter 11 十一

*CeO₂-based anodes and their electrochemical
characterization in humidified H₂ and CH₄*

CeO₂-based anodes and their electrochemical characterization in humidified H₂ and CH₄*

Abstract

Electrocatalytic properties of Nb and Gd-doped ceria anodes deposited on 8YSZ and 20CGdO electrolytes were addressed using *I/V* and impedance analysis. The effects of the electrode thickness and morphology, the addition of a pore former and Ni or Cu metallic catalysts, the polarization as well as the gas composition (H₂, H₂O, CH₄ and CO₂) were taken into account. Sealed, non-sealed and symmetrical measurements were performed. Inlet and outlet gas composition analysis (gas chromatography and mass spectroscopy) were made with the sealed systems. The low activity of Nb and Gd-doped ceria for the oxidation of CH₄ confirmed the previous catalytic runs made in a catalytic reactor (Chapter 10). No carbon deposition was observed in the sealed set-ups as expected from the catalytic runs. This study demonstrated again that it is possible to oxidize CH₄ electrochemically in a SOFC without prior steam-reforming provided that a suitable catalyst is added to promote its activation. As for LaCrO₃-based anodes, a direct relationship between the catalytic activity and electrocatalytic performance was evidenced. Also, the polarization resistance was observed to decrease significantly for anodes made of a fine structure where high performances were reached in H₂ (430 mW/cm² and 1750 mA/cm² between 850-900°C, for the best cells). The performance in CH₄ depended on the presence of a catalyst. In CH₄, at 900°C, with Pt-meshes the best performance was of 350 mW/cm² with a short circuit current (*i*_{sc}) of 1050 mA/cm², whereas with Au-meshes it was only of 100 mW/cm² with a *i*_{sc} of 420 mA/cm². The anode contributed slightly to the ohmic losses of the electrolyte as the series resistance tended to increase upon polarization. As for the case of LaCrO₃-based anodes, this was most probably due to bad current collection as the ohmic losses of these electrodes are expected to be quite small. Inductive loops were observed on cells measured in a SOFC mode in both H₂ and CH₄, but they were not detected with symmetrical cells. One electrode process was observed to increase upon polarization. Analysis of the impedance data against temperature, gas composition and polarization shows a possible mechanism where an adsorbed species is undergoing a charge transfer reaction in a similar manner to the so-called ‘*Gerischer impedance*’, and where a diffusion process is taking place. Limiting currents were observed at high overpotentials. The origins and the interpretations of these processes are discussed. A possible reaction mechanism is proposed as the chemisorption of H₂ over the ceria-based anodes and its electrochemical oxidation through an adsorbed intermediate, with oxygen ions diffusing to the reaction sites. The reaction zone is thought to spread over some parts of the anode so that it should not be confined only to the triple phase boundary area. Surface kinetics limitations play also a role in the reactions. This interpretation allows a rationalization of observations made concerning the influence of the catalyst and the gas composition. Finally, analysis of the reaction orders in CH₄ indicated that, under OCV conditions at least, the reaction was determined by H species activity, produced by steam reforming of methane. Also, gas equilibrium was not reached under CH₄ fuel as the OCV was observed to be determined by the local equilibrium between H₂ and H₂O, as for the case of LaCrO₃-based anodes.

Introduction

In the previous chapters (Chapter 9 and 10) the fabrication and characterization of ceria based powders were discussed. Catalytic runs showed the high stability of ceria compounds in CH₄ feed.

In the present chapter, an attempt was made to apply some of these powders as electrodes for their use as anodes in CH₄. Different parameters were addressed. The effects of the electrode thickness and morphology, the addition of a pore former and Ni or Cu metallic

* Some of the results dealt with in this chapter were published as J. Van herle, J. Sfeir, R. Ihringer, N. M. Sammes, G. Tompsett, K. Kendal, K. Yamada, C. Wen, M. Ihara, T. Kawada, J. Mizusaki, ‘Improved tubular SOFC for quick thermal cycling’, in the Forth European Solid Oxide Fuel Cell Forum, Lucerne, ed. A. J. McEvoy, 2000, 251-260

catalysts, the polarization as well as the gas composition (H₂, H₂O, CH₄ and CO₂) were taken into account. Here, as dopants, only Nb and Gd were investigated.

Experimental

Powder and cell preparation

Nb and Gd doped ceria powders were prepared following the modified liquid/solid-state route and the coprecipitation method respectively (Chapter 9). Terpeneol-ethyl cellulose-based slurries were prepared with the ball-milled powders, using isopropanol as solvent (Chapter 2). Some of these slurries were prepared by adding 50 vol% of graphite powder or teflon balls as described in Chapter 9, to increase the porosity. One electrode slurry was also made by adding 1 wt% of Ni catalyst, taken in the form of a nitrate salt and dissolved in the organics, and one other by mixing a 50 wt% Ni taken as NiO with the CeNbO powder. Electrodes of 1 cm² area were then screen-printed on 150 μm 8YSZ sheets and in one case on a 770 μm thick 20%CeGdO home-made pellet. In the latter case, a CeGdO electrode was screen-printed and sintered and then impregnated with an aqueous solution of Cu-nitrate, as described in Chapter 9. The CeGdO electrolyte was considered in order to get round the adhesion problem of CeGdO over YSZ. The different cells discussed here are presented in Table 1.

Electrochemical testing

All three testing configurations were used in this study. Two types of systematic studies were made in order to estimate the effect of different parameters on the ceria-based anodes.

The first type of study was made using symmetrical cells in order to analyze the influence of H₂, CH₄, H₂O and P_{O_2} on the electrochemical reaction. In this case, the inlet gas composition was controlled through mixing with N₂, using calibrated gas rotameters and saturating the whole with the desired amount of H₂O in a thermostated bubbler. Inlet and outlet gas lines were heated to around 120°C to prevent water condensation. At the outlet, a condenser was used to remove H₂O prior to gas chromatography (GC) analysis. In the case of a constant P_{O_2} , the H₂O/H₂ or H₂O/CH₄ ratio was maintained constant, by passing H₂ or CH₄ in the bubbler, then diluting the whole in N₂. Globally, H₂ or CH₄ were modified between 5 to near 100%, H₂O between 3 to 50%, whereas the temperature was varied from 680 to 880°C. The exhaust gas composition (CH₄, H₂, N₂, CO, CO₂, C₂H₂, C₂H₄ and C₂H₆) was analyzed by GC through syringe injection over a Carlo Erba MFC500 (Porapak Q, He carrier) and a Gowmac (Molecular Sieve 5Å, Ar carrier) instruments. It is important to see that these different parameters are related together, either through the Nernst potential relating the temperature, the electrode potential, H₂O and H₂ partial pressure (and possibly other gases such as CO and CO₂), or due to local equilibrium between CH₄ and H₂, H₂O, CO and CO₂ (and possibly C₂H₂, C₂H₄ and C₂H₆). All experiments intended to study one parameter could possibly involve some other parameters. So cross analysis was undertaken to verify the dependencies.

The other type of study rested on the analysis of the potential and gas composition effect in SOFC mode. The evolution of *I/V* and overpotential curves was analyzed with respect to temperature and anode gas composition.

In both cases, impedance spectroscopy analysis was performed with an IM5 Zahner impedance analyzer, at open circuit potential (OCV) or under bias (in the case of cells working in the SOFC mode), between the two symmetrical anode electrodes. The impedance responses were best fitted by the $LR_e(R_1Y_1)(R_2Y_2)(R_3Y_3)$ circuit, using the Zahner fitting software. Y_i was, as presented previously, a constant phase element (CPE)¹

$$Y_i = Y_{i,o} (j\omega)^n = j\omega C \quad (1)$$

with $Y_{i,o}$ an admittance, j the imaginary unit, ω the angular frequency, n the frequency power, C a frequency-dependent capacitance, R_e the series electrolyte resistance between the two electrodes, R_i a resistance, and L the current/potential collectors inductance. R and C had positive or negative values, depending on the mechanism used for interpreting the data. The general values for L , n_1 , n_2 , and n_3 were of 220 nH, 0.9, 0.6-0.8, and 0.7-0.8. The mean fitting error was of 0.1%, whereas the maximum errors were of 0.6-3%. The R and C were analyzed with respect to the different parameters for possible dependencies.

Table 1: A summary of the different anodes presented in this study.

Anode cell Nr	Composition	Pore former	Nr of layers	Screen printer Screen	Current collector	Sintering temperature [°C]	Power density/ i_{sc} , H ₂ 900°C	Power density/ i_{sc} , H ₂ 850°C	Power density/ i_{sc} , CH ₄ 900°C	Power density/ i_{sc} , CH ₄ 850°C
B40	CNbO	-	3	250mesh, 50 μ	Pt-mesh	1100°C/4h		100/350		
A24	CNbO	-	2	250mesh, 50 μ	Pt-mesh	1100°C/4h	250/900	190/600	90/250	60/140
B36	CNbO	-	2	250mesh, 50 μ	fine Au-mesh	1000°C/4h	230/800	150/400		20/45
D1	CNbO	carbon 50vol%	2	250mesh, 50 μ	Pt-mesh	1100°C/4h	105/390	60/210	30/90	12.5/50
B62	CNbO	-	2	325mesh, 30 μ	Pt-mesh	1100°C/4h		430/1700	350/1050	120/400
E7h	CNbO	-	2	325mesh, 30 μ	Pt-Au-mesh	1100°C/4h	400/1750	250/800	100/420	50/220
D13d	CNbO	-	3	325mesh, 30 μ	fine Pt-Au-mesh	1200°C/4h				
D10c	CNbO+1%Ni	-	3	325mesh, 30 μ	fine Pt-Au-mesh	1200°C/4h				
<i>B17</i>	CNbO	-	2	325mesh, 30 μ	fine Au-mesh	1100°C/4h		250/1180		
<i>D39</i>	CGdO+Cu*	teflon 50vol%	3	250mesh, 50 μ	Au-CGdO/Au-mesh	1250°C/4h		200/1000		80/400
B32	46%CNbO/54%Ni	-	2	250mesh, 50 μ	Pt-mesh	1150°C/3h		160/550		6.25/25
A-3	50%CNbO/50%YSZ	-	3	250mesh, 50 μ	Pt-mesh	1200°C/4h		46/180		

Cell numbers in bold and in italic are measurements made in the symmetrical and sealed set-up configurations respectively. i_{sc} represents the short circuit current. The power density is given in mW/cm² and the short circuit current in mA/cm². * screen-printed over a 20% CeGdO electrolyte.

Results

Effect of the electrode thickness and morphology

As discussed in Chapter 9, CeNbO electrodes adhered well on YSZ sheets when sintered at 1100°C and 1200°C but tended to densify at higher sintering temperature. The electrodes were observed to be quite dense even when sintered at 1100°C-1200°C so that no optimization of the sintering temperature was undertaken.

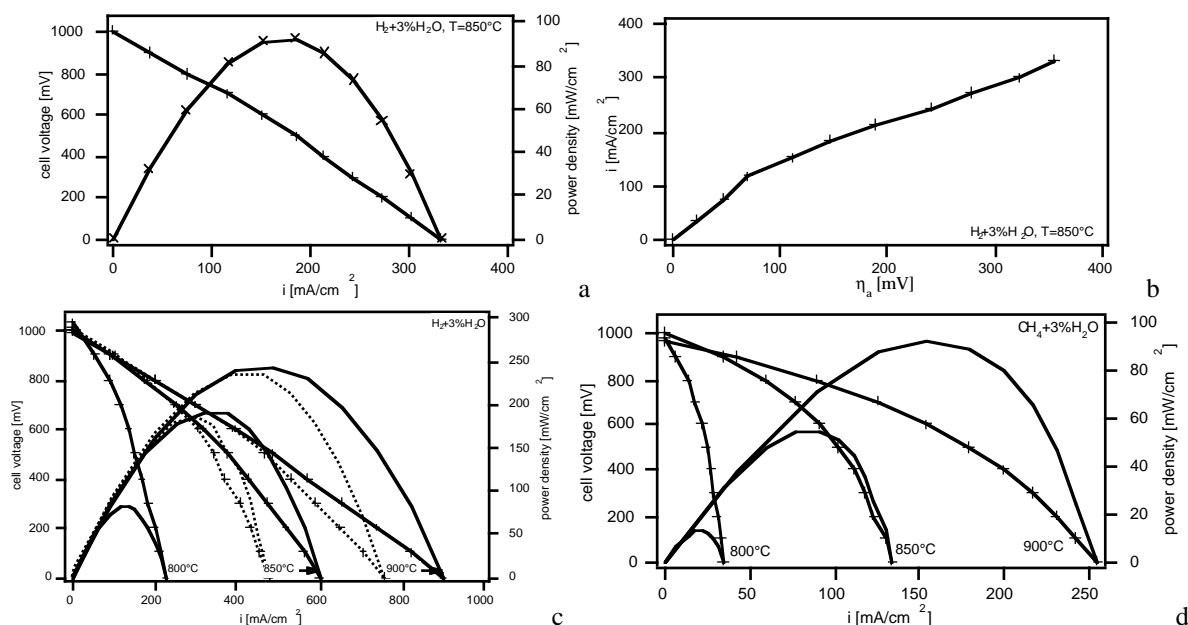


Figure 1: *I/V* and power density curves of CeNbO anodes made of a. and b.: 3 layers (B40) and c. and d.: 2 layers (A24).

On the other hand, the effect of the electrode thickness and its morphology was observed to be important in achieving a better performance. Figure 1 compares two CeNbO electrodes, one with 3 layers and one with only 2 layers. One can see that the overall performance was higher in the second case. This was due to a lower R_p of 0.3 instead of 0.7 Ωcm^2 . The power density, recorded at 850°C in humidified H₂, was almost double being of 190 mW/cm^2 instead of 100 mW/cm^2 . As can be seen in Figure 1c and as will be discussed in more detail later, a limiting current seems to be attained at high overpotential and low temperature. As with LaCrO₃-based anodes, CeNbO anodes seemed to withstand direct CH₄ feed as expected from the catalytic runs described in Chapter 10. Similarly, the anode performance with CH₄ was lower than with H₂ by a factor of 4 to 6 at 900°C and 800°C respectively. A limiting current was observed in all cases for CH₄ (Figure 1d). Also, the series resistance, R_s , was observed to increase upon polarization (Figure 2), in a reverse manner to the LaCrO₃-based anodes. The performance of these anodes was observed to be strongly activated with temperature, however being very low below 800°C.

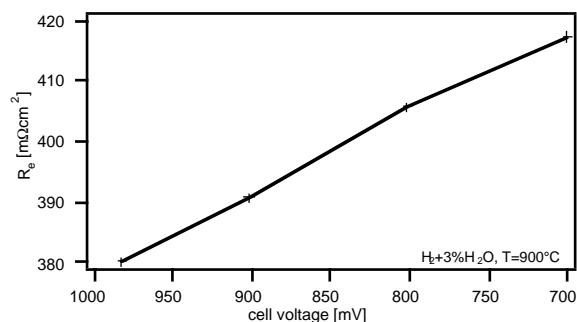


Figure 2: The evolution of the series resistance as a function of the cell polarization as observed by impedance spectroscopy.

Figure 1c shows the *I/V* curves in humidified H₂ taken just after CH₄ runs (broken lines in Figure 1c) and after reoxidation with air (850°C and 950°C). It was observed that the initial

performance was somewhat lower than after air treatment, most probably due to carbon deposition over the Pt-mesh current collector, as Pt is a good CH₄ cracking catalyst. However, this mild deactivation did not lead to a deterioration of the cell performance. These redox cycles did not cause the delamination of the electrode.

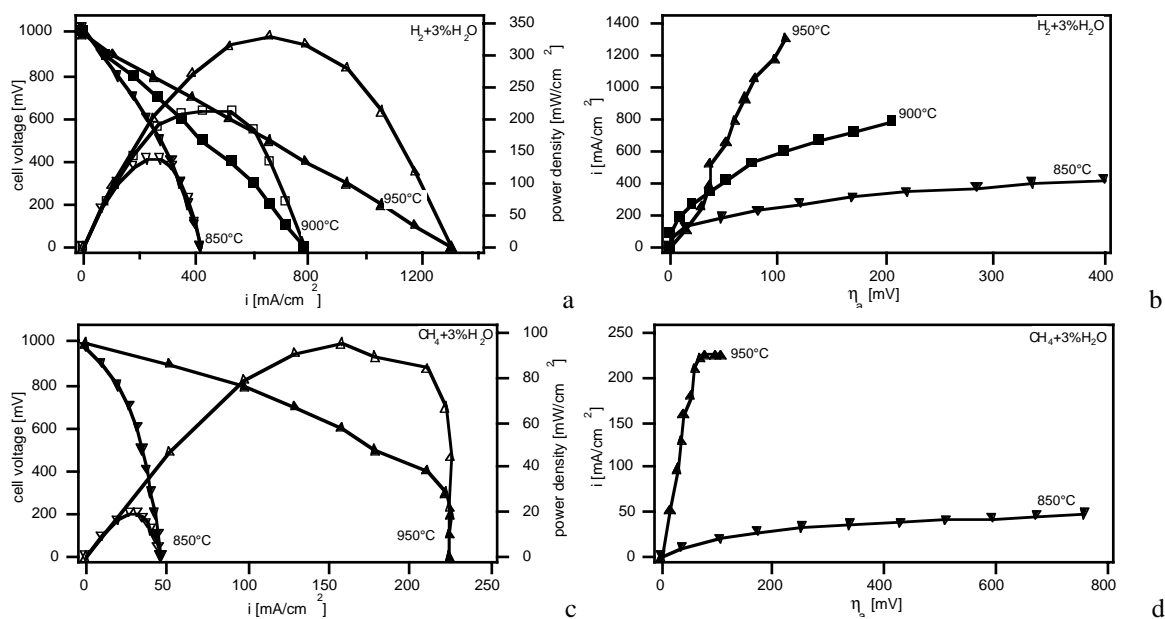


Figure 3: Performance of a CeNbO anode (B36) using an Au-mesh current collector. The effect of temperature and the gas atmosphere is highlighted.

In order to evaluate the effect of the current collector on the cell performance in humidified CH₄, an Au-mesh current collector was used instead of Pt. Au is known to show almost no interaction with CH₄ (Chapter 6 and 8) so that the measured activity should be close to that of pure CeNbO. In this case, the electrode was sintered at 1000°C in order to prevent melting of the Au-mesh. This is illustrated in Figure 3. The performance in H₂ at lower temperatures was somewhat lower than in the previous case (A24), most probably due to the sintering temperature and / or to the catalytic effect of Pt. The output in 3% humidified CH₄ was poor when compared to the case with Pt mesh. The cell performance in CH₄ in this case was 1/6 to 1/8 of that in H₂. The limiting current behavior was observed clearly in this case, most probably indicating a diffusion limited process. In accordance with the previous catalytic measurements (Chapter 10), these results indicate the low CH₄ activity of the CeNbO material. The addition of a catalyst is needed in order to increase the activity towards CH₄. Also, by the fact that CeO₂ as well as LaCrO₃-based anodes are poor electronic conductors, a good current collection is needed in order to attain high current densities. Preliminary work done on CeNbO anodes, where a Pt-mesh was simply contacted with the anode structure, pointed out the necessity of appropriate current collection for reaching higher current densities.

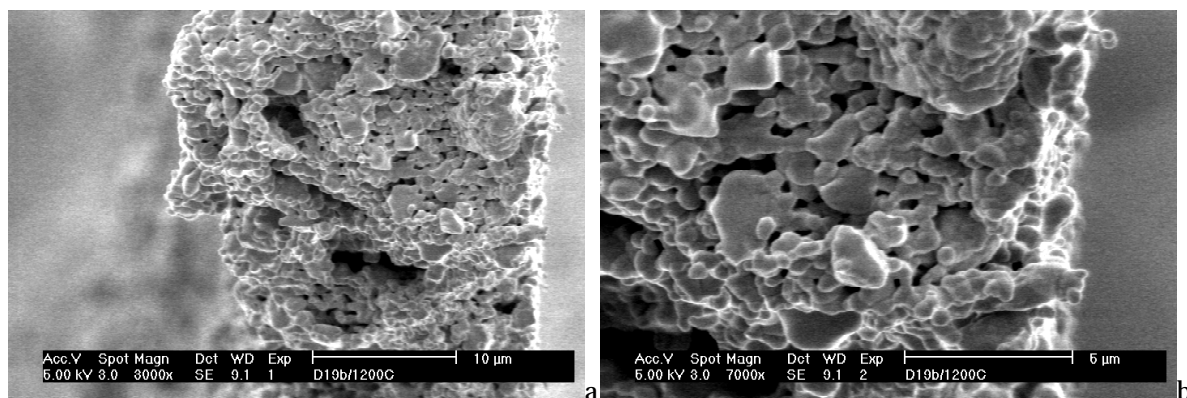


Figure 4: SEM micrographs of a CeNbO electrode screen-printed using a 250 mesh, 50μ screen and sintered at 1200°C.

SEM micrographs taken on some of these anodes show, as discussed previously in Chapter 9, a fairly dense structure. This is illustrated again in Figure 4. Trials were made to increase the porosity of the anode by adding pore formers like carbon powder. The microstructure of such an anode is shown in Figure 5. In the case of CeNbO, carbon powder tended to induce a very fine porosity but also lead to some fragility and delamination.

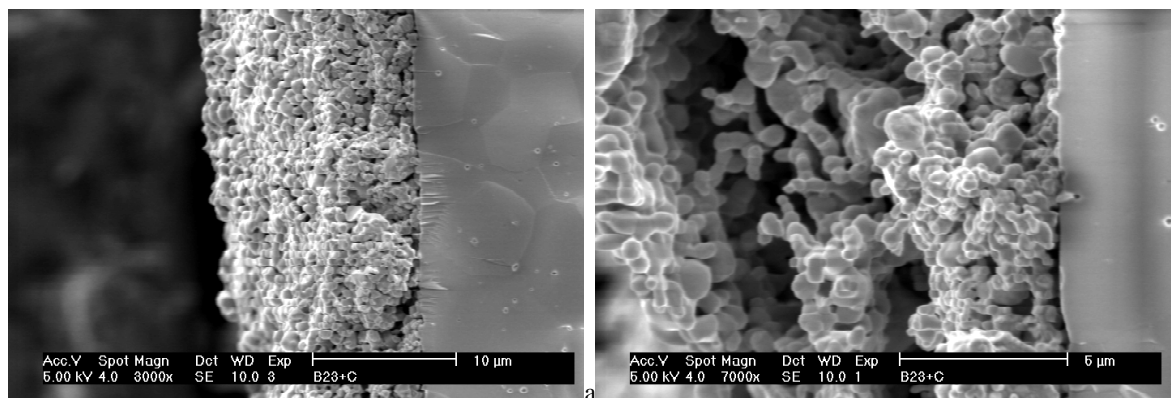


Figure 5: SEM micrographs of a CeNbO electrode made using graphite as pore former (D1). Screen-printed electrode using a 250 mesh, 50 μ screen and sintered at 1100°C.

The performance of a CeNbO anode made using a carbon powder pore former was much lower than the one made without addition of carbon (Figure 6 and 7, and Table 1 for a summary) showing 60 mW/cm² of power output versus 190 mW/cm², at 850°C in humidified H₂. The measured ohmic series resistance at 850°C was of 895 m Ω cm² (expected value of 380 m Ω cm²), with an R_p of 1.1 Ω cm² at OCV. Here also, a limiting current was observed (Figure 7).

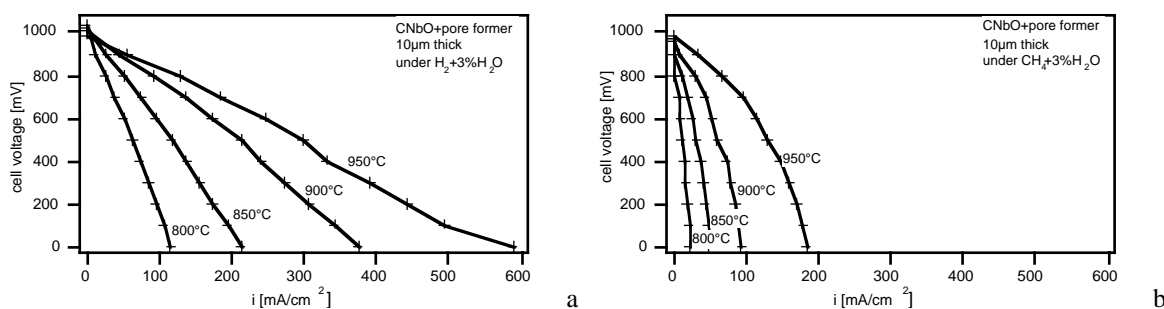


Figure 6: IV plots of a CeNbO anode having the microstructure of Figure 5. a: in H₂ and b: in CH₄ (D1).

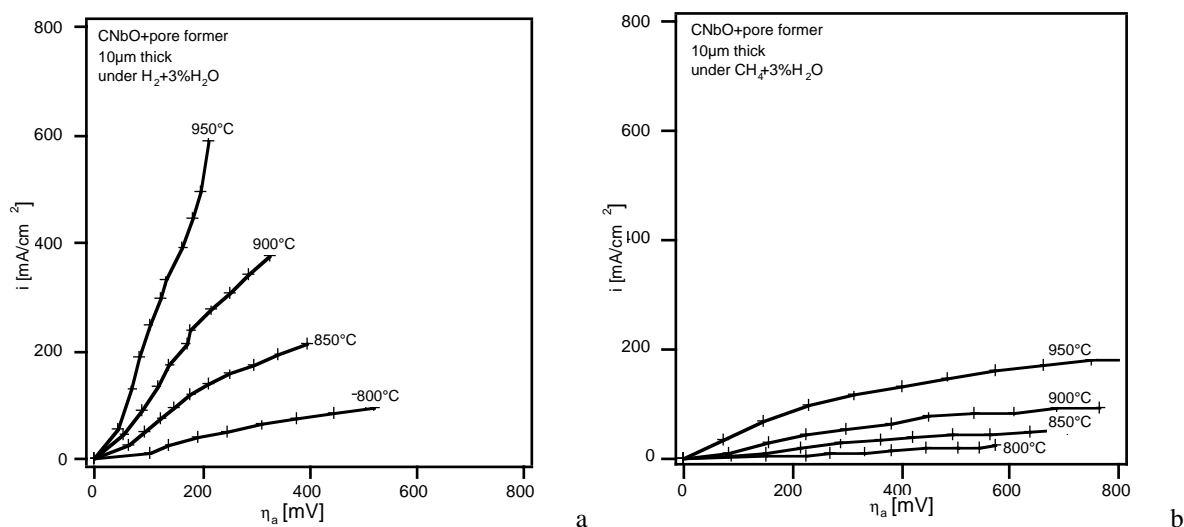


Figure 7: Overpotential curves of a CeNbO anode with graphite made pores (D1).

As a last parameter, the mesh of the screen of the screen-printer was modified from 250 to 325 mesh (woven wires per inch). The morphology change is observed in Figure 8 (to compare with Figure 5). In this case, the electrodes show a higher porosity and a finer structure, most probably due to the sieving effect of the screen, which retained large CeNbO powder grains.

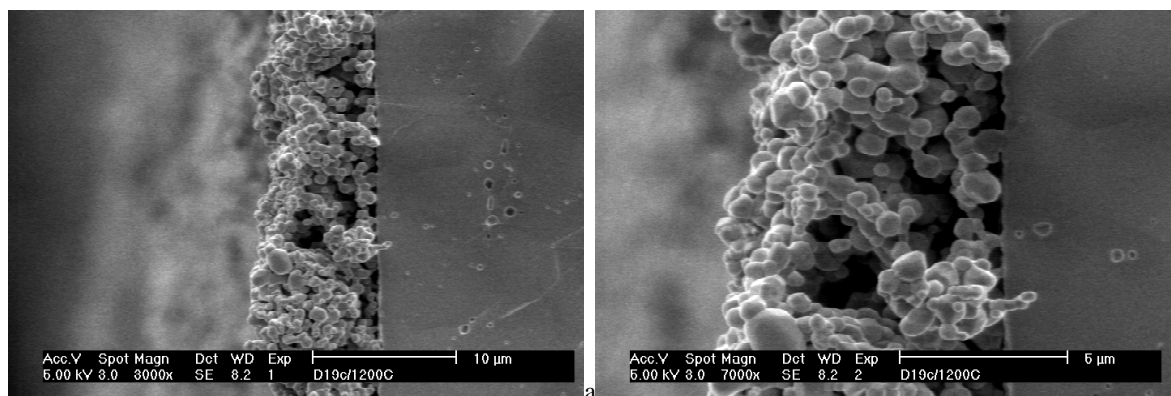


Figure 8: SEM micrographs of a CeNbO anode screen-printed using a 325 mesh, 30 μ screen, sintered at 1200°C/4h.

The performance of such an anode is illustrated by two examples (Figure 9). The performances reached here are of 430 and 250 mW/cm² in humidified H₂ at 850°C, with a short circuit current of 1700 mA/cm² and 800 mA/cm² (see Table 1 for a summary). In humidified (3% H₂O) CH₄, the output was of 120 and 50 mW/cm² with a short circuit current of 400 and 220 mA/cm² at 850°C. The overpotential varied linearly with the current (Figure 9b). The difference in performance between these two cells might stem again from the nature of the current collector, the highest performance being reached with a Pt-mesh and the lowest with an Au electroplated Pt-mesh. An experiment in sealed conditions (Au-mesh) seems to confirm this observation as the performance was near 250 mW/cm² at 850°C (Figure 10).

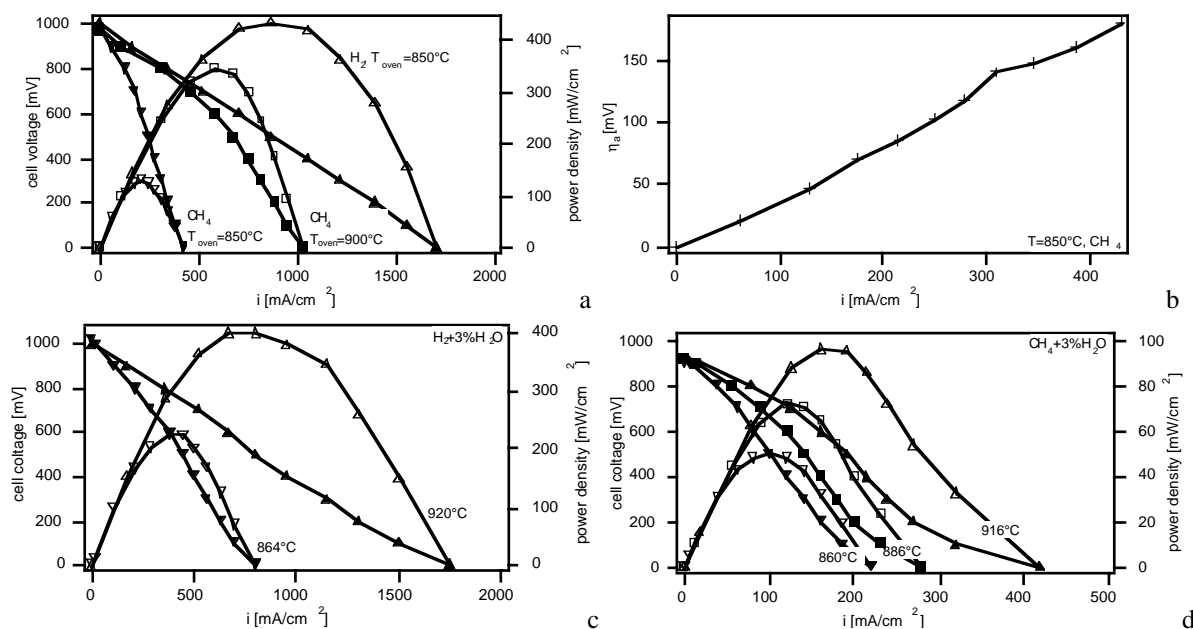


Figure 9: Performance of a CeNbO anode made using a 325 mesh screen. a. and b. case of B62 and c. and d. case of E7h. The exchange current density calculated from b. using $i_o = RT/(4FR_p)$ is of about 130 mA/cm².

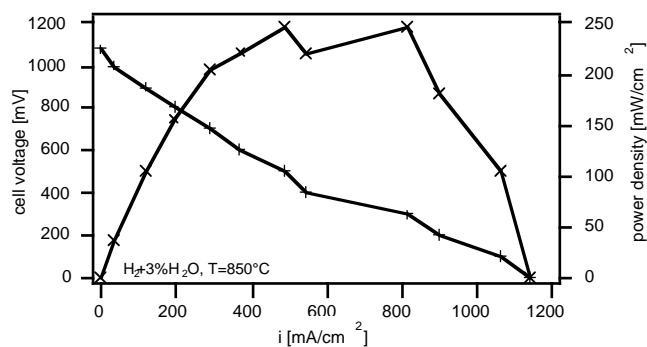


Figure 10: A CeNbO anode (B17) having 0.7 cm in diameter, screen-printed with a 325 mesh screen, sintered at 1100°C/4h, on a 140 μm thick YSZ circular sheet. The anode was connected to an Au-mesh current collector with a CeNbO/Au paste. The measurement was made in the sealed configuration (Chapter 2). The OCV was near theoretical being of 1078 mV in H₂ + \approx 3% H₂O.

The cell B62 was run under CH₄ for more than 150 h. A steady degradation of 11% was observed over this time span (Figure 11) under a cell polarization of 700 mV, which could be due, as discussed above, to carbon deposition around the Pt-mesh current collector. Switching the cell to OCV lead to a further degradation which was resorbed in 10 h after further polarization.

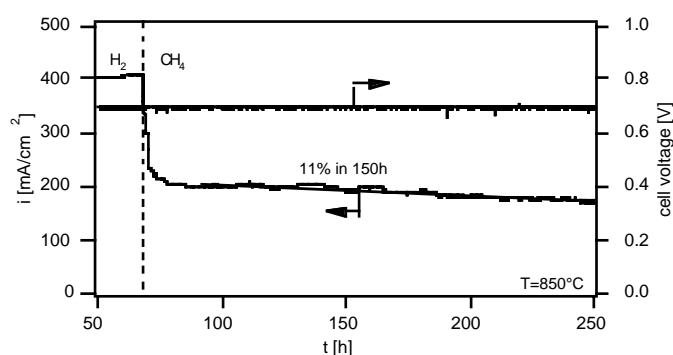


Figure 11: Stability monitoring of the B62 cell at 850°C after switching the cell to humidified CH₄.

As for LaCrO₃-based anodes, the high current density flow induced the heating of the cell by a Joule effect (Figure 12). A temperature increase of about 20°C was monitored by a S-type thermocouple placed beneath the anode (but protected from it by an alumina wool).

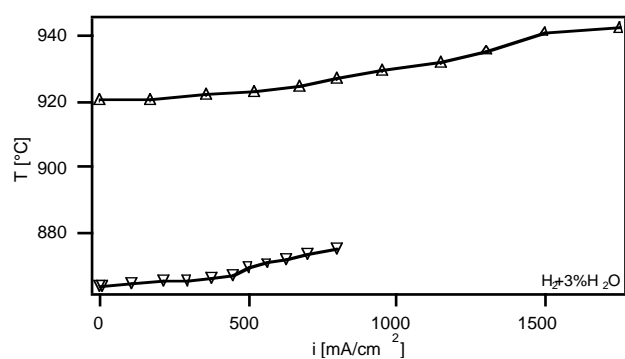


Figure 12: Temperature evolution of the anode upon cell polarization. Two initial temperatures are shown here (E7h).

All these results indicate that CeNbO is an interesting ceramic material for its use as H₂ oxidation anode at middle range temperatures (800-900°C). However, CH₄ activation was quite low over this anode as expected from the corresponding catalytic tests (Chapter 10). A further modification of the ceria material and the use of CeGdO or CePrO could lead to an increase in activity. The addition of a catalyst, such as Ni, Cu or Cu/Ni, is also possible. Another possibility to improve the performance could be the addition of a composite ceria/YSZ layer between the electrolyte and the anode, especially in the case of CeGdO and CePrO-based anodes, as means to improve the adhesion to YSZ. One trial was made in this direction by mixing 50 wt% Mel-YSZ (Magnesium Elektron, U.K.) with CeNbO, but as seen in Chapter 8, the performance was lower than with CeNbO alone (46 mW/cm² in H₂ at 850°C). No trial was yet made with 22 wt% YSZ.

Effect of the catalyst on the performance: case of Ni and Cu

The addition of Ni to CeNbO, in a trial to make a Ni-CeNbO cermet, did not improve the anode performance (Figure 13, to compare with Figure 1). At 850°C, a power output of 160 mW/cm² was achieved in H₂ (see Table 1), a value similar to case A24 (Figure 1). The cell performance dropped dramatically upon introduction of CH₄ (6.25 mW/cm²). From the catalytic runs (Chapter 10) this is expected to proceed due to carbon formation around the Ni particles leading to their extraction off the CeNbO matrix.

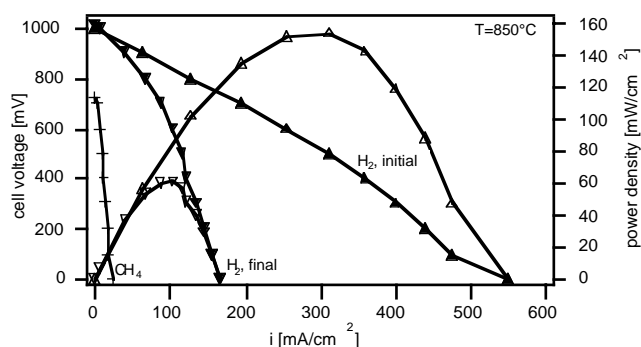


Figure 13: 46%CeNbO/54%Ni anode sintered at 1150°C, B32. I/V curves in H₂ and in CH₄ at 850°C. After CH₄ introduction, the cell performance dropped dramatically. Switching back to H₂ after 24 h run in CH₄ leads to the reactivation of the cell but with a lower power density. This remaining activity might be related to the CeNbO skeleton.

For Cu addition, a CeGdO-based anode with 50 vol% teflon balls was made and applied following the procedure described in Chapter 9 on a 20% CeGdO electrolyte. This combination was chosen, as discussed in Chapter 9, for the ease of pore fabrication with large free volumes required for Cu-nitrate impregnations. A Cu loading of 17% max was obtained after calcining at 900°C/1h. Low OCVs were obtained in H₂ as expected² from the mixed conductance through the ceria electrolyte (Figure 14). The obtained performances agreed well with those mentioned above in H₂ (200 mW/cm², and a short circuit current of 950 mA/cm²). In this case, the electrolyte had a thickness of 770 μm. The series ohmic loss was only 500 mΩcm² at OCV but 1400 mΩcm² at short circuit. Considering these ohmic losses, the performance reached here is comparable to the best cases for CeNbO anodes (case B62 and E7h). In CH₄, the performance was higher than for CeNbO (80 mW/cm², 400 mA/cm² short circuit current), keeping in mind that an Au-mesh was used as current collector (Figure 14). Globally, the combination of Cu and CeGdO lead to about twofold increase in performance in CH₄ (see Table 1 case E7h and D39). The performance of the anode in CH₄ was almost equivalent to that obtained in 10% H₂ in Ar, which would imply a CH₄ conversion of 2 to 5%, if the behavior in methane is governed by hydrogen production.

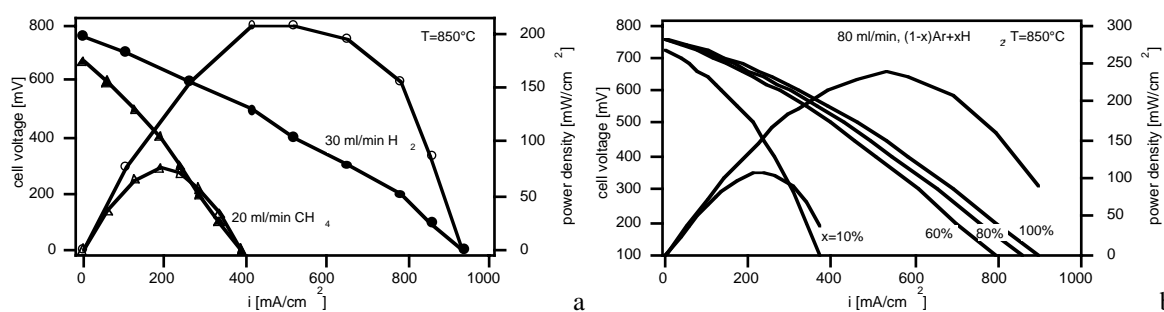


Figure 14: CeGdO+17% Cu anode (impregnation) on a 770 μm thick CeGdO electrolyte sintered at 1250°C (D39). a. Effect of the fuel on the performance, b. effect of the H₂ concentration on the performance of the cell. All tests were made with 3% H₂O. The low OCVs are due to the reduction of ceria².

Effect of the polarization on the performance of the CeNbO anode

The effect of the potential on the anode performance is well depicted in the impedance spectra shown hereafter. All CeNbO anodes treated above showed inductive loops at middle range frequencies appearing at conditions near 'OCV' (see Figure 15). It is to be noted that the Zahner impedance analyzer has the potentiostat and the frequency analyzer coupled together so that, even under OCV conditions, a bias was always applied to the cell. No real OCV condition

could be thus reached and the values were usually shifting by 2 to 10 mV from the desired cell potential. On the impedance spectra, a low frequency semi-circle was observed (see Figure 15) growing at an angle near to 45°. At increasing overpotential, the inductive loops tended to vanish while the low frequency impedances increased. Simultaneously, and as discussed before, the series ohmic resistance shifted to higher values. Globally, the anode R_p tended to increase upon polarization which explains the limiting current reached in most of the cases.

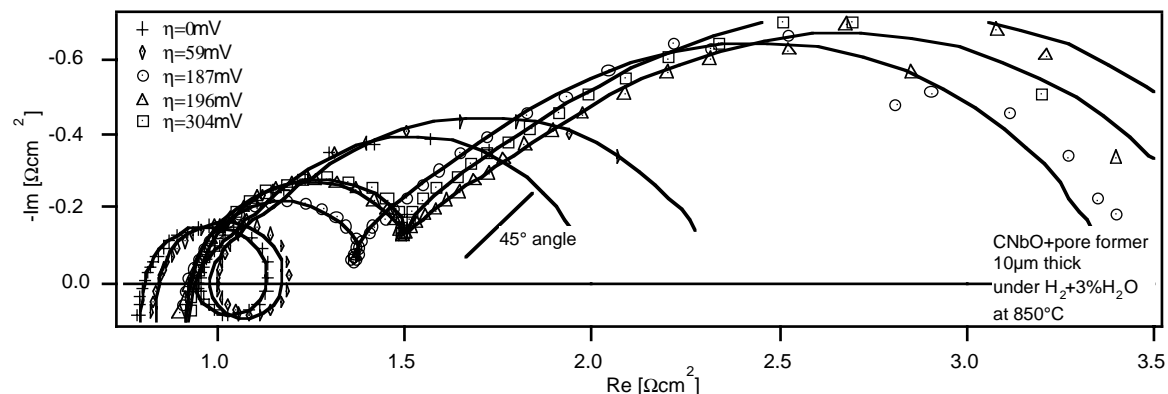


Figure 15: CeNbO anode (D1). Effect of the cell polarization on the anode impedance in humidified H₂. The anode R_p tended to increase upon polarization. Full lines correspond to the fitting data using the impedance equivalent circuit discussed in the text.

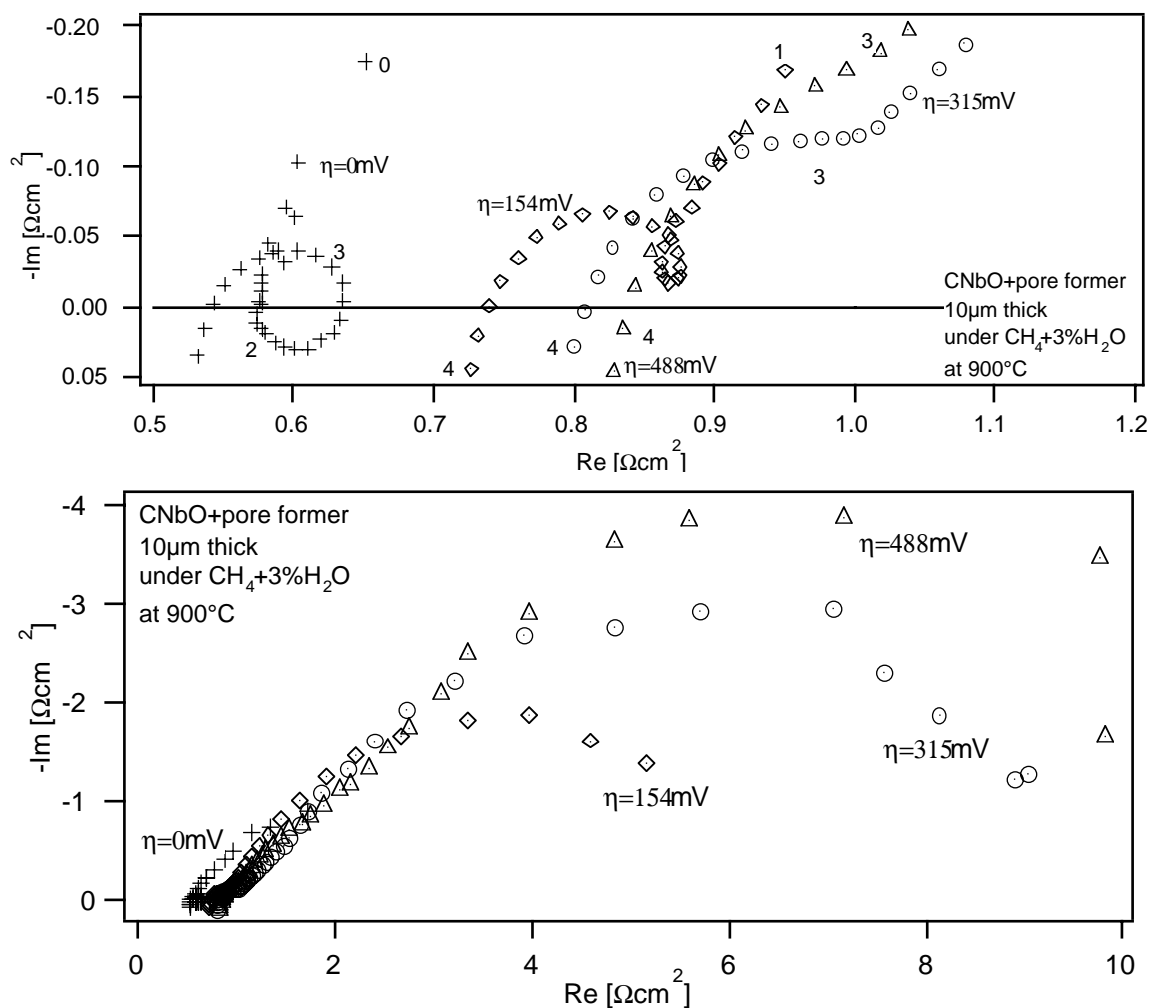


Figure 16: CeNbO anode (D1). Effect of the cell polarization on the anode impedance in humidified CH₄. The first part is a magnification of the full spectra in the high frequency range. The anode R_p tended to increase upon polarization.

Similarly, in CH₄ the R_p increased too, but here the low frequency arcs were dominating so that the inductive loops were too small to be observed on scale (Figure 16). The impedance spectra were highly activated with temperature (see Figures 17) in both hydrogen and methane atmospheres. Moreover, such impedance spectra were observed independently of the location of the reference electrode, i.e. on the cathode or the anode side.

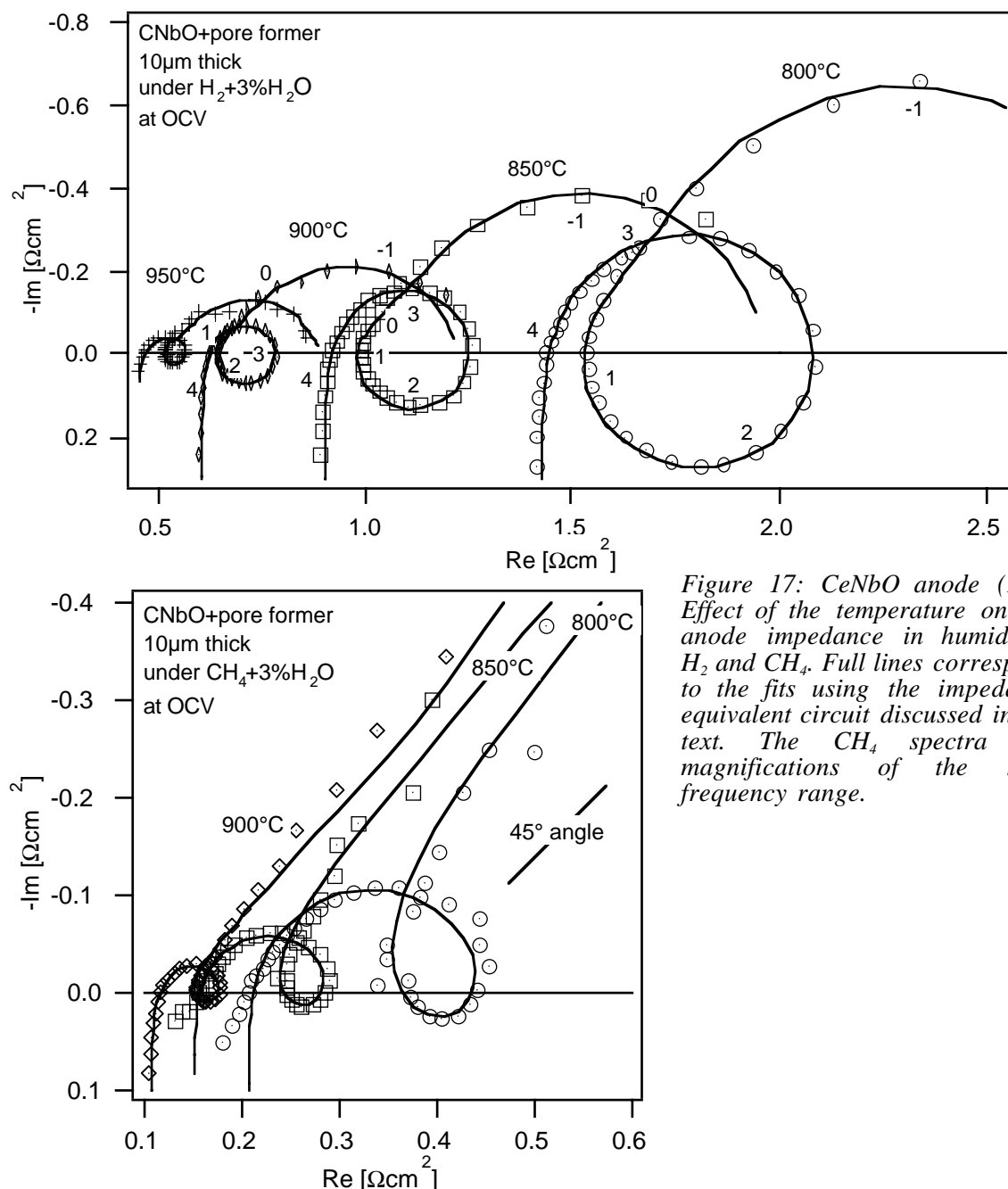


Figure 17: CeNbO anode (D1). Effect of the temperature on the anode impedance in humidified H₂ and CH₄. Full lines correspond to the fits using the impedance equivalent circuit discussed in the text. The CH₄ spectra are magnifications of the high frequency range.

In literature examples of inductive loops were observed at low frequencies (1 Hz to 1 mHz) with corrosion or electro-crystallization of metals as well as for SOFC electrodes³⁻¹³. Different interpretations were advanced in SOFC, as step charge transfer of intermediate adsorbates^{7, 9-11}, as a spreading of the reaction surface and the appearance of a parallel diffusion path (e.g. LSM¹²), as electrocatalysis due to superficial electronic conductivity⁸ (i.e. equally a spreading of the reaction surface), as 'cross-talk' between the working electrode and the reference electrode¹³ or as an artefact caused by electrical shielding¹⁴. As discussed in Chapter 2, our electrochemical setups were all shielded by a faradaic cage and if such artefacts were to happen they should have been systematically observed on the LaCrO₃-based anodes too, which was not the case. The

cross-talk was interpreted as the diffusion of charged species between the working and the reference electrode on the surface of a mixed conducting electrolyte or surface. In our case, these observed loops occurred whether the reference was at the anode or the cathode side. This leaves two remaining interpretations, the non-linear behavior due to a spread of the surface reaction or the presence of intermediate adsorbed species undergoing a charge transfer reaction.

Several models were advanced describing a two-step electron transfer process under bias conditions in the form of



where I is an adsorbed intermediate (Gerischer et al: Epelboin et al.; Frumkin and Armstrong et al. ^{5, 15}). A mathematical derivation of the mechanism with an adsorbed intermediate was first presented by Gerischer and Mehl ⁴ and later generalized by Armstrong and Henderson ¹⁵ and Harrington and Conway ¹⁶, the latter adding a recombination reaction between 2 adsorbed intermediates. Analysis of the model shows that, under bias, an adsorption related negative capacitance is related to a negative resistance (see Figure 18, R₃ and CPE₃) leading to the inductive loop, R₂ and CPE₂ being the charge transfer resistance and the double layer capacitance. Other models were proposed such as the use of an inductance instead of the CPE₃ ^{5, 16}. In the following approach, the model generalized by Armstrong and Henderson ¹⁵ (i.e. negative resistance and capacitance) is considered for its easy physical meaning.

The impedance data generated under bias were best fitted using the so-called ‘Gerischer impedance’ (Figure 18) by adding the electrolyte series resistance (R₁) and a non-uniform diffusion impedance (Z_{NUD}) or a resistance and a CPE in parallel. An inductance was added for the simulation of the impedance system at high frequencies (≥ 10 kHz).

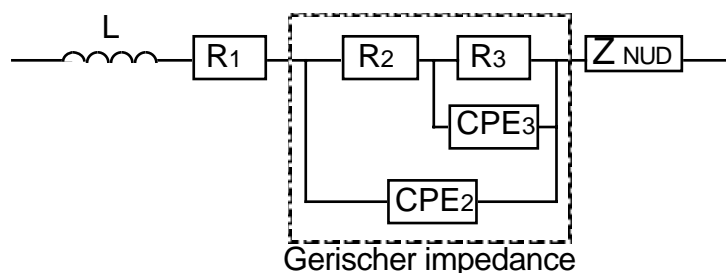


Figure 18: Equivalent circuit used for fitting the impedance data measured in the fuel cell condition. The central part is a modified Gerischer impedance where the capacities are replaced by constant phase elements. Z_{NUD} corresponds to the impedance of a non-uniform diffusion, but could also be replaced by a resistance and CPE in parallel.

The ‘Gerischer impedance’ has the following physical meaning. R₂ is the charge transfer resistance of the electroadsorption step, CPE₂ to the double layer ‘capacitance’. R₃ and C₃ are defined as ¹⁵

$$R_3 = -\frac{R_2^2}{R_o + R_2} \quad (3)$$

$$C_3 = -\frac{R_o \tau}{R_2^2} \quad (4)$$

with R_o a concentration impedance of the adsorbed phase, C₃ the pseudocapacitance of the adsorbed species and τ the adsorption reaction relaxation time. It should be noted that these identifications are not always straightforward and could be related to these parameters in a rather complicated way ¹⁶. The non-uniform diffusion impedance is defined as ¹

$$Z_{NUD} = \frac{\sigma \cdot \tanh(\delta \cdot (i\omega)^p)}{(i\omega)^p} \quad (5)$$

$$\text{with} \quad \sigma = \frac{RT}{n^2 F^2 A C_s \sqrt{D_s}} \quad (6)$$

$$\text{and} \quad \delta = \frac{L}{\sqrt{D_s}} \quad (7)$$

where C_s and D_s represent the bulk concentration and the diffusion coefficient of the diffusing species, L the finite length diffusion, i.e. the thickness of the diffusion layer, n the charge of the species and A the surface area. On the real axis of the impedance, R_{NUD} can be expressed as

$$R_{NUD} = \sigma \delta \quad (8)$$

From equation (7), the value of the diffusion coefficient can be estimated as

$$\left(\frac{1}{\delta}\right)^2 = \frac{D_s}{L^2} \quad (9)$$

whereas the concentration can be derived from equations (6) and (7) as

$$C_s \left(\frac{n^2 F^2 A L}{R} \right) = \frac{T \delta}{\sigma} \quad (10)$$

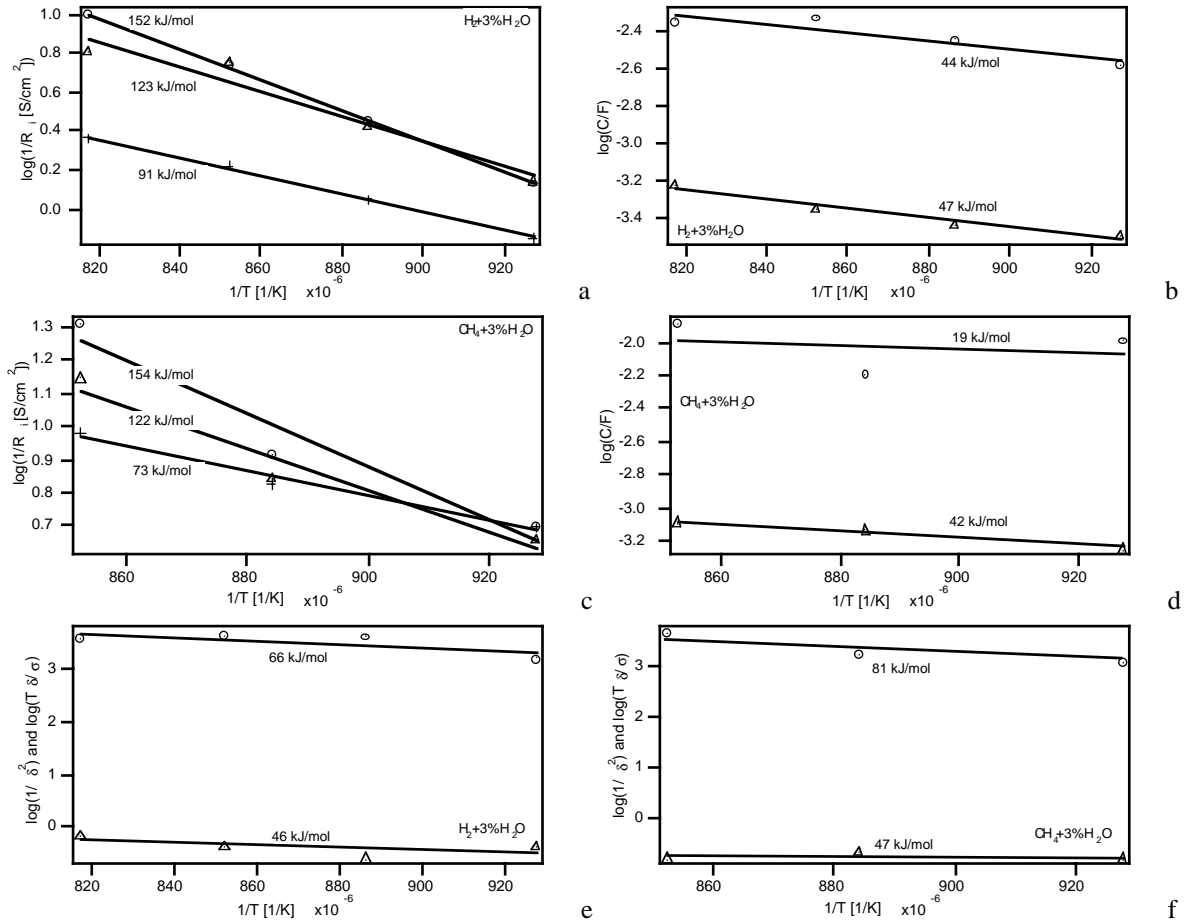


Figure 19: CeNbO anode (D1). Effect of the temperature on the elements of the equivalent circuit used to fit the data. (+) R_1 , (Δ) R_2 or C_2 or $1/\delta^2$, (o) $-R_3$ or $-C_3$ or $T\delta/\sigma$.

Fitting of the impedance data to this model gave a maximum fitting error of 2 to 3% over the whole range of frequency, and in both gas atmospheres (H₂ and CH₄). C_2 was in the range of 400 $\mu\text{F}/\text{cm}^2$, C_3 of -4 mF/cm², and $n_2 \approx 0.87$ and $n_3 \approx 0.93$ in H₂ while in CH₄ the values were of 600 $\mu\text{F}/\text{cm}^2$ for C_2 , -10 mF/cm² for C_3 and $n_2 \approx 0.9$ and $n_3 \approx 0.89$.

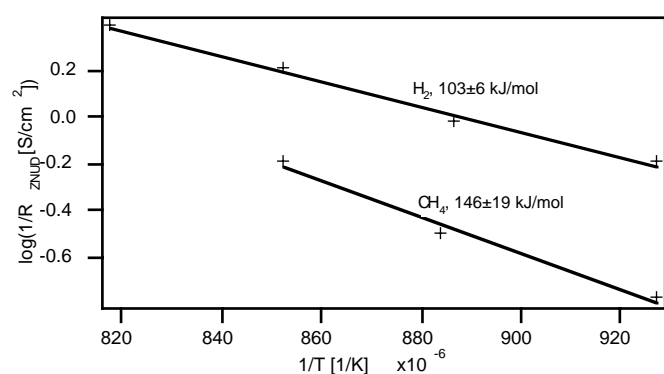


Figure 20: Temperature dependence of the real part of Z_{NUD} for a CeNbO anode (D1). Inset numbers correspond to the activation energies.

The evolution of the different elements in this equivalent circuit as a function of the different parameters will be discussed hereafter. To begin with the effect of temperature (780-980°C) is reflected in Figure 19 (see also Table 2). The evolution of R_1 with temperature, in both gas atmospheres, is similar with activation energies of 91 to 73 kJ/mol, lying near that for YSZ (77 kJ/mol) but also those for CeO₂ solid solutions (see Chapter 9). As observed above, the electronic resistance of the CeNbO anode did participate in the series resistance of the cell, so that the observed activation energy could reflect the participation of the CeNbO electrode. R_2 and $-R_3$ were also similar in both atmospheres, as well as C_2 . On the other hand, $-C_3$ had different values with H₂ and CH₄, perhaps due to the dispersion of the data in CH₄. $1/\delta^2$ and $T\delta/\sigma$ which correspond to the diffusion coefficient and the concentration of the eventual diffusion species were also similar in both atmospheres. If the impedance resistance of the last part of the equivalent circuit in Figure 18 is taken into account, the activation energy of the process is different between H₂ (103±6 kJ/mol) and CH₄ (146±19 kJ/mol) (see Figure 20). But here again due to the dispersion of the data in CH₄, the activation energies could be similar. Summarized, the activation energies seemed to be quite similar in CH₄ and H₂ fuel for many of the simulated processes (see Table 2).

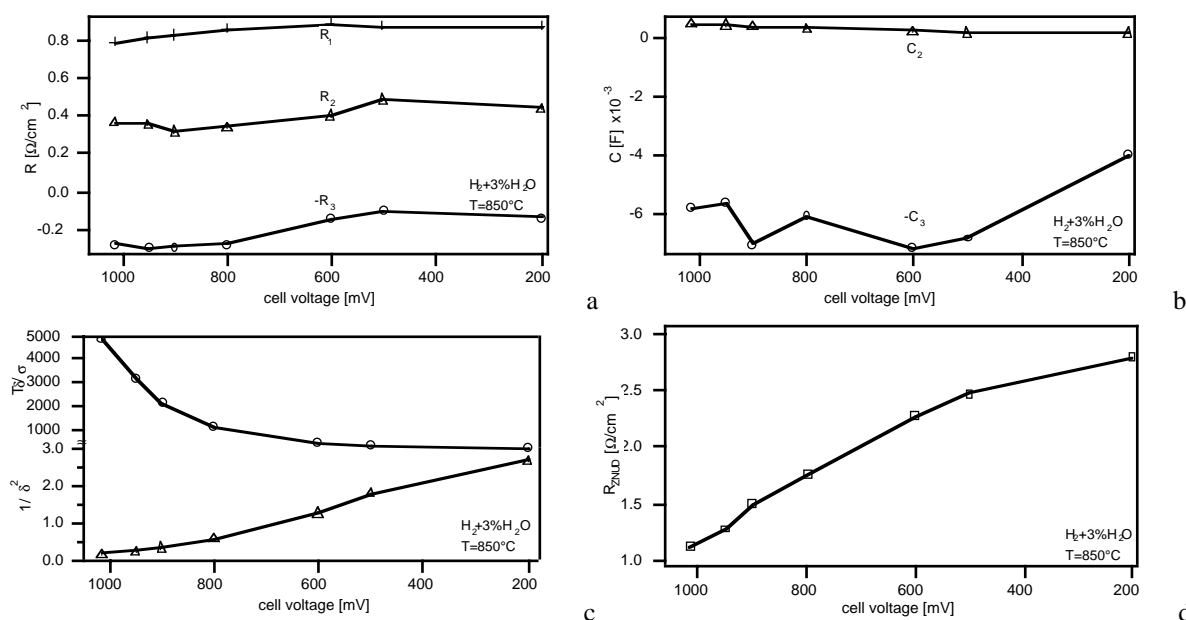


Figure 21: CeNbO anode (D1). Effect of the overpotential on the elements of the equivalent circuit used to fit the data. (+) R_1 , (Δ) R_2 or C_2 or $1/\delta^2$, (o) $-R_3$ or $-C_3$ or $T\delta/\sigma$, (\square) R_{NUD} .

The evolution of the equivalent circuit elements as a function of the cell voltage is treated hereafter (see Figure 21). The resistances R_1 and R_2 tended to increase slightly whereas $-R_3$ tended to decrease with the overpotential. The fact that $-R_3$ is decreasing with the potential may

indicate an activated process in which the adsorbed species catalyzes the reaction. The capacities, C_2 seemed to decrease slightly with the potential, whereas $-C_3$ was dispersed. $1/\delta^2$ and $T\delta/\sigma$ showed opposite evolution, the first increasing and the second decreasing with the potential. The fact that $1/\delta^2$ increases would mean, if the diffusivity of the species did not vary upon polarization, that the diffusion length was reduced. Globally, the most limiting process seemed to stem from the non-uniform diffusion impedance the real part of which almost tripled upon polarization (Figure 21d). Also, from equation (3), R_o can be calculated and its activation energy lies between 64 to 152 kJ/mol in H₂ and 52 kJ/mol in CH₄. A summary of all these activation energies is given in Table 2.

Table 2: Summary of the activation energies of an CeNbO anode run in the non-sealed configuration. Case of D1.

E_a [kJ/mol]	$1/R_1$	$1/R_2$	C_2	$1/-R_3$	$-C_3$	$1/\delta^2$	$T\delta/\sigma$	$1/R_{NUD}$	$1/R_o$
H ₂	73	122	47	154	44	46	66	103	64-152
CH ₄	91	123	42	152	19	47	81	146	52

Effect of H₂, H₂O, CH₄ and p_{O₂} on CeNbO anodes

Here two kinds of measurements were done, one in a SOFC configuration and others on symmetrical cells. The treatment of the data from the SOFC configuration is similar to the one presented above, using the modified 'Gerischer impedance' equivalent circuit. The impedance spectroscopy data were measured at OCV.

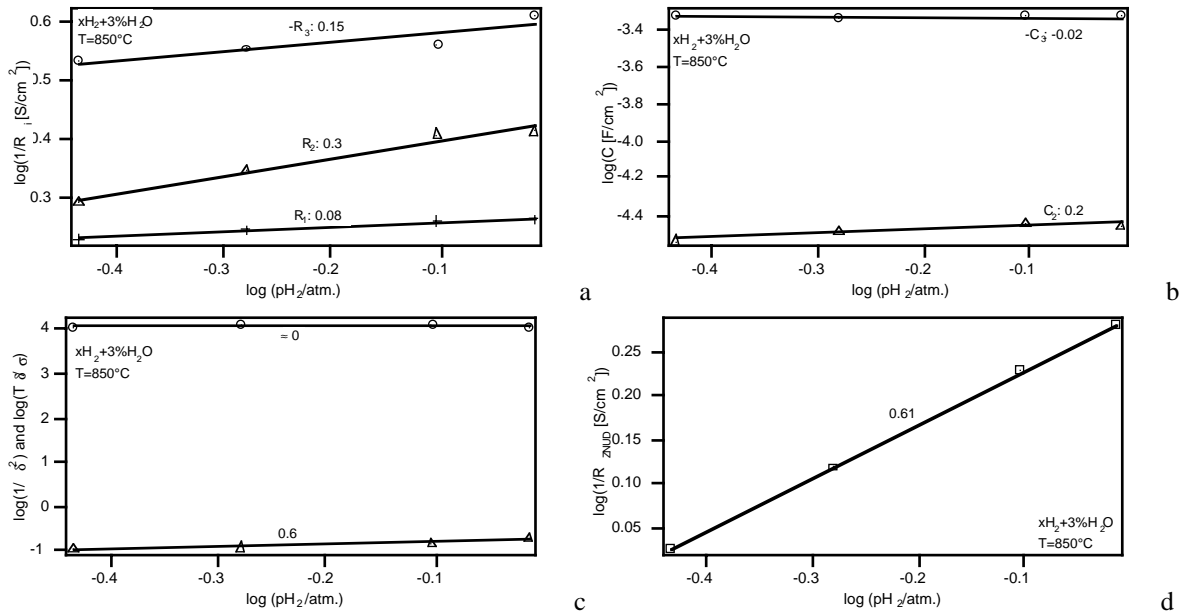


Figure 22: CeNbO anode (B40). Effect of the H₂ partial pressure on the elements of the equivalent circuit used to fit the data. (+) R_1 , (Δ) R_2 or C_2 or $1/\delta^2$, (o) $-R_3$ or $-C_3$ or $T\delta/\sigma$, (\square) R_{NUD} . Inset numbers correspond to the reaction orders towards H₂.

The effects of H₂ and H₂O in a real SOFC setup are presented hereafter (Figure 22 and 23). As can be seen from these figures, there is only a slight effect of H₂ and H₂O on the series resistance, at least at these concentrations (see later). R_2 and $-R_3$ were affected by H₂ as well as H₂O partial pressures, decreasing with increasing P_{H_2} , while increasing with increasing P_{H_2O} , but to a lesser extent. C_2 on the other hand increased with both H₂ and H₂O partial pressures.

$-C_3$ was sensitive to H₂ but not to H₂O. $1/\delta^2$ increased with H₂ and H₂O, while $T\delta/\sigma$ was constant in H₂ but decreased with H₂O. Globally, the non-uniform diffusion impedance decreased upon increasing H₂O but did not vary upon H₂ increase. The little effect of H₂O on

R_{NUD} stems from the similar reaction order for $T\delta/\sigma$ and $1/\delta^2$ towards H₂O but with reverse signs.

Table 3: Summary of the reaction orders of an CeNbO anode run in the non-sealed configuration at 850°C. Case of B40.

Reaction order	$1/R_1$	$1/R_2$	C_2	$1/-R_3$	$-C_3$	$1/\delta^2$	$T\delta/s$	$1/R_{NUD}$
H ₂	0.08	0.3	0.2	0.15	-0.02	0.6	0	0.61
H ₂ O	-0.08	-0.18	0.12	-0.1	0.29	0.37	-0.39	-0.02

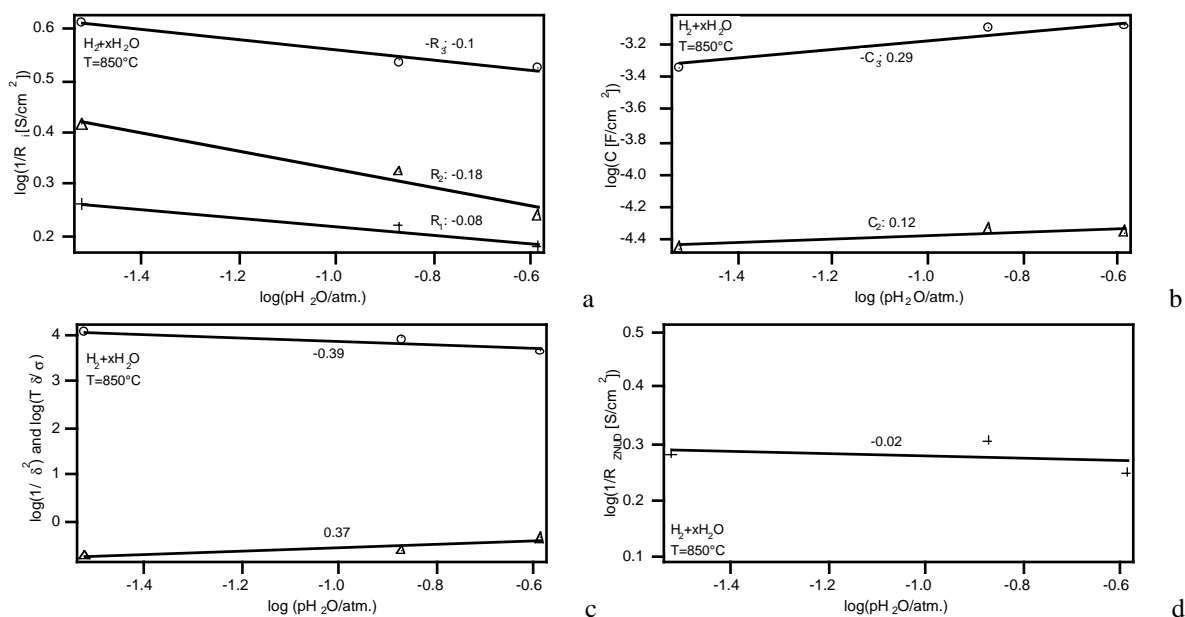


Figure 23: CeNbO anode (B40). Effect of the H₂O partial pressure on the elements of the equivalent circuit used to fit the data. (+) R_1 , (Δ) R_2 or C_2 or $1/\delta^2$, (o) $-R_3$ or $-C_3$ or $T\delta/\sigma$, (\square) R_{NUD} . Inset numbers correspond to the reaction orders towards H₂O.

Also, from equation (3), R_o reaction orders were estimated to 0.53 in H₂ and -0.37 in H₂O. Table 3 summarizes all values.

The effects of H₂, H₂O, CH₄ and P_{O_2} on symmetrical cells are presented hereafter. In this study two types of cell were tested: CeNbO and CeNbO+1%Ni, sintered at 1200°C/4h (see Table 1). A GC analysis was conducted in parallel to analyze the reacted gas composition at the outlet of the reactor (Figure 24). The catalytic reaction over these anodes showed an activation energy of about 160 kJ/mol on both anode types (see Figure 24a), a value slightly different from the value (140 kJ/mol) obtained in the catalytic reactor (Chapter 10) in humidified CH₄ for CeNbO powders. However, this activation energy matches well the reported value for CH₄ oxidation by CeO₂¹⁷. Also, the temperature of 800°C was observed to be the limit above which the reaction rate increased significantly (Figure 24a). This was also observed over the powder catalyst. From the outlet gas composition of H₂O and H₂ partial pressures (mass balance), the expected OCV was calculated in the manner as described before in Chapter 6 and 10 using HSC 4.1 thermodynamic equilibria calculation software (Figure 24b and e). The observed values were confirmed during a sealed measurement at 850°C (Figure 24f). Also, the evolution of the gas product as a function of CH₄ partial pressure showed a linear relation between CH₄ and H₂, whereas CO₂ formation tended to level off with a concomitant increase in the CO selectivity (Figure 24c). With increasing H₂O partial pressure, H₂ and CO₂ production tended to increase but leveled off at high H₂O content (Figure 24d). In all cases, CO₂ formation was favored at $T \leq 800^\circ\text{C}$, while CO was favored at $T \geq 850^\circ\text{C}$ as expected from the catalytic runs (Chapter 10). An estimate of the reaction order for H₂O was of 0.5 over CeNbO and 0.7 over CeNbO+1%Ni whereas it was of about 0.8 for CH₄.

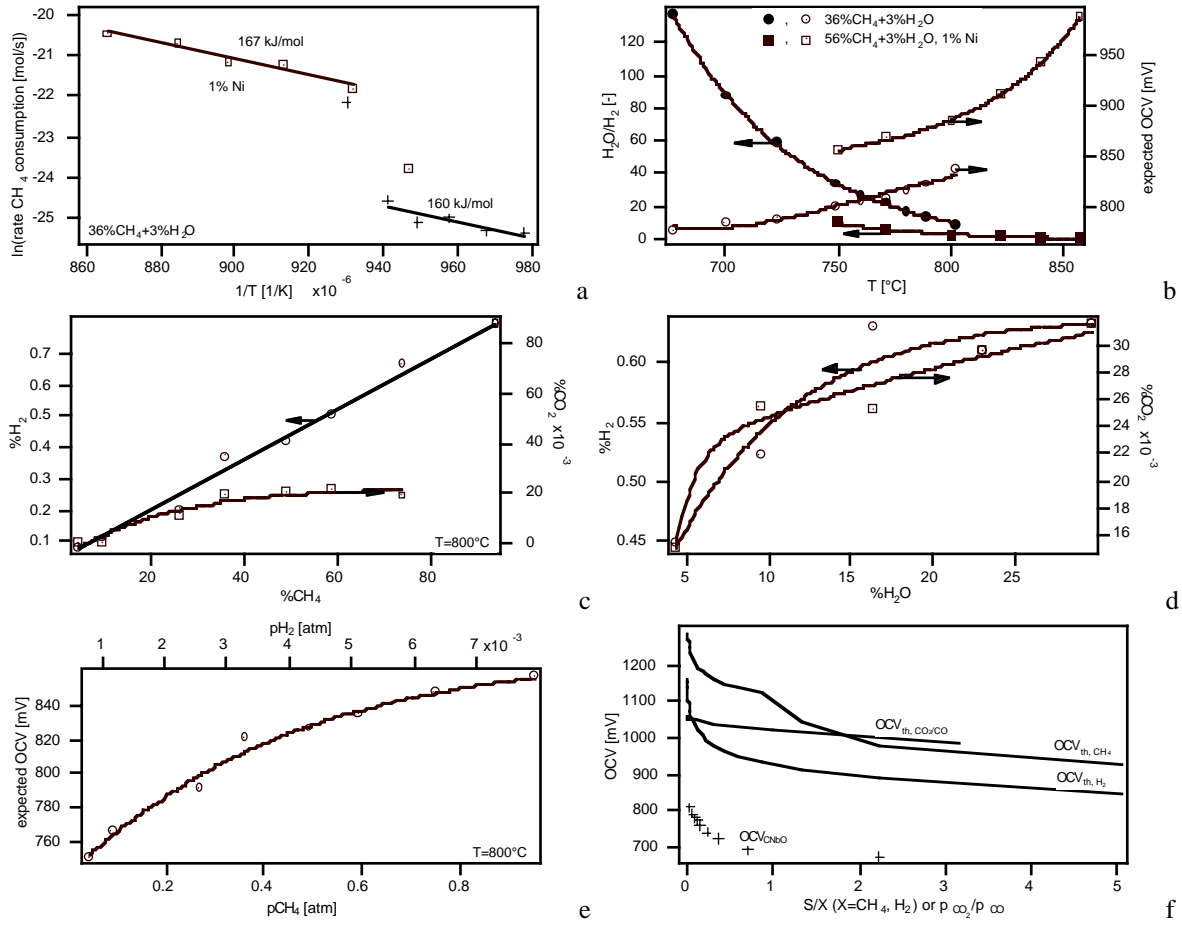


Figure 24: CeNbO anode (D13d, D10c and B17). GC analysis of the exhaust gas in the symmetrical cell configuration. a. activation energies, b. expected OCV from the outlet gas composition (D13d and D10c), evolution of the gas composition as a function of c. CH₄ and d. H₂O, e. expected OCV as a function of CH₄ (D13d) and f. measured OCV in a sealed set-up (B17).

The influence of these different parameters on the electrochemical behavior of the cell is shown hereafter. The impedance response of the symmetrical cells is somewhat different from what has been described above (Figure 15-17). No inductive loop is observed in this case (Figure 25, 26). This difference might stem, as discussed above, from the imposed potential at OCV by the Zahner system in the case of the real SOFC test (from 2 to 10 mV) leading to a polarization of the anode ($\approx 1\text{--}3\text{ mA/cm}^2$). In the case of the symmetrical cells, the voltage differences between the two symmetrical anodes was of 1 mV, leading to a negligible current ($\approx 1\text{ }\mu\text{A/cm}^2$). Two semi-circles were observed. At high frequency a semi-circle was introduced to better fit the data (the relevance of this will be discussed later). The low frequency arc increased following a 45° angle, similarly to the other data reported before.

The effect of the different gas atmospheres can be seen on Figure 25, 26. By lowering the H₂ concentration, the spectra tended to shift to higher impedances, with an increasing lower frequency arc. Water had a similar effect on the high frequency impedance but influenced the low frequency arc less (Figure 25). In CH₄, these effects were similar, with a pronounced influence on the low frequency arc (Figure 26).

The system was best fitted by a series of 3 (RY) as described in the experimental part. Here the summit frequency for each arc, defined as

$$f_i[\text{Hz}] = \frac{1}{2\pi R_i C_i} \quad (11)$$

was around 10 kHz, 0.5~1 kHz and 0.5~1 Hz for the first, the second and the third arc respectively. These summit frequencies were similar to those observed for the 3 steps in the modified 'Gerischer impedance' described above.

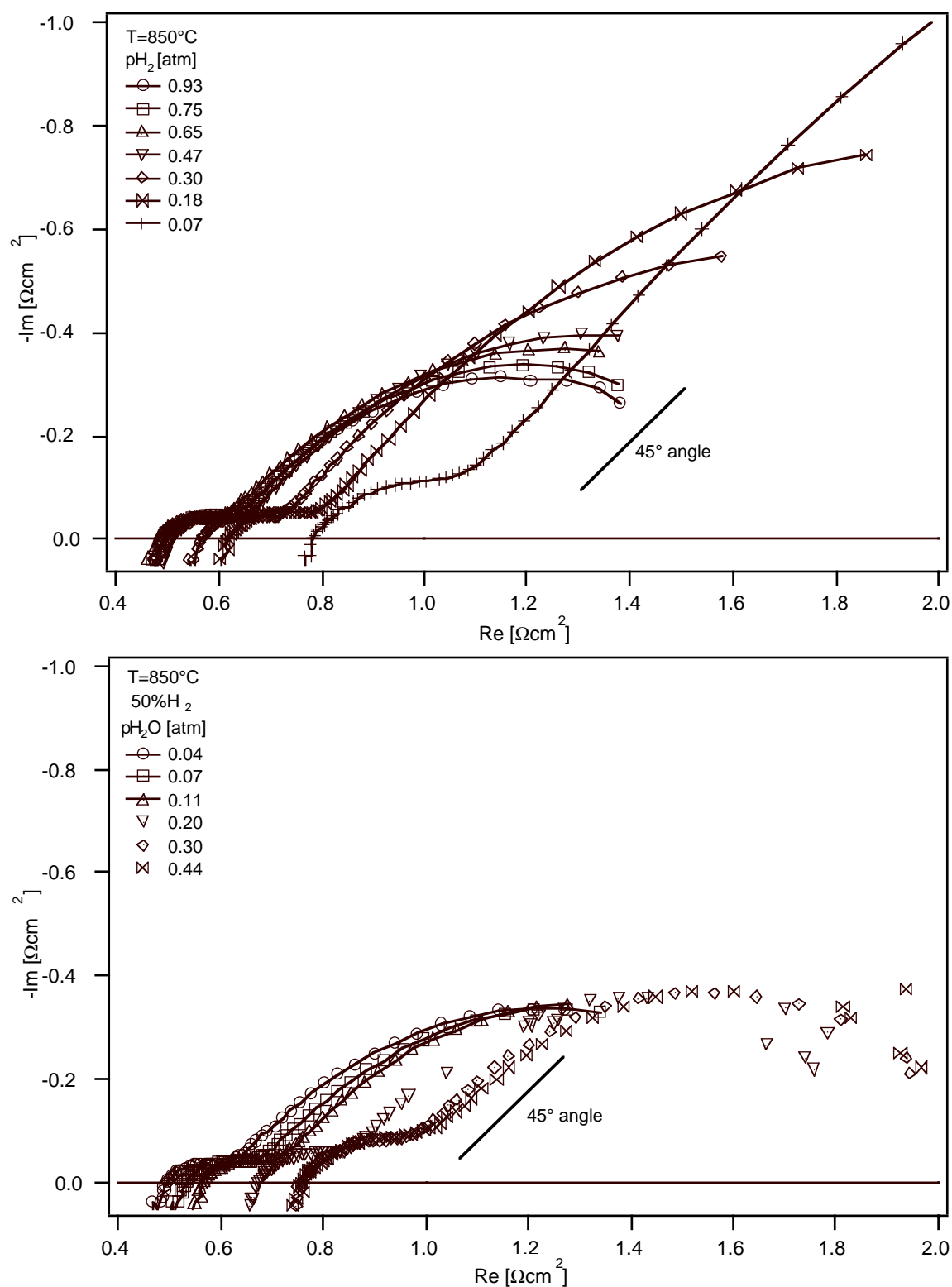


Figure 25: CeNbO anode (D13d). Impedance spectra as a function of H₂ and H₂O partial pressure at 850°C.

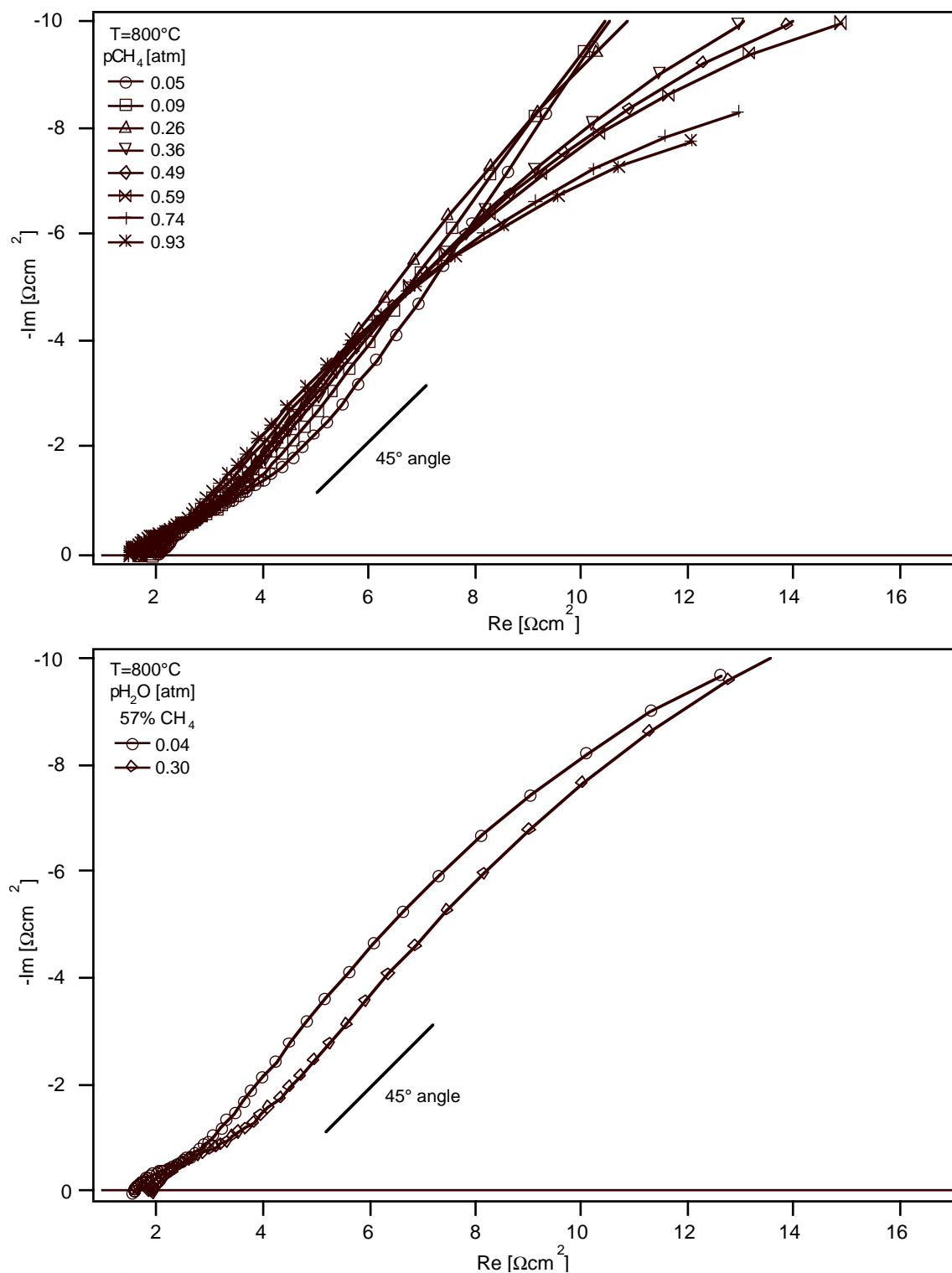


Figure 26: CeNbO anode (D13d). Impedance spectra as a function of CH₄ and H₂O partial pressure at 800°C.

From the fitting of the impedance data to the equivalent circuit (3 arcs) its was possible to follow the evolution of the different elements with the parameters. This is illustrated in Figure 27-31.

Effect of T: All processes were activated with temperature. The electrolyte series resistance had an activation energy of 70~74 kJ/mol in H₂ and CH₄ respectively, a value near to that of YSZ (77 kJ/mol). R_1 had a gas atmosphere independent activation energy. As R_1 appeared at high frequency (10 kHz), where the influence of the inductance by the measuring set-up became significant, and as its value was quite negligible (40 mΩcm²), its was regarded as not further relevant. R_2 and R_3 , on the other hand, depended on the gas atmosphere, showing higher activation energies in CH₄. In CH₄, R_3 was activated by 308 kJ/mol, a value near to 370-435 kJ/mol reported for gas phase splitting of CH₄ to CH₃ and H radicals¹⁸. The addition of 1%Ni reduced the activation energies in most cases (see Table 4 for a summary, and Figure 27).

Table 4: Summary of the activation energies in the symmetrical cell configuration.

CeNb			C	CeNb+1%Ni		
Gas	Parameter	E_a	E_a	Gas	Parameter	E_a
H ₂	1/R _e	70		H ₂	1/R _e	87
	1/R ₁ -C ₁	122	122		1/R ₁	45
	1/R ₂ -C ₂	105	92		1/R ₂	107
	1/R ₃ -C ₃	85	45		1/R ₃	149
CH ₄	1/R _e	74		CH ₄ *	1/R _e	72~74
	1/R ₁ -C ₁	125	82		1/R ₁	77~78
	1/R ₂ -C ₂	174	60		1/R ₂	136~140
	1/R ₃ -C ₃	308	30		1/R ₃	140~147

*two different water content used: 3 and 70% H₂O. E_a in kJ/mol.

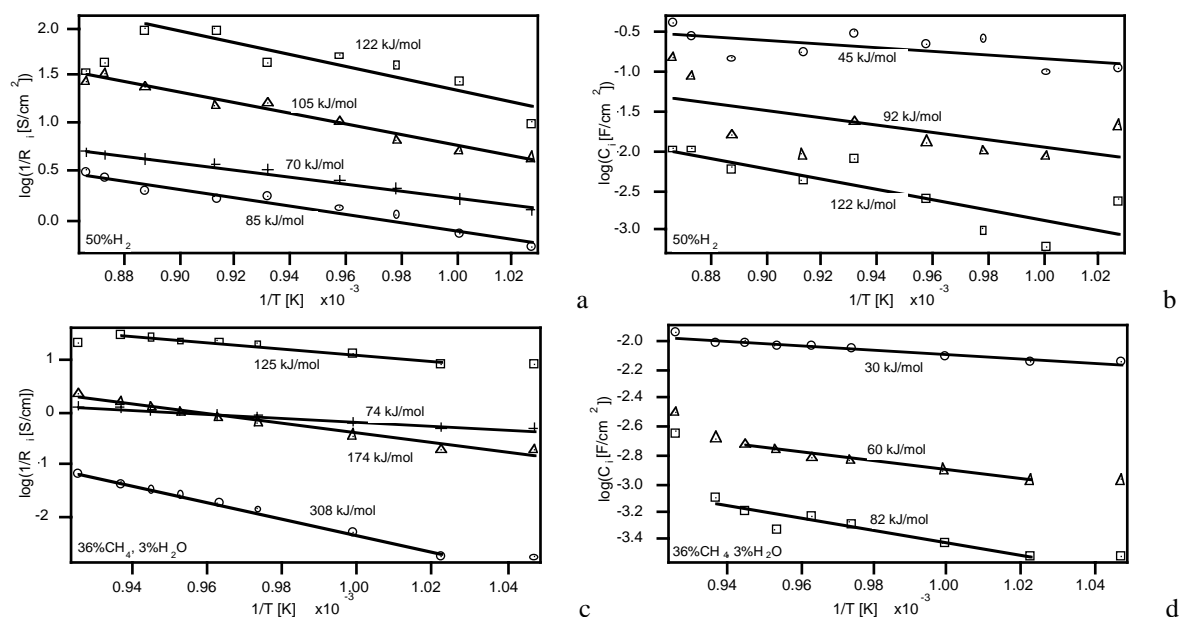


Figure 27: CeNbO anodes (D13d): Temperature dependence in both H₂ and CH₄. (+) R_e, (□) R₁ or C₁, (Δ) R₂ or C₂ and (O) R₃ or C₃.

Effect of H₂, H₂O, CH₄ and P_{O₂}: Figures 28-31 display the evolution of the equivalent circuit elements as a function of these parameters (see Table 5, 6 and 7 for an overview). Globally, it is observed that all reaction steps depended more on H₂ than on CH₄ partial pressures when the results in CH₄ are plotted against the H₂ partial pressure as measured by GC (see Table 5 and Figure 28). In all cases the dependence towards H₂ was more significant or equal to that in CH₄. When the data are plotted against P_{O₂}, as estimated from the thermodynamic calculations based on the exhaust gas, the influence of P_{O₂} was also apparently

less significant than that of H₂ (see Table 5 and Figure 29). However, 2 different regimes were observed depending on the P_{O_2} : the dependencies towards H₂ were almost nil for all the elements except for R₃ and C₃, with the slope changing at a P_{O_2} level below 10⁻²⁰ at 800°C or 10⁻¹⁹ at 850°C (Figure 29). These oxygen partial pressures correspond to the region where a drastic change in the electronic conductivity of CeNbO occurs (Chapter 9).

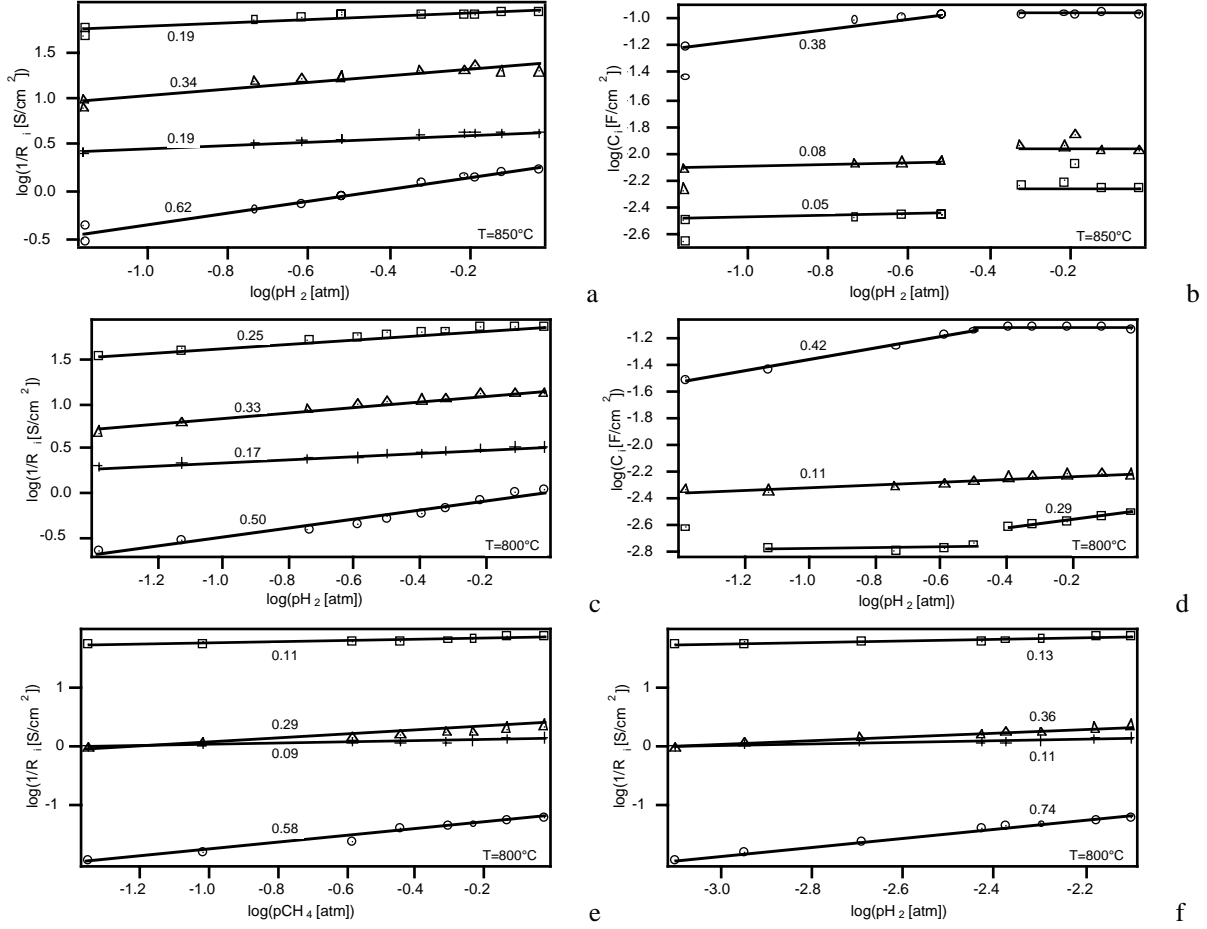


Figure 28: Evolution of the equivalent circuit elements as a function of the different parameters. a. and b. in H₂ at 850°C, c. and d. in H₂ at 800°C and e. and f. in CH₄ at 800°C. (Case of D13d)

Table 5: Summary of the reaction orders for a CeNbO anode (case of D13d).

CeNb		Parameter	1/R		C		1/R		C		1/R		C		
Gas	T[°C]		pH ₂	pO ₂	pH ₂ O	pO ₂	pH ₂ O	pO ₂	pH ₂ O	pO ₂	pH ₂ O	pO ₂	pH ₂ O	pO ₂	
H ₂	850°C	1/R _e	0.19	-0.08	-0.19										
		1/R ₁ -C ₁	0.19	0	-0.3	0	-0.49								
		1/R ₂ -C ₂	0.37	0	-0.35	0	-0.45								
		1/R ₃ -C ₃	0.62	0~-0.38	-0.28	0~-0.19	0.37	-0.09							
H ₂	800°C	1/R _e	0.17	-0.09	-0.14		-0.06								
		1/R ₁ -C ₁	0.25	0~-0.29	-0.2	0~-0.16	0.09	-0.1	0.04						
		1/R ₂ -C ₂	0.33	0.11	-0.3	-0.06	-0.3	-0.03	-0.15	-0.02					
		1/R ₃ -C ₃	0.5	0.42~0	-0.27	0~-0.22	0.5	-0.03	-0.03						
CH ₄	800°C	1/R _e	0.09	-0.06	0.11		-0.09		-0.06						
		1/R ₁ -C ₁	0.11	0.05	0.13	0.1	-0.19		-0.12						
		1/R ₂ -C ₂	0.29	0.09	0.36	0.17	-0.35	-0.15	-0.21	-0.09					
		1/R ₃ -C ₃	0.58	0.1~0.25	0.74	0.25	0.17	0	0.1	0					

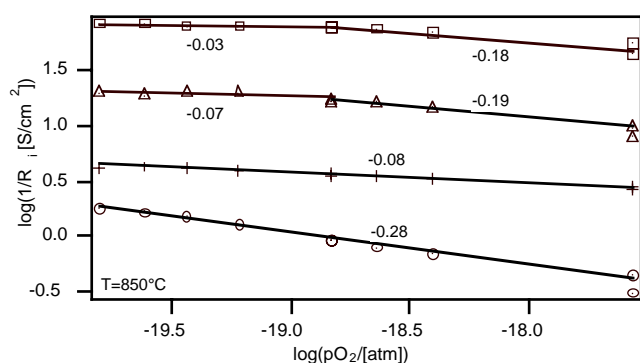


Figure 29: Effect of P_{O_2} on the different equivalent circuit elements. This graph is equivalent to that of Figure 28a. (Case of D13d).

To examine further the effect of the oxygen partial pressure on the the R and C elements, experiments were made at constant potential values (see Figure 30 and Table 6). The evolution with H₂ and H₂O shows clearly that these gases more than the partial pressure of oxygen are responsible for the measured dependencies. Again, at very high H₂ partial pressures (or low P_{O_2}) the dependencies were almost nil, whereas at low H₂ partial pressures (or high P_{O_2}) the dependencies were very marked. Only R_3 depended much on H₂ and H₂O in the whole pressure span (see Figure 30 and Table 6).

H₂O was observed to have a negative effect on the reaction rate as all reaction orders but for R_3 were negative. The effect of water was negligible at very low concentrations. This was also confirmed at constant P_{O_2} (Figure 31 and Table 5 and 6). Globally, water seemed to behave in a reverse manner to H₂, i.e. the reaction orders were equivalent but opposite in sign (except for R_3). This could be a hint that for R_1 and R_2 , H₂O in one form or the other is the reaction product of a hydrogen species. R_3 , on the other hand, decreased with increasing H₂O concentration as confirmed by constant P_{O_2} measurements (Figure 28 and 30).

The addition of 1%Ni to the anode tended to decrease the activation energies of most steps of the reaction (Table 4) but it did not alter much the dependencies to the gas composition, except for H₂O (see Table 7). The activation energies in H₂ and CH₄ for R_1 , R_2 and R_3 tended to decrease, except for R_3 in H₂, indicating that this catalyst facilitated some of these reactions. The activation towards CH₄ for R_3 was very marked as its E_a passed from 308 to 140-147 kJ/mol. The difference in the activation energies for R_3 in H₂ between the two cases (CeNbO and CeNbO + 1%Ni \approx 64 kJ/mol) is almost equal to the adsorption energy of H₂ over Ni as reported by Leach at al.¹⁹ (63 kJ/mol).

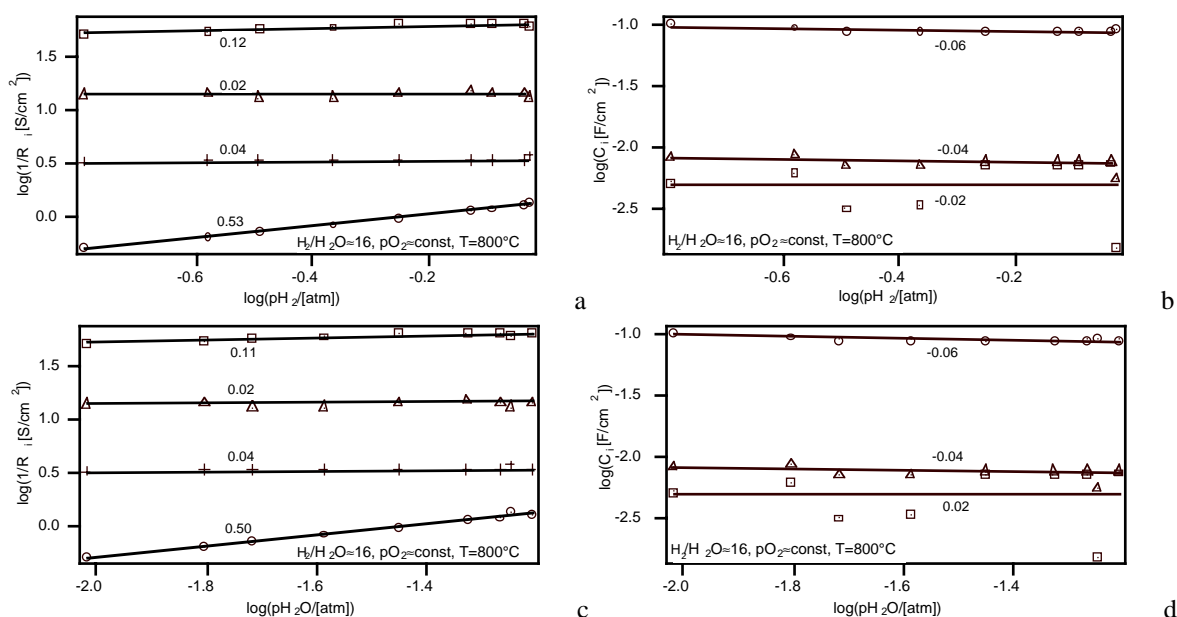


Figure 30: Effect of H₂ and H₂O at constant P_{O_2} of about 1.73×10^{-21} atm. (Case of D13d).

Table 6: Summary of the H₂, H₂O and CH₄ reaction orders at constant P_{O₂} for a CeNbO anode (case of D13d).

CeNb, const. pO ₂ effect		1/R	C	1/R	C	1/R	C
Gas	T [°C]	Parameter	pH ₂		pH ₂ O		
H ₂	800°C	1/R _e	0.04		0.04		
H ₂ /H ₂ O	16	1/R ₁ -C ₁	0.12	0	0.11	0	
P _{O₂}	≈10 ⁻²¹	1/R ₂ -C ₂	0.02	-0.04	0.02	-0.04	
OCV*	1.07 V	1/R ₃ -C ₃	0.53	-0.06	0.5	-0.06	
Gas	T [°C]	Parameter	pCH ₄		pH ₂ O		pH ₂
CH ₄	800°C	1/R _e	0.1		0.09		0.1
H ₂ /H ₂ O	0.29	1/R ₁ -C ₁	0.15	0.37	0.15	0.35	0.16
P _{O₂}	≈10 ⁻¹⁸	1/R ₂ -C ₂	0.17	0.06	0.16	0.06	0.17
OCV*	0.88 V	1/R ₃ -C ₃	0.6	0.03	0.6	0.03	0.6

*expected OCV from H₂/H₂O ratio calculated from the Nernst equation.

 Table 7: Summary of the H₂, H₂O and CH₄ reaction orders at constant P_{O₂} for a CeNbO + 1%Ni anode (case of D10c).

CeNb+1%Ni		1/R	1/R	1/R	
Gas	T[°C]	Parameter	pH ₂	pH ₂ O	
H ₂	850°C	1/R _e	0.1	-0.1	
		1/R ₁	0.22	-0.08	
		1/R ₂	0.26	-0.08	
		1/R ₃	0.49	0	
H ₂	800°C	1/R _e	0.06	0.05	
		1/R ₁	0.05	0.04	
		1/R ₂	0.23	-0.08	
		1/R ₃	0.36	0.12	
Gas	T[°C]	Parameter	pCH ₄	pH ₂	pH ₂ O
CH ₄	850°C	1/R _e	0.08	0.09	0
		1/R ₁	0.07	0.07	-0.05
		1/R ₂	0.3	0.33	-0.07
		1/R ₃	0.36	0.4	0.08

Discussion - Nature of the CeNbO electrode reaction

By comparing the results of both configurations (non-sealed and symmetrical configurations), it appears that the so-called charge transfer resistance in the modified Gerischer equivalent circuit (Figure 18) corresponds to R₁ or R₂ of the symmetrical cell as their activation energies and reaction orders lye close to each other (Table 2 and 3 versus Table 4 and 5). R₁ in the symmetrical analysis, due to its low value (40 mΩcm²), could be related to an artefact as its summit frequency was quite high (10 kHz) and affected by the measurement apparatus. R_{NUD} could correspond to R₃, even though the activation energy in CH₄ for R₃ was much higher than that for R_{NUD}. However, this could be rationalized by the fact that un-coated Pt-meshes were used in the case of the non-sealed configuration (see Table 1 case of D1 versus D13d) and could be compared to the case of CeNbO + 1%Ni (E_a=140-147 kJ/mol). Also, both configurations showed clearly arcs having almost a 45° slope (see for example Figure 15 and 25) which could indicate a diffusion limited process. The fact, that no inductive loops were observed in the symmetrical case could be related to the difference in OCV conditions as discussed earlier.

The electrolyte resistance in both cases is observed to have an activation energy similar to that of YSZ (77 kJ/mol) but the influence of the anode conductivity cannot be excluded as its own activation energy in reducing atmospheres is also of 79 kJ/mol (see Chapter 9, Figure 6). The effect of the different gas atmospheres (see Table 5) and polarization (Figure 2) on this resistance show clearly that its value tend to increase upon increasing the local oxygen partial

pressure. CeNbO as an *n*-type conductor shows a rapid decrease in its conductivity above an oxygen partial pressure of 10⁻²⁰ atm, at 850°C, related to its reoxidation. At about an oxygen partial pressure of 10⁻¹⁵ atm the conductivity reaches a constant value. This behavior is very similar to that of the electrolyte resistance as measured by impedance spectroscopy (see Figure 32) where a net drop in its conductivity was observed around 10⁻²⁰ atm of *P*_{O₂}. The conductivity stabilized ultimately beginning from 10⁻¹⁵ atm of *P*_{O₂}.

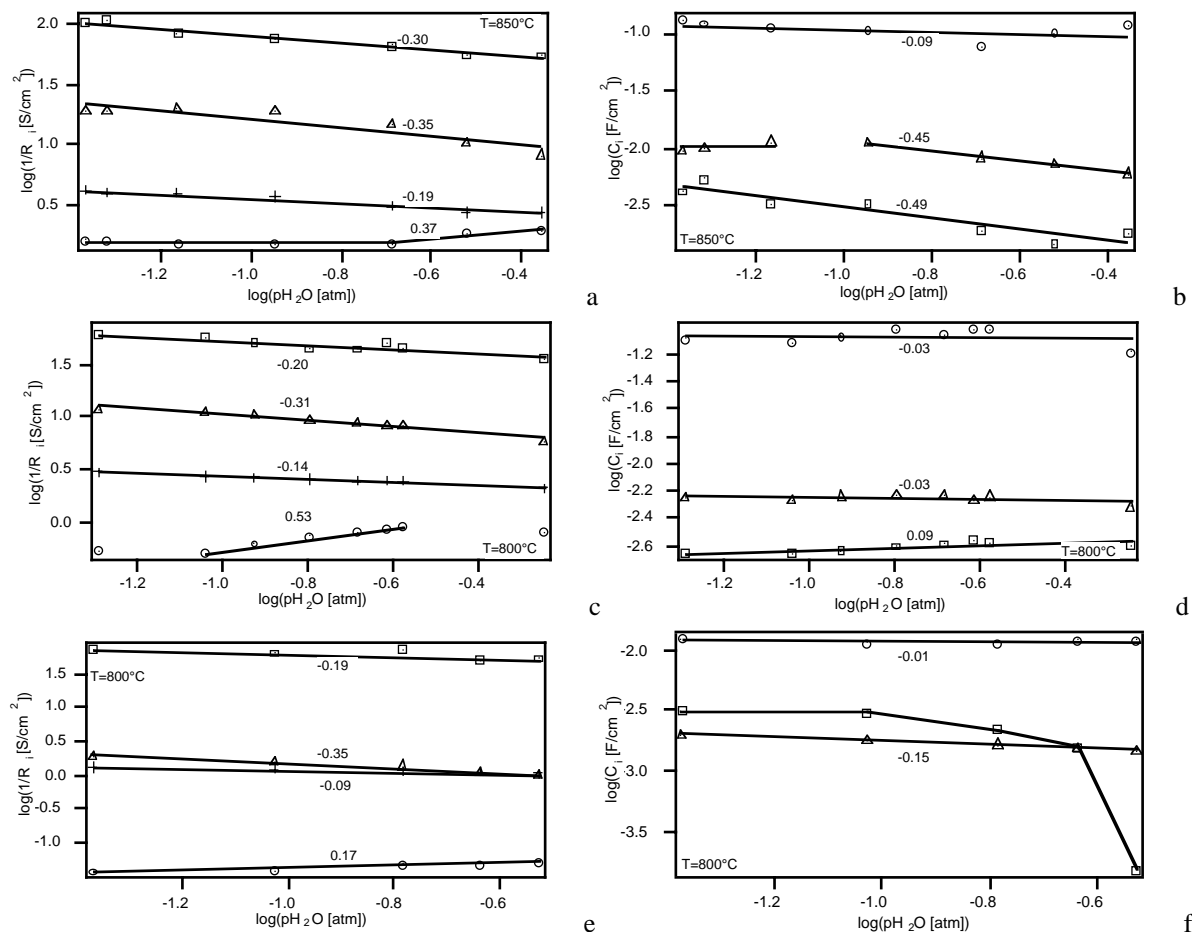


Figure 31: Effect of H₂O in H₂ a., b., c. and d. and CH₄ e. and f. (Case of D13d).

This slope change at around 10⁻²⁰ atm of *P*_{O₂} was also observed for the other processes in the reaction (see Figure 32) and for the capacities (see for example Figure 28 b. and d.). This may indicate that the activity of oxygen plays a role in all the observed processes, even though under constant *P*_{O₂} these were markedly more dependent towards H₂, H₂O and CH₄ (see Table 5 and 6). The indication that the capacities did not change much with the gas composition, except for the case of *R*₁, at constant *P*_{O₂} (Table 6) could be a further hint to the implication of oxygen activity in the different steps of the reaction as revealed from the analysis of the different elements of the equivalent circuit used to interpret impedance spectroscopy data.

From the hypothesis made by using a modified 'Gerischer impedance', one adsorbed species resulting from an electrochemical reaction should also undergo an electrochemical reaction as already discussed by equation (2). As the absolute reaction orders for CH₄ or H₂ were similar to those of H₂O (those being negative, see Table 3 and 5), H₂O or one of its intermediates should be the products of the electrochemical reactions. One can think of the electrochemical reaction of an oxygen species with H₂ leading to an adsorbed hydroxyl group which further reacts with a hydrogen species to lead to H₂O in the following manner:





where equation (12) and (13) are the charge transfer reactions with $\cdot H$ (adatom) the intermediate species, equation (14) the recombination reaction leading to adsorbed H₂O which desorbs following equation(15) liberating an oxygen vacancy $V_o^{\cdot\cdot}$. The ionic conductivity allows to replenish these vacancies (equation (16)). The electron donations of equation (12) and (13) are made through the ceria matrix following equation (17). An alternative model could be the charge transfer of hydrogen species and their reaction with oxygen species from YSZ or CeNbO as follows



One should keep in mind that H^+ is a species bonded to oxygen sites on the surface. Another possibility is O_o^x discharging (partially or totally) followed by its reaction with the fuel following a catalytic reaction.

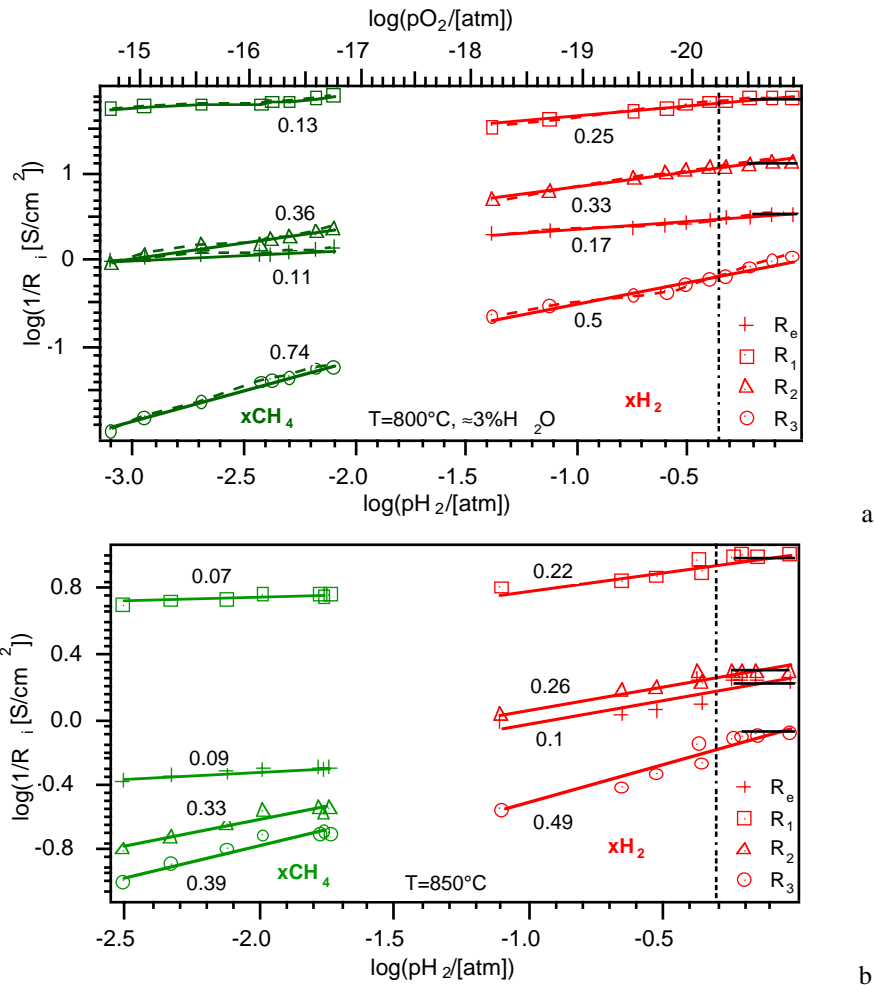


Figure 32: Summary of the influences of the gas composition on the different resistances defined by the used equivalent circuit. a. case of CeNbO, b. case of CeNbO + 1%Ni symmetrical cells. The vertical dashed lines represent the slope changes in the diagrams.

These are simplified schemes as none of the adsorbed or intermediate species are known. This is only a trial to rationalize the impedance response as observed in both the symmetrical and the non-sealed configurations. The reaction order towards H₂ predicted from equation (12) is not fully respected in the experimental results, but such situations often occur in catalysis when a change in the degree of coverage modifies the apparent orders and the activation energy of the reaction²⁰. To be able to analyze the effect of coverage on the reaction, further analysis should be made in order to complete the cross influence of variables (changing H₂ concentration under different H₂O concentrations and so on, effect of the oxygen activity, the analysis of the current curves towards the gas composition at fixed potentials ...²¹). Such a mechanism implies that the reaction can also take place on the oxide anode which has a relatively high ionic conductivity, and that the reaction is not necessarily limited to the triple phase boundary. Such an approach is also based on the observation that the reduction of ceria was sluggish by *TPR* (Chapter 10, Figure 1), at least when compared with LaCrO₃-based materials (Chapter 6, Figure 3), as the bulk reduction started 300°C higher than for LCs. Also, as discussed in Chapter 10, H₂O is not expected to have an inhibiting effect on ceria as it does not seem to adhere well when compared to La₂O₃ for example²². So the desorption of H₂O is not expected to be relevant here (equation (15)). The similar reaction order of H₂O and H₂ might stem from the *OH* reaction product as H₂O chemisorption could lead to this species through the reverse of reactions (15) and (14). By increasing H₂O partial pressure, this species coverage increases and thus influences reactions (12) and (13) or (18) and (19).

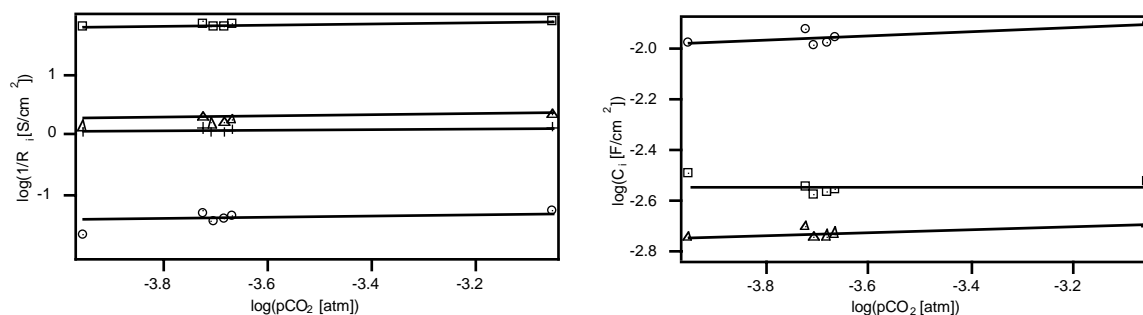


Figure 33: Evolution of the equivalent circuit elements as a function of CO₂ partial pressure generated by the reaction of CH₄ with water over the anode at 800°C. This graph is a redrawing of Figure 27e.

The reaction orders in CH₄ were found to depend more on hydrogen than on CH₄ itself (Table 5). From Figure 24c one can see the linearity existing between CH₄ and H₂ in the symmetrical cell configuration running at OCV. H₂ was produced by the catalytic reaction of CH₄ with H₂O over the CeNbO anode in a similar manner to the catalytic reaction initiated over CeNbO powders (Chapter 10). CH₄ conversion was as expected from the catalytic runs and the reaction rates observed were similar in both cases (see Figure 24a). Even the measured OCV (Figure 24f) matched well with the expected OCV calculated on the basis of H₂/H₂O equilibrium (see Chapter 6). All this indicates that H₂ was primarily responsible of the reaction near the OCV condition at least. One has to see that the presented reaction orders in CH₄ (Table 5) were made near OCV, i.e. in the catalytic regime where H₂ is produced by steam-reforming. The measured rate of CH₄ electrocatalytic reaction was by far lower than that of H₂ (Figure 3b and d). However, the very similar activation energies obtained in both H₂ and CH₄ in the presence of the catalytic Pt-meshes (Table 2) indicates similarity in the reaction mechanism. Also, as previously observed one can simulate the *I/V* curves of a CH₄ run cell by taking a diluted H₂/Ar gas mixture (Figure 14a and b) simulating a low CH₄ conversion. At OCV at least, H₂ production is thought to determine the reaction orders as presented by Table 5. The differences in the activation energies between H₂ and CH₄ in the symmetric configuration (Table 4) indicate clearly that the reacting species stem from CH₄ rather than directly from the locally produced H₂. The reaction of the hydrogen species could follow the same scheme as presented in equations (12) to (20). For a clearer insight of the reaction with CH₄ more measurements are needed such as the study of the evolution of the reaction orders with the anode overpotential, or the analysis of the effect of the reaction product on the reaction or a cross variation of the

different gas species (e.g. variation of the CH₄ partial pressure at different H₂O partial pressures, ...). Such analysis could give a better idea of the evolution of reaction and its activation energy with the coverage of the different species. At OCV again, plotting the different resistances as a function of the CO₂ partial pressure showed no influence of this product gas on the reaction (Figure 33). CO₂ is not expected to inhibit the reaction as discussed in Chapter 10. The addition of Ni to the anode did not modify the reaction orders as the reaction steps were still similarly sensitive to H₂. Ni was more effective in reducing the activation energy, most probably by activating H₂ and CH₄ dissociation over the anode. CeO₂-based materials are known to be poor H₂ and CH₄ catalysts²³. This explains the effect of catalysts such as Ni or Cu (see for example Figure 14) on the activation of the reaction. So globally, at OCV at least, CeNbO behaves similarly to LaCrO₃-based anodes in the sense that H₂ originating from the steam-reforming of CH₄ is responsible for the OCV response.

The identification of the equivalent circuit of the modified ‘*Gerischer impedance*’ to a physical process is not always straightforward¹⁶. The R_2 of Figure 18 is expected to be the charge transfer resistance of the electroadsorption step. It should thus decrease with increasing overpotential which is obviously not observed in the experiments (Figure 21a). This might stem from the decrease in oxygen conductivity due to the reoxidation of CeNbO which transforms it to a merely electronic conductor (the ionic transference number is of about 5×10^{-4} , see Chapter 9, Table 2). $-R_3$ was observed to decrease. It should indicate an electrocatalytic effect of the adsorbate as an increase of the overpotential should result in a larger amount of oxygen ions on the surface of the anode. Due to the affinity of H₂ to oxygen, its adsorption could be enhanced and thus the polarization resistance should decrease. However, here again, as the overpotential increases, the ionic conductivity of the anode drops, canceling the beneficial effect of polarization. Thus, an increase of the ionic conductivity of the anode, either by using a composite with YSZ, or by modifying its composition (e.g. Y instead of Nb as dopant thus increasing its ionic conductivity) could be appropriate. C_2 and $-C_3$ did not change much.

By considering the simple model given by equations (12) to (20), the finite diffusion impedance could be attributed to many diffusion species, either in the bulk of the anode (i.e. protonic conduction, ionic conduction, electronic conduction) or on its surface (i.e. hydrogen, hydroxyl groups or possibly some oxygen species diffusion) or gas phase diffusion. We will try to discuss these possibilities hereafter.

For the bulk diffusion in ceria, it is possible to make some assumptions on the results obtained from the analysis of the non-uniform diffusion impedance. As the conductivity of a species s in ceria can be written as

$$\sigma_s = \frac{D_s C_s n_s^2 F^2}{RT} \quad (21)$$

it can be rewritten to be inserted in equation (6) by using equation (7) as

$$\sigma = \frac{L}{\sigma_s \delta A} \quad (22)$$

with σ the fitting parameter (Equation (6)). This would allow to calculate the conductivity of the diffusing species from the deconvolution of the impedance data by giving an estimate for D_s .

Protonic conduction in ceria has been reported by several research groups²⁴⁻²⁷. Nigara et al.^{25, 26} pointed out to a protonic conductivity of about 10^{-5} S/cm or 2×10^{-6} S/cm at 850°C for CeO₂ and Ce_{0.8}Yb_{0.2}O_{1.9}, respectively with activation energies of 28.9~55.9 kJ/mol at temperatures lower than 1000°C or 67.5~106.0 kJ/mol above 1000°C as measured by permeability methods. Sakai et al.²⁴ indicated a hydrogen solubility of 10^{-2} mol of H /mol oxide, in other words 0.04 atoms of H per lattice unit of ceria doped with Yb, and showed that this solubility increases when the lattice distortion of ceria decreases. Doping with low amounts of Nb is expected to lead to a low distortion of the lattice parameter as shown in Chapter 9, Figure 2. Measurements made by Larring and Norby²⁸ on rare earth oxides also showed protonic conductivities ranging from $3.6\text{--}6.3 \times 10^{-6}$ S/cm to $5.6 \times 10^{-4}\text{--}3.2 \times 10^{-5}$ S/cm at 850°C for Er_{1.98}Ca_{0.02}O₃ and Gd_{1.98}Ca_{0.02}O₃ respectively, the highest values being in humid atmospheres. So we could expect for ceria solution a value going from 5×10^{-4} to 10^{-6} S/cm for protonic conduction. To the best of our knowledge no value for the diffusion coefficient of protons is

available in the literature for ceria. We rely on values given by Matsumoto et al.²⁹ for SrCe_{0.95}Yb_{0.05}O_{3-δ} for the mobilities (u_H) of protons at 900°C (2×10^{-4} cm²/sV). From

$$u_s = nF \frac{D_s}{RT} \quad (23)$$

a value of 3×10^{-9} m²/s can be estimated for D_s . By taking a value of 10^{-9} m²/s the evolution of the diffusion length, the concentration and the conductivity of the proton are presented in Figure 34. By taking a value of 10^{-10} m²/s, the diffusion length is divided, the concentration and conductivity multiplied by $\sqrt{10}$. A value of 10^{-9} m²/s gives a better agreement with the expected concentration of protons in ceria (i.e. 0.04 atoms/lattice unit²⁴). The conductivities are however too high, about 6×10^{-3} S/cm compared to the highest estimate of 10^{-4} S/cm. However, this could be due to the very low oxygen and to the high hydrogen partial pressures. The diffusion length almost corresponds to the electrode thickness representing thus large distances. This is consistent with the dense structure of the electrodes studied here (B40 and D1, see Figure 4). These calculations would lead to a limiting current, taken as

$$i_l = \frac{nD_s A F C_s}{L} \quad (24)$$

of 0.7 A/cm² at 200 mV cell voltage. The last value is about 3 times the one observed at short circuit when using thick electrodes (Case of D1, see Figure 6). Using a diffusion coefficient of 10^{-10} m²/s leads to current densities $\sqrt{10}$ lower. The activation energies obtained in H₂ and CH₄ for these conductivities are of 89.6 and 153.5 kJ/mol respectively and were calculated without taking into account any activation energy for the diffusivity (i.e. $D_H = \text{const}$ with T). These values are higher than reported (29-106 kJ/mol^{25,26}). The difference between H₂ and CH₄ could be due to one in oxygen partial pressure. Also, one can expect that upon polarization the protonic conduction decreases due to the local increase in oxygen activity leading to a lower ionic and electronic conductivity. Protonic conduction is tempting as it explains the reaction orders of the diffusion impedance toward H₂ and H₂O (about 0.5, see Table 5). Indeed protonic conductivity is thought to stem from H₂ or H₂O insertion in the lattice following the reactions^{29,30}



Equation (25) and (26) lead to a dependency in $\sqrt{H_2O}$, whereas equation (27) follows $\sqrt{H_2}$, hence the observed dependencies. The effects of H₂ and H₂O on the same parameters are shown in Figure 35. The higher the H₂ concentration the higher the proton conductivity and thus the diffusion length drops (Figure 35a). With H₂O, the fact that the oxygen partial pressure increases leads to a lowering of the conductivity (Figure 35b). However, these conductivities are too high.

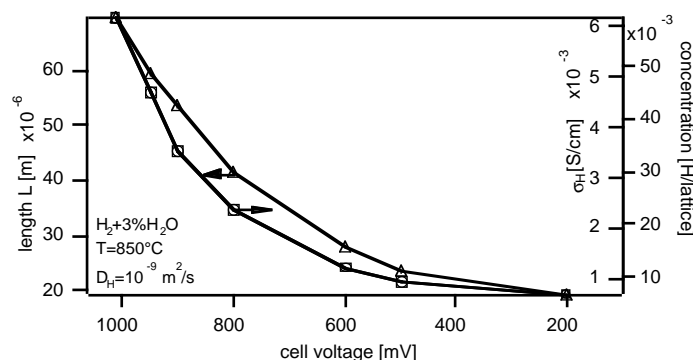


Figure 34: Evolution of the diffusion length (L), the concentration and conductivity of proton estimated from the deconvolution of the impedance data. The data are for H₂ at 850°C and the proton diffusivity is taken as 10^{-9} m²/s. (Case of D1).

The possibility of ionic diffusion limitation inside the bulk of the anode will be considered hereafter. Oxygen self-diffusion coefficients, D_o , (that is in oxygen rich atmospheres) in ceria-based compounds vary between 10^{-7} cm²/s for Ce_{0.8}Y_{0.2}O_{2-δ}³¹ at 700°C, 2.7×10^{-7} cm²/s for Ce_{0.9}Gd_{0.1}O_{2-δ}³² at 850°C, and even lower for Ce_{0.985}Nb_{0.015}O_{2-δ} with a value of 2×10^{-11} cm²/s at 800°C³³. Activation energies vary a lot and spread from 57 kJ/mol to 127 kJ/mol³³. For the ionic conductivity, the vacancy diffusion coefficient is needed and it is defined as

$$D_v = \frac{2 - \delta}{\delta} D_o \quad (28)$$

For CeNbO, the non-stoichiometry, δ , in reducing atmospheres is of 0.15 as measured by TPR (see Chapter 9) so that the vacancy diffusion coefficient is about 12 times higher than the oxygen self-diffusion coefficient, i.e. the values will spread from 3.3×10^{-6} to 2.5×10^{-10} cm²/s. The ionic conductivity depends thus much on the non-stoichiometry, i.e. on the oxygen partial pressure. Here, the two extremes are considered (10^{-6} and 10^{-10} cm²/s).

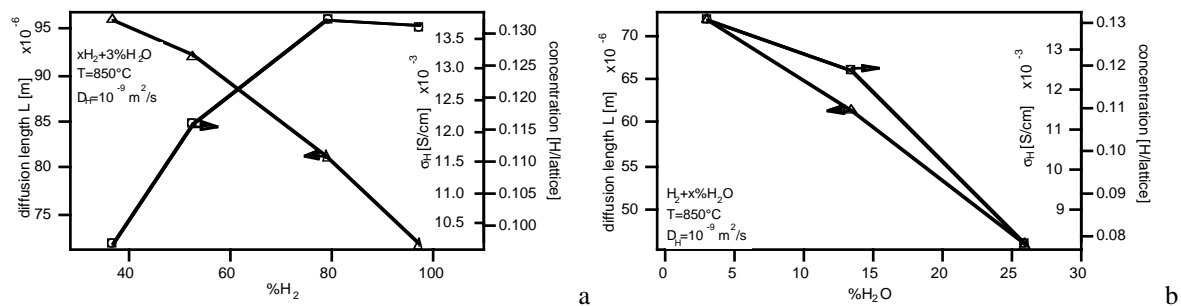


Figure 35: Evolution of the diffusion length (L), the concentration and conduction of protons estimated from the deconvolution of the impedance data. The data are for H₂ at 850°C and the proton diffusivity is taken as 10^{-9} m²/s. (Case of B40).

The results for the highest diffusivity (10^{-6} cm²/s) is shown in Figure 36. The general trends are similar to that for proton conduction. However, all the parameters here seem to match the observed values. The ionic conductivity is of 1.9×10^{-3} S/cm at OCV which is very near to that of ceria (see Chapter 9, Table 2) and drops to 2×10^{-4} at 200 mV cell voltage as expected for CeNbO in its oxidized form ($t_i \approx 5 \times 10^{-4}$ ³³). The oxygen vacancy concentration is also as expected (if $\delta \approx 0.15$ than a max of $0.6 V_o^{\bullet\bullet}$ / lattice is expected). The diffusion length is also nearer to the anode effective thickness (about 20 μ m) and its evolution could be understood in the sense of a lowered ionic conductivity. Also, the limiting current calculated is of 0.21 A/cm², very near to the one observed on the same sample (Case D1, Figure 6, ≈ 0.21 V). Moreover, the activation energy measured for $1/\delta^2$ (Table 2, 47 kJ/mol) which corresponds to that of D_v , for both CH₄ and H₂ matches the literature values (57 to 127 kJ/mol).

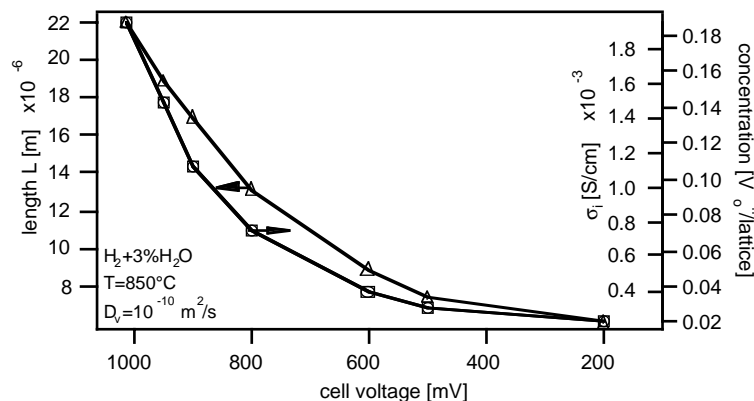


Figure 36: Evolution of the diffusion length (L), the concentration and conductivity of oxygen vacancies estimated from the deconvolution of the impedance data. The data are for H₂ at 850°C and the oxygen vacancies diffusivity is taken as 10^{-10} m²/s. (Case of D1).

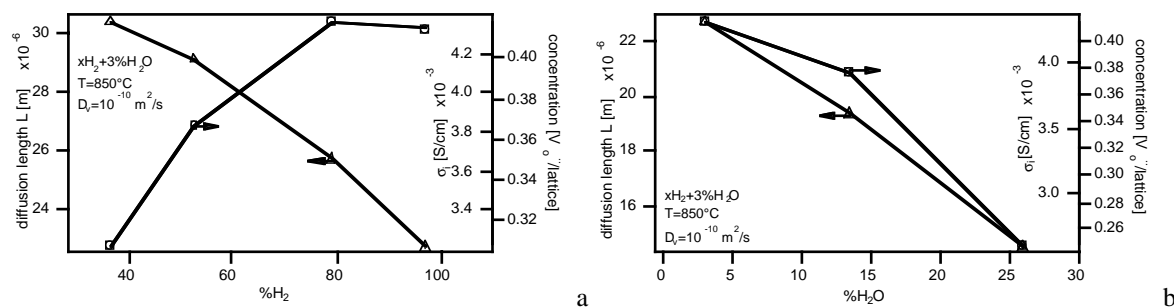


Figure 37: Evolution of the diffusion length (L), the concentration and conductivity of oxygen vacancies estimated from the deconvolution of the impedance data. The data are for H₂ at 850°C and the oxygen vacancy diffusivity is taken as 10⁻¹⁰ m²/s. (Case of B40).

The effects of H₂ and H₂O on the same parameters are shown in Figure 37. The higher the H₂ concentration the higher the ionic conductivity due to the reduction of ceria and the creation of oxygen vacancies and thus the diffusion length drops (Figure 37a). With H₂O, the fact that the oxygen partial pressure increases leads to a lowering of the conductivity (Figure 35b). Globally these values fit the expected tendencies of the ionic conductivity. If this is the limiting step for diffusion, this could mean that the surface exchange reactions are very slow, something expected from the high reducing temperature observed for ceria-based powders (Chapter 10). The reaction orders for H₂ and H₂O could stem from the effect of the surface exchange reaction dealing with adsorbed H₂ and H₂O species. However, water's reaction order cannot be easily rationalized. Perhaps hydroxyl groups enhance H₂ and CH₄ chemisorption on ceria. One way to reduce the diffusion effect is to produce an anode with a fine porosity and to add a catalyst. The addition of YSZ as for LaCrO₃-based anodes would increase the ionic conductivity of the anode and thus its performance. Better performances have been partly achieved when the anode was made more porous and fine by using a printing screen allowing the deposition of fine powders (case of B62 and E7h). Finally, in these calculation one has assumed that D_v is constant with polarization, but from its definition (equation (28)) it is expected to change with the variation of the oxygen partial pressure. This should modify the diffusion length evolution.

If smaller values for D_v are taken into consideration (down to 10⁻¹⁰ instead of 10⁻⁶ cm²/s), the direct correlation with the experiments does not hold any more. The length of diffusion, the conductivity and the limiting current are divided, and the concentration multiplied by a factor of up to 100.

If one considers gas phase H₂ diffusion, one gets diffusion lengths of about 20 cm when using the impedance generated data. No limiting current would be expected. H₂O local production on the anode should not be responsible for the diffusion process as its increasing partial pressure should have a negative effect on the diffusion resistance whereas the reaction order towards H₂O is positive (Table 5). Gas conversion impedance should also be excluded for both effects of H₂O and the very high activation energy observed do not fit this impedance. Also, electronic conductivity is unlikely to explain the diffusion impedance as it is the major component of the conductivity in CeNbO. From Naik and Tien³⁴ and Tuller and Nowick³⁵ the mobility of electrons is of 1.99×10⁻² to 2.2×10⁻³ cm²/Vs which leads to a diffusivity of about 1.9×10⁻⁷ to 2.1×10⁻⁸ m²/s (equation (23)). This value is too high and does not fit the experimental data.

A last possibility for the diffusion limitation might stem from the surface diffusion of reacting species. For this purpose, equations (6), (10), (21) and (22) should be modified as follows

$$\sigma = \frac{RT}{n^2 F^2 l C_{sur} \sqrt{D_{sur}}} = \frac{RT \delta}{n^2 F^2 l C_{sur} L} \quad (29)$$

$$C_{sur} = \left(\frac{RT \delta}{n^2 F^2 l L \sigma} \right) \quad (30)$$

$$\sigma_{sur} = \frac{D_{sur} C_{sur} n^2 F^2}{RTd} \quad (31)$$

$$\sigma = \frac{L}{\sigma_{sur} l d \delta} \quad (32)$$

where l represents the triple phase boundary length (*TPBL*), d the thickness of the conduction layer on the anode grains, and the subscript ‘*sur*’ associated with the surface diffusing species. In this case the limiting current would be given by

$$i_{l,sur} = \frac{nFD_{sur} C_{sur} l}{L} \quad (33)$$

From SEM observation (Figure 4), the anode grains for the rough structures have a mean diameter of 2.5 μm and are spaced by 0.5 μm . The number of grains attached to YSZ is calculated by supposing cubic grains of 2.5x2.5 μm^2 area and 2.5x4 μm of perimeter, giving thus 4.4x10⁷ grains/cm², or a *TPBL* of 111 m/cm². The thickness of the conduction layer can be taken as 1 nm³⁶. Skaarup et al.³⁷ showed that, over Ni at least, the surface coverage θ_H was relatively high at 850°C, reaching 0.36 at a H₂ partial pressure of 1 atm. This seems to be the case even though no intermediates were found over metal electrodes by cyclic voltammetry³⁸. Over oxides, as discussed previously in Chapter 10, *FTIR* did not allow the detection of any hydroxyl species at very high temperature, thus indicating that the life time of such species is very short and undetectable by such techniques. So for simplification, a surface coverage with hydrogen species of 0.3 will be considered. This gives 0.6 sites / lattice, or 3.41x10⁻⁶ mol/m². Data on the diffusion of hydrogen or hydroxyl groups over ceria were not found. However, a recent paper of Raz et al.³⁶ discussed the hydroxyl conduction on the surface of YSZ from room temperature to 450°C. For our purpose, these results will be implemented here for ceria in order to analyze the possibility of surface diffusion of hydrogen or hydroxyl groups. Raz et al.³⁶ measured chemisorption enthalpies for water of 70 and 94 kJ/mol over YSZ. These two enthalpies correspond to two different sites of adsorption, namely Y and Zr sites (Holtappels et al.³⁹ give a diffusion activation enthalpy of 120 to 160 kJ/mol). Following their discussion, hydrogen would have an equal or even higher chemisorption enthalpy. The activation energy for ionic conduction in the temperature range of 150°C-450°C in the almost completely chemisorbed water layer was of 29 kJ/mol. This activation energy is somewhat smaller than the one measured from $1/\delta^2$ (47 kJ/mol). At 450°C, they measured a surface protonic conductivity of 1.25x10⁻³ S/cm. As with temperature the mobility of the protons increases but their coverage decreases (let us suppose from 1 to 0.3), the extent of conduction is not very clear. One can extrapolate that the conductivity increases or decreases by 2 orders of magnitudes. From equation (21) and the above discussion using equation (29) to (33), estimates for the diffusion coefficient could be advanced. These thus vary from 3.7x10⁻¹³ to 3.7x10⁻⁸ m²/s. For example, surface diffusion of Ni over Ni is of 6.5x10⁻¹¹ m²/s, that of H over Ni of 5.2x10⁻⁸ m²/s at 850°C³⁷ and that of O over Pt of 5.5x10⁻¹¹ m²/s at 800°C⁴⁰. The values derived for surface protonic diffusivity would give too high surface concentration of adsorbed species (at least a θ of 0.5 or higher than 1), and too low limiting currents (8 mA/cm² with the calculated L). Symmetrically, surface conduction of protons over the YSZ would not be an interesting explanation neither.

Thus, the limiting current observed due to the diffusion limited process could be best explained by an ionic conduction inside the CeNbO anode. This limiting process can be overcome by making a fine anode structure (small grains) and by using a more ionically conducting matrix either by using a composite with YSZ or another ionically conducting ceria like Ce(Y, Pr, Gd, Sm)O or by using another dopant which could promote both the ionic and the electronic conduction like Pr (see Chapter 9, Table 2). The promotion of CH₄ and H₂ oxidation could be implemented by the addition of carbon resistant catalysts such as Cu or Cu-Ni alloys (see Chapter 10). A first trial in that direction was presented in Figure 14 with a porous CeGdO+17%Cu anode, where in spite of the high ohmic resistance of the CeGdO thick pellet (770 μm) a power output of 200 mW/cm² or 80 mW/cm² in H₂ and CH₄ respectively could be

achieved. Due to the electrolyte thickness, about 700 mA/cm² were lost at least for the case of H₂ oxidation.

The effect of this diffusion impedance is similar to Adler's model on mixed conducting electrodes^{41,42} (see Chapter 8). It is possible to calculate the diffusion polarization losses using Adler's model and compare it with the above mentioned results. For that purpose, we take a mean value of 10⁻⁷ cm/s for the surface exchange coefficient (κ) from Carter et al.³³, a value obtained at high oxygen partial pressure. It is possible to derive a value of κ of 10⁻⁶ cm/s in wet H₂ by assuming the same dependency to P_{O_2} as measured by Horita et al.³¹ (i.e. $\log(\kappa_{H_2}) = \log(\kappa_{O_2}) - \frac{1}{20} \log(p_{O_2})$). The evolution of D_v with the oxygen partial pressure can also be taken into account by using equation (28). The results are summarized in Table 8 and indicate a similar increase of the real impedance resistance as shown in Figure 21d. This would mean that the reaction spreads away from the TPB as would be expected for mixed ionic-electronic conductors. However, the anode reaction length increases here. It should be noted that the effect of the non-stoichiometry was taken into account for these calculations, whereas it was neglected when using the deconvoluted data of Z_{NUD} .

Table 8: Effect of κ and D_o on a presumed chemical diffusion impedance, at 850°C.

Parameters	values	calculated values	wet H ₂	air
τ	1	D_v [cm ² /s]	1.2x10 ⁻⁷	3.9x10 ⁻⁷
ϵ	0.3	c_v [mol/cm ³]	0.006	0.002
a [cm ² /cm ³]	10000	c_{mc} [mol/cm ³]	0.077	0.081
κ_{H_2}	1x10 ⁻⁶	δ [μm]	8.4	26.4
κ_{air}	1x10 ⁻⁷	R_{chem} [Ωcm ²]	0.77	2.32
D_o [cm ² /s]	1x10 ⁻⁸	L_c [cm]	1x10 ⁻²	1x10 ⁻¹

Table 9: Effect of temperature on the chemical impedance.

T [°C]	D_o [cm ² /s]	κ_{H_2} [cm/s]	κ_{air} [cm/s]	R_{chem, H_2} [Ωcm ²]	δ [μm]	E_a [kJ/mol]	$R_{chem, air}$ [Ωcm ²]	δ [μm]	E_a [kJ/mol]
950	1.5x10 ⁻⁸	4.7x10 ⁻⁶	4.710 ⁻⁷	0.29	4.8	110.3	0.93	15.2	103.7
850	1.0x10 ⁻⁸	1.0x10 ⁻⁶	1.0x10 ⁻⁷	0.77	8.4		2.32	26.4	
800	7.8x10 ⁻⁹	4.1x10 ⁻⁷	4.1x10 ⁻⁸	1.29	11.5		3.89	36.2	

The same parameters as in Table 8 were used in these calculations.

The evolution with temperature is given in Table 9, using the temperature dependence given for D_o and κ by Carter et al.³³ (50 and 176 kJ/mol respectively). The temperature dependence of $1/R_{chem}$ is of 110 kJ/mol, a value similar to that derived in our system (see Table 2 and 4: 103 (Pt-mesh) to 149 kJ/mol (Ni catalyst) in H₂). Following this model, it is predicted that the losses will decrease the higher the surface area of the anode, as δ and R_{chem} are a function of \sqrt{a} (see Chapter 8), where a is the surface area. This would explain the effect of the finer structure of the anode on lowering the anode polarization losses. Also, the effect of a catalyst dispersed over the ceria-based anode would be to increase the surface exchange coefficient and thus to lower the polarization losses. These positive effects were clearly observed in this study (see for example Figure 9 and Figure 14 as well as Table 4). This also shows that the activation of the gas species (CH₄ but also H₂) is very important in achieving better performances. Finally, the linear increase of the current with the overpotential, at low and intermediate values (e.g. Figure 9b) could be related to this dominating loss.

Literature survey on ceria-based anodes

In literature ceria has been used for different purposes, mainly as an additive for the Ni-cermet anode and in most of the cases it was tested in H₂ or reformed gases. Globally, CeO₂-

based anodes can be grouped into three types: (i) doped ceria anodes without any metal component⁴³⁻⁴⁹; (ii) doped ceria anodes with highly dispersed metal catalysts⁴³⁻⁴⁸; and (iii) Ni and doped (or undoped) ceria cermet anodes⁵⁰. The anodes were based on CeGdO or CeSmO. The performances varied a lot and the best ones were reported by Uchida and Watanabe⁴³⁻⁴⁷ whereas Putna et al.⁴⁸ presented the lowest values (6 mW/cm² at 800°C). Uchida and Watanabe reported overpotential values in H₂ at 900°C of about 175 mV for 400 mA/cm², for the unloaded CeSmO, a value slightly worse than that obtained here for CeNbO (150 mV at 400 mA/cm² in CH₄ using Pt-mesh (see Figure 9b)). The performance was increased upon loading with Ru (50 mV, 400 mA/cm², 900°C, H₂). No measurements were made in CH₄ and no long-term stability operation tests were presented by Uchida and Watanabe. The performances of our cells are thus comparable even under CH₄ fuel conditions. Metal loading, as discussed above, would enhance the surface reaction kinetics and promote the reaction. Ru loading presented by Watanabe and Uchida go in that direction. However, there is a need to apply a carbon resistant catalyst such as Cu or Cu-Ni as discussed in Chapter 10.

Marina et al.⁵¹ worked with CH₄ at 1000°C over a Ce_{0.6}Gd_{0.4}O_{1.8} anode and reported similar values of 500 mW/cm² in H₂ and 80 mW/cm² in CH₄ when using Pt-meshes. They reported similarly lower values in CH₄ when using Au-meshes⁴⁹.

Conclusion

This study demonstrated again that oxide-based anodes can be used instead of the conventional Ni-cermet anodes for H₂ oxidation. CeO₂ doped with Nb or Gd has shown, as for the case of LaCrO₃-based materials, an ability to oxidize CH₄ directly without prior fuel processing (steam or carbon dioxide reforming or partial oxidation). These anodes were very resistant toward carbon deposition in very rich CH₄ fuels (97% CH₄ + 3% H₂O). However, CH₄ activation was observed to be low as steam-reforming and direct oxidation were slow. The addition of a stable catalyst is required in order to activate CH₄. One candidate is Cu or Cu-Ni alloy, or even another oxide catalyst like Ni-substituted LaCrO₃.

On the studied electrodes, inductive loops were observed along with a diffusion-like limitation, by impedance spectroscopy. Analysis of the data pointed to a mechanism where a hydrogen species is chemisorbed undergoing an electrochemical reaction (a so-called Gerischer impedance) and where the ceria lattice oxygens diffuse to the active sites to supply them with active oxygen species. The diffusion of oxide ions more than any other species (protons, electrons or surface species) is thought to be responsible of the observed limiting currents. These results point to the necessity of making fine powder ceria anodes and to the necessity of adding a catalyst that is able to promote the surface reaction kinetics involving most probably the chemisorption of H₂ or CH₄. Trials were made with fine anode structures and with catalyst addition and the promising results obtained supported these interpretations.

Furthermore, a direct influence of hydrogen on the electrochemical reaction of CH₄ showed that, at OCV conditions at least, the reaction was governed by H₂-H₂O equilibration. CH₄ oxidation was easily catalyzed by the presence of Pt-mesh current collectors or by the addition of a small percentage of Ni or Cu. The *I/V* curves bent rapidly upon polarization indicating a limiting process, most probably due to the lack of active *H* species. As with LaCrO₃-based anodes, the electrochemical oxidation of H₂ is faster than that of CH₄. Kinetic data were presented in this study in a trial to better understand the electrochemical reaction in H₂ as well as in CH₄.

These results and those presented for LaCrO₃-based anodes show that optimizations are still possible. Poor catalysts for CH₄ oxidation can be modified in an appropriate manner to make them interesting candidates for direct CH₄ oxidation, knowing that the state of the art Ni-cermet anodes cannot withstand, in their actual formulation, direct CH₄ feed without a prior fuel processing step. In hydrogen a power density of 430-400 mW/cm² and a short circuit current of 1750-1700 mA/cm² was observed at 800-900°C. In CH₄, depending on the nature of the current collector, the performance varied between 350 mW/cm² (short circuit current of 1050 mA/cm²) when Pt-mesh was used, and 100 mW/cm² (short circuit current of 420 mA/cm²) with Au-electroplated Pt-mesh, at 900°C. The CeNbO anodes sustained well thermal cycling as well as redox cycling (H₂ ↔ air) without degradation.

References

- (1) Macdonald, J. R. *Impedance Spectroscopy. Emphasizing Solid Materials and Systems*; John Wiley & Sons, **1987**.
- (2) Gödickemeier, M., Ph.D. thesis Nr. 11348, Swiss Federal Institute of Technology Zürich, Switzerland, **1996**.
- (3) Macdonald, D. D.; Sikora, E.; Engelhardt, G., *Electrochimica Acta* **1998**, *43*, 87-107.
- (4) Sluyters-Rehbach, M.; Sluyters, J. H. A. C. *techniques*; Plenum Press.
- (5) Gabrielli, C. "Identification of electrochemical processes by frequency response analysis," Solartron Instruments, Schlumberger, **1984**.
- (6) Gharbage, B.; Pagnier, T.; Hammou, A., *J. Electrochem. Soc.* **1994**, *141*, 2118-2121.
- (7) Wippermann, K.; Stimming, U.; Jansen, H.; Stöver, D. The Third International Symposium on Solid Oxide Fuel Cell, Honolulu, Hawaii, **1993**; p 180-189.
- (8) Schouler, E. L.; Kleitz, M., *J. Electrochem. Soc.* **1987**, *134*, 1045-1050.
- (9) Hassel, B. A. v.; Boukamp, B. A.; Burggraaf, A. J., *Solid State Ionics* **1991**, *48*, 139-154.
- (10) Hassel, B. A. v.; Boukamp, B. A.; Burggraaf, A. J., *Solid State Ionics* **1991**, *48*, 155-171.
- (11) Hassel, B. A. v.; Boukamp, B. A.; Burggraaf, A. J., *Solid State Ionics* **1992**, *51*, 161-174.
- (12) Hammouche, A., Institut National Polytechnique de Grenoble, 1989.
- (13) Boukamp, B. A., *Solid State Ionics* **2001**, *143*, 47-55.
- (14) Fleig, J.; Jamnik, J.; Maier, J., *J. Electrochem. Soc.* **1996**, *143*, 3636-3641.
- (15) Armstrong, R. D.; Henderson, M., *Electoanalytical Chemistry and Interfacial Electrochemistry* **1972**, *39*, 81-90.
- (16) Harrington, D. A.; Conway, B. E., *Electrochimica Acta* **1987**, *12*, 1703-1712.
- (17) Otsuka, K.; Wang, Y.; Sunada, E.; Yamanaka, I., *Journal of Catalysis* **1998**, *175*, 152-160.
- (18) Westley, F.; Herron, J. T.; Cvetanovic, R. J. *Compilation of Chemical Kinetic Data for Combustion Chemistry. Part 1. Non-Aromatic C, H, O, N and S Containing Compounds. (1971-1982)*; U.S. Department of Commerce, National Bureau of Standards, **1987**.
- (19) Leach, H. F.; Mirodatos, C.; Whan, D. A., *Journal of Catalysis* **1980**, *63*, 138-151.
- (20) Frennet, A.; Liénard, G.; Crucq, A.; Degols, L., *Journal of Catalysis* **1978**, *53*, 150-163.
- (21) Bockris, J. O. M.; Reddy, A. K. N. *Modern Electrochemistry*, 3 ed.; Plenum/Rosetta, **1977**.
- (22) Hewett, K. B.; Anderson, L. C.; Rosynek, M. P.; Lunsford, J. H., *J. Am. Chem. Soc.* **1996**, *118*, 6992-6997.
- (23) Trovarelli, A., *Catal. Rev. -Sci. Eng.* **1996**, *38*, 439-520.
- (24) Sakai, N.; Yamaji, K.; Horita, T.; Yokokawa, H.; Hirata, Y.; Sameshima, S.; Nigara, Y.; Mizusaki, J., *Solid State Ionics* **1999**, *125*, 325-331.
- (25) Nigara, Y.; Kawamura, K.; Kawada, T.; Mizusaki, J., *Solid State Ionics* **2000**, *136-137*, 215-221.
- (26) Nigara, Y.; Kawamura, K.; Kawada, T.; Mizusaki, J.; Ishigame, M., *J. Electrochem. Soc.* **1999**, *146*, 2948-2953.
- (27) Nigara, Y.; Mizusaki, J.; Kawamura, K.; Kawada, T.; Ishigame, M., *Solid State Ionics* **1998**, *113-115*, 347-354.
- (28) Larring, Y.; Norby, T., *Solid State Ionics* **1995**, *77*, 147-151.
- (29) Matsumoto, H.; Asakura, F.; Takeuchi, K.; Iwahara, H., *Solid State Ionics* **2000**, *129*, 209-218.
- (30) Steinsvik, S.; Larring, Y.; Norby, T., *Solid State Ionics* **2001**, *143*, 103-116.
- (31) Horita, T.; Yamaji, K.; Sakai, N.; Ishikawa, M.; Yokokawa, H.; Kawada, T.; Dokiya, M., *Electrochemical and Solid-State Letters* **1998**, *1*, 4-6.
- (32) Lane, J. A.; Kilner, J. A., *Solid State Ionics* **2000**, *136-137*, 927-932.
- (33) Carter, S.; Chater, R. J.; Kajda, J.; Liddicott, K. M.; Kilner, J. A.; Steele, B. C. H. Proceedings of the first international symposium on ionic and mixed conducting ceramics., **1989**; p 84-94.
- (34) Naik, I. K.; Tien, T. Y., *J. Phys. Chem. Solids* **1978**, *39*.
- (35) Tuller, H. T.; Nowick, A. S., *J. Phys. Chem. Solids* **1977**, *38*, 859-867.
- (36) Raz, S.; Sasaki, K.; Maier, J.; Riess, I., *143* **2001**.

- (37) Skaarup, S.; Zachau-Christiansen, B.; Jacobsen, T. High Temperature Electrochemistry: Ceramics and Metals, Risø National Laboratory, Roskilde, Denmark, **1996**; p 423-430.
- (38) Zachau-Christiansen, B.; Jacobsen, T.; Bay, L.; Skaarup, S., *Solid State Ionics* **1998**, *113-115*, 271-277.
- (39) Holtappels, P.; Vinke, I. C.; Haart, L. G. J. d.; Stimming, U., *J. Electrochem. Soc.* **1999**, *146*, 2976-2982.
- (40) Van herle, J., Ph.D. thesis Nr. 1187, Swiss Federal Institute of Technology Lausanne (EPFL), **1993**.
- (41) Adler, S. B., *Solid State Ionics* **1998**, *111*, 125-134.
- (42) Adler, S. B.; Lane, J. A.; Steele, B. C. H., *J. Electrochem. Soc.* **1996**, *143*, 3554-3564.
- (43) Uchida, H.; Mochizuki, N.; Watanabe, M., *J. Electrochem. Soc.* **1996**, *143*, 1700-1705.
- (44) Uchida, H.; Osuga, T.; Watanabe, M., *J. Electrochem. Soc.* **1999**, *146*, 1677-1682.
- (45) Uchida, H.; Suzuki, H.; Watanabe, M., *J. Electrochem. Soc.* **1998**, *145*, 615-620.
- (46) Watanabe, M.; Uchida, H.; Shibata, M.; Mochizuki, N.; Amikura, K., *J. Electrochem. Soc.* **1994**, *141*, 342-346.
- (47) Watanabe, M.; Uchida, H.; Yoshida, M., *J. Electrochem. Soc.* **1997**, *144*, 1739-1743.
- (48) Putna, E. S.; Stubenrauch, J.; Vohs, J. M.; Gorte, R. J., *Langmuir* **1995**, *11*, 4832-4837.
- (49) Marina, O. A.; Mogensen, M., *Applied Catalysis A: General* **1999**, *189*, 117-126.
- (50) Maric, R.; Ohara, S.; Fukui, T.; Inagaki, T.; Fujita, J., *Electrochemical and Solid-State Letters* **1998**, *1*.
- (51) Marina, O. A.; Bagger, C.; Primdahl, S.; Mogensen, M. Third European Solid oxide Fuel Cell Forum, Nantes, France, **1998**; p 427-436.

General conclusion

General conclusion

LaCrO₃ and CeO₂ and Cu/Ni-based catalysts were investigated for their potential use as anode materials in SOFC for the direct oxidation of CH₄ without prior external fuel processing. LaCrO₃ possesses a perovskite structure, easily substituted on the La A-site and Cr B-site with alkali earth and transition metal elements, allowing interesting modifications of their electronic as well as their catalytic properties. CeO₂ belongs to the family of fluorites and, like LaCrO₃, can be substituted by a wide range of other elements which allow equally the modification of its electronic and catalytic properties.

LaCrO₃-based anodes

22 different LaCrO₃ compositions were produced following a modified citrate route. Different substituents were used, mainly Mg, Ca, Mn, Fe, Co, Ni and Sr. Powders of 1 to 6 m²/g and 0.7 to 6 μm average size were obtained. In most cases, residual, unidentified peaks of low intensity (< 2%), not matching the usually admitted orthorhombic lattice structure were detected in the powder X-ray diffractogrammes. XRD-pure phases were obtained at calcination temperatures above 1100°C. Conductivity measurements made on some of these compositions sintered into bars at 1500°C showed the low conductivity of these materials in reducing conditions (0.2 to 6 S/cm in humidified H₂ versus 5 to 24 S/cm in air). A-site substituents gave rise to a higher conductivity than the B-site substituents.

The catalytic activity of LaCrO₃-based powders towards CH₄ was simulated using three different gas mixtures: 5:1 CH₄:O₂ for partial oxidation; 5:1:0.6 CH₄:O₂:CO₂ for mixed reforming in a recycling mode and 56:x:y CH₄:Ar:H₂O (x+y=44) for steam reforming. By substituting the inactive LaCrO₃ catalyst with alkaline earth and first series transition metal elements, a noticeable improvement in activity towards CH₄ conversion was achieved. Three different behavioural patterns were observed depending on the catalyst composition. It was observed that among the alkaline earth elements, Mg had an inhibiting effect whereas Ca and Sr substitution improved the catalytic activity for CH₄ oxidation, and CO₂ and H₂O reforming reactions. Transition metal substitution experiments on the B-site indicated that Co had an inhibiting effect whereas Mn and Fe showed an enhancement in activity when compared to the activity of the base material, LaCrO₃. The LaCrO₃ activity was however not drastically modified. On the other hand, Ni substitution caused a considerable change in the turn-over frequency (4 fold when compared to LaCrO₃). Among the transition metal substituents, Co and Mn showed the lowest cracking activity whereas Fe deposited high amounts of C as confirmed by TEM analysis. Thus, by suitable substitution of the stable but rather inactive LaCrO₃ catalyst with Ni, an improved catalyst for CH₄ oxidation, with low coking activity, was produced.

Furthermore, thermodynamic calculations, based on correlations developed in literature as well as experimental work, have been conducted in an attempt to analyze the stability of the LaCrO₃ system when doped with Mg, Ca, Sr, Mn, Fe, Co and Ni. Various gas atmospheres were simulated (air, humidified H₂, CO and CO₂). It was possible to correlate some of the experimental results (electrochemical, XRD, XPS-Augur, SIMS and TEM-EDS) with the thermodynamic calculations. It was found that on the A-site, Sr substitution is more favorable than Ca in reducing atmospheres. H₂O and H₂ are expected to corrode the perovskites, as the volatility of Ca, Sr and Cr are more pronounced due to the formation of hydroxy-species. Furthermore, the higher the substitution with Ca or Sr the larger the destabilization of the perovskite, both in air and in reducing atmospheres – LaCrO₃ seems to accommodate more Sr in reducing atmospheres. The secondary phases formed during the decomposition could react readily with YSZ at 800°C, as observed experimentally. Overall, the LaCrO₃ are thermodynamically quite reactive toward YSZ but this was not observed experimentally unless treated above 1100°C. Although Mg, Mn, Fe, Co and Ni, B-site substituted compounds, are thermodynamically unstable, they are quite stable experimentally suggesting that their decomposition is hindered kinetically. The A-site substitution seems to be more problematic. This difference in behavior might stem from a difference in the diffusion coefficient of the A and B-site cations. From this analysis, Sr seem to be more favorable than Ca and is thus a more convenient substituent in SOFC anodes, as its presence allows a higher electrical conductivity in the material.

Based on these results, the electrochemical properties of Ca, Sr, Mg, Co and Ni substituted LaCrO_3 anodes deposited on 150 μm thick 8YSZ electrolytes were compared under humidified H_2 and CH_4 . The nature of the substituent was observed to have an influence on the anodic ohmic and polarization resistances. Globally, the higher the conductivity, the better was the performance of the electrode. The catalytic activity of the electrode material was also observed to play a role in the electrochemical reaction. The polarization losses in humidified CH_4 were observed to decrease almost in the same trend as the increase in the catalytic activity, i.e. $\text{LaCrO}_3 \approx \text{LaCr}_{0.9}\text{Co}_{0.1}\text{O}_3 < \text{LaCr}_{0.9}\text{Ni}_{0.1}\text{O}_3 < \text{La}_{0.85}\text{Sr}_{0.15}\text{CrO}_3 < \text{La}_{0.85}\text{Sr}_{0.15}\text{Cr}_{0.9}\text{Ni}_{0.1}\text{O}_3$. A direct relationship between the electronic and catalytic activities and the electrocatalytic performance was evidenced. Also, the surface exchange coefficient might have an influence on the performance of the cell, as it was observed to decrease upon reduction of the electrode material.

LaCrO_3 -based anode performances were higher in H_2 than in CH_4 and in turn higher than in CO_2/CO . OCV measurements made on sealed cells were very sensitive to $\text{H}_2/\text{H}_2\text{O}$ equilibrium rather than to the whole gas composition produced after the partial steam-reforming reaction taking place on the surface of the electrodes. H_2 oxidation could be thought to mask CH_4 oxidation. Further, full oxidation did not seem to take place over $\text{La}_{0.85}\text{Ca}_{0.15}\text{Cr}_{0.9}\text{Mg}_{0.1}\text{O}_3$, at least at low current densities, in accordance with the catalytic measurements. On the contrary, CO_2 had an influence on the cell polarization, and as in the case of the catalytic reactions, this is thought to be related to the formation of surface carbonates.

From the impedance analyses, 2 limiting processes were identified. The first one might be related to charge transfer or to a chemical step (R_1 and C_1 did not depend much on the gas atmosphere and the polarization), while the second might stem from a chemical process dealing with H species. The latter process could be related to a chemical impedance taking into account the surface chemical exchange coefficient as well as the oxygen diffusion coefficient. In general, for both processes, the summit frequency tended to increase as the cell was polarized, showing an electrocatalyzed process. Further analyses based on polarization curves and impedance spectroscopy made in different gas atmospheres are needed to confirm these results.

The cells were observed to be more stable when the anodes were sintered at 1100°C. At higher sintering temperatures, some topotactic reactions were observed, linked with the formation of $(\text{Sr,Ca})\text{ZrO}_3$ at the interface with YSZ. At lower sintering temperatures, adhesion was insufficient. Further, the stability of the electrode was increased by intercalating a composite layer between the electrolyte and the electrode. The best performance was obtained with a layer of 78:22 wt% $\text{La}_{0.85}\text{Sr}_{0.15}\text{Cr}_{0.9}\text{Ni}_{0.1}\text{O}_3 + 8\text{YSZ}$ covered with 3 layers of $\text{La}_{0.85}\text{Sr}_{0.15}\text{Cr}_{0.9}\text{Ni}_{0.1}\text{O}_3$, with a power output of 450 mW/cm^2 in H_2 and 300 mW/cm^2 in CH_4 , at 875°C. The measured R_p in H_2 was of 0.11 Ωcm^2 . The performance of the electrode was sustained for 136 h in CH_4 . This work led to the deposition of an European patent. As pointed out in the catalytic and thermodynamic studies, Sr and Ni elements turned out to be the most favorable substituents among those analyzed for the electrocatalysis. Sr addition is required to enhance the electronic conductivity of the electrode. Sr is better than Ca from the thermodynamic point of view and also for achieving a lower expansion of the substituted LaCrO_3 under reducing conditions.

CeO₂-based anodes

14 different CeO_2 -based powders were prepared using three different techniques. Different dopants were studied: Y, Nb, Pr and Gd. Oxalate coprecipitation was implemented for Y, Pr and Gd doped ceria, all synthesized at 700°C/1h. Nb doped ceria was synthesized following a modified route, using Nb_2O_5 or NbCl_5 as precursors. Powders of 1 to 18 m^2/g were produced. Among all dopants studied, Nb enhanced most the CeO_2 densification. Nb was also observed to induce the highest electronic conductivity in ceria, both in air and in humidified H_2 . However, concomitant doping with Gd and Nb pointed to the negative effect of Nb on the total conductivity in air of Gd-doped ceria. Nevertheless, Nb induced a marked electronic conductivity in reducing conditions. Among all powders, $\text{Ce}_{0.992}\text{Nb}_{0.008}\text{O}_{2-\delta}$ adhered best on YSZ electrolyte sheets and withstood the reducing conditions. In that case, a sintering temperature of 1100°C/4h was necessary to make the electrode stick. The adhesion did not deteriorate in reducing atmospheres. Ceria was also observed to be relatively inert to YSZ when sintered at temperatures $\leq 1200^\circ\text{C}$, as evidenced by *HRTEM*.

Ceria-based catalysts have shown a poor activity toward CH_4 activation, at least with three studied dopants (Nb, Pr and Gd). The higher activity was reached with 15%CePrO followed by 20%CeGdO and 0.8%CeNbO. In 3% humidified CH_4 , CH_4 conversion was of 2.7, 1.3 and 0.4% at 850°C respectively. This poor activity was equivalent to the unsubstituted LaCrO_3 (1.7%). Interestingly, all three CeO_2 -based catalysts did not deposit carbon and seemed to resist much better to CH_4 cracking than LaCrO_3 -based catalysts. Globally, the activity of these oxides seemed to be higher the higher the electronic and ionic conductivity as in the case of Pr-doping. However, XPS measurements revealed a high surface segregation in the case of Nb- and Gd-doping which could affect the ionic conductivity. The use of CePrO is advantageous for its higher activity in CH_4 and its expected higher OCV. The overall reaction mechanism might be as well very similar to that over LaCrO_3 . However, CeO_2 presents some differences in that it has strong acid sites, deposits less carbon, and does not adsorb strongly CO_2 . Also, the high doping level in CeO_2 used in this study did not seem to enhance much the overall activity of this material when compared to LaCrO_3 . The addition of an extra catalyst seems thus needed. Catalysts such as Ni or Cu can be either impregnated over ceria, as studied here, or added as dopants.

Cermet compounds with metallic Ni, Ni-Cu, Cu and Ru were also studied in order to enhance the total activity of ceria. A major problem in processing CH_4 containing feeds over metal catalysts is extensive carbon deposition. The present study shows that for all these catalysts, even when supported on CeNbO, carbon was deposited. Impregnation of 1%Ni or Ru allowed an increase of the activity but at the same time the growth of filamentous carbon around the metallic particles, as evidenced by TEM, lifted the catalyst off the support leading eventually to plugging of the reactor. Cu alone resisted longer to CH_4 , as a long induction period was needed before carbon precipitation. Interestingly, alloying Ni with Cu allowed to temper the activity of Ni and limited the carbon formation. Thus the use of metal less liable to carbide formation and carbon dissolution might prevent carbon formation. A strong interaction with the support, reached by a high temperature treatment, was observed and found to be necessary for this improved performance. However, over a sufficiently long period the catalyst inevitably deposited carbon indicating the necessity to polarize such a material when used as anode.

CeO_2 anodes doped with Nb or Gd showed, as for the case of LaCrO_3 -based anodes, an ability to oxidize CH_4 directly without prior fuel processing (steam or carbon dioxide reforming or partial oxidation). These anodes were very resistant toward carbon deposition in very rich CH_4 fuels (97% CH_4 + 3% H_2O). However, CH_4 activation was observed to be low as the catalytic steam-reforming and direct oxidation modes were slow. The addition of a stable catalyst is required in order to activate CH_4 . Candidates are Cu or Cu-Ni alloy, or even another oxide catalyst such as Ni-substituted LaCrO_3 .

On the studied electrodes, inductive loops were observed along with a diffusion-like limitation, by impedance spectroscopy. Analysis of the data pointed to a mechanism where a hydrogen species is chemisorbed undergoing an electrochemical reaction (a so-called Gerischer impedance) and where the ceria lattice oxygen diffuses to the active sites to supply them with active oxygen species. In H_2 , the diffusion of oxide ions more than any other species (protons, electrons, surface or gaseous species) is thought to be responsible for the observed limiting currents. These results point out to the necessity of making porous ceria anodes and the addition of a catalyst that is able to promote the surface reaction kinetics involving most probably the chemisorption of H_2 or CH_4 . Trials were made with fine anode structures and with Cu catalyst and the promising results obtained support these interpretations (e.g. 200 mW/cm² in H_2 and 100 mW/cm² in CH_4 with Cu catalyst and 20% CeGdO electrolyte, measured in sealed conditions).

Furthermore, a direct influence of hydrogen on the electrochemical reaction of CH_4 showed that, at OCV conditions at least, the reaction was governed by H_2 - H_2O electrochemical equilibration. CH_4 oxidation was easily catalyzed by the presence of Pt-mesh current collectors or by the addition of a small percentage of Ni or Cu. In CH_4 , the I/V curves bent rapidly upon polarization indicating a limiting process, again most probably due to the lack of active O species but also possibly due to the low H species content stemming from the CH_4 reactions. As with LaCrO_3 -based anodes, the electrochemical oxidation of H_2 is faster than that of CH_4 . Kinetic data were presented in this study in a trial to better understand the electrochemical reaction in H_2 as well as in CH_4 . But, as in the case of LaCrO_3 , further analysis is needed

mainly by changing the electrochemical as well as the gas composition conditions. Labeled reactions could also be implemented.

These results and those presented for LaCrO_3 -based anodes show that optimizations are still possible. Poor catalysts for CH_4 oxidation can be modified in an appropriate manner to make them interesting candidates for direct CH_4 oxidation, knowing that the state-of-the-art Ni-cermet anodes cannot withstand, in their actual formulation, direct CH_4 feed without a prior fuel processing step. In H_2 a power density of 430-400 mW/cm^2 and a short circuit current of 1750 mA/cm^2 was observed at 850°C for Nb-doped ceria. In CH_4 , depending on the nature of the current collector, the performance varied between 420 mW/cm^2 (short circuit current of 1050 mA/cm^2) when Pt-meshes were used, and 100 mW/cm^2 (short circuit current of 420 mA/cm^2) with Au-electroplated Pt-meshes, at 900°C. Pr-doped ceria could be tested when implementing an adhesion layer as in the case of LaCrO_3 .

Globally, this study demonstrated that stable oxide-based anodes can be used instead of the conventional Ni-cermet anodes for H_2 oxidation. Oxide anodes based on LaCrO_3 and CeO_2 withstand also CH_4 rich feeds without excessive carbon formation on the contrary to the Ni-based anodes. However, these materials possess a rather low electrical conductivity (on the order of 1 S/cm in reducing conditions), necessitating the application of an extra material for proper current collection.

For a detailed analysis of the reaction mechanism over the LaCrO_3 and CeO_2 -based anodes, further measurements are needed. The analysis of the gas phase dependency at OCV as well as under polarization and eventually the determination of the transfer coefficients and their temperature dependencies would lead to a better comprehension of the reaction. Labeled reactions are also of interest. In the case of LaCrO_3 -based anodes, further variations on the B-site are to be considered for a better tuning of their electrochemical activity. The addition of a catalyst has also a practical interest. For CeO_2 -based anodes, Pr doping has to be considered, its application needing the use of an adhesion layer made of ceria and YSZ. The use of a Cu-Ni alloy is a mean to enhance the activity towards CH_4 and to lower the working temperature of the cell (< 800°C). For a practical use, these two oxide anodes have to be implemented with a current collecting layer made of a good metallic conducting oxide such as the Nb or Ti-based bronze-like materials. Cu could also serve for that purpose.

Acknowledgements

I would like to express my sincere thanks to the following people:

to Professor Michael Grätzel, for giving me the opportunity to make this thesis in his group, for the liberty he offered me in my research and for the interest he showed in my work;

to Dr. K. Ravindranathan Thampi for his unlimited willingness to help and listen, for having put at my disposal his gas chromatography installation, for having pushed me to write a paper, for having read a big part of my thesis, for his advice on many subjects and the many talks we had concerning scientific and most of all social matters; for his sympathy and tolerance and for having encouraged me to keep going;

to Dr. Jan Van herle, for the considerable time he generously spent reading my thesis and all my papers, bringing in many corrections, for all the discussions and advices, for having spent many hours to introduce me to many topics, for having organized part of the financial support through the Brite/Euram and NEDO funding, giving me the opportunity to take part in many discussions with many European colleagues, and for his constant availability and help;

to Dr. Augustin McEvoy, for helping me get a Japanese scholarship to the University of Tokyo which allowed me to broaden my thinking, offering me the opportunity to meet many interesting people, for having organized part of the financial support through the PPM funding and for having read part of my thesis;

to Professor Philippe Buffat, for the tremendous time he spent generously behind transmission electronic microscopes (*TEM*) hunting small changes of my catalysts, looking for carbon filaments and deposits, giving me a clear sight of the changes occurring on my catalysts, and most of all giving me a real push and more confidence in my work, for his research enthusiasm and sympathy;

to Dr. Pedro Möckli, for all the time he generously spent analyzing by *XRD* many powders of mine, for his constant availability, for all the discussions and for his help;

to Nikolas Xanthopoulos, for all the time he spent analyzing by *XPS-Auger* many powders of mine, for his joviality and humour;

to my colleague, Dr. Stefan Diethelm, for his humor and kindness, for his help and for all the interesting discussions we had;

to Brian Senior, for having trained me on the secondary electronic microscopy;

to Ms Danielle Laub, for having prepared some samples for *TEM* measurements;

to Dr. Marco Cantoni, for having performed some *HRTEM* measurements on ceria samples;

to Dr. Didier Leonard, for having performed some *SIMS* analysis on lanthanum chromite samples;

to Dr. Paul Bowen, for having introduced me to the powder size distribution analysis;

to Ruben Vasquez, my lab colleague for two years, for helping me in conductivity measurements;

to Dr. Hugh Middleton, for his advice and for the many discussions we had during his very short visits to our lab, for his sympathy and joviality and for having accepted to act as external expert;

to Dr. Mogens Mogensen for having accepted to act as external expert of my thesis, and for all the interesting discussions we had during all the Brite/Euram meetings;

to Professor Albert Renken, for having accepted to act as internal expert of my thesis;

to Dr. Harumi Yokokawa, for all the advice he gave me concerning the thermodynamic calculations;

to Dr. Layla Grahl-Madsen, for introducing me, in the frame of the Brite/Euram project, to the thermodynamic calculations using the HSC thermodynamic calculation program;

to many people in the Material Science Department in EPFL, Professor Hans Jörg Mathieu, Professor Mortensen, Dr. Alain Sfera, Raymond Oesch, for their help and for giving me access to their lab and instruments;

to my colleague Hami Öz, for having put at my disposal many lab instruments;

to Dr. Pierre Infelta, for helping me in many computer issues;

to my colleagues and friends, Dr. Dhananjeyan Rajaram Mugunthu, Richard Meir, Dr. Serge Rambert, Dr Pierre Infelta, Dr. Raphaël Ihringer, Laurent Constantin, Dilan Seneviratne;

to Alexandre Closset, Olivier Bücheli and Joseph Schweizer from HTCeramix, for their friendship and for their interest in my work;

to the mechanical workshop of the department, for their tremendous skills;

to the electronic workshop, especially Gabriel Roch, for having tried a year long to build a tubular oven, 'mille excuses';

to Alfred Neuenschwander, for his extreme quality glass blowing;

to Anita Shori, Catherine Vinckenbosch and many other for their help and compassion;

and last but not least, to my parents, my sister, and my late grand-mother, for their never-ending encouragement, support and confidence, 'Kopf Hoch', without which I would have never brought my thesis to an end;

and to Souad for her love, for being there, for her joviality and all the marvelous moments we spent together. You are always on my mind إن شئتُم أو ابيتم

List of publications

'LaCrO₃ based anodes for methane oxidation', J. Sfeir, J. Van Herle and A. J. McEvoy, in *Third European Solid Oxide Fuel Cell Forum*, P. Stevens ed., Nantes, France, **1998**, 2, 267-276.

'Stability of Calcium Substituted Lanthanum Chromites used as SOFC Anodes for Methane Oxidation', J. Sfeir, J. Van herle and A. J. McEvoy, in *Journal of the European Ceramic Society*, **1999**, 19, 897-902.

'Lanthanum Chromite Based Catalysts for Oxidation of Methane Directly on SOFC Anodes', J. Sfeir, P. A. Buffat, P. Möckli, N. Xanthopoulos, R. Vasquez, H. J. Mathieu, J. Van herle and K. R. Thampi, in *Journal of Catalysis*, **2001**, 202, 229-244.

'LaCrO₃-based anodes: stability considerations', J. Sfeir, in *Solid Oxide Fuel Cell Materials and Mechanisms*, Joint Topical Meeting, IEA-ESF, **2001**, 55-67.

'Improved Tubular SOFC for Quick Thermal Cycling', J. Van herle, J. Sfeir, R. Ihringer, N. M. Sammes, G. Tompsett, K. Kendall, K. Yamada, C. Wen, M. Ihara, T. Kawada, J. Mizusaki, in *Fouth European Solid Oxide Fuel Cell Forum*, A. J. McEvoy ed., Lucerne, Switzerland, **2000**, 1, 251-260.

Curriculum Vitae

Name: Joseph Sfeir
Birth date: 20 August 1971
Nationality: Swiss
Languages: French, English, Swiss-German, Arabic and some Japanese

Education

1998-2001: Ph.D. thesis with Professor M. Grätzel at the Swiss Federal Institute of Technology in Lausanne (EPFL), Switzerland, in the field of solid oxide fuel cells.

1996-1997: Exchange student at the University of Tokyo, Japan.

1995-1996: Industrial experience in the field of organic chemistry in Rohner AG, Pratteln, Switzerland.

1991-1995: Undergraduate studies in Chemical Engineering at EPFL.

Droits d'auteur attachés à la thèse

1. *Le rédacteur de la thèse est considéré comme auteur au sens de la législation sur le droit d'auteur. Sous réserve de l'alinéa 2, il détient tous les droits qui relèvent du droit d'auteur.*
2. *Pour faire connaître à d'autres les résultats des recherches consignés dans la thèse, l'EPFL peut remettre des versions abrégées ou des copies de la thèse à des établissements d'enseignement, à des instituts scientifiques ou à des bibliothèques ou d'autres administrations publiques.*

Art. 21 de l'Ordonnance sur le doctorat.